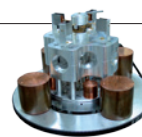


THIS WEEK

EDITORIALS

MEMOIRS The pleasure and pitfalls of a written scientific life **p.136**

WORLD VIEW Time to think the unthinkable on federal funds **p.137**



BIG-G What goes up must come down slightly faster **p.139**

Sequenced from the start

Four US studies are set to explore how genomic data can best help healthy and ill newborns. They must also settle some questions of ethics.

Genetic sequencing has established itself as a powerful tool for diagnosis, but it is not yet clear how useful it will be for disease prevention or health management. A US\$25-million project announced last week aims to explore that issue in perhaps the most high-stakes patient group: newborn babies.

In the Genomic Sequencing and Newborn Screening Disorders (GSNSD) programme, four teams will sequence the exomes — the protein-coding portions of the genome — or the whole genomes of more than 1,500 babies, including not only infants who are ill, whether or not the disease has been diagnosed, but also healthy babies. The programme is funded by the US National Human Genome Research Institute and the Eunice Shriver Kennedy National Institute of Child Health and Human Development (NICHD). The studies will examine how useful sequencing information is for families and doctors, and whether it is superior to data gathered through conventional newborn-screening methods, which check for about 60 genetic disorders.

The project joins a short but growing list of studies testing the utility of clinical sequencing in otherwise healthy individuals, but it is the first to focus on healthy and ill babies. As such, it will highlight five hot questions.

First, do we yet know enough about how genes code for health to make genomic data useful in preventing disease? Studies have found that sequencing can diagnose 15–50% of children with otherwise undiagnosable illnesses, but no one has yet asked what use it has for healthy children. Not all genetic traits will influence a person's health, and it is still not possible to say with any certainty what a given genetic variant will mean for a given individual.

Second, what kind of genetic findings should doctors return to patients, and does the answer differ between children and adults, or between ill and healthy people? The family that is unsure whether its ill baby will live or die is not in a good position to absorb information about a hypothetical future cancer risk. The family that has a baby's genome sequenced just to see what might be found may spend years worrying about that cancer risk in their perfectly healthy child. The key will be to find the children who will best benefit from this knowledge, because their individual disease risks are real enough that routine screening could save their lives. In the US health-care system, which is prone to over-diagnosis and over-treatment of cancer, for example, this is a tricky balance. Some of the GSNSD projects will check babies' genomes for genes not linked to any immediate illness, although each study is taking a different approach to how it will inform parents about risks.

Third, what is the quickest and cheapest way to conduct clinical sequencing so that it returns accurate information to patients in time to influence care decisions? Increasing the number of conditions being screened for will necessarily cause more false positives — as many as 20 for every true positive, according to one estimate. Those false positives will lead to increased medical costs and anxiety for families.

Fourth, who owns the genetic data? None of the GSNSD studies

plans to give the raw genetic data to the children's families, even though that could allow the children to benefit from it throughout their lives.

Finally, should the data be shared with other researchers? This would be the best way for scientists to help tackle the tough question of how genes contribute to disease. But it is increasingly difficult to guarantee the privacy of genetic data (see *Nature* **493**, 451; 2013), and this is an

"The day when all children will be sequenced at birth — if not before — draws ever nearer."

important issue for babies, whose information will be known for their entire lives even though they themselves have not consented to the disclosure. One of the GSNSD projects will share data with the NICHD's Newborn Screening Translational Research Network, and another with the National Center for Biotechnology Information's Database of Genotypes and Phenotypes. The other two are still deciding.

As researchers explore these questions, sequencing costs continue to drop and the day when all children will be sequenced at birth — if not before — draws ever nearer. Some people are wary of this, and are already warning of the dangers of what they consider to be a government-funded plan to store all citizens' data. If newborn sequencing is to fulfil its potential to save many children's lives, it is imperative that scientists get the ethics and the science right. ■

Under threat

The grey wolf is at risk of losing its endangered status under US law.

In the mid-1990s in the United States, several courts were asked to decide whether wolves were illegal immigrants. Ranching groups that were against the proposed reintroduction of the wild animals to Idaho, Wyoming and Montana were trying to block their transport across the border from Canada. The appeal failed and the foreign wolves were delivered and released.

In recent decades, many more in the legal profession have become familiar with *Canis lupus*. The grey wolf, and its place in the US landscape, sharply divides opinion — both scientific and political. Broadly speaking, conservationists want the wolf population to expand into its historical range, whereas the ranching community is anxious about large numbers of a top predator roaming free. Both sides can point to scientific research and ecological opinion to support their stance.

The battle over the fate of the grey wolf is gearing up for a new conflict, perhaps the most significant yet. As we report on page 143, the US Fish and Wildlife Service (FWS) has extended the period for which

it will allow public comment on its controversial proposal to strip the grey wolf of its federal protection. The agency wants to remove the animal from the list of those protected under the 1973 Endangered Species Act, and to hand responsibility for its management and conservation to individual states. The FWS claims that the move follows the “successful recovery” of the wolf in two key regions. Scratch the surface, though, and it looks more like a cost-cutting exercise and, to some, a politically convenient one. Gary Frazer, assistant director for endangered species at the FWS, told *Nature* that he expects hundreds of thousands of people to comment.

Many of these will be rightly suspicious of the true motives. The proposed delisting of the grey wolf comes barely two years after the notorious ‘wolf rider’ that saw a clause to remove legal protection of the animals in Montana and Idaho tagged by local politicians to an unrelated, and essential, budget appropriations bill. The move, this journal noted at the time, set a “dangerous precedent” (see *Nature* 475, 5; 2011), and was the first time that Congress had removed a species from the list. The clumsy political manoeuvre came after a decade of court-rebuffed attempts to change the status of the wolf through the proper regulatory channels.

Grey wolves are certainly doing better in the United States than a century or so ago, when rewards for their killing made them locally extinct. Controlled reintroduction under the 1973 act has led to populations in the thousands around the Great Lakes and Northern Rockies — and to the loss of livestock. According to the US Department of Agriculture, between 1995 and 2007, wolves killed 298 cattle, 46 sheep, 13 llamas, 24 goats and 7 horses in Montana. Enough is enough, critics say; the grey wolf is no longer endangered. Yet the 1973 act is clear: such a judgement must be made over all, or a significant proportion, of the animal’s range.

“We still haven’t figured out how to handle a situation where experts have outspoken views,” Frazer says of the divergent opinions on the

topic. It is a lament that will strike a chord with many policy-makers, not least those in Britain, where government-sanctioned marksmen are busy reducing the population of another emblematic — and previously protected — species. After years of similar arguments and conflicting scientific advice, the environment department DEFRA has embarked on two pilot culls of badgers, which farmers blame for the spread of bovine tuberculosis (TB).

Ian Boyd, science adviser to DEFRA, writes on page 159 that, too often, the evidence used to set policy is biased and unreliable, even when published in scientific journals. He wants to introduce a Kitemark (indicator of quality approval) for studies that meet an audited standard of scientific evidence. But he should be careful what he wishes for. As *Nature* has repeatedly pointed out, the published evidence on badger culls does not indicate that bovine TB will be reduced by DEFRA’s strategy, which relies on untested tactics such as free shooting.

Politics can trump science, of course, for politicians are elected to make decisions. But so can sentiment. A few miles along the M4 motorway from where the badger culls and the protests against them are under way is the base of the Wolf Conservation Trust. Wolves vanished from Britain centuries ago, but they retain mystique and appeal — even to Brits. US lawmakers must bear this in mind as they invoke science to argue for the delisting of the grey wolf.

The protection of the 1973 Endangered Species Act for vulnerable animals does not end at the US border. Several overseas and foreign species are listed too, and US citizens are forbidden from, for instance, trading in them. But a US law that gives sanctuary to the Chinese alligator and the great Indian bustard but not to the native grey wolf would be a strange beast indeed. ■

“Enough is enough, critics say; the grey wolf is no longer endangered.”

Reality at risk

Don’t treat a memoir as anything other than one person’s interpretation of events.

“It was the afternoon of my eighty-first birthday and I was in bed with my catamite when Ali announced that the archbishop had come to see me.” So runs the first sentence of *Earthly Powers*, Anthony Burgess’s memoir of the fictional novelist Kenneth Toomey. “I have lost none of my old cunning in the contrivance of what is known as an arresting opening,” he writes a few lines later — noting that, whereas every supposed fact in the first sentence is true, the context is one of pure artifice, designed to portray an image of the writer as he would wish to be seen, not necessarily as he really is. Toomey is clearly a writer of some skill (as is Burgess, his inventor and rapporteur), so we, the poor readers, are at his mercy. We can do no other than take what he claims as truth at face value, whether it is true or not. Such is the *caveat emptor* of the memoir in general.

This week, *Nature* publishes book reviews of two memoirs by very real people. On page 162, Robert Crease reviews *My Brief History* by theoretical physicist Stephen Hawking, and notes that it is more akin to a PR exercise than a warts-and-all confession: “It does not take the reader behind any scenes... It is a concise, gleaming portrait, not unlike those issued by the public relations department of an institution.” Eugenie Scott on page 163, by contrast, finds *An Appetite for Wonder*, the first volume of memoirs by evolutionary biologist Richard Dawkins, “a very honest book”, in which we get a taste of the upbringing and early experiences of the author of *The Selfish Gene* and *The God Delusion*. From which we are entitled to get a flavour, at least, of how Dawkins got to be the man he is today — in other words, what makes him tick.

But do we? Get a flavour of what makes someone tick from their own, self-selected, self-redacted reminiscence? Memoirs are more vehicles of entertainment than any reflection of reality. When one reads *The Double Helix*, James Watson’s knockabout account of the discovery of the structure of DNA, one should take any facts presented therein strictly as having been heavily filtered by the unashamedly biased reminiscence of just one of the protagonists, not as a scholarly account. And there’s nothing wrong with that. *The Double Helix* works beautifully as entertainment.

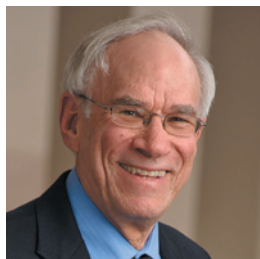
There is another layer of selection. Those memoirs that get published as books are not so much about scientists (say) as celebrities. Readers of *My Brief History* will want to know about Hawking’s triumph over his disability more than how he came to this or that conclusion about black holes. More people are likely to have encountered Dawkins as the doctrinaire neo-atheist of *The God Delusion* than as the peerless commentator on the machinery of evolution in *The Selfish Gene* — and vastly more than as the author of scientific papers on animal behaviour.

To understand what working scientists free from the constraints of celebrity actually do all day, one might turn to the blogosphere and follow (to mention just two of thousands) Jenny Rohn’s ‘Mind the gap’ (<http://occamstypewriter.org/mindthegap>) and, perhaps more pertinently, the notes of the anonymously eponymous Female Science Professor (<http://science-professor.blogspot.co.uk>).

Even then, such writings demonstrate the self-selection of those scientists (a tiny proportion) who feel that they have something to say. For everyone else, life is something that is lived undocumented, unshared and in real time. Perhaps the only really ‘true’ experiences are those that one has lived oneself. To which one can

➔ **NATURE.COM**
To comment online,
click on Editorials at:
go.nature.com/xhunq

only ask whether one is talking to oneself, or whether the Universe has gone solipsistic all of a sudden. Then again, to quote that koan from Jewish Buddhist wisdom — if there is no self, whose arthritis is this? ■



It is time to update US biomedical funding

The effects of federal budget cuts provide an opportunity to revisit the funding structure of the National Institutes of Health, says Frederick Grinnell.

As the 30 September deadline looms for US lawmakers to complete budget appropriations for the fiscal year 2014 with no realistic prospect of success, drastic cuts to public spending on science seem likely to continue. The effect has been severe: many grant-renewal applications at the US National Institutes of Health (NIH), which were easily fundable a few years ago, are not even close to being funded this year. Things are tough, as reflected by an outpouring of comment and opinion in the media about the potential decline of US science.

We have been here before. Around 1970, US spending on science was cut to help pay for the Vietnam War. Faculty positions were scarce and winning a research grant became much more difficult. But the research community survived and thrived. I believe that we will survive the current cuts, but because of their depth and arbitrary nature, their effects will take years to overcome.

We should take this opportunity to examine and debate the NIH funding structure for biomedical research, and focus on how it could be made stronger, more resilient and more diverse in the future. To begin, here are four suggestions.

First, we should revisit the relationship between how NIH grants are assessed and funded. Grant applications are evaluated on a relative scale, but are funded in absolute terms: all or nothing. This is illogical. Applications that fall on either side of the funding cut-off, or payroll, are more or less of equal quality. As overall success rates decline, this practice becomes more difficult to justify. A better approach would be to link funding levels with the percentile scores used to rank applications. NIH institutes should agree on the total number of grants to be funded, then give full funding to applications with the best scores and partial funding to those with slightly lower scores.

If the total available funds declined, then the curve of percentage funding versus percentile score would become steeper — perhaps down to 50% of the approved budget for grants with percentile scores just within the payroll. If funds increased, then the curve would flatten out. In times of severe budget constraint, this would allow more laboratories to stay open — albeit on a smaller scale — preserving research infrastructure and lab continuity. Many will argue that this would produce labs that are unable to achieve their proposed specific aims, but investigators could always drop an aim.

Second, we should look closer at research productivity and the size of grants. Some data on the scientific output of researchers funded by the US National Institute of General Medical Sciences (NIGMS) suggest that productivity (measured by number of publications or average journal impact factor) peaks when principal investigators have annual funding levels of roughly US\$750,000. When the productivity metrics were normalized to grant

dollars, however, smaller labs were more productive per dollar.

The NIGMS findings are preliminary. Moreover, some types of research are much more expensive than others. However, if NIH scientific-review groups evaluating grant-renewal applications paid more attention to normalized rather than total productivity, then principal investigators with smaller labs might become more competitive for funding, resulting in a wider distribution of research dollars.

At present, when a scientist wins an NIH grant, a percentage of the funding is often used for his or her salary. In my view, that percentage is too high when faculty members are asked by their institutions to raise most or all of their own salaries through grant awards. Doing so creates both potential conflicts of commitment and challenges to research integrity. Faculty members with NIH funding bring benefits

beyond the successful completion of research projects. They boost student education and the development of intellectual property and technology transfer. My third suggestion is that universities should chip in more to pay these academics, freeing up federal money for the research itself.

My final suggestion is to consider the broader impact of research grants. As pressure on public funds intensifies, scientists are increasingly being asked to articulate the economic benefits of their discoveries. Yet the economic impact of biomedical research goes

beyond its ability to improve human health. It includes education of the scientific workforce, expansion of institutional and community resources, and development of regional technology centres.

Funding for academic research and technology development tends to be concentrated in a relatively small number of institutions. If 'scientific merit' remains the singular basis for decision-making on grants, then historically underfunded institutions are at a disadvantage — and the wider economic benefits cannot be shared. Yet incremental increases in funding would have a bigger relative impact for such institutions than for those already receiving the most research dollars. Perhaps grant applications from underfunded institutions should be funded at a different payroll. That would be controversial but there is precedent: the NIH has already modified the payroll to increase funding for new investigators, another underfunded group.

These are important points to debate, and some will be unpopular. The last consultation effort with the broad US biomedical community was in 1992, when I and many others served on the NIH Strategic Plan Task Force. That failed because the process was too top-down. We should try again. ■

Frederick Grinnell is in the Department of Cell Biology at the University of Texas Southwestern Medical Center in Dallas. e-mail: frederick.grinnell@utsouthwestern.edu

THE NIH FUNDING
STRUCTURE COULD BE
STRONGER,
MORE RESILIENT AND
MORE DIVERSE.

➔ **NATURE.COM**
Discuss this article
online at:
go.nature.com/xx9uw3

RESEARCH HIGHLIGHTS

Selections from the
scientific literature

CHEMISTRY

Power from deep-sea vents

Researchers have harnessed deep-sea hydrothermal vents to produce electricity.

Masahiro Yamamoto of the Japan Agency for Marine-Earth Science and Technology in Yokosuka and Ryuhei Nakamura of the RIKEN Center for Sustainable Resource Science in Wako and their team exploited the differences in chemistry between sea water and fluids that leak from hydrothermal vents. Steep concentration gradients of chemicals such as hydrogen sulphide allowed the researchers to generate more than 21 milliwatts of power from a fuel cell based on a platinum cathode and an iridium anode.

This successfully powered three light-emitting diodes 1,000 metres below the surface, both at an artificial vent created by deep-sea drilling and a natural vent. *Angew. Chem.* <http://doi.org/f2dtrm> (2013)

GEOLOGY

Meet the world's largest volcano

A submarine mountain in the northwest Pacific could be the largest single volcano on Earth, rivalling even the mighty Olympic Mons on Mars.

Tamu Massif, situated 1,500 kilometres east of Japan, is roughly the size of the British Isles. Seismic-profiling studies penetrated its depths and revealed that its lava flows dip away from the volcano's summit in all directions. This suggests that all the lava came from a single eruptive vent, say William Sager of the University of Houston in



ANIMAL BEHAVIOUR

Clumping caterpillars

Entomologists sometimes see caterpillars clumping together, but the reason for this behaviour has defied explanation.

Researchers had proposed that the aggregations conserved water or energy, but John Terblanche of Stellenbosch University in South Africa and his colleagues have dispatched those ideas. They collected Cape Lappet moth caterpillars (*Eutricha capensis*) and reared them as individuals and in groups of up to 100. Metabolic rates and water use did not decrease with group size.

Given that aggregating caterpillars did not conserve energy, the researchers suggest that the behaviour may confer other advantages, such as faster growth rates or safety in numbers. *J. Exp. Biol.* <http://doi.org/npp> (2013)

Texas and his colleagues.

The dome-shaped mountain probably formed in a single eruptive blast that began some 140 million years ago.

Nature Geosci. <http://doi.org/nqd> (2013)

For a longer story on this research, see go.nature.com/beeqp4

ECOLOGY

US forests grow to be different

Trees have made a major comeback in the northeastern United States, but the regrown forest is in some

ways markedly different from that of 400 years ago, when European colonists started clearing trees for agriculture.

Jonathan Thompson of the Smithsonian Conservation Biology Institute in Front Royal, Virginia, and his colleagues examined land-survey records from 1620 to 1825 in nine northeastern states. Colonial surveyors often divided up plots of land using 'witness trees' to mark the corners, generally noting the genus, so the authors were able to compare these data with modern forest inventories.

Although most of the same tree species were present in both time periods (with the exception of the now-rare American chestnut, *Castanea dentata*), their relative abundances differ greatly. Colonists removed a forest dominated by species such as beech and hemlock conifers, but today's trees form a canopy of mostly maple and birch.

PLoS ONE 8, e72540 (2013)

TECHNOLOGY

A cheaper, quieter MRI machine

Magnetic resonance imaging (MRI) is expensive, noisy and requires bulky equipment. It can also have side effects, such as stimulating nerves in patients. These problems arise from the constant switching between positive and negative magnetic-field gradients used to manipulate the spin of hydrogen nuclei throughout the patient's body. The energized nuclei produce radiofrequency signals, which carry the information used to build up an image.

By exploiting the radiofrequency pulses used to prepare the nuclei, Jonathan Sharp at Alberta Innovates Technology Futures in Calgary, Canada, and his

HENNO GOUS

colleagues removed the need for switched magnetic fields. Instead, they manipulated the nuclei using pairs of resonant radiofrequency fields twisted in opposing directions and a static magnetic field. The technique could make MRI cheaper, accessible and quieter. *NMR Biomed.* <http://doi.org/nqf> (2013)

LANGUAGE

Babies hear a primate's call

Babies listen to lemur vocalizations in the same way that they listen to human speech.

A baby's language skills develop rapidly during the first year, and previous research has shown that by three months, hearing human speech while viewing objects helps infants to group objects into categories. Alissa Ferry at the International School for Advanced Studies in Trieste, Italy, and her colleagues examined how recordings of calls from a lemur (*Eulemur macaco flavifrons*; pictured) influenced how infants performed when they were asked to discriminate between images of dinosaurs and fish.

The team found that lemur calls helped three- to four-month-old infants to categorize objects but did not help six-month-olds. The study suggests that the link between language and the capacity to categorize objects is initially broad enough to include calls from non-human primates, but quickly becomes tuned to human language. *Proc. Natl Acad. Sci. USA* <http://doi.org/nqx> (2013)



TERRY QUINN

EDWIN GIESBERS/NATURE PICTURE LIBRARY

SYNTHETIC BIOLOGY

Forcing fluorine into molecules

Researchers have discovered a pathway for introducing fluorine atoms into naturally occurring molecules.

Fluorine is present in up to 30% of pharmaceuticals and can expand the usefulness of natural products by, for example, increasing the time they take to break down in the body. But until now, chemists have been using a single method — the fluoroacetate pathway — to insert fluorine into organic molecules.

Michelle Chang of the University of California, Berkeley, and her colleagues have found a different way to insert atoms of the element into a useful group of molecules called polyketides. Their method enlists a soil bacterium (*Streptomyces cattleya*) for the first steps. The bacterium binds fluorine to carbon, making building blocks such as fluoroacetate monomers that can then be inserted into polyketides in the place of acetate.

The team demonstrated the method in the laboratory and in living cells, in which they were able to control where the fluorine atoms ended up in the polyketide molecules. *Science* 341, 1089–1094 (2013)

PHYSICS

A startling value for gravitation

The quest to pin down the fundamental constants of nature usually results in increased precision over time, but knowledge of the Newtonian constant of gravitation (G), known among physicists as Big G , has not improved much in recent years because different measurement methods continue to disagree.

Now, Terry Quinn and his colleagues at the International

COMMUNITY CHOICE

The most viewed papers in science

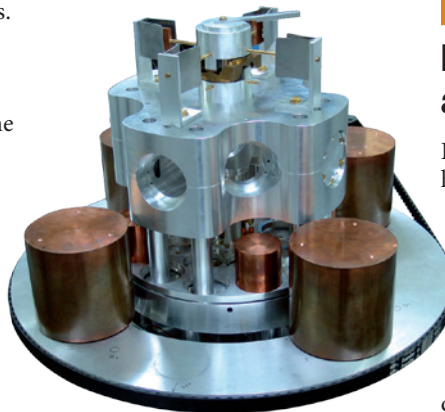
CELL BIOLOGY

Nuclear receptor linked to fitness

HIGHLY READ
on nature.com/nm
8 Aug–4 Sept

Would-be dopers may have a new target: the Rev-erb- α protein. Known to regulate sugar and fat metabolism, the nuclear receptor has now been linked to the production and function of mitochondria — the cell's metabolic powerhouses.

A team led by Bart Staels and Hélène Duez, jointly at the Lille II University of Health and Law and the Pasteur Institute in Lille, France, showed that mouse muscle cells lacking Rev-erb- α contain dysfunctional mitochondria, and that mice lacking the gene encoding it, *Nr1d1*, could not run as fast as normal mice. The reverse occurred when the protein was overexpressed or when a synthetic agonist was given, suggesting that Rev-erb- α could be targeted by drugs to improve exercise capacity by boosting mitochondrial number and function in muscle cells. *Nature Med.* 19, 1039–1046 (2013)



Bureau of Weights and Measures in Paris have added to the uncertainty by finding a value for G of $6.67545 \times 10^{-11} \text{ m}^3 \text{ kg}^{-1} \text{ s}^{-2}$. This is significantly larger than several other measurements from the past decade, but is in agreement with a 2001 result by the same group using a similar but independent experimental set-up.

The researchers used a torsion balance (pictured), in which a thin metal strip changes orientation in response to test masses. The authors say that they do not know why their apparatus gives a different result from other approaches. *Phys. Rev. Lett.* 111, 101102 (2013)

PRIMATE COGNITION

Monkeys raise the alarm on predators

For the first time, researchers have shown that non-human primates emit calls in specific sequences to convey the type and location of the threat.

Non-human primates are known to produce calls that signal different kinds of danger. Richard W. Byrne at the University of St Andrews, UK, and his colleagues conducted an experiment on five groups of titi monkeys (*Callicebus nigrifrons*) living in a reserve to find out whether monkey vocalization encoded predator type (raptor or snake), elevation (tree or ground) or both.

A raptor in the air elicited only calls of type A; a raptor on the ground, calls of type A, followed by B. Conversely, a predator on the ground elicited pure B calls, but a ground predator in the trees brought forth B calls, followed by A. *Biol. Lett.* 9, 20130535 (2013)

NATURE.COM

For the latest research published by Nature visit:

www.nature.com/latestresearch

SEVEN DAYS

The news in brief

RESEARCH

Dark-energy survey

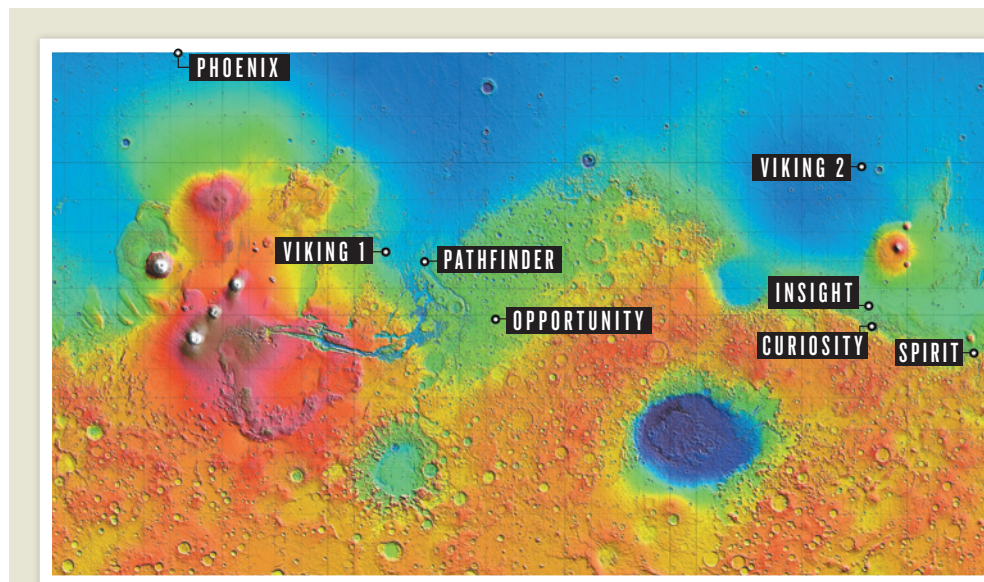
A massive sky-mapping project to study dark energy has begun, announced by Fermilab in Batavia, Illinois, on 3 September. The Dark Energy Survey at the Cerro Tololo Inter-American Observatory in Chile launched on 31 August. Over the next five years, it will map 300 million galaxies covering one-eighth of the night sky. Data from its 570-megapixel camera may lead to a better understanding of the mysterious dark energy that is thought to drive the Universe's accelerating expansion. See go.nature.com/ybcueb for more.

Baby-genome plan

Hundreds of babies in the United States will have their genomes sequenced as part of a US\$25-million programme unveiled on 4 September by the US National Institute of Child Health and Human Development and the National Human Genome Research Institute. The agencies have chosen four research teams, which will receive grants over the next five years, to test whether sequencing can provide more information than conventional tests that screen newborns for genetic and other disorders. See page 135 and go.nature.com/izz7u9 for more.

High-tech probe

Making better devices for measuring brain activity in animals is the goal of a US\$5.5-million collaboration announced on 4 September. Partners include the Howard Hughes Medical Institute in Chevy Chase, Maryland; the Allen Institute for Brain Science in Seattle, Washington; and the nanoelectronics-research company imec in Leuven, Belgium. The project, which also involves



JPL-CALTECH/NASA

NASA homes in on next Mars landing site

The next US Mars lander will touch down on one of four candidate sites announced by NASA on 4 September. The lander, dubbed Interior Exploration Using Seismic Investigations, Geodesy and Heat Transport (InSight), is set to launch in March 2016 and will study the planet's deep interior to help researchers to understand how rocky planets formed. There were 22

candidate sites; the semi-finalists were chosen for their level and smooth terrain. The sites are all on an equatorial plain in an area called Elysium Planitia, close to where other landers have set up home (pictured). InSight will drill 2–5 metres into the Martian surface, so scientists wanted sites that would not harbour large rocks or solid bedrock that could block the probe.

University College London and UK biomedical charity the Wellcome Trust, aims to pack more electrodes than ever onto brain probes that record signals between neurons. The group hopes to make the devices available for sale by the end of 2016.

but they are powerful greenhouse gases. Parties to the protocol will debate amending the treaty to implement a global phase-down of HFCs at a meeting in October in Bangkok.

Carbon-tax repeal

The newly elected prime minister of Australia, Tony Abbott, has committed to scrapping the previous government's plans to put a price on carbon emissions. He vowed as part of his campaign to repeal the carbon tax, which outgoing Prime Minister Kevin Rudd had already promised to soften to a carbon-trading scheme. Abbott, who beat Rudd in national elections on 7 September, said that it

would be "a very early item of business". But Abbott may face a fight to push the repeal through parliament.

FACILITIES

Spanish clash

Plans to build a particle accelerator and neutron source in Bilbao, Spain, have come to an abrupt halt. The governing board of the €180-million (US\$238-million) European Spallation Source-Bilbao (ESS-Bilbao) announced on 29 August that the project's scientific director had been removed, and that the executive director's contract would not be renewed. The board cited a need to analyse and refocus the initiative. ESS-Bilbao, which has encountered budget

POLICY

Gas phase-down

Leaders of the Group of 20 (G20), representing the world's largest economies, agreed on 6 September to regulate hydrofluorocarbons (HFCs) under the Montreal Protocol on Substances that Deplete the Ozone Layer. Primarily used as refrigerants, HFCs were developed as alternatives to ozone-depleting chemicals,

shortfalls, was launched in 2009 as a test-bed for a larger facility planned for Lund, Sweden.

PEOPLE

Libel suit tossed

On 4 September, the Taipei District Court in Taiwan dismissed a criminal libel suit against environmental engineer Ben-Jei Tsuang of National Chung Hsing University in Taichung. The petrochemical company Formosa Plastics Group (FPG) in Taipei had sued Tsuang for US\$1.3 million in damages for suggesting that its emissions were linked to an increased risk of cancer. Tsuang presented his results at a scientific meeting in 2010 and a press conference in 2011, and has since submitted a paper on the topic. A civil lawsuit against Tsuang by FPG is still pending. See go.nature.com/ukmxye for more.

AWARDS

Balzan prizes

Pascale Cossart (**pictured**), a microbiologist at the Pasteur Institute in Paris, has been awarded one of four 750,000-Swiss-franc (US\$800,000) Balzan prizes for her work on the molecular biology of pathogenic bacteria and their interaction with host cells. Physicist Alain Aspect of the École Polytechnique in Palaiseau, France, won



another of the prizes for his contributions to quantum information processing.

Lasker award

Richard Scheller of Genentech in South San Francisco, California, and Thomas Südhof of Stanford University in California have won this year's US\$250,000 Lasker Award for Basic Medical Research for their work on the molecular mechanisms that underlie the rapid release of neurotransmitters in the brain. Winners of the award, which this year was announced on 9 September, often go on to get a Nobel prize. See go.nature.com/ubuzgy for more.

Ocean contest

The X Prize Foundation is offering US\$2 million in a competition, sponsored by US philanthropist Wendy Schmidt, to improve ocean pH monitors, it announced on 9 September. Researchers can compete for one or both of

two \$1-million prize pots — one for the most accurate and another for the most cost-effective sensor. Subtle changes in ocean acidity can have marked effects on marine life, but existing sensors do not work well at depth or over long periods of time, and are too expensive to deploy widely. See go.nature.com/ttlysw for more.

EVENTS

Lunar orbiter up

On 6 September, NASA launched the Lunar Atmosphere and Dust Environment Explorer (LADEE) from Wallops Flight Facility in Virginia. The orbiter should arrive at the Moon in about 30 days, and will fly 20–50 kilometres above the surface. LADEE will collect dust and gas molecules in the lunar atmosphere, searching for silicon, magnesium and other elements ejected from Moon rocks. Researchers hope that data from LADEE could help to explain the twilight glow above the Moon's horizon seen by missions in the 1960s. See go.nature.com/j2tzmh for more.

Labour row ends

The Atacama Large Millimeter/submillimeter Array (ALMA) observatory restarted operations in Chile on 9 September, after a labour strike shut down the

COMING UP

16–21 SEPTEMBER

The Seventh International Congress on Advanced Electromagnetic Materials in Microwaves and Optics takes place in Bordeaux, France, where scientists will share the latest results in metamaterials research. Topics will include advances in cloaking, and medical applications of metamaterials.

go.nature.com/yqmli6

centre for 17 days. Contract negotiations had broken down between the union that represents most of ALMA's Chilean staff and Associated Universities Incorporated, based in Washington DC, which employs the workers (see go.nature.com/vhxfrv). The two-year contract signed on 7 September includes shorter working shifts, a 4% pay rise for union workers at the low end of the wage scale, and a bonus for workers at the highest-elevation ALMA site.

BUSINESS

Drug resurrected

On 4 September, AstraZeneca launched clinical studies of a previously abandoned experimental ovarian-cancer drug. Researchers had hoped that olaparib would herald a new class of drug targeting a DNA-repair protein called PARP, but the London-based pharmaceutical firm halted the drug's development in 2011 after a failed clinical trial (see *Nature* **483**, 519; 2012). Further analysis suggested that olaparib may work best against cancers bearing mutations that affect other DNA-repair proteins, leading the company to launch the latest trial in patients with BRCA-mutant cancers.

► **NATURE.COM**

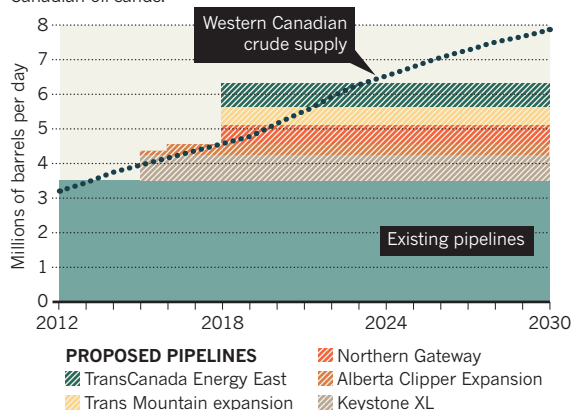
For daily news updates see:
www.nature.com/news

TREND WATCH

With existing oil pipelines at near full capacity, increased production in the oil sands of Alberta, Canada, will depend on new projects such as the controversial Keystone XL, says a report from the Sierra Club in San Francisco, California. The environmental group argues that halting Keystone — expected to carry about 730,000 barrels of oil per day from 2015 — would prevent an increase in greenhouse-gas emissions by impeding further development of carbon-rich oil in the region.

OIL SAND EXPORTS

Companies need new pipelines to sustain production from Canadian oil sands.



NEWS IN FOCUS



UK POLICY Plan to offload labs vexes environmental scientists **p.145**

ENERGY Chemical databases pave the way for 'greener' fracking fluids **p.146**

FUNDING More cuts loom for US science as sequestration drags on ... and on **p.147**

TAXONOMY On the trail of the spy who chased lizards and frogs **p.150**

LYNN M. STONE/NATURE PICTURE LIBRARY



The grey wolf, protected for more than 30 years, could see its endangered status removed nationwide.

CONSERVATION

Grey wolves left out in the cold

US plan to remove federal protection elicits howls of protest.

BY CHRIS WOOLSTON

Central Kentucky is coyote country. But the 33-kilogram animal shot by a hunter near Munfordville this spring was definitely not a coyote. Its huge paws, broad snout and massive build suggested that it was a grey wolf (*Canis lupus*) — the first to be shot in Kentucky in more than 150 years. DNA tests confirmed the animal's identity in August.

The animal, a possible stray from hundreds of kilometres away in Michigan or Minnesota (although it cannot be ruled out that it was

once captive), was also a player in a growing debate that mixes science, politics and passionate public opinion. From Kentucky to California, wolves are forcing biologists and policy-makers to re-examine the US Endangered Species Act (ESA) and the very definition of an 'endangered' species.

The act, introduced in 1973, was a landmark piece of legislation. Its purpose has been contentious ever since, but it is intended to save

NATURE.COM
Why the US wildlife service wants to list a new wolf species:
go.nature.com/7nujx9

species "in danger of extinction throughout all or a significant portion" of their range. Although wolves have never been at risk of extinction in the United States as a whole, those in the 48 contiguous states were classified as endangered in 1978.

After decades of federal protection and reintroduction programmes, the US Fish and Wildlife Service (FWS) undertook a comprehensive review, which found that wolf populations near the western Great Lakes and the northern Rocky Mountains had recovered sufficiently to warrant removing ESA protection (see 'Wolf pack'). (There are now about 4,000 wolves in the Great Lakes area and nearly 1,700 in the northern Rockies.) Wolves in these areas were 'delisted' between May 2011 and August 2012.

But in June this year, the FWS proposed removing ESA protection from all US grey wolves, citing the earlier review as evidence of their recovery and arguing that the original listing had erroneously included regions outside the species' historical range. The agency says that by delisting the rest of the US wolf population, it can concentrate its resources on ESA protection for the Mexican wolf (*Canis lupus baileyi*), a subspecies of the grey wolf.

The proposal marks a turning point for the grey wolf. A century ago, the animals had been hunted almost out of existence south of the United States–Canada border. Now, as a result of the partial delisting, six states have wolf-hunting seasons. In Montana, 225 wolves were legally trapped or shot in the 2012–13 season.

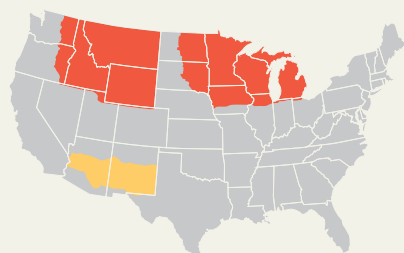
Grey wolves removed from the ESA programme would be managed by states, some of which have in the past shown little interest in protecting wolves or expanding their territory. Delisting the wolves would essentially prevent them from reclaiming large parts of their historic range in places such as California, the southern Rockies and the northeast, says John Vucetich, a forest scientist at Michigan Technological University in Houghton. And, as the appearance of the wolf in Kentucky suggests, pushing boundaries is a wolf speciality.

"The Fish and Wildlife Service is essentially saying that this is the best that wolves can do, and it's not even close," he says. "Wolves are on the verge of setting a precedent for the Endangered Species Act."

Robert Wayne, an ecologist and evolutionary biologist at the University of California, Los Angeles, says that wolves need broad ranges and large populations to return to their historic

WOLF PACK

By October 2012, grey wolf populations in six US states had recovered such that they no longer needed protecting by the Endangered Species Act.



■ Not protected ■ Endangered
■ Experimental population

► levels of gene flow and diversity. In 2005, he and his colleagues analysed mitochondrial DNA from specimens collected before wolves were decimated in the 1900s, and found that it contained twice as many variations as DNA from modern wolves (J. A. Leonard *et al. Mol. Ecol.* **14**, 9–17; 2005). The researchers estimated that the wolf populations in Mexico and the western United States had once reached 380,000 individuals. “Wolves have not recovered over a large part of their range,” Wayne says.

But Gary Frazer, assistant director for endangered species at the FWS in Arlington, Virginia, says that the service exceeded its own minimum targets for wolf recovery as early as 2001, and thus it is a case of mission accomplished. “That was the plan from the beginning: to declare recovery, to delist the species, and to move on to other species that need our attention,” he says, noting that the agency’s resources are limited.

Wolves might occupy only a fraction of their historic range, but they are not in danger of extinction, adds Mark Boyce, a biologist at the University of Alberta in Edmonton, Canada. “We have 6,000 wolves in Alberta alone,” he says. “Except for Mexican wolves, the populations in the lower 48 states add nothing to the genetic diversity of the species.” Boyce believes that any expansion of the wolves’ range would be costly for ranchers. In 2011, he co-authored a study that tracked wolves using the Global Positioning System, showing that each wolf pack in southwestern Alberta killed an average of 17 cattle every year (A. T. Morehouse and M. S. Boyce *Front. Ecol. Environ.* **9**, 440–445; 2011).

The wolf controversy highlights the strained relationship between science and politics. Vucetich and Wayne, along with Roland Kays of the North Carolina Museum of Natural

Sciences in Raleigh, were, they claim, dropped in August from a panel to review the FWS proposal because they had publicly opposed the wolf’s delisting. “I’m not mad about not being on the panel, but it doesn’t seem like they were following proper procedure,” Wayne says. “It was punitive,” he claims.

The review process has since been restarted. “We still haven’t figured out how to handle a situation where experts have outspoken views,” Frazer says. “We are not an academic institution. We’re trying to implement federal law.” The public consultation period will close in October, but because the panel’s peer review will not be complete by then, Frazer plans to reopen public comments in January 2014. “People are very passionate about wolves,” he says. The final decision may take a year or more.

The future of US wolves will hinge mainly on public acceptance of their delisting. Groups such as Defenders of Wildlife in Washington DC protest against wolf hunting, whereas those affiliated with hunters and ranchers want wolves to be aggressively controlled. Some individuals have made death threats to ranchers who legally shot wolves that attacked livestock.

Vucetich thinks that the government is eager to pass the issue on to the states. “It saps the energy of people working on it,” he says. ■

SOURCE: US FISH AND WILDLIFE SERVICE

MATHEMATICS

Physicists net fractal butterfly

Decades-old search closes in on recursive pattern that describes electron behaviour.

BY DEVIN POWELL

After a nearly 40-year chase, physicists have found experimental proof for one of the first fractal patterns known to quantum physics: the Hofstadter butterfly. Named after Douglas Hofstadter, the Pulitzer prizewinning author of the 1979 book *Gödel, Escher, Bach*, the pattern describes the behaviour of electrons in extreme magnetic fields.

To catch the butterfly, scientists have had to fashion innovative nets. Since May, several groups have published experiments that sought the pattern using hexagonal lattices of atoms; last month, others reported seeking it with atomic laser traps. Some physicists say that studying the pattern could help in the development of materials with exotic electric properties. But the main point of the chase was to check whether the butterfly looks as predicted.

“Hofstadter’s concept was initially disturbing to a lot of people,” says Cory Dean, an experimental physicist at the City College of New York. “Now we can say his proposal wasn’t



Hofstadter’s butterfly describes electron motion.

so crazy after all.”

Hofstadter, now a cognitive scientist at Indiana University Bloomington, sketched out the pattern in the 1970s while a graduate student in physics. It was known at the time that electrons under the influence of a magnetic field would race around in circles. But Hofstadter found that in theory, if the electrons were confined inside a crystalline atomic lattice, their motion would become complicated.

As the magnetic field was cranked up, the energy levels that define the motion of electrons would split again and again. When represented on a graph, those energy levels revealed a pattern that looked like a butterfly — and continued to do so, even when zoomed in to infinitely small scales.

Mathematician Benoit Mandelbrot had yet to popularize the term ‘fractal’ for such recursive patterns, and Hofstadter’s adviser was unimpressed. “He scornfully called the nesting pattern that this upstart youngster claimed to see, ‘mere numerology,’” says Hofstadter. “He even told me that I would be unable to get a PhD for this kind of work.” Hofstadter published¹ his description of the butterfly in 1976, after finishing his PhD.

The idea was difficult to test. The strength of the required magnetic field depends on the spacing between the atoms in the lattice. In conventional materials, in which atoms are separated by less than one-billionth of a metre, the pattern can emerge only in fields on the order of tens of thousands of tesla. The best available magnets can reach only about

DOUGLAS HOFSTADTER

ENVIRONMENTAL SCIENCES

Hackles rise over privatization plan

UK Natural Environment Research Council proposes to cut four institutes loose, but scientists fear for long-term data.

BY DANIEL CRESSEY

The UK Natural Environment Research Council (NERC) is in a quandary. The government body, which channels money to environmental scientists, has for weeks been soliciting evidence on whether it should hand funding control of four of its five key research institutes to the private sector. The move is meant in part to decrease the institutes' reliance on waning government funds, but leading scientists have now gone public with their concerns that it could jeopardize research and data of crucial importance to environmental science in the United Kingdom and around the world.

At stake are the futures of the National Oceanography Centre, the British Geological Survey, the Centre for Ecology and Hydrology and the National Centre for Atmospheric Science. (The British Antarctic Survey, which NERC also runs, is not affected.) As well as conducting research on a variety of environmental topics, all four are closely linked to specialist centres that collect long-term data, such as the British Oceanographic Data Centre, hosted by the National Oceanography Centre in Liverpool. In total, the institutes have a budget of about £400 million (US\$628 million).

"The NERC centres uniquely provide long-term consistent data, and make them freely available for the benefit of ecological science and to improve our understanding of the natural world," says William Sutherland, president of the British Ecological Society in London. "These data include studies that are undertaken over the course of decades, protected from changes in fashion or the fluctuations of short-term demands. Any change in ownership of the centres must preserve this."

Helen Snaith, a remote-sensing researcher at the National Oceanography Centre in Southampton and a trade-union representative, notes that advice that the centres provide to the government could be compromised if they start generating significant income

from private sources. "There's the potential for a very clear perceived conflict of interest," she says. She also worries that the roughly 1,750 members of staff at the four centres, about two-thirds of whom are researchers, could get a worse deal on pay and benefits under private ownership.

Duncan Wingham, NERC's chief executive, stresses that no decision has yet been taken. If the centres are moved out of the public sector, he says, it would not necessarily mean that they become profit-making. They could, for example, become part of universities. He has also emphasized that the decision on the centres' futures will not consider cost savings, which most interested parties concede.

There may also be advantages, adds Wingham — notably that freeing the institutes of public-sector constraints on pay and promotion, and from reliance on government funding, could give them better flexibility to respond to new opportunities.

Steve Ormerod, an ecologist at Cardiff University and chairman of the Royal Society for the Protection of Birds, acknowledges this. He sees advantages if the Centre for Ecology and Hydrology can develop partnerships on its own terms with international agencies and businesses, and says that being independent might allow the centre to win more funding and attract more researchers.

But there are risks, he says. "We need safeguards for these unique assets, skills and long-term, large-scale perspectives that have always provided crucial support for impartial, highly rigorous, evidence-based advice."

NERC's call for evidence on the proposal closed at the end of August, and submissions are being reviewed. The NERC board will decide on the institutes' futures in December. If the research council does choose to divest itself of these centres, the decision would represent almost the end of an era for government-controlled science in the United Kingdom. According to its 2011–12 report, the UK Biotechnology and Biological Sciences Research Council has made arrangements to "remove [its] ability to exert control" over some of its institutes; and the Medical Research Council is transferring some of its in-house units to universities. ■

100 tesla, and for just a fraction of a second.

But smaller fields are sufficient in lattices with larger spacings, which can be created by layering materials in stacks. In May, researchers reported² that they had stacked a single sheet of graphene, in which carbon atoms are arranged like a honeycomb, on top of a sheet of honeycombed boron nitride. The layers create a repeating pattern that provides a larger target for magnetic fields than the hexagons in each material — effectively magnifying the field.

After applying a field, the researchers measured discrete changes in the conductivity of the composite material — stepwise jumps that result from splits in the energy levels of its electrons. These were not a direct detection of the expected electron behaviour, but were a proxy for it. Hofstadter's butterfly had not quite flown into the net, but it had revealed its existence. "We found a cocoon," says Pablo Jarillo-Herrero, an experimental physicist at the Massachusetts Institute of Technology (MIT) in Cambridge. "No one doubts that there's a butterfly inside."

Nobel laureate Wolfgang Ketterle, another physicist at MIT, is going after the butterfly in a different way: by making atoms act like electrons. To do this, he chills rubidium atoms to a few billionths of a degree above absolute zero, and uses lasers to trap them in a lattice with egg-carton-like pockets.

When zapped by an extra pair of crisscrossed lasers, the atoms tunnel from one pocket to another. Tilting the grid allows gravity to guide the atoms into paths that mimic the circular motions of an electron in a magnetic field — although no actual magnetic fields are involved. The system can easily track the motion of individual atoms, and should be able to mimic a magnetic field strong enough to produce a Hofstadter's butterfly. "Cold atoms will give us an enormous freedom," says Ketterle, whose team posted its study on the preprint server arXiv last month³. But the set-up has a liability: the lasers tend to heat the cold atoms, limiting the ability to control the energies of the particles and reveal the fractal pattern.

Still, if the heat can be handled and the butterfly simulated, this system could be a starting point for exploring quantum behaviours in solids, such as materials that can conduct electricity on the surface but are insulators at the core. Dieter Jaksch, a physicist at the University of Oxford, UK, says, "I expect that a wealth of new phenomena and insights will be found when exploring the butterfly." ■

1. Hofstadter, D. R. *Phys. Rev. B* **14**, 2239–2249 (1976).

2. Hunt, B. *et al. Science* **340**, 1427–1430 (2013).

3. Miyake, H., Siviloglou, G. A., Kennedy, C. J., Burton, W. C. & Ketterle, W. Preprint at <http://arxiv.org/abs/1308.1431> (2013).

Secrets of fracking fluids pave way for cleaner recipe

Disclosure of chemicals used in hydraulic fracturing will empower green chemistry.

BY JEFF TOLLEFSON

The myriad liquid concoctions used in hydraulic fracturing make for quite a recipe book. Since January 2011, FracFocus, an online chemical-disclosure registry, has assembled a list of the mixtures used at more than 52,000 oil and gas wells across the United States. In these data, geochemist Brian Ellis sees opportunity. He plans to mix different chemicals into oil- and gas-rich shale rock inside a pair of high-pressure chambers that he is building. This will allow him to explore the reactions that occur when these ‘fracking’ fluids are injected deep underground.

The fluids, which are mixed with sand, are predominantly water, laced with 1% ‘special sauce’. The recipes for that fraction — a mixture that includes acids, solvents and corrosion inhibitors — were until the last few years secrets guarded by the companies that seek to penetrate shale formations to release stores of fossil fuels. But in the face of widespread concern about water contamination, 21 US states have adopted mandatory disclosure rules for the mixtures, making it easier for scientists such as Ellis, of the University of Michigan at Ann Arbor, to assess their impacts.

Much of the data end up in registries such as FracFocus, which is overseen by state energy and water organizations (see ‘A recipe for fracking’). “There are still a lot of bugs, but the vast majority of companies are now disclosing their chemicals,” says Scott Anderson, a senior policy adviser for the Environmental Defense Fund in Austin, Texas, which advocates for greener fracking procedures.

More than 500 companies have reported data to FracFocus so far. Academic researchers, advocacy groups and companies are now poring over those recipes to assess their toxicity in the hope of narrowing them down to a group of environmentally acceptable ones — and perhaps spurring the synthesis of even greener alternatives.

The boom in the disclosure of fracking-fluid components has occurred despite the fact that the federal government has yet to weigh in with its own rules. The Department of the Interior has proposed requiring the disclosure of chemicals used during hydraulic-fracturing operations on public lands, but much of the current oil and gas development



The chemicals used in hydraulic fracturing to extract oil and gas are being disclosed to online registries.

is taking place on private land. Many companies are volunteering the information anyway, even in states that have no disclosure requirements. And companies that do the hydraulic fracturing, such as Halliburton and Baker Hughes, both based in Houston, Texas, are developing their own chemical-assessment programmes in an apparent effort to address public concerns and reduce their environmental footprint.

The data in these registries, although increasingly abundant, remain incomplete, unconsolidated and difficult to compare. The European Union is phasing in a unified chemical-regulation programme that governs reporting across all commercial sectors. Energy companies operating in the North Sea, for example, must all play by the same rules and abide by strict reporting requirements. But in the United States, the regulations on chemical reporting remain a mixture of state

and national policies that vary by industry.

Even in states with disclosure laws, companies can omit information in the interests of protecting intellectual property. For example, a subsidiary of ExxonMobil, based in Irving, Texas, declined to list the components of a gelling agent — used to help to suspend sand in water — at one of its wells in Wyoming, calling the information a “trade secret”.

The result is that companies are still operating under their own risk assessments and not disclosing all of the information that might be needed for independent verification. “If everybody has a different definition of what is hazardous and doesn’t fully disclose the chemicals they use, then it is going to be awfully difficult to compare,” says Lauren Heine, co-director of Clean Production Action, an advocacy group based in Somerville, Massachusetts.

Heine’s group is sifting through company disclosures to perform a risk assessment on the most commonly used chemicals. The effort is designed to provide a single point of

➔ **NATURE.COM**
For concerns
about the impact of
fracking, see:
go.nature.com/193vas

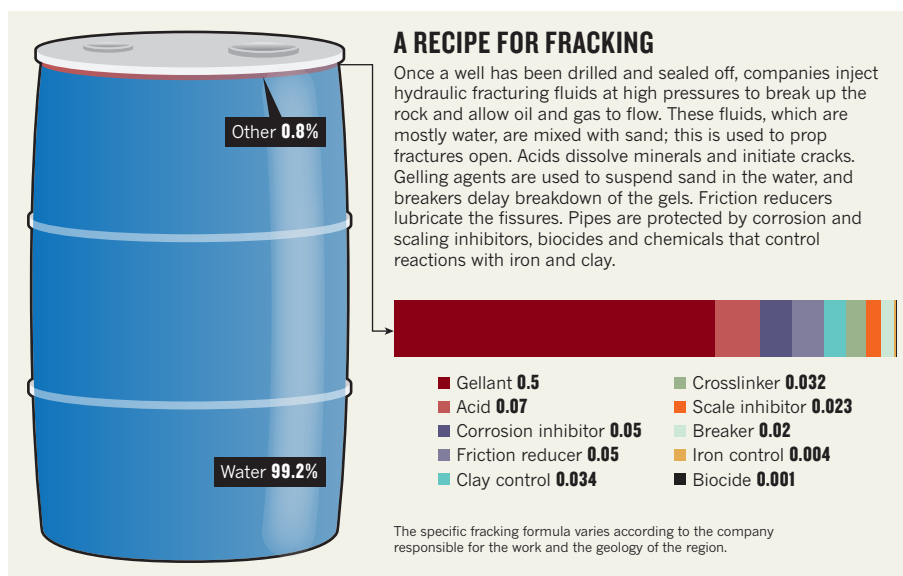
DAVID ZALUBOWSKI/AP/PRESS ASSOC. IMAGES

comparison so that scientists, industry and the public can make informed decisions about which chemicals are best.

Daniel Durham, who heads a chemical-assessment programme at the Houston-based energy company Apache, says that although Heine's effort is promising, companies do not need to wait. The US Environmental Protection Agency (EPA) already maintains its own public registry of preferred chemicals for various industrial processes. Companies that want to register their chemicals provide the EPA with toxicity and environmental-assessment data; the registry also allows companies to keep certain data confidential if intellectual property is involved.

The upshot is a growing — albeit incomplete — list of preferred chemicals that companies such as Apache can choose from as they design their fracking fluids. A company that wants to avoid using a solvent such as ethylene glycol monobutyl ether, for example — used to reduce viscosity but possibly toxic to the endocrine system — could look through the EPA list for alternatives. "It's a very good road map to green chemistry," Durham says.

Eventually, Durham hopes that researchers will help to develop novel chemicals that could be used to make the entire hydraulic-fracturing process cleaner and more efficient.



Scientists such as Ellis could play an important part.

Ellis wants to know whether fracking fluids are contributing to geochemical reactions within the shale rock that might free up potentially dangerous metals and radionuclides, such as arsenic, barium, strontium and uranium. These elements are often found in trace concentrations in the waste water produced

by oil and gas companies, but can also be found naturally in groundwater. Ellis eventually hopes to help companies to select better chemicals that would minimize the potential for contamination and the need for wastewater treatment. But for now, he says, he is focused on the basic science. "Fundamentally, I just want to understand those reactions a little better." ■

POLICY

More cuts loom for US science

Stalemate in Congress puts spending plans on hold.

BY LAUREN MORELLO

Laura Niedernhofer is counting her pennies. The mid-career molecular biologist moved last year to the Scripps Research Institute's campus in Jupiter, Florida — a risky decision that saw her building a new laboratory group at a time when the US government was cutting its support for science. In June, Niedernhofer abandoned one of her main lines of research — reducing the toxicity of cancer drugs — after the National Institutes of Health (NIH) rejected her grant application. In July, the agency approved a second grant, allowing her to keep another research thrust alive — on the molecular mechanisms of ageing. But the NIH cut the award by 18%, preventing her from hiring an additional postdoctoral researcher.

Niedernhofer is not alone. In a survey of more than 3,700 US scientists released on 29 August by the American Society for Biochemistry and Molecular Biology in Rockville, Maryland, one-third said that they had laid off researchers, and close to two-thirds had seen their funding fall

since 2010. Federal spending on research and development has declined by 16.3% since 2010, the fastest drop in a three-year period since the end of the space race in the 1970s, according to an analysis published on 3 September by the American Association for the Advancement of Science in Washington DC.

The most drastic reduction occurred on 1 March, when across-the-board budget cuts known as sequestration lopped 5% from the budgets of most government agencies. Science powerhouses such as the NIH in Bethesda, Maryland, and the National Science Foundation in Arlington, Virginia, began to scrimp by reducing the values and durations of grants, and the number of recipients per application cycle.

The situation could worsen in the coming months. Congress, which returned to Washington DC this week, has made little progress

on setting government spending for the 2014 fiscal year, which begins on 1 October. An attempt by a group of Republican senators and the White House to negotiate an agreement on deficit reduction broke down in late August, and since then the crisis in Syria has diverted the attention of Congress. To avoid a government shutdown, lawmakers are expected to extend current funding levels until December. That extension, known as a continuing resolution, would run out at about the same time that the country confronts another financial matter: surpassing its borrowing limit, or debt ceiling.

That could set up a budget battle royal in the next few months. A similar fight in the summer of 2011 led to the law that created sequestration; it specifies annual spending reductions until 2021, if Congress does nothing to override it. The next round of cuts, scheduled to take effect in January 2014, would trim spending to 2% below the already-whittled-down 2013 level.

Indications of how the various science agencies will fare can be found in Congress's ►

"There is continuing pressure for additional budget cuts as a price for raising the debt ceiling."

► unfinished spending bills. The Democratic-controlled Senate would eliminate sequestration and give science agencies modest boosts. The Republican-controlled House of Representatives would cut funding in many areas to keep total spending in line with the 2% cut that sequestration prescribes. One relatively bright spot is the House's proposed allocation of \$7.0 billion for the National Science Foundation, the same amount that the agency received in 2012 — a bountiful level in House terms. But Barry Toiv, vice-president for public affairs at the Association of American Universities in Washington DC, worries that House Republicans will now end up seeking cuts beyond 2%. "There is continuing pressure for additional budget cuts as a price for raising the debt ceiling," he says.

The situation leaves US research institutions in an uneasy position, unsure whether 2013 funding levels will have been the nadir, or a prelude to something worse. Many are just beginning to feel the effects, because of the delay between the sequestration cuts and grants being awarded. At the University of Maryland in College Park, the haul of grants from the NIH was 7% below projections in the 2012–13 academic year, and its share of defence-department cash was 3% lower than expected, says chief research officer Patrick O'Shea. At Johns Hopkins University in Baltimore, Maryland, four doctoral programmes in the department for environmental health sciences each accepted just one student this year, instead of the usual two or three, says Jonathan Links, a medical physicist who handles the university's crisis planning.

But US universities collect tuition fees and generally have endowments, which means that they have ways to provide stop-gap funding to scientists in tight spots. At a 'soft-money' research institute such as Scripps, grants are needed to pay almost all the bills — so Niedernhofer's situation was more dire.

Although she is continuing her ageing research with her three postdocs, she has a new standard question she asks before hiring them: will they consider only academic research as a job? "I can't guarantee that they will get that," she says, "and I don't want to be the one to break their hearts." ■

PHYSICS

Ultimate upgrade for US synchrotron

Argonne lab banks on beam-bending magnets in bid for world's most focused X-ray light source.

BY EUGENIE SAMUEL REICH

Every day, in dozens of synchrotrons around the globe, electrons are whipped around in circular storage rings to provoke them into emitting X-rays, useful for imaging materials, identifying chemical-reaction products and determining crystal structures.

But photon scientists do not want just any old storage ring. For more than a decade, they have dreamt of 'ultimate' storage rings — ones that use specialized magnets to produce X-ray beams that are as tightly focused as theory allows.

Now, researchers at the largest US synchrotron, the Advanced Photon Source (APS) at the Argonne National Laboratory in Illinois, are taking steps to develop this technology. In the process, they hope to leapfrog several international facilities that have a head start.

In Sweden, ultimate-storage-ring technology is being pioneered at MAX IV, a 528-metre-circumference synchrotron in Lund. Scientists there first sought to increase the intensity and brightness of the synchrotron's X-ray light in 2006 by focusing electron beams more tightly. The design relied on groups of seven magnets, known as multi-bend achromats, that could be used in as many as 20 places around the ring to nudge the paths of electrons back and forth until they lined up more-or-less perfectly. Machine director Mikael Eriksson recalls that when he toured US light sources to describe the project, "few believed it".

Eriksson now has believers. In a report posted online on 29 August, researchers at the Argonne lab describe how they are hoping to upgrade the 1.1-kilometre-circumference APS with multi-



Magnets for the Swedish MAX IV synchrotron.

bend achromats (see go.nature.com/asxrbq). "There's a new technology that has come along and it's pretty revolutionary," says APS director Brian Stephenson. Current storage rings have at most double-bend achromats, which contain two magnets rather than seven. Physicists had thought that including more magnets would make the beam unstable by bending it too much and introducing too many fluctuations. But the work at MAX IV showed that very compact magnets enable bending paths that are short enough to stop fluctuations from building up.

The US Department of Energy, which funds the APS, still needs to approve the plan. In July, one of the department's advisory committees suggested that US labs were being left behind while other countries push towards ultimate storage rings. The committee had also recommended pursuing a next-generation X-ray

DANFYSIK

MORE ONLINE

TOP STORY

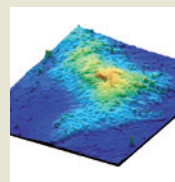


Indian parliament accuses HPV-vaccination programme of violating ethical standards
go.nature.com/flnwzy

MORE NEWS

- Bacteria in faecal feast help mice stay slim go.nature.com/spfyx8
- Yellow warblers protect coffee crops against borer beetle go.nature.com/nvtk5w
- Physics Nobel laureate responds to criticism of his 'time crystals' proposal go.nature.com/yypwjt

IMAGE OF THE WEEK

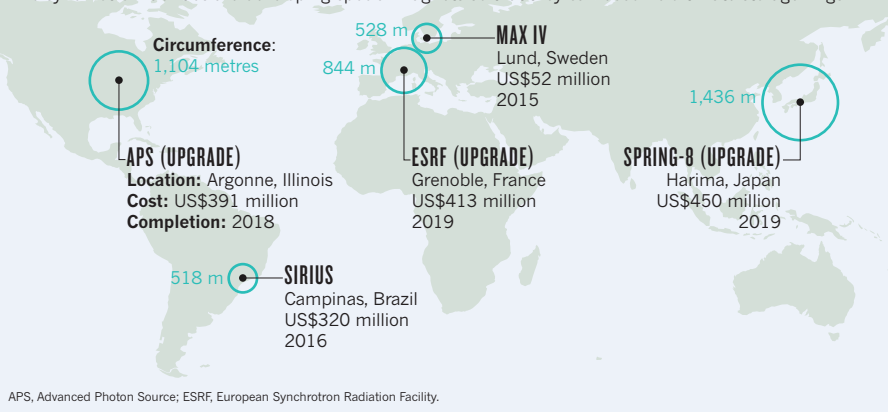


Volcano found under Pacific Ocean is Earth's largest at 650 kilometres wide
go.nature.com/beeqp4

WILLIAM SAGER/UNIV. HOUSTON

FOCUSED BEAMS

Five synchrotron facilities are developing special magnets so that they can become ultimate storage rings.



laser, useful for making ‘molecular movies’ of chemical reactions, among other things (see *Nature* **500**, 13–14; 2013). But such a laser would have limitations: its strongly peaked light pulses would destroy delicate materials. Ultimate storage rings, by contrast, satisfy a need for more gradually peaked pulses of light.

Researchers say that these storage rings could revolutionize X-ray imaging by making it possible to map evolving chemical processes. Current X-ray sources are not bright enough to track changes in materials with nanometre and nanosecond resolution, because there are not enough coordinated photons in the beams. Ultimate storage rings would change that. “A whole class of new problems opens up,” says Paul Evans, a materials scientist at the University of Wisconsin–Madison. For example, he says that the rings could be used to investigate what happens chemically and electrically at the interface between materials inside a battery as it runs out.

The APS is seeking to tack the installation of ultimate-storage-ring technology on to a separate upgrade that had already been approved. Cost calculations are still ongoing, but Stephenson hopes that the multi-bend achromats can be included without raising the upgrade budget much above US\$391 million. MAX IV is implementing the technology for only 340 million Swedish kronor (\$52 million), but that ring is smaller and the price tag would not include the overhead costs that are charged at US energy-department labs.

After its upgrade, the APS could surpass MAX IV by approaching the theoretical limit for the most focused beam possible. The Swedish synchrotron will contain 20 multi-bend achromats, whereas the APS upgrade calls for around 40. In 2012, physicists at SLAC National Accelerator Laboratory in Menlo Park, California, showed that the number of multi-bend achromats around a larger ring could be pushed even higher without fundamentally destabilizing the electron beam. “The key is to make the bending gentle,” says Yunhai Cai, head of beam physics at SLAC.

Alongside APS, the European Synchrotron Radiation Facility (ESRF) in Grenoble, France, has also opted for a multi-bend-achromat upgrade, after a working group concluded last October that the technology was affordable. ESRF director-general Francesco Sette says that accelerator physicists there showed that multi-bend achromats could work with the facility’s existing injector, a part of the machine that supplies extra electrons to the main ring a few times each day. He had previously thought that a new injector would be needed. “We are today in full swing to launch as soon as possible,” he says.

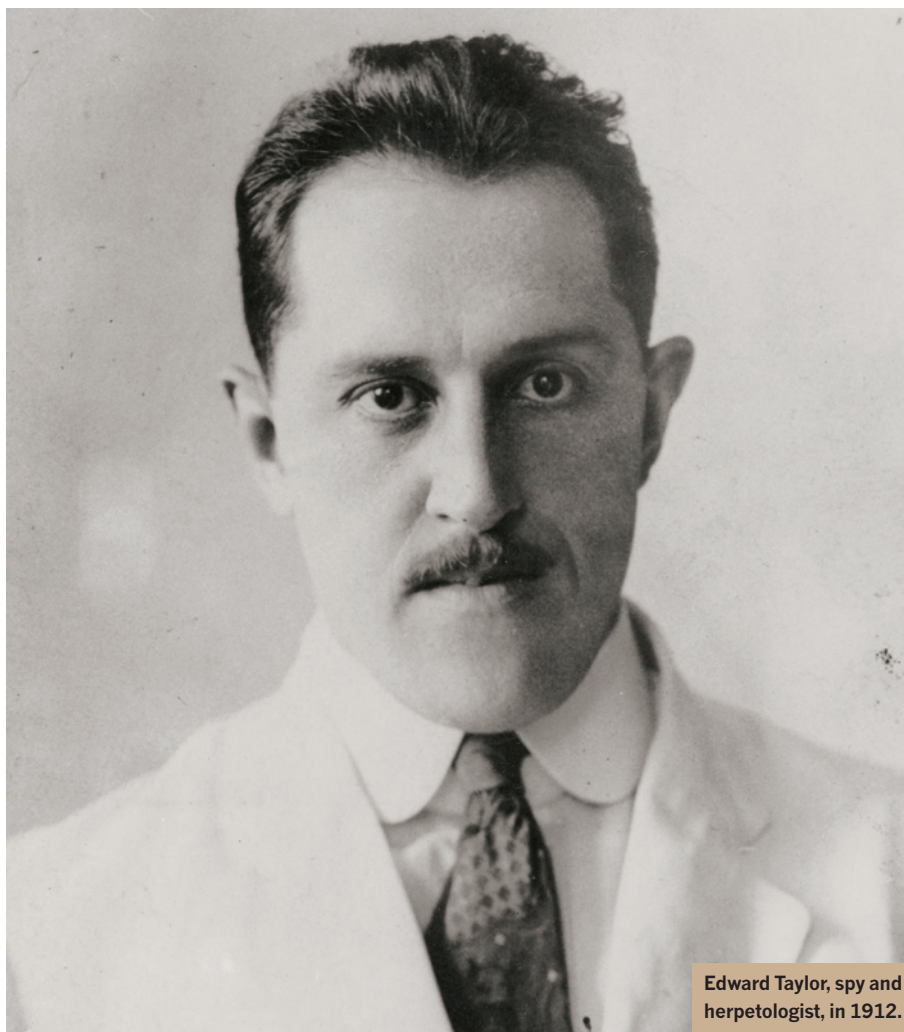
Storage rings in Brazil and Japan will also be upgraded with multi-bend achromats, giving MAX IV a window of only one year from its projected completion date of 2015 before it faces competition (see ‘Focused beams’).

Some have suggested that particle-physics tunnels, too, could eventually be turned into light sources with multi-bend achromats. SLAC has an idle 2.2-kilometre-circumference tunnel that originally housed a particle accelerator used to compare the decay rates of matter and antimatter. And a 6.3-kilometre tunnel used by the now-closed Tevatron particle accelerator at Fermilab near Batavia, Illinois, is another candidate for conversion. Eriksson says that building ultimate storage rings of that size would not be realistic for Sweden, given the relative size of its science budget.

He knows that Sweden’s time in the vanguard will be short-lived, and has mixed feelings about seeing other countries adopting the technology that he and his colleagues pioneered so enthusiastically. “We are both happy and a little sorry,” he says. ■

CORRECTION

The News story ‘NASA ponders Kepler’s future’ (*Nature* **501**, 16–17; 2013) inflated the size of asteroids that the probe could watch for — they would be several hundred metres in diameter rather than several hundred kilometres.



Edward Taylor, spy and herpetologist, in 1912.

SPENCER RESEARCH LIBRARY/UNIV. KANSAS LIBRARIES

THE SPY WHO LOVED FROGS

To track the fate of threatened species, a young scientist must follow the jungle path of a herpetologist who led a secret double life.

BY BRENDAN BORRELL

Before leaving for the Philippines as an undergraduate in 1992, Rafe Brown scoured his supervisor's bookshelf to learn as much as he could about the creatures he might encounter. He flipped through a photocopy of a 1922 monograph by the prolific herpetologist Edward Taylor, and became mesmerized by a particular lizard, *Ptychozoon intermedium*, the Philippine parachute gecko. With marbled skin, webs between its toes and aerodynamic flaps along its body that allow it to glide down from the treetops, it was just about the strangest animal that Brown had ever seen.

Brown learned that Taylor had collected the first known example, or type specimen, near the town of Bunawan in 1912, and had deposited it at the Philippine Bureau of Science in

Manila. But the specimen had been destroyed along with the building during the Second World War, and the species had never been documented again in that part of the country. "What are the chances I'm going to see one of the rarest geckos in the world?" he wondered.

He was driven by more than curiosity. Given the rampant deforestation in that part of the Philippines, he wanted to determine whether the species still existed there and if so, how similar it was to geckos collected in other areas. He wanted to see, in other words, whether Taylor's 70-year-old taxonomic decisions were still valid.

On their first night in the field, Brown and his colleagues drove to the edge of the forest and caught two red eyes in the beam of a

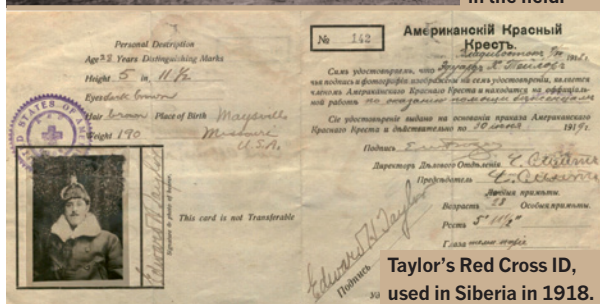
headlamp. It was a *Ptychozoon*. Back at their hotel, Brown photographed the gecko, took tissue samples for DNA sequencing, and carefully prepped it and stuck it in a jar. It became the neotype to replace Taylor's lost specimen, and in 1997, Brown published a new description of the species¹. It marked the start of an obsession.

As Brown made his career studying biodiversity in the Philippines over the next two decades, he could not escape Taylor's long shadow. The elder herpetologist had logged 23 years in the field over his lifetime, collecting more than 75,000 specimens around the world, and naming hundreds of new species.

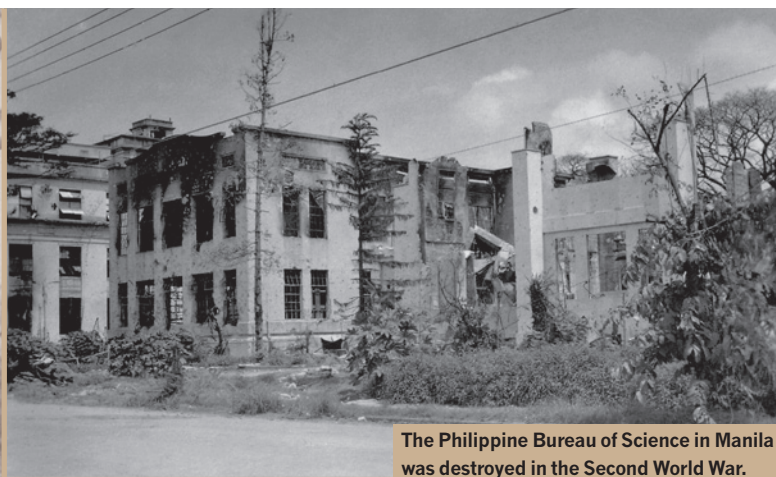
There is a darker side to Taylor's legacy, however. He was a racist curmudgeon beset by paranoia — possibly a result of his mysterious



Edward Taylor in the field.



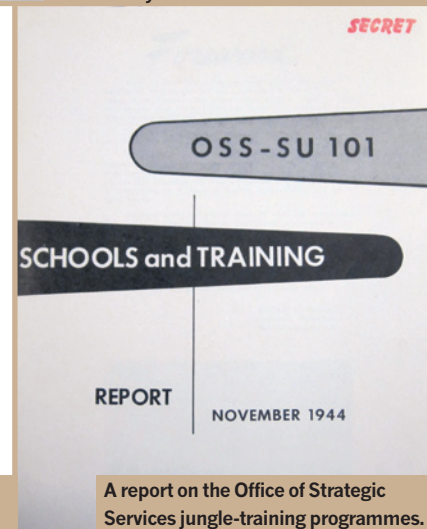
Taylor's Red Cross ID, used in Siberia in 1918.



The Philippine Bureau of Science in Manila was destroyed in the Second World War.



The Philippine parachute gecko.



A report on the Office of Strategic Services jungle-training programmes.

double life as a spy for the US government. He had amassed no shortage of enemies by the time he died in 1978. An obituary noted that he was, to many, “a veritable ogre—and woe to anyone who incurred his wrath”². More damaging, perhaps, were the attacks on his scientific reputation. After the loss of his collection in the Philippines, many of the species he had named were declared invalid or duplicates. The standards of taxonomy had advanced beyond Taylor’s quaint descriptions, and without the specimens to refer to, his evidence seemed flimsy.

Nevertheless, Brown felt a connection with his maligned predecessor. It was a bond that intensified when, in 2005, Brown became curator of herpetology at the University of Kansas Natural History Museum in Lawrence, the same institution at which Taylor had spent much of his career. Over the years, Brown has rebuilt some of Taylor’s collection and resurrected many of his species. Now, as he finishes a major monograph on a group of Philippine frogs, he is more convinced than ever: “Taylor was right.”

Brown’s reassessment could prove crucial. Since Taylor’s time, taxonomy has become more than just a naming exercise. Designating a group of organisms as a new species, or lumping it in with an old one, can affect the

animals’ legal protection and influence the allocation of scarce conservation resources. Amphibian declines, in particular, have made headlines around the world, and the Philippines ranks second only to Sri Lanka for sheer proportions of imperilled species: 79% of Philippine amphibians are found nowhere else on Earth, and 46% are under threat of extinction. But following Taylor’s trail has given Brown

“HE WAS A VERITABLE OGRE — AND WOE TO ANYONE WHO INCURRED HIS WRATH.”

cause for optimism. “A lot of the things people thought were extinct,” he says, “if you go right where Taylor said to go, you can find them.”

A LUST FOR ADVENTURE

On the fourth floor of the Kansas museum, Brown is walking through the herpetological collections. Lizards float upside down in yellow-tinged alcohol. Snakes coil like corkscrews,

and two dozen tiny, dark frogs embrace in a specimen jar. On one shelf, the jars have red ribbons tied around their lids to signify that their contents are type specimens: the standards on which species descriptions are based.

When scientists disagree on whether something is a new species or a variant of a known one, they often need to refer back to the type specimen or even return to where it was collected. Brown opens a jar and extracts a small lizard that has a tin tag tied to its waist with twine. It is one of Taylor’s originals, on loan from the California Academy of Sciences in San Francisco. “Preserved properly, well labelled and deposited in a safe institution,” says Brown, “these will last forever.”

That is the kind of legacy to which every taxonomist aspires, and Taylor was no exception. Born in Maysville, Missouri, on 23 April 1889, he was still a teenager when he began depositing specimens at this museum. At 23, he joined the civil service and became what he called “a one-man Peace Corps” in the Philippines — then a US territory — setting up a school for members of a headhunting tribe in central Mindanao, where he collected the parachute gecko among other species. Next, he worked for the fisheries department in Manila and then completed his PhD on Philippine

mammals, but his true passion was always herpetology. It came at the expense of just about everything else in his life. “I named about 500 species,” he would later tell a reporter, “but I can’t always remember the names of my own children.” His wife, Hazel, could not bear his long absences, and they divorced in 1925.

By then, Taylor had described more species than most of his peers could achieve in a lifetime: 42 amphibians, 40 lizards and 30 snakes. He sold some of his specimens to museums in the United States, but many remained at the Bureau of Science in Manila, where he thought they would be secure forever. He joined the faculty at Kansas in 1926, and over the next two decades he wandered the globe from Mexico and Costa Rica to parts of Africa, lugging a folding army cot and subsisting on rice and evaporated milk as he collected specimens.

In his 60s, however, Taylor found himself under attack. In 1954, Robert Inger, a herpetologist at the Field Museum in Chicago, Illinois, published a withering taxonomic review of Philippine amphibians³. Inger, who studied only specimens in museums, axed 44 of the 87 species that Taylor had personally named or approved. “The differences between Taylor’s frogs will be recognized as the differences to be expected between individuals,” Inger wrote. In other words, Taylor was a hack. On his personal copy of Inger’s text, Taylor scribbled the word, “Hooley.”

More recently, herpetologists have levelled other serious allegations against Taylor’s character. In 1993, the Kansas Herpetological Society posthumously published his 1916 master’s thesis on Kansas reptiles. In a foreword, one of his former students, Hobart Smith, revealed that Taylor had plagiarized large sections from the nineteenth-century palaeontologist and herpetologist Edward Drinker Cope. For those who knew Taylor as a man of principle, it was a devastating revelation, but it also explained why Taylor had never tried to publish the work himself. Then, in 2002, herpetologist Jay Savage at the University of Miami in Coral Gables, Florida, charged that Taylor had secretly copied the field notes of a rival in order to scoop him on his next collecting trip to Costa Rica⁴.

Taylor had other demons. He had voiced support for eugenics programmes and reportedly refused to take on Jewish students. Brown makes no apologies for the man, but Taylor’s reputation — for good or ill — is intertwined with the history of the Kansas museum. “In the end, we consider him our own,” says Brown.

A LEGACY REVISITED

Brown’s interest in Taylor grew when he was a graduate student at the University of Texas at Austin in the late 1990s. He devoured Taylor’s monographs to plan his own collecting. He hunted through museum records to find out where Taylor’s specimens were, and made

visits to see them at the Field Museum and the California academy. But time and time again, he came to a dead end when he wanted information on type specimens that Taylor had deposited at the Philippine Bureau of Science.

He soon learned the tragic story of that institution: in February 1945, when US General Douglas MacArthur launched an all-out attack on Manila to expel the Japanese occupiers, the Bureau of Science was reduced to rubble, and all of its botanical and zoological specimens were destroyed, including 32 of Taylor’s type specimens. “The loss is an irreplaceable one,” Taylor’s friend Elmer Merrill, a legendary botanist, wrote in *Science*⁵. Plant specimens were gradually replenished, but no one had systematically tried to replicate Taylor’s efforts. For many years, hostile tribes kept most interlopers away from species-rich regions. In the 1990s, threats of terrorism made it difficult to access places such as the Sulu Archipelago, where Taylor collected types for a dozen species. Despite the danger, Brown resolved to retrace Taylor’s steps.

In July 1998, he hired a boy to guide his team through the mountains of northern Luzon Island. It was the same place where Taylor had been ambushed by a machete-wielding native in a loincloth. While Brown tromped through streams on his quest, a rumour spread through a town below that Westerners had

Over the past two decades, Brown and his close collaborator Arvin Diesmos, a herpetologist at the National Museum of the Philippines in Manila, have collected more than 15,000 Philippine specimens — about one-fifth of Taylor’s lifetime haul. To establish evolutionary relationships, Brown also collects DNA, which cannot be extracted from Taylor’s formaldehyde-preserved specimens, and he records frog mating calls, a key tool for identifying species. By the time he has finished his own review of the Philippine *Platymantis* frogs, which has been in the works since 2003, he expects to have doubled the number of species from 30 to 60, resurrecting many of Taylor’s names.

CROAK AND DAGGER

Brown’s fascination with Taylor has gone beyond taxonomy. Early in his research, he became intrigued by “herpetology gossip” about Taylor’s extracurricular activities. As he trotted around the globe, Taylor seemed to be conducting field work in conflict zones and, in his memoirs, he alluded to duties outside science⁷. While working for the fisheries department in Manila, he helped to investigate the murder of an Englishman, traded tips with the Swedish secret service and scouted for mercury that could be used in munitions during the First World War. On his river journeys,

he occasionally noticed Japanese people, and warned the local governor that they were “spying out of the land”.

It was never clear to Taylor’s few confidantes whether he used wars as an excuse to get into the field, or vice versa. In his obituary,

a former student suggested that Taylor’s later activities during the Second World War “probably will never be known in detail”².

But the true nature of Taylor’s work is finally coming into focus as intelligence records are declassified and research materials surface. They reveal that Taylor was indeed a spy, and that he continued to do intelligence work after the First World War, when he was sent to Siberia. His official purpose was to join the Red Cross to stop a typhus epidemic, but he was also gathering information on the Communist revolt in Russia and, later, the fate of grand duchess Anastasia, daughter of murdered tsar Nicholas II.

Taylor was called to duty again in 1944, when he was 54 and war raged in the Pacific. According to records in the US National Archives, he joined the Office of Strategic Services (OSS), a precursor to the Central Intelligence Agency (CIA), to train agents in Sri Lanka — then a British territory that provided ready access to Myanmar, Malaysia, Indonesia and other areas that the Japanese had infiltrated. Scientific work, an OSS officer explained to one of Taylor’s superiors, was “excellent cover”.

“A LOT OF THE THINGS PEOPLE THOUGHT WERE EXTINCT, IF YOU GO RIGHT WHERE TAYLOR SAID, YOU CAN FIND THEM.”

kidnapped the boy. A dozen locals took up torches, canes and machetes and marched to the home of the village chief on their way to find the kidnappers. When Brown returned, he diffused the situation by producing sacks of amphibians — his only captives. Taylor, when ambushed, had produced a rifle.

During the 1998 trip, Brown and his collaborators found 5 species of reptiles and amphibians not seen for many decades; 13 potentially new to science; and 30 never before reported from the region⁶. One night, Brown caught several *Platymantis* frogs making an insect-like chirp high in the trees. They turned out to be from a species that Taylor had caught and named *rivularis* in 1920. The type specimen still existed, but it was bleached of colour and in pretty bad shape, and there were not many other examples to examine. Accordingly, Inger had lumped *rivularis* in with another species, *hazelae* (named after Taylor’s wife). But after hearing its mating calls and seeing its colours in life, Brown decided he would resurrect *P. rivularis* as its own species. Inger, says Brown, favoured more inclusive groupings and was draconian in his decisions. “If he had any doubt, he would sink a species.”

Taylor taught jungle survival at Camp Y, a steamy settlement on the coast. With a penetrating stare and a lantern jaw, he seemed more imposing than his 1.8 metres. In his spare time, he occasionally dodged gunfire to nab specimens, which he studied for two monographs published after the war. "Have just described five new forms of blind snakes from the island," he wrote to S. Dillon Ripley, a young ornithologist who served with him and would later lead the Smithsonian Institution in Washington DC. In a later letter, he offered "some 500 species" of mollusc shells to the Smithsonian.

After the war, Taylor helped the British in Malaysia to investigate Japanese war crimes against civilians. His work documenting rape, torture and murder may have contributed to his antipathy towards the Japanese people. Never an easy-going person, his experiences at war seem to have wounded him. He failed in a bid to become head of the Kansas museum, and grew increasingly paranoid in daily life. He studied Russian and made inquiries about working for the CIA. Smith, who died in March this year, told *Nature* that Taylor sprinkled flour on the floor of his office to detect trespassers during his absences. "I was wary of him," said Smith. William Duellman, a herpetologist at the University of Kansas who first met Taylor in 1951, thinks that Taylor's symptoms could today meet the standards of post-traumatic stress disorder. Nevertheless, Taylor kept working. In his later years, he studied a group of poorly known, legless amphibians called caecilians. He published a sprawling, 800-page taxonomic review⁸ of them in 1968.

ON THE BRINK

Taylor's herpetological legacy in the Philippines has taken on new importance now that the country has lost more than 95% of its native forest. Species collectors such as Brown know that their work has conservation implications, but there are often differences between scientific studies and conservation classifications. In the late 1990s, for example, the International Union for Conservation of Nature (IUCN) labelled the Polillo Island frog — *Platymantis polillensis*, first described by Taylor — as critically endangered. All but 4 square kilometres of Polillo's forests had been razed for coconut plantations.

But in 2004, Brown was listening to his recordings when he noticed that the Polillo frog had a mating call similar to that of a frog that he had collected on Luzon. Brown applied for permission to get genetic samples from Taylor's original collecting site, and confirmed his hunch: the frog is widespread. Last year, he reported⁹ that seven frog species once considered vulnerable or endangered by the IUCN are actually widespread on Luzon.

The challenge for taxonomists is that although many agree that global biodiversity



Rafe Brown holds a specimen of an adult snake, collected by Edward Taylor in the 1920s.

is in crisis, threat levels are hard to gauge accurately because advocates for every taxon and ecosystem are clamouring for attention and real data are scarce. "Global threat assessments for large taxonomic groups is a very inexact science," says Walter Jetz, an ecologist at Yale University in New Haven, Connecticut. "We need more boots on the ground."

Brown is sceptical about conservation assessments in general, but one threat to Philippine amphibians does concern him: the chytrid fungus *Batrachochytrium dendrobatidis*, which has been linked to the decline or extinction of hundreds of amphibian species around the world (see *Nature* 465, 680–681; 2010). In 2009, Brown identified the fungus on five species in the Philippines, and it has since been found on more. The chytrid threat, he says, combined with habitat destruction and climate change, could push Philippine amphibians over the edge.

Time is running out to document the biodiversity of the Philippines, but also to determine Taylor's place in history. Brown has found that Taylor's species descriptions, although brief, often zeroed in on the precise trait that set one group apart from its relatives. "He had a sharp eye," says Brown. More than a dozen species whose names were erased by Inger and others have proved to be valid after all.

Inger, who is 93, is impressed by the emerging evidence and the way that Brown has approached the subject. "I think he's probably right," he says, but adds, "I'm still a little uneasy about over-fragmentation."

Back at the University of Kansas, Brown takes a seat inside an archival library and dips once more into some of Taylor's work, including the battered leather books that the man used for his field notes and specimen catalogues. Paging through one of those catalogues for the first time, Brown is stunned to find that Taylor had crossed out the name attached to an Asian spadefoot toad that he caught on Mindoro Island — a strange, gangly creature that crawls rather than hops. Next to it, Taylor had written, "new sp!!". As recently as 2009, Brown had designated it as a new species, *Leptobrachium mangyanorum*, because it was so different from previously described relatives¹⁰.

"Ed was way ahead of us," says Brown. "Why he never named it, we'll never know. But it's pretty satisfying to come along 90 to 100 years later and arrive at the same conclusion." ■

Brendan Borrell is a biologist-turned-journalist based in New York. He contributed to a 2007 review paper on gliding animals, which also included work by Brown.

1. Brown, R. M., Ferner, J. W. & Diesmos, A. C. *Herpetologica* **53**, 357–373 (1997).
2. Webb, R. G. *Herpetologica* **34**, 422–425 (1978).
3. Inger, R. F. *Fieldiana Zool.* **33**, 183–531 (1954).
4. Savage, J. M. *The Amphibians and Reptiles of Costa Rica* (Univ. Chicago Press, 2002).
5. Merrill, E. D. *Science* **101**, 401 (1945).
6. Diesmos, A. C., Brown, R. M. & Gee, G. V. A. *Sylvatrop* **13**, 63–80 (2003).
7. Taylor, E. H., Leonard, A. B., Smith, H. M. & Pisani, G. R. *Monogr. Mus. Nat. Hist. Univ. Kansas* **4**, 1–160 (1975).
8. Taylor, E. H. *The Caecilians of the World* (Univ. Kansas Press, 1968).
9. Brown, R. M. et al. *Check List* **8**, 469–490 (2012).
10. Brown, R. M., Siler, C. D., Diesmos, A. C. & Alcalá, A. C. *Herpetol. Monogr.* **23**, 1–44 (2009).

➔ NATURE.COM

For a podcast and slideshow about Taylor and Brown, see: go.nature.com/hnform

QUANTUM QUEST

PHYSICISTS HAVE
SPENT A CENTURY
PUZZLING OVER
THE PARADOXES OF
QUANTUM THEORY.
NOW A FEW OF THEM
ARE TRYING TO
REINVENT IT.

BY PHILIP BALL

If the truth be told, few physicists have ever really felt comfortable with quantum theory. Having lived with it now for more than a century, they have managed to forge a good working relationship; physicists now routinely use the mathematics of quantum behaviour to make stunningly accurate calculations about molecular structure, high-energy particle collisions, semiconductor behaviour, spectral emissions and much more.

But the interactions tend to be strictly formal. As soon as researchers try to get behind the mask and ask what the mathematics mean, they run straight into a seemingly impenetrable wall of paradoxes. Can something really be a particle and a wave at the same time? Is Schrödinger's cat really both alive and dead? Is it true that even the gentlest conceivable measurement can somehow have an effect on particles half-way across the Universe?

Many physicists respond to this inner weirdness by retreating into the 'Copenhagen interpretation' articulated by Niels Bohr, Werner Heisenberg and their colleagues as they were putting quantum theory into its modern form in the 1920s. The interpretation says that the weirdness reflects fundamental limits on what can be known about the world, and just has to be accepted as the way things are — or, as famously phrased by physicist David Mermin of Cornell University in Ithaca, New York, "shut up and calculate!"¹

But there have always been some who are not content to shut up — who are determined to get behind the mask and fathom quantum theory's meaning. "What is it about this world that forces us to navigate it with the help of such an abstract entity?" wonders physicist Maximilian Schlosshauer of the University of Portland in Oregon, referring to the uncertainty principle; the wave function that describes the probability of finding a system in various states; and all the other mathematical paraphernalia found in textbooks on quantum theory.

Over the past decade or so, a small community of these questioners have begun to argue that the only way forward is to demolish the abstract entity and start again.

ILLUSTRATION BY ANDY POTTS



They are a diverse bunch, each with a different idea of how such a ‘quantum reconstruction’ should proceed. But they share a conviction that physicists have spent the past century looking at quantum theory from the wrong angle, making its shadow odd, spiky and hard to decode. If they could only find the right perspective, they believe, all would become clear, and long-standing mysteries such as the quantum nature of gravity might resolve themselves in some natural, obvious way — perhaps as an aspect of some generalized theory of probability.

“The very best quantum-foundational effort,” says Christopher Fuchs of the Perimeter Institute for Theoretical Physics in Waterloo, Canada, “will be the one that can write a story — literally a story, all in plain words — so compelling and so masterful in its imagery that the mathematics of quantum mechanics in all its exact technical detail will fall out as a matter of course”.

A VERY REASONABLE PROPOSAL

One of the earliest attempts to tell such a story came in 2001, when Lucien Hardy, then at the University of Oxford, UK, proposed that quantum theory might be derived from a small set of “very reasonable” axioms about how probabilities can be measured in any system², such as a coin tossed into the air.

Hardy began by noting that a classical system can be specified completely by measuring a certain number of ‘pure’ states, which he denoted N . For a coin toss, in which the result is always either heads or tails, N equals two. For the roll of a dice, whereby the cube must end up with one of six faces uppermost, N equals six.

Probability works differently in the quantum world, however. Measuring the spin of an electron, for example, can distinguish two

pure states, which can be crudely pictured as a rotation clockwise or anticlockwise around, say, a vertical axis. But, unlike in the classical world, the electron’s spin is a mixture of the two quantum states before a measurement is made, and that mixture varies along a continuum. Hardy accounted for that through a ‘continuity axiom’, which demands that pure states transform from one to another in a smooth way. This axiom turns out to imply that at least N^2 measurements are required to completely specify a system — a relationship that corresponds to the standard quantum picture.

But, in principle, said Hardy, the continuity axiom also allows for higher-order theories in which a complete definition of the system requires N^3 , N^4 or more measurements³, resulting in subtle deviations from standard quantum behaviour that might be observable in the lab. He did not attempt to analyse such possibilities in any detail, however; his larger goal was to show how quantum physics might be reframed as a general theory of probability. Conceivably, he says, such a theory could have been derived by nineteenth-century mathematicians without any knowledge of the empirical motivations that led Max Planck and Albert Einstein to initiate quantum mechanics at the start of the twentieth century.

Fuchs, for one, found Hardy’s paper electrifying. “It hit me over the head like a hammer and has shaped my thinking ever since,” he says, convincing him to pursue the probability approach wholeheartedly.

Fuchs was especially eager to reinterpret the troubling concept of entanglement: a situation in which the quantum states of two or more particles are interdependent, meaning that a measurement of one of them will instantaneously allow the measurer to determine the state of the other. For example, two photons emitted from an atomic nucleus in opposite directions might be entangled so that one is polarized horizontally and the

other is polarized vertically. Before any measurement is made, the polarizations of the photons are correlated but not fixed. Once a measurement on one photon is made, however, the other also becomes instantaneously determined — even if it is already light years away.

As Einstein and his co-workers pointed out in 1935, such an instantaneous action over arbitrarily large distances seems to violate the theory of relativity, which holds that nothing can travel faster than light. They argued that this paradox was proof that quantum theory was incomplete.

But the other pioneers stood fast. According to Erwin Schrödinger, who coined the term ‘entanglement’, this feature is the essential trait of quantum mechanics, “the one that enforces its entire departure from classical lines of thought”. Subsequent analysis has resolved the paradox, by showing that measurements of an entangled system cannot actually be used to transmit information faster than light. And experiments on photons in the 1980s showed that entanglements really do work this way.

Still, this does seem an odd way for the Universe to behave. And this is what prompted Fuchs to call for a fresh approach to quantum foundations⁴. He rejected the idea, held by many in the field, that wave functions, entanglement and all the rest represent something real out in the world (see *Nature* **485**, 157–158; 2012). Instead, extending a line of argument that dates back to the Copenhagen interpretation, he insisted that these mathematical constructs are just a way to quantify “observers’ personal information, expectations, degrees of belief”⁵.

He is encouraged in this view by the work of his Perimeter Institute colleague Robert Spekkens, who carried out a thought experiment asking what physics would look like if nature somehow limited what any observer could know about a system by imposing a “knowledge balance principle”: no observer’s information about the system, as measured in bits, can ever exceed the amount of information he or she lacks. Spekkens’ calculations show that this principle, arbitrary as it seems, is sufficient to reproduce many of the characteristics of quantum theory, including entanglement⁶. Other kinds of restriction on what can be known about a suite of states have also been shown to produce quantum-like behaviours^{7,8}.

KNOWLEDGE GAP

The lesson, says Fuchs, isn’t that Spekkens’s model is realistic — it was never meant to be — but that entanglement and all the other strange phenomena of quantum theory are not a completely new form of physics. They could just as easily arise from a theory of knowledge and its limits.

To get a better sense of how, Fuchs has rewritten standard quantum theory into a form that closely resembles a branch of classical probability theory known as Bayesian inference, which has its roots in the eighteenth century. In the Bayesian view, probabilities aren’t intrinsic quantities ‘attached’ to objects. Rather, they quantify an observer’s personal degree of belief of what might happen to the object. Fuchs’ quantum Bayesian view, or QBism (pronounced ‘cubism’)^{9,10}, is a framework that allows known quantum phenomena to be recovered from new axioms that do not require mathematical constructs such as wavefunctions. QBism is already motivating experimental proposals, he says. Such experiments might reveal, for example, new, deep structures within quantum mechanics that would allow quantum probability laws to be re-expressed as minor variations of standard probability theory¹¹.

“That new view, if it proves valid, could change our understanding of how to build quantum computers and other quantum-information kits,” he says, noting that all such applications are critically dependent on the behaviour of quantum probability.

Knowledge — which is typically measured in terms of how many bits of information an observer has about a system — is the focus of many other approaches to reconstruction, too. As physicists Časlav Brukner and Anton Zeilinger of the University of Vienna put it, “quantum physics is an elementary theory of information”¹². Meanwhile, physicist Marcin Pawłowski at the University of Gdańsk in Poland and his colleagues are exploring a principle they call ‘information causality’¹³. This postulate says that if one experimenter (call her Alice) sends m bits of information about her data to another observer (Bob), then Bob can gain no more than m classical bits of information about that data — no

matter how much he may know about Alice’s experiment.

Pawłowski and his colleagues have found that this postulate is respected by classical physics and by standard quantum mechanics, but not by alternative theories that allow for stronger forms of entanglement-like correlations between information-carrying particles. For that reason, the group writes in their paper, “information causality

might be one of the foundational properties of nature” — in other words, an axiom of some future, reconstructed quantum theory.

What is striking about several of these attempts at quantum reconstruction is that they suggest that the set of laws governing our Universe is just one of many mathematical possibilities. “It turns out that many principles lead to a whole class of probabilistic theories, and not specifically quantum theory,” says Schlosshauer. This is in itself a valuable insight. “A lot of the features we

think of as uniquely quantum,” he says, “are actually generic to many probabilistic theories. This allows us to focus on the question of what makes quantum theory unique.”

POISED FOR SUCCESS?

Hardy says that the pace of quantum-reconstruction efforts has really picked up during the past few years as investigators begin to sense they are getting some good handles on the issue. “We’re now poised for some really significant breakthroughs,” he says.

But how can anyone judge the success of these efforts? Hardy notes that some investigators are looking for experimental signs of the higher-order quantum correlations allowed in his theory. “However, I would say that the real criterion for success is more theoretical,” he says. “Do we have a better understanding of quantum theory, and do the axioms give us new ideas as to how to go beyond current-day physics?” He is hopeful that some of these principles might eventually assist in the development of a theory of quantum gravity.

There is plenty of room for scepticism. “Reconstructing quantum theory from a set of basic principles seems like an idea with the odds greatly against it,” says Daniel Greenberger, a physicist who works on quantum foundations at the City College of New York⁵. Yet Schlosshauer argues that “even if no single reconstruction program can actually find a universally accepted set of principles that works, it’s not a wasted effort, because we will have learned so much along the way”.

He is cautiously optimistic. “Once we have a set of simple and physically intuitive principles, and a convincing story to go with them, quantum mechanics will look a lot less mysterious,” he says. “I think a lot of the outstanding questions will then go away. I’m probably not the only one who would love to be around to witness the discovery of these principles.” ■

Philip Ball is a freelance writer based in London.

1. Mermin, D. *Phys. Today* p.9 (April 1989).
2. Hardy, L. Preprint at <http://arxiv.org/abs/quant-ph/0101012> (2001).
3. Sorkin, R. D. Preprint at <http://arxiv.org/abs/gr-qc/9401003> (1994).
4. Fuchs, C. A. Preprint at <http://arxiv.org/abs/quant-ph/0106166> (2001).
5. Schlosshauer, M. (ed.) *Elegance and Enigma: The Quantum Interviews* (Springer, 2011).
6. Spekkens, R. W. Preprint at <http://arxiv.org/abs/quant-ph/0401052> (2004).
7. Kirkpatrick, K. A. *Found. Phys. Lett.* **16**, 199–224 (2003).
8. Smolin, J. A. *Quantum Inform. Comput.* **5**, 161–169 (2005).
9. Fuchs, C. A. Preprint at <http://arxiv.org/abs/1003.5209> (2010).
10. Fuchs, C. A. Preprint at <http://arxiv.org/abs/1207.2141> (2012).
11. Renes, J. M., Blume-Kohout, R., Scott, A. J. & Caves, C. M. *J. Math. Phys.* **45**, 2171–2180 (2004).
12. Brukner, Č. & Zeilinger, A. Preprint at <http://arxiv.org/abs/quant-ph/0212084> (2002).
13. Pawłowski, M. et al. *Nature* **461**, 1101–1104 (2009).

COMMENT



ADVICE A call to help policy-makers to navigate research bias **p.159**

HEALTH CARE Is patient involvement good for medicine? **p.160**

PHYSICS Film and memoir drop intriguing hints about Stephen Hawking **p.162**

EVOLUTION First volume of Richard Dawkins' memoir reviewed **p.163**

NEIL WEBB



A single market for European research

European collaboration is not far behind that in the United States, but there is still work to be done on cross-border funding and financial inequalities, says **Paul Boyle**.

Building the European Research Area (ERA) has been the priority of Máire Geoghegan-Quinn since her appointment as the European Commissioner for Research, Innovation and Science in 2009. Her mandate stipulates that the ERA should “ensure the free circulation of researchers, knowledge, ideas and technology” across the European Union (EU; see go.nature.com/qdlyri) — like an academic equivalent of the European single market for goods and services. In March 2012, the European Council called for it to be completed by 2014 (see go.nature.com/meukwn). One focus, of

particular relevance to the national funding agencies, has been on increasing researcher collaboration and mobility within Europe.

As president of Science Europe (representing 53 research-funding and -performing organizations from 27 countries) and chief executive of the UK Economic and Social Research Council (ESRC), I believe that the proposed timetable for implementing the ERA is worryingly short, particularly if changes to funding agencies and other institutional practices are necessary. I am also concerned that the changes may produce some undesirable, unintended consequences.

To agree on how much collaboration is optimal, we need to know how researchers collaborate and move within Europe. At Science Europe's request, such an analysis, produced by scientific publisher Elsevier's SciVal Analytics Team, will be released this week¹. The report shows that internal European collaboration is not far behind that in the United States, but that connections with countries outside Europe need nurturing too. Researcher mobility between institutions in different European countries is also relatively low compared with movement between US states. To further the ERA vision, we ►

► should promote best practices for cross-border funding and minimize inequalities in salaries, pensions and benefits.

In Europe, most scientific research is supported by national agencies, rather than through European or international programmes. Different agencies take different approaches to collaboration. Some allocate resources across borders: the ESRC, for example, allows up to 30% of any grant to be spent on international collaborations. By contrast, many agencies restrict their spending to their home nations, and legislation to alter this requirement would be impossible to attain by 2014, even if they wished to do so.

Some organizations pay proportionately for researchers from their country in transnational projects. One approach is that collaborators submit a proposal to a single 'lead agency', which reviews the bid and takes the funding decision. Agencies from other countries recognize the decision and pay their share. Although this is efficient, negating the need for peer review in multiple nations, problems can arise. Committing high proportions of an agency's budget on the basis of decisions taken in another nation could lead to local funding panels feeling deprived of power. Lead-agency agreements work best when those involved have similar peer-review standards, success rates and views on research priorities. Agreements cannot be imposed on unwilling partners.

STATE OF THE UNION

Comparisons are often made with the greater level of partnership across US states (see go.nature.com/w87clf). But, unlike Europe, the US states are part of a federal system, with one language, consistent labour-market conditions and a single national funding system.

To provide a benchmark, Science Europe asked Elsevier to draw on publication data

from their bibliographic database Scopus on the level of collaboration and mobility in Europe and the United States. The report¹ will be launched in Brussels on 16 September.

The analysis found that, in 2011, 13% of papers with a European primary author included co-authors from more than one country in Europe, compared with 16% of US primary-author papers that involved inter-state collaborations (see 'Affiliation trends'). This difference is small. But it is intercontinental collaborations — those that involve authors outside Europe or the United States, respectively — that tend to produce the most highly cited papers. So it is concerning that European scientists have fewer such partnerships (23% of joint papers) than their US counterparts (30%).

Relatively few academics seem to move between countries in Europe. The report finds that between 1996 and 2011, only 7% of researchers' affiliations switched between European countries, according to their addresses. In the United States, 22% of researchers published from institutions in more than one state in the same period. Barriers to movement across European borders might include language, benefits systems and cultural differences.

Although many funding agencies cannot legally allocate their resources to another nation, some have agreed a 'money follows researcher' policy, allowing researchers to transfer grants if they relocate within Europe. But even this simple scheme has challenges.

Who owns the intellectual property from the grant-funded work when a researcher moves? Why would an academic move to a country where salaries or pensions are lower?

How long would a national agency support such a policy if several researchers and their grants emigrated but few immigrated? And would the strongest researchers concentrate in the best-performing countries and institutions, perhaps increasing European excellence overall, but punishing nations that are still building their science portfolios?

Progress on various fronts is required². First, regular monitoring of researcher collaborations and movements in Europe is needed. Funding agencies, universities and the EU should work together to collect different parts of this information.

Second, best practices, drawn from the various schemes, should be adopted across Europe. These should be administratively simple and avoid double peer review, where possible. Clarity is required on terminology — even words such as 'grant' or 'evaluation' can mean different things in different organizations — and on how funding mechanisms are implemented and communicated to researchers. Science Europe's working group on cross-border collaboration is now preparing such guidance.

Third, we need a forum that brings together research-funding and -performing organizations, the European Commission and ministerial representatives from member states. Science Europe has committed to hosting such a high-level ERA workshop annually.

Fourth, European funding agencies should not overemphasize European collaboration at the expense of global partnerships. Best-with-best partnerships should be encouraged, wherever they might be.

Fifth, research-funding and -performing organizations, through Science Europe, and universities must work with the European Commission to identify and solve barriers to mobility in the labour market, welfare and administrative systems. These include issues such as pensions portability, coordination of social-security systems and transparent recognition of educational qualifications.

The ERA should be an evolving, flexible and creative space in which researchers, ideas and knowledge circulate freely to respond to society's challenges. At its heart will be trust. The establishment of Science Europe is itself testament to the willingness of European research agencies to engage in shaping a better research landscape. ■

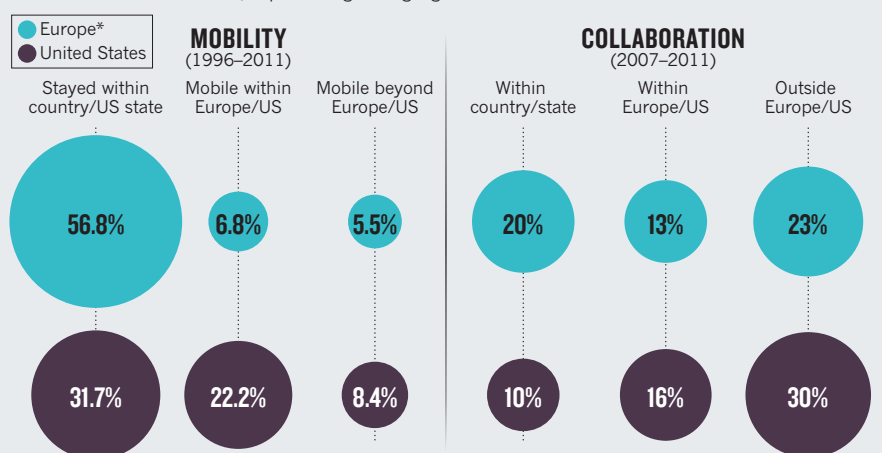
Paul Boyle is chief executive of the UK Economic and Social Research Council in Swindon, UK, and president of Science Europe in Brussels.
e-mail: esrc.ceo@esrc.ac.uk

1. Elsevier SciVal Analytics Team. *Comparative Benchmarking of European and US Research Collaboration and Researcher Mobility* (Elsevier, 2013).
2. *EUROHORCS and ESF Vision on a Globally Competitive ERA and their Road Map for Actions* (EUROHORCS, ESF; 2009).

SOURCE: REF. 1

AFFILIATION TRENDS

Researcher mobility and collaboration, revealed through publication data, are lower across Europe than across the United States, in part owing to language and cultural barriers.



*Percentages exclude transitory mobility and single-author/institute papers. Europe refers to the 41 countries eligible for Seventh Framework Programme funding: 27 EU member states and 14 associated countries.



The purported decline in bee numbers raises questions about evidence quality.

A standard for policy-relevant science

Ian Boyd calls for an auditing process to help policy-makers to navigate research bias.

The increasing concern about unreliability in scientific literature^{1,2} is a problem for people like me — I am the science adviser to DEFRA, the UK government department for environment, food and rural affairs. To counsel politicians, I must recognize systematic bias in research. Bias is cryptic enough in individual studies, let alone in whole bodies of literature that contain important inaccuracies^{2,3}.

It worries me that because of bias, some parts of the published scientific literature, such as studies on the safety of genetically modified (GM) organisms and pesticides, or trends in biodiversity measurements, might have only limited use in policy-making.

To mitigate this problem, policy-makers should consider holding published scientific evidence to an audited standard that can be replicated and is robust to variations in assessor competence. A weighting factor, or 'kite mark', applied to journals or individual articles, could help policy-makers to assess the robustness of studies for use in particular applications. Similar methods established by non-profit standards associations are used in research to certify laboratory practice and in

engineering to certify building standards.

The quality of research results fluctuates because of varying tractability in the problems being probed^{1,4}. For example, it is easy to judge the efficacy of an experiment to engineer a tomato to produce the pigment anthocyanin⁵, because if it succeeds, that tomato is the colour of a ripe plum. It is much harder to judge the reliability of a study investigating whether a GM crop is toxic to animals⁶. The latter situation is much more susceptible to inaccuracy and interpretation.

These problems are amplified in complex issues such as the environmental effects of GM organisms or chemical pollutants, including pesticides and endocrine disrupters. In these cases, experimentation is needed at scales large enough to provide statistical power in the presence of high background noise. The problem is amplified further when statistical inference is used.

SCOPING THE PROBLEM

Systematic bias across whole fields of science is even more cryptic and therefore more problematic. It could stem from the combined effects of how science is commissioned,

conducted, reported and used, and also from how scientists themselves are incentivized to conduct certain research⁷. Such bias results from actively searching for a particular outcome, rather than performing balanced hypothesis testing. For example, in 2006, researchers in the United Kingdom and in the Netherlands found that the number of insect pollinators might have declined⁸. A consequent call for proposals (see go.nature.com/audhny) contained the underlying assumption that there was a decline, rather than conveying a need to establish whether current information about declines was robust.

Another problem is the tendency to treat different studies as statistically independent, even when they have emerged from connected commissioning processes and could therefore amount to multiple testing of the same hypothesis, meaning that every extra study must overcome an increasingly rigorous statistical hurdle to demonstrate efficacy. In combination, these kinds of bias can make individual or groups of studies that report certain effects seem more important than they really are. I suspect that these effects could be a factor in the continuing controversies

surrounding genetic modification and the failure of the EU regulatory system to process applications to license new GM products.

A common reaction to such controversy is to commission subject reviews or meta-analyses¹ that assess the weight of evidence for certain effects across many individual studies. Ideally, reviewers would use processes similar to those deployed in the Cochrane Reviews that inform decision-making in health care⁹.

But reviews also contain pitfalls. First, they risk amplifying rather than eliminating systematic bias — which could be more common in some subjects than others. Second, they can be affected by the increasing tendency not to publish ‘negative’ results⁴. Meta-analyses can compound the prevalence of false positives in the literature, and can be blind to unreported true negatives. We need rules for how to deal with these issues when compiling literature reviews for policy-relevant research.

SEAL OF APPROVAL

Strict procedures govern experimental design and the evidence standards for trials that are used to determine the efficacy and safety of GM organisms, pesticides or drug therapies. But once products are licensed for use, they are often subject to less formal investigations. The same relaxation of rules applies to testing the efficacy of policy interventions. Ad hoc studies, with all the problems outlined above, can then carry disproportionate political

weight when their results question the operational integrity of a licensed product, or the effectiveness of a policy¹⁰. Quality-control criteria are needed for these studies that are outside a regulatory framework.

We need an international audited standard that grades studies, or perhaps journals. It would evaluate how research was commissioned, designed, conducted and reported. This audit procedure would assess

“What I propose augments rather than replaces peer review.”

many of the fundamental components of scientific studies, such as appropriate statistical power; precision and accuracy of measurements; and validation data for assays and models. It would also consider conflicts of interest, actual or implied, and more challenging issues about the extent to which the conclusions follow from the data. Any research paper or journal that does not present all the information needed for audit would automatically attract a low grade.

Such a system would provide policy officials and others with a reliable way of assessing evidence quality, and it would drive up standards in scientific research to reverse the worrying trends that suggest underlying bias^{1–4,7}.

Critics will counter that my proposed certification standard would be subjective and

would shift the job of assessing quality away from expert peer reviewers. But in its current form, peer review fails to set a consistent standard. What I propose augments rather than replaces peer review, and assessment could be carried out on behalf of authors, journals or users of information through the use of third-party certified auditors.

I do not underestimate the challenge of establishing such a system, but it would bring standards to scientific publishing that are common practice in other disciplines. Ultimately, this will increase the rigour and transparency around the scientific literature that is used in policy decisions. ■

Ian Boyd is chief scientific adviser at the UK Department of Environment, Food and Rural Affairs in London. He is also professor in biology at the University of St Andrews, UK. e-mail: ian.boyd@defra.gsi.gov.uk

1. Egger, M., Davey Smith, G., Schneider, M. & Minder, C. *Br. Med. J.* **315**, 629–634 (1997).
2. Begley, C. G. *Nature* **497**, 433–434 (2013).
3. Fanelli, D. *PLoS ONE* **4**, e5738 (2009).
4. Fanelli, D. *Scientometrics* **90**, 891–904 (2012).
5. Zhang, Y. et al. *Curr. Biol.* **23**, 1094–1100 (2013).
6. Doull, J. et al. *Food Chem. Toxicol.* **45**, 2073–2085 (2007).
7. Fanelli, D. *PLoS ONE* **5**, e10271 (2010).
8. Biesmeijer, J. C. et al. *Science* **313**, 351–354 (2006).
9. Jadad, A. R. et al. *J. Am. Med. Assoc.* **280**, 278–280 (1998).
10. Stokstad, E. *Science* **340**, 674–676 (2013).

Bring on the evidence

It is time to probe whether the trend for patient and public involvement in medical research is beneficial, say **Sophie Petit-Zeman** and **Louise Locock**.

Involving patients and the public as partners in medical research — from deciding what to study to influencing how results are used — is an emerging force. For some, the approach is based on common sense and justice¹. Others, such as the chief medical officer for England, Sally Davies, feel that the advice of patients and the public “invariably makes studies more effective, more credible and often more cost efficient”².

The Seventh Framework Programme (FP7), the European Union’s current research-funding instrument, stresses³ the importance of patient and public involvement, known as PPI. And the Patient-Centered Outcomes Research Institute in Washington DC has allocated US\$68 million to a research network predicated on the principle that “the interests of patients will be central to decision-making” (see go.nature.com/mdhy6i).

PPI is a prerequisite for much UK

government research funding and it is spreading among funders, health-care organizations and charities⁴. The James Lind Alliance (JLA), with which one of us (S.P.-Z.) has worked since its inception in 2004, enables patients, carers and clinicians to agree on what research matters most. It explicitly excludes the pharmaceutical industry and pure researchers. After a decade of arms-length government support, the JLA is now part of the National Institute for Health Research (NIHR) based in Southampton, UK, and JLA partnerships are complete or underway for 25 medical conditions (see go.nature.com/twhvzx). For example, the NIHR Oxford Biomedical Research Centre is running partnerships in spinal-cord injury and joint-replacement surgery, and it is the first major research institution to be appointing staff to use the JLA method ‘in house’, closing the loop between what matters to

patients and what is researched in their name.

This international growth of PPI is rightly paralleled by unease at the paucity of evidence for its impact. And the evidence there is, including the findings that PPI improves recruitment to studies and changes what is researched^{2,5}, is weak. As Simon Denegri, the United Kingdom’s first national director for public participation and engagement in research, put it: “The evidence-base for PPI’s impact is meagre, patchy and largely observational.”

SELF-EXAMINATION

Those of us working in PPI must robustly examine our own practices with a common set of tools. Otherwise, we will struggle to answer PPI sceptics, such as one researcher who asked: “Why should patients have useful opinions about what directions research should take?”⁶.

A first crucial step is to ensure consistent, accurate reporting of what PPI has been done and how. We can assess whether an activity is useful only if it is clear what it was.

This challenge is being addressed through GRIPP⁷ (Guidance for Reporting Involvement of Patients and Public), a checklist published in 2011 for studies that include PPI to help authors and readers to critically appraise the work. GRIPP is being used to generate consensus through the EQUATOR Network, an international initiative that promotes the development and spread of guidelines for health-research reporting⁴.

A key element of reporting PPI is to make clear who was involved, in part to allow us to gauge when it matters to distinguish between public and patient input. One demonstrable effect of PPI is that it helps to create user-friendly information, questionnaires and interview schedules for patients⁵. But this sort of reality check about jargon differs from gathering and heeding patient experiences.

We must also probe whether PPI is valuable for all research types. Will it ever, for example, have a place in basic science? Anecdotal evidence suggests that it might, in part because patients push for research into causes. The UK Alzheimer's Society, the only funder that works with people with dementia and their carers to select research projects, backs work from the lab bench to the clinic. And priorities in sight-loss research, identified through the JLA approach, revealed patient interest in causation, as well as treatments using stem cells and gene therapy.

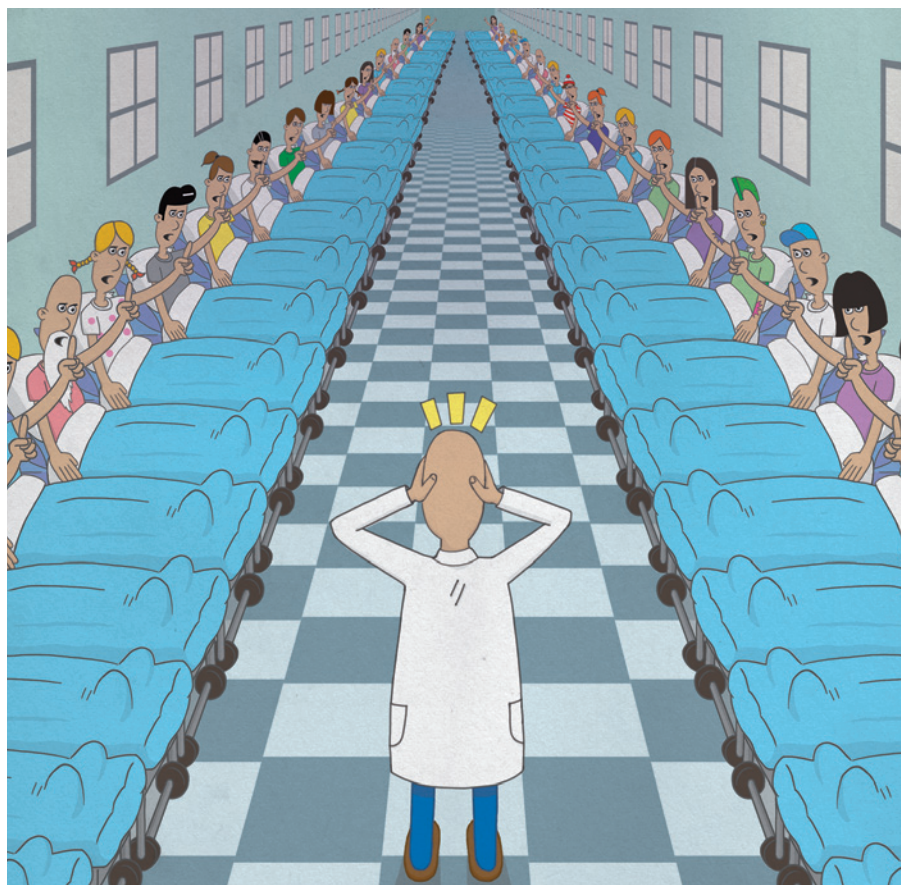
One of the knottiest problems in PPI is how to best weigh up anecdotes and evidence. How are the patients involved chosen? Do they bring more than their own views? Are diverse voices heard, or just those that are loudest?

Ignore such questions, and PPI might unwittingly perpetuate power imbalances. Patients can achieve involvement through existing networks, but not all will be part of these, or they might be chosen by a researcher who is keen to work with a kindred spirit. The most well-meaning approaches can simply extend input from educated, middle-class professionals to input from educated, middle-class patients.

Yet we must also avoid double standards. Just as people will always want the best researchers or clinicians, we must not exclude the most informed or articulate patients⁶.

There is no easy fix, but the ability of involved patients to represent wider views can be optimized through routes such as the website www.healthtalkonline.org, led by the University of Oxford's Health Experiences Research Group (HERG), where one of us (L.L.) is deputy research director.

Healthtalkonline and its sister site, www.youthhealthtalk.org, contain video,



audio and written records of nearly 3,000 people's experiences of more than 75 health-related issues. The websites allow patients and professionals to broaden their knowledge of what it is like to be ill or to make difficult health-care decisions.

Using qualitative research, interviews with subjects continue until no major new themes emerge, indicating that a comprehensive set of views has been gathered. As Sue Ziebland, HERG's research director, explains: "Supporting patients involved in research to draw from a pool of views helps defend them from accusations that they bring only their own agenda."

BUILDING A CASE

Gathering the evidence base for PPI will take time. The methodological issues described here must be addressed, and the crucial question — whether research using PPI makes life better for patients — is complex. A project funded by the UK Medical Research Council last week launched its Public Involvement Impact Assessment Framework, a resource to support research teams to develop impact-assessment tools appropriate for their work.

As PPI matures, we must find ways to ensure that those who do it, be they professionals, patients or public participants, are offered support and training — perhaps most crucially to help them to understand each others' worlds. We must then report,

dissect and assess involvement, devising impact measures with patients as partners, in ways that optimize the potential of patient-centred science. ■

Sophie Petit-Zeman is director of patient involvement in research at the NIHR Oxford Biomedical Research Centre, Oxford University Hospitals NHS Trust, UK.

Louise Locock is deputy research director, Health Experiences Research Group, Department of Primary Care Health Sciences, University of Oxford, UK.
e-mail: sophie.petit-zeman@ouh.nhs.uk.

1. Chalmers, I. *Br. Med. J.* **310**, 1315–1318 (1995).
2. Staley, K. *Exploring Impact: Public Involvement in NHS, Public Health and Social Care Research* (INVOLVE, 2009).
3. European Commission. *FP7 Cooperation Work Programme: Health 2013* (EC, 2012).
4. Staniszewska, S. & Denegri, S. *Evid. Based Nurs.* **16**, 69 (2013).
5. Brett, J. *et al. Health Expect.* <http://dx.doi.org/10.1111/j.1369-7625.2012.00795.x> (2012).
6. Petit-Zeman, S. & Uhm, S. *Infant* **8**, 71–72 (2012).
7. Staniszewska, S., Brett, J., Mockford, C. & Barber, R. *Int. J. Technol. Assess. Health Care* **27**, 391–399 (2011).
8. Lindow, V. in *Ethics and Community in the Health Care Professions* (ed. Parker, M.), 154–172 (Routledge, 1999).

The views expressed are those of the authors and not necessarily those of the National Health Service, the National Institute for Health Research or the UK Department of Health. The authors declare competing financial interests: see go.nature.com/jedv2a for details.



Stephen Hawking, the subject of both a new memoir and a documentary film.

PHYSICS

A cosmological life

Robert P. Crease weighs up two takes on Stephen Hawking — including the theoretical physicist's own.

True to its name, Stephen Hawking's autobiography *My Brief History* is a model of brevity, at just 20,000 words. A new documentary about the renowned theoretical physicist, *Hawking*, takes longer to watch than the book does to read. These separate projects add little to our understanding of Hawking, but do feed our insatiable curiosity about him.

Both vehicles do a creditable job of reviewing the outlines of Hawking's story, which is a compelling one. In 1963, while a graduate student at the University of Cambridge, UK, Hawking learned that he had motor neuron disease (known in the United States as Lou Gehrig's disease). In 1970, he began work on the theory of black holes, predicting in 1974 that they emit radiation and could therefore potentially evaporate: 'Hawking radiation' is probably his most significant scientific contribution. Gradually losing mobility and speech, he survived thanks to an indomitable spirit, devoted assistants and increasingly sophisticated technology. (He wrote the memoir using a sensor attached to his glasses that responds to cheek-muscle twitches.) Hawking's *A Brief History of Time* (Bantam, 1988) is surely the most popular science book ever. And he has become, to the public, the greatest living scientist — as well as a media

My Brief History

STEPHEN HAWKING
Bantam: 2013.

Hawking

DIRECTED BY STEPHEN FINNIGAN
Cambridge Film Festival, UK, 19 September 2013.

magnet who enjoys making outrageous claims ("Philosophy is dead").

Meanwhile, Hawking has a solid, if not superhuman, reputation among scientists. In 1999, a *Physics World* survey asked eminent physicists to name the five physicists they thought had made the most significant contributions. Of the 61 named — 11 of them living — Hawking received only one vote.

My Brief History does not do what we expect of a memoir. It does not take the reader behind any scenes. Hawking narrates his life non-introspectively, celebrating its triumphs and burnishing its sensitive moments. It is a concise, gleaming portrait, not unlike those issued by the public relations department of an institution. "Not knowing what was going to happen to me or how rapidly the disease would progress, I was at a loose end," he writes of his reaction to being diagnosed. Nor is he reflective about his relationships with his ex-wives Jane Wilde and Elaine Mason. "My marriage

to Elaine was passionate and tempestuous," he writes. "We had our ups and downs."

The book provides no revelations, deep insight, messy details or score-settling, and does not explore his celebrity status. Hints of emotion are rare. At one point he recalls thinking himself a tragic figure, and begins to listen to Wagner. At another he remembers seeing a boy in the hospital bed next to him die of leukaemia. "Whenever I feel inclined to be sorry for myself, I remember that boy." You sense something like a soul behind Hawking's dispassionate account, but, like a black hole, its existence has to be deduced from external indications.

Hawking, directed by Stephen Finnigan, is a good celebrity biopic. In it, Hawking narrates many of the same events as in *My Brief History*, often in the same words. But the film is diverting in a way that the book is not: we get to see clips of Hawking's appearances as himself or in cartoon form on US television shows such as *Star Trek* and *The Simpsons*. We hear Wagner and Pink Floyd on the soundtrack, watch re-enactments of episodes from Hawking's early life, and see a snapshot of Hawking with President Obama and First Lady Michelle.

Hawking's synthesized voice can lend an aura of gravitas to words that would come off as platitudes on the page. "When you are faced with the possibility of an early death, it makes you realize that life is worth living," he says. Occasionally, even the synthesizer cannot rescue his pronouncements from sounding naive: "Sometimes I wonder if I am as famous for my wheelchair and disabilities as I am for my discoveries." The film concludes with spectacular footage from the 2012 Paralympics in London, at which Hawking opened the ceremonies.

These two offerings add to a growing list that do offer new knowledge about the cosmologist. Jane Hawking's *Travelling to Infinity* (Alma Books, revised, 2008) divulges aspects of their relationship. Kitty Ferguson's *Stephen Hawking: An Unfettered Mind* (Palgrave Macmillan, 2012) explores his life and illness. Hélène Mialet's *Hawking Incorporated* (University of Chicago Press, 2012) analyses the networks of people, media and technologies without which there would be no Stephen Hawking as we know him.

Mialet demolishes the popular myth of Hawking as a solitary genius. But it is an irresistible one. "Thank you for coming on a journey through my world," Hawking says at the conclusion of the documentary. In truth, *Hawking* is a carefully stage-managed tour of only part of that world, yet it is a skilful, entertaining and moving trip nonetheless. ■

Robert P. Crease is professor of philosophy at Stony Brook University, New York, and author of *World in the Balance*.
e-mail: robert.crease@stonybrook.edu

BIOLOGY

Evolution of a mind

Eugenie C. Scott revels in the first volume of Richard Dawkins's frank new memoir.

Richard Dawkins is one of the world's best-known scientists — largely because of his tireless promotion of evolution and, more recently, atheism, through a succession of best-sellers, videos and public appearances. In *An Appetite for Wonder*, the first part of a two-volume memoir, Dawkins presents his life up to the publication of *The Selfish Gene* (Oxford University Press, 1976), the popular-science blockbuster that kick-started his career as a spokesperson for evolutionary biology.

As befits someone whose life's work has focused on the cumulative changes through time that we call evolution, Dawkins wants to share the forces and factors in his life that have shaped the person he has become. A bookish child, he neglected many opportunities provided by his nature-loving parents to explore and be inspired by the natural world. Given that he was born in Nairobi and spent his early years in what is now Malawi, it seems curious that the natural abundance around him did not kindle that spark. He does speak of developing a fondness for animals, but more through reading children's books such as Hugh Lofting's *Doctor Dolittle* series, noting, "I learned late to love watching wild creatures, and I have never been such an outdoor person as either my father or my grandfather."

The African interlude came about because Dawkins's father, Clinton John Dawkins, followed family tradition by working in the British foreign service. Dawkins presents his father, who was a forester, as independent, resourceful, inventive and willing to take big risks. When a distant relative unexpectedly bequeathed to John Dawkins the country estate Over Norton Park in Oxfordshire, UK, he moved the family back to England, renounced his government pension and turned the land into a working farm. Richard, then eight, was soon packed off to boarding school.

The picture Dawkins paints of his schools is, if not quite Dickensian, pretty awful: little boys lining up naked for cold morning baths, shivering in unheated rooms, choking down bad-tasting food, enduring corporal punishment and bullying, and not always receiving a sterling education. Dawkins was, he

confesses, an indifferent student, but a few teachers managed to stimulate an interest in science. It is clear that he did not come into his own intellectually until he was admitted — by the skin of his teeth — into the University of Oxford. There, at Balliol College, Dawkins was lucky enough to be tutored by the great ethologist Nikolaas 'Niko' Tin-

book put the young Dawkins on that short list of scientists who are able to make complicated scientific ideas understandable and exciting without oversimplifying them.

Dawkins is a polarizing figure, both widely praised and widely criticized. Supporters as well as detractors may be surprised at the honest depiction of an individual who comes across as both less saintly and less diabolical than media caricatures may have led them to expect. He loves poetry, and readily confesses to choking up when reading sentimental verse such as Hilaire Belloc's 1910 *To the Balliol Men Still in Africa*. He reflects with chagrin on his lack of concern about the rampant bullying that took place at his schools, and his support of what he now considers the bullying of some Berkeley faculty members by radical professors and students during the Vietnam War protests. Of the Berkeley experience, he notes, "I was still young, but not all that young. Should have known better." He readily confesses that scientific habits were slow in coming. It is a very honest book.

Charles Darwin wrote his autobiography for his family; for whom is Dawkins's written? I found the enumeration of ancestors in early chapters a bit of a slog. The middle chapters describing his childhood in Africa and school days in England should be of interest to all. The latter chapters, dealing with his mathematical modelling of evolution, might appeal more to scientists.

Dawkins's atheist fans are not all necessarily in that camp, and might find the graphs and diagrams of behaviour patterns daunting.

However, throughout and as usual, Dawkins's writing is graceful, sparkling with anecdotes and wit. Those of us who struggle in our writing will be comforted to read the words: "Pretty much every sentence I write is revised, fiddled with, re-ordered, crossed out and re-worked." In other words, the elegant, functional design of his writing is accomplished through variation and selection. Why am I not surprised? ■

Eugenie Scott is executive director of the National Center for Science Education in Oakland, California.
e-mail: scott@ncse.com



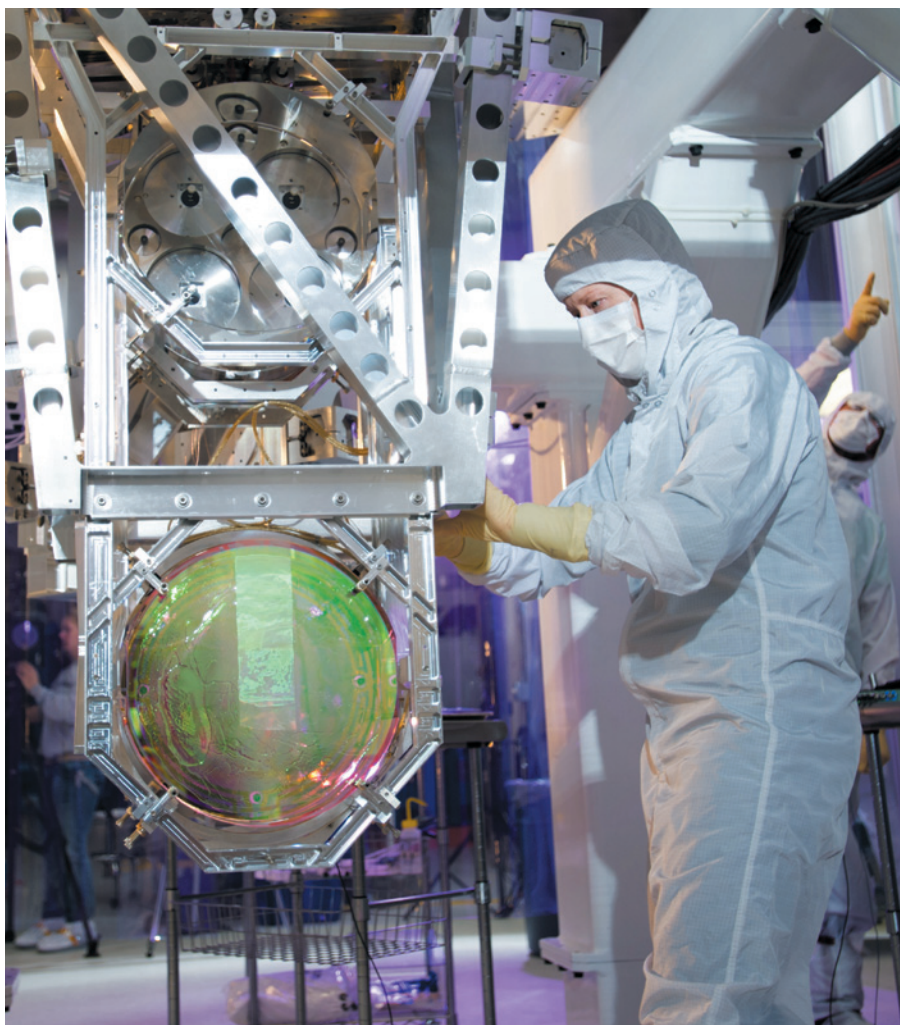
Richard Dawkins studying mating calls in crickets in 1976.

bergen, and became fascinated by animal behaviour.

The latter part of the book traces Dawkins's intellectual path from Oxford to his assistant professorship in zoology at the University of California, Berkeley (where he was swept up in the movement against the Vietnam War), and his return to Oxford as a young scientist. It describes his transition from a quantitatively oriented computer-programming experimentalist who modelled chick behaviour to the more theoretically oriented scientist we know today. I doubt if more than 1 in 10,000 readers of *The Selfish Gene* ever read his earlier experimental work. (I hadn't, either.) Inspired by the 1970s ferment over group and individual selection, kin selection and the like, that

An Appetite for Wonder: The Making of a Scientist

RICHARD DAWKINS
Bantam: 2013.



Researchers working at the Laser Interferometer Gravitational-Wave Observatory.

SOCIOLOGY OF SCIENCE

Chasing the gravitational wave

Marianne de Laet enjoys a sociological analysis of how a select group of physicists works.

In *Gravity's Ghost and Big Dog*, British sociologist Harry Collins documents the astrophysical search for the elusive gravitational wave. In part an account of sociological fieldwork among scientists in the field and part astronomy-history mystery, Collins's book is a terrific read informed by almost 40 years of research.

The book homes in on two sudden energy surges, thought to be the first truly significant detections of gravitational-wave signals, that got the astrophysics community in a stir: the

Equinox Event in 2007 and Big Dog in 2010. The book's first part was previously published in 2010 as *Gravity's Ghost* (University of Chicago Press), a stand-alone account of the Equinox Event. The new, second part documents the frenzy over Big Dog — so named because the signal was bigger than the 2007 surge and seemed to come from the constellation Canis Major — when the stakes were higher and the future of the field hung in the balance. As an 'embedded' observer, participant, apprentice and analyst working

among the astrophysicists, Collins reports on meetings, telephone conferences, e-mail discussions and social events. By conversing with and analysing scientists at research facilities, scientific conferences and home institutions, he offers a glimpse of the ways in which knowledge is made in this esoteric field.

Predicted by Albert Einstein's general theory of relativity, first published in 1915, gravitational waves are formed when the mass of an imploding star disappears, causing ripples in space time. Ground-based interferometers built to detect them have been in use for decades, but Collins focuses on the Laser Interferometer Gravitational-Wave Observatory (LIGO), which has sites at Hanford, Washington, and Livingston, Louisiana.

Two questions drive the narrative: are the signals real? And do they prove that gravitational waves exist? Collins lets us in on the conversations among the scientists. At times, they focus on the rigour of statistical margins by asking at which margin error can be ruled out; at others, they discuss the semantics of knowing, pondering whether they are confronted with observation, evidence or fact. He intersperses these exchanges with historical information and his own sociological analysis of gravitational-wave research. As the astrophysicists debate the two detection events, it emerges that deciding whether a gravitational wave exists is not just a matter of observation, calibration and learning to understand LIGO's idiosyncrasies. It also involves semantics, political considerations and attending to expectations from funders, media and the public.

A debate among key collaborators about how to announce Big Dog is a case in point. The degree of certainty with which a finding is announced sets expectations, and these find their way into the rationales for retooling or building new instruments. The validity of past research, the promise embedded in future instruments and scientific reputations are all explicitly at stake in the exchanges among the collaborators. Collins has turned the minutiae of these conversations into an exciting detective story.

Collins finds himself immersed, learning so much science that he becomes a force to be reckoned with. His queries are pertinent to the research and, by his own account, that gets the scientists to rethink strategies or interpretations of their findings. Collins even tries his hand at physics, and suggests an alternative strategy for some of the calculations for Big Dog. Flirting with the



Gravity's Ghost and Big Dog: Scientific Discovery and Social Analysis in the Twenty-first Century
HARRY COLLINS
University of Chicago Press: 2013.

LIGO LABORATORY

science, he begins to think not only about the astrophysicists, but with them. With Collins, we begin to wonder what it takes to be an expert in the field.

In social science, going native in this way is a tricky business. In an effort not to alienate his subjects, the sociologist may end up relying too much on the group's own interpretations of their actions, leading to less insightful renderings of their world. If, by contrast, he lacks credibility with the group, his presumption to reveal something new may offend. Collins walks a tight line deftly; although his interlocutors are somewhat incredulous at his

"Collins learns so much science that he becomes a force to be reckoned with."

efforts to do physics, the group does engage with them.

That does not make Collins an expert within their culture — only about it. And here, in trying to justify his calculations by asserting that they are not far off, he violates a golden rule of the sociology of science. Understanding the process of knowledge-making is not predicated on whether the knowledge in question is right or wrong. At the same time, Collins defies a best practice of anthropology — to examine one's motifs and motivations. He is not the first researcher in the sociology of science whose observation of scientific expertise turns into the desire to possess it. This interesting feature of the analysis of science remains unexamined in Collins's book.

That said, Collins's respect for science compels him to make a lovely observation: that there is something admirable about the modes of science — its aspiration to honesty, persistence and truth-seeking — and that this should serve as a moral and epistemological model for how to behave. And if, as US anthropologist Stefan Helmreich suggests in his book *Silicon Second Nature* (UC Press, 1998), social analysis of science enables participants to "recognize something new of themselves", Collins's serial monograph is on point. It tells of scientists who are well aware of their own practices — perhaps not least as a result of having a sociologist in their midst. ■

Marianne de Laet is an associate professor of anthropology and science, technology, and society at Harvey Mudd College in Claremont, California, USA. She observed the emerging collaboration of the California Extremely Large Telescope, renamed in 2003 as the Thirty Meter Telescope.

e-mail: delaelaet@g.hmc.edu

PSYCHOLOGY

Mapping memory's lanes

Alison Abbott sees the science and poetry in a penetrating study of reminiscence in the elderly.

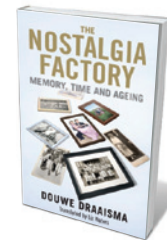
In 1688, Swiss physician Johannes Hofer coined the term nostalgia to describe the clinical symptoms of homesickness. Hofer linked the Greek words *nostos*, for homecoming, and *algia*, for pain. Nostalgia could even be life-threatening, he noted. In *The Nostalgia Factory*, psychologist Douwe Draaisma touches on this phenomenon in his exploration of memory and ageing, which draws on scientific work and anecdotal case studies.

He tells of the Dutch emigrants after the Second World War who, crippled by homesickness, later found that return offered no respite: 'home' no longer matched their memories of it. He describes the twentieth-century emigration agencies as 'nostalgia factories'. But the real nostalgia factory, he says, is time — which "makes emigrants of us all". In old age, memories are all that remain of the land of our youth, even if we never left home. His beautifully written book attempts to capture the nebulous essence of reminiscence in eight elegant, authoritative essays.

Draaisma's style is both literary and scientific. It calls to mind the works of Oliver Sacks, who popularized neuroscience through the intriguing stories of his neurological patients. (In fact, one of Draaisma's essays is based on a conversation with Sacks about "what time does to memories and what memories do to time".) But Draaisma's style is perhaps the more poetic, which is what makes the powerful insights in his book so penetrating.

It is disconcerting to learn from Draaisma how unstable and adrift our own biographies are: we constantly reconstruct our lives as our memories are refiltered through new experiences. Draaisma offers both reassurance and warnings. Forgetting names rarely foretells dementia, and many old people who describe themselves as forgetful have a well-functioning memory when tested objectively. But claims that food supplements, enriched environments or computer training programs can halt the natural process of harmless age-related forgetfulness are hokum. "Anyone who thinks that such tricks ... can actually give them a better memory probably also thinks they would be able to walk better if they used a walking frame," notes Draaisma.

For many, *The Nostalgia Factory* will be what Draaisma refers to as a 'decisive' book, one that changes one's perspective on life. Or maybe that would be true only for the young? Because in this book we also learn



The Nostalgia Factory: Memory, Time and Ageing
DOUWE DRAAISMA
Yale University Press:
2013.

about the 'reminiscence-curve bump'.

Modern psychological research into reminiscences uses cue words — such as 'flag' or 'circus' — to prompt memories in elderly people, and researchers then date these to the year they happened. The number of memories recalled for each age, beginning at age three or four, follows a predictable

pattern. Numbers rise to a peak at around 20 years old, then fall rapidly, flattening out at an alarmingly low level well before middle age. The curve rises again in later life, when people recall things simply because they happened recently. Middle age barely registers.

So it is not surprising that most people, if asked to name a decisive book, cite one they read before they were 23 — a time they will also describe, unprompted, as 'their era', when pop music was best. Its reflection can be seen in almost all autobiographies. In *Peeling the Onion* (Harville Secker, 2007), Nobel-prize-winning author Günter Grass devotes the majority of pages on the first 30 years of his life to those between the ages of 17 and 21.

Draaisma argues that the bump in the reminiscence curve has less to do with the ability of the young adult brain to store memories efficiently and more to do with the quality of memories accrued as we set out on independent adult life. Indeed, the bump advanced by more than a decade in a study of people who had migrated in their mid-thirties. Sacks, who emigrated from England to the United States in the 1960s at the age of 27, muses in his conversation with Draaisma that when he recorded his own year-by-year reminiscences during long driving trips, his tapes for the 1970s overflowed, but thereafter the length of the tape "decreased almost linearly".

Rigorous psychological research into the reminiscence phenomenon, whether healthy or distorted, is relatively new. This short book shows that it can reveal much about who we are at different stages of our lives. ■

Alison Abbott is Nature's senior European correspondent.

Correspondence

Turkey's scientists can't ignore politics

Given the severity of the political problems that scientists face in Turkey, academics need to become more politically involved — not less, as you suggest — to help bring about reform to the country's academic system (see *Nature* **500**, 253; 2013).

There is no clear evidence to support your implication that the debate over the headscarf ban in Turkish universities has affected the quality of their scientific research. Other long-standing impediments are the real culprits.

Scientists in Turkey have had to contend for years with a lack of academic freedom and transparency in grant-review and faculty-recruitment processes. The small size of the academic community and a clumsy bureaucracy further obstruct the nation's research potential.

There are some notable successes, however. Contrary to your description of Boğaziçi University as “cash-starved”, in 2010 researchers there gained funding of close to US\$13 million, of which more than \$2 million came from highly competitive international sources (see go.nature.com/wik8xn).

Ozan Aygün *Massachusetts Institute of Technology, Cambridge, USA.*
oyaygun@mit.edu

Transcranial devices are not playthings

Controlled investigation of transcranial direct-current stimulation (tDCS) for treating neuropsychiatric disorders or for neurorehabilitation should not be confused with improvised devices or practices that apply electricity to the brain without reference to established protocols (see *Nature* **498**, 271–272; 2013). Unorthodox technologies and applications must not be allowed to distort the long-term validation of tDCS.

Experimentation outside

established and tested norms may put subjects at risk. In tDCS, the delivered dose of electrical brain stimulation (defined by the waveform and intensity applied) and the electrode size, number and position are all crucial. Safe and effective dose ranges have been established in clinical trials. Patients receiving tDCS do so in a controlled environment, under guidance from institutional ethics review boards and with strict criteria for patient inclusion.

Meddling with the tDCS dose is potentially as dangerous as tampering with a drug's chemical composition. Painstaking efforts by researchers to understand the risks and benefits of tDCS should never be interpreted as encouraging such practices.

Marom Bikson *City College of New York, USA.*

bikson@ccny.cuny.edu

Sven Bestmann *University College London, UK.*

Dylan Edwards *Burke–Cornell Medical Research Institute, New York, USA.*

M. B. declares competing financial interests: see go.nature.com/lxuxfq for details.

Don't compromise on informed consent

I urge researchers responding to the call for information about sharing data sets (M. Bobrow *Nature* **500**, 123; 2013) to defend the important principle of informed consent by patients participating in medical research.

The UK Health and Social Care Act 2012 requires the transfer of all National Health Service electronic medical records in England from general practitioners to the Health and Social Care Information Centre. The biomedical research charity the Wellcome Trust and the Human Genomics Strategy Group have proposed that variant files, which contain whole human genomes minus the Sanger Institute reference genome, should be attached to the records.

The UK government's

intention is to share these data with accredited researchers — ranging from the Google-funded gene-testing company 23andMe to private health-care companies and Chinese research institutes — but without people's knowledge or consent.

Most data will be ‘pseudo-anonymized’, with some identifiers (such as names) stripped out, but with the ability to link back to the individual retained. People can opt out of this data-sharing system (see go.nature.com/azkyru), but that will in effect prevent members of the public from taking part in medical research.

Abandoning informed consent is unlikely to benefit biomedical research (J. P. A. Ioannidis *Am. J. Bioethics* **13**, 40–42; 2013). Researchers could face a dwindling source of data as people withdraw from participation to protect their confidentiality.

Helen Wallace *GeneWatch UK, Buxton, UK.*

helen.wallace@genewatch.org

HeLa genome versus donor's genome

I contend that the continual divergence of chromosomal features (‘karyotype’) and DNA sequence in dynamic cancer-cell populations undermines debate over ownership of the HeLa cancer-cell line derived from Henrietta Lacks six decades ago (see *Nature* **500**, 121 and 132–133; 2013).

The HeLa genome is no longer Henrietta Lacks's personal genome. Although the two share some DNA sequences, the similarity ends there. Lacks's genome had the usual number of 46 normal chromosomes, whereas most HeLa cells have 70–90 chromosomes and more than 20 translocations, some of which are highly complex.

Changes in the HeLa genome in the past few decades have resulted from multiple cycles of genome reorganization during

the cancer process and from the initial cell-culture experiments. Considering that chromosomes provide the genome identity and blueprint, it might even be argued that the HeLa genome is no longer a human genome.

Henry H. Heng *Wayne State University School of Medicine, Detroit, USA.*

hheng@med.wayne.edu

A forgotten history of sex research

Elizabeth Pollitzer's point about sex mattering in all areas of biology has long been considered an important topic (see *Nature* **500**, 23–24; 2013).

For example, the Endocrine Society's flagship journal *Endocrinology*, of which I am editor-in-chief, has since 2012 required authors to include the sex of animals, tissues and even cell lines in their papers (J. D. Blaustein *Endocrinology* **153**, 2539–2540; 2012). Authors must justify the use of single-sex animals or tissues, and consider sex in interpreting their data.

Research in neurobiology and psychology has also consistently recognized sex differences in physiology, pathophysiology, pharmacology and toxicology (see, for example, G. E. Gillies & S. McArthur *Pharmacol. Rev.* **62**, 155–198; 2010). The US National Institutes of Health supports such research and has emphasized its importance in programme announcements.

From 1922, the US Committee for Research in Problems of Sex was funded by the Rockefeller Foundation for decades. In 2006, the Organization for the Study of Sex Differences, based in Atlanta, Georgia, was founded for researchers and clinicians.

Studies on sex differences published before the PubMed online archive, electronic journals and searchable keywords should not be overlooked.

Andrea C. Gore *University of Texas at Austin, USA.*
andrea.gore@austin.utexas.edu

Anthony James Pawson

(1952–2013)

Biochemist whose vision of cell signalling transformed cancer research.

Tony Pawson's research on protein interactions transformed the thinking about how cells communicate, how proteins evolve and how cellular messaging goes awry in cancer. A creative experimenter, his synthesis of diverse observations in areas from biochemistry to mouse genetics and developmental biology led to a coherent picture of how cellular processes work.

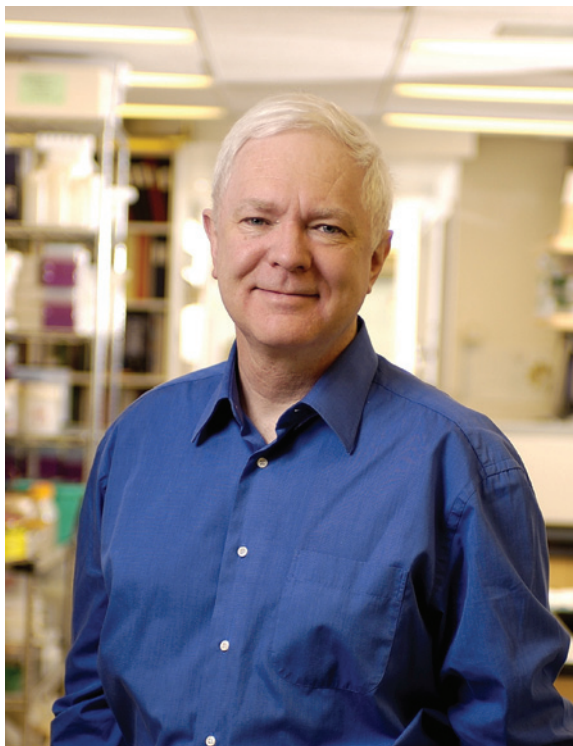
In the 1980s, early in his career, Pawson and his team discovered the Src homology region 2 (SH2). A subunit, or domain, of many proteins, SH2 directs how proteins interact and governs how cells respond to external cues. This finding set a path for all his future work.

Pawson went on to show that combinations of a small number of domains could produce an enormous range of cellular responses. This 'modular' vision reshaped scientists' understanding of cellular regulation and paved the way for the development of drug classes that interfere with these protein interactions.

But recognition did not come immediately for Pawson. The existence of modular binding domains, now standard textbook fare, was initially received with scepticism by biochemists, and with benign neglect by molecular biologists. But as the evidence, largely from Pawson's lab, grew more compelling, it could no longer be ignored.

Pawson, who died suddenly at home on 7 August aged 60, was born in Maidstone, UK, to an eminent British family. His father, to some the more famous Tony Pawson, was a champion sportsman and a household name in Britain. A fly fisher, cricketer, footballer and, later, sports writer, his multivalent skills loomed large for the younger Pawson, who was often mistaken for his father. It was his mother, Hilarie, a biology teacher, who stimulated his interest in science.

Pawson read biochemistry at the University of Cambridge, UK, and obtained his PhD in 1976, working with Alan Smith at the Imperial Cancer Research Fund (now Cancer Research UK) on proteins encoded by the Rous sarcoma retrovirus. While visiting a friend in Cambridge, Tony met his American wife-to-be, Maggie. They married in 1975, and in 1976 moved to Berkeley, California,



where Tony began postdoctoral work on the protein products of avian retroviruses.

In 1981, the couple moved to Vancouver, Canada, where Pawson was assistant professor in the department of microbiology at the University of British Columbia. Pawson's lab became immediately productive, publishing important papers on oncoproteins — proteins coded by genes that have the potential to cause cancer. There, Pawson struck up collaboration with Mike Smith, a Nobel-prizewinning chemist who invented the technique of site-specific mutagenesis that Pawson used in his SH2 discovery.

In 1985, when a research institute was launched at the Mount Sinai Hospital in Toronto (now the Lunenfeld–Tanenbaum Research Institute), Pawson joined us as one of the first appointments in its molecular and developmental biology division. With the addition of developmental biologist Alexandra Joyner and the late molecular biologist Martin Breitman, the five of us — young, ambitious and with a pioneering spirit — knew that we were building something important.

The division was created at a propitious time: developmental biology was about to be transformed by the latest genetic technologies

from a descriptive to a mechanistic science, and cancer research was accelerating with the discovery of oncogenes, tumour-suppressor genes and related signalling pathways. The two fields were about to converge with the discovery that the normal equivalents of viral oncogenes have crucial roles in embryo development.

Within a few years, the division grew from having just a handful of students and postdocs to having more than 100 members. Pawson was at the centre, partly because cell signalling was core to all our science, but largely because he loved to collaborate. To him, collaboration was as much about camaraderie and friendship as it was about getting a piece of science done. Working with Tony was fun, and although he was invited to give ten times the number of talks as everybody else, he would always give credit to his collaborators.

Pawson's seminars were virtuoso performances, and they were eagerly attended. His talks and more than 450 published papers were not just assemblages of data, but elegantly

presented expositions of how cells and organisms evolve, develop and function. At the time of his death, he was one of the most highly cited biomedical researchers.

When Pawson received the Heineken Prize for biochemistry and biophysics in 1998, he spoke at the ceremony in Amsterdam about the joy of discovery, the privilege of working with talented young people, the potential for advances to lead to new treatments for disease, and about the importance of family in a scientist's life. One could have heard a pin drop.

Our strongest memories of Tony are in those early years at the Lunenfeld, sharing our latest results, writing grants, exchanging gossip and sharing family joys and sorrows — and watching Tony gesticulating wildly with his arms when he got excited. His enthusiasm was infectious. He will be greatly missed. ■

Alan Bernstein is president and chief executive officer of the Canadian Institute for Advanced Research in Toronto.

Janet Rossant is chief of research at the Hospital for Sick Children in Toronto.
e-mails: abernstein@cifar.ca;
janet.rossant@sickkids.ca

UNIV. TORONTO

The mathematics of murder

A mathematical model of gun ownership has been developed that clarifies the debate on gun control and tentatively suggests that firearms restrictions may reduce the homicide rate.

ADELINE LO & JAMES H. FOWLER

The mass killing of 20 children and 6 adults on 14 December 2012 at Sandy Hook Elementary School in Newtown, Connecticut (Fig. 1), has revived an enduring controversy about gun control in the United States. Gun-control advocates believe that widespread gun ownership increases the rate of gun-related crime and homicide, whereas critics argue that gun availability actually decreases gun violence because potential assailants are less likely to commit such crimes if they believe citizens are armed. But who is right? In an article published in *PLoS ONE*, Wodarz and Komarova¹ describe an elegant and highly parsimonious mathematical model designed to answer exactly this question. And, in an extremely cautious way, they suggest that more guns make things worse.

The scientific literature suggests that gun homicides are influenced by various interwoven factors, including the rate of legal and illegal gun possession, the national prevalence of armed and unarmed attacks, the likelihood of fatalities in such attacks, and the quality and quantity of general law enforcement^{2–5}. Gun-control policy is clearly only one key variable in a complex social system. But work on the issue is typically conducted by scholars who collect data on types of gun-control policy and numbers of gun homicides, and look for correlations while controlling for certain important variables — such as whether the locations of the homicides are rural or urban, or whether it is easy to obtain arms illegally.

The problem is that many of these correlations are difficult to interpret. If gun deaths are higher in states with stricter gun-control laws, is this because gun restrictions cause higher crime or because politicians react to higher crime by enacting more restrictions? It is with this difficulty in mind that Wodarz and Komarova have created their formal model of gun ownership.

The modelling of complex social



Figure 1 | A prayer vigil for the victims of the Sandy Hook shooting.

phenomena is not new. As early as 1974, the economist Gary Becker took a supply-and-demand approach to the 'production' of crime and punishment, using his model to show how crime might be minimized with various public and private policies that make criminal behaviours 'costly'⁶. But Becker's analysis did not explicitly tackle the thorny problem of gun control, and the scholars who followed also tended to focus more on abstract models.

By contrast, Wodarz and Komarova's model is explicitly designed to address gun-control policies and their effects. At the core of the model is the rate of gun ownership. Strict laws might lower the rate and permissive laws might increase it, but the mechanism itself does not matter — the goal of the model is to clarify what assumptions are necessary to measure the effect of overall gun ownership on the

rate of firearms-related homicides.

Wodarz and Komarova assume that there is a positive relationship between the number of gun owners and the number of potential gun-related attackers. This is reasonable: if there are no guns, there will be no attacks with guns. But the authors also assume that there is a negative relationship between the rate of gun ownership and the likelihood that a gun-wielding attacker actually uses his or her weapon. This is because non-criminals may own guns, too. If a potential victim possesses a gun, a potential attacker might think twice about attacking.

A few other factors are also included in the model, such as the risk of dying in a gun attack, and the availability and take-up of illegal arms in the face of varying levels of gun control. But the key insight is that there are essentially two perfect worlds, one in which no one owns a gun (meaning no one is able to attack) and one in which everyone owns a gun (meaning no one is willing to attack). In between, we get the worst of both worlds because some criminals have guns and they choose to use them. This means that the effect of gun availability is crucially dependent on where we sit between these two worlds.

This is social science at its very best. Rather than crafting yet another highly abstract formal model, Wodarz and Komarova create a model that is directly relevant to an extremely important societal issue. And rather than overly emphasizing the results of their model, they conduct an exercise in caution, highlighting the importance of grounding models in sound and accurate assumptions — because a model is only as good as the assumptions from which it proceeds.

Using their best guess about values estimated or implied from the existing literature, Wodarz and Komarova show that their model implies that stricter laws are the best way to reduce gun deaths. But they are quick to point out that there are some assumptions that are vital to the model for which we have no reliable measurement. So although the model does lend support to arguments in favour of gun

DAMIAN DOVARGANES/AP/PRESS ASSOCIATION IMAGES

control, it is fair to say that the jury is still out.

The most obvious contribution Wodarz and Komarova make towards the study of gun-control policies is in highlighting key parameters that require further empirical investigation. Collaborative efforts between sociologists, political scientists and other scholars can now move forward in an objective way to advance our understanding of gun-control policies by focusing on the assumed values that are

currently less well measured. Armed with these, the model might help us to resolve — perhaps once and for all — the debate on gun ownership. ■

Adeline Lo and James H. Fowler are in the Political Science Department, University of California, San Diego, La Jolla, California 92093-0521, USA.
e-mail: fowler@ucsd.edu

BIOLOGICAL TECHNIQUES

An embryonic view of tumour development

A genome-wide screen of developing mouse embryos, performed using RNA-interference techniques, finds new suspects in skin cancer. But some factors seem to have opposing roles in cancer and normal-tissue maintenance. [SEE ARTICLE P.185](#)

PAWEŁ J. SCHWEIGER & KIM B. JENSEN

Gene function has traditionally been studied using organisms in which individual genes have been either eliminated or artificially expressed in excess. The discovery in the 1990s of RNA interference (RNAi) — the process by which small RNA molecules specifically inhibit gene expression by binding to and destroying messenger RNAs — established a new framework for investigating gene function. Until now, however, genome-wide screens using RNAi techniques have been limited mainly to cultured cells, and so cannot take into account the complex cellular interactions that govern normal tissue behaviour or that lead to the development of diseases such as cancer. On page 185 of this issue, Beronja *et al.*¹ describe the first *in vivo* genome-wide RNAi screen, which was performed in mouse embryos with the aim of identifying genes involved in the development of non-melanoma skin cancer*.

Non-melanoma skin cancer — one of the most prevalent tumour types — occurs in the epidermal cells that make up the outer layer of the skin. In the developing embryo, the epidermis forms during mid-gestation from the surface ectoderm and gradually matures into an impermeable barrier with associated structures, such as hair follicles. Early studies of non-melanoma skin cancer identified members of the *Ras* gene family as potent drivers of the disease², but a lack of techniques for studying gene activity at the single-cell level³ has meant that little is known about other genes involved in the maintenance of these, and other, tumours.

The team presenting the current paper

previously described an approach⁴ for achieving RNAi in the developing epidermis. In this technique, cells in the surface ectoderm of mouse embryos are transduced by means of lentiviral vectors carrying short hairpin RNAs (shRNAs), which are cleaved to RNAi sequences once the shRNAs are expressed in a cell. The researchers have now extended this approach to screen the entire genome of the epidermal cells, using a library of shRNA molecules designed to interfere with every mRNA in mouse cells. Because cells in the developing epidermis divide in an extremely

1. Wodarz, D. & Komarova, N. L. *PLoS ONE* **8**, e71606 (2013).
2. Kaplan, M. S. & Geling, O. *Soc. Sci. Med.* **46**, 1227–1233 (1998).
3. Kleck, G. & Patterson, E. B. *J. Quant. Criminol.* **9**, 249–287 (1993).
4. Papachristos, A. V., Braga, A. A. & Hureau, D. M. *J. Urban Health* **89**, 992–1003 (2012).
5. Zimring, F. *Univ. Chicago Law Rev.* **35**, 721–737 (1968).
6. Becker, G. in *Essays in the Economics of Crime and Punishment* (eds Becker, G. & Landes, W. M.) 1–54 (Nat'l Bureau Econ. Res., 1974).

reproducible manner, any RNAi sequence that alters the normal rate of proliferation can be identified as either enriched or depleted in a pool of RNAi sequences. Thus, by comparing the relative abundance of shRNA sequences in the embryos' genomic DNA at the time of RNAi induction (embryonic day 9.5) and nine days later, the authors were able to identify genes that, when inhibited, cause proliferative advantages or disadvantages.

Beronja and colleagues conducted two such screens: one to assess genes involved in normal epidermal development and the other to assess genes implicated in the development of tumours induced by enhanced expression of *Hras*. The top candidate gene to emerge in both screens, but with an opposite effect on proliferation, was that encoding the β -catenin protein. This finding is in line with previous reports^{5,6} showing that β -catenin is required for the development of non-melanoma skin cancer and that loss of this protein specifically in the epidermis causes hyperproliferation.

β -Catenin is an integral component of adherens junctions — protein complexes that form between cells in epithelial and endothelial tissues — and is therefore key to

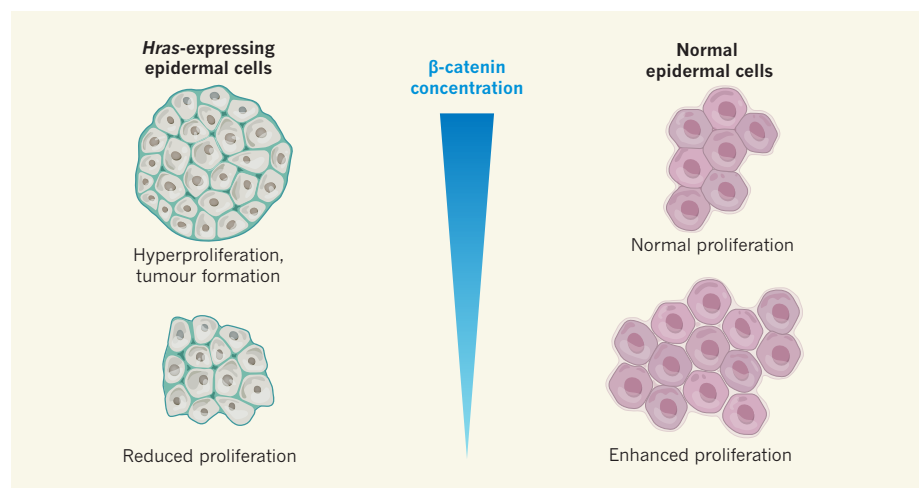


Figure 1 | Role of β -catenin in normal and cancer-prone skin cells. Beronja and colleagues' *in vivo* whole-genome RNA interference (RNAi) screen¹ of epidermal cells expressing the oncogene *Hras* identified β -catenin as essential for maintaining cellular hyperproliferation in this model of cancer; inhibiting expression of the protein led to decreased proliferation. The authors infer that this effect is mediated through β -catenin's involvement in the Wnt signalling pathway. By contrast, the same screen in normal epidermal cells revealed that RNAi-induced inhibition of β -catenin led to enhanced proliferation in such cells. Follow-up experiments suggest that this effect results from β -catenin's role in maintaining the adherens-junction protein complexes between epidermal cells; disruption of these junctions impairs the contact-inhibition processes that keep cell proliferation in check.

*This article and the paper under discussion¹ were published online on 14 August 2013.

intercellular adhesion. It is also a cofactor of the Lef1/Tcf family of transcription factors, which are effector molecules in signalling pathways involving Wnt proteins⁷. β -Catenin thereby regulates several fundamental cellular processes. In the authors' screen for regulators of normal epidermal-cell behaviour, β -catenin emerges as a negative regulator of epidermal-cell growth (Fig. 1). Follow-up *in vitro* experiments suggested that this effect is independent of Wnt signalling, and that it stems from a loss of contact-mediated inhibition of proliferation. By contrast, the authors show that β -catenin is required for *Hras1*-induced hyperproliferation, and that this correlates with increased Wnt signalling *in vivo*. Intriguingly, however, a previous study showed⁸ that blocking Wnt signalling in the epidermis by expression of an inhibitory form of Lef1 does not impede epidermal tumour formation. Future work is therefore needed to evaluate the involvement of β -catenin and Wnt signalling in tumour development.

Whereas β -catenin has already been implicated in numerous malignancies, Beronja and colleagues' screen identified another gene, *Mllt6*, as also being involved in *Hras1*-induced epidermal-cell hyperproliferation. Chromosomal translocations of this gene have previously been associated with mixed myeloid leukaemia⁹. Although the exact function of the *Mllt6* protein is unclear, it is known to influence the subcellular localization of the Dot1a-histone methyltransferase protein complex and to regulate specific gene networks¹⁰. Like β -catenin, *Mllt6* is required for tumour growth induced by *Ras*-gene mutations. The existence of multiple Lef1/Tcf binding sites in the *Mllt6* promoter indicates that it is a potential downstream target of β -catenin-mediated Wnt signalling. However, further investigations are required to determine whether *Mllt6* is directly regulated by β -catenin, whether concerted action of the two proteins drives hyperproliferation, or whether *Mllt6* is an essential component of another signalling pathway. This will be important to resolve, because it influences the number of potential downstream drug targets.

The bird's-eye perspective taken by Beronja *et al.* to identify regulators of growth has produced a wealth of information. The extensive data sets generated in their study provide the basis for further comprehensive computational analysis. A subset of the genes identified is probably involved in epidermal-appendage formation, rather than strictly in proliferation. Filtering the data on the basis of gene-expression patterns during this phase of embryo development would provide an excellent framework for categorizing genes into those with functions in homeostasis, development and oncogene-induced growth. Moreover, it will be exciting to see whether the genes implicated in Ras-protein-induced growth represent universal mechanisms for abnormal

proliferation, or if different tissues have evolved discrete mechanisms for controlling homeostasis. ■

Pawel J. Schweiger and Kim B. Jensen are at the Biotech Research and Innovation Center, University of Copenhagen, DK-2200 Copenhagen N, Denmark. K.B.J. is also at the Wellcome Trust and Medical Research Council Cambridge Stem Cell Institute, Cambridge, UK. e-mail: kim.jensen@bric.ku.dk

1. Beronja, S. *et al.* *Nature* **501**, 185–190 (2013).

MATERIALS SCIENCE

Boosting X-ray emission

A spectroscopic technique has been demonstrated that uses stimulated emission to enhance weak X-ray signals for fundamental studies in materials science. SEE LETTER P191

ERNST FILL

During the past decade or so, a spectroscopic technique called resonant inelastic X-ray scattering (RIXS) has evolved as a powerful tool for probing elementary excitations in materials^{1,2}. Excitations accessible to RIXS include charge transfer, crystal-field excitations, magnons, molecular vibrations and even phonons. Recent progress in this field is due to the availability of third-generation synchrotrons as X-ray sources and to advances in X-ray photon detection². However, the method still suffers from a low photon yield because of dominant radiationless processes, requiring high incident photon fluxes that cause damage to the sample under investigation. On page 191 of this issue, Beye *et al.*³ demonstrate an ingenious way to greatly increase the photon yield for RIXS.

In RIXS, a beam of X-ray photons is directed at a sample, and the photon energy is chosen such that photon absorption elevates an electron from a deep-lying atomic-core energy level to a previously unoccupied state in the material's valence energy band. This process generates a hole — a particle created by the absence of an electron — in the atomic core. This highly unstable state typically decays within a few femtoseconds (1 fs is 10^{-15} s; in the current experiment the core-hole lifetime is 19 fs). Usually, the main decay channel is the Auger process, in which an electron jumps to the core hole and another electron is emitted. RIXS relies on a different decay process in which, again, an electron jumps to the core but, instead of an electron, a photon is emitted

2. Feinberg, A. P., Vogelstein, B., Droller, M. J., Baylin, S. B. & Nelkin, B. D. *Science* **220**, 1175–1177 (1983).
3. Copeland, N. G. & Jenkins, N. A. *Nature Rev. Cancer* **10**, 696–706 (2010).
4. Beronja, S., Livshits, G., Williams, S. & Fuchs, E. *Nature Med.* **16**, 821–827 (2010).
5. Malanchi, I. *et al.* *Nature* **452**, 650–653 (2008).
6. Huelsken, J., Vogel, R., Erdmann, B., Cotsarelis, G. & Birchmeier, W. *Cell* **105**, 533–545 (2001).
7. Clevers, H. & Nusse, R. *Cell* **149**, 1192–1205 (2012).
8. Niemann, C., Owens, D. M., Schettina, P. & Watt, F. M. *Cancer Res.* **67**, 2916–2921 (2007).
9. Meyer, C. *et al.* *Leukemia* **23**, 1490–1499 (2009).
10. Reisenauer, M. R. *et al.* *J. Biol. Chem.* **284**, 35659–35669 (2009).

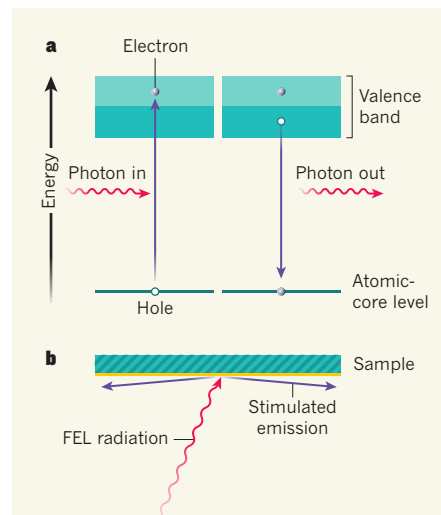


Figure 1 | RIXS spectroscopy using stimulated emission. **a**, In conventional RIXS, an incident photon generates a hole in a deep-lying atomic-core energy level and an electron in the unoccupied part of the valence energy band (left). An electron from the occupied part of the valence band fills the core hole, leaving a hole in the valence band and emitting a photon (right). The emitted photon provides information about energy states of the underlying material. **b**, In Beye and colleagues' experiment³, the downward transition is amplified by stimulated emission. A brilliant soft-X-ray free-electron laser (FEL) beam is focused on a crystalline silicon sample and penetrates only about 1 micrometre into the sample (yellow). A high percentage of atoms is excited, allowing stimulated emission to predominate over spontaneous emission and other decay channels. This results in a highly directional emission close to the surface.

(Fig. 1a). The fluorescence yield (the ratio of the rate of radiative decay to total decay rate) is very low, and thus the RIXS signal is weak. Nevertheless, RIXS provides a large amount of information on the chemical and physical features of materials.

In their study, Beye *et al.* irradiated a solid-state sample with a soft-X-ray free-electron laser (FEL), which allows a large fraction of atoms to be excited. In this way, a mechanism known as stimulated emission takes over and the radiative channel is significantly enhanced at the expense of non-radiative processes; in stimulated emission, an incident photon de-excites an excited state by generating a second photon with exactly the same energy and direction. FEL radiation had previously been proposed for excitation². FELs emit brilliant, tunable, monoenergetic photon beams that can be focused to spot sizes smaller than 10 micrometres, inducing a high density of photons (intensity) on the sample. But Beye and colleagues went one step further and applied FEL radiation to generate the sizeable atomic population inversion that is required to induce X-ray amplification (gain) and generate laser light at the energies of the transitions investigated.

The method is related to the concept of an inner-shell X-ray laser. This laser scheme had already been suggested in the 1960s⁴, but has only quite recently been realized, also using FEL radiation⁵. In the current experiment, the gain generated is so high that the laser transition becomes saturated — that is, almost all of the excited states are converted into photons and the non-radiative channel is effectively quenched. The emitted radiation is highly directional and radiated close to the sample surface (Fig. 1b). Directionality and amplification may lead to an enhancement of the brilliance of the emitted photon beam by several orders of magnitude, solving the problem of the weak RIXS signal.

In Beye and colleagues' pioneering experiment, the conditions for observing stimulated emission were not optimal. Owing to experimental constraints, the spectroscopic observation had to be limited to a detection angle to the surface of 15°, whereas the emission maximum was found to occur at 9°. Because of this problem, an enhancement of only a bit more than a factor of two was measured. However, the high directionality of the beam was demonstrated clearly, showing the effect of stimulated emission.

The authors' experiment is an important first step towards a new way of using RIXS for fundamental studies. Possible improvements include an elongation of the irradiated spot for increasing the directionality; travelling-wave excitation (in which the excitation sweeps over the sample at the speed of light, with the generated radiation exactly following the excitation) to avoid decay of population inversion before the beam has left the excited material; and a

better match of the observation direction to the emission direction.

An open question is how the signal in various spectral regions might be altered by the stimulated-emission process. If all transitions are ensured to be saturated, this may not be a problem. Another challenge pertains to the high directionality of the emission: how can the information on the excitations, which depends on the change in momentum that the photons undergo, be retrieved under this condition? In ordinary RIXS, photons are emitted in different directions and such information is derived from this feature.

Another point concerns the incident-photon energy at which stimulated-emission RIXS can be carried out. With a photon energy of around 100 electronvolts, Beye and colleagues' experiment falls into the very-low-energy regime of RIXS. Higher photon energies are already available with FELs — for example, at the Linac Coherent Light Source at the SLAC National Accelerator Laboratory in Menlo Park, California, which emits photons with energies of up to 10 keV (ref. 6). With more-energetic photons, stimulated-emission RIXS may revolutionize investigations of many chemical elements. However, the shorter lifetime of the excited states that are reached at

such photon energies will make inducing stimulated emission more challenging. Application of the technique may be extended to liquids or even gases in order to investigate free atoms or molecules⁷. Owing to the method's increased spectral resolution, the investigation of new low-energy excitations (for example, phonons with energies much below 0.1 eV) may be possible.

This work could open up a new chapter in RIXS studies and lead to the discovery of novel excitations. A further exciting prospect is the potential to make time-resolved measurements using two incident photon beams⁸. ■

Ernst Fill is at the Max Planck Institute of Quantum Optics, D 85748 Garching, Germany. e-mail: ernst.fill@mpq.mpg.de

1. Kotani, A. & Shin, S. *Rev. Mod. Phys.* **73**, 203–246 (2001).
2. Ament, L. J. P., van Veenendaal, M., Devereaux, T. P., Hill, J. P. & van den Brink, J. *Rev. Mod. Phys.* **83**, 705–767 (2011).
3. Beye, M. *et al. Nature* **501**, 191–194 (2013).
4. Duguay, M. A. & Rentzepis, P. M. *Appl. Phys. Lett.* **10**, 350–352 (1967).
5. Rohringer, N. *et al. Nature* **481**, 488–491 (2012).
6. McNeil, B. W. J. & Thompson, N. R. *Nature Photon.* **4**, 814–821 (2010).
7. Hennies, F. *et al. Phys. Rev. Lett.* **104**, 193002 (2010).
8. Harbola, U. & Mukamel, S. *Phys. Rev. B* **79**, 085108 (2009).

IMMUNOLOGY

Lipopolysaccharide sensing on the inside

Host-cell detection of lipopolysaccharide in the outer membrane of Gram-negative bacteria was thought to be restricted to the cell-surface receptor TLR4. It emerges that lipopolysaccharide can also be sensed in the cytoplasm.

**VIJAY A. K. RATHINAM
& KATHERINE A. FITZGERALD**

The innate immune system provides an exquisite defence system against microorganisms, but its excessive engagement can be dangerous. Overproduction of cell-signalling molecules called cytokines and excessive release of other components of dying cells can directly or indirectly injure host tissues and, in extreme cases, may lead to blood poisoning, or sepsis. The primary trigger of such reactions is lipopolysaccharide, the main component of the outer membrane of Gram-negative bacteria. Genetic studies suggested that this component is sensed exclusively through Toll-like receptor 4 (TLR4), a member of an ancient receptor family dedicated to the detection of infectious microorganisms^{1,2}, but there were some hints of TLR4-independent sensing of lipopolysaccharide³.

In an exciting paper published in *Science*, Kayagaki *et al.*⁴ describe a TLR4-independent sensing mechanism for lipopolysaccharide (LPS) that occurs in the cytoplasm of macrophages — a type of innate immune cell*. Although the identity of the novel LPS receptor remains unknown, the authors show that its engagement results in activation of the inflammatory enzyme caspase-11. The findings greatly enhance our understanding of LPS responses and may have implications for the treatment of sepsis.

The discovery emerged from the authors' examination of inflammasome activation during Gram-negative bacterial infections. Inflammasomes are large, multi-protein complexes found in the cytoplasm that couple pathogen recognition to the maturation of IL-1 β and other cytokines. Inflammasomes

*This News & Views article was published online on 4 September 2013.

also trigger an inflammatory cell-death response called pyroptosis. The best-studied inflammasome contains the protein NLRP3, a sensor of microbial infection that engages the adapter molecule ASC, which then recruits and activates the effector enzyme caspase-1. Although most activators of NLRP3 lead to caspase-1 engagement by this mechanism, previous work⁵ from the research group presenting the current paper showed that, during infections with gut pathogens such as *Escherichia coli* and *Vibrio cholerae*, engagement of caspase-11 was essential to facilitate NLRP3–ASC-dependent caspase-1 activation and IL-1 β maturation (Fig. 1). The caspase-11 pathway was also shown to play a part in LPS-induced septic shock.

Several other studies^{6–13} subsequently linked caspase-11 to inflammasome responses for a broad range of Gram-negative (but not Gram-positive) bacterial pathogens, and attempted to understand how caspase-11 is activated in these infections. Kayagaki and colleagues now show that cytoplasmic LPS recognition has a role.

The findings came by a circuitous route. The group's previous work⁵ had identified cholera toxin B (CTB) as a trigger of the caspase-11 pathway in cells exposed to LPS. The latest work describes how one form of LPS, O111:B4, facilitates caspase-11 activation by CTB, whereas other LPS serotypes or lipid A — the portion of LPS that is responsible for TLR4 activation — do not. It turns out that CTB is not itself a trigger of caspase-11 activation but instead acts as a vehicle to deliver O111:B4 LPS into the cell. This finding led the authors to speculate that cytoplasmic LPS is the trigger that activates caspase-11, and they validated this idea by showing that LPS and lipid A led to caspase-11 activation when they were delivered directly to the cytoplasm.

Following experiments showing that a modified form of LPS that still activates TLR4 failed to trigger the cytoplasmic LPS-sensing pathway, Kayagaki *et al.* hypothesized that cytoplasmic LPS is sensed in a TLR4-independent manner. In support of this idea, they show that TLR4-deficient macrophages undergo normal caspase-11-pathway activation in response to LPS or lipid A, as long as the cells are first primed with ligands of other Toll-like receptors, TLR2 or TLR3, to induce expression of NLRP3, IL-1 β and caspase-11. The authors also provide compelling evidence linking the cytoplasmic LPS-sensing pathway to the recognition of Gram-negative bacteria, by monitoring caspase-11 activation in primed macrophages infected either with mutant *E. coli* that lacked biologically active LPS or with wild-type *E. coli*. Both normal and TLR4-deficient macrophages responded to the wild-type bacteria, but the mutant *E. coli* failed to drive responses that depended on caspase-11.

It has been known for more than a decade that TLR4-deficient mice survive doses of LPS

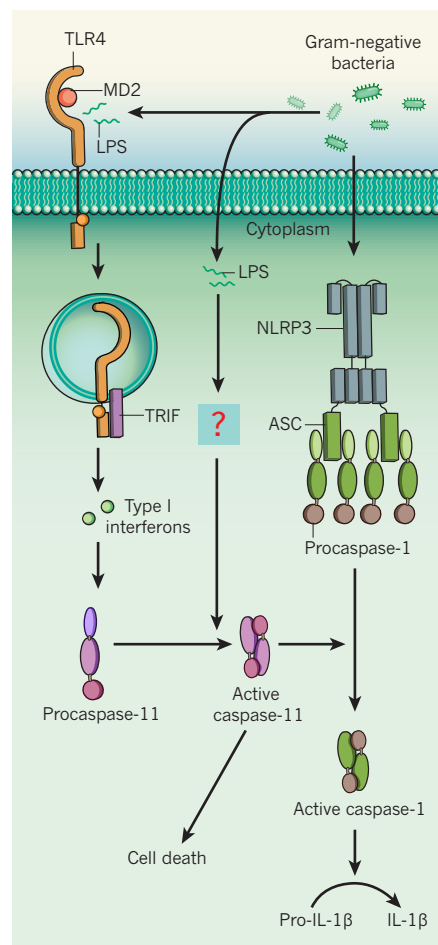


Figure 1 | Inflammasome activation by caspase-11. Infections with Gram-negative bacteria trigger the formation of an inflammasome protein complex comprising NLRP3, ASC and procaspase-1 in host cells. Active caspase-1 subsequently triggers the maturation of cytokines such as IL-1 β . During responses to Gram-negative bacteria, including *Escherichia coli*, the progression of procaspase-1 to caspase-1 requires caspase-11. Caspase-11 expression is regulated by a signalling pathway involving the adapter protein TRIF and type-1 interferon proteins. This is initiated following the recognition of lipopolysaccharide (LPS), a major component of the outer membrane of Gram-negative bacteria, by the cell-surface receptor TLR4 in complex with its co-receptor MD2. Kayagaki *et al.*⁴ show that LPS can also be sensed in a TLR4-independent manner in the cytoplasm of host cells through an as-yet-unidentified receptor, and that this leads to the activation of caspase-11. In addition to its role in triggering caspase-1 activation, caspase-11 can cause host-cell death in a caspase-1-independent way.

that are lethal to normal animals, and Kayagaki and colleagues' earlier work⁵ found similar responses in mice that are missing caspase-11. The authors assessed the relevance of the cytosolic LPS-sensing pathway to these responses in TLR4-deficient or wild-type mice by first priming the mice with a non-lethal dose of a TLR3 ligand, to induce sufficient caspase-11 expression. Under these conditions, the TLR4-deficient mice were as susceptible as

wild-type mice to LPS-induced septic shock.

Collectively, these findings provide compelling evidence for an LPS sensor in the cytoplasm that is involved in detecting Gram-negative bacterial infections, and highlight the importance of both TLR4 and this sensor in eliciting the severe inflammatory responses that result in LPS-induced mortality (Fig. 1). The study also reinforces an emerging theme in our understanding of antimicrobial defence: that multiple sensors recognize the same microbial product in a way that is specific to different cellular compartments. This strategy might help the host to gauge the severity of microbial invasion and tailor the response so that it is commensurate with the threat. For example, a tiny quantity of LPS will drive a TLR4-dependent proinflammatory response that alerts the host to the presence of infection. Higher quantities of LPS, which reach the cytoplasm, will trigger inflammasome activation, IL-1 β production and, ultimately, cell death. This strategy might also be deliberate, because the cytoplasmic LPS-sensing pathway seems to be much more detrimental to the host than TLR4-based recognition. As a result, the cytoplasmic pathway would only be engaged following an overwhelming infection.

Several pressing questions arise from this study. The most crucial is: what is the identity of the sensor? We lack a detailed understanding of its ability to coordinate caspase-11 activation. Another key issue not yet addressed is whether cytoplasmic LPS triggers similar events in human cells. If it does, this understanding may be useful in the development of drugs for treating sepsis. For example, eritoran, a highly specific TLR4-inhibiting drug, recently failed in human clinical trials that aimed to reduce deaths from sepsis¹⁴; could this be because eritoran fails to block the cytoplasmic pathway of LPS recognition? About one-third of cases of septic shock result from Gram-negative bacterial infections, and these cases have a high mortality rate. A better understanding of the clinical relevance of the caspase-11 pathway in Gram-negative bacterial recognition in humans may improve the outcome of these infections. ■

Vijay A. K. Rathinam and Katherine A. Fitzgerald are in the Division of Infectious Disease and Immunology, Department of Medicine, University of Massachusetts Medical School, Worcester, Massachusetts 01605, USA. e-mail: kate.fitzgerald@umassmed.edu

- Poltorak, A. *et al.* *Science* **282**, 2085–2088 (1998).
- Meng, J., Gong, M., Björkbacka, H. & Golenbock, D. T. *J. Immunol.* **187**, 3683–3693 (2011).
- Haziot, A., Hijiya, N., Gangloff, S. C., Silver, J. & Goyert, S. M. *J. Immunol.* **166**, 1075–1078 (2001).
- Kayagaki, N. *et al.* *Science* <http://dx.doi.org/10.1126/science.1240248> (2013).
- Kayagaki, N. *et al.* *Nature* **479**, 117–121 (2011).
- Gurung, P. *et al.* *J. Biol. Chem.* **287**, 34474–34483 (2012).
- Broz, P. *et al.* *Nature* **490**, 288–291 (2012).

8. Rathinam, V. A. *et al. Cell* **150**, 606–619 (2012).
9. Achoui, Y. *et al. Science* **339**, 975–978 (2013).
10. Case, C. L. *et al. Proc. Natl Acad. Sci. USA* **110**, 1851–1856 (2013).
11. Casson, C. N. *et al. PLoS Pathogens* **9**, e1003400 (2013).
12. Schauvliege, R., Vanrobaeys, J., Schotte, P. & Beyaert, R. *J. Biol. Chem.* **277**, 41624–41630 (2002).
13. Suk, K., Kim, S. Y. & Kim, H. *J. Neurochem.* **80**, 230–238 (2002).
14. Opal, S. M. *et al. J. Am. Med. Assoc.* **309**, 1154–1162 (2013).

GEOCHEMISTRY

Sulphur from heaven and hell

Fingerprints of sulphur isotopes in rocks from the ridge beneath the Atlantic Ocean suggest that a substantial fraction of sulphur at Earth's surface is left over from the formation of the planet's core. [SEE LETTER P.208](#)

NICOLAS DAUPHAS

The relative abundances and isotopic signatures of sulphur found in rocks exhumed from Earth's mantle act as fingerprints of how and where our planet acquired its complement of this biochemically important element. Textbooks say that Earth's sulphur has the same isotopic composition as chondrites, a type of meteorite that is thought to best represent the building blocks of terrestrial planets. With dashes of audacity and insight, Labidi and co-workers¹ question this assumption in a paper on page 208 of this issue. They report measurements of rocks derived

from Earth's mantle that reveal isotopic patterns unlike any others previously reported, with implications for how the planet formed*.

Most of us take Earth's chemical composition for granted, but unique circumstances may have been at play in delivering the right mix of elements for life to develop and flourish. For example, this is true of the noble metals needed in the electronic devices used to print or display this page. It is also true of sulphur, which is found in the amino acids cysteine and methionine and represents around 0.2% of our body weight. These elements and a few others

*This article and the paper under discussion¹ were published online on 4 September 2013.

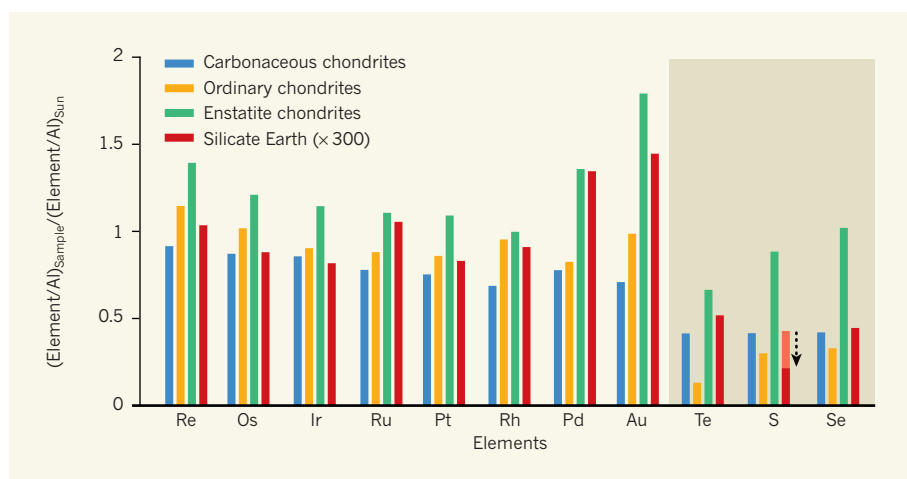


Figure 1 | Abundances of elements in Earth's mantle and in chondritic meteorites. The elements shown have strong affinities with metallic iron^{9,11,12} and are in order of increasing volatility. Shaded region indicates elements that are not noble metals. Data are normalized to the abundance of aluminium (Al), because this element was neither lost to space during Earth's accretion nor scavenged by metallic iron during core formation. The data are also normalized to solar abundances to prevent them from spanning many orders of magnitude. The 'silicate Earth' pattern shows abundances in the mantle, and has been multiplied by a factor of 300 to allow easy comparison with the chondrite data. The depicted elements are thought to have segregated into Earth's core as the planet formed, but were subsequently replenished in the mantle by the accretion of chondritic material — which is why these elements are found in proportions similar to those of chondrites. However, Labidi *et al.*¹ suggest that about half or more of the sulphur in Earth's mantle may be left over from core formation (black arrow), with the remainder coming from chondrites; the upper part (light red) for sulphur represents the total abundance of the element in the mantle, and the lower part indicates the abundance left over from core formation.



50 Years Ago

Prof. L. Egged has recently summarized a number of hypotheses concerning the expansion of the Earth, and has suggested that the Earth's radius is expanding at a rate of 0.5–1.0 mm per year. There appears to be a remarkably close agreement between the rate of increase of the Earth's radius and that of the universe according to Hubble's law. Using the at present accepted value for Hubble's constant, $H = 100 \text{ km/s/megaparsec}$, which is $1.65 \times 10^{-4} \text{ mm per year per mile}$, and substituting the value of the Earth's radius in the Hubble equation, $v = RH$, we obtain a radial expansion for the Earth of 0.66 mm per year. While this agreement may be fortuitous it may suggest a fundamental concordance between expansion processes in the Earth's core and those responsible for the expansion of the universe.

From *Nature* 14 September 1963

100 Years Ago

In a paper on the psychology of insects, read before the General Malarial Committee at Madras in November, 1912, Prof. Howlett, after giving an account of experiments carried out by him on the response of insects to stimuli, comes to the conclusion that insects are to be regarded "not as intelligent beings consciously shaping a path through life, but as being in a sort of active hypnotic trance." It is claimed that this view of insect-psychology opens up great possibilities in the study of insect carriers of disease, since "it is no intelligent foe we have to fight, but a mere battalion of somnambulists." If we discover the stimuli or particular conditions which determine the actions of an insect, we can apply them to its undoing.

From *Nature* 11 September 1913

have strong affinities for metallic iron — so much so that when Earth's metallic, iron-rich core formed, it scavenged all these elements, leaving behind a rocky mantle barren of sulphur, selenium, tellurium and noble metals. The prevailing view regarding the origin of these elements is that they were replenished in the mantle by a rain of asteroids from the heavens, known as the late veneer^{2–5}. This late accretion of meteoritic material may also have delivered a fraction of the elements needed for life (hydrogen, carbon and nitrogen), as well as prebiotic organic molecules that could have served as the seeds for life.

The late-veneer hypothesis for the origin of Earth's sulphur is supported by strong observational evidence. First, laboratory experiments to reproduce the conditions of core–mantle segregation indicate that sulphur, selenium, tellurium and the noble metals are efficiently scavenged into metallic iron. Second, these elements are present in the mantle in proportions similar to those found in chondrites (Fig. 1). And third, the isotopic composition of sulphur in mantle rocks is identical to that of chondrites^{6,7}. It is this third point that Labidi *et al.* call into question. They find that the ratio of sulphur-34 to sulphur-32 in Earth's mantle is 0.13% lower than that of chondrites.

To arrive at this conclusion, the authors used an analytical technique that provides a more complete recovery of sulphur from rock samples than has previously been possible. The difference in sulphur isotopic ratios that they infer between Earth's mantle and meteorites corresponds approximately to the difference measured in laboratory experiments when sulphur is partitioned between (core-like) metal and (mantle-like) silicate. An appealing possibility is therefore that a large fraction (maybe half or more) of the sulphur in Earth's mantle originated in the bowels of the Earth — that is, it is left over from core formation. If correct, there is no need to invoke unique circumstances to explain the presence of sulphur at Earth's surface. Furthermore, this element should be ubiquitous in Earth-like planets, raising the possibility of one day detecting sulphur-bearing molecules in the atmospheres of such extrasolar planets.

A difficulty with a dynamically active planet such as Earth is that geological processes, for example partial melting of the interior to form magmas and recycling of surface rocks into the interior at subduction zones, can blur isotopic signals and complicate interpretations. For instance, Labidi and co-workers identify the isotopic signatures of two distinct sulphur-containing components in rocks formed by melting of the mantle. One has a sulphur-isotope composition distinct from that of chondrites, which they interpret to be representative of the mantle. The other has a sulphur-isotope composition similar to that of chondrites, but the authors ascribe it to recycling of sulphur from sediments. This

interpretation is reasonable, but a question lingers as to whether or not these components are representative of their mantle sources. During magma formation and extraction from the mantle, considerable amounts of sulphide minerals can remain behind at the magma's source, potentially affecting the sulphur isotopic ratios of magma-derived rocks⁸. Labidi *et al.* argue against this interpretation of their results, but insufficient experimental data are available on sulphur-isotope partitioning between sulphide and silicate melts to definitely rule out this possibility.

The relative abundances of selenium, sulphur and tellurium in the mantle have been used to gain insight into the nature of the late veneer⁹. These relative abundances best match the composition of carbonaceous chondrites (Fig. 1), suggesting that Earth received a late veneer of material rich in volatile compounds and organic molecules. Other isotopic evidence¹⁰ suggests that the nature of the meteoritic material accreted by Earth was not very different before and after the completion of core formation. If Labidi and colleagues are correct and a substantial fraction of sulphur in the mantle is left over from core formation, this undermines the argument for a volatile-rich later veneer.

However, one is left wondering whether the good match between the selenium/sulphur and tellurium/sulphur ratios of chondrites and those of Earth can be coincidental. Labidi and co-workers' measurements are of the highest quality and will endure, but the same can be said of another study⁹, published earlier this year, the conclusions of which contradict the present findings. The questions raised by these two conflicting studies will undoubtedly stimulate further discussion and experiments. ■

Nicolas Dauphas is in the Origins Laboratory, Department of the Geophysical Sciences and the Enrico Fermi Institute, The University of Chicago, Chicago, Illinois 60637, USA.
e-mail: dauphas@uchicago.edu

1. Labidi, J., Cartigny, P. & Moreira, M. *Nature* **501**, 208–211 (2013).
2. Kimura, K., Lewis, R. S. & Anders, E. *Geochim. Cosmochim. Acta* **38**, 683–701 (1974).
3. Chou, C. L. *Proc. Lunar Planet. Sci. Conf.* **9**, 219–230 (1978).
4. Jagoutz, E. *et al. Proc. Lunar Planet. Sci. Conf.* **10**, 2031–2050 (1979).
5. Morgan, J. W. *J. Geophys. Res.* **91**, 12375–12387 (1986).
6. Sakai, H., Des Marais, D. J., Ueda, A. & Moore, J. G. *Geochim. Cosmochim. Acta* **48**, 2433–2441 (1984).
7. Chaussidon, M., Sheppard, S. M. F. & Michard, A. in *Stable Isotope Geochemistry: A Tribute to Samuel Epstein* (eds Taylor, H. P. Jr, O'Neill, J. R. & Kaplan, I. R.) 325–338 (Geochem. Soc., 1991).
8. Chaussidon, M., Albarède, F. & Sheppard, S. M. F. *Earth Planet. Sci. Lett.* **92**, 144–156 (1989).
9. Wang, Z. & Becker, H. *Nature* **499**, 328–331 (2013).
10. Dauphas, N., Davis, A. M., Marty, B. & Reisberg, L. *Earth Planet. Sci. Lett.* **226**, 465–475 (2004).
11. Walker, R. J. *Chem. Erde* **69**, 101–125 (2009).
12. Fischer-Gödde, M., Becker, H. & Wombacher, F. *Chem. Geol.* **280**, 365–383 (2011).

ASTROCHEMISTRY

Extracts of meteorite

The Sutter's Mill meteorite exploded in a dazzling fireball over California last year (pictured). Writing in *Proceedings of the National Academy of Sciences*, Pizzarello *et al.* report that it contained organic molecules not found in any previously analysed meteorites (S. Pizzarello *et al.* *Proc. Natl Acad. Sci. USA* <http://dx.doi.org/10.1073/pnas.1309113110>; 2013).

The authors' analysis of extracts of organic matter from the meteorite revealed a complex mixture of oxygen-rich compounds, which probably resulted from oxidative processes that occurred in the parent body. Intriguingly, the authors suggest that such compounds could have been released to prebiotic Earth during or after meteorite bombardments, adding to the roster of organic molecules that might have contributed to the evolution of life. [Andrew Mitchinson](#)



COMPUTATIONAL BIOLOGY

A recipe for ligand-binding proteins

Cellular cross-talk, enzymatic catalysis and regulation of gene expression all depend on molecular recognition. A method that allows the design of proteins with desired recognition sites could thus be revolutionary. [SEE LETTER P.212](#)

GIOVANNA GHIRLANDA

To support cellular processes, natural proteins have evolved to recognize a relatively small set of ligand molecules with high affinity and specificity. Broadening this set of protein–ligand pairs with synthetic proteins that are specific for ligands of choice could transform the development of biosensors, protein-based drugs, artificial enzymes and tools for chemical biology. Current *in vitro* approaches to the design of protein–ligand pairs rely on laborious directed-evolution techniques to engineer binding sites in existing protein scaffolds, and cannot be generalized. In this issue, Tinberg *et al.*¹ (page 212) describe a computational method that promises to streamline and greatly facilitate the

development of tailored ligand-binding proteins*.

One way to engineer synthetic ligand-binding proteins is repurposing existing proteins through directed evolution. This approach involves selecting a few amino acids within an existing protein, typically located in a cavity, and randomly mutating them to create libraries of millions of protein variants, which are then selected for their ability to bind the target. Depending on the ligand and the scaffold protein, successive rounds of directed evolution yield binding proteins with dissociation constants in the physiologically relevant micromolar to nanomolar ranges^{2,3}. The process is arduous, and success is not guaranteed: current methods limit the size of combinatorial libraries to about 10⁹, which is often insufficient to explore a large number of positions and so limits the fitness of the resulting

binders. Furthermore, the process works best when the starting protein already binds weakly to the desired ligand, rather than when starting from scratch.

Computational methods hold great promise to bypass this lengthy process by using virtual selection on a large number of scaffolds. Such approaches have enjoyed much success lately, with the design of artificial enzymes for a variety of reactions^{4–8}. Despite these feats, the design of high-affinity ligand-binding proteins has remained elusive⁹.

Tinberg *et al.* now present a generalizable strategy for designing artificial recognition modules for any desired target molecule. As their target they chose digoxigenin — a natural steroid that forms part of the cardiac drug digoxin, and that has found a second life as a recognition tag in biotechnology applications. Consequently, a few digoxigenin-binding agents, including both antibodies and non-antibody proteins, have been developed through traditional protein-engineering methods^{10–12}.

Taking some clues from the previously developed binding agents, Tinberg and colleagues sketched out a couple of possible ways to bind ligands to digoxigenin using amino acids that could provide hydrogen bonds and hydrophobic interactions (Fig. 1a). They then transposed these minimalistic sets into three-dimensional models, which were used as probes to interrogate a selected set of 401 proteins, encompassing several classes of

*This article and the paper under discussion¹ were published online on 4 September 2013.

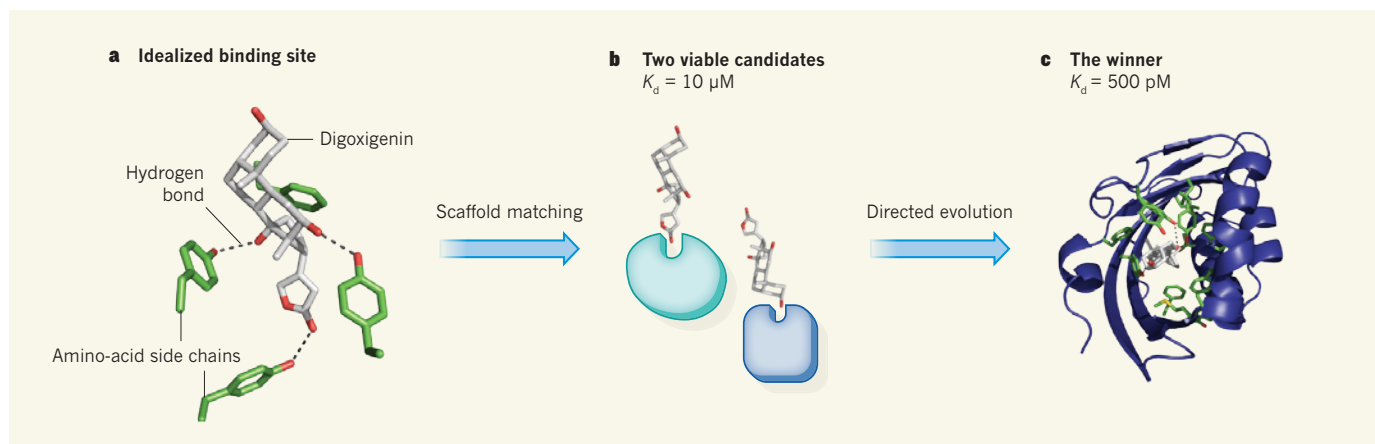


Figure 1 | Steps to making a ligand-binding protein. **a**, To design a protein with high binding affinity for the steroid digoxigenin, Tinberg *et al.*¹ created a minimal digoxigenin-binding site made with amino-acid side chains positioned to maximize hydrogen bonding and hydrophobic interactions to the target. They then sifted through a selected set of 401 scaffold-protein structures to find all (17) possible matches for the digoxigenin-binding site

and ranked them by best fit. **b**, After validating the predictions through protein expression, they subjected the two best performers, which had micromolar binding affinities (K_d), to directed-evolution methods, randomizing amino acids farther away from the binding site. **c**, Finally, a protein with picomolar binding affinity emerged as winner, and the authors obtained its crystal structure to confirm the design features.

protein fold, for geometrical compatibility. Powerful computational methods available in the authors' lab enabled them to rapidly sift through all possible matches, rank the candidates and perform optimization through rounds of redesign and scoring.

Seventeen proteins emerged as candidates for experimental characterization, on the basis of optimal shape complementarity to the ligand, pre-organization of the site in the absence of ligand and predicted protein stability. Of these, only two bound the ligand with micromolar affinity (Fig. 1b). Although an impressive result for a computational approach, these binding affinities are far from the nanomolar ranges needed for practical applications. The authors, therefore, turned to directed-evolution methods to improve binding affinity.

To explore the effect of all 20 possible amino acids at each of 34 residues located within roughly 10 Å of the binding site would have required an astronomical number (more than 10^{44}) of possible protein sequences. Fortunately, a new method¹³ allowed Tinberg *et al.* to circumvent this limitation — by randomizing each of the 34 positions independently, selecting for binding to labelled digoxigenin, and using deep sequencing to build a fitness map that correlates amino-acid identity at each position to function. On the basis of this information, the authors combined favourable substitutions in successive generations of libraries to obtain mutants with affinity in the low-nanomolar to high-picomolar ranges (Fig. 1c).

The litmus test for measuring successful protein design is obtaining high-resolution structures of the final product and comparing it with the designed features in the models. Tinberg and colleagues' proteins pass this test with flying colours: structural characterization of the two best mutants, DIG10.2 and

its improved version, DIG10.3, showed the presence of hydrogen bonding between three designed tyrosine residues and the ligand. Tyrosine is frequently found in the binding pockets of antibodies and of synthetic ligand-binding proteins: its ability to form hydrophobic and hydrogen-bonding interactions, as well as its size and conformational rigidity, fulfil many roles in molecular recognition¹⁴. In addition to the designed features, subjecting the proteins to directed evolution allowed the exchange of small hydrophobic amino acids with larger ones, and the introduction of two additional tyrosines within the binding site. These mutations reinforce design principles incorporated in the computational selection, such as shape complementarity and binding-site pre-organization, which maximize the entropic contribution to binding as well as maximizing specificity.

Tinberg *et al.* also exploited hydrogen-bonding interactions, which impart strong geometric constraints and thus contribute to specificity for binding to digoxigenin as opposed to other steroids. This point is elegantly illustrated by a series of mutants in which the authors correlate the number of hydrogen-bonding groups on the target steroids with the effect of swapping each tyrosine for phenylalanine, which cannot hydrogen bond, and demonstrate the large energetic penalty paid for each mismatch.

The success of this protocol overcomes a long-standing issue in protein design, and promises to have an impact on the effectiveness of designed enzymes, which has often been limited by low affinity for the substrate. This work also opens up many exciting challenges. Digoxigenin proved a wise choice of target ligand, and contributed to the authors' success: the molecule offers several hydrogen-bonding 'hooks', which helped to achieve high binding specificity in the protein, and the

steroid's rigid scaffold helped to maximize entropic contributions to binding. The authors were also able to gather information on what the binding site should look like from existing structures. Future work will, no doubt, implement ways to deal with flexible ligands and to design minimalistic binding sites in the absence of structural information. More powerful computational methods would enable affinity maturation *in silico* rather than *in vitro*, and would overcome the need for an existing scaffold as a starting point, by designing novel proteins around each target ligand¹⁵. Finally, molecular recognition could be coupled to functional activity, for example by using small-molecule binding to modulate protein activity. ■

Giovanna Ghirlanda is in the Department of Chemistry and Biochemistry, Arizona State University, Tempe, Arizona 85287-1604, USA. e-mail: gghirlanda@asu.edu

1. Tinberg, C. E. *et al.* *Nature* **501**, 212–216 (2013).
2. Gebauer, M. & Skerra, A. *Meth. Enzymol.* **503**, 157–188 (2012).
3. Gilbreth, R. N. & Koide, S. *Curr. Opin. Struct. Biol.* **22**, 413–420 (2012).
4. Jiang, L. *et al.* *Science* **319**, 1387–1391 (2008).
5. Siegel, J. B. *et al.* *Science* **329**, 309–313 (2010).
6. Röthlisberger, D. *et al.* *Nature* **453**, 190–195 (2008).
7. Privett, H. K. *et al.* *Proc. Natl Acad. Sci. USA* **109**, 3790–3795 (2012).
8. Korendovych, I. V. *et al.* *Org. Lett.* **12**, 5142–5145 (2010).
9. Schreier, B., Stumpp, C., Wiesner, S. & Höcker, B. *Proc. Natl Acad. Sci. USA* **106**, 18491–18496 (2009).
10. Metz, S. *et al.* *Proc. Natl Acad. Sci. USA* **108**, 8194–8199 (2011).
11. Jeffrey, P. D. *et al.* *Proc. Natl Acad. Sci. USA* **90**, 10310–10314 (1993).
12. Korndörfer, I. P., Schlehuber, S. & Skerra, A. *J. Mol. Biol.* **330**, 385–396 (2003).
13. Fowler, D. M. *et al.* *Nature Meth.* **7**, 741–746 (2010).
14. Koide, S. & Sidhu, S. S. *ACS Chem. Biol.* **4**, 325–334 (2009).
15. Koga, N. *et al.* *Nature* **491**, 222–227 (2012).

Social reward requires coordinated activity of nucleus accumbens oxytocin and serotonin

Gül Dölen^{1†}, Ayeh Darvishzadeh¹, Kee Wui Huang¹ & Robert C. Malenka¹

Social behaviours in species as diverse as honey bees and humans promote group survival but often come at some cost to the individual. Although reinforcement of adaptive social interactions is ostensibly required for the evolutionary persistence of these behaviours, the neural mechanisms by which social reward is encoded by the brain are largely unknown. Here we demonstrate that in mice oxytocin acts as a social reinforcement signal within the nucleus accumbens core, where it elicits a presynaptically expressed long-term depression of excitatory synaptic transmission in medium spiny neurons. Although the nucleus accumbens receives oxytocin-receptor-containing inputs from several brain regions, genetic deletion of these receptors specifically from dorsal raphe nucleus, which provides serotonergic (5-hydroxytryptamine; 5-HT) innervation to the nucleus accumbens, abolishes the reinforcing properties of social interaction. Furthermore, oxytocin-induced synaptic plasticity requires activation of nucleus accumbens 5-HT_{1B} receptors, the blockade of which prevents social reward. These results demonstrate that the rewarding properties of social interaction in mice require the coordinated activity of oxytocin and 5-HT in the nucleus accumbens, a mechanistic insight with implications for understanding the pathogenesis of social dysfunction in neuropsychiatric disorders such as autism.

The mesocorticolimbic (MCL) circuit, implicated in encoding the rewarding properties of addictive drugs, is likely to have evolved to motivate behaviours that were important for survival and reproduction. Such incentive behaviours include eating, drinking and copulation, and are reinforced by so-called 'natural rewards' (for example, food, water, pheromones)¹. Growing evidence suggests that social interaction itself can act as a natural reward². However, given the diversity of social behaviours (for example, parental investment, mating, cooperation) and the selection pressures that shaped their emergence (reproductive, predation, limited resources)³, it remains unclear whether evolutionarily conserved neural mechanisms exist to encode social reward.

An important clue comes from studies that have related pair-bonding behaviour in prairie voles (*Microtus ochrogaster*) to elevated expression of oxytocin receptors (OTRs) in the nucleus accumbens (NAc), a key component of the brain's MCL reward circuit⁴. However, the species-specific nature of this mating behaviour and the reported paucity of OTR expression in the NAc of mice^{2,5,6} questions the relevance of NAc OTRs to consociate social behaviours. This topic is of particular interest given that polymorphisms in the OTR gene have been associated with autism spectrum disorders, which are characterized by profound social deficits, and may be amenable to treatment with oxytocin (OT)⁷.

Mice are social animals: they live in consociate 'demes' consisting of five to ten adult members that share territorial defence⁸ and alloparental responsibilities⁹, and exhibit several behaviours (for example, vocal communication, imitation, and empathy)^{10–12} that are the hallmarks of sociality. As in several other species including humans, OT has been linked to social behaviours in mice⁷. However, OT and OTR knockout mice show a number of related behavioural deficits (such as memory impairment, anxiety, stress, aggressivity)⁵ that make it difficult to parse the function of OT as a social reward signal in the central nervous system. To examine the hypothesis that OT signalling in mice is required for the rewarding properties of social interactions, we used

a conditioned place preference (CPP) assay that has traditionally been used to study the rewarding properties of drugs of abuse¹³ and recently has been expanded to include social reward¹⁴.

Social reward requires oxytocin

Male wild-type mice were conditioned for social CPP (Fig. 1a, b) while receiving intraperitoneal injections of either saline or the OTR antagonist (OTR-A), L-368,899 hydrochloride (5 mg kg⁻¹, twice a day for 2 days). Saline-treated wild-type mice showed a robust place preference for the socially conditioned context, whereas OTR-A treated mice showed no preference (Fig. 1c–e). Neither locomotor activity (Supplementary Fig. 1a–i) nor cocaine CPP (Supplementary Fig. 2a–d) was altered by OTR-A treatment, demonstrating the specificity of the effects of OTR-A for the social domain. Furthermore, OTR-A, but not saline, localized to the NAc using Andalman probes (Fig. 1f and Supplementary Fig. 3a, b) prevented social CPP (Fig. 1g–i), demonstrating that OT action in the NAc is required for consociate social reward.

Given the known species- and sex-specific variation in OTR expression^{2,5,15,16}, it is notable that no study so far^{6,17–19} has determined whether hypothalamic OTRergic inputs to the NAc exist in male mice. Here we injected recombinant rabies virus expressing enhanced green fluorescent protein (eGFP) (RBV-eGFP) into the NAc, where it is taken up by presynaptic terminals and retrogradely transported to cell bodies (Supplementary Fig. 4). In a substantial subset of hypothalamic neurons in the paraventricular nucleus (PVN), but not the supraoptic nucleus (SON), robust eGFP expression co-localizes with OT, indicating a direct axonal OTRergic projection to the NAc (Supplementary Figs 4 and 5). Furthermore, these results suggest that it is the magnocellular projection from the SON that distinguishes prairie voles⁶ from rats¹⁹ and mice. Although they do not rule out an additional contribution of paracrine release, our findings demonstrate a significant synaptic source for OT in the NAc of male mice.

¹Nancy Pritzker Laboratory, Department of Psychiatry and Behavioral Sciences, Stanford University School of Medicine, 265 Campus Drive, Stanford, California 94305, USA. †Present address: Department of Neuroscience, Johns Hopkins University, 855 North Wolfe Street, Baltimore, Maryland 21205, USA.

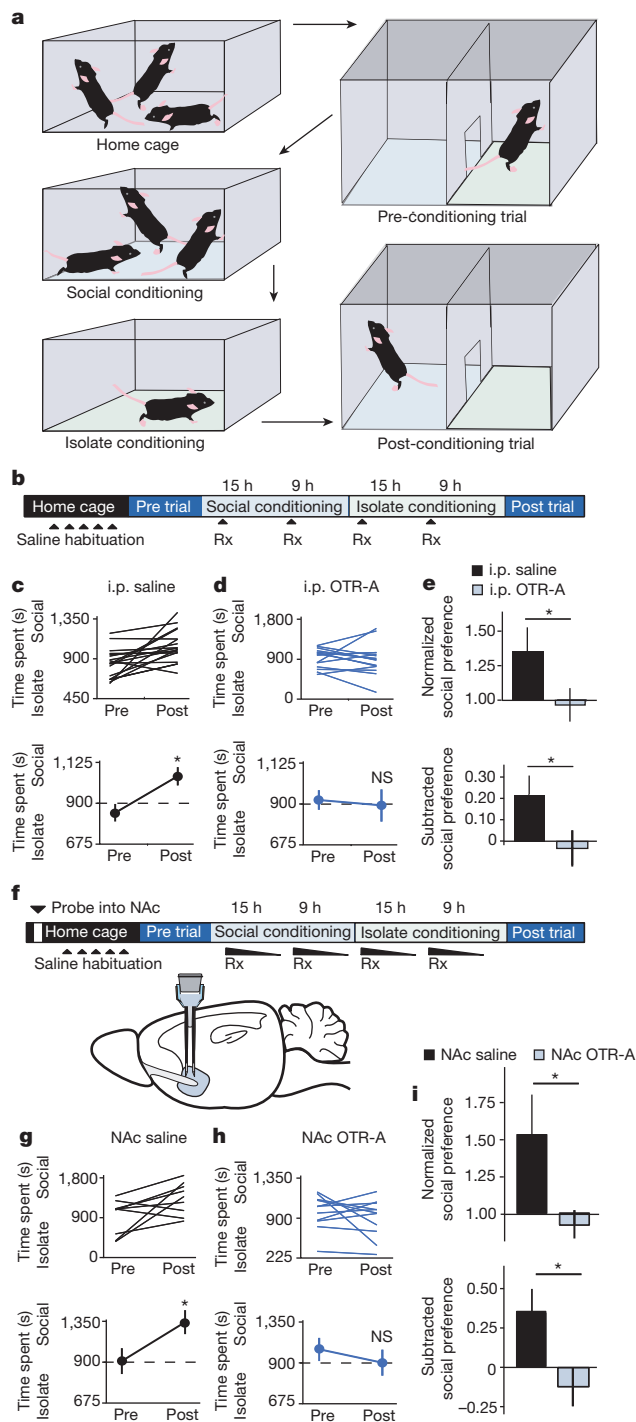


Figure 1 | Oxytocin is required for social CPP. **a–i**, Protocol for social CPP (**a**). Experimental time course of intraperitoneal (i.p.) injections (**b**) and NAC reverse microdialysis (**f**) in social CPP. Individual (top) and average (bottom) responses in animals receiving intraperitoneal (i.p.) (**c**) or NAC (**g**) saline versus animals receiving i.p. (**d**) or NAC (**h**) OTR-A. For both i.p. and NAC delivery routes, saline- but not OTR-A-treated animals spend more time in social bedding cue following conditioning ($n = 18$ i.p. saline, $n = 15$ i.p. OTR-A; $n = 9$ NAC saline and $n = 11$ NAC OTR-A animals). Values below 900 indicate that subjects preferred isolate bedding; values above 900 indicate that subjects preferred social bedding. **e, i**, Comparisons between treatment (Rx) groups reveal significantly decreased normalized and subtracted social preference in both i.p. and NAC OTR-A-treated animals. Summary data are presented as mean \pm s.e.m. (* $P < 0.05$, Student's t -test). Each arrowhead indicates an application of saline or OTR-A.

Oxytocin induces presynaptic LTD in NAc MSNs

To interrogate directly the synaptic role of OT within the NAc, we recorded excitatory postsynaptic currents (EPSCs) from NAc medium spiny neurons (MSNs) in acute slices. Bath application of OT ($1 \mu\text{M}$, 10 min) caused a long-term depression (LTD) of EPSCs that was blocked (Fig. 2a–c) but not reversed (Fig. d–f) by the OTR-A L-368,899 hydrochloride ($1 \mu\text{M}$, continuous or 10 min application respectively). The magnitude of this oxytocin-induced LTD was significantly decreased in slices from socially conditioned versus isolation conditioned animals (Fig. 2g–i), consistent with the hypothesis that social experience elicits or influences the generation of OT-LTD.

To determine whether social experience preferentially influenced OT-LTD in one of the two major components of the basal ganglia circuit, direct (D1-receptor-expressing) versus indirect (D2-receptor-expressing) pathway MSNs²⁰, targeted recordings were made from NAc slices prepared from bacterial artificial chromosome (BAC) transgenic D1-TdTomato, and D2-eGFP reporter mice^{21,22}. Application of OT induced robust LTD (Fig. 2j–l) and isolation conditioning resulted in increased magnitude of OT-LTD (Supplementary Fig. 6) in both D1- and D2-receptor-expressing MSNs, suggesting that these phenomena do not display direct and indirect pathway specificity.

To determine whether the OT-LTD was expressed pre- or postsynaptically, we performed a number of standard electrophysiological synaptic assays. The frequency, but not the amplitude, of miniature EPSCs, was significantly decreased by OT application (Fig. 2m–q). Furthermore, both the paired-pulse ratio (PPR) of EPSCs (50-ms inter-stimulus interval) and the coefficient of variation of the EPSCs increased following OT application (Fig. 2r–t). Together, these findings suggest that OT-LTD results from a decrease in presynaptic neurotransmitter release probability.

Social reward requires presynaptic OTRs in NAc

Anatomical studies have revealed sparse expression of OTRs in mouse NAc^{2,5}. Moreover, immunostaining in OTR-Venus reporter mice²³ indicates that the small subset of cells that do express OTRs in the NAc are either inhibitory interneurons or glial cells (Supplementary Fig. 7). To test the hypothesis that OTRs in the NAc are preferentially localized to presynaptic boutons deriving from afferent inputs, we injected TdTomato-expressing RBV (RBV-TdTomato) into the NAc of OTR-Venus reporter mice (Supplementary Fig. 8). Cellular co-localization of TdTomato and Venus was detected in several, but not all, brain regions projecting to the NAc (Supplementary Fig. 8), identifying a number of putative sources of presynaptic OTRs in the NAc.

To extend the anatomical mapping of OTRs to their functional role in social reward *in vivo*, we used conditional OTR knockout mice²⁴ combined with Cre recombinase (Cre)-expressing RBV or adeno-associated virus (AAV) injected into the NAc, an approach that enabled selective ablation of pre- or postsynaptic NAc OTRs, respectively. Normal social CPP was observed in both sham-injected wild-type and conditional OTR mice (Fig. 3a–d). Injection of the AAV-Cre-eGFP to delete OTRs from cells within the NAc did not affect social CPP in either wild-type or conditional OTR mice (Fig. 3e–h). Consistent with this lack of effect of deleting OTRs from cells within the NAc, OT application did not induce long-lasting changes at inhibitory synapses onto MSNs (Supplementary Fig. 9). In contrast, injection of RBV-Cre-eGFP to delete presynaptic OTRs in the NAc, completely blocked social CPP in conditional OTR knockout mice but had no effect in wild-type mice (Fig. 3i–l). Injection sites and viral expression were confirmed for all animals (Supplementary Figs 10 and 11). Considered together with the pharmacological results showing OTRs within the NAc are required for social CPP (Fig. 1f–i), these results indicate that OTRs on presynaptic boutons within the NAc are required for social reward.

Social CPP and LTD require dorsal raphe inputs and 5HT_{1B} receptors

To determine which of the afferent inputs expressing OTRs identified by RBV-mediated molecular ablation are required for social CPP,

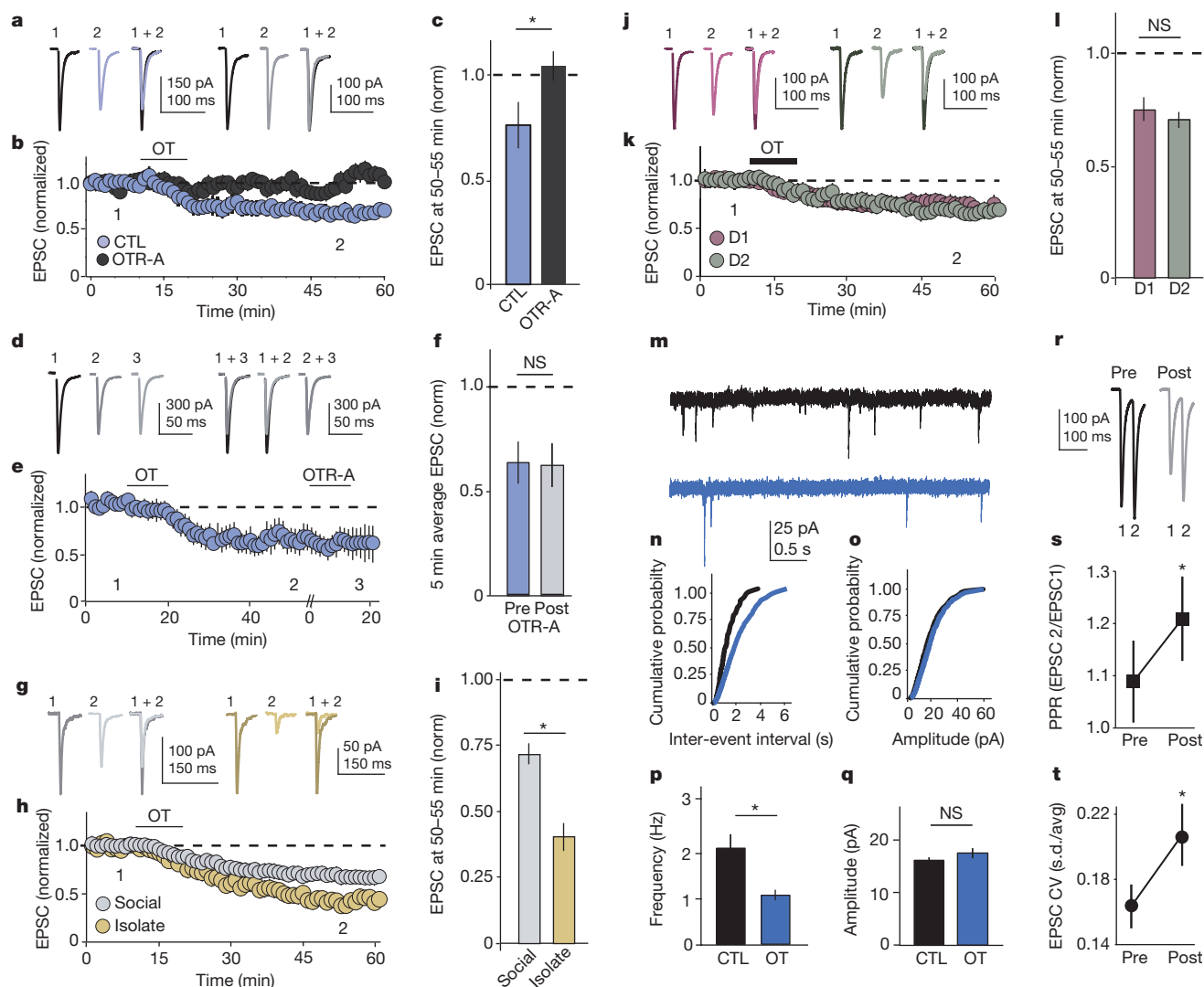


Figure 2 | Oxytocin induces LTD in the NAc. **a–h**, Representative traces (**a**, **d**, **g**, **j**), summary time course (**b**, **e**, **h**, **k**), and average post-treatment magnitude comparisons (**c**, **f**, **i**, **l**) reveal significant EPSC response depression in oxytocin-treated but not OTR-A-pre-incubated cells (**a–c**, $n = 6$ OT (oxytocin), $n = 6$ OT + OTR-A pre-incubation cells). OT-response depression is not reversed by post-induction OTR-A chase (**d–f**, $n = 7$ cells). The magnitude of OT-LTD is significantly increased in cells from isolation versus socially reared animals (**g–i**, isolate, $n = 14$, social $n = 27$ cells). The magnitude of EPSC OT-LTD is not different in D1 versus D2 MSNs (**j–l**, $n = 9$ D1, and

$n = 11$ D2 cells). **m–q** Representative miniature EPSC traces (**m**), cumulative probability (**n**, **o**), and average (**p**, **q**) comparisons reveal that miniature EPSC frequency (**n**, **p**), but not amplitude (**o**, **q**), is decreased in OT-treated versus control cells (control, $n = 11$, OT, $n = 11$ cells). **r–t**, Comparisons of representative traces (**r**) and average (**s**) paired-pulse ratios PPR ($n = 6$ cells) as well as average (**t**) coefficient of variance, CV ($n = 32$ cells) reveal significant increases following induction of OT-LTD. Summary data are presented as mean \pm s.e.m. (* $P < 0.05$, Student's t -test). Numbered traces (1, 2 and 3) were taken at the times indicated by numbers below the graphs.

we next injected AAV-eCre-eGFP into selected brain regions of conditional OTR mice. Deleting OTRs in either the anterior cingulate cortex or the ventral subiculum had no effect on social CPP (Supplementary Fig. 12), whereas AAV-Cre-eGFP injections into the dorsal raphe nucleus of conditional OTR mice, but not wild-type mice, prevented social CPP (Fig. 4a–d). This same manipulation also significantly reduced OT-LTD recorded *ex vivo* (Fig. 4e–g). Together these results provide support for the hypothesis that presynaptic OTRs on dorsal raphe nucleus axon terminals within the NAc are specifically required for social reward.

Since the dorsal raphe nucleus is one of the major sources of serotonin (5-HT) in the brain, we further characterized NAc projection neurons in the dorsal raphe nucleus and found substantial overlap between OTR- and 5-HT-expressing cells (Supplementary Fig. 13), raising the possibility of coordinated activity of these transmitters in the NAc. Given that 5HT1B receptors have been implicated in social behaviours^{25,26} and autism²⁷, and their activation elicits a presynaptic LTD in the striatum²⁸, we reasoned that OT may induce LTD in the NAc through activation of 5HT1B receptors. Consistent with previous

results²⁸, application of the 5HT1B selective agonist CP-93129 induced robust LTD in NAc MSNs (Fig. 5a–c). Subsequent application of OT caused no further depression (Fig. 5a–c), suggesting that the 5HT1B receptor-induced LTD had occluded OT-LTD. To test whether OT-LTD required release of 5HT within the NAc, we applied the 5HT1B receptor antagonist NAS-181 (20 μ M) to NAc slices, a manipulation that largely prevented the LTD normally induced by OT (Fig. 5d–f). In contrast, 5HT1B receptor-induced LTD was readily induced in slices in which OTRs had been pharmacologically blocked (Fig. 5g–i) or molecularly ablated from dorsal raphe nucleus projections (Supplementary Fig. 14). Application of NAS-181 also prevented the decrease in miniature EPSC frequency normally elicited by OT (Fig. 5j–n), but had no effect on its own (Supplementary Fig. 15).

Together these results support the hypothesis that activation of OTRs on the terminals of dorsal raphe nucleus axons within the NAc leads to a 5HT1B receptor-dependent form of LTD (Supplementary Fig. 16) and that this synaptic modulation is necessary for social reward, as measured by social CPP. A strong prediction of this hypothesis is that

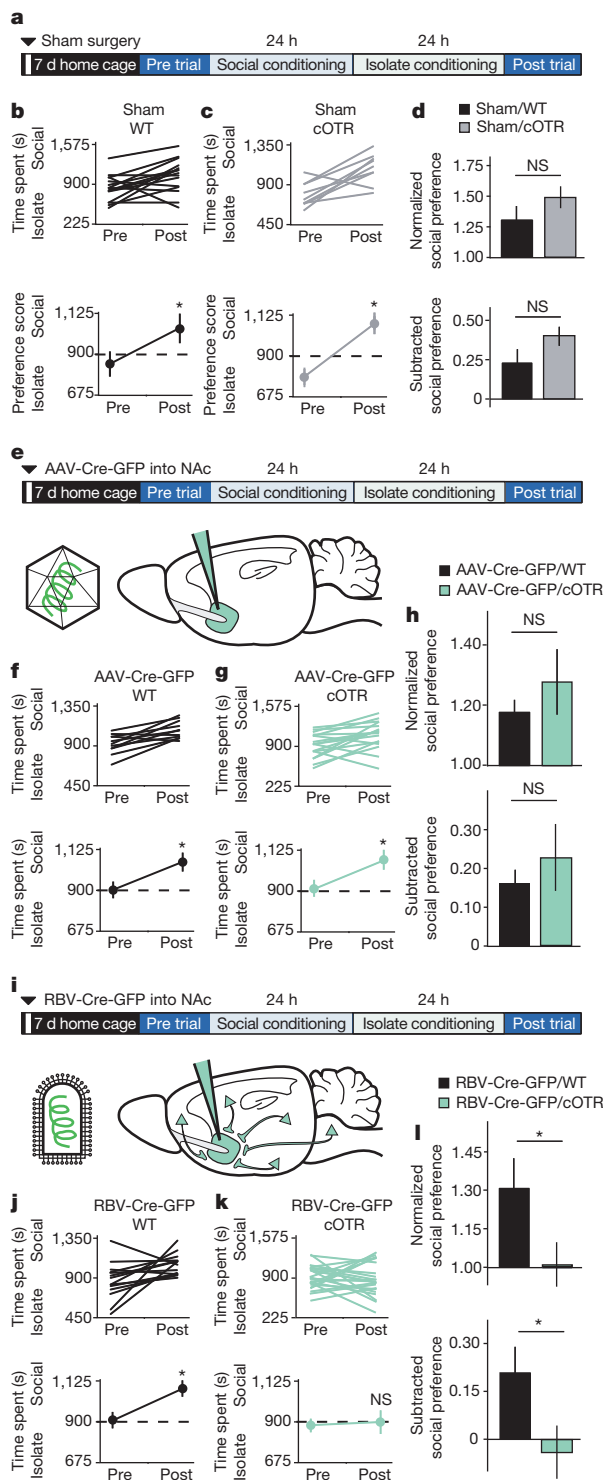


Figure 3 | Presynaptic OTRs are required for social CPP. **a–l**, Experimental time course for sham (**a**), NAc AAV-Cre-eGFP injection showing AAV particle and spread of Cre-eGFP from injection site (**e**), and NAc RBV-Cre-eGFP injection showing RBV particle and spread of Cre-eGFP from injection site (**i**). Individual (top) and average (bottom) responses in wild-type (WT) (**b, f, j**), versus conditional OTR (cOTR) (**c, g, k**) animals receiving sham (**b, c**), NAc AAV-Cre-eGFP (**f, g**) or NAc-RbV-Cre-eGFP (**j, k**). WT animals, as well as sham and NAc AAV-Cre-eGFP-injected cOTR animals, but not cOTR animals injected with NAc RBV-Cre-eGFP, spend more time in the social bedding cue following conditioning (sham WT, $n = 15$, cOTR, $n = 8$; NAc AAV-Cre-eGFP WT, $n = 15$, cOTR, $n = 19$; NAc RBV-Cre-eGFP WT, $n = 14$, cOTR, $n = 22$ animals). **d, h, l**, Comparisons between WT and cOTR animals reveal normal social CPP in sham and NAc AAV-Cre-eGFP-injected animals, whereas in NAc RBV-Cre-eGFP-injected animals social CPP is significantly decreased in cOTR versus WT controls. Summary data are presented as mean \pm s.e.m. (* $P < 0.05$, Student's t -test).

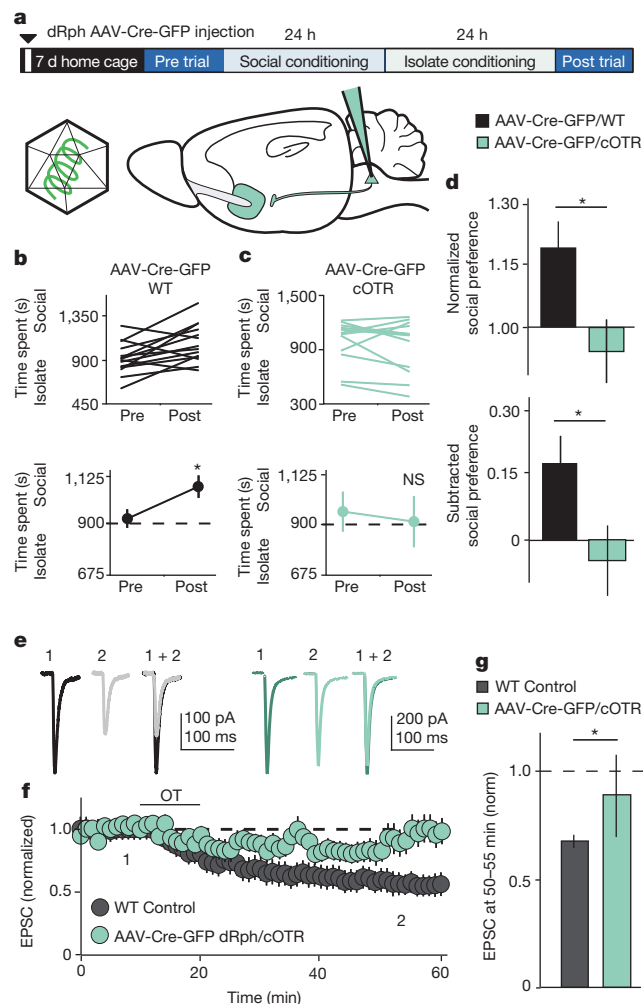


Figure 4 | NAc OTRs in presynaptic terminals originating from the dorsal raphe nucleus are required for social CPP and OT-LTD. **a**, Experimental time course of dorsal raphe nucleus (dRph) AAV-Cre-eGFP injections in social CPP. **b, c** Individual (top) and average (bottom) comparisons reveal that dRph AAV-Cre-eGFP-injected WT (**b**), but not cOTR (**c**) animals spend significantly more time in the social bedding cue following conditioning (WT, $n = 14$, cOTR, $n = 10$ animals). **d**, Comparisons between dRph AAV-Cre-eGFP-injected groups reveal significantly decreased social CPP in cOTR animals compared to WT controls. **e–g**, Representative traces (**e**), summary time course (**f**) and average post-treatment magnitude comparisons (**g**) reveal absence of OT-LTD in EPSCs recorded from dRph AAV-Cre-eGFP-injected cOTR knockout versus pooled WT control animals (dRph AAV-Cre-eGFP-injected cOTR, $n = 6$ cells; pooled WT control, $n = 30$ cells). Summary data are presented as mean \pm s.e.m. (* $P < 0.05$, Student's t -test).

blockade of 5HT1B receptors within the NAc should prevent social CPP. Consistent with this prediction, NAS-181, but not saline, infusions into the NAc during conditioning (Fig. 6a) prevented the occurrence of social CPP (Fig. 6b–d).

Concluding remarks

We have demonstrated that the coordinated activity of OT and 5-HT is required for the reward associated with social interactions and modifies MCL circuit properties by generating LTD of excitatory synapses onto MSNs in the NAc. Moreover, our findings specifically implicate OT-mediated 5-HT release in the NAc in the regulation of social reward. Since OT-LTD occurs in both D1- and D2-receptor-expressing MSN subtypes, as does 5HT1B-LTD²⁸, these results suggest that social reward is not expressly governed by the dichotomies proposed by prevailing models of striatal function²⁰. Indeed, the two-pathway framework for striatal function is almost certainly oversimplified^{29–32} and computational

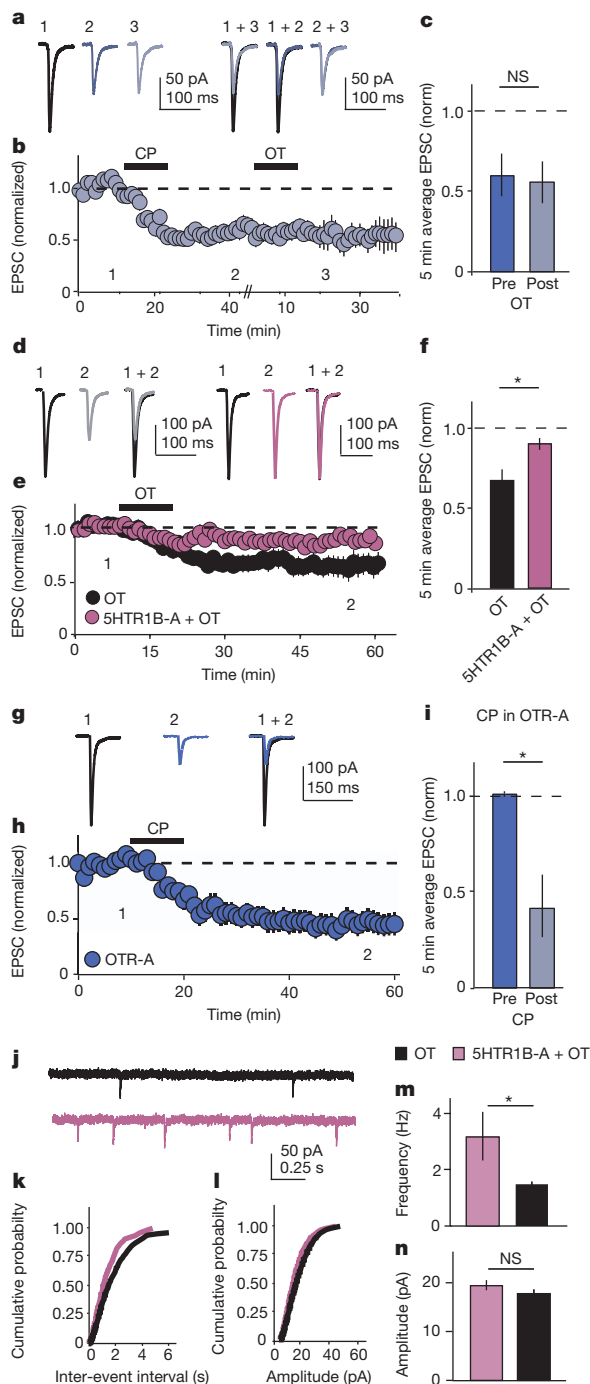


Figure 5 | OT-LTD in NAc requires 5HT1B receptors. **a–i**, Representative traces (**a**, **d**, **g**), summary time course (**b**, **e**, **h**) and average post-treatment magnitude comparisons (**c**, **f**, **i**) reveal that EPSC depression in cells treated with 5HT1B agonist (CP-93129 dihydrochloride) is not augmented by subsequent application of OT (**a–c**, $n = 5$ cells); OT-LTD is significantly reduced in cells pre-treated with the 5HT1B-antagonist (NAS-181) (**d–f**, control, $n = 7$, 5HT1B antagonist, $n = 7$ cells); 5HT1B-mediated LTD induced by application of CP-93129 is not affected by pharmacological blockade of OTRs (**g–i**, $n = 5$ cells). **j–n** Representative miniature EPSC traces (**j**), cumulative probability (**k**, **l**), and average (**m**, **n**) comparisons reveal miniature EPSC frequency (**k**, **m**), but not amplitude (**l**, **n**), is decreased in OT-treated cells versus cells treated with OT in the presence of NAS-181 (OT, $n = 17$, OT + 5HT1B-A, $n = 17$ cells). Summary data are presented as mean \pm s.e.m. (* $P < 0.05$, Student's t -test).

modelling studies have proposed that reinforcement learning engages multiple neuromodulatory reward circuits in parallel³³. Furthermore, 5-HT and dopamine systems may represent reward in fundamentally

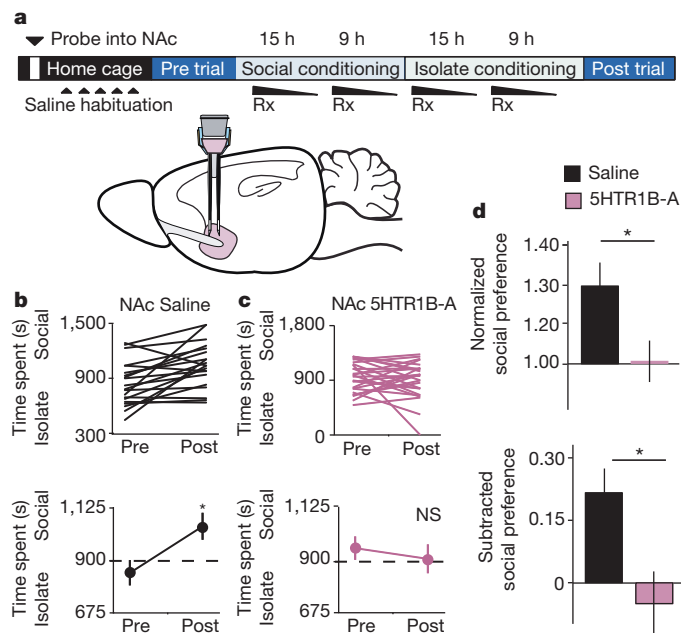


Figure 6 | Social CPP requires NAc 5HT1B receptors. **a**, Experimental time course of NAc reverse microdialysis. **b**, **c**, Individual (top) and average (bottom) responses in animals receiving NAc saline (**b**) versus 5HT1B antagonist (5HT1B-A) (**c**). Saline-treated animals, but not 5HT1B-A-treated animals, spend more time in social bedding cue following conditioning (Nac saline, $n = 20$, NAc 5HT1B-A, $n = 26$ animals). **d**, Comparisons between treatment groups reveal significantly decreased normalized and subtracted social preference in NAc 5HT1B-A-treated animals compared to saline controls. Summary data are presented as mean \pm s.e.m. (* $P < 0.05$, Student's t -test).

different ways^{34–36}. Future studies examining the interplay between dopamine and 5-HT in the regulation of social reward will therefore be informative.

In light of estimates that the shift to social living preceded the emergence of pair-living by 35 million years³, we suggest that the NAc-dependent social reward mechanisms described here are the predecessors of evolutionary specializations seen in prairie voles^{2,5,6}. These mechanisms utilize presynaptically localized OTRs, which couple to G-proteins⁵, and thus may have been overlooked by previous studies that relied on receptor autoradiography and transcript tagging to conclude that OTRs do not exist in the NAc of consociate species like mice^{2,6}. Moreover, as it is these antecedent social behaviours that are disrupted in neuropsychiatric diseases such as autism³⁷, the elucidation of the neural mechanisms mediating social reward is a critical step towards the development of rational, mechanism-based treatments for brain disorders that involve dysfunction in social behaviours.

METHODS SUMMARY

All procedures were conducted in accordance with the animal care standards set forth by the National Institutes of Health and were approved by Stanford University's Administrative Panel on Laboratory Animal Care. Male young adult mice (4 to 6 weeks of age) on a C57BL/6 background were used for all studies.

Full Methods and any associated references are available in the online version of the paper.

Received 26 November 2012; accepted 1 August 2013.

- Kelley, A. E. & Berridge, K. C. The neuroscience of natural rewards: relevance to addictive drugs. *J. Neurosci.* **22**, 3306–3311 (2002).
- Insel, T. R. Is social attachment an addictive disorder? *Physiol. Behav.* **79**, 351–357 (2003).
- Shultz, S., Opie, C. & Atkinson, Q. D. Stepwise evolution of stable sociality in primates. *Nature* **479**, 219–222 (2011).
- Young, L. J. & Wang, Z. The neurobiology of pair bonding. *Nature Neurosci.* **7**, 1048–1054 (2004).
- Lee, H.-J., Macbeth, A. H., Pagani, J. H. & Young, W. S. Oxytocin: the great facilitator of life. *Prog. Neurobiol.* **88**, 127–151 (2009).

6. Ross, H. E. *et al.* Characterization of the oxytocin system regulating affiliative behavior in female prairie voles. *Neurosci.* **162**, 892–903 (2009).
7. Yamasue, H. *et al.* Integrative approaches utilizing oxytocin to enhance prosocial behavior: from animal and human social behavior to autistic social dysfunction. *J. Neuroscience* **32**, 14109–14117 (2012).
8. Anderson, P. K. & Hill, J. *Mus musculus*: experimental induction of territory formation. *Science* **148**, 1753–1755 (1965).
9. Riedman, M. L. The evolution of alloparental care and adoption in mammals and birds. *Q. Rev. Biol.* **57**, 405–435 (1982).
10. Holy, T. E. & Guo, Z. Ultrasonic songs of male mice. *PLoS Biol.* **3**, e386 (2005).
11. Panksepp, J. Behavior. Empathy and the laws of affect. *Science* **334**, 1358–1359 (2011).
12. Hodgson, S. R., Hofford, R. S., Roberts, K. W., Wellman, P. J. & Eitan, S. Socially induced morphine pseudosensitization in adolescent mice. *Behav. Pharmacol.* **21**, 112–120 (2010).
13. Tszchentke, T. M. Measuring reward with the conditioned place preference (CPP) paradigm: update of the last decade. *Addict. Biol.* **12**, 227–462 (2007).
14. Panksepp, J. B. & Lahvis, G. P. Social reward among juvenile mice. *Genes Brain Behav.* **6**, 661–671 (2007).
15. Rosen, G. J., de Vries, G. J., Goldman, S. L., Goldman, B. D. & Forger, N. G. Distribution of oxytocin in the brain of a eusocial rodent. *Neuroscience* **155**, 809–817 (2008).
16. Hermes, M. L., Buijs, R. M., Masson-Pévet, M. & Pévet, P. Oxytocinergic innervation of the brain of the garden dormouse (*Eliomys quercinus* L.). *J. Comp. Neurol.* **273**, 252–262 (1988).
17. Phillipson, O. T. & Griffiths, A. C. The topographic order of inputs to nucleus accumbens in the rat. *Neuroscience* **16**, 275–296 (1985).
18. Brog, J. S., Ongse, A. S., Deutch, A. Y. & Zahm, D. S. The patterns of afferent innervation of the core and shell in the “accumbens” part of the rat ventral striatum: immunohistochemical detection of retrogradely transported fluoro-gold. *J. Comp. Neurol.* **278**, 255–278 (1993).
19. Knobloch, H. S. *et al.* Evoked axonal oxytocin release in the central amygdala attenuates fear response. *Neuron* **73**, 553–566 (2012).
20. Lobo, M. K. & Nestler, E. J. The striatal balancing act in drug addiction: distinct roles of direct and indirect pathway medium spiny neurons. *Front. Neuroanat.* **5**, 41 (2011).
21. Shuen, J. A., Chen, M., Gloss, B. & Calakos, N. Drd1a-tdTomato BAC transgenic mice for simultaneous visualization of medium spiny neurons in the direct and indirect pathways of the basal ganglia. *J. Neurosci.* **28**, 2681–2685 (2008).
22. Gong, S. *et al.* A gene expression atlas of the central nervous system based on bacterial artificial chromosomes. *Nature* **425**, 917–925 (2003).
23. Yoshida, M. *et al.* Evidence that oxytocin exerts anxiolytic effects via oxytocin receptor expressed in serotonergic neurons in mice. *J. Neurosci.* **29**, 2259–2271 (2009).
24. Lee, H.-J., Caldwell, H. K., Macbeth, A. H., Tolu, S. G. & Young, W. S. A conditional knockout mouse line of the oxytocin receptor. *Endocrinology* **149**, 3256–3263 (2008).
25. Brunner, D., Buhot, M. C., Hen, R. & Hofer, M. Anxiety, motor activation, and maternal-infant interactions in 5HT1B knockout mice. *Behav. Neurosci.* **113**, 587–601 (1999).
26. Furay, A. R., McDevitt, R. A., Miczek, K. A. & Neumaier, J. F. 5-HT1B mRNA expression after chronic social stress. *Behav. Brain Res.* **224**, 350–357 (2011).
27. Orabona, G. M. *et al.* HTR1B and HTR2C in autism spectrum disorders in Brazilian families. *Brain Res.* **1250**, 14–19 (2009); erratum **1264**, 127 (2009).
28. Mathur, B. N., Capik, N. A., Alvarez, V. A. & Lovinger, D. M. Serotonin induces long-term depression at corticostriatal synapses. *J. Neurosci.* **31**, 7402–7411 (2011).
29. Cui, G. *et al.* Concurrent activation of striatal direct and indirect pathways during action initiation. *Nature* **494**, 238–242 (2013).
30. Capper-Loup, C., Canales, J. J., Kadaba, N. & Graybiel, A. M. Concurrent activation of dopamine D1 and D2 receptors is required to evoke neural and behavioral phenotypes of cocaine sensitization. *J. Neurosci.* **22**, 6218–6227 (2002).
31. Nambu, A. Seven problems on the basal ganglia. *Curr. Opin. Neurobiol.* **18**, 595–604 (2008).
32. Perreault, M. L., Hasbi, A., O'Dowd, B. F. & George, S. R. The dopamine d1-d2 receptor heteromer in striatal medium spiny neurons: evidence for a third distinct neuronal pathway in Basal Ganglia. *Front. Neuroanat.* **5**, 31 (2011).
33. Doya, K. Metalearning and neuromodulation. *Neural Netw.* **15**, 495–506 (2002).
34. Nakamura, K., Matsumoto, M. & Hikosaka, O. Reward-dependent modulation of neuronal activity in the primate dorsal raphe nucleus. *J. Neurosci.* **28**, 5331–5343 (2008).
35. Tanaka, S. C. *et al.* Prediction of immediate and future rewards differentially recruits cortico-basal ganglia loops. *Nature Neurosci.* **7**, 887–893 (2004).
36. Boureau, Y.-L. & Dayan, P. Opponency revisited: competition and cooperation between dopamine and serotonin. *Neuropsychopharmacology* **36**, 74–97 (2011).
37. Silverman, J. L., Yang, M., Lord, C. & Crawley, J. N. Behavioural phenotyping assays for mouse models of autism. *Nature Rev. Neurosci.* **11**, 490–502 (2010).

Supplementary Information is available in the online version of the paper.

Acknowledgements We thank members of the Malenka laboratory for comments; A. Andalman, W. Xu, B.K. Lim and T. Sudhof for technical advice; and the SIM1 Animal Care facility for husbandry support. The OT-neurophysin antibody was a gift of H. Gainer. OTR-Venus reporter mice were a gift of L. J. Young. D1-TdTomato BAC transgenic mice were provided by N. Calakos. The rabies virus complementary DNA plasmid and viral component-expressing plasmids were gifts from K. Conzelmann and I. Wickersham. HHK-B19G cells were a gift from E. Callaway. AAVs were produced by the Stanford NGVVC (supported by National Institutes of Health grant NIH NS069375). The AAV-DJ helper plasmid was a gift from M. Kay. This work was supported by funding from the Simons Foundation Autism Research Initiative (R.C.M.), N.I.H. (R.C.M.), and a Berry Foundation Postdoctoral Fellowship (G.D.).

Author Contributions G.D. and R.C.M. designed the study, interpreted results and wrote the paper. G.D. performed behavioural experiments, electrophysiology, and confocal microscopy. G.D., A.D. and K.W.H. performed stereotaxic injections and immunohistochemistry. K.W.H. generated RBV viruses. All authors edited the paper.

Author Information Reprints and permissions information is available at www.nature.com/reprints. The authors declare no competing financial interests. Readers are welcome to comment on the online version of the paper. Correspondence and requests for materials should be addressed to R.C.M. (malenka@stanford.edu).

METHODS

Animals. Male young adult (4 to 6 weeks of age) C57BL/6 (Charles River), DRD1A–TdTomato BAC transgenic²¹ (D1–TdTomato, gift of N. Calakos), DRD2–eGFP BAC transgenic²² (D2–eGFP), Oxtm1.1Wsy homozygous²⁴ (conditional OTR knockout, Jackson Laboratory), or OTR Venus Neo/+²³ (heterozygous OTR–Venus reporter, gift of L. J. Young) mice backcrossed to C57BL/6 were used for all experiments. All procedures complied with the animal care standards set forth by the National Institutes of Health and were approved by Stanford University's Administrative Panel on Laboratory Animal Care. All animals were maintained on a 12 h–12 h light–dark cycle. Experimenters were blind to the treatment condition when subjective criteria were used as a component of data analysis, and control and test conditions were interleaved for all experiments.

Behavioural assays. The protocol for social conditioned place preference (social CPP) was shortened to 2 days of conditioning (Fig. 1a) from 10 days of conditioning^{14,38}. Animals were weaned (or delivered from Charles River) at 3 weeks of age into 'home' cages containing 3 to 5 cage-mates, and housed on corn cob bedding (Bed-O'Cobs, 0.125 inches, PharmaServ). One to two weeks later, animals were subjected to experimental manipulations and returned to their home cage (all cage-mates were of the same genotype and received the same experimental manipulation). Animals were then placed in open field activity chamber (ENV-510, Med Associates) equipped with infrared beams and a software interface (Activity Monitor, Med Associates) that monitors the position of the mouse. The apparatus was divided into two equally sized zones using a clear plastic wall, with a 5-cm diameter circular opening at the base; each zone contained one type of novel bedding (Alpha-Dri, PharmaServ, Alpha Chip, PharmaServ; Bed-O'Cobs, 0.25 inches, PharmaServ; or Kaytee Soft Granule, Petco). The amount of time spent freely exploring each zone was recorded during 30-min test sessions. After an initial test (pre-conditioning trial) to establish baseline preference for the two sets of bedding cues, mice were assigned to receive social conditioning (with cage-mates) for 24 h on one type of bedding, followed by 24 h on the isolate bedding cue (without cage-mates) on the other type of bedding. Bedding assignments (social versus isolate) were counter-balanced for an unbiased design. Twenty-four hours later, animals received a 30-min post-conditioning trial to establish preference for the two conditioned cues. Animals were excluded (pre-established criteria) if they exhibited a pre-conditioning preference score of >1.5 or <0.5 (for an unbiased procedure); pre-conditioning versus post-conditioning social preference scores were considered significant if paired student's *t*-test *P* values were <0.05 . Comparisons between experimental conditions were made using both normalized social preference scores (time spent in social zone; post-trial divided by pre-trial), and subtracted social preference scores (time spent in social zone; post-trial minus pre-trial); these were considered significant if unpaired student's *t*-test (two conditions), or analysis of variance (ANOVA) (three conditions, Supplementary Fig. 12) *P* values were <0.05 .

For cocaine-conditioned place preference (cocaine CPP), the apparatus was divided into two equally sized zones using plastic floor tiles with distinct visual and tactile cues (grey and smooth, or white and rough). After 5 days of saline injections twice a day for habituation in the home cage, the amount of time spent freely exploring each zone was recorded during 30-min test sessions. After an initial test to establish baseline preference for the two sets of cues, mice in each of the two treatment groups (intraperitoneal saline or intraperitoneal OTR-A) were randomly assigned in a counterbalanced fashion to receive cocaine (20 mg kg⁻¹) or saline in the presence of one set of cues (that is, an unbiased design). The second conditioning session was conducted 24 h later in the presence of the other set of cues. The post-conditioning test session was conducted 24 h after the second conditioning session to determine time spent in the presence of the cocaine versus saline associated cue. Isolation and socially housed animals were not different in terms of cocaine CPP so they were pooled for further analysis. Pre-conditioning, post-conditioning, subtracted, and normalized cocaine preference scores were calculated as for social CPP.

Andalman probes. Modified Andalman probes were constructed as described previously³⁹ (Supplementary Fig. 3). In brief, probes consisted of a reservoir (Polypropylene Luer Hub) attached to a double cannula guide (C235gs, 26GA, C/C distance 2 mm, 5 mm pedestal, cut 4 mm below pedestal, custom specified for mouse bilateral NAc coordinates, Plastics One). Polyimide tubing (40 American Wire Gauge, 0.0031 inches internal diameter, 0.0046 inches outside diameter, 0.00075 inches Wall, Small Parts) was threaded through the stainless steel tubing of the cannula guide on one end, and out of a hole drilled into the luer hub to act as a flush outlet (outflow tube) on the other end. The dialysis membrane (Spectra/Por, 13-kD molecular weight cut-off, Spectrum Laboratories) was then threaded over the outflow tube and through the cannula guide; ends were cut such that ~ 500 μ m of dialysis membrane was exposed below the cannula guide and above the sealed end. Junctions were sealed with bio-compatible epoxies (Epo-Tek 730, Epo-Tek 301, Epoxy Technologies). In this design, a pharmacological agent could

be intracranially delivered rapidly, continually and concurrently to all members of the social group, without anaesthesia.

Once male mice reached age postnatal day 35 to 40, probes were implanted into the NAc of male mice following bilateral craniotomy (bregma 1.54 mm; lateral 1.0 mm) and attached to the skull using dental acrylic. Previous reports indicate that for complete pharmacological effect, drug concentration in the reservoir must be ~ 500 times the dose used for direct injections^{39,40}, thus OTR and 5HT1B antagonists were applied at 10 mM (L-368,899) and 85 mM (NAS-181) concentrations in a volume of 25 μ l saline. Probe placement and competency was verified by post-hoc application of concentrated Fluorescein sodium salt (Sigma-Aldrich) to reservoir before intracardial PFA perfusion and histology (Supplementary Fig. 3).

Virus generation. Rabies virus (RBV) was generated from a full-length complementary DNA plasmid containing all components of RBV (SAD L16; gift from K.-K. Conzelmann)⁴¹. We replaced the rabies virus glycoprotein with eGFP (RBV–eGFP), TdTomato (RBV–TdTomato) or Cre–eGFP to generate RBV-expressing Cre–eGFP (RBV–Cre–eGFP), eGFP (RBV–eGFP) or TdTomato (RBV–TdTomato). To rescue RBV from this cDNA we used a modified version of a published protocol^{41,42}. In brief, HEK293T cells were transfected with a total of 6 plasmids; 4 plasmids expressing the RBV components pTIT–N, pTIT–P, pTIT–G and pTIT–L; one plasmid expressing T7 RNA polymerase (pCAGGS–T7), and the aforementioned glycoprotein-deleted RBV cDNA plasmid expressing Cre–eGFP, eGFP or TdTomato. For the amplification of RBV, the media bathing these HEK293T (ATCC) cells was collected 3 to 4 days post transfection and moved to baby hamster kidney (BHK) cells stably expressing RBV glycoprotein (BHK–B19G)⁴³. After 3 days, the media from BHK–B19G cells were collected, centrifuged for 5 min at 3,000g to remove cell debris, and concentrated by ultracentrifugation (55,000g for 2 h). Pellets were suspended in Dulbecco's PBS, aliquoted and stored at -80°C . The titre of concentrated RBV was measured by infecting HEK293 cell and monitoring fluorescence. Plasmids expressing the RBV components were gifts from K.-K. Conzelmann and I. Wickersham. BHK cells stably expressing B19G were a gift from E. Callaway.

The adeno-associated viruses (AAVs) used in this study were produced by the Stanford Neuroscience Gene Vector and Virus Core. In brief, AAV–DJ⁴⁴ was produced by transfection of AAV 293 cells (Agilent) with three plasmids: an AAV vector expressing Cre–eGFP, AAV helper plasmid (pHELPER, Agilent), and AAV rep–cap helper plasmid (pRC–DJ, gift from M. Kay). At 72 h after transfection, the cells were collected and lysed by a freeze-and-thaw procedure. Viral particles were then purified by an iodixanol step gradient ultracentrifugation method. The iodixanol was diluted and the AAV was concentrated using a 100-kDa molecular weight cut-off ultrafiltration device. The genomic titre was determined by quantitative PCR. **Stereotaxic injections.** Stereotaxic injection of viruses into NAc was performed under general ketamine–medetomidine anaesthesia using a stereotaxic instrument (David Kopf). A small volume (~ 1 μ l) of concentrated virus solution was injected bilaterally into NAc core (bregma 1.54 mm; lateral 1.0 mm; ventral 4.0 mm), unilaterally into the dorsal raphe nucleus (bregma -3.3 mm; lateral 0.0 mm; ventral 3.35 mm), bilaterally into the ventral subiculum (bregma -2.95 mm; lateral 3.1 mm; ventral 4.35 mm), or bilaterally anterior cingulate (bregma 1.0 mm; lateral 0.3 mm; ventral 1.25 mm) at a slow rate (100 nl per min) using a syringe pump (Harvard Apparatus). The injection needle was withdrawn 5 min after the end of the infusion. Animals were tested 7 days after AAV or RBV injections. Injection sites and viral infectivity were confirmed in all animals post-hoc by preparing sections (50 μ m) containing the relevant brain region (Supplementary Fig. 10).

Immunohistochemistry. Immunohistochemistry and confocal microscopy were performed as described previously⁴⁵. In brief, after intracardial perfusion with 4% paraformaldehyde in PBS (pH 7.4), the brains were post fixed overnight in this same solution and the following day 50 μ M coronal, sagittal or horizontal sections were prepared. Primary antibodies were used at the following concentrations: mouse anti-oxytocin–neurophysin (1:50; gift of H. Gainer^{46,47}); rat anti-green fluorescent protein (GFP, 1:1000; Nacalai); rabbit anti-parvalbumin (1:750; Swant); rabbit anti-neuronal nitric oxide synthase (1:100; BD Transduction Laboratories); rabbit anti-glial fibrillary protein (1:80; Sigma-Aldrich); rabbit anti-choline acetyltransferase (1:100; Millipore); rabbit anti-dopamine receptor protein (1:100, Millipore); sheep anti-tryptophan hydroxylase (1:100 Millipore) diluted in a solution containing 1% horse serum, 0.2% BSA and 0.5% Triton X-100 in PBS. After overnight incubation in primary antibody at room temperature (20–22 $^{\circ}\text{C}$) with slow agitation, slices were washed four times in PBS and then incubated with appropriate secondary antibody diluted at 1:750 for 2 h in PBS containing 0.5% Triton X-100. Subsequently, slices were washed 5 times and mounted using Vectashield mounting medium (Vector Laboratories). To identify cells expressing GFP or TdTomato due to the injection of RBV–eGFP or RBV–TdTomato into the NAc, raw fluorescence was visualized. Image acquisition was performed with a confocal microscope (Zeiss LSM510) using a $10\times/0.30$ Plan Neofluar and a $40\times/1.3$ Oil DIC Plan Apochromat objective. Confocal images were examined using the Zeiss LSM Image Browser software.

Electrophysiology. Parasagittal slices (250 μm) containing the NAC core were prepared from C57BL/6 and D1-TdTomato/D2-eGFP BAC transgenic mice on a C57BL/6 background using standard procedures. In brief, after mice were anaesthetized with isoflurane and decapitated, brains were quickly removed and placed in ice-cold low sodium, high sucrose dissecting solution. Slices were cut by adhering the two sagittal hemispheres brain containing the NAC core to the stage of a Leica vibroslicer. Slices were allowed to recover for a minimum of 60 min in a submerged holding chamber ($\sim 25^\circ\text{C}$) containing artificial cerebrospinal fluid (ACSF) consisting of 119 mM NaCl, 2.5 mM KCl, 2.5 mM CaCl_2 , 1.3 mM MgSO_4 , 1 mM NaH_2PO_4 , 11 mM glucose and 26.2 mM NaHCO_3 . Slices were then removed from the holding chamber and placed in the recording chamber where they were continuously perfused with oxygenated (95% O_2 , 5% CO_2) ACSF at a rate of 2 ml per min at $26 \pm 2^\circ\text{C}$. For EPSC recordings, bicuculline (20 μM) was added to the ACSF to block GABA_A (γ -aminobutyric acid type A)-receptor-mediated inhibitory synaptic currents. For inhibitory postsynaptic current (IPSC) recordings, dl-2-amino-5-phosphonovalerate (dAPV, 10 μM) and 2,3-Dioxo-6-nitro-1,2,3,4-tetrahydrobenzo[f]quinoxaline-7-sulfonamide (NBQX, 5 μM) dissolved in DMSO were added to block NMDA and AMPA receptors, respectively. Whole-cell voltage-clamp recordings from MSNs were obtained under visual control using a 40 \times objective. The NAC core was identified by the presence of the anterior commissure. D1 and D2 MSNs in the NAC core were identified by the presence of TdTomato and eGFP, respectively, which were excited with ultraviolet light using bandpass filters (HQ545/30 \times EX (excitation) for TdTomato; HQ470/40 \times EX for eGFP). Recordings were made with electrodes (3.5–6.5 M Ω) filled with 115 mM CsMeSO_4 , 20 mM CsCl, 10 mM HEPES, 0.6 mM EGTA, 2.5 mM MgCl, 10 mM Na-phosphocreatine, 4 mM Na-ATP, 0.3 mM Na-GTP, and 1 mM QX-314. Excitatory and inhibitory afferents were stimulated with a bipolar nichrome wire electrode placed at the border between the NAC core and cortex dorsal to the anterior commissure. Recordings were performed using a Multiclamp 700B (Molecular Devices), filtered at 2 kHz and digitized at 10 kHz. EPSCs were evoked at a frequency of 0.1 Hz while MSNs were voltage-clamped at -70 mV. Data acquisition and analysis were performed on-line using custom Igor Pro software. Input resistance and access resistance were monitored continuously throughout each experiment; experiments were terminated if these changed by $>15\%$.

Summary LTD graphs were generated by averaging the peak amplitudes of individual EPSCs in 1-min bins (six consecutive sweeps) and normalizing these to the mean value of EPSCs collected during the 10 min baseline immediately before the LTD-induction protocol. Individual experiments were then averaged together. Oxytocin (Tocris Biosciences, 1 μM , 10 min) was applied via the bath following the collection of baseline for induction of OT-LTD. For experiments examining the blockade of OT-LTD, slices were pre-incubated in antagonist (OTR-A, 1 μM L-368,899 hydrochloride or 5HTR1B-A, 20 μM NAS-181; Tocris Biosciences) for at least 30 min before recording. For experiments examining the reversal of OT-LTD, 30 to 40 min post induction, OTR-A was bath applied for 10 min. After the collection of stable baseline EPSCs, 5HT1B-LTD was induced by 10-min bath application of 2 μM CP-93129 dihydrochloride (Tocris Biosciences)

as described previously²⁸. For experiments examining the occlusion of OT-LTD, after stabilization of 5HT1B-LTD (at 30 to 40 min post induction), 1 μM oxytocin was applied via the bath for 10 min. Miniature EPSCs were collected at a holding potential of -70 mV in the presence of TTX (0.5 μM). Two minutes after break-in (sweep number 5, 30-s sweeps), 30-s blocks of events (total of 200 events per cell) were acquired and analysed using Mini-analysis software (Synaptosoft) with threshold parameters set at 5 pA amplitude and <3 ms rise time. All events included in the final data analysis were confirmed to be miniature EPSCs by visual examination, based on their rapid rise time and shape. Slices were incubated in the appropriate drug (dissolved in ACSF-bicuculline) for 10 min before recording, and cross-cell comparisons were made. Paired-pulse ratios (PPRs) were acquired by applying a second afferent stimulus of equal intensity, 50 ms after the first stimulus, and then calculating the ratio of EPSC2/EPSC1. Coefficient of variance was calculated from the standard deviation divided by the average (STDEV/AVG) of 10-min blocks (minutes 0–10, pre trial; minutes 40–50, post trial). Comparisons between different experimental manipulations were made using a two-tailed, Students *t*-test (paired or unpaired, as appropriate) with $P < 0.05$ considered to be significant. All statements in the text regarding differences between grouped data indicate that statistical significance was achieved, assuming normal distribution and equal variance. Sample size was estimated based on published literature^{14,28}. All values are reported as mean \pm s.e.m.

38. Panksepp, J. B. *et al.* Affiliative behavior, ultrasonic communication and social reward are influenced by genetic variation in adolescent mice. *PLoS ONE* **2**, e351 (2007).
39. Aronov, D., Andalman, A. S. & Fee, M. S. A specialized forebrain circuit for vocal babbling in the juvenile songbird. *Science* **320**, 630–634 (2008).
40. Andalman, A. S. & Fee, M. S. A basal ganglia-forebrain circuit in the songbird biases motor output to avoid vocal errors. *Proc. Natl Acad. Sci. USA* **106**, 12518–12523 (2009).
41. Mebatsion, T., König, M. & Conzelmann, K. K. Budding of rabies virus particles in the absence of the spike glycoprotein. *Cell* **84**, 941–951 (1996).
42. Wickersham, I. R., Sullivan, H. A. & Seung, H. S. Production of glycoprotein-deleted rabies viruses for monosynaptic tracing and high-level gene expression in neurons. *Nature Protocols* **5**, 595–606 (2010).
43. Wickersham, I. R., Finke, S., Conzelmann, K. & Callaway, E. M. Retrograde neuronal tracing with a deletion-mutant rabies virus. *Nature Methods* **4**, 47–49 (2007).
44. Grimm, D. *et al.* In vitro and in vivo gene therapy vector evolution via multispecies interbreeding and retargeting of adeno-associated viruses. *J. Virol.* **82**, 5887–5911 (2008).
45. Lammel, S. *et al.* Input-specific control of reward and aversion in the ventral tegmental area. *Nature* **491**, 212–217 (2012).
46. Ben-Barak, Y., Russell, J., Whitnall, M., Ozato, K. & Gainer, H. Neurophysin in the hypothalamo-neurohypophyseal system. I. Production and characterization of monoclonal antibodies. *J. Neurosci.* **5**, 81–97 (1985).
47. Whitnall, M. H., Key, S., Ben-Barak, Y., Ozato, K. & Gainer, H. Neurophysin in the hypothalamo-neurohypophyseal system. II. Immunocytochemical studies of the ontogeny of oxytocinergic and vasopressinergic neurons. *J. Neurosci.* **5**, 98–109 (1985).

RNAi screens in mice identify physiological regulators of oncogenic growth

Slobodan Beronja¹, Peter Janki¹, Evan Heller¹, Wen-Hui Lien¹, Brice E. Keyes¹, Naoki Oshimori¹ & Elaine Fuchs¹

Tissue growth is the multifaceted outcome of a cell's intrinsic capabilities and its interactions with the surrounding environment. Decoding these complexities is essential for understanding human development and tumorigenesis. Here we tackle this problem by carrying out the first genome-wide RNA-interference-mediated screens in mice. Focusing on skin development and oncogenic (Hras^{G12V}-induced) hyperplasia, our screens uncover previously unknown as well as anticipated regulators of embryonic epidermal growth. Among the top oncogenic screen hits are Mllt6 and the Wnt effector β -catenin, which maintain Hras^{G12V}-dependent hyperproliferation. We also expose β -catenin as an unanticipated antagonist of normal epidermal growth, functioning through Wnt-independent intercellular adhesion. Finally, we validate functional significance in mouse and human cancers, thereby establishing the feasibility of *in vivo* mammalian genome-wide investigations to dissect tissue development and tumorigenesis. By documenting some oncogenic growth regulators, we pave the way for future investigations of other hits and raise promise for unearthing new targets for cancer therapies.

Genome-wide cellular RNA interference (RNAi) screening has advanced the identification of genes involved in oncogenic growth control. To date, however, high-throughput screens in mammalian cells have been limited to cultures, in which even the best systems incompletely model physiological environments. We have overcome this impediment by devising methods to efficiently and selectively transduce murine epidermis through *in utero* lentiviral targeting of progenitors in embryonic day (E)9.5 embryos¹. When coupled with short hairpin RNA (shRNA) expression, lentiviral transduction is stably propagated throughout skin epithelium, resulting in RNAi-mediated reductions in target transcript and protein levels. This enables rapid analysis of complex genetic pathways in mammals, something previously only possible in lower eukaryotes^{2–4}.

The correlation between a tissue's growth and turnover rates and its susceptibility to cancer makes embryonic epidermis an attractive model for exploring how rapidly growing tissues balance proliferation and differentiation, and what prevents them from doing so in tumour progression. Given the efficacy of our system in single-gene studies, we have now expanded this scale by more than four orders of magnitude to conduct genome-wide RNAi screens. Our objectives were to first, demonstrate the feasibility of such screens in mammals; second, identify epidermal growth regulators in their native, physiological environment; third, uncover how epidermal growth control changes when it is propelled by a well-known oncogene; and fourth, demonstrate the implications of our findings for tumour progression in mice and humans.

Epidermal growth is rapid and uniform

Following completion of gastrulation and continuing to birth, mouse surface ectoderm commences rapid growth to match embryo expansion (Fig. 1a). Beginning as a monolayer, E9.5 ectoderm differentiates into a stratified, multi-layered epidermis that by birth constitutes a barrier that retains fluids and excludes microbes. Mature epidermis maintains an inner progenitor layer, which fuels tissue homeostasis and wound repair.

To quantify epidermal growth, we randomly marked single cells at clonal density by infecting E9.5 *Rosa26*^{lox-stop-lox-(LSL)-yfp} Cre-reporter embryos (*R26*^{yfp/+})⁵ with an LV-Cre lentivirus¹, and then monitored their expansion during development (Fig. 1b). By E18.5, single yellow

fluorescent protein (YFP)⁺ cells at E10.5 had grown to clones constituting ~40 cells (Fig. 1b, c; ~5–6 divisions per cell). Variability in clone size ranged within 1–2 cell divisions, indicating strikingly uniform growth throughout the epidermis.

We next examined how growth is affected by oncogenic *Hras1*, which is found mutated in many cancers and is the primary target in skin carcinogenesis models^{6,7}. *K14*-Cre⁸-driven, epidermal-specific expression of Hras^{G12V} from its endogenous locus (*Hras*^{lox-wild-type-stop-lox-G12V})⁹ resulted in mice whose skin displayed epidermal overgrowth as well as oncogenic Hras dose-dependency for one (*K14-cre; Hras*^{LSL-G12V/+}; Hras^{oncoX1}) or two (*K14-cre; Hras*^{LSL-G12V/LSL-G12V}; Hras^{oncoX2}) copies (Supplementary Fig. 1). Additional distinctions included the expansion of both progenitors (keratin 5⁺) and differentiating layers (spinous keratin 10⁺; granular filaggrin⁺) (Supplementary Figs 1–3).

To quantify the impact of oncogenic Hras on epidermal growth, we used a cellular growth index (CGI) assay¹ (Fig. 1d). Cre-reporter (*R26*^{yfp/+}) embryos, transduced with a LV-Cre and red fluorescent protein-expressing lentivirus (LV-RFP) mix showed similar relative numbers of YFP⁺ to RFP⁺ keratinocytes across several embryos, indicating that control YFP⁺ and RFP⁺ populations grew at comparable rates (Fig. 1e, f). Transduction of the same lentiviral mixture into test animals (where Cre-transduction induces Hras^{G12V}) revealed consistently more YFP⁺ (Hras^{G12V}) than RFP⁺ (control) cells (CGI = 1.82, Hras^{oncoX1}; 3.32, Hras^{oncoX2}; Fig. 1e, f). These findings demonstrate that Hras^{G12V} confers a dose-dependent growth advantage to skin epidermis and that growth rates can be documented and quantified.

Hras^{G12V} not only conferred a dose-dependent increase in proliferation, but also in suppression of apoptosis (Supplementary Fig. 4). In addition, consistent with established pro-inflammatory effects of Hras^{G12V}, innate and adaptive immune cells infiltrated underlying dermis. Last, real-time PCR revealed no evidence for oncogenic induction of cellular senescence-associated cyclin-dependent kinase (CDK) inhibitors¹⁰.

Establishing pooled screen parameters

On the basis of our CGI assay principle, we expected that, after epidermal transduction with a pool of shRNA-expressing lentivirus, any

¹Howard Hughes Medical Institute, Laboratory of Mammalian Cell Biology & Development, The Rockefeller University, New York, New York 10065, USA.

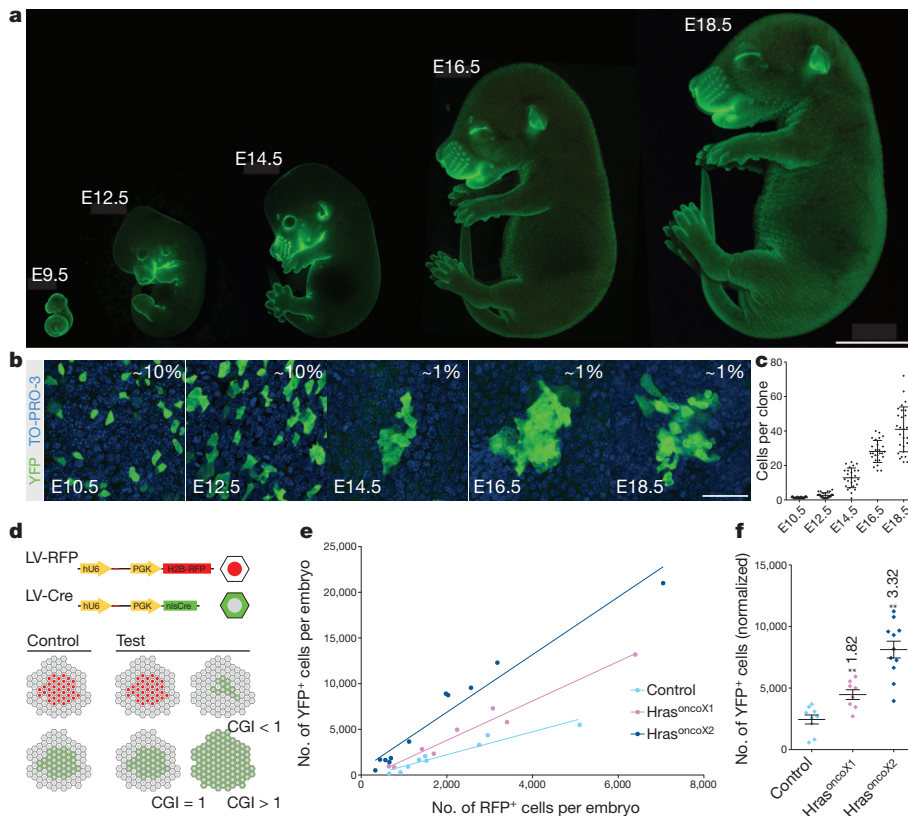


Figure 1 | Embryonic epidermal tissue growth is rapid and responsive to oncogenic Hras.

a, Mouse embryogenesis, highlighted by propidium iodide (E9.5) or K14-actin-GFP (E12.5–18.5). **b**, $R26^{YFP/+}$ Cre-reporter embryos infected at E9.5 with LV-Cre and analysed at days shown. Transduced cells are YFP⁺. Transduction levels (% YFP⁺ cells) depend upon viral titre. **c**, Cell numbers in transduced YFP⁺ clones at ages shown. **d**, Schematic of CGI assay. E9.5 $R26^{YFP/+}$ Cre-reporter (control) or $gene^{lox/lox} R26^{YFP/+}$ (test) embryos are infected with a LV-Cre and LV-RFP mix. At E18.5, numbers of RFP⁺:YFP⁺ cells in control and test animals are compared, and phenotypes scored as neutral (CGI = 1), growth advantaged (CGI > 1) or disadvantaged (CGI < 1). **e**, Numbers of RFP⁺ and YFP⁺ cells at E18.5 in control, $Hras^{oncoX1}$ and $Hras^{oncoX2}$ embryos. Upper shift is consistent with growth advantage. **f**, RFP⁺ cell numbers normalized to YFP⁺ cells in control, $Hras^{oncoX1}$ and $Hras^{oncoX2}$ animals. CGI assay suggests a 1.8-fold overgrowth ($P = 0.002$) in $Hras^{oncoX1}$ and 3.3-fold overgrowth ($P < 0.0001$) in $Hras^{oncoX2}$ epidermis. Error bars indicate \pm s.d. (**c**) and \pm s.e.m. (**f**). ** ($P \leq 0.01$) in **f** indicates statistical significance of comparison to control. For CGI assay (**e**, **f**), data points are individual embryos: control ($n = 9$), $Hras^{oncoX1}$ ($n = 8$) and $Hras^{oncoX2}$ ($n = 11$). Scale bars, 5 mm (**a**) and 50 μ m (**b**).

shRNA that targets an essential mediator of growth will be reduced or lost during development, whereas shRNAs targeting negative growth regulators will become overrepresented. By comparing relative shRNA abundance in the initial pool and at E18.5, we expected to identify shRNAs and their targets that confer either growth advantage or disadvantage.

The success of the approach depended upon our ability to: (1) modify growth at a low multiplicity of infection ($MOI \leq 1$); (2) measure individual shRNA abundance in the pool; (3) transduce embryonic epidermis at a $MOI \leq 1$; and (4) achieve complete screen coverage, in which every shRNA in the pool is tested. We set up a series of controls to ensure that these parameters were met. Underscoring the feasibility of pooled-formats for *in vivo* RNAi screens, we demonstrated that targeting of (1) anaphase promoting complex component *Anapc5* during normal growth, and (2) *Hras1* during oncogenic hyperplasia, reduced average clone sizes, even with transductions where most cells harboured only a single shRNA (Supplementary Fig. 5).

To quantify individual shRNA representation in a complex pool, we used the Illumina-based count-by-sequencing principle (Supplementary Fig. 6). We designed oligonucleotides to amplify the target sequence of each shRNA, and optimized pre-amplification and clean-up pipelines to yield a product to apply directly to the sequencing cell. We tested our protocol against a defined template generated by combining genomic DNAs from independently transduced cell lines, so that individual genome-integrated shRNAs were present in amounts corresponding from a single cell (6 pg) up to 2,048 cells (12.3 ng).

We amplified and sequenced this standard set, and showed that reactions were: (1) quantitative, with increased sequencing reads corresponding to shRNA abundance in the pool; (2) sensitive, detecting all three single-copy shRNAs; and (3) highly reproducible (Supplementary Fig. 6). Independent counts of the standard set showed identical sequencing bias for a given shRNA, and thus became neutralized in relative comparisons of absolute counts, especially with ≥ 32 copies of the shRNA. Indeed, a >30-fold screen coverage proved sufficient to sample all shRNAs in our pool (see below). At this level, growth-neutral

shRNAs were >1,000-fold represented in the E18.5 sequencing quantification reaction, because each E9.5 epidermal cell generates ~ 40 cells by E18.5.

We next determined that at an infection level of 13–27%, most transduced epidermal keratinocytes carried a single lentivirus ($MOI \leq 1$) (Supplementary Fig. 7). To ensure that at least 30 individual cells were infected with each shRNA at E9.5, a pool of $\sim 78,000$ shRNAs required $\sim 10^6$ cells to be targeted. We used high-resolution imaging of TO-PRO3-labelled embryos and established that at E9.5, surface ectoderm contained $\geq 120,000$ cells per embryo. Together, this suggested that transducing ≥ 90 embryos would achieve the requisite coverage (Supplementary Fig. 8).

Screens identify known growth regulators

We pooled the genome-wide collection of murine shRNA lentiviruses in roughly equal concentrations¹¹, and profiled the starting composition of the pool ($t = 0$) in transduced primary mouse keratinocytes (Fig. 2a). Physiological screens were performed in control and $Hras^{oncoX2}$ embryos transduced at E9.5 *in utero* (Fig. 2b). Epidermal cells were collected after 24 hours (initial pool) and 9 days of development, and integrated lentiviral hairpins from genomic DNAs were sequenced and quantified (Fig. 2c).

Our pre-amplification and sequencing reactions did not bias shRNA quantification, and Illumina sequencing reads were of high quality. They mapped to the shRNA library with predictable efficiency and indicated complete coverage of the pool (Supplementary Figs 9, 10). Significantly altered shRNAs were identified and ranked on the basis of two independent methods. To ensure reproducibility, we used DESeq statistical package¹², which accounted for biological variability among our replicates (sets of 30 embryos per condition) and is the best method to identify candidates per se (Fig. 2d–k). However, informative yet variable shRNAs can be excluded by the high stringency of DESeq, which reduces the ability to control for off-target effects by requiring that multiple shRNAs show consistent behaviour. We therefore also analysed pooled data sets (90 embryos per condition;

Supplementary Fig. 11) using Fisher's exact test, which reduces variability by averaging individual shRNA abundance. By maximizing screen coverage, this method produces a more inclusive list of significantly altered shRNAs, and hence was preferred for ranking candidates identified by DESeq (Fig. 2f, j, k). Importantly, the overlap between these approaches was extensive (Supplementary Fig. 11), underscoring the robustness of our data.

We identified ~1,800 genes as essential for normal growth (Fig. 2d, e and Supplementary Tables 1, 2) and significantly enriched for function in protein synthesis ($P = 3.1 \times 10^{-10}$) and gene expression ($P = 2.6 \times 10^{-10}$). Genes encoding 60S and 40S ribosomal proteins were also highly represented and among the top 10% of all hits for normal growth, underscoring our screen's power to identify regulators of normal growth/viability (Fig. 2f and Supplementary Fig. 12). Indeed, our top 10 candidates for regulators of normal growth featured six ribosomal genes and two genes essential for messenger RNA splicing (Fig. 2j).

In our screen for specific regulators of Hras^{G12V}-dependent oncogenic growth, ~160 genes surfaced as candidates (Fig. 2g and Supplementary Tables 3, 4). They diverged in identity and function from those implicated in normal growth regulation, as most housekeeping growth regulators were eliminated by pair-wise comparison of control and Hras^{oncoX2} shRNA abundance (Fig. 2h). The oncogene-specific

regulators included Hras1, and downstream Ras pathway members Raf1, and Mek and Akt proteins (Fig. 2i). Equally notable was the absence of upstream oncogenic Ras regulators, for example, guanine nucleotide exchange factors (GEFs) and GTPase-activating proteins (GAPs), which are not expected to arise in a screen for hairpins suppressing Hras^{G12V}-induced growth. Our top 10 hits for regulators of oncogenic growth included well-established Ras pathway members *Akt3* and *Raf1*, as well as the Ras-regulated *Pawr*¹³ (Fig. 2k). Cyclin C (*Ccnc*), a putative regulator of haematopoietic stem cell quiescence¹⁴, was also on this list, as was *Mllt6*, encoding a myeloid/lymphoid, or mixed-lineage, leukaemia (MLL) translocation partner and a component of an epigenetic modifier complex¹⁵.

The very top candidate for preferential regulation of oncogenic growth was *Ctnnb1*, encoding the Wnt signalling and intercellular adhesion effector β -catenin. At first glance, β -catenin seemed obvious, as its over-activation has been implicated in a variety of cancers, including those of skin^{16–18}. However, β -catenin is also thought to be essential for stem cells¹⁹. Hence, it was surprising that its hairpins surfaced in a screen for selective inhibitors of oncogenic and not normal growth. Even more paradoxical was that in our parallel genome-wide screen, *Ctnnb1* was the top candidate for negative regulation of normal epidermal growth (Supplementary Tables 1, 2).

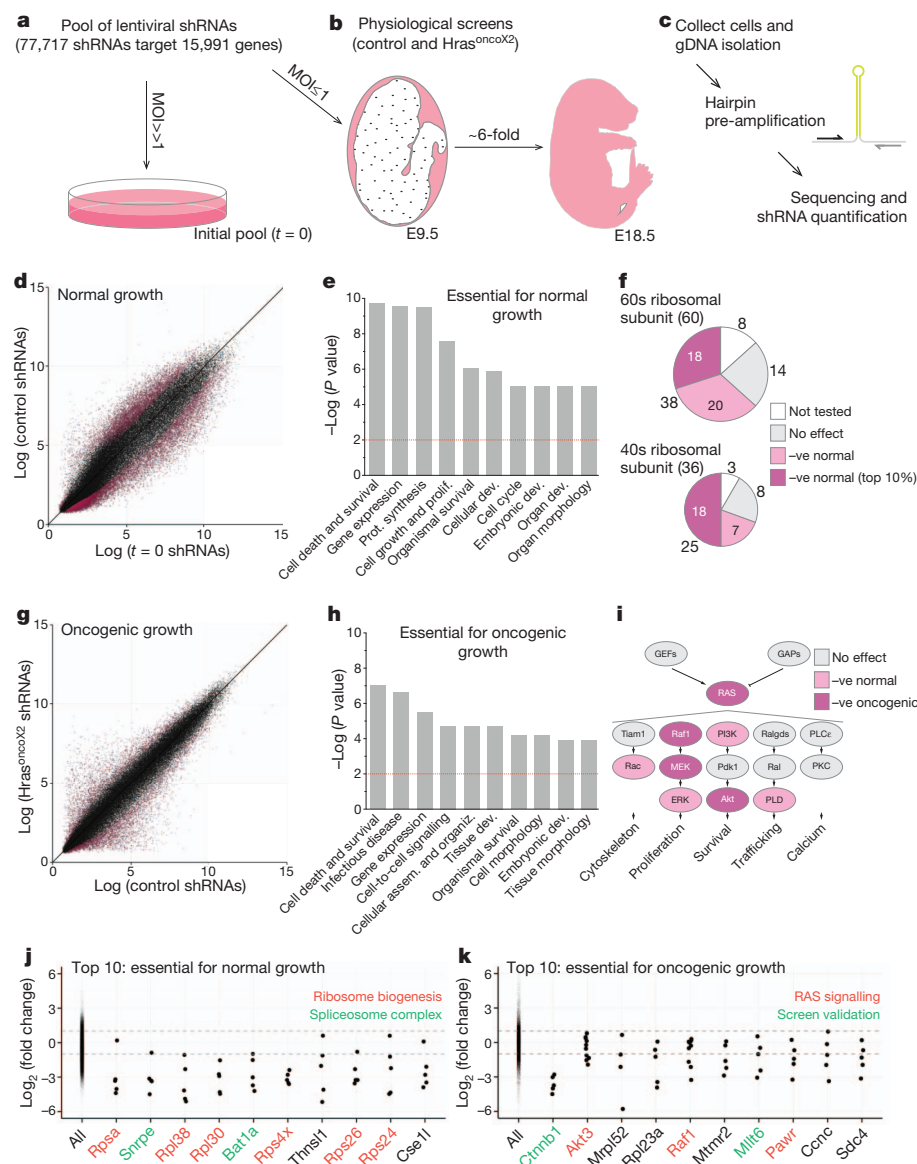


Figure 2 | Genome-wide RNAi screens for physiological regulators of normal and oncogenic growth identify expected and surprising regulators. **a–c**, Schematic of the RNAi screens based on relative enrichment/depletion of individual shRNAs over time. **a**, shRNAs against 15,991 mouse genes are combined into a lentiviral pool whose composition is determined from the ‘initial pool’ ($t = 0$) experiment, in which transduced cells are analysed 24 h after infection. **b**, Genes that regulate normal and oncogenic growth are identified in two screens, in which E9.5 control or K14-Cre⁺; Hras^{oncoX2} embryos are infected *in utero*, allowed to develop for 9 days, and processed. **c**, After epidermal tissues are collected and used in genomic DNA (gDNA) isolation, individual shRNAs are pre-amplified and quantified by sequencing unique hairpin regions. **d–k**, Significantly enriched/depleted shRNAs identified using DESeq analysis. **d**, Dot plot of relative abundance of 77,717 shRNAs at $t = 0$ and in E18.5 epidermis. **e**, Putative normal growth regulators are significantly enriched ($P \geq 0.01$) for gene function categories promoting cell viability and development. **f**, Normal growth regulators encode for ribosomal 60S and 40S subunit components ($P = 1.12 \times 10^{-9}$ and $P = 3.26 \times 10^{-7}$, respectively), with many in the top 10% of all hits (maroon). **g**, Relative shRNA abundance in control and Hras^{G12V} animals reveal oncogenic growth-altering shRNAs. **h**, Putative oncogenic growth regulators are enriched ($P \geq 0.01$) in gene categories that support cell growth. **i**, Downstream effectors of Ras signalling score as essential for growth (pink), with many exhibiting an oncogene-specific requirement (maroon). **j**, **k**, shRNAs for the top ten essential regulators of normal (**d**) and oncogenic (**g**) growth are markedly depleted relative to the genome-wide pool (all).

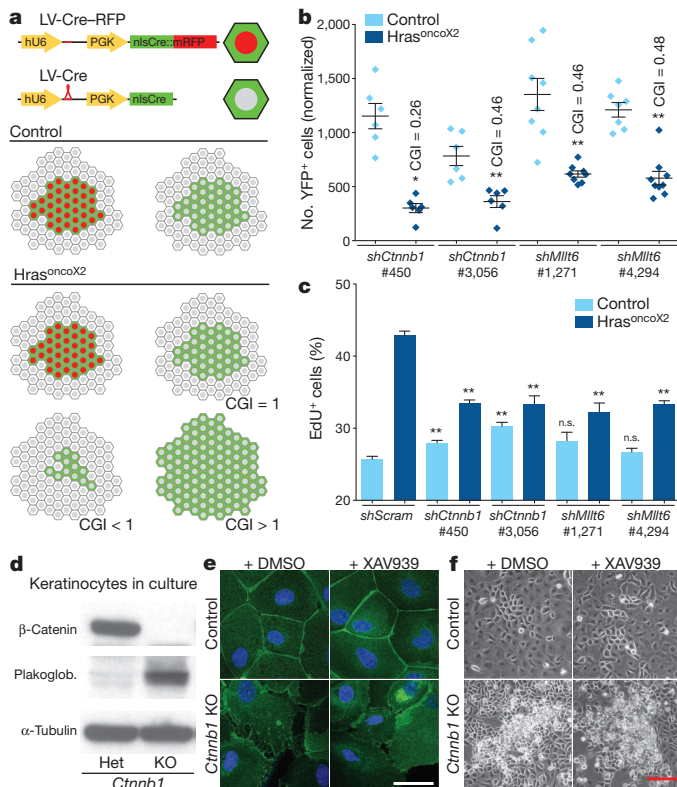


Figure 3 | Suppressing β -catenin and *Mllt6* selectively affects *Hras*^{G12V}-dependent epidermal hyperplasia. **a**, Modified CGI assay measures effect of shRNA-mediated gene knockdown in animals with Cre-activated transgene expression. Transduction with LV-Cre-RFP co-expressing scrambled (scram) shRNA, and LV-Cre co-expressing candidate-targeting shRNA, leads to generation of YFP⁺ RFP⁺ scrambled and YFP⁺ knockdown clones in control or *Hras*^{G12V} animals. Numbers of YFP⁺ cells (normalized to YFP⁺ RFP⁺) in control and *Hras*^{G12V} animals reflect lentiviral mix composition after normal and oncogenic growth, respectively. **b**, Fewer YFP⁺ cells are found in oncogenic animals upon knockdown of *Ctnnb1* and *Mllt6* with independent shRNAs. **c**, Reduced EdU incorporation following *Ctnnb1* knockdown in *Hras*^{G12V} animals contrasts with increased proliferation in control epidermis. *Mllt6* depletion also reduces EdU labelling in oncogenic growth. **d**, Immunoblot of control (*Ctnnb1* heterozygous (Het)) and *Ctnnb1* knockout (KO) keratinocyte lysates shows upregulation of plakoglobin. **e**, Establishment of cell adhesion 48 h after Ca²⁺ shift is unaffected in keratinocytes treated with a Wnt-signalling inhibitor (XAV939) but impaired in *Ctnnb1* knockout cells. E-cadherin (green) marks adherens junctions and DAPI (4',6-diamidino-2-phenylindole; blue) labels the nuclei. **f**, Unlike control cells or cells treated with a Wnt-inhibitor, *Ctnnb1* knockout keratinocytes form overgrown foci upon reaching confluence. Error bars (**b**, **c**) indicate \pm s.e.m. Data points (**b**, **c**) represent individual embryos with $n = 6$ (*shCtnnb1* and *shScram* in control), $n = 7$ (*shMllt6* no. 4,294 in control), $n = 8$ (*shMllt6* no. 1,271), $n = 9$ (*shMllt6* no. 4,294 in *Hras*^{G12V}), or $n = 10$ (*shScram* in *Hras*^{G12V}), each scored through immunofluorescence analysis of ten 425.1 μm^2 images. NS, not significant ($P > 0.05$); * $P \leq 0.05$ and ** $P \leq 0.01$ indicate statistical significance. Scale bars, 50 μm (**e**), 10 μm (**f**).

Validating oncogene-specific regulators

We chose *Ctnnb1* and *Mllt6* for further study. For both *Ctnnb1* and *Mllt6*, a direct correlation was observed between transcript knockdown *in vitro* and severity of growth defects *in vivo* (Supplementary Fig. 13), strongly arguing against off-target effects. We validated our candidates as oncogenic growth regulators with a modified *in vivo* CGI assay involving two lentiviral vectors (Fig. 3a). In one, Cre-recombinase fused to monomeric RFP (LV-Cre-mRFP) contained a scrambled shRNA control. In the other vector, untagged Cre was used; this vector encoded the test shRNA against the candidate. Transduction of E9.5 control or *Hras*^{G12V} Cre-reporter embryos marked two separate populations: RFP⁺ YFP⁺ cells represented the

baseline rate of normal (in control) or oncogenic growth (in *Hras*^{G12V}); YFP⁺ cells represented the rate of growth that occurs when the target transcript is depleted.

The ratios of YFP⁺ cells normalized to YFP⁺ RFP⁺ cells in *Hras*^{G12V} and control animals revealed that two independent *Ctnnb1* shRNAs displayed reductions of ~ 2 –4-fold in oncogenic relative to normal growth. Similar ~ 2 -fold reductions in YFP⁺ cells were observed in the *Hras*^{G12V} background when *Mllt6* transcripts were diminished (Fig. 3b). The physiological effects of *Ctnnb1* or *Mllt6* knockdown were profound: the neonatal oncogenic phenotype was significantly ameliorated, and epidermal proliferation in *Hras*^{G12V} embryos was markedly and reproducibly suppressed. By contrast, no significant effects were seen on apoptosis (Fig. 3c and Supplementary Fig. 13).

Equally interesting to the selective effects of *Ctnnb1* knockdown on suppressing *Hras*^{G12V}-dependent oncogenic growth were its positive effects on normal growth. These differences seemed to be physiologically relevant, as they were reflected at the level of EdU-incorporation and thickness of epidermal tissue (Fig. 3c and Supplementary Fig. 14). Although hitherto overlooked, the proliferative effects of *Ctnnb1* hairpins on normal epidermis are recapitulated upon conditional targeting of β -catenin^{20,21}.

β -Catenin is both an adherens junction component and a nuclear cofactor for Wnt regulators in the LEF/TCF family and other DNA-binding proteins²². However in contrast to its nuclear functions, β -catenin's role in adhesion has been assumed to be redundant with plakoglobin²³. Given that intercellular defects can promote proliferation, we revisited this issue using a sensitive *in vitro* adhesion assay (Fig. 3d–f and Supplementary Fig. 15)²⁴. Despite plakoglobin upregulation, *Ctnnb1*-null keratinocytes inefficiently formed cell–cell adhesions upon calcium induction. Moreover, the Wnt inhibitor XAV939 (ref. 25) failed to phenocopy these defects. Finally, consistent with the view that loss of β -catenin compromises contact inhibition and leads to cellular overgrowth, *Ctnnb1*-null cells were hyperproliferative and formed overgrown foci upon reaching confluence.

Oncogenic growth and Wnt signalling

Although intercellular adhesion is often viewed as tumour suppressive, Wnt signalling is often associated with oncogenic growth. To test whether this might contribute to the negative effects of *Ctnnb1* knockdown on *Hras*^{G12V} skins, we transduced embryos with both a Wnt-reporter and LV-Cre (Fig. 4a). In E18.5 control animals, reporter expression was predictably restricted to developing hair follicles²⁶ and largely abolished with concomitant *Ctnnb1* knockdown.

Intriguingly, Wnt-reporter expression was expanded throughout transduced *Hras*^{G12V} interfollicular epidermis. In addition, *Hras*^{G12V}-expressing epidermis displayed ectopic nuclear β -catenin and >6-fold upregulation of *Axin2* transcripts (Fig. 4a and Supplementary Fig. 16a–c). Conversely, bone morphogenetic protein signalling, which is antagonistic to Wnt signalling in skin²⁷, was downregulated in *Hras*^{G12V} epidermis, and was not rescued by β -catenin depletion, suggesting its independence of Wnt in this oncogenic context (Supplementary Fig. 18).

Mllt6 expression paralleled β -catenin and Wnt-reporter activity, both in normal hair follicles and in evaginating structures of *Hras*^{G12V} skin (Supplementary Fig. 16b). Chromatin immunoprecipitation followed by next-generation sequencing (ChIP-seq) analysis showed that Tcf3 and Tcf4 bound to a conserved LEF/TCF motif upstream of *Mllt6* (Fig. 4b). A 299-base-pair (bp) segment (green line) encompassing this site drove LEF1/ β -catenin-dependent luciferase reporter activity in a manner comparable to the 331-bp Tcf3/4 binding site of *Axin2*, an established Wnt-target gene (Fig. 4c and Supplementary Fig. 16d). In agreement, depletion or loss of β -catenin in embryonic epidermis *in vivo* reduced *Mllt6* transcript levels (Fig. 4d).

β -catenin and *Mllt6* in epidermal tumours

Although our screens were conducted on embryonic mouse skin, our findings showed relevance to cancer. RNA-seq analysis revealed that

Ctnnb1 or *Mllt6* depletion in oncogenic Hras epidermis affected a shared set of transcripts ($P = 2.48 \times 10^{-40}$ and $P = 8.16 \times 10^{-25}$) that globally suppressed pathways promoting tumorigenesis (for example, *Myc*, *E2f1*) and enhanced those restricting growth (for example, *Trp53*, *Cdkn2a*; Fig. 4e, f). Moreover, in human squamous cell carcinomas (SCC), β -catenin and MLLT6 were often upregulated and nuclear (notably in the basal layer, where cancer stem cells reside²⁸). Our analysis of 75 different human skin SCCs showed that most tumours expressed both proteins, with significant correlation in their expression (Supplementary Fig. 18). It remains to be seen whether their co-expression in tumours and a shared effect on transcriptional profile during oncogenic growth reflects a functional interaction between our candidates, or is a result of their independent

effect/importance on the cellular machinery at the heart of oncogenic growth.

We next tested whether β -catenin and *Mllt6* are physiologically relevant to Hras^{G12V}-dependent tumour initiation and maintenance. Whereas clonal LV-Cre-mediated activation of Hras^{G12V} expression in mice resulted in squamous papilloma formation as early as 3 weeks of age, concomitant constitutive expression of *Ctnnb1* or *Mllt6* shRNAs delayed tumour initiation (Fig. 5a). Moreover, growth of orthotopically transplanted SCC cells was significantly reduced following candidate depletion (Fig. 5b and Supplementary Fig. 19).

We extended this physiological relevance by performing xenografts of human SCC cells transduced with lentivirus harbouring scrambled or shRNAs targeting human *CTNNB1* or human *MLLT6*. Tumour initiation was significantly delayed, with *MLLT6* showing stronger effect than *CTNNB1* (Fig. 5c and Supplementary Fig. 19).

Finally, to assess whether *Ctnnb1* and *Mllt6* are required for tumour maintenance, we engineered an LV-Cre vector that allows for doxycycline-regulated shRNA expression, thereby enabling induced depletion of *Mllt6* and *Ctnnb1* following tumour formation in adult animals (Fig. 5d and Supplementary Fig. 20). Both had negative effects on tumour maintenance, with some tumours showing partial regression. Thus, the tumour-suppressive effects of *Ctnnb1* and *Mllt6* shRNAs as first revealed in embryogenesis appeared to be functionally relevant to adult tumorigenesis.

Discussion

The urgent need to understand cancer has fuelled human cancer genome sequencing and *in vitro* RNAi-based screening efforts to

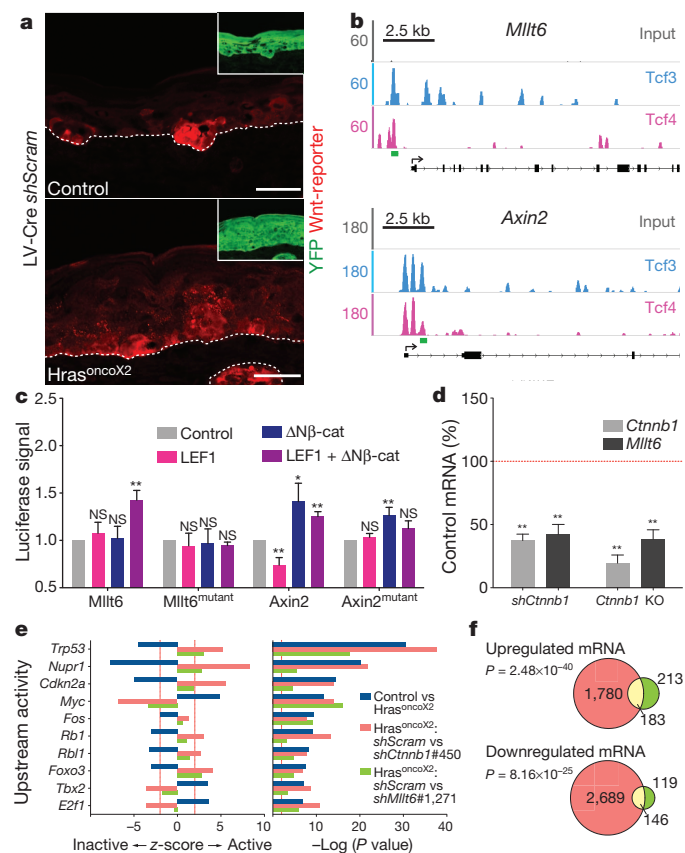


Figure 4 | Hras^{G12V}-induced epidermal growth affects other signalling pathways. **a**, Wnt-reporter activity (red) is restricted to hair placodes in control skin (top) but extends to interfollicular epidermis in Hras^{oncoX2} animals (bottom). YFP (inset) marks LV-Cre-transduced epidermis. White dotted line demarcates dermal-epidermal boundary. **b**, ChIP-seq peaks on chromosome 11 reveal Tcf3 (blue) and Tcf4 (pink) binding sites in *Mllt6* and *Axin2* promoter regions. Negative control (grey) is total genome DNA. Green bars represent the ~300-bp fragment used to validate Tcf3/4 binding. **c**, Human LEF1 (TCF3/4 family member) and stabilized β -catenin ($\Delta N\beta$ -cat) together promote luciferase activity when putative TCF3/4 binding sites of *Mllt6* and *Axin2* are used as drivers. These effects are not observed when the TCF3/4 binding motifs are mutated. **d**, *Mllt6* and *Ctnnb1* mRNA epidermal levels are reduced by *Ctnnb1* knockdown (*shCtnnb1* no. 450) or knockout (KO). **e**, Transcriptional profile of Hras^{G12V} epidermal progenitors reveals repression of tumour suppressors (for example, *Trp53*, *Cdkn2a*, *Rb1*) and activation of oncogenic signalling (for example, *Myc*, *E2f1*). shRNA-mediated depletion of *Ctnnb1* or *Mllt6* in Hras^{G12V} epidermis significantly counter these transcriptional changes. Red vertical lines represent significant activation z-score (twofold) and P value of a correct prediction ($P = 0.01$). **f**, Significant overlap in differentially regulated transcripts is observed following depletion of β -catenin and *Mllt6* in Hras^{G12V} epidermal progenitors. Error bars indicate \pm s.e.m. (c) and \pm s.d. (d). In the real-time PCR experiment (d), data are shown for three embryos assayed in two independent reactions ($n = 6$). * $P \leq 0.05$, ** $P \leq 0.01$. Scale bars, 50 μ m.

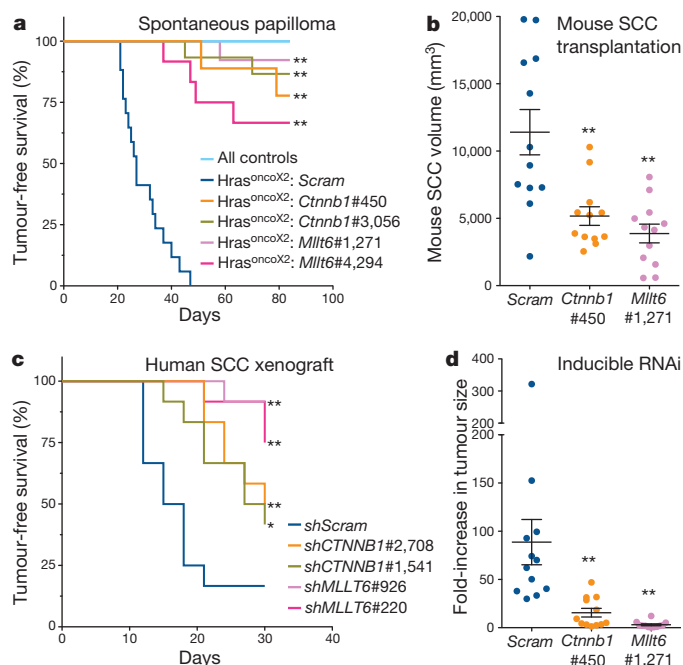


Figure 5 | β -catenin and *Mllt6* depletion impair Hras^{G12V}-dependent tumorigenesis. **a**, shRNA-mediated depletion of *Ctnnb1* or *Mllt6* delays spontaneous tumour initiation in Hras^{oncoX2} mice ($n = 9$ in all conditions except LV-Scram-transduced Hras^{oncoX2} ($n = 18$)). Control lines correspond to animals transduced with shRNAs with no effect on tumorigenesis. **b**, Tumour volumes of *Ctnnb1*- and *Mllt6*-depleted mouse SCCs transplants are significantly reduced after 30 days of growth. **c**, Tumour initiation following xenotransplantation of shRNA-transduced human SCC cells is significantly delayed following knockdown of human *CTNNB1* or *MLLT6*. **d**, Induction of *Ctnnb1* or *Mllt6* knockdown in pre-existing spontaneous mouse papillomas results in impaired growth and sometimes regression. **a–d**, Transduction of scrambled shRNA served as control. Error bars (b, d) indicate s.e.m. **b–d**, $n = 12$ transplants (b, c) or tumours (d). * $P \leq 0.05$ and ** $P \leq 0.01$ indicate statistical significance of the observed differences.

identify genes that preferentially affect cancer cells but not their normal counterparts. Although promising in concept, assay conditions and cell-line histories can profoundly affect genes identified in these screens^{29,30}. Although xenogeneic transplantations of transduced human cells offer improvements³¹, they often incompletely simulate carcinoma ontogeny, which depends upon complex interactions with local and systemic environments. By targeting cells in their normal physiological context, we correct these deficits and abrogate many caveats, including epigenetic, genetic and stress-induced alterations in gene expression, all of which introduce heterogeneity and increase coverage requirements when cells are grown on plastic.

Our study accentuates a particular importance of β -catenin in promoting oncogenic effects, as it surfaced at the top of >15,000 genes in our screen. Moreover, increased Hras-mitogen-activated protein kinase signalling drove β -catenin's effects from negative to positive, as normal epidermal growth was actually impeded by β -catenin. In this regard, it is interesting that leukaemias also seem to be more sensitive to activated β -catenin than their normal counterparts³². Our findings further suggest that β -catenin's ability to balance tissue growth is exerted through its antagonistic functions in intercellular adhesion and transcriptional activation.

A myriad of new candidates from our screen await further investigation. Among them are chromatin modifiers, which have been increasingly implicated in human cancers³³. In this regard, our validation of Mllt6 is intriguing, as MLL proteins are known to associate with DOT1L H3K79-methyltransferase complexes³⁴. Given Mllt6's selective effects on oncogenic growth, it is tempting to speculate that this protein might function by guiding its histone modifier complex to a key cancer target gene(s). Although detailed understanding of this and other candidates awaits experimentation, our methodology paves the way for future studies aimed at uncovering mechanisms of SCC progression, with the hope of identifying targets that selectively compromise growth of one of the world's most prevalent and life-threatening cancers.

METHODS SUMMARY

Animals were on a C57BL/6 background. Lentiviral production and ultrasound-guided injection into E9.5 amniotic space are as described^{1,35}. Transduced embryos were developed to E18.5, after which epidermal suspensions were prepared for gDNA isolation. gDNAs from sets of 30 transduced embryos were combined and used as template for a 21-cycle pre-amplification PCR. For identification and quantification of shRNAs, clean pre-amplification product was sequenced using Illumina HiSeq2000, and the sequencing output was aligned to the TRC 2.x library with Burrows-Wheeler Aligner (BWA) with a maximum edit distance of three. Bioinformatics analyses of RNA-seq data and candidates identified by our screens were performed using IPA software (Ingenuity Systems). Figures were prepared using Adobe Photoshop and Illustrator CS5. Graphing and statistical analyses were performed using Prism 5 (GraphPad Software). Descriptions of antibodies and mouse strains are provided in Methods.

Full Methods and any associated references are available in the online version of the paper.

Received 28 December 2012; accepted 12 July 2013.

Published online 14 August 2013.

- Beronja, S., Livshits, G., Williams, S. & Fuchs, E. Rapid functional dissection of genetic networks via tissue-specific transduction and RNAi in mouse embryos. *Nature Med.* **16**, 821–827 (2010).
- Williams, S. E., Beronja, S., Pasoli, H. A. & Fuchs, E. Asymmetric cell divisions promote Notch-dependent epidermal differentiation. *Nature* **470**, 353–358 (2011).
- Ezraty, E. J. et al. A role for the primary cilium in Notch signaling and epidermal differentiation during skin development. *Cell* **145**, 1129–1141 (2011).
- Oshimori, N. & Fuchs, E. Paracrine TGF- β signaling counterbalances BMP-mediated repression in hair follicle stem cell activation. *Cell Stem Cell* **10**, 63–75 (2012).
- Srinivas, S. et al. Cre reporter strains produced by targeted insertion of *EYFP* and *ECFP* into the *ROSA26* locus. *BMC Dev. Biol.* **1**, 4 (2001).
- Karnoub, A. E. & Weinberg, R. A. Ras oncogenes: split personalities. *Nature Rev. Mol. Cell Biol.* **9**, 517–531 (2008).
- Balmain, A. & Pragnell, I. B. Mouse skin carcinomas induced *in vivo* by chemical carcinogens have a transforming Harvey-ras oncogene. *Nature* **303**, 72–74 (1983).

- Vasioukhin, V., Degenstein, L., Wise, B. & Fuchs, E. The magical touch: genome targeting in epidermal stem cells induced by tamoxifen application to mouse skin. *Proc. Natl Acad. Sci. USA* **96**, 8551–8556 (1999).
- Chen, X. et al. Endogenous expression of Hras^{G12V} induces developmental defects and neoplasms with copy number imbalances of the oncogene. *Proc. Natl Acad. Sci. USA* **106**, 7979–7984 (2009).
- Serrano, M., Lin, A. W., McCurrach, M. E., Beach, D. & Lowe, S. W. Oncogenic ras provokes premature cell senescence associated with accumulation of p53 and p16INK4a. *Cell* **88**, 593–602 (1997).
- Moffat, J. et al. A lentiviral RNAi library for human and mouse genes applied to an arrayed viral high-content screen. *Cell* **124**, 1283–1298 (2006).
- Anders, S. & Huber, W. Differential expression analysis for sequence count data. *Genome Biol.* **11**, R106 (2010).
- Donninger, H. et al. The Ras effector RASSF2 controls the PAR-4 tumor suppressor. *Mol. Cell. Biol.* **30**, 2608–2620 (2010).
- Miyata, Y. et al. Cyclin C regulates human hematopoietic stem/progenitor cell quiescence. *Stem Cells* **28**, 308–317 (2010).
- Prasad, R. et al. Leucine-zipper dimerization motif encoded by the AF17 gene fused to ALL-1 (MLL) in acute leukemia. *Proc. Natl Acad. Sci. USA* **91**, 8107–8111 (1994).
- Gat, U., DasGupta, R., Degenstein, L. & Fuchs, E. *De novo* hair follicle morphogenesis and hair tumors in mice expressing a truncated β -catenin in skin. *Cell* **95**, 605–614 (1998).
- Chan, E. F., Gat, U., McNiff, J. M. & Fuchs, E. A common human skin tumour is caused by activating mutations in beta-catenin. *Nature Genet.* **21**, 410–413 (1999).
- Malanchi, I. et al. Cutaneous cancer stem cell maintenance is dependent on β -catenin signalling. *Nature* **452**, 650–653 (2008).
- Nusse, R. Wnt signaling and stem cell control. *Cell Res.* **18**, 523–527 (2008).
- Huelsken, J., Vogel, R., Erdmann, B., Cotsarelis, G. & Birchmeier, W. β -Catenin controls hair follicle morphogenesis and stem cell differentiation in the skin. *Cell* **105**, 533–545 (2001).
- Nguyen, H. et al. Tcf3 and Tcf4 are essential for long-term homeostasis of skin epithelia. *Nature Genet.* **41**, 1068–1075 (2009).
- Clevers, H. & Nusse, R. Wnt/ β -catenin signaling and disease. *Cell* **149**, 1192–1205 (2012).
- Posthaus, H. et al. β -Catenin is not required for proliferation and differentiation of epidermal mouse keratinocytes. *J. Cell Sci.* **115**, 4587–4595 (2002).
- Vasioukhin, V., Bauer, C., Yin, M. & Fuchs, E. Direct actin polymerization is the driving force for epithelial cell-cell adhesion. *Cell* **100**, 209–219 (2000).
- Huang, S. M. et al. Tankyrase inhibition stabilizes axin and antagonizes Wnt signaling. *Nature* **461**, 614–620 (2009).
- DasGupta, R. & Fuchs, E. Multiple roles for activated LEF/TCF transcription complexes during hair follicle development and differentiation. *Development* **126**, 4557–4568 (1999).
- Kandyba, E. et al. Competitive balance of intrabulge BMP/Wnt signaling reveals a robust gene network ruling stem cell homeostasis and cyclic activation. *Proc. Natl Acad. Sci. USA* **110**, 1351–1356 (2013).
- Schober, M. & Fuchs, E. Tumor-initiating stem cells of squamous cell carcinomas and their control by TGF- β and integrin/focal adhesion kinase (FAK) signaling. *Proc. Natl Acad. Sci. USA* **108**, 10544–10549 (2011).
- Scholl, C. et al. Synthetic lethal interaction between oncogenic KRAS dependency and STK33 suppression in human cancer cells. *Cell* **137**, 821–834 (2009).
- Babij, C. et al. STK33 kinase activity is nonessential in KRAS-dependent cancer cells. *Cancer Res.* **71**, 5818–5826 (2011).
- Zuber, J. et al. RNAi screen identifies Brd4 as a therapeutic target in acute myeloid leukaemia. *Nature* **478**, 524–528 (2011).
- Wang, Y. et al. The Wnt/ β -catenin pathway is required for the development of leukemia stem cells in AML. *Science* **327**, 1650–1653 (2010).
- Suvà, M. L., Riggi, N. & Bernstein, B. E. Epigenetic reprogramming in cancer. *Science* **339**, 1567–1570 (2013).
- Bernt, K. M. et al. MLL-rearranged leukemia is dependent on aberrant H3K79 methylation by DOT1L. *Cancer Cell* **20**, 66–78 (2011).
- Beronja, S. & Fuchs, E. RNAi-mediated gene function analysis in skin. *Methods Mol. Biol.* **961**, 351–361 (2013).

Supplementary Information is available in the online version of the paper.

Acknowledgements We thank J. Fagin for inducible oncogenic Hras mice; S. Williams, M. Schober, A. Rodriguez Folgueras, S. Dewell and D. Schramek for intellectual input; D. Oristian and N. Stokes as mouse specialists; Comparative Bioscience Center (AAALAC accredited) for care of mice in accordance with National Institutes of Health (NIH) guidelines; Genomics Resource Center (C. Zhao, Director) for sequencing; Bioimaging Center (A. North, Director) for advice; Flow Cytometry facility (S. Mazel, Director) for FACS sorting. E.F. is an Investigator of the Howard Hughes Medical Institute. This research was supported by grants from the NIH (R37-AR27883 (E.F.) and K99-AR061469 (S.B.)), Emerald Foundation (E.F.) and Human Frontiers Science Program Postdoctoral Fellowship (S.B.).

Author Contributions S.B., P.J. and E.F. designed the experiments. S.B. and P.J. made shRNA pools and lentivirus, and performed the screens. Illumina sequence analysis was done by E.H. and S.B. RNAseq and IPA analyses were performed by S.B., B.E.K. and P.J. Imaging was done by S.B. and N.O., and image analysis by S.B. and E.H. CHIP-seq data was generated by W.-H.L., and P.J. performed luciferase assays. S.B. and E.F. wrote the paper. All authors provided intellectual input, vetted and approved the final manuscript.

Author Information Raw RNAseq data can be accessed at Gene Expression Omnibus under accession number GSE48480 and permissions information is available at www.nature.com/reprints. The authors declare no competing financial interests. Readers are welcome to comment on the online version of the paper. Correspondence and requests for materials should be addressed to E.F. (fuchslb@rockefeller.edu).

METHODS

Lentivirus production and *in vivo* and *in vitro* transductions. Large-scale production and concentration of lentivirus were performed as previously described¹. Male and female animals was used in equal numbers, and all mice were on the C57BL/6 background, including *Gt(Rosa)26Sor^{tm1(eYFP)Cosl}+* (Jackson Laboratories, donated by A. McMahon), *FR-Hras^{G12V}* (9) and *Tg(K14-cre)1Efl^u*. Mice were housed and cared for in an AAALAC-accredited facility, and all animal experiments were conducted in accordance with IACUC-approved protocols. Randomization and blinding were not used in this study. Detailed description of the *in vivo* lentiviral transductions can be found elsewhere^{1,35}. For lentiviral infections in culture, cells were plated in 12-well dishes at 70,000 cells per well and incubated with lentivirus in the presence of polybrene (100 mg ml⁻¹) overnight. After 2 days, infected cells were sorted on the basis of RFP expression (mouse and human SCC cells) or positively selected with puromycin (1 mg ml⁻¹) for 4 days and processed for mRNA analysis. **mRNA quantifications.** Total RNAs were isolated from FACS-sorted cells from E18.5 epidermis or from flash-frozen, pulverized kidney, using the Absolutely RNA Microprep kit (Stratagene). Complementary DNAs were generated from 1 µg of total RNA using the SuperScript Vilo cDNA synthesis kit (Life Technologies). Real-time PCR was performed using the 7900HT Fast Real-Time PCR System (Applied Biosystems) and gene-specific and *Ppib* control primers. Real-time experiments were done on cells isolated from three transduced animals, or three independently transduced cell culture plates, and all reactions were performed in triplicate and in two separate runs. BRE-ZsGreen activity was measured using real-time PCR with ZsGreen-specific primers on cDNA from transduced epidermal cells as previously described⁴.

Immunostaining and histological analyses. The following primary antibodies were used: chicken anti-GFP (1:2,000; Abcam); mouse anti-β-catenin (15B8, 1:1,000; Sigma); guinea pig anti-K5 (1:500; E. Fuchs); rat anti-CD34 (RAM34, 1:100; eBioscience), anti-Ecad (ECCD-1, 1:200; M. Takeichi) and anti-nidogen (ELM1, 1:2,000; Santa Cruz); rabbit anti-caspase 3 (AF835, 1:1,000; R&D), anti-RFP (PM005, 1:2,000; MBL), anti-K10 (PRB-159P, 1:1,000; Covance), anti-filaggrin (PRB-417P, 1:2,000; Covance), anti-pSmad1/5/8 (AB3848, 1:1,000; Millipore) and anti-Mllt6 (NBP1-89222, 1:100; Novus Biologicals). Secondary antibodies were conjugated to Alexa-488, 546 or 647 (1:1,000, Life Technologies). Detection of pSmad1/5/8 was enhanced using the Tyramide Signal Amplification (Perkin Elmer). Cells and tissues were processed as previously reported¹, and mounted in ProLong Gold with DAPI (Life Technologies). Skin squamous cell cancer tissue array (SK802a) was obtained from US Biomax Inc. Immunohistochemistry preparations were developed using ImmPRESS Universal Antibody Polymer Detection method (Vector Laboratories). Confocal images were captured by a scanning laser confocal microscope (LSM510 and LSM780; Carl Zeiss) using Plan-Apochromat 20×/0.8 oil and C-Apochromat 40×/1.2 water lenses. Images were processed using ImageJ and Adobe Photoshop CS3. To quantify the number of ectodermal cells at E9.5, embryos were fixed in 4% paraformaldehyde, permeabilized in PBS + 0.1% Triton (Sigma), and the nuclei were labelled with TO-PRO-3 as recommended (Life Technologies). Tiled Z-stack images of were collected on a Zeiss LSM780 using a Plan-Apochromat 63×/1.4 oil lens. Stacks and metadata were imported into MATLAB (Mathworks) using the LOCI Bio-Formats Importer³⁶. For each stack, the surface was located by finding the first Z position with an average intensity threefold above background, and the stack was cropped to 6 µm corresponding to the surface epithelium. The resulting images were segmented in three dimensions using Imaris (Bitplane AG) to obtain counts of nuclei.

Flow cytometry. Primary epidermal keratinocytes were isolated³⁷ and then purified by fluorescence activated cell sorting (FACS) using BD FACSaria II (BD Biosciences). Nucleotide analogue EdU (50 mg per g body weight) was injected intraperitoneally 2 h before processing, and EdU (Life Technologies) incorporation and active caspase 3 (BD Pharmingen) assays were performed as recommended. Immune cell infiltration was analysed in whole skin dissociated with a sequential incubation in collagenase (Sigma; 0.25% in HBSS for 90 min) and trypsin (Gibco; 0.25% in PBS for 15 min) at 37 °C. The following biotin-conjugated rat antibodies (1:100; Pharmingen) were used: anti-CD11b (M1/70), anti-CD103 (M290), anti-Ly-6G/C (RB6-8C5), anti-CD3e (145-2C11), anti-CD45 (30-F11) and anti-CD45R (RA3-6B2). YFP/RFP quantification was based on detection of the native protein in unfixed cells. Flow cytometric analysis was performed on BD LSR II.

Cell culture assays. Cells were cultured in 0.05 mM Ca²⁺ (E18.5 mouse epidermal keratinocytes and SCC cells) or 1.5 mM Ca²⁺ (human SCC) E-media supplemented with 15% serum. Cell adhesion in primary epidermal keratinocytes seeded at low confluence was assayed by replacing their growth medium with a 1.5 mM Ca²⁺ E-media, and fixing them at different times thereafter. Nucleotide analogue EdU (10 µM) was added to cell culture media 90 min before processing, and contact inhibition was analysed in cells 3 days after reaching confluence. Inhibition of Wnt signalling was achieved by addition of 5 µM tankyrase inhibitor

XAV939 (IC₅₀ values 11 nM (Tnks1) and 4 nM (Tnks2)) to the media 12 h before the start of the experiments.

Lentiviral constructs. Sequences of RNAi constructs are listed in Supplementary Table 5. Design of LV-RFP, LV-GFP and LV-Cre has been previously reported¹. Lentiviral construct for inducible shRNA expression is a modification of tet-pLKO-puro³⁸ (Addgene plasmid 21915), where the IRES-Puro cassette was replaced between the XmaI and KpnI sites with the ligation of PCR-amplified XmaI/NheI-flanked *P2A* fragment and NheI/KpnI-flanked *nlsCre* cDNA. The lentiviral Wnt-reporter was fashioned after the lentiviral Beta-catenin Activated Reporter³⁹. It includes 12 *Tcf/Lef* binding sites followed by a minimal TK promoter and an *mRFP1* transgene that were subcloned into a pLKO.1 backbone between KpnI and NheI sites. Lentiviral bone morphogenetic protein-reporter that contains a pair of bone morphogenetic protein response elements is a derivative of BRE-ZsGreen⁴, where the reporter cassette between XhoI and NheI sites has been placed between SalI and NheI sites of the pLKO-nlsCre-MCS vector.

Tumour-free survival. Control and *Hras^{oncX2}* animals were transduced at E9.5 with low-titre LV-Cre containing constitutively expressing or inducible shRNA against scrambled control or test *Ctnnb1* and *Mllt6* shRNAs. Transductions were confirmed by real-time PCR of P7 (newborn) littermates, and the remaining animals were monitored for an additional 12 weeks. Animals were assessed every 2–3 days, and scored positive when tumours were larger than 2 mm in diameter. Animals transduced with an LV-Cre containing inducible shRNAs were allowed to form tumours for 60 days, at which point individual tumours were measured along their short and long axis using a digital caliper ($t = 0$). Next, tumour-bearing animals were treated by a single intraperitoneal injection of doxycycline (100 µl of 50 mg ml⁻¹) and maintained on doxycycline-containing chow for 8 weeks, and tumour size was assayed every 7 days. Because the tumour volumes at $t = 0$ showed a range between 4–20 mm³, the assayed tumour size was normalized to the initial tumour volume, and expressed as fold-change over time. Transplantation of SCC cells transduced with control shRNA, or shRNAs targeting mouse and human *Ctnnb1* and *Mllt6*, into immunocompromised nude recipients were performed as previously described²⁸, and animals were monitored every 3 days for a month. Tumour size was measured using a digital caliper, and tumour volume was calculated using the formula $[(\text{length} \times \text{width})^2 \times \pi]/6$.

Tcf3/4 ChIP-seq and luciferase assay. Details of the Tcf3/4 ChIP-seq will be reported elsewhere. For luciferase assays, passage 9–14 293FT cells were seeded in 96-well culture plates and transfected at 60–70% confluence using standard calcium phosphate procedures. Cells were co-transfected with control Renilla pRL-TK, and combinations of 50 ng pGL3-Mllt6, Mllt6^{mutant}, Axin2 or Axin2^{mutant} and 200 ng of K14-expression vectors encoding Lef1, ΔNβ-cat or control (empty vector). After 44 h, cells were collected and luciferase activity was measured using the TD-20/20 luminometer (Turner Biosystems) and the Dual-Glo Luciferase Assay System (Promega). Each transfection was performed in duplicate and repeated seven times.

Sample preparation and pre-amplification. Epidermal cells were isolated from E18.5 mouse skin using previously established procedures³⁷. Cells from individual embryos were used for genomic DNA isolation with the DNeasy Blood & Tissue Kit (Qiagen), and each sample was analysed for target transduction using real-time PCR. gDNAs from 30 transduced embryos were pooled, and 200 µg of the total was used as template in a 10-ml pre-amplification reaction with 21 cycles and Phusion High-Fidelity DNA Polymerase (NEB). PCR products were run on a 2% agarose gel, and a clean ~200-bp band was isolated using QIAquick Gel Extraction Kit as recommended by the manufacturer (Qiagen). Final samples were then sent for Illumina HiSeq 2000 sequencing.

Sequence processing and relative shRNA quantification. For each genotype, DNA from 30 embryos was pooled and independently sequenced using custom forward (5′-AATGATACGCGACACCGAGATCTACACTCTTTCCCTACACGAGCTCTTCCGATCTATCTTGTGGAAAGGACGAACACC-3′) and reverse (5′-CAAGCAGAGACGGCAGGATACGAGCTCTCCGATCTAATTGTGGATGAATACTGCCATTGTGTC-3′) oligonucleotides. Illumina reads were trimmed to the 21-nucleotide hairpin sequence using the FASTX-Toolkit and aligned to the TRC 2.x library with BWA (v0.6.2)⁴⁰ using a maximum edit distance of 3. Putative growth regulators were identified by combining two methodologies. First, Illumina reads from 3 sets of 30 embryos were treated as independent biological replicates in the DESeq R package⁴². Dispersions (variability) for each hairpin were estimated using a local fit to the data for each genotype, and hairpins with a P value < 0.05 by the negative binomial test were considered for downstream analysis. Second, an analysis was carried out on a pooled data set in which the reads from three sets of embryos were combined to maximize screen coverage and average biological variability. Although this precludes estimation of within-group variability, it has the effect of reducing noise for poorly counted hairpins when operating close to the minimum required screen coverage. Fisher's exact test was applied on a per-hairpin basis using combined reads by assembling a 2 × 2 contingency table⁴¹. The columns of the table

are the treatment conditions (for example, control and Hras^{oncoX2}), and the rows correspond to the sequencing counts for a given hairpin in the first, and the counts for all other hairpins in the pool in the second. The test thus calculates the probability of observing a difference in hairpin representation relative to the expected representation in the pool. We further adjust the *P* value for multiple testing using the Benjamini–Hochberg correction. Hairpins with a *P* value < 0.05 were considered for further analysis. A gene was considered significantly enriched or depleted if at least two hairpins exhibited a twofold or greater change in normalized reads with a significant *P* value, and no hairpins in the set exhibited a change of equal magnitude in the opposite direction. Hits common to both analyses were ranked by number of significant hairpins and the magnitude of their effect. All analyses were carried out in the R statistical environment⁴², with some plots produced using the ggplot2 package⁴³. Gene lists were imported into the Ingenuity Pathway Analysis software (Ingenuity Systems), and analyses and graphic outputs of relative enrichment in functional gene categories were performed as recommended.

Choice of statistical analysis of relative shRNA abundance. The strength of the Fisher's exact test is that it can calculate a probability of observing a difference in shRNA representation in a comparison of pooled data sets. When operating close to the minimum required screen coverage or when it is not feasible to perform many independent replicates, this strategy can be advantageous to increase coverage and reduce noise if combined with additional stringent criteria (that is, requiring a gene to be targeted by multiple hairpins) and validation.

Because this methodology does not explicitly account for sample-to-sample variability (instead maximizing coverage and averaging out variability), we independently analysed our data using two additional statistical methodologies that directly address variability within biological replicates. Importantly, both of these methods used the same stringent set of thresholds (twofold change in hairpin count, and a requirement for least two hairpins to show a significant effect in same direction, and none in the opposite). First, we used DESeq¹², an R package designed for the analysis of Illumina sequencing-based assays, which estimates and accounts for biological variability in a statistical test based on the negative binomial distribution. Second, we treated independently sequenced sets of 30 embryos as biological replicates, and generated replicate-specific lists of candidate genes. Comparison of hits shared between these replicates to the hits identified in our analysis of pooled samples yielded a highly conserved set of candidate genes consistent with strong reproducibility of our data. Both analyses identify a list of candidates that substantially overlaps with those identified by our pooling and ranking scheme, with nearly all of our top hits identified regardless of the methodology.

When conducting shRNA drop-out screens, perhaps the most important criteria in identifying potential candidates is that a gene be targeted by multiple, independent hairpins to avoid off-target effects. We thus felt our data would be best-served by combining an analysis of pooled data, which tends to be more

inclusive at the level of hairpins and enables ranking by number of independent hairpins, and the results of DESeq, which ensures reproducibility of hits.

RNA-seq and IPA network analyses. Epidermal progenitors were FACS sorted into TrizolLS (Invitrogen) and RNA was purified using Direct-zol RNA MiniPrep kit (Zymo Research) per manufacturer's instructions. Quality of the RNA was determined using Agilent 2100 Bioanalyzer, with all samples passing the quality threshold of RNA integrity numbers (RIN) > 8. Library preparation using Illumina TrueSeq mRNA sample preparation kit was performed at the Weill Cornell Medical College Genomic Core facility, and cDNA was sequenced on Illumina HiSeq 2000. Reads were mapped to mm9 build of the mouse genome using TopHat, and transcript assembly and differential expression were determined using Cufflinks⁴⁴. Differentially regulated transcripts were analysed in IPA (Ingenuity Systems), and the upstream transcriptional regulators were predicted using the Upstream Regulator Analysis package, with a significant overlap between the data set genes and transcription factor targets set at *P* < 0.01, and the regulation direction (activated or inhibited) at *z*-score = 2.

Statistics. All quantitative data were collected from experiments performed in at least triplicate, and expressed as mean ± s.d. or s.e.m. The fits of cellular and tumour growth were compared using the extra sum-of-squares F-test, and expression of CTNNB1 and MLLT6 in human SCC tissue was analysed using a non-parametric (Spearman) correlation. Differences between groups were assayed using two-tailed student *t*-test using Prism 5 (GraphPad Software). Significant differences were considered when *P* < 0.05.

36. Linkert, M. *et al.* Metadata matters: access to image data in the real world. *J. Cell Biol.* **189**, 777–782 (2010).
37. Nowak, J. A. & Fuchs, E. Isolation and culture of epithelial stem cells. *Methods Mol. Biol.* **482**, 215–232 (2009).
38. Wiederschain, D. *et al.* Single-vector inducible lentiviral RNAi system for oncology target validation. *Cell Cycle* **8**, 498–504 (2009).
39. Davidson, K. C. *et al.* Wnt/β-catenin signaling promotes differentiation, not self-renewal, of human embryonic stem cells and is repressed by Oct4. *Proc. Natl Acad. Sci. USA* **109**, 4485–4490 (2012).
40. Li, H. & Durbin, R. Fast and accurate short read alignment with Burrows–Wheeler transform. *Bioinformatics* **25**, 1754–1760 (2009).
41. Auer, P. L. & Doerge, R. W. Statistical design and analysis of RNA sequencing data. *Genetics* **185**, 405–416 (2010).
42. R Research Development Team. R: A language and environment for statistical computing. R Foundation for Statistical Computing, Vienna, Austria. <http://www.R-project.org> (2012).
43. Wickham, H. *ggplot2: Elegant Graphics for Data Analysis* (Springer, 2009).
44. Trapnell, C. *et al.* Transcript assembly and quantification by RNA-Seq reveals unannotated transcripts and isoform switching during cell differentiation. *Nature Biotechnol.* **28**, 511–515 (2010).

Stimulated X-ray emission for materials science

M. Beye¹, S. Schreck^{1,2}, F. Sorgenfrei^{1,3}, C. Trabant^{1,2,4}, N. Pontius¹, C. Schüßler-Langeheine¹, W. Wurth³ & A. Föhlisch^{1,2}

Resonant inelastic X-ray scattering and X-ray emission spectroscopy can be used to probe the energy and dispersion of the elementary low-energy excitations that govern functionality in matter: vibronic, charge, spin and orbital excitations^{1–7}. A key drawback of resonant inelastic X-ray scattering has been the need for high photon densities to compensate for fluorescence yields of less than a per cent for soft X-rays⁸. Sample damage from the dominant non-radiative decays thus limits the materials to which such techniques can be applied and the spectral resolution that can be obtained. A means of improving the yield is therefore highly desirable. Here we demonstrate stimulated X-ray emission for crystalline silicon at photon densities that are easily achievable with free-electron lasers⁹. The stimulated radiative decay of core excited species at the expense of non-radiative processes reduces sample damage and permits narrow-bandwidth detection in the directed beam of stimulated radiation. We deduce how stimulated X-ray emission can be enhanced by several orders of magnitude to provide, with high yield and reduced sample damage, a superior probe for low-energy excitations and their dispersion in matter. This is the first step to bringing nonlinear X-ray physics in the condensed phase from theory^{10–16} to application.

In the soft X-ray region, the use of nonlinear techniques to enhance the signal levels has been prevented by the small cross-sections and the short lifetimes of core-excited states in the regime of a few femtoseconds. In the past few years, free-electron lasers have become available, producing ultrashort, intense soft X-ray pulses^{9,17–20}. Recently, the stimulation of emission from a single fluorescence line in a rare gas²¹ and hard X-ray/optical sum frequency generation²² have been demonstrated.

We present here stimulated X-ray emission from a solid-state sample recorded at the free-electron laser in Hamburg (FLASH) for non-resonant silicon *L*-edge excitation at a photon energy of 115 eV. With free-electron laser radiation we produce regions with high *2p* core excitation densities. The spontaneously emitted radiation from recombination of the *2p* core holes (photon energy of 85 eV to nearly 100 eV) seeds the stimulated emission of soft X-ray photons. The emitted spectrum is determined by the spontaneous emission as observed in a typical resonant inelastic X-ray scattering (RIXS) or X-ray emission spectroscopy (XES) experiment and thus conserves all the information and specificity of these methods. By carefully choosing the geometry, we can significantly enhance the weak fluorescence signal at the expense of Auger decays. Fewer electrons are emitted and electronic damage to the sample is minimized. By properly shaping the free-electron laser beam footprint on the sample the detected signal can be enhanced by orders of magnitude because the usually isotropic emission can be directed towards the detector. This opens up the possibility of nonlinear spectroscopy in the X-ray region by combining concepts from nonlinear optics with the high information depth of X-ray spectroscopy, which is intrinsically able to resolve femtosecond dynamics^{10–16,23–25}.

The absorption and stimulated emission probabilities P can be approximated for infinitesimally thin samples where the photons interact on a short length dx as:

$$P = \sigma \rho_{\text{atom}} dx \text{ and } P = \sigma \rho_{\text{ch}} dx \quad (1)$$

where ρ_{atom} is the number density of absorbing atoms and ρ_{ch} (for core hole) is the number density of excited atoms for stimulation. The X-ray absorption or stimulation cross-sections σ are determined by the dipole transition matrix elements between the core level and unoccupied (absorption) or occupied (stimulated emission) valence states and are assumed at this point to be approximately the same. The cross-section is connected with the absorption length $\lambda = (\sigma \rho_{\text{atom}})^{-1}$. The effect of stimulated emission is large, when the stimulation probability approaches unity $P \stackrel{!}{=} 1 = \sigma \rho_{\text{ch}} dx$, yielding:

$$\frac{\rho_{\text{ch}}}{\rho_{\text{atom}}} = \frac{\lambda}{dx} \quad (2)$$

For effective stimulation, the absorption length relative to the interaction lengths of stimulating photons has to be similar to the fraction of core-excited atoms. For comparable interaction and absorption lengths, every atom needs to be core-excited; a population inversion is required.

In the forward direction, stimulated X-ray emission has been demonstrated in the gas phase²¹. In this geometry, the maximum interaction length at which stimulating photons can interact with core holes is intrinsically given by the absorption length. The sample has to absorb one X-ray photon per atom. If applied to solids, this energy usually destroys the bonding network and is hence not suited for spectroscopic studies of the undisturbed system.

The situation is very different for other geometries. Along the lateral dimension of the X-ray focus, the interaction length can be significantly larger. With soft X-rays on solids, the absorption length of the exciting radiation with a photon energy that is slightly above an absorption edge is typically tens or hundreds of nanometres, whereas the lateral dimensions of typical X-ray foci are a few to hundreds of micrometres. The interaction length is then limited by the absorption length of the RIXS and XES signals with a photon energy below the absorption edge, which are typically an order of magnitude larger than for the exciting radiation. Consequently, lower excitation densities are needed, when the observation direction is chosen to be along the lateral dimension of the projected focus instead. This situation is sketched in Fig. 1, together with measured data of the total emission signal detected at several angles to the surface. We observe an emission maximum at around 9°, which is the result of the balance between the absorption length of the exciting radiation and the interaction length of the emitted radiation inside the excited volume.

We also studied the emission with a spectrometer. Experimental constraints meant that it was placed at around 15° to the sample surface. We observed a characteristic dependence of the total number and the spectral distribution of the outgoing photons on the incoming photon flux (Figs 2 and 3).

Before we analyse the experimental data, we discuss the relevant processes that have to be considered to derive the number of stimulated photons. The explicit formulation is given in the Methods section. Stimulated emission can be treated along the same lines as absorption. We can hence formulate a differential equation as a function of the interaction length in an ansatz similar to the derivation of the Lambert–Beer law for absorption. This approach is inherently time-independent. Auger

¹Institute for Methods and Instrumentation of Synchrotron Radiation Research G-ISRR, Helmholtz-Zentrum Berlin für Materialien und Energie GmbH, Albert-Einstein-Straße 15, 12489 Berlin, Germany.

²Fakultät für Physik und Astronomie, Universität Potsdam, Karl-Liebknecht-Straße 24–25, 14476 Potsdam, Germany. ³Institut für Experimentalphysik, Universität Hamburg and Centre for Free-Electron Laser Science, Luruper Chaussee 149, 22761 Hamburg, Germany. ⁴II. Physikalisches Institut, Universität zu Köln, Zùlpicher Straße 77, 50937 Köln, Germany.

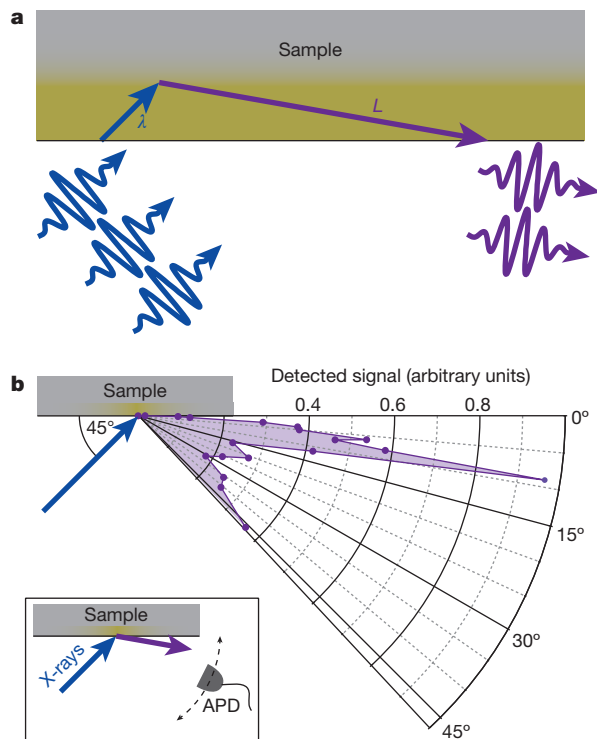


Figure 1 | Geometry to observe spontaneously stimulated X-ray emission from solids. **a**, X-rays create core excitations in the solid (yellow). A cascade of stimulated emission builds up in a direction where the penetration depth λ of incoming photons is balanced by the absorption length L for emission. **b**, The total emission is detected as a function of glancing angle at fluences where stimulated emission saturates. An enhancement is observed for shallow angles, where the interaction length for emitted photons is longest. This direction is far away from the specular reflection increase around 45° . The inset displays the layout of the experiment. APD, avalanche photodiode.

decays are not explicitly treated, because Auger processes and radiative emission are independent processes and are only related through the number of core holes. Auger decays are implicitly included, though, through the core-hole lifetime. Auger decays are the only other significant decay channel of the core holes and stimulated emission reduces the number of core holes, so we expect a substantial decrease in the number of Auger processes. The effective lifetime of the core holes, taking all decay channels into account, should be shortened.

We formulate a differential equation for the gain in the number of observed stimulated photons. $N_{\text{stim,obs}}$ is the number of stimulated photons that are emitted into a detector with a finite acceptance angle and detection efficiency:

$$\frac{dN_{\text{stim,obs}}}{dx} = N_{\text{obs}} \rho_{\text{ch}} \sigma_{\text{stim}} \quad (3)$$

where the cross-section for transitions between the respective valence and the core state is σ_{stim} (now generally different from σ_{abs}). The total number of photons in the observation direction N_{obs} drives the observed stimulation and is the sum of the number of spontaneously emitted photons in this direction $N_{\text{sp,obs}}$ (initially acting as a seed) and the increasing contribution of $N_{\text{stim,obs}}$ itself. Without stimulation, $N_{\text{sp,obs}}$ is proportional to the number of the incoming photons. Stimulated photons are available to stimulate further, which leads to a nonlinear increase of the stimulated signal. At low photon numbers stimulation is negligible and the spontaneous emission forms a linear lower limit for the dependence of the observed number of photons as a function of incoming photon numbers.

The next important factor is the instantaneous density of the core holes available for stimulated decays. Although every photon in an X-ray pulse is absorbed in the sample, the instantaneous number of core

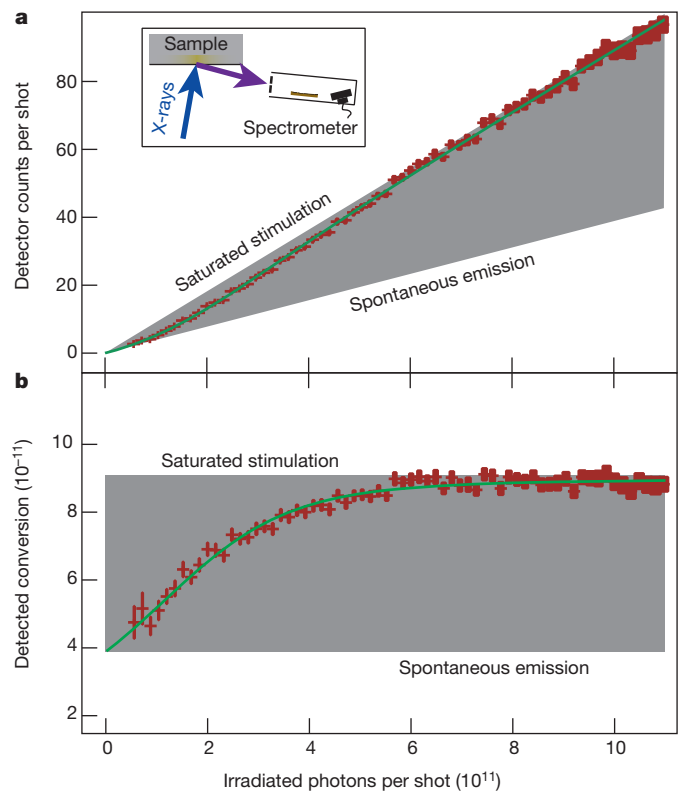


Figure 2 | Observing stimulated emission from a solid. **a**, Red symbols show the measured number of counts per shot versus the number of incoming photons. The error bars are one standard deviation of the averaged values. The grey area falls between the limiting cases of spontaneous emission and saturation of stimulated emission. The green line is a fit to the derived formula. The inset shows the geometry of the experiment. **b**, The same data are plotted as detected conversion, after dividing the detector counts by the number of incoming photons. The linear limits now become constants.

holes is smaller than one per incoming photon, depending on the pulse length and the core-hole lifetime: some core holes have already decayed before the pulse is over. Besides the reduction through spontaneous decay, the number of core holes is reduced by each stimulated photon. To treat this effect, we split the decay rate of the core holes into two parts: the Auger decays enter through the fixed core-hole lifetime, and the stimulation directly reduces the number of core holes. Thus, the change in the number of stimulated photons depends on $N_{\text{stim,obs}}$ itself, this time with a negative sign leading to saturation. An upper limit for stimulated emission is reached, at which every core hole is stimulated. For high incoming photon numbers, the observed number of photons will thus saturate towards an upper linear limit as a function of incoming photon numbers.

The solution of the differential equation provides the dependence of the observed number of stimulated photons on the experimental parameters. We approximate the lateral distribution of the incoming beam and the exponentially decaying absorption profile into the depth of the sample with a constant core-hole density (albeit modified through stimulated emission), inside a cylindrically shaped excitation volume, the size of which is given by the focal sizes and the absorption length of the incoming radiation. The interaction length for stimulation in this volume extends from the bottom of the excited cylinder to the sample surface in the direction of observation and is thus given only through the geometry of the experiment.

For soft X-rays from current free-electron lasers, focal sizes of the order of $10 \mu\text{m}$ and pulse lengths around the core-hole lifetime are well within reach. With typical absorption lengths in solids for the incoming photons of around 100 nm and for the emission of around $1 \mu\text{m}$ and with stimulation cross-sections of 1 Mbarn (ref. 26), stimulation

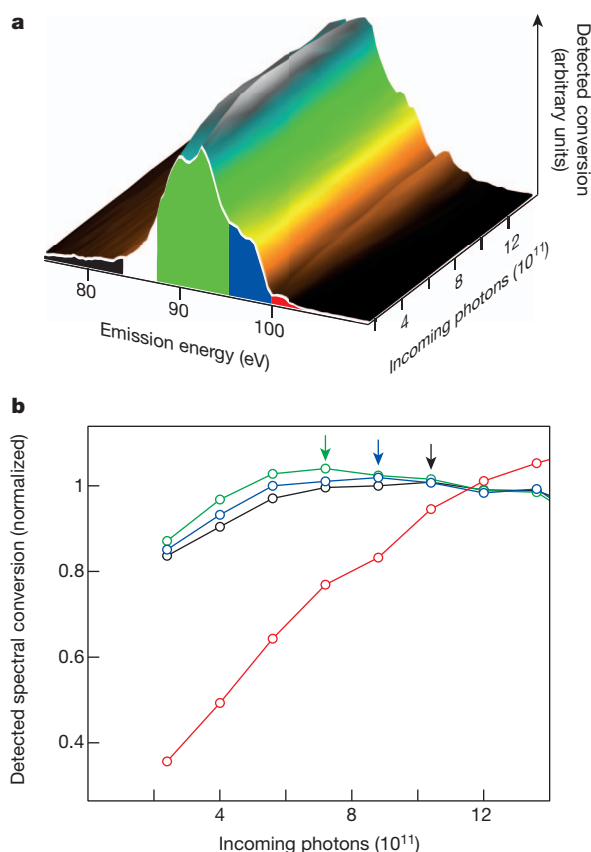


Figure 3 | Spectrally resolved stimulated emission. **a**, The detected conversion is shown, highlighting the integration regions for data plotted in **b**. **b**, The maximum detected conversions for different spectral regions are marked with arrows. The most intense features saturate first (green, 87–95 eV), followed by the emission shoulder (blue, 95–99.5 eV) and the weak multiple scattering background (black, 71–84 eV). The onset of saturation can be connected with the stimulation cross-section. Emission above the band gap (red, 99.5–108 eV) is not observed at low intensities. The signal is connected with X-ray-induced electronic excitations.

becomes important at about 10^{11} incoming photons per pulse. Typical soft X-ray free-electron lasers produce up to 10^{13} photons per shot, so that stimulated emission has to be considered as a dominating effect.

We now turn to the experimental observations. In Fig. 1b, we show the angular dependence of the emission signal. The incidence angle is chosen to be 45° and we find enhanced intensity for the specular geometry with the detector at 45° . Additionally, we find a strong enhancement of the signal by about a factor of five at grazing angles around 9° , far from the specular reflection. It appears in a narrow angular window and is indeed the result of a nonlinear effect. With the used excitation conditions, we are deep in the regime where the stimulated emission saturates and the observed effects are variations in the angular distribution of the stimulated emission. The maximum signal is expected in a direction for which the interaction length inside the core excited volume is as large as possible and for which the reabsorption probability is minimized. Because the absorption length for the incoming radiation is about an order of magnitude shorter than the reabsorption length, the optimal angle is expected around $\arcsin(0.1) \approx 6^\circ$ which is in reasonably good agreement with the experiment.

In Fig. 2a, we show the total number of observed photons in our spectrometer placed at 15° to the surface plane, along with a fit to the expected dependence. We also include the linear limits derived from the fit. We observe that already in the lower fluence range studied, there is a deviation from linearity and the stimulated emission quickly saturates to the upper limit. In the chosen experimental geometry, the enhancement of the emission between purely spontaneous and saturated

stimulation is only about a factor of two. This is because the majority of the stimulated photons are radiated more grazing to the surface and do not reach our detector, as shown in Fig. 1b. Still, the nonlinear enhancement and saturation of the signal through stimulated emission are clearly observed.

It is instructive to display the total number of observed photons divided by the number of incoming photons (see Fig. 2b). This yields the conversion efficiency from incoming photons to emitted photons, as seen by the detector—the detected conversion. The limiting linear dependences turn into limiting constant conversion efficiencies and are determined by the experimental parameters. The nonlinearity of the curve becomes obvious as a monotonous change from the lower to the upper limit.

The photon number needed for the nonlinear part between the limiting lines is directly related also to the emission-energy-dependent stimulation cross-section. For larger stimulation cross-sections, the nonlinearity and thus the saturation of stimulated emission will occur at smaller incoming photon numbers. In Fig. 3a, we show the spectral evolution of the silicon *L*-edge emission depending on the number of incoming photons and how we separate the spectrum into parts of different emission intensity. The stimulation cross-section contains the same matrix elements as the spontaneous emission probability, which is in turn proportional to the measured spectral emission intensity, so the stimulation of emission becomes more effective for emission-energy regions that already show a high intensity at low fluences. Figure 3b displays the dependence of the normalized detected conversion on the number of incoming photons in specific emission-energy regions. The peak region around an emission energy of 90 eV, as the most intense feature, approaches saturated stimulation fastest, and the other regions follow in the order of spectral intensity.

The emission energy region for usually unoccupied states above the bandgap shows a strikingly different behaviour. Here, a secondary effect sets in. Photo-emitted electrons and electrons from Auger decays scatter inelastically in the sample, very quickly creating a multitude of delocalized electron–hole pair excitations around the bandgap. This effect becomes stronger with an increasing number of incoming photons and the connected radiative decays annihilate core holes that contributed to the stimulated emission of other parts of the spectrum at lower photon numbers. Therefore, the detected conversion in other parts of the spectrum actually shrinks rather than becoming constant. Nevertheless, because all emission processes saturate when all the core holes are stimulated down, the total detected conversion still becomes constant (compare the integral detected conversion shown in Fig. 2b).

In the direction of 15° from the surface, the detected conversion increases by a bit more than a factor of two between the limiting cases of spontaneous emission and saturated stimulated emission. By using a shallower angle, we can increase the gain further by another factor of five (see the difference in the saturated emission signal in Fig. 1b). This value is limited by the round shape of the free-electron laser beam footprint on the sample. The shape of the beam leads to the same maximized interaction length in every azimuthal direction in the sample surface plane and thus to a stimulated emission profile which is rotationally symmetric around the sample normal at the centre of the beam.

The observed gain can clearly be further increased when the footprint of the irradiated photons is specifically shaped. An elongation of the footprint in the observation direction will further enhance the observed photon numbers, whereas in other directions the signal will be reduced. To ensure temporal overlap of the core excitations in the sample and the majority of the stimulated photons travelling with the speed of light, the footprint of the exciting beam needs to be elongated by placing the sample grazing to the incident beam. In this way, the exciting wavefront will travel along the sample surface in time with the stimulated photons and the enhancement of the emission signal will be maximized while X-ray-induced sample damage is further minimized.

The same applies to soft X-ray experiments from other systems, because the determining parameters are very similar for most materials.

The signal gain that we expect as compared to normal RIXS or XES experiments stems from two sources. On one hand, the saturation of stimulated emission is an indicator that most core holes decay via the emission of photons instead of decaying via Auger processes. This pushes the observed fluorescence yield from the 10^{-3} level in the direction of unity. On the other hand, directing the majority of the emission towards the detector can substantially increase the signal, given that typical fluorescence detectors (and our spectrometer) have a geometrical acceptance of less than 10^{-4} of the full solid angle. Therefore, stimulated emission can enhance the detected signal by several orders of magnitude. In our experiment we did observe traces of sample damage. Generally though, with optimized geometries at optimized X-ray sources, the signal gain can be used to minimize acquisition times in the non-damaging regime, or alternatively to record full spectra in a single X-ray shot, so that the spectroscopic information is essentially generated before X-ray-induced changes set in.

Such enhanced signal levels enable highly selective RIXS and XES studies with considerably improved energy resolution, so that new low-energy excitations may be discovered. Through the combination with pump-probe techniques, huge parameter spaces in the ultrafast time domain can quickly be mapped. Finally, through the combination of non-linear techniques from optical lasers with the high specificity of X-rays, small signals from extremely dilute active centres can now be dissected.

METHODS SUMMARY

Photon parameters. The experiments were conducted at the free-electron laser FLASH at Hamburg, Germany, operating at a photon energy of 115 eV. The spectrally resolved data was recorded at a repetition rate of 5 Hz with 30-fs pulses^{17,27}. We used the grating of beamline PG2 as a mirror²⁸. The focus was round with a diameter of 45 μm , leading to fluences up to 1 J cm^{-2} . The angular dependence was measured at beamline BL2 (ref. 29) at a burst repetition rate of 10 Hz, each including 100 pulses at 250 kHz. The focal size was adjusted to be about 40 μm to compensate for the now 50-fs-long pulses. With a gas attenuator, we set the fluence around 1 J cm^{-2} . The incoming photon numbers have been measured for each shot by a gas monitor detector²⁹.

Experimental setup. We scanned hydrogen-passivated silicon (100) surfaces through the beam. Spectra were recorded with a Scienta XES 355 spectrometer³⁰ and a single-photon-counting, multi-hit-capable detector centred at 92 eV with a resolution of 0.4 eV. The scattering plane was the horizontal plane of polarization of the incoming photons with the spectrometer at around 85° to the beam (15° to the sample surface), while the pulses impinged at an angle of 80° to the surface. For the angular dependence, we used an avalanche photodiode with an aluminium filter to block optical light. The incidence angle was 45° , whereas the detection angle was varied.

Analysis. With our spectrometer, we recorded around 40,000 single shots. The data was sorted, binned and the standard deviations of the averaged values were computed for each bin. With the photodiode, we analysed 15,000 bursts. During free-electron laser irradiation, the emission from a plasma plume was optically visible at the sample and slight ablation was observed.

Full Methods and any associated references are available in the online version of the paper.

Received 17 October 2012; accepted 9 July 2013.

Published online 21 August 2013.

- Kotani, A. & Shin, S. Resonant inelastic x-ray scattering spectra for electrons in solids. *Rev. Mod. Phys.* **73**, 203–246 (2001).
- Schlappa, J. *et al.* Collective magnetic excitations in the spin ladder $\text{Sr}_{14}\text{Cu}_{24}\text{O}_{41}$ measured using high-resolution resonant inelastic x-ray scattering. *Phys. Rev. Lett.* **103**, 047401 (2009).
- Hennies, F. *et al.* Resonant inelastic scattering spectra of free molecules with vibrational resolution. *Phys. Rev. Lett.* **104**, 193002 (2010).
- Ament, L. J. P., van Veenendaal, M., Devereaux, T., Hill, J. P. & van den Brink, J. Resonant inelastic x-ray scattering studies of elementary excitations. *Rev. Mod. Phys.* **83**, 705–767 (2011).
- Le Tacon, M. *et al.* Intense paramagnon excitations in a large family of high-temperature superconductors. *Nature Phys.* **7**, 725–730 (2011).

- Pietzsch, A. *et al.* Spatial quantum beats in vibrational resonant inelastic soft x-ray scattering at dissociating states in oxygen. *Phys. Rev. Lett.* **106**, 153004 (2011).
- Schlappa, J. *et al.* Spin-orbital separation in the quasi-one-dimensional mott insulator Sr_2CuO_3 . *Nature* **485**, 82–85 (2012).
- Krause, M. O. Atomic radiative and radiationless yields for K and L shells. *J. Phys. Chem. Ref. Data* **8**, 307 (1979).
- McNeil, B. W. J. & Thompson, N. R. X-ray free-electron lasers. *Nature Photon.* **4**, 814–821 (2010).
- Tanaka, S. & Mukamel, S. Coherent x-ray Raman spectroscopy: a nonlinear local probe for electronic excitations. *Phys. Rev. Lett.* **89**, 043001 (2002).
- Mukamel, S. Multiple core-hole coherence in x-ray four-wave-mixing spectroscopies. *Phys. Rev. B* **72**, 235110 (2005).
- Schweigert, I. & Mukamel, S. Probing valence electronic wave-packet dynamics by all x-ray stimulated Raman spectroscopy: a simulation study. *Phys. Rev. A* **76**, 012504 (2007).
- Harbola, U. & Mukamel, S. Coherent stimulated x-ray Raman spectroscopy: attosecond extension of resonant inelastic x-ray Raman scattering. *Phys. Rev. B* **79**, 085108 (2009).
- Patterson, B. D. Resource letter on stimulated inelastic x-ray scattering at an XFEL. (SLAC Technical Note SLAC-TN-10-026, SLAC National Accelerator Laboratory, Menlo Park, California, 2010).
- Sun, Y.-P., Liu, J.-C., Wang, C.-K. & Gel'mukhanov, F. Propagation of a strong x-ray pulse: pulse compression, stimulated raman scattering, amplified spontaneous emission, lasing without inversion, and four-wave mixing. *Phys. Rev. A* **81**, 013812 (2010).
- Biggs, J. D., Zhang, Y., Healion, D. & Mukamel, S. Two-dimensional stimulated resonance Raman spectroscopy of molecules with broadband x-ray pulses. *J. Chem. Phys.* **136**, 174117 (2012).
- Ackermann, W. *et al.* Operation of a free-electron laser from the extreme ultraviolet to the water window. *Nature Photon.* **1**, 336–342 (2007).
- Emma, P. *et al.* First lasing and operation of an angstrom-wavelength free-electron laser. *Nature Photon.* **4**, 641–647 (2010).
- Di Mitri, S. *et al.* in *Advances in X-ray Free-Electron Lasers: Radiation Schemes, X-Ray Optics, and Instrumentation* (eds Tschentscher, T. & Cocco, D.) Vol. 8078, 807802, doi:10.1117/12.886491 (Proc. SPIE, 2011).
- Pile, D. X-rays: first light from SACLA. *Nature Photon.* **5**, 456–457 (2011).
- Rohringer, N. *et al.* Atomic inner-shell x-ray laser at 1.46 nanometres pumped by an x-ray free-electron laser. *Nature* **481**, 488–491 (2012).
- Glover, T. E. *et al.* X-ray and optical wave mixing. *Nature* **488**, 603–608 (2012).
- Beye, M., Sorgenfrei, F., Schlotter, W. F., Wurth, W. & Föhlisch, A. The liquid-liquid phase transition in silicon revealed by snapshots of valence electrons. *Proc. Natl Acad. Sci. USA* **107**, 16772–16776 (2010).
- Wernet, P. Electronic structure in real time: mapping valence electron rearrangements during chemical reactions. *Phys. Chem. Chem. Phys.* **13**, 16941–16954 (2011).
- Salén, P. *et al.* Experimental verification of the chemical sensitivity of two-site double core-hole states formed by an x-ray free-electron laser. *Phys. Rev. Lett.* **108**, 153003 (2012).
- Yeh, J. J. & Lindau, I. Atomic subshell photoionization cross-sections and asymmetry parameters— $1 \leq Z \leq 103$. *Atom. Data Nucl. Data Tab.* **32**, 1–155 (1985).
- Frühling, U. *et al.* Single-shot terahertz-field-driven x-ray streak camera. *Nature Photon.* **3**, 523–528 (2009).
- Martins, M. *et al.* Monochromator beamline for FLASH. *Rev. Sci. Instrum.* **77**, 115108 (2006).
- Tiedtke, K. *et al.* The soft x-ray free-electron laser FLASH at DESY: beamlines, diagnostics and end-stations. *New J. Phys.* **11**, 023029 (2009).
- Nordgren, J. Soft x-ray emission spectroscopy—preface. *J. Electron Spectrosc.* **110–111**, ix–x (2000).

Acknowledgements We thank N. Rohringer, A. Scherz and J. Stöhr for discussions. We acknowledge support from the FLASH staff. Financial support was given to M.B. by the VolkswagenStiftung. Further support was given by the German Federal Ministry of Education and Research through the priority programme FLASH: “Matter in the light of ultrashort and extremely intense X-ray pulses” and contract number 05K10PK2, and also by the Deutsche Forschungsgemeinschaft through the graduate school: “Physics with new advanced coherent radiation sources”.

Author Contributions All authors contributed to planning parts of the experiment. Research was conducted by F.S., C.T., N.P., C.S.-L. and M.B. Data analysis and interpretation was done by M.B., S.S. and A.F. The formalism was developed and the manuscript was written by M.B. with input from all co-authors.

Author Information Reprints and permissions information is available at www.nature.com/reprints. The authors declare no competing financial interests. Readers are welcome to comment on the online version of the paper. Correspondence and requests for materials should be addressed to M.B. (martin.beye@helmholtz-berlin.de).

METHODS

Photon parameters. The experiments have been conducted during two separate runs at the free-electron laser FLASH at Hamburg, Germany. The machine was operated at a central photon energy of about 115 eV. In one run, we recorded the spectral resolved data. The machine was operated at a repetition rate of 5 Hz with typically 30-fs pulses^{17,27}. We used beamline PG 2 with the 1,200-lines-per-millimetre grating in zero order, thus reflecting the incident beam without dispersion²⁸. To maximize the photon flux, a grazing angle of 3.5° was used on the grating. The spot on the sample was round with a diameter of about 45 µm, determined through measurements on a fluorescence screen and permanent imprints studied under a microscope. These parameters lead to fluences up to 1 J cm⁻². The incoming photon numbers have been measured for each shot by a gas monitor detector²⁹.

In another experimental campaign, the angular dependence of the stimulated emission signal was studied. Our setup was placed at beamline BL 2 (ref. 29). After an upgrade of the FLASH accelerator, a burst repetition rate of 10 Hz became available, each burst including 100 pulses at 250 kHz. The pulse length was, at about 50 fs, slightly longer and the spot size on the sample was adjusted to be about 40 µm for compensation. With a gas attenuator, we set the fluence at around 1 J cm⁻², the upper limit of the spectrally resolved data.

Experimental setup. Hydrogen-passivated silicon (100) surfaces were scanned through the beam. The spectra have been recorded with a commercial Scienta XES 355 spectrometer³⁰ using the 300-lines-per-millimetre grating. The counts have been detected by a multi-channel-plate, phosphor-screen combination that can count single photons and is multi-hit capable. The detection window was centred at 92 eV and the resolution was set to 0.4 eV. The scattering plane was the horizontal plane of polarization of the incoming photons. The spectrometer was mounted at around 85° to the beam (15° to the sample surface), while the pulses impinged at an angle of 80° to the surface.

For the angular dependence, we used an avalanche photodiode with an aluminium filter to block optical light. The incidence angle on the sample was 45°, whereas the detection angle was varied.

Data analysis. With our spectrometer, we recorded around 40,000 single shots. The data was sorted and binned and the standard deviations of the averaged values were computed for each bin. With the photodiode, we analysed 15,000 bursts. During free-electron laser irradiation, the emission from a plasma plume was optically visible at the sample and slight ablation was observed.

The instantaneous core-hole density. As described in the main text, the instantaneous core-hole density contains the main approximations in our theoretical treatment. Without stimulation, the core-hole density is assumed to be constant inside a cylinder formed by the exciting radiation, and outside it is assumed to be zero. The dimensions of this cylinder in the surface plane of the sample are given by the distribution of the incoming photons: the measured focal width and height (w and h). The depth of the cylinder is taken as the tabulated absorption length of the incoming radiation λ . By choosing $1/e$ dimensions for this volume, the integral number of core holes is the same as for the actual distributions and given through the number of incoming photons. We thus scale the core-hole density to yield the same integrals and the same second moments as the actual distributions.

We treat the temporal distribution of the core holes as follows: Core-hole decays during the pulse length reduce the instantaneous core-hole density. The temporal distribution of the number of core holes in the sample at a given time t , that is, $N_{\text{ch}}(t)$, is the solution of the following differential equation:

$$\frac{dN_{\text{ch}}(t)}{dt} = N_{\text{in}}(t) - \frac{N_{\text{ch}}(t)}{\tau_{\text{lt}}}$$

with the temporal distribution of the exciting photons $N_{\text{in}}(t)$ as the source term of this inhomogeneous differential equation and the core-hole lifetime τ_{lt} . For a temporal Gaussian pulse of incoming photons, the solution is the product of an exponential decaying function and an error function for the creation of core holes. To cast the analytical solution into the same approximation as above, where the core-hole density (without stimulation) is constant during a specific time period, we analyse $N_{\text{ch}}(t)$ as follows.

The integral of $N_{\text{ch}}(t)$ per incoming photon, that is, the total number of core holes per photon present at each moment in time is proportional to τ_{lt} . The longer the lifetime, the more core holes are present, because they have not yet decayed. The second central moment of $N_{\text{ch}}(t)$ for temporal Gaussian pulses is $\tau_{\text{lt}}^2 + \tau_{\text{pl}}^2$ with the pulse length τ_{pl} . The width of this function is approximated by the square root of the second moment. The constant function that yields the same integral over time (τ_{lt}), and is zero outside a window as large as the square root of the second moment of $N_{\text{ch}}(t)$, is thus given by:

$$T = \frac{\tau_{\text{lt}}}{\sqrt{\tau_{\text{lt}}^2 + \tau_{\text{pl}}^2}} = \frac{1}{\sqrt{1 + \frac{\tau_{\text{pl}}^2}{\tau_{\text{lt}}^2}}}$$

This expression also accounts for the lowering of the number of core holes through spontaneous decay, because the decays are included in the core-hole lifetime.

The instantaneous core-hole density without stimulation is taken to be constant; only stimulation is taken to annihilate core holes. The number of total stimulated photons is taken to be K times bigger than observed (accounting for angular dependences and the finite detector acceptance and efficiency). The instantaneous core-hole density ρ_{ch} for the differential equation is thus given by:

$$\rho_{\text{ch}} = p(N_{\text{in}} - KN_{\text{stim,obs}})$$

$$p = \frac{4T}{\pi wh\lambda}$$

The number of stimulating photons. The number of stimulating photons in the observation direction has been termed N_{obs} . This value is given by the sum of the spontaneously emitted photons in the observation direction and the stimulated photons in the observation direction $N_{\text{stim,obs}}$. We introduce the acceptance and detection efficiency A of our spectrometer, weighted with the possible angular distributions of the spontaneous emission.

The total number of photons that are spontaneously emitted in the observed direction increases across the interaction region, starting from zero at the far end of the observed volume to the number of incoming photons N_{in} times the fluorescence yield ω_{fy} and the acceptance ($A\omega_{\text{fy}}N_{\text{in}}$). We approximate this increase with a constant across the interaction region. We take half the maximal value to yield the correct average value for a linear increase. This approximation ensures integrability and neglects the aspects around the temporal evolution, travel times of photons inside the interaction region and so on.

Given that stimulated emission annihilates core holes (and K times more stimulated photons are emitted than are observed because of the finite acceptance of the detector), the number of spontaneously emitted photons is reduced with higher stimulation. We thus introduce the source term for stimulated emission as:

$$N_{\text{obs}} = q(N_{\text{in}} - KN_{\text{stim,obs}}) + N_{\text{stim,obs}}$$

$$q = \frac{1}{2}A\omega_{\text{fy}}$$

The full source term should in principle also reflect the spatial growth of the seeding spontaneous emission across the interaction region, which would lead to a slightly different nonlinearity in the stimulated emission signal, especially for low photon numbers. In reality, this effect is more than compensated by the bigger effect of the temporal mismatch of the seeding spontaneous emission (for near-normal impinging irradiation, the seed appears at the same time across the whole interaction region in a time window of around $\sqrt{\tau_{\text{lt}}^2 + \tau_{\text{pl}}^2} \approx 35$ fs (see above), whereas the travel time of the stimulated field across the 50-µm-long interaction region is already around 170 fs.) This can only be overcome by using a different geometry, as proposed in the main text.

The full differential equation. In the differential equation for the growth of stimulated emission along the interaction region, we also treat the reabsorption of emitted photons explicitly, with reabsorption length L . With the above introduced abbreviations, we thus solve:

$$\frac{dN_{\text{stim,obs}}}{dx} = (qN_{\text{in}} + (1 - qK)N_{\text{stim,obs}})(pN_{\text{in}} - pKN_{\text{stim,obs}})\sigma_{\text{stim}} - \frac{N_{\text{stim,obs}}}{L}$$

with $N_{\text{stim,obs}}(x=0) \stackrel{!}{=} 0$

To get the total number of photons measured by the detector $N_{\text{tot,obs}}$, we must add the spontaneous emission, including the reduction through stimulated emission and the reabsorption along the interaction length x , which is $\exp(-x/L)$:

$$N_{\text{tot,obs}} = 2qe^{(-x/L)}(N_{\text{in}} - KN_{\text{stim,obs}}) + N_{\text{stim,obs}}$$

The solution and its limits. In the solution of the differential equation further combinations of parameters appear. $X = x/L$ is the ratio between the actual interaction length and the reabsorption length. This number is given by the experimental geometry and can thus be derived from tabulated values. $\Phi = pL\sigma_{\text{stim}}$, a dimensionless number that relates the excited volume p^{-1} to a stimulation volume $L\sigma_{\text{stim}}$. The inverse value of Φ is connected to the number of photons that is needed to observe the nonlinear increase in signal due to stimulated emission.

The full solution thus reads:

$$N_{\text{tot,obs}} = 2e^{-X}qN_{\text{in}} + \frac{1}{2K\Phi(qK-1)}(1-2e^{-X}qK) \\ \left\{ \left(1 + \Phi N_{\text{in}}(2qK-1) - \sqrt{1 + \Phi N_{\text{in}}(\Phi N_{\text{in}} + 4qK - 2)} \right) \right. \\ \left. \tanh \left[\frac{\sqrt{1 + \Phi N_{\text{in}}(\Phi N_{\text{in}} + 4qK - 2)}X}{2} \right] + \right. \\ \left. \left. \operatorname{arctanh} \left(\frac{1 + \Phi N_{\text{in}}(2qK-1)}{\sqrt{1 + \Phi N_{\text{in}}(\Phi N_{\text{in}} + 4qK - 2)}} \right) \right] \right\}$$

For small incoming photon numbers, the signal is proportional to the number of incoming photons, with purely spontaneous emission (with reabsorption) as linear limit:

$$N_{\text{tot,obs}} \xrightarrow{N_{\text{in}} \rightarrow 0} 2e^{-X}qN_{\text{in}} = e^{-X}A\omega_{\text{fy}}N_{\text{in}}$$

For very high numbers of incoming photons, the tanh in the formula nears unity and we obtain the following expression for the number of observed photons:

$$N_{\text{obs}} \xrightarrow{N_{\text{in}} \rightarrow \infty} \frac{1}{K}N_{\text{in}}$$

This expression relates the saturation of stimulated emission to the geometry-dependent K factor that describes how much more stimulated emission happens in other directions than observed. Because stimulated emission is a highly nonlinear effect, this factor can vary largely, depending on the shape of the interaction region and how the observation direction is oriented relatively.

In our time-independent constant average discussion, the saturation of stimulated emission means a complete suppression of the Auger channel. In reality, Auger processes will still take place during the less intense beginning of the pulse, at the edges of the irradiated volume, as well as when the excited volume and the stimulated photons lose temporal overlap. Nevertheless, these contributions take out a constant fraction of the temporal and spatial evolution of stimulated emission and are thus linearly dependent on N_{in} . Therefore, the convergence to a linear dependence is not altered.

Fitting the model to the experimental data. We fit the obtained solution of the differential equation for $N_{\text{tot,obs}}$ to the observed dependence of the signal on the incoming photon numbers recorded with the spectrometer as shown in Fig. 2a and b. We determine the interaction length x from the experimental geometry: with the incoming beam at 80° to the surface, the observation direction at 15° to the surface and an absorption length of the exciting radiation of 45 nm (ref. 31), we estimate

an interaction length of 171 nm and obtain $X = 0.285$ with reabsorption length $L = 600$ nm (ref. 31). The parameters q , K and Φ are then fitted to the data. We obtain $q = (2.6 \times 10^{-11}) \pm (0.3 \times 10^{-11})$, $K = (1.100 \times 10^{10}) \pm (0.003 \times 10^{10})$ and $\Phi = (3.1 \times 10^{-11}) \pm (0.3 \times 10^{-11})$. The fitting error is given as one standard deviation.

Although we did not record many data points at very low intensities, the extrapolation of our data towards zero incoming photons can readily be done (Fig. 2b). Besides the reabsorption factor e^{-X} this value directly yields the parameter q with a rather small error. The fitted value agrees well with our expectations and can be decomposed into the fluorescence yield⁸ ($\omega_{\text{fy}} = 3.8 \times 10^{-4}$), the angular acceptance of our spectrometer³⁰ of around 10^{-5} and the grating and detection efficiency³² of 7×10^{-3} .

The saturation limit $1/K$ of the signal is close to the value of q . Owing to the good data quality at higher photon numbers, we find a very small fitting error. The value of K signifies that many more stimulated photons are emitted in other directions than what we observe with our spectrometer. This finding is corroborated by our angle-dependent study and can be further optimized by choosing different geometries, as described in the main text.

The fitting parameter Φ is the main unknown in this study and accounts for the theoretical approximations as well as uncertainties in determining experimental parameters and further unconsidered nonlinear effects. We decompose Φ into the factors $P = 7.5 \times 10^{15} \text{ m}^{-3}$ given through the experimental parameters (focal width and height 45 μm , absorption length³¹ 45 nm, pulse length²⁷ 30 fs and the core-hole lifetime³³ of 19 fs), the reabsorption length³¹ of 600 nm and the stimulation cross-section σ_{stim} . For σ_{stim} , we thus obtain a value of $6.9 \times 10^{-21} \text{ m}^2$ which is about a factor of 25 bigger than the absorption cross-section. We have indications from rough calculations that the overlap between valence band and core states is actually about a factor of 2–3 bigger than for conduction band and core states, which leads to a larger stimulation cross-section than absorption cross-section. The remaining order of magnitude can be explained through the nonlinearity of the effect. This will nonlinearly enhance the signal from regions with higher excitation density, so that the effective focal size, excitation depth and duration are actually shorter than estimated. Therefore, we conclude that the fitted parameters agree reasonably well with our expectations.

31. Henke, B. L., Gullikson, E. M. & Davis, J. C. X-ray interactions: photoabsorption, scattering, transmission, and reflection at $E=50\text{--}30,000$ eV, $Z=1\text{--}92$. *Atom. Data Nucl. Data Tab.* **54**, 181–342 (1993).
32. Kunnus, K. *et al.* A setup for resonant inelastic soft x-ray scattering on liquids at free electron laser light sources. *Rev. Sci. Instrum.* **83**, 123109 (2012).
33. Hricovini, K. *et al.* Electronic structure and its dependence on local order for H/Si(111)-(1 \times 1) surfaces. *Phys. Rev. Lett.* **70**, 1992–1995 (1993).

Stereoinversion of tertiary alcohols to tertiary-alkyl isonitriles and amines

Sergey V. Pronin¹, Christopher A. Reiher¹ & Ryan A. Shenvi¹

The S_N2 reaction (bimolecular nucleophilic substitution) is a well-known chemical transformation that can be used to join two smaller molecules together into a larger molecule or to exchange one functional group for another. The S_N2 reaction proceeds in a very predictable manner: substitution occurs with inversion of stereochemistry, resulting from the ‘backside attack’ of the electrophilic carbon by the nucleophile. A significant limitation of the S_N2 reaction is its intolerance for tertiary carbon atoms: whereas primary and secondary alcohols are viable precursor substrates, tertiary alcohols and their derivatives usually either fail to react or produce stereochemical mixtures of products^{1–3}. Here we report the stereochemical inversion of chiral tertiary alcohols with a nitrogenous nucleophile facilitated by a Lewis-acid-catalysed solvolysis. The method is chemoselective against secondary and primary alcohols, thereby complementing the selectivity of the S_N2 reaction. Furthermore, this method for carbon–nitrogen bond formation mimics a putative biosynthetic step in the synthesis of marine terpenoids⁴ and enables their preparation from the corresponding terrestrial terpenes. We expect that the general attributes of the methodology will allow chiral tertiary alcohols to be considered viable substrates for stereoinversion reactions.

The incorporation of nitrogen during secondary metabolite biosynthesis occurs almost exclusively through the chemistry of carbonyls and imines: reductive amination, Mannich reactions and transamination⁵. The ability to mimic these biosynthetic pathways by chemical synthesis has vastly simplified the production of complex alkaloids. However, many alkaloids produced in marine environments do not adhere to the established biosynthetic patterns of terrestrial organisms (see Fig. 1a). For example, the nitrogen atoms in the terpenoid metabolites **1–6** derive from inorganic cyanide by means of reactions that are not well characterized but certainly do not involve carbonyl or imine substrates. These reactions may involve the attack of high energy, unstabilized carbocations by cyanide or a nucleophile derived from cyanide (Fig. 1b)⁴. Indeed, the primary products of these pathways are isonitriles⁶.

Mimicry of this proposed biosynthetic transformation is challenging because, apart from substrate control⁷, intermolecular attack of unstabilized carbocations by cyanide or organonitriles is non-stereoselective. Furthermore, the high acidity of protons adjacent to carbocations facilitates E1 (unimolecular) elimination with most counteranions⁸, which can erase adjacent stereogenic centres. Therefore, even if reprotonation of the nascent alkene is possible with Brønsted acid, regioisomers and further stereoisomers can result.

Here we demonstrate a chemoselective and stereoselective method for incorporating cyanide into terpenoid frameworks by the stereoinversion of tertiary alcohols. This method is uniquely competent to generate in concise synthetic sequences the primary pharmacophores of isocyanoterpenes⁹, some of which have shown potent antimalarial activity¹⁰. The method is also generally useful for the conversion of alcohols to amines and is chemoselective for tertiary alcohol displacement in preference to secondary or primary alcohols. Previous approaches to the synthesis of terpenoids exemplified by Fig. 1 have relied on either abiotic strategies for formation of the C–N bond¹¹ or biomimetic reactions

of nitriles with carbocations that rely on stereocontrol imparted by a cyclic scaffold¹². This latter strategy has proved to be capricious, because many terpenoid cations lead to isomeric mixtures or non-natural stereoisomers on capturing nitriles^{13–15}. Previous studies did, however, establish the idea of using a Lewis acidic reagent to ionize a tertiary leaving group in the presence of trimethylsilyl cyanide (TMSCN) as a competent nucleophile and isonitrile precursor. For instance, tertiary halides will react with TMSCN in the presence of $TiCl_4$ to produce isonitriles¹⁶. Similar reactions have simplified the synthesis of a marine bisonitrile; however, the late-stage isocyanation resulted in a near equimolar mixture of four stereoisomers¹³. Subsequently the ionization of tertiary alcohols with superstoichiometric zinc halides in the presence of TMSCN was developed¹⁷. However, this latter method is neither stereoselective nor chemoselective and results in indiscriminate isocyanation, elimination and isomerization of, for example, α -bisabolol **10** (Fig. 2a). A stereocontrolled Mitsunobu isocyanation of tertiary alcohols was also reported¹⁸, but in our hands this reaction could not be successfully applied to the isocyanoterpenes⁹.

We believed that a stereocontrolled displacement of alcohols or esters could be effected if TMSCN were used in excess and could therefore stereoselectively trap the nascent cation at the contact ion-pair stage^{1,20}.

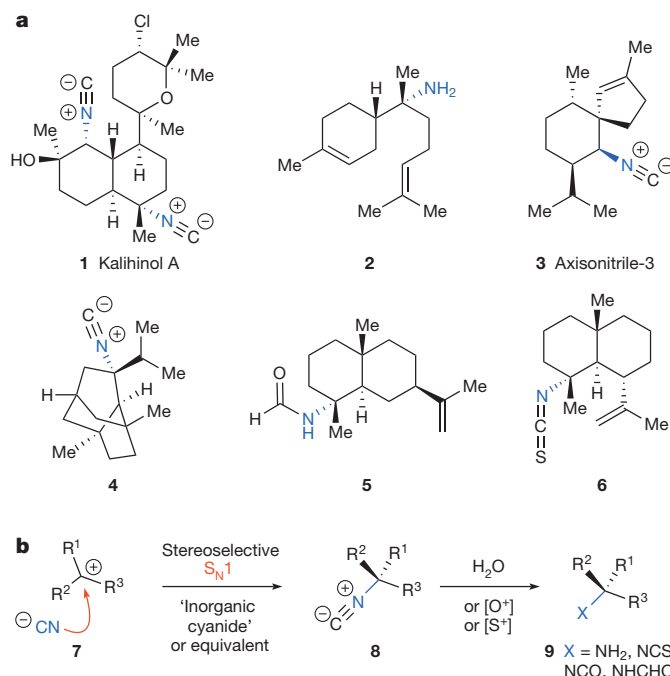


Figure 1 | Nitrogenous marine terpenoids derived from inorganic cyanide. **a**, A subfamily of marine terpenoids represented by **1–6** are decorated with nitrogen atoms in a different pattern from that observed in most terrestrially derived metabolites. **b**, From isotope-feeding studies the hypothetical biosynthetic path (**7**→**8**→**9**) common to **1–6** is known to incorporate inorganic cyanide and is proposed to involve unstabilized carbocations as biosynthetic intermediates.

¹Department of Chemistry, The Scripps Research Institute, 10550 North Torrey Pines Road, La Jolla, California 92037, USA.

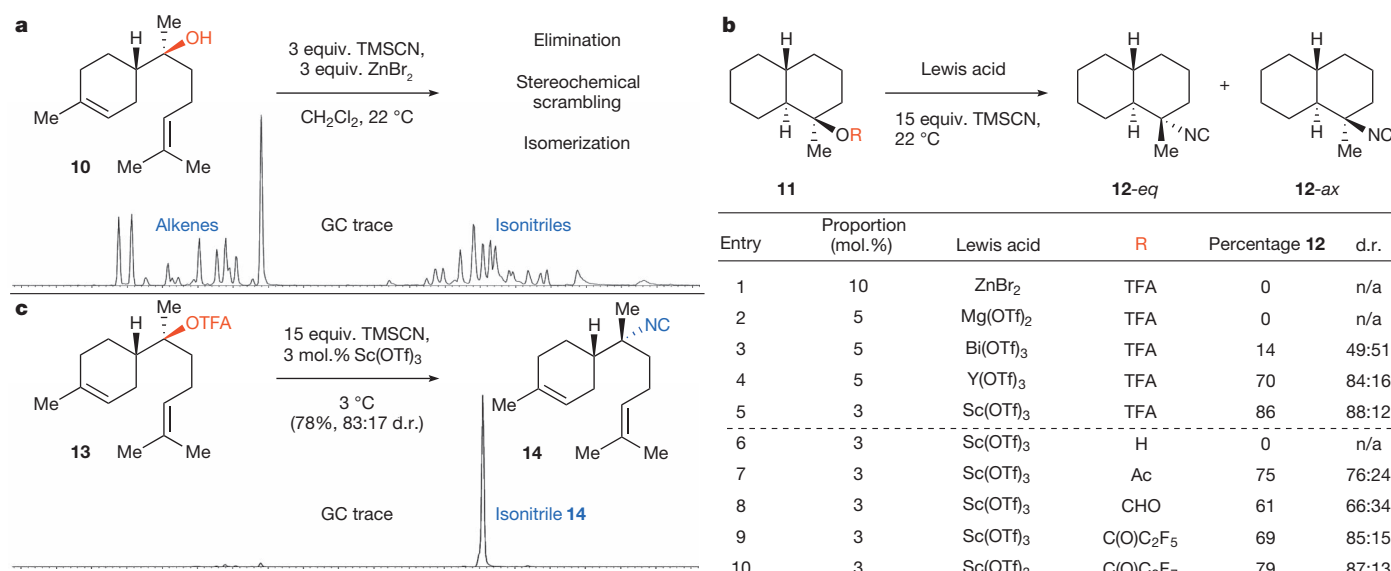


Figure 2 | Development of a stereoselective Ritter-type reaction through tertiary alcohol inversion. **a**, Prior state-of-the-art isocyanation of tertiary alcohols applied to α -bisabolol **10** produces complex mixtures. GC, gas chromatography. **b**, Optimization studies identify $\text{Sc}(\text{OTf})_3$ as an optimal

Lewis acid and fluoroesters as optimal substrates for stereoinverting isocyanation. Eq, equatorial; ax, axial; d.r., diastereomeric ratio; n/a, not applicable. **c**, Application of this method to bisabolyl trifluoroacetate **13** provides isonitrile **14** cleanly and with high stereoselectivity.

The challenge of this approach lies in the competitive equilibria of Lewis acid-catalysed solvolysis. First, the Lewis-basic TMSCN and the Lewis-basic leaving group compete for association with the requisite Lewis acid. In the extreme case of solvolysis, the Lewis acid might be coordinatively saturated with non-labile solvent and rendered unreactive. Second, the counteranion that is necessary for steric and/or electronic shielding of one face of the carbocation can undergo equilibrium displacement with TMSCN²⁰, which would result in a stereoisomeric mixture of solvolysis products. Unfortunately, whereas chiral tertiary chlorides²¹ are viable substrates for solvolysis in alkaline methanol¹, tertiary esters are known to undergo almost complete racemization in acid².

Indeed, attempted solvolysis in TMSCN with zinc and magnesium Lewis acids fails to consume any decalyl trifluoroacetate **11** (Fig. 2b, entries 1 and 2; see also Supplementary Information for a complete list of Lewis acids screened). Bismuth triflate (entry 3) shows slow conversion of **11** to decalyl isonitriles, but as an equimolar mixture of equatorial and axial stereoisomers. However, we found that early transition metal triflates (entries 4 and 5) yield a high ratio of diastereomers favouring stereoinversion (**12**). Scandium(III) trifluoromethanesulphonate (scandium(III) triflate; $\text{Sc}(\text{OTf})_3$) catalyses²² solvolysis much more rapidly than $\text{Y}(\text{OTf})_3$, possibly as a result of its high rate of ligand exchange²³, it therefore can be conveniently run at catalyst loadings as low as 3 mol%. The solvolysis was found to be ineffective with alcohols, and to be less stereoselective with acetyl and formyl esters, although the reaction rate for these latter substrates was much higher than for the trifluoroacetate. Given this trend, we expected selectivity to increase with greater fluorination of the leaving group. For **11**, the results are roughly equivalent (entries 9 and 10), although linear substrates show improved selectivity when the leaving group is a longer-chain perfluoroalkanoate (see below).

The optimal conditions for the solvolysis of decalin **11** were found to be generally applicable to stereogenic tertiary trifluoroacetates, and as a result **13** can be cleanly converted to isonitrile **14**, which is the enantiomer of a naturally occurring marine terpenoid (Fig. 2c)⁴.

The generality, functional group tolerance and utility of this solvolysis reaction are illustrated by Fig. 3. When a tertiary alcohol is the sole stereocentre in a molecule, the percentage inversion of **15**, for instance, is 90%, accounting for enantiomeric purity of the alcohol. It should be noted that acyclic perfluorobutyrate showed slightly higher stereoselectivity in solvolysis (at -5°C with 10% (v/v) CH_2Cl_2) than the

corresponding trifluoroacetates: **14** (diastereomeric ratio 85:15) and **15** (enantiomeric ratio 87:13, corresponding to 93% inversion). Proximal unsaturation (for example **16**) has little or no effect on stereoselectivity. The diastereomeric ratio of isonitriles **17** is almost identical to the percentage inversion of **15**, and so the distal stereocentre seems to have essentially no influence but serves as a useful stereochemical probe. Lewis basic groups such as esters (**16**) and nitriles (**17**) are tolerated but tend to decrease reaction rates; so catalyst loading was therefore increased to 6 mol%. Not surprisingly, alkynes **20** are tolerated, as are primary alcohols **21**, which are also subjected to solvolysis conditions as their corresponding trifluoroacetates but do not ionize.

Naturally occurring marine terpenes are easily accessible with this method (also see Fig. 4). For instance, isocyanocadinene⁴ **22** is synthesized in two steps from its terrestrial counterpart, cedrelanol (seven steps from commercial material), whereas **22** was previously prepared in 29 steps²⁴. Additionally, *trans*-androsterone can be elaborated to the corresponding tris-trifluoroacetate (see Supplementary Information), which on solvolysis selectively produces isonitrile **23** with excellent stereoselectivity and chemoselectivity. This stereoinversion reaction shows the same stereochemical preference as an $\text{S}_{\text{N}}2$ reaction, but with reverse substitution demands. Tocopherol-derived quinone **24** can be accessed with high diastereoselectivity, obviously independently of its two other stereocentres. The monoisonitrile **25** and bisisonitrile **26** can be derived from dihydrosclareol by means of one and two stereoinversions, in which selectivity presumably reflects the different heterolytic stabilities of the two trifluoroacetates.

This procedure enables the stereoinversion of tertiary alcohols to the corresponding tertiary-alkyl amines and their derivatives (Fig. 4). For instance, 1.11 g of α -bisabolol (**10**) can be trifluoroacetylated and solvolysed to isonitrile **14**, which in turn can be hydrolysed to 1.10 g of amine **2**, which was isolated as a 5:1 ratio of diastereomers. The enantiomer of **27** was previously synthesized in nine steps (19 mg)²⁵. Simple hydrolysis also converts androsterone-derived isonitrile **23** into amine **30**, and quinone **24** into aza-tocopherol **31** (after reduction of the intermediate iminoquinone). Naturally occurring cadinenes **28** and **29** (ref. 4) are simple to access from **22** by means of hydrolysis or sulphurization (see Supplementary Information).

This isocyanation is of course not without limitation (Fig. 5). Highly branched tertiary alcohols (**31–33**) generally give poor diastereoselectivity, probably because of an encumbered approach of the nucleophile.

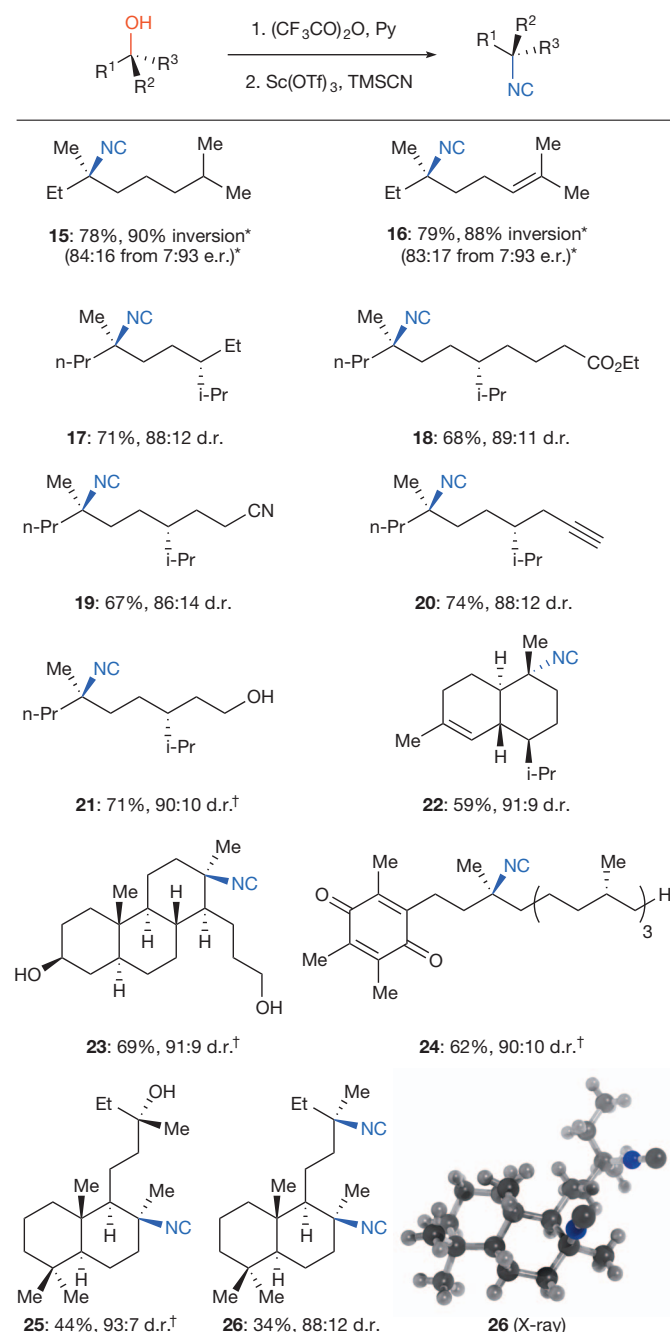


Figure 3 | Probing the selectivity and functional group tolerance of isocyanation. Py, pyridine; e.r., enantiomeric ratio; d.r., diastereomeric ratio. *Determined by Mosher analysis. †After treatment with methanol and triethylamine.

Furthermore, we discovered early on that cyclohexanols are problematic substrates. Whereas equatorial trifluoroacetate **34** is solvolysed to the axial isocyanide **36** with high stereoselectivity, the displacement of axial trifluoroacetate **35** is slower and poorly diastereoselective, and actually favours stereoretention. We suspect that this low stereoselectivity is due to the imperfection of the 4-*t*-butyl conformational 'lock'²⁶ that allows enough torsional mobility for ionization at the 1 position to proceed preferentially through a twist-boat conformer²⁷. The exact relationship between torsional freedom and stereoselection is not clear, but nevertheless the more rigid decalins **37** and **11** do not suffer from the same promiscuity. It remains unclear whether C–N bond formation occurs at the contact ion pairs of equatorial esters **34** and **37**, because solvent-separated cations of **34** and **37** yield the same axial isocyanide

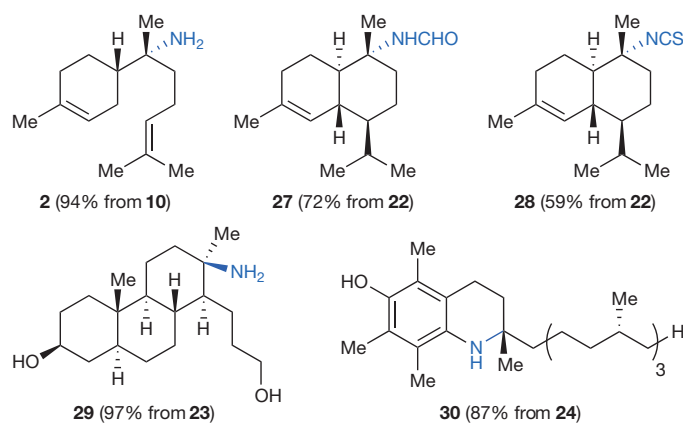


Figure 4 | Amines, amides and isothiocyanates synthesized from the corresponding isocyanides. Chemoselective and stereoselective isocyanation allows access to a variety of marine metabolites and allows terrestrial terpenoids to be converted to their theoretical marine counterparts.

products⁹. Nevertheless, we are optimistic that these solvolysis conditions may help to shed light on the still obscure stereoelectronic basis for stereoselective addition to cyclohexyl cations²⁸.

A detailed mechanistic picture of the solvolysis (for example, **13**→**14**) is not yet available, but a general sketch (Fig. 6) and relevant observations are worth discussion. Because $\text{Sc}(\text{OTf})_3$ is a strong Lewis acid, we suspect that it becomes coordinatively saturated (**A**) on addition to TMSCN, and we observe that it dissolves completely. By analogy with the high rate constant for inner-sphere water ligand exchange of $\text{Sc}(\text{OTf})_3$ observed previously²³, we suspect that **A** rapidly exchanges a TMSCN ligand for ester **B** to provide activated substrate **C**. Two reactions are then available to **C**: either $\text{S}_{\text{N}}2$ or $\text{S}_{\text{N}}1$ displacement (path

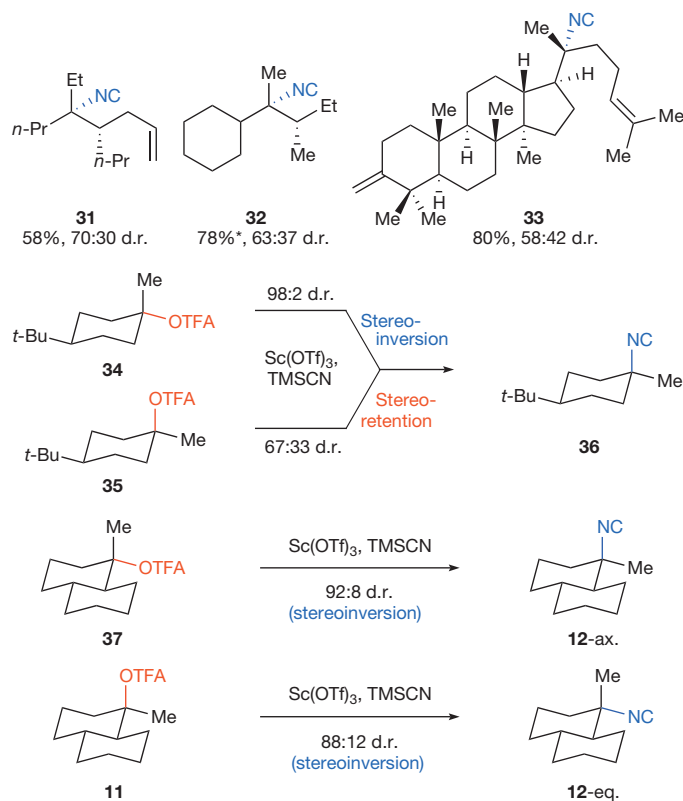


Figure 5 | Limitations of tertiary alcohol stereoinversion. Highly branched substrates provide lower diastereomeric ratios of isocyanides, as do conformationally flexible cyclohexanol derivatives. OTFA, trifluoroacetate. *Isolated along with regioisomeric isocyanides.

1 or path 2). It is possible that departure of the ester and attack by TMSCN occur concurrently (path 1), in which the nucleophile stabilizes the developing positive charge by means of nascent bond formation (**D**), but this occurrence is rare³ and has been ruled out in related solvolysis reactions¹⁹. An alternative possibility is that ionization of **C** occurs (path 2) to provide contact ion pair **E**, and TMSCN approaches the planar carbocation opposite the large and electron-rich counteranion to provide stereochemically inverted isonitrile **8** after silyl transfer to the trifluoroacetate. If instead of attack **E** undergoes ion dissociation to solvated cation **F** (path 3), then attack of **F** from either face would provide the stereochemically scrambled isonitrile **rac-8**. Thus, the stereochemical ratio of product isonitriles should depend on the relative rates of attack (**E**→**8**) versus anion–solvent exchange (**E**→**F**), and two observations are worth noting. First, the identity of the ester ($R = H, CH_3, CF_3, C_3F_7$) affects the stereochemical outcome, but the contribution of these esters to the relative rates of attack versus anion–solvent exchange is unclear. Transient interactions between the fluorines on the perfluoroalkanoates and the carbocation²⁹, or differential distribution of charge between the alkanoate and metal centre³⁰, could explain this trend. The overall reaction rates of acetates are higher than those of trifluoroacetates, but the inverse relationship of reaction rate and stereochemical outcome may be coincidental. Second, the percentage inversion of trifluoroacetyl ester **13** to isonitrile **14** was found to be inversely proportional to temperature: 79:21 at 22 °C, compared with 83:17 at 3 °C. Given these trends, further investigation is necessary to provide a clear mechanistic picture; however, three control experiments were also performed in support of Fig. 6. Replacement of $Sc(OTf)_3$ with trimethylsilyl triflate (TMSOTf) under otherwise identical conditions did not

promote any reaction of trifluoroacetyl esters, which excludes electrophilic silicon as the active Lewis acid. Addition of 2,6-di-*t*-butylpyridine (3:1 with catalyst) did not inhibit product formation, which excludes Brønsted acid catalysis, although increased amounts of elimination were observed. Finally, addition of stoichiometric trimethylsilyl trifluoroacetate ($TMSO_2CCF_3$) did not affect the rate or stereoselectivity of the reaction, which indicates no participation of the product acetate in stereochemical scrambling. We are working to expand this methodology to include other nucleophiles, but preliminary data suggest that the current reaction cannot be directly applied to different reactants, and in fact is surprising in its uniqueness. For instance, in acetonitrile or trimethylsilylacetonitrile, the perfluoroalkanoates do not react at all, whereas trimethylsilylazide and trimethylsilylisothiocyanate solvents produce complex mixtures.

Here we have developed a method for the stereoselective conversion of tertiary alcohols to tertiary-alkyl amines, which fills a major methodological gap in organic chemistry. The reaction entails a Lewis-acid-catalysed solvolysis of tertiary alcohol derivatives, a conceptual advance that may enable the expansion of this chemistry to related systems. The reaction proceeds with inversion of configuration by means of an isonitrile and works best on minimally branched linear tertiary alcohols, and conformationally inflexible alicyclic alcohols. The reaction is chemoselective for tertiary-trifluoroacetyl esters in preference to secondary or primary ones, which do not react even on prolonged exposure to the solvolysis conditions. This reactivity complements standard stereoinversion (S_N2) reactions, which favour secondary and primary substrates, whereas most tertiary substrates fail. In addition, this method converts readily available terrestrial terpenoid alcohols into their marine counterparts, which should greatly facilitate the preparation of these fascinating and potentially useful molecules. It is possible that the same overall transformation is used in biosynthetic pathways. This reaction adds a new retrosynthetic manoeuvre to the cache of transforms available to organic chemistry. We expect that the general attributes of this reaction will lead to the development of other stereoinversion reactions of tertiary alcohols and stimulate further advances in carbocation chemistry.

METHODS SUMMARY

A solution of trifluoroacetate **13** (32.0 mg, 0.1 mmol) in TMSCN (0.1 ml) was cooled to 0 °C and treated with a solution of anhydrous $Sc(OTf)_3$ (1.5 mg, 0.003 mmol) in TMSCN (0.1 ml). The reaction mixture was left for 18 h at 3 °C and quenched with tetramethylethylenediamine (7.5 µl, 0.05 mmol). The resulting solution was concentrated under reduced pressure, and the residue was purified by flash column chromatography on silica gel (elution with 35% dichloromethane in hexanes) to deliver 18.0 mg (78% yield) of 7-isocyano-7,8-dihydro- α -bisabolene (**14**). See the notes in Supplementary Information regarding safety.

Received 14 March; accepted 16 July 2013.

- Hughes, E. D., Ingold, C. K., Martin, R. J. L. & Meigh, D. F. Walden inversion and reaction mechanism: Walden inversion in unimolecular reactions of secondary and tertiary alkyl halides. *Nature* **166**, 679–680 (1950).
- Bunton, C. A., Hughes, E. D., Ingold, C. K. & Meigh, D. F. Walden inversion and reaction mechanism: Walden inversion in the acid hydrolysis of carboxylic esters by unimolecular alkyl fission. *Nature* **166**, 680 (1950).
- Mascal, M., Hafezi, N. & Toney, M. D. 1,4,7-Trimethyloxatriquinane: S_N2 reaction at tertiary carbon. *J. Am. Chem. Soc.* **132**, 10662–10664 (2010).
- Garson, M. J. & Simpson, J. S. Marine isocyanides and related natural products—structure, biosynthesis and ecology. *Nat. Prod. Rep.* **21**, 164–179 (2004).
- Dewick, P. M. *Medicinal Natural Products: A Biosynthetic Approach* (Wiley, 2009).
- Hagadone, M. R. & Scheuer, P. J. On the origin of the isocyano function in marine sponges. *J. Am. Chem. Soc.* **106**, 2447–2449 (1984).
- Rubenbauer, P. & Bach, T. Diastereoselective Ritter reactions of chiral secondary benzylic alcohols. *Chem. Commun. (Camb.)* 2130–2132 (2009).
- Pronin, S. V. & Shenvi, R. A. Synthesis of highly strained terpenes by nonstop tail-to-head polycyclization. *Nat. Chem.* **4**, 915–920 (2012).
- Pronin, S. V. & Shenvi, R. A. Synthesis of a potent antimalarial amphilectene. *J. Am. Chem. Soc.* **134**, 19604–19606 (2012).
- Miyaoka, H., Shimomura, M., Kimura, H. & Yamada, Y. Antimalarial activity of kalihinol A and new relative diterpenoids from the Okinawan sponge, *Acanthella* sp. *Tetrahedron* **54**, 13467–13474 (1998).
- White, R. D., Keaney, G. F., Slown, C. D. & Wood, J. L. Total synthesis of (\pm)-kalihinol C. *Org. Lett.* **6**, 1123–1126 (2004).

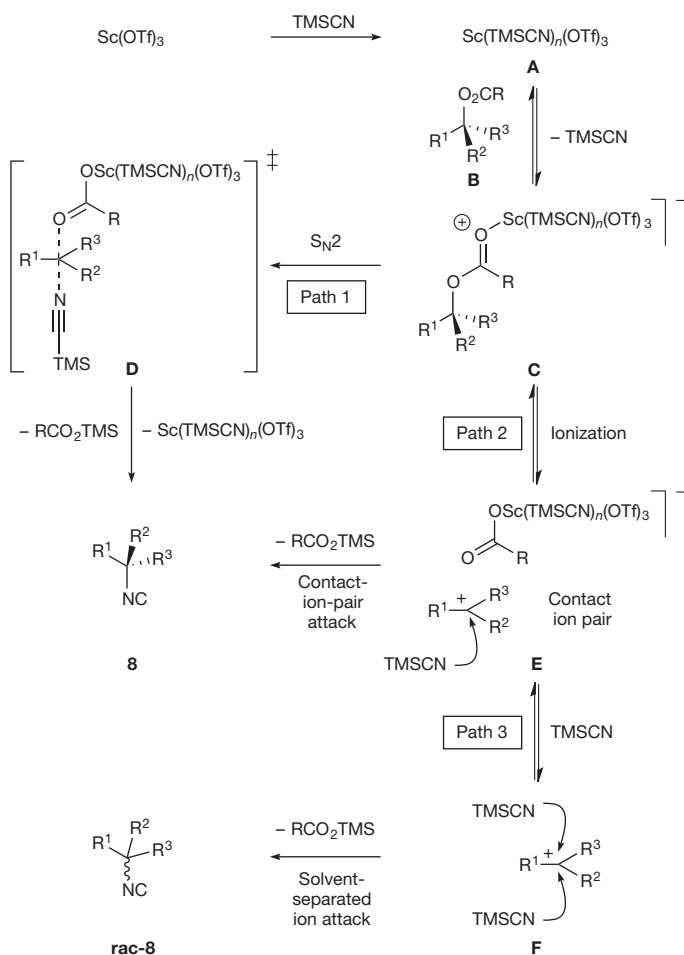


Figure 6 | Possible reaction pathways. A sketch of mechanistic possibilities according to experimental observation.

12. Srikrishna, A., Ravi, G. & Subbaiah, D. R. C. V. Enantioselective first total syntheses of 2-(formylamino)trachyopsane and ent-2-(isocyano)trachyopsane via a biomimetic approach. *Synlett* 32–34 (2009).
13. Corey, E. J. & Magriotis, P. A. Total synthesis and absolute configuration of 7,20-diisocyanoadociane. *J. Am. Chem. Soc.* **109**, 287–289 (1987).
14. Castellanos, L., Duque, C., Rodríguez, J. & Jiménez, C. Stereoselective synthesis of (–)-4-epiaxinysamine. *Tetrahedron* **63**, 1544–1552 (2007).
15. Kitano, Y. *et al.* Synthesis and antifouling activity of 3-isocyanothreonellin and its analogues. *J. Chem. Soc. Perkin Trans. 1* 2251–2255 (2002).
16. Sasaki, T., Nakanishi, A. & Ohno, M. Synthesis of adamantane derivatives. 56. Reaction of 1-adamantyl chloride with trimethylsilyl pseudohalide. *J. Org. Chem.* **46**, 5445–5447 (1981).
17. Kitano, Y., Chiba, K. & Tada, M. A direct conversion of alcohols to isocyanides. *Tetrahedr. Lett.* **39**, 1911–1912 (1998).
18. Masutani, K., Minowa, T., Hagiwara, Y. & Mukaiyama, T. Cyanation of alcohols with diethyl cyanophosphonate and 2,6-dimethyl-1,4-benzoquinone by a new type of oxidation–reduction condensation. *Bull. Chem. Soc. Jpn.* **79**, 1106–1117 (2006).
19. Richard, J. P., Toteva, M. M. & Amyes, T. L. What is the stabilizing interaction with nucleophilic solvents in the transition state for solvolysis of tertiary derivatives: nucleophilic solvent participation or nucleophilic solvation? *Org. Lett.* **3**, 2225–2228 (2001).
20. Winstein, S., Clippinger, E., Fainberg, A. H., Heck, R. & Robinson, G. C. Salt effects and ion pairs in solvolysis and related reactions. III. 1. Common ion rate depression and exchange of anions during acetolysis. *J. Am. Chem. Soc.* **78**, 328–335 (1956).
21. Stevens, P. G. & McNiven, N. L. Halogenation of optically active tertiary carbinols. *J. Am. Chem. Soc.* **61**, 1295–1296 (1939).
22. Kobayashi, S., Hachiya, I., Araki, M. & Ishitani, H. Scandium trifluoromethanesulfonate (Sc(OTf)₃). A novel reusable catalyst in the Diels–Alder reaction. *Tetrahedr. Lett.* **34**, 3755–3758 (1993).
23. Kobayashi, S., Nagayama, S. & Busujima, T. Lewis acid catalysts stable in water. Correlation between catalytic activity in water and hydrolysis constants and exchange rate constants for substitution of inner-sphere water ligands. *J. Am. Chem. Soc.* **120**, 8287–8288 (1998).
24. Nishikawa, K. *et al.* Total synthesis of 10-isocyano-4-cadinene and determination of its absolute configuration. *Org. Lett.* **12**, 904–907 (2010).
25. Kochi, T. & Ellman, J. A. Asymmetric α -alkylation of *N*′-tert-butanefulfonyl amidines. Application to the total synthesis of (6*R*,7*S*)-7-amino-7,8-dihydro- α -bisabolene. *J. Am. Chem. Soc.* **126**, 15652–15653 (2004).
26. Winstein, S. & Holness, N. J. Neighboring carbon and hydrogen. XIX. *t*-Butylcyclohexyl derivatives. Quantitative conformational analysis. *J. Am. Chem. Soc.* **77**, 5562–5578 (1955).
27. Shiner, V. J., Jr & Jewett, J. G. The transition state in acetolysis of cyclohexyl tosylate. *J. Am. Chem. Soc.* **87**, 1384–1385 (1965).
28. Rauk, A., Sorensen, T. S. & Schleyer, P. V. Tertiary cyclohexyl cations. Definitive evidence for the existence of isomeric structures (hyperconjugomers). *J. Chem. Soc., Perkin Trans. 2* **6**, 869–874 (2001).
29. Ferraris, D., Cox, C., Anand, R. & Lectka, T. C–F bond activation by aryl carbocations: conclusive intramolecular fluoride shifts between carbon atoms in solution and the first examples of intermolecular fluoride ion abstractions. *J. Am. Chem. Soc.* **119**, 4319–4320 (1997).
30. Lanza, G., Fraga, I. L. & Marks, T. J. Ligand substituent, anion, and solvation effects on ion pair structure, thermodynamic stability, and structural mobility in ‘constrained geometry’ olefin polymerization catalysts: an ab initio quantum chemical investigation. *J. Am. Chem. Soc.* **122**, 12764–12777 (2000).

Supplementary Information is available in the online version of the paper.

Acknowledgements We thank C. Moore and A. L. Rheingold for X-ray crystallographic analysis. We thank the Yu laboratory for the use of their liquid chromatography–mass spectrometry equipment, the Boger laboratory for the use of their polarimeter, the Baran laboratory for the use of their cold room. Financial support for this work was provided by Eli Lilly, Boehringer Ingelheim and the Scripps Research Institute.

Author Contributions S.V.P. and R.A.S. conceived the work. S.V.P. and C.A.R. performed the experiments. S.V.P., C.A.R. and R.A.S. designed the experiments and analysed the data. R.A.S. wrote the manuscript.

Author Information Crystallographic data are deposited with the Cambridge Crystallographic Data Centre under accession numbers CCDC 949094 (**25**) and CCDC 948968 (**26**). Reprints and permissions information is available at www.nature.com/reprints. The authors declare no competing financial interests. Readers are welcome to comment on the online version of the paper. Correspondence and requests for materials should be addressed to R.A.S. (rshevi@scripps.edu).

Changes in North Atlantic nitrogen fixation controlled by ocean circulation

Marietta Straub¹, Daniel M. Sigman², Haojia Ren³, Alfredo Martínez-García¹, A. Nele Meckler¹, Mathis P. Hain² & Gerald H. Haug¹

In the ocean, the chemical forms of nitrogen that are readily available for biological use (known collectively as ‘fixed’ nitrogen) fuel the global phytoplankton productivity that exports carbon to the deep ocean^{1–3}. Accordingly, variation in the oceanic fixed nitrogen reservoir has been proposed as a cause of glacial–interglacial changes in atmospheric carbon dioxide concentration^{2,3}. Marine nitrogen fixation, which produces most of the ocean’s fixed nitrogen, is thought to be affected by multiple factors, including ocean temperature⁴ and the availability of iron^{2,3,5} and phosphorus⁶. Here we reconstruct changes in North Atlantic nitrogen fixation over the past 160,000 years from the shell-bound nitrogen isotope ratio ($^{15}\text{N}/^{14}\text{N}$) of planktonic foraminifera in Caribbean Sea sediments. The observed changes cannot be explained by reconstructed changes in temperature, the supply of (iron-bearing) dust or water column denitrification. We identify a strong, roughly 23,000-year cycle in nitrogen fixation and suggest that it is a response to orbitally driven changes in equatorial Atlantic upwelling⁷, which imports ‘excess’ phosphorus (phosphorus in stoichiometric excess of fixed nitrogen) into the tropical North Atlantic surface^{5,6}. In addition, we find that nitrogen fixation was reduced during glacial stages 6 and 4, when North Atlantic Deep Water had shoaled to become glacial North Atlantic intermediate water⁸, which isolated the Atlantic thermocline from excess phosphorus-rich mid-depth waters that today enter from the Southern Ocean. Although modern studies have yielded diverse views of the controls on nitrogen fixation^{1,2,4,5}, our palaeobiogeochemical data suggest that excess phosphorus is the master variable in the North Atlantic Ocean and indicate that the variations in its supply over the most recent glacial cycle were dominated by the response of regional ocean circulation to the orbital cycles.

Nitrogen fixation, the conversion of N_2 to ammonia, by cyanobacteria in surface waters seems to dominate the input of fixed N to the ocean. The main loss of fixed N is biological reduction to N_2 (generalized here as ‘denitrification’) in marine sediments and in the suboxic zones of the water column in the eastern tropical Pacific Ocean and the Arabian Sea¹. Nitrogen fixation introduces N with $\delta^{15}\text{N}$ of about -1‰ ($\delta^{15}\text{N} = (^{15}\text{N}/^{14}\text{N})_{\text{sample}} / (^{15}\text{N}/^{14}\text{N})_{\text{reference}} - 1$, where the reference is atmospheric N_2), whereas water column denitrification preferentially removes ^{14}N -bearing nitrate⁹ (NO_3^-). In total, global ocean denitrification raises the $\delta^{15}\text{N}$ of mean ocean nitrate above that of newly fixed N (ref. 10).

Sediment records show N isotopic evidence of reduced water column denitrification during the Last Glacial Maximum (LGM) and other cold phases of the most recent glacial cycle, relative to the current interglacial (the Holocene epoch) and times of intermediate climate states¹¹ (for example Marine Isotope Stage (MIS) 3, from 57 to 29 kyr ago). Benthic denitrification, because of its weak effect on the $\delta^{15}\text{N}$ value of nitrate in the water column¹⁰, has not been directly reconstructed, but it may also have decreased during ice ages because of reduced continental shelf area due to lower sea level¹².

The history of N fixation has been vigorously debated^{2,3,13}. As with water column denitrification, N fixation is apparent in the spatial pattern of nitrate $\delta^{15}\text{N}$. Against the background of the mean ocean nitrate $\delta^{15}\text{N}$ of $\sim 5\text{‰}$, N fixation in the euphotic zone followed by the sinking and remineralization of organic matter adds low- $\delta^{15}\text{N}$ nitrate to the thermocline, which is observed across the western subtropical and tropical North Atlantic¹⁴. This low $\delta^{15}\text{N}$ value is recorded by the organic N bound within the shell walls of planktonic foraminifera^{15,16}. Foraminifera-bound $\delta^{15}\text{N}$ (FB- $\delta^{15}\text{N}$) from the Caribbean Sea and the Gulf of Mexico indicates that N fixation was reduced during the LGM^{15,17}.

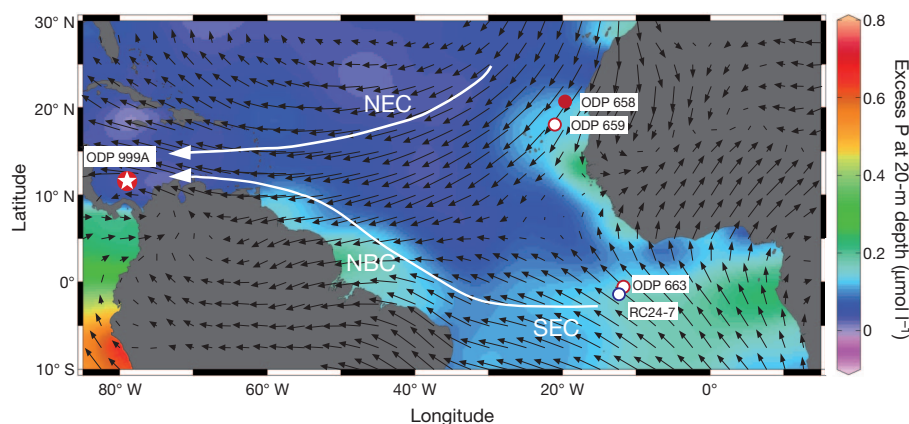


Figure 1 | Core locations, surface winds, excess P at 20-m depth and main surface currents. The star indicates ODP Site 999 Hole A ($12^{\circ} 45' \text{N}$, $78^{\circ} 44' \text{W}$; 2,828 m), the core in which FB- $\delta^{15}\text{N}$ was measured to reconstruct North Atlantic N fixation. The filled red circle indicates ODP Site 658 ($20^{\circ} 45' \text{N}$, $18^{\circ} 35' \text{W}$; 2,263 m), from which sediment Zr/Al data are reported in relation to North African aeolian flux. The open blue circle indicates core RC24-7 ($1^{\circ} 21' \text{S}$, $11^{\circ} 55' \text{W}$; 3,899 m), previously published data from which

reveal precession cycles in equatorial Atlantic upwelling⁷. The open red circles indicate ODP Site 659 ($18^{\circ} 05' \text{N}$, $21^{\circ} 02' \text{W}$; 3,070 m) and ODP Site 663 ($1^{\circ} 11.9' \text{S}$, $11^{\circ} 52.7' \text{W}$; 3,708 m), from which come previously published data pertaining to the aeolian flux^{21,22}. Excess P ($[\text{PO}_4^{3-}] - [\text{NO}_3^-]/16$; ref. 6) is an annual average. Black arrows show June–August winds, with length indicating speed. NBC, north Brazil current; NEC, north equatorial current; SEC, south equatorial current.

¹Geological Institute, Department of Earth Sciences, ETH Zurich, 8092 Zurich, Switzerland. ²Department of Geosciences, Princeton University, Princeton, New Jersey 08544, USA. ³Lamont-Doherty Earth Observatory, Columbia University, New York, New York 10964, USA.

Here we build on the FB- $\delta^{15}\text{N}$ results of ref. 15 with new data from the same core, Ocean Drilling Program (ODP) Site 999 Hole A in the Caribbean Sea (Fig. 1), extending the record back over the past 160 kyr through a full glacial cycle (Fig. 2a, b). We measured FB- $\delta^{15}\text{N}$ in two euphotic-zone-dwelling species of planktonic foraminifera, *Globigerinoides ruber* and *Globigerinoides sacculifer*. The records from the two species are very similar (Fig. 2a and Supplementary Fig. 1) and highly coherent (Supplementary Fig. 6). The FB- $\delta^{15}\text{N}$ of *G. ruber* (Fig. 2a, green symbols) is typically slightly ($\sim 0.3\text{‰}$) lower than that of *G. sacculifer* (Fig. 2a, blue symbols). There is a greater ($\geq 0.6\text{‰}$) interspecies difference during the LGM, in glacial MIS 4 and during the transition from MIS 6 to MIS 5 (Fig. 2a and Supplementary Fig. 1). Although changes in the interspecies

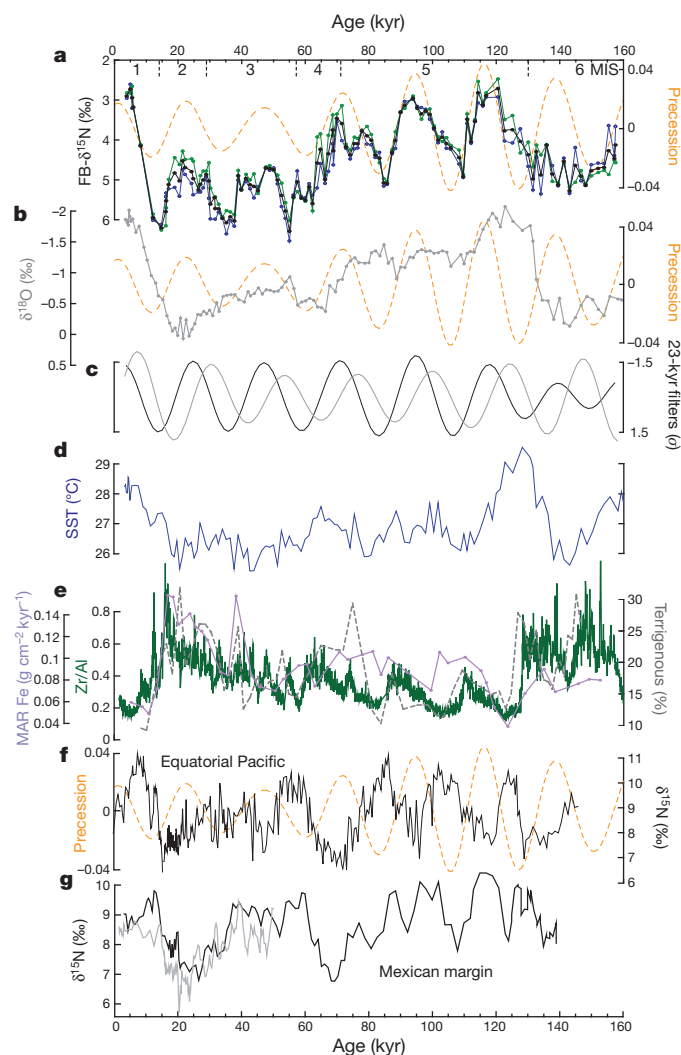


Figure 2 | FB- $\delta^{15}\text{N}$ in ODP Site 999 and its relationship to SST, dust flux and water column denitrification. **a**, FB- $\delta^{15}\text{N}$ was measured separately in two species, *G. sacculifer* (blue) and *G. ruber* (green). The black symbols show the two-species average FB- $\delta^{15}\text{N}$ at each sampling depth. As plotted, increasing N fixation is upward. **b**, *Globigerinoides ruber* $\delta^{18}\text{O}$ at ODP Site 999²⁰. In **a** and **b**, precession is dashed orange. **c**, The 23-kyr precession-band-filtered FB- $\delta^{15}\text{N}$ (black) and *G. ruber* $\delta^{18}\text{O}$ (grey) illustrate the 4–7-kyr phase lag between $\delta^{15}\text{N}$ and $\delta^{18}\text{O}$ at the precession band (Supplementary Figs 6 and 9). Given an average phase lag of 4–7 kyr between $\delta^{18}\text{O}$ and precession¹⁹, this observation confirms the correspondence of $\delta^{15}\text{N}$ minima with precession maxima (June aphelion). ($\delta^{18}\text{O} = (^{18}\text{O}/^{16}\text{O})_{\text{sample}} / (^{18}\text{O}/^{16}\text{O})_{\text{reference}} - 1$, where the reference is Vienna PeeDee Belemnite). **d**, *Globigerinoides ruber* Mg/Ca-derived SST at ODP Site 999²⁰. **e**, Atlantic dust-related records are mass accumulation rate of iron (MAR Fe) at ODP Site 999²³, Zr/Al at ODP Site 658 and terrigenous material abundance at ODP Site 663²². **f**, **g**, The Pacific bulk sediment $\delta^{15}\text{N}$ records are from the Mexican margin²⁹ (**g**) and the equatorial Pacific³⁰ (**f**), with increasing denitrification plotted upward (see also Supplementary Fig. 5).

$\delta^{15}\text{N}$ difference probably hold valuable information¹⁶, given the overarching similarity of the *G. ruber* and *G. sacculifer* FB- $\delta^{15}\text{N}$ records, we focus hereafter on the FB- $\delta^{15}\text{N}$ record generated by averaging the two species-specific records (Fig. 2a, black symbols).

The FB- $\delta^{15}\text{N}$ of the previous interglacial (early MIS 5) is similar to that of the Holocene, and the FB- $\delta^{15}\text{N}$ of the penultimate glacial maximum (MIS 6) is similar to that of the LGM. There is no evidence from previous work for mean ocean nitrate $\delta^{15}\text{N}$ changes across the most recent glacial cycle that mimic the FB- $\delta^{15}\text{N}$ record of Site 999, with the exception of a possible $\delta^{15}\text{N}$ maximum during the most recent deglaciation^{15,18}. Furthermore, South China Sea FB- $\delta^{15}\text{N}$ data support the interpretation of the Caribbean LGM-to-Holocene FB- $\delta^{15}\text{N}$ decrease as recording a regional change in N fixation¹⁸. The FB- $\delta^{15}\text{N}$ change through the Caribbean Sea record is of similar amplitude to the regional isotopic imprint of N fixation, in which nitrate $\delta^{15}\text{N}$ decreases from $\sim 5.3\text{‰}$ at $\sim 1,200\text{-m}$ depth in the water column to $\sim 2.5\text{‰}$ at $\sim 200\text{ m}$ (ref. 14). Thus, the FB- $\delta^{15}\text{N}$ record indicates proportionally large variations in N fixation¹⁵. The record of bulk sediment $\delta^{15}\text{N}$ at Site 999 shows a number of minor changes that coincide with changes in FB- $\delta^{15}\text{N}$, but they are so weak as to be unnoticeable without the benefit of the larger FB- $\delta^{15}\text{N}$ changes (Supplementary Fig. 2). The apparent muting of the variations suggests an allochthonous N input to the bulk sediment that does not respond to open-ocean changes¹⁷.

The FB- $\delta^{15}\text{N}$ variation is highly correlated with Earth's 19–23-kyr orbital precession cycle (Fig. 2a and Supplementary Figs 6, 8 and 10). FB- $\delta^{15}\text{N}$ minima consistently lag *G. ruber* calcite $\delta^{18}\text{O}$ minima by 4–7 kyr (Fig. 2c and Supplementary Figs 6 and 9), and they thus lag peak Northern Hemisphere summer insolation at the precession frequency band by 10–12 kyr (ref. 19). That is, minima in Caribbean FB- $\delta^{15}\text{N}$ (maxima in N fixation) occur during aphelion in the northern summer (precession maxima; Fig. 2a), which is the opposite of the precession phase that encourages Northern Hemisphere summer warming and deglaciation. Despite this precessional phasing, FB- $\delta^{15}\text{N}$ is higher (N fixation is reduced) during the major glacial periods (MIS 6 and MISs 4–2) relative to the interglacials (MISs 5 and 1). This implies that there are non-precessional step changes in FB- $\delta^{15}\text{N}$ at each of the major deglaciations (the transitions between MISs 6 and 5 and between MISs 2 and 1) and at the intensification of glaciation at the transition between MISs 5 and 4.

Temperature is recognized as a control on the distribution of N fixation, both in the ocean and on land⁴. Thus, ice-age cooling might be expected to reduce N fixation, consistent with the basic LGM–Holocene change in N fixation. However, the full record indicates that N fixation does not track Caribbean sea surface temperature (SST) as reconstructed from the Mg/Ca ratio of *G. ruber* at Site 999²⁰ (Fig. 2d and Supplementary Fig. 9c). SST rose early in the penultimate deglaciation (the transition between MISs 6 and 5) and had already begun to decline before N fixation reached the first of its three maxima in MIS 5, with the subsequent maxima in N fixation occurring against a relatively stable baseline of low SST (Fig. 2d and Supplementary Fig. 7a, b). Hence, SST change does not seem to explain the history of N fixation reconstructed from FB- $\delta^{15}\text{N}$.

Iron is a critical nutrient for N fixers, and iron-bearing dust has been suggested to cause ice-age enhancements in N fixation^{2,3}. In our comparison of the N fixation record at Site 999 with records of dust input, we include a new reconstruction of dust transport from ODP Site 658, a coring site off the coast of North Africa, which is the dominant source of dust to the Caribbean (Fig. 1). The Zr/Al ratio increases with high-energy aeolian transport (Supplementary Fig. 3). Focusing first on the large-scale glacial–interglacial changes, the FB- $\delta^{15}\text{N}$ record at Site 999 indicates that N fixation was, if anything, inversely correlated with Zr/Al at Site 658; reconstructed dust flux at Site 659²¹, which is farther offshore; terrigenous material abundance at equatorial Atlantic Site 663²²; and iron accumulation rate at Site 999²³ (Fig. 2e and Supplementary Fig. 4). The correlation of N fixation with dust over the precession cycle is more difficult to assess. North African aridity has

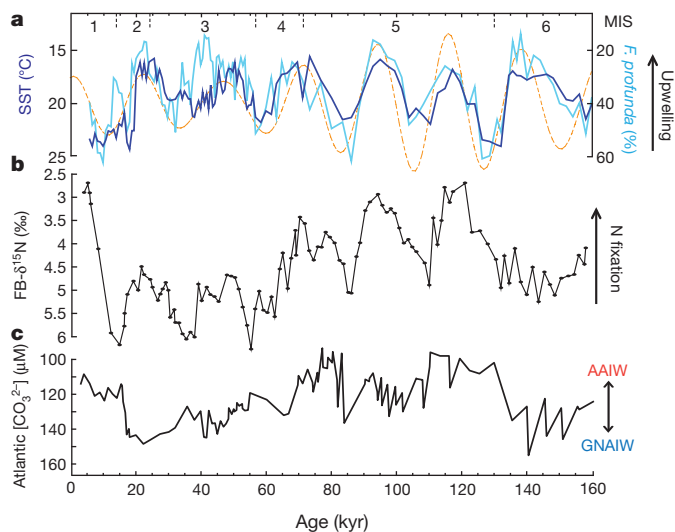


Figure 3 | Comparison of FB- $\delta^{15}\text{N}$ with changes in precession-paced equatorial Atlantic upwelling and glacial-interglacial Atlantic intermediate water source. **a**, *Florisphaera profunda* abundance (light blue) and foraminifera-species-derived SST (dark blue) from equatorial Atlantic core RC24-77. **b**, FB- $\delta^{15}\text{N}$ from ODP Site 999. **c**, Bottom water carbonate ion reconstruction from Caribbean Sea core VM28-122³¹ (12° N, 79° W; 3,620 m). The orange dashed line in **a** is the precession parameter. Episodes of higher equatorial Atlantic upwelling led to higher N fixation in the North Atlantic, observed as lower FB- $\delta^{15}\text{N}$. In **c**, the switches in North Atlantic intermediate water source between AAIW, the dominant source of excess P to the Atlantic⁵, and GNAIW, which was low in $[\text{PO}_4^{3-}]$ (refs 28,32) and presumably also in excess P, can be seen. Periods of inflow of AAIW stimulated N fixation.

been reported to increase during northern summer aphelion²⁴, when we observe higher N fixation. However, available records suggest, on balance, that dust input is out of phase with the precessional cycles in N fixation (Fig. 2 and Supplementary Information). All things considered, it does not seem that a dust-derived iron supply can explain the reconstructed N fixation changes.

North Atlantic N fixation might be expected to change so as to balance denitrification changes¹³. Bulk sediment $\delta^{15}\text{N}$ records near the major suboxic zones indicate a lower rate of water column denitrification during cold periods¹¹, in the same sense as the N fixation decrease that we reconstruct for the LGM, the glacial of MIS 4 and the glacial maximum of MIS 6 (Fig. 2f, g and Supplementary Fig. 5). However, beyond this coarsest scale, there are major differences. For example, in contrast to the sediment $\delta^{15}\text{N}$ records from the denitrification zones, FB- $\delta^{15}\text{N}$ at Site 999 during early MIS 3 is similar to that during the LGM, with these local $\delta^{15}\text{N}$ minima separated by the highest sustained $\delta^{15}\text{N}$ of the record at ~35 kyr ago in late MIS 3 (Fig. 2a). In addition, tropical Pacific bulk sediment $\delta^{15}\text{N}$ maxima (water column denitrification maxima) seem to be associated with minima in Earth's orbital precession cycle (Fig. 2f), when perihelion coincides with northern summer. The FB- $\delta^{15}\text{N}$ record indicates that these times represent minima, not maxima, in Atlantic N fixation. Although a global ocean reconstruction of denitrification does not yet exist, the available records do not provide clear signs that changes in water column denitrification are responsible for the timing of changes in North Atlantic N fixation over the most recent glacial cycle.

The importance of precession in Caribbean FB- $\delta^{15}\text{N}$ suggests a connection to low-latitude climate. Over recent glacial cycles, equatorial Atlantic upwelling varied with a precession frequency⁷. In the eastern equatorial Atlantic, climatic precession maxima (aphelion in northern summer) coincide with minima in reconstructed SST (Fig. 3a). In addition, these times are characterized by minima in the fraction of the nanofossils represented by the nutricline dwelling form *Florisphaera profunda* (Fig. 3a), reflecting a shoaling of the nutricline⁷. These observations indicate that precession maxima yielded stronger equatorial Atlantic upwelling⁷.

Precession-paced change in the equatorial Atlantic upwelling, coupled with a tendency of N fixation to occur in N-depleted, phosphorus-bearing water⁶, explains the precession signal in Caribbean FB- $\delta^{15}\text{N}$. Compared with the thermocline and surface layer of the western North Atlantic, subsurface water upwelled along the Equator has higher 'excess P'^{5,6} (defined as the phosphate concentration minus 1/16th of the nitrate concentration; Fig. 1). In waters with positive excess P, phytoplankton tends to deplete the water of nitrate before the complete consumption of phosphate. The residual phosphate in this nitrate-free water should encourage the growth of N-fixing phytoplankton¹³. In line with this expectation, data-assimilating model calculations suggest that the transport into the tropical North Atlantic of equatorial water bearing excess P leads to a band of high N fixation in this region^{6,25}. Moreover, N fixation seems to respond in the equatorial Atlantic upwelling region itself, before lateral transport of surface waters²⁶. The excess P of the waters upwelled along the Equator originates in sub-Antarctic mode water (SAMW) and Antarctic intermediate water⁵ (AAIW). With climatic precession maxima, increased equatorial upwelling of excess-P-bearing water coupled with northwestward transport of equatorial surface waters into the western tropical North Atlantic by the north Brazil current would increase the supply of excess P to the latter region, intensifying N fixation there (Fig. 3). Although the Amazon outflow may also contribute to the excess P in the north Brazil current (Fig. 1), its response to precession²⁷ seems to be inconsistent with our reconstructed N fixation changes.

The baseline shifts in FB- $\delta^{15}\text{N}$ at the respective transitions between MISs 6 and 5, 5 and 4, and 2 and 1 parallel well-known changes in the depth of North Atlantic ventilation (Fig. 3c): glacial North Atlantic intermediate water (GNAIW) formed during glacial stages 6 and 4–2, rather than the North Atlantic Deep Water (NADW) of interglacial stages⁸. GNAIW formation reduced the nutrient concentration at the base of the Atlantic thermocline²⁸ by preventing the influx of AAIW and SAMW or by diluting their impact, or both (Fig. 4). The low nutrient content of GNAIW implies that it formed from nutrient-depleted, low-latitude North Atlantic surface water, which today lacks excess P (ref. 5). Thus, the switch from NADW to GNAIW lowered the excess P of the subsurface waters to be upwelled (Fig. 4). A plausible alternative for the step changes in FB- $\delta^{15}\text{N}$ is that Atlantic N fixation was responding to sea-level-driven reductions in sedimentary denitrification during glacial stages 6 and 4–2. However, a shelf-associated decrease in sedimentary denitrification would have lowered excess P in the low-latitude upper ocean within decades to centuries of the sea-level decline at the onset of MIS 4. The FB- $\delta^{15}\text{N}$ increase in glacial stage 4 occurred ~7 kyr after the sea-level decrease (Fig. 2a, b and Supplementary Fig. 9a), inconsistent with a response to regional sedimentary denitrification but consistent with the timing of the switch to GNAIW⁸.

Although variations in Atlantic N fixation do not seem to have paralleled global water column denitrification over the past 160 kyr, this does not require an imbalance between N fixation and denitrification on a global ocean basis; indeed, a sensitivity to phosphorus would encourage a global balance¹³. At the same time, this study recalibrates our expectations regarding the regional drivers of biogeochemical change in the low-nutrient tropical and subtropical ocean. Water column denitrification is broadly recognized as being sensitive to the physical circulation, given that the major ocean suboxic regions are located in the tropical 'shadow zones', the poorly ventilated subsurface volumes east of the subtropical gyres. Our results indicate that ocean circulation, through its control of nutrient transport, can also drive changes in regional rates of N fixation⁶.

Although iron limitation of phytoplankton is fundamental to ocean biogeochemistry^{2,3,5}, the data reported here suggest that, in the North Atlantic, the rate of N fixation over the past 160 kyr has not been tightly constrained by iron supply. The entire ocean N and P reservoirs must flow through the North Atlantic on the timescale of ocean ventilation (~1 kyr), which is probably shorter than the residence time of the ocean's fixed N reservoir¹. Thus, if N fixation in the rest of the ocean is significantly limited

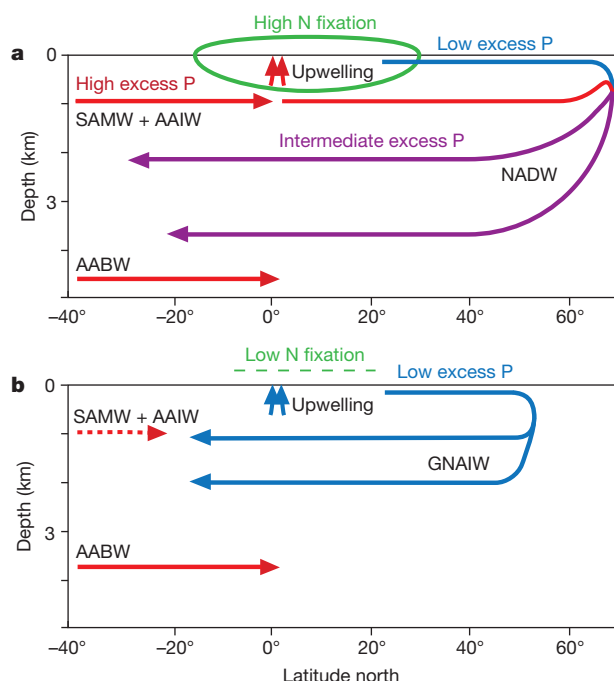


Figure 4 | Effect of changes in glacial-interglacial circulation on N fixation in the Atlantic. **a**, During the Holocene and MIS 5, SAMW and AAIW import high excess P (red) to the low latitudes, where its upwelling stimulates N fixation, which removes the excess P (conversion from red to blue). North Atlantic surface water, SAMW and AAIW are incorporated into newly formed NADW, which is thus intermediate in excess P (purple; ref. 5). **b**, In glacial stages MIS 6 and MISs 4–2 (where MIS 2 is the LGM), the low excess P of southward-flowing GNAIW would have diluted or replaced the high excess P of SAMW and AAIW, reducing the concentration of excess P available to be upwelled, and thus lowering N fixation. The precession-paced changes in equatorial Atlantic upwelling are not indicated in this diagram.

by iron, then the North Atlantic may have an important role in maintaining the relationship between the global ocean N and P reservoirs.

METHODS SUMMARY

FB- $\delta^{15}\text{N}$ was analysed by oxidizing organic N to nitrate and then using a bacterial method to convert the nitrate to nitrous oxide for isotope ratio mass spectrometry¹⁵. The individual species were picked manually, to obtain 3–7 mg of foraminifera per sample. The picked sample was crushed and underwent reductive and then oxidative cleaning to remove all N not bound within (and thus physically protected by) the calcite walls of the foraminifera tests. Dissolution of the tests with HCl released the test-bound organic N, which was then oxidized to nitrate. Sediment Zr/Al was measured with an Avaatech XRF Core Scanner at MARUM, University of Bremen. Data are of X-ray fluorescence count ratios and were obtained at a resolution of 1 cm over an area of 1.2 cm² directly at the split-core surface of the archive half.

Full Methods and any associated references are available in the online version of the paper.

Received 22 August 2012; accepted 13 June 2013.

Published online 21 August 2013.

- Gruber, N. & Galloway, J. N. An Earth-system perspective of the global nitrogen cycle. *Nature* **451**, 293–296 (2008).
- Falkowski, P. G. Evolution of the nitrogen cycle and its influence on the biological sequestration of CO₂ in the ocean. *Nature* **387**, 272–275 (1997).
- Broecker, W. S. & Henderson, G. M. The sequence of events surrounding Termination II and their implications for the cause of glacial-interglacial CO₂ changes. *Paleoceanography* **13**, 352–364 (1998).
- Houltton, B. Z., Wang, Y., Vitousek, P. M. & Field, C. B. A unifying framework for dinitrogen fixation in the terrestrial biosphere. *Nature* **454**, 327–330 (2008).
- Moore, C. M. *et al.* Large-scale distribution of Atlantic nitrogen fixation controlled by iron availability. *Nature Geosci.* **2**, 867–871 (2009).
- Deutsch, C., Sarmiento, J. L., Sigman, D. M., Gruber, N. & Dunne, J. P. Spatial coupling of nitrogen inputs and losses in the ocean. *Nature* **445**, 163–167 (2007).
- Molifino, B. & McIntyre, A. Precessional forcing of nutrient dynamics in the equatorial Atlantic. *Science* **249**, 766–769 (1990).

- Piotrowski, A. M., Goldstein, S. L., Hemming, S. R. & Fairbanks, R. G. Temporal relationships of carbon cycling and ocean circulation at glacial boundaries. *Science* **307**, 1933–1938 (2005).
- Brandes, J. A., Devol, A. H., Yoshinari, T., Jayakumar, D. A. & Naqvi, S. W. A. Isotopic composition of nitrate in the central Arabian Sea and eastern tropical North Pacific: a tracer for mixing and nitrogen cycles. *Limnol. Oceanogr.* **43**, 1680–1689 (1998).
- Brandes, J. A. & Devol, A. H. A global marine-fixed nitrogen isotopic budget: implications for Holocene nitrogen cycling. *Glob. Biogeochem. Cycles* **16**, 1120 (2002).
- Altabet, M. A., Francois, R., Murray, D. W. & Prell, W. L. Climate-related variations in denitrification in the Arabian Sea from sediment ¹⁵N/¹⁴N ratios. *Nature* **373**, 506–509 (1995).
- Christensen, J. P. Carbon export from continental shelves, denitrification and atmospheric carbon dioxide. *Cont. Shelf Res.* **14**, 547–576 (1994).
- Tyrrell, T. The relative influences of nitrogen and phosphorus on oceanic primary production. *Nature* **400**, 525–531 (1999).
- Knapp, A. N., DiFiore, P. J., Deutsch, C., Sigman, D. M. & Lipschultz, F. Nitrate isotopic composition between Bermuda and Puerto Rico: implications for N₂ fixation in the Atlantic Ocean. *Glob. Biogeochem. Cycles* **22**, GB3014 (2008).
- Ren, H. *et al.* Foraminiferal isotope evidence of reduced nitrogen fixation in the ice age Atlantic Ocean. *Science* **323**, 244–248 (2009).
- Ren, H., Sigman, D. M., Thunell, R. C. & Prokopenko, M. G. Nitrogen isotopic composition of planktonic foraminifera from the modern ocean and recent sediments. *Limnol. Oceanogr.* **57**, 1011–1024 (2012).
- Meckler, A. N. *et al.* Deglacial nitrogen isotope changes in the Gulf of Mexico: evidence from bulk sedimentary and foraminifera-bound nitrogen in Orca Basin sediments. *Paleoceanography* **26**, PA4216 (2011).
- Ren, H., Sigman, D. M., Chen, M. C. & Kao, S. Elevated foraminifera-bound nitrogen isotopic composition during the last ice age in the South China Sea and its global and regional implications. *Glob. Biogeochem. Cycles* **26**, GB1031 (2012).
- Imbrie, J. *et al.* On the structure and origin of major glaciation cycles 1. Linear responses to Milankovitch forcing. *Paleoceanography* **7**, 701–738 (1992).
- Schmidt, M. W., Vautravers, M. J. & Spero, H. J. Western Caribbean sea surface temperatures during the late Quaternary. *Geochim. Geophys. Geosyst.* **7**, Q02P10 (2006).
- Tiedemann, R., Sarnthein, M. & Shackleton, N. J. Astronomic timescale for the Pliocene Atlantic $\delta^{18}\text{O}$ and dust flux records of Ocean Drilling Program site 659. *Paleoceanography* **9**, 619–638 (1994).
- deMenocal, P. B., Ruddiman, W. F. & Pokras, E. M. Influences of high- and low-latitude processes on African terrestrial climate: Pleistocene eolian records from equatorial Atlantic Ocean Drilling Program Site 663. *Paleoceanography* **8**, 209–242 (1993).
- Mora, G. & Martínez, J. I. Sedimentary metal ratios in the Colombia Basin as indicators for water balance change in northern South America during the past 400,000 years. *Paleoceanography* **20**, PA4013 (2005).
- Pokras, E. M. & Mix, A. C. Earth's precession cycle and Quaternary climatic change in tropical Africa. *Nature* **326**, 486–487 (1987).
- Coles, V. J. & Hood, R. R. Modeling the impact of iron and phosphorus limitations on nitrogen fixation in the Atlantic Ocean. *Biogeochemistry* **4**, 455–479 (2007).
- Subramaniam, A., Mahaffey, C., Johns, W. & Mahowald, N. Equatorial upwelling enhances nitrogen fixation in the Atlantic Ocean. *Geophys. Res. Lett.* **40**, 1766–1771 (2013).
- Harris, S. E. & Mix, A. C. Pleistocene precipitation balance in the Amazon basin recorded in deep sea sediments. *Quat. Res.* **51**, 14–26 (1999).
- Marchitto, T. M., Curry, W. B. & Oppo, D. W. Millennial-scale changes in North Atlantic circulation since the last glaciation. *Nature* **393**, 557–561 (1998).
- Ganeshram, R. S., Pedersen, T. F., Calvert, S. E. & Murray, D. W. Large changes in oceanic nutrient inventories from glacial to interglacial periods. *Nature* **376**, 755–758 (1995).
- Jia, G. & Li, Z. Easterly denitrification signal and nitrogen fixation feedback documented in the western Pacific sediments. *Geophys. Res. Lett.* **38**, L24605 (2011).
- Yu, J. *et al.* An evaluation of benthic foraminiferal B/Ca and $\delta^{11}\text{B}$ for deep ocean carbonate ion and pH reconstructions. *Earth Planet. Sci. Lett.* **293**, 114–120 (2010).
- Marchitto, T. M. & Broecker, W. S. Deep water mass geometry in the glacial Atlantic Ocean: a review of constraints from the paleonutrient proxy Cd/Ca. *Geochim. Geophys. Geosyst.* **7**, Q12003 (2006).

Supplementary Information is available in the online version of the paper.

Acknowledgements We thank M. A. Weigand, S. Oleynik and S. Bishop for technical assistance and U. Röhl and V. Lukies for X-ray fluorescence scanning support. Funding was from SNF grant 200021-131886/1, US NSF grant OCE-1060947 and the Grand Challenges Program of Princeton University. This research used samples provided by the ODP, which is sponsored by the NSF and participating countries under the management of the Joint Oceanographic Institutions. X-ray fluorescence scanning was supported by the DFG-Leibniz Center for Surface Process and Climate Studies at the University of Potsdam.

Author Contributions M.S., D.M.S. and G.H.H. designed the study. M.S. performed the FB- $\delta^{15}\text{N}$ analysis and wrote the first version of the manuscript with D.M.S.; A.N.M. generated the Zr/Al record at ODP Site 658. A.M.-G. performed the statistical analysis of the data with M.S.; H.R. was involved in the laboratory and data analysis. All authors contributed to the interpretation of the data and provided significant input to the final manuscript.

Author Information Reprints and permissions information is available at www.nature.com/reprints. The authors declare no competing financial interests. Readers are welcome to comment on the online version of the paper. Correspondence and requests for materials should be addressed to M.S. (marietta.straub@alumni.ethz.ch).

METHODS

Sample preparation for $\text{FB-}\delta^{15}\text{N}$. The protocol follows that of ref. 15. The individual species are picked manually under a dissecting microscope (315–425- μm size fraction). Foraminifera (3–7 mg, or 600–800 specimens, per sample) are used to carry out the analysis and are gently crushed. Clay particles are removed using a 2% polyphosphate solution and 5-min sonication in an ultrasonic bath. The samples are then rinsed with deionized water. Dithionite-citric acid (10 ml) is added to each sample, and the solution is kept for 1 h in a water bath at 80 °C to remove any metal coatings. After being rinsed with deionized water, the sample undergoes oxidative cleaning with a basic potassium persulphate solution at 100 °C for 1 h to remove external organic N. The cleaned samples are rinsed in deionized water and dried overnight at 60 °C.

Conversion of foraminifera-bound N to nitrate. Foraminifera (3–6 mg per sample) are weighed into a previously combusted glass vial and dissolved in 4 N HCl (40–60 μl per sample). To convert the released organic N to nitrate, basic potassium persulphate oxidizing solution is added to each vial and to vials containing organic standards and procedural blanks, and the vials are then autoclaved for 1 h on a slow-vent setting (1.5 h including warm-up and cool-down times). To lower the N blank associated with the oxidizing solution, the potassium persulphate is recrystallized two to three times. At the time of processing, 1 g NaOH and 1 g potassium persulphate are dissolved in 100 ml of deionized water. Organic standards are used to constrain the $\delta^{15}\text{N}$ of the persulphate reagent blank. The two organic standards used here are mixtures of 6-aminocaproic acid and glycine. A minimum of 10 organic standards and 3–5 blanks are analysed per batch of samples, allowing for a correction for the persulphate blank. We used 1 ml of persulphate reagent for the blanks, oxidation standards and foraminifera samples. **Determination of N content.** To determine sample N content, we measure nitrate concentration in the oxidation solutions after autoclaving. The nitrate analysis is done by reduction to nitric oxide using vanadium(III) followed by chemiluminescence detection³³. The blank is also quantified in this way. The *G. ruber* and *G. sacculifer* samples have average N content of 3–4 $\mu\text{mol N}$ per gram of sample, yielding nitrate concentrations in the oxidation solutions of 10–20 μM , whereas the blank concentration ranges between 0.3 and 0.7 μM .

Denitrifier method. A detailed explanation of the denitrifier method can be found in ref. 34. Before adding the foraminifera samples to the bacteria, the sample solution is acidified to pH 3–6. The denitrifier *Pseudomonas chlororaphis* was used for this work. Normally, 5 nmol samples are added to 1 ml of bacterial concentrate after the degassing. Oxidation standards, as well as replicate analyses of nitrate reference material IAEA-N3 (with $\delta^{15}\text{N}$ of 4.7‰) and a bacterial blank, are also measured. The IAEA-N3 standards are used to monitor the bacterial conversion and mass spectrometry, and the oxidation standards are used for the final correction of the data. If possible, samples are oxidized in duplicate, and all oxidized samples are analysed by the denitrifier method in duplicate at least. The reported error is the standard deviation (1σ) estimated from the means of separate oxidations of cleaned foraminiferal material.

Age model. We use the age model in refs 20,35. This age model is based on radiocarbon dating for the past 21.6 kyr. For the rest of the record, the age model is based on the alignment between the $\delta^{18}\text{O}$ record of *G. ruber* and the LR04 benthic stack reference curve³⁶.

Bulk sediment $\delta^{15}\text{N}$ analysis. The total N content of the sediment was analysed as N_2 using a Thermo Fisher Series 1112 elemental analyser coupled with a Thermo Fisher Delta V Plus mass spectrometer at ETH Zurich. Between 40 and 60 mg of sediment was analysed. In-house standards of atropine and peptone were measured in the same runs, and the final corrections were based on the peptone standard, which has been referenced to international reference materials. Standard deviations for both standards were <0.2‰.

X-ray fluorescence scanning. Sediment Zr/Al X-ray fluorescence (XRF) count ratios were obtained with an Avaatech XRF Core Scanner at MARUM, University of Bremen. Data were obtained at a resolution of 1 cm over an area of 1.2 cm^2 directly at the split-core surface of the archive half, with different settings for light elements such as Al (10 kV, 20 s and 150 mA) and heavy elements such as Zr (50 kV, 20 s and 800 mA). The core surface was covered with a 4- μm -thick

SPEX Certi Prep Ultralene1 foil to avoid contamination of the XRF measurement unit. The core scanner includes a Canberra X-PIPS Silicon Drift Detector (SDD; Model SXD 15C-150-500) with 150-eV X-ray resolution, a Canberra Digital Spectrum Analyzer DAS 1000 and an Oxford Instruments 100W Neptune X-ray tube with rhodium target material. Raw data spectra were processed using the WIN AXIL package from Canberra Eurisys.

To bridge coring gaps and hiatuses, cores from all three parallel holes (A, B and C) were used, and a new composite depth was derived from the XRF data. Because cores from hole C had been frozen and re-thawed, we used this hole only where material from the other two holes was unavailable. The higher water content of Site 658C resulting from the different treatment affected the Al measurements, as is commonly observed. We therefore adjusted the Zr/Al ratios from Site 658C by regression to Zr/Al from Site 658B for a section with overlapping data (Supplementary Fig. 3).

The age model for the record from Site 658 was derived by transferring the published benthic $\delta^{18}\text{O}$ record³⁷ onto the new composite depth and aligning the record to the same data as contained in the LR04³⁶ benthic stack (Supplementary Fig. 3). For the past 15 kyr, the age model was further refined by aligning XRF Ca counts from Site 658A and Site 658B to percentage CaCO_3 data from radiocarbon-dated Site 658C^{38,39}, and for the period between 20 and 130 kyr ago, additional tie-points were derived by matching Zr/Al to the humidity index of core GeoB7920-2^{40,41}.

Because Zr from zircon minerals is dominantly present in the coarse silt fraction, whereas Al is most abundant in clay minerals, the Zr/Al ratio is interpreted to reflect grain size (Supplementary Fig. 3). Similarly, the Zr/Rb ratio has been shown to covary with grain size in this region^{40,42}, but the low signal-to-noise ratio of Rb in our XRF measurements led us to use Al instead. The dust deposited at Site 658 is mainly transported by the northeast trade winds, and its dominant grain type is coarse silt⁴³. Increasing Zr/Al ratios at Site 658 should therefore reflect increasing aeolian transport of Saharan dust.

Map of excess phosphorus and wind velocities. The excess phosphorus map shown in Fig. 1 uses World Ocean Atlas data⁴⁴ and the software Ocean Data View⁴⁵. Winds were plotted using the IRI Climate and Society Map Room (<http://iridl.ldeo.columbia.edu/maproom>).

33. Braman, R. S. & Hendrix, S. A. Nanogram nitrite and nitrate determination in environmental and biological materials by vanadium(III) reduction with chemiluminescence detection. *Anal. Chem.* **61**, 2715–2718 (1989).
34. Sigman, D. M. *et al.* A bacterial method for the nitrogen isotopic analysis of nitrate in seawater and freshwater. *Anal. Chem.* **73**, 4145–4153 (2001).
35. Schmidt, D. W., Spero, H. J. & Lea, D. W. Links between salinity variation in the Caribbean and North Atlantic thermohaline circulation. *Nature* **428**, 160–163 (2004).
36. Lisiecki, L. E. & Raymo, M. E. A. Pliocene-Pleistocene stack of 57 globally distributed benthic $\delta^{18}\text{O}$ records. *Paleoceanography* **20**, PA1003 (2005).
37. Sarnthein, M. & Tiedemann, R. Toward a high-resolution stable isotope stratigraphy of the last 3.4 million years: Sites 658 and 659 off Northwest Africa. *Proc. ODP Sci. Res.* **108**, 167–661 (1989).
38. deMenocal, P. *et al.* Abrupt onset and termination of the African Humid Period: rapid climate responses to gradual insolation forcing. *Quat. Sci. Rev.* **19**, 347–361 (2000).
39. Adkins, J., deMenocal, P. & Eshel, G. The “African humid period” and the record of marine upwelling from excess ^{230}Th in Ocean Drilling Program Hole 658C. *Paleoceanography* **21**, PA4203 (2006).
40. Tjallingii, R. *Application and Quality of X-Ray Fluorescence Core Scanning in Reconstructing Late Pleistocene NW African Continental Margin Sedimentation Patterns and Paleoclimate Variations* 65–84. PhD thesis, Univ. Bremen (2006).
41. Tjallingii, R. *et al.* Coherent high- and low-latitude control of the northwest African hydrological balance. *Nature Geosci.* **1**, 670–675 (2008).
42. Matthewson, A. P., Shimmield, G. B., Kroon, D. & Fallick, A. E. A 300-kyr high-resolution aridity record of the North-African continent. *Paleoceanography* **10**, 677–692 (1995).
43. Holz, C., Stuetz, J. B. W. & Henrich, R. Terrigenous sedimentation processes along the continental margin off NW Africa: implications from grain-size analysis of seabed sediments. *Sedimentology* **51**, 1145–1154 (2004).
44. Garcia, H. E. *et al.* *World Ocean Atlas 2009* Vol. 4, 398 (Government Printing Office, 2010).
45. Schlitzer, R. Ocean Data View. <http://odv.awi.de> (2012).

Retardation of arsenic transport through a Pleistocene aquifer

Alexander van Geen¹, Benjamin C. Bostick¹, Pham Thi Kim Trang², Vi Mai Lan², Nguyen-Ngoc Mai², Phu Dao Manh², Pham Hung Viet², Kathleen Radloff¹†, Zahid Aziz¹†, Jacob L. Mey^{1,3}, Mason O. Stahl⁴, Charles F. Harvey⁴, Peter Oates⁵, Beth Weinman⁶†, Caroline Stengel⁷, Felix Frei⁷, Rolf Kipfer^{7,8} & Michael Berg⁷

Groundwater drawn daily from shallow alluvial sands by millions of wells over large areas of south and southeast Asia exposes an estimated population of over a hundred million people to toxic levels of arsenic¹. Holocene aquifers are the source of widespread arsenic poisoning across the region^{2,3}. In contrast, Pleistocene sands deposited in this region more than 12,000 years ago mostly do not host groundwater with high levels of arsenic. Pleistocene aquifers are increasingly used as a safe source of drinking water⁴ and it is therefore important to understand under what conditions low levels of arsenic can be maintained. Here we reconstruct the initial phase of contamination of a Pleistocene aquifer near Hanoi, Vietnam. We demonstrate that changes in groundwater flow conditions and the redox state of the aquifer sands induced by groundwater pumping caused the lateral intrusion of arsenic contamination more than 120 metres from a Holocene aquifer into a previously uncontaminated Pleistocene aquifer. We also find that arsenic adsorbs onto the aquifer sands and that there is a 16–20-fold retardation in the extent of the contamination relative to the reconstructed lateral movement of groundwater over the same period. Our findings suggest that arsenic contamination of Pleistocene aquifers in south and southeast Asia as a consequence of increasing levels of groundwater pumping may have been delayed by the retardation of arsenic transport.

This study reconstructs the initial phase of contamination of an aquifer containing low levels of arsenic (low-As) in the village of Van Phuc, located 10 km southeast of Hanoi on the banks of the Red River. A key feature of the site is the juxtaposition of a high-As aquifer upstream of a low-As aquifer in an area where pumping for the city of Hanoi has dominated lateral groundwater flow for the past several decades (Fig. 1a). Many residents of the village of Van Phuc still draw water from their 30–50-m-deep private wells. In the western portion of the village, the wells typically contain less than 10 µg of As per litre of water and therefore meet the World Health Organization guideline for As in drinking water, whereas As in the groundwater from most wells in eastern Van Phuc exceeds this guideline by a factor of 10–50 (ref. 5).

Drilling and sediment dating in the area has shown that low-As groundwater is drawn from orange-coloured sands deposited over 12,000 years ago, whereas high-As groundwater is typically in contact with grey sands deposited less than 5,000 years ago^{6,7}. We examined to what extent the boundary between the low-As and high-As aquifers of Van Phuc has shifted in response to groundwater withdrawals in Hanoi. This large-scale perturbation spanning several decades has implications for low-As aquifers throughout Asia that are vulnerable to contamination owing to accelerated groundwater flow.

The collection of sediment cores and the installation of monitoring wells was concentrated along a transect trending southeast to northwest that extends over a distance of 2.2 km from the bank of the Red

River (Fig. 1b). Groundwater heads, and therefore the groundwater velocity field, within Van Phuc respond rapidly to the daily and seasonal cycles in the water level of the river (Supplementary Information). Before large-scale groundwater withdrawals, rainfall was sufficient to maintain groundwater discharge to the river, as is still observed elsewhere along the Red River⁸. In Van Phuc, however, the groundwater level was on average 40 cm below that of the water level of the Red River in 2010–11 and the hydraulic gradient nearly always indicated flow from the river into the aquifer. The reversal of the natural head gradient is caused by the large depression in groundwater level centred 10 km to the northwest that induces groundwater flow along the Van Phuc transect from the river towards Hanoi (Fig. 1a). This perturbation of groundwater flow is caused by massive pumping for the municipal water supply of Hanoi^{9–11}, which nearly doubled from 0.55 million to 0.90 million cubic metres per day between 2000 and 2010 owing to the rapid expansion of the city (Supplementary Fig. 1).

A change in the colour of a clay layer capping sandy sediment along the transect defines a geological boundary between the two portions of the Van Phuc aquifer. Up to a distance of 1.7 km from the river bank, the clay capping the aquifer is uniformly grey with the exception of a thin brown interval at the very surface (Fig. 2b). In contrast, a readily identifiable sequence of highly oxidized bright yellow, red and white clays was encountered between 12 m and 17 m depth at all drill sites along the transect beyond a distance of 1.7 km from the river bank. This oxidized clay layer is probably a palaeosol dating to the last sea-level low-stand about 20,000 years ago^{7,12}.

The colour of aquifer sands below the upper clay layer also changes markedly along the Van Phuc transect. Sand colour in fluvio-deltaic deposits is controlled primarily by the extent to which Fe(III) has been reduced to Fe(II) by the decomposition of organic carbon¹³. Up to a distance of 1.6 km from the river bank, sandy drill cuttings within the 20–40 m depth range are uniformly grey. The predominance of orange sands beyond 1.6 km indicates oxidation during the previous sea-level low-stand. After the sea level rose back to its current level, the nature of the remaining organic carbon precluded a new cycle of Fe(III) reduction¹⁴.

Independently of sediment colour, the calcium (Ca) content of sand cuttings collected while drilling along the Van Phuc transect confirms that a geological boundary extends to the underlying aquifer sands. Within the southeastern portion of the aquifer that is not capped by the presumed palaeosol, X-ray fluorescence measurements indicate Ca concentrations of over 2,000 mg Ca per kg of sand in cuttings to a depth of 30 m (Fig. 2a). The groundwater in this portion of the aquifer is supersaturated with respect to calcite and dolomite⁶, suggesting that authigenic precipitation is the source of Ca in the grey drill cuttings, as previously proposed elsewhere¹² (Supplementary Fig. 2). At a distance of 1.7 km from the river and further to the northwest, instead, the Ca

¹Lamont-Doherty Earth Observatory (LDEO), Columbia University, Palisades, New York 10964, USA. ²Research Centre for Environmental Technology and Sustainable Development (CETASD), Hanoi University of Science, Vietnam National University, Hanoi, Vietnam. ³Department of Physical Sciences, Kingsborough Community College, Brooklyn, New York 11235, USA. ⁴Massachusetts Institute of Technology, Cambridge, Massachusetts 02139, USA. ⁵Anchor QEA, Montvale, New Jersey 07645, USA. ⁶Earth and Environmental Sciences, Vanderbilt University, Nashville, Tennessee 37235, USA. ⁷Eawag, Swiss Federal Institute of Aquatic Science and Technology, 8600 Dübendorf, Switzerland. ⁸Institute of Geochemistry and Petrology, Swiss Federal Institute of Technology, Zurich ETHZ 8092, Switzerland. ⁹Present addresses: Gradient, Cambridge, Massachusetts 02138, USA (K.R.); Sadat Associates, Trenton, New Jersey 08610, USA (Z.A.); Earth and Environmental Sciences, California State University, Fresno, California 93740, USA (B.W.).



content of orange sand cuttings systematically remains less than 100 mg Ca per kg and the groundwater is undersaturated with respect to calcite and dolomite. Unlike surficial shallow grey clays, the Ca content of the presumed palaeosol is also very low (<100 mg Ca per kg) and consistent with extensive weathering.

The redox state of the aquifer has a major impact on the composition of groundwater in Van Phuc, as reported elsewhere in Vietnam¹⁵ and across south and east Asia more generally³. High but harmless Fe(II) concentrations in groundwater (10–20 mg per litre) associated with grey reducing sediments are apparent to residents of eastern Van Phuc as an orange Fe(III) precipitate that forms in their water upon exposure to air (Supplementary Fig. 3). In contrast, the high and toxic concentrations of As in groundwater at 20–30 m depth within the

Figure 1 | Map of the Hanoi area extending south to the study site.

a, Location of the village of Van Phuc in relation to the cone of depression formed by groundwater pumping for the municipal water supply of Hanoi (white contours, adapted from ref. 10). Urbanized areas are shown in grey; largely open fields are shown in green. **b**, Enlarged view of Van Phuc (box shows location in **a**) from Google Earth showing the location of the transect along which groundwater and sediment were collected, with tickmark labels indicating distance from the Red River bank in kilometres. Symbol colour distinguishes the uniformly grey Holocene aquifer (red), the Pleistocene aquifer contaminated with As (yellow), the Pleistocene aquifer where the groundwater conductivity and dissolved inorganic carbon concentrations are high but As concentrations are not (green), and the Pleistocene aquifer without indication of contamination (blue), all within the 25–30-m depth interval. Three white asterisks identify the wells that were used to determine flow direction. Image copyright 2012 Digital Globe Google Earth. **c**, Rose diagram frequency plot of the head gradient direction based on data collected at 5-min intervals (numbers indicate the number of observations) from these three wells from September 2010 to June 2011.

same portion of the transect, ranging from 200 µg per litre near the river to levels as high as 600 µg per litre at 1.2–1.6 km from the river bank, are invisible (Fig. 2c). The groundwater in contact with Pleistocene sands in northwestern Van Phuc is also anaerobic but contains less than 0.5 mg Fe(II) per litre and less than 10 µg As per litre and shows little indication of organic carbon mineralization compared to the Holocene aquifer (Supplementary Fig. 4).

The Pleistocene portion of the Van Phuc aquifer adjacent to the Holocene sediment is not uniformly orange or low in As. Of particular interest is a layer of grey sand at 25–30 m depth extending to the northwest at a distance of 1.7–1.8 km from the river bank (Fig. 2b). The intercalation of grey sand between orange sands above and below, combined with the low Ca content of sand cuttings within this layer, indicate that it was deposited during the Pleistocene and therefore until recently oxidized and orange in colour. Within the portion of the Pleistocene aquifer that became grey and is closest to the geological boundary, groundwater As concentrations are therefore presumed to have been originally very low (<5 µg per litre). Actual As concentrations of 100–500 µg per litre, as high as in the adjacent Holocene aquifer, indicate contamination extending over a distance of about 120 m into the Pleistocene aquifer (Fig. 3a).

A subset of the transect wells was sampled in 2006 and analysed for tritium (^3H) as well as noble gases in order to measure groundwater ages and determine the rate of As intrusion into the Pleistocene aquifer. Atmospheric nuclear weapons testing in the 1950s and 1960s is the main source of ^3H that entered the hydrological cycle¹⁶. The distribution of ^3H indicates that only groundwater in the southeastern high-As portion of the aquifer contains a plume of recharge dating from the 1950s and later. Concentrations of ^3He , the stable decay product of ^3H , were used to calculate groundwater ages for eight wells in the 24–42-m depth range with detectable levels of ^3H . In 2006, the oldest water dated by the ^3H – ^3He method (Supplementary Fig. 5) was sampled at a distance of 1.6 km from the river, which is the most northwestern location along the transect where the aquifer is uniformly grey (Fig. 2b, d). Younger ages of 15 years and 17 years were measured closer to the river at 1.3 km and 1.5 km, respectively. Concentrations of ^3H , groundwater ^3H – ^3He ages, and hydraulic head gradients consistently indicate that the Holocene aquifer has been recharged by the river from the southeast within the past few decades.

Drilling and geophysical data indicate that the main groundwater recharge area extends from the centre of the Red River to the inland area where a surficial clay layer thickens markedly, that is, from 100 m southeast to 300 m northwest of the river bank (Supplementary Fig. 6). The relationship between groundwater ages and travel distance from the recharge area implies accelerating flow drawn by increased Hanoi pumping (Supplementary Fig. 7). A simple transient flow model for the Van Phuc aquifer yields average advection rates of 38 m yr⁻¹ and 48 m yr⁻¹ towards Hanoi since 1951 and 1971, respectively (Supplementary Discussion). According to these two pumping scenarios,

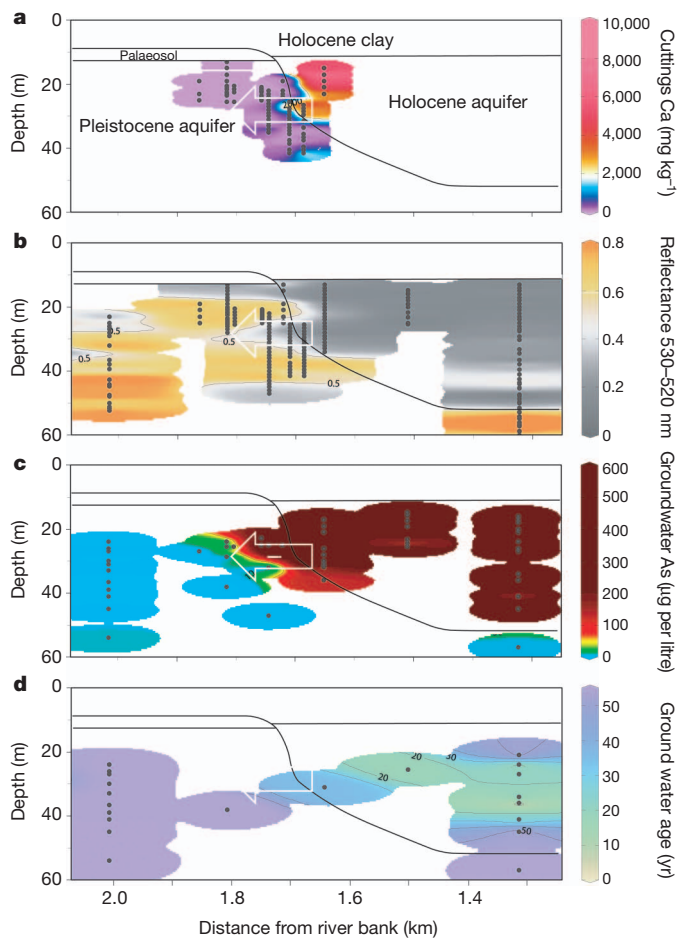


Figure 2 | Contoured sections of sediment and water properties based on data collected between 1.3 km and 2.0 km from the Red River bank. The location and number of samples indicated as black dots varies by type of measurement. **a**, Concentration of Ca in sand cuttings measured by X-ray fluorescence. Also shown are the boundaries separating the two main aquifers and the palaeosol overlying the Pleistocene aquifer. '2000' labels the contour for 2,000 mg Ca per kg. **b**, Difference in diffuse spectral reflectance between 530 nm and 520 nm, indicative of the colour of freshly collected drill cuttings¹³. The contour labels correspond to the percentage difference in reflectance shown by the colour scale. **c**, Concentrations of As in groundwater collected in 2006 with the needle sampler and in 2011 by monitoring wells along the transect. '10' labels the contour for the WHO guideline, 10 µg As per litre. **d**, Groundwater ages relative to recharge determined by ^3H - ^3He dating of groundwater samples collected from a subset of the monitoring wells in 2006. The portion of the Pleistocene aquifer that became reduced and where As concentrations presumably increased over time is located within the large white arrow pointing in the direction of flow. The plot was drawn with Ocean Data View (<http://odv.awi.de/>).

groundwater originating from the Holocene portion of the aquifer was transported 2,000–2,300 m into the Pleistocene sands by 2011, when the transect was sampled for analysis of As and other groundwater constituents.

The sharp decline in As concentrations between 1.60 km and 1.75 km from the river bank indicates that migration of the As front across the geological boundary was retarded by a factor of 16 to 20 relative to the movement of the groundwater (Fig. 3a). Without retardation, attributable to As adsorption onto aquifer sands, the entire Pleistocene aquifer of Van Phuc would already be contaminated. The retardation is derived from several decades of perturbation and is at the low end of previous estimates by other methods, typically measured within days to weeks^{17–22}, and therefore predicts greater As mobility than most previous studies. The retardation measured in Van Phuc integrates the effect of competing ions typically present at higher concentrations in the Holocene aquifer (Supplementary Fig. 4) as well as

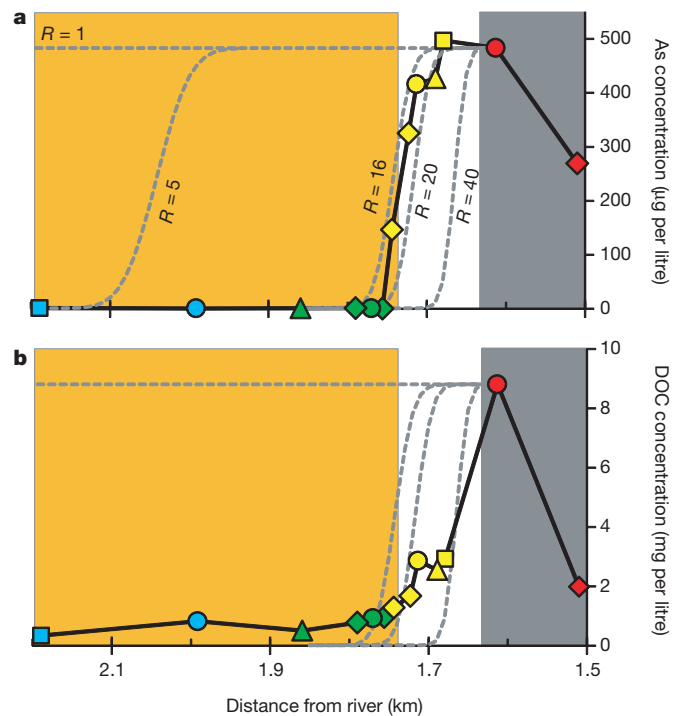


Figure 3 | Distribution of arsenic and dissolved organic carbon in groundwater within the 25–30-m depth interval along the Van Phuc transect. Symbols are coloured according to the classification in Fig. 1. Grey and orange shading indicates the extent of the grey Holocene aquifer and the portion of the Pleistocene aquifer that is still orange, respectively. The intermediate area without shading indicates the portion of the Pleistocene aquifer that became grey. Shown as dotted lines are predicted As concentrations bracketing the observations with retardation factors R of 16 and 20 and an average advection velocity of 43 m yr^{-1} over the 50 years preceding the 2011 sampling (Supplementary Discussion). **a**, Also shown are predicted concentrations for As assuming retardation factors of 1, 5 and 40 and the same average rate of advection. **b**, For visual reference, predicted dissolved organic carbon concentrations are shown as dotted lines according to the same advection velocity and retardation factors of 16, 20 and 40, assuming there was no detectable dissolved organic carbon in the Pleistocene aquifer before the perturbation.

the impact of Fe oxyhydroxide reduction. However, the extent to which contamination was caused by either As transport from the adjacent Holocene aquifer or reductive dissolution of Fe(III) oxyhydroxides and *in situ* As release to groundwater cannot be determined from the available data (Supplementary Fig. 8).

The sharp drop in dissolved organic carbon concentrations across the geological boundary from 9 mg per litre to about 1 mg per litre indicates rapid organic carbon mineralization coupled to the reduction of Fe(III) oxyhydroxides and explains the formation of a plume of grey sands within the Pleistocene aquifer (Fig. 3b). On the basis of a stoichiometric Fe/C ratio of 4 (ref. 15), the dissolved organic carbon supplied by flushing the aquifer 30 times with groundwater from the Holocene aquifer would be required to turn Pleistocene sands from orange to grey by reducing half of their 0.1% reactive Fe(III) oxyhydroxide content²³, assuming a porosity of 0.25. Given that groundwater was advected over a distance of 2,000–2,300 m across the geological boundary over the past 40–60 years, we would predict that the plume of grey sands extends 65–75 m into the Pleistocene aquifer. This is somewhat less than is observed (Fig. 3), possibly due to additional reduction by H_2 advected from the Holocene portion of the aquifer¹⁴. The Van Phuc observations indicate that dissolved organic carbon advected from a Holocene aquifer can be at least as important for the release of As to groundwater as autochthonous organic carbon^{12,24–27}.

Contamination of Pleistocene aquifers has previously been invoked in the Red River and the Bengal basins^{11,12,28}, but without the benefit of

a well-defined hydrogeological context. The Pleistocene aquifer of Van Phuc was contaminated under the conducive circumstances of accelerated lateral flow. Although downward groundwater flow and therefore penetration of As will typically be slower, the Van Phuc findings confirm that the vulnerability of Pleistocene aquifers will depend on the local spatial density of incised palaeo-channels that were subsequently filled with Holocene sediments¹². Owing to retardation, concentrations of As in a Pleistocene aquifer will not increase suddenly but over timescales of decades even in the close vicinity of a Holocene aquifer. This is consistent with the gradual increase in groundwater As concentrations documented by the few extended time series available from such a vulnerable setting²⁹. However, concentrations of As could rise more rapidly where flow accelerates beyond the rate documented in Van Phuc, closer to Hanoi for instance.

METHODS SUMMARY

A total of 41 wells were installed in Van Phuc in 2006–11. The water levels of the river and in the wells were recorded from September 2010 to June 2011 using pressure transducers and adjusted to the same elevation datum after barometric corrections. The magnitude and direction of the head gradient within the 25–30-m depth interval was calculated from water level measurements in three wells (Fig. 1b). In 2006, a subset of the wells was sampled for noble gas and tritium (³H) analysis at a high flow rate using a submersible pump to avoid degassing. The samples were analysed by mass spectrometry in the Noble Gas Laboratory at ETH Zurich. ³H concentrations were determined by the ³He ingrowth method³⁰. Groundwater As, Fe and Mn concentrations measured by high-resolution inductively coupled plasma mass spectrometry at LDEO represent the average for acidified samples collected in April and May 2012. Further details are provided in the Supplementary Information.

Full Methods and any associated references are available in the online version of the paper.

Received 17 December 2012; accepted 11 July 2013.

- Ravenscroft, P., Brammer, H. & Richards, K. *Arsenic Pollution: A Global Synthesis* (RGS-IBG Book Series, Wiley-Blackwell, 2009).
- BGS/DPHE (British Geological Survey, Department of Public Health Engineering) *Arsenic Contamination of Groundwater in Bangladesh* Final Report, <http://www.bgs.ac.uk/arsenic/bangladesh/> (British Geological Survey, 2001).
- Fendorf, S., Michael, H. A. & van Geen, A. Spatial and temporal variations of groundwater arsenic in south and southeast Asia. *Science* **328**, 1123–1127 (2010).
- Ahmed, M. F. *et al.* Epidemiology: ensuring safe drinking water in Bangladesh. *Science* **314**, 1687–1688 (2006).
- Berg, M. *et al.* Magnitude of arsenic pollution in the Mekong and Red River deltas—Cambodia and Vietnam. *Sci. Total Environ.* **372**, 413–425 (2007).
- Eiche, E. *et al.* Geochemical processes underlying a sharp contrast in groundwater arsenic concentrations in a village on the Red River delta, Vietnam. *Appl. Geochem.* **23**, 3143–3154 (2008).
- Funabiki, A., Haruyama, S., Quy, N. V., Hai, P. V. & Thai, D. H. Holocene delta plain development in the Song Hong (Red River) delta, Vietnam. *J. Asian Earth Sci.* **30**, 518–529 (2007).
- Larsen, F. *et al.* Controlling geological and hydrogeological processes in an arsenic contaminated aquifer on the Red River flood plain, Vietnam. *Appl. Geochem.* **23**, 3099–3115 (2008).
- Thu, T. M. & Fredlund, D. G. Modelling subsidence in the Hanoi City area, Vietnam. *Can. Geotech. J.* **37**, 621–637 (2000).
- Berg, M. *et al.* Hydrological and sedimentary controls leading to arsenic contamination of groundwater in the Hanoi area, Vietnam: the impact of iron-arsenic ratios, peat, river bank deposits, and excessive groundwater abstraction. *Chem. Geol.* **249**, 91–112 (2008).
- Winkel, L. H. E. *et al.* Arsenic pollution of groundwater in Vietnam exacerbated by deep aquifer exploitation for more than a century. *Proc. Natl Acad. Sci. USA* **108**, 1246–1251 (2011).
- McArthur, J. M. *et al.* How paleosols influence groundwater flow and arsenic pollution: a model from the Bengal Basin and its worldwide implication. *Wat. Resour. Res.* **44**, W11411 (2008).
- Horneman, A. *et al.* Decoupling of As and Fe release to Bangladesh groundwater under reducing conditions. Part I: evidence from sediment profiles. *Geochim. Cosmochim. Acta* **68**, 3459–3473 (2004).
- Postma, D. *et al.* Groundwater arsenic concentrations in Vietnam controlled by sediment age. *Nature Geosci.* **5**, 656–661 (2012).
- Postma, D. *et al.* Arsenic in groundwater of the Red River floodplain, Vietnam: controlling geochemical processes and reactive transport modeling. *Geochim. Cosmochim. Acta* **71**, 5054–5071 (2007).
- Kipfer, R., Aeschbach-Hertig, W., Peeters, F. & Stute, M. Noble gases in lakes and ground waters. *Rev. Mineral. Geochem.* **47**, 615–700 (2002).
- Stollenwerk, K. G. *et al.* Arsenic attenuation by oxidized aquifer sediments in Bangladesh. *Sci. Total Environ.* **379**, 133–150 (2007).
- van Geen, A. *et al.* Flushing history as a hydrogeological control on the regional distribution of arsenic in shallow groundwater of the Bengal Basin. *Environ. Sci. Technol.* **42**, 2283–2288 (2008).
- Nath, B. *et al.* Mobility of arsenic in the sub-surface environment: an integrated hydrogeochemical study and sorption model of the sandy aquifer materials. *J. Hydrol.* **364**, 236–248 (2009).
- Itai, T. *et al.* Variations in the redox state of As and Fe measured by X-ray absorption spectroscopy in aquifers of Bangladesh and their effect on As adsorption. *Appl. Geochem.* **25**, 34–47 (2010).
- Radloff, K. A. *et al.* Arsenic migration to deep groundwater in Bangladesh influenced by adsorption and water demand. *Nature Geosci.* **4**, 793–798 (2011).
- Jessen, S. *et al.* Surface complexation modeling of groundwater arsenic mobility: results of a forced gradient experiment in a Red River flood plain aquifer, Vietnam. *Geochim. Cosmochim. Acta* **98**, 186–201 (2012).
- Dhar, R. K. *et al.* Microbes enhance mobility of arsenic in Pleistocene aquifer sand from Bangladesh. *Environ. Sci. Technol.* **45**, 2648–2654 (2011).
- Islam, F. S. *et al.* Role of metal-reducing bacteria in arsenic release from Bengal delta sediments. *Nature* **430**, 68–71 (2004).
- Polizzotto, M. L., Kocar, B. D., Benner, S. B., Sampson, M. & Fendorf, S. Near-surface wetland sediments as a source of arsenic release to ground water in Asia. *Nature* **454**, 505–508 (2008).
- Neumann, R. B. *et al.* Anthropogenic influences on groundwater arsenic concentrations in Bangladesh. *Nature Geosci.* **3**, 46–52 (2010).
- Mailloux, B. J. *et al.* Advection of surface-derived organic carbon fuels microbial reduction in Bangladesh groundwater. *Proc. Natl Acad. Sci. USA* **110**, 5331–5335 (2013).
- Mukherjee, A. *et al.* Elevated arsenic in deeper groundwater of the western Bengal basin, India: extent and controls from regional to local scale. *Appl. Geochem.* **26**, 600–613 (2011).
- McArthur, J. M. *et al.* Migration of As, and ³H-³He ages, in groundwater from West Bengal: implications for monitoring. *Water Res.* **44**, 4171–4185 (2010).
- Beyerle, U. *et al.* A mass spectrometric system for the analysis of noble gases and tritium from water samples. *Environ. Sci. Technol.* **34**, 2042–2050 (2000).

Supplementary Information is available in the online version of the paper.

Acknowledgements This study was supported by NSF grant EAR 09-11557, the Swiss Agency for Development and Cooperation, grant NAFOSTED 105-09-59-09 to CETASD, and NIEHS grants P42 ES010349 and P42 ES016454. This is Lamont-Doherty Earth Observatory contribution number 7698.

Author Contributions A.v.G., M.B., P.T.K.T., P.O. and B.C.B. conceived the study. V.M.L., N.-N.M., P.D.M., P.T.K.T. and P.H.V. were responsible for organizing the field work and carrying out the monitoring throughout the study. K.R., Z.A. and B.W. participated in the field work in 2006. M.O.S. processed the hydrological data and carried out the flow modelling under the supervision of C.F.H. and P.O. J.L.M. was responsible for groundwater analyses at LDEO, C.S. for those at Eawag, and F.F. for noble gas measurements in R.K.'s laboratory. A.v.G. drafted the paper, which was then edited by all co-authors.

Author Information Reprints and permissions information is available at www.nature.com/reprints. The authors declare no competing financial interests. Readers are welcome to comment on the online version of the paper. Correspondence and requests for materials should be addressed to A.v.G. (avangeen@deo.columbia.edu).

METHODS

Drilling. A first set of 25 wells, including two nests of nine and ten wells tapping the depth range of the Holocene and Pleistocene aquifers, respectively, were installed in Van Phuc in 2006 (ref. 6). Another 16 monitoring wells were installed between December 2009 and November 2011. Three additional holes were drilled to collect cuttings without installing a well. All holes were drilled by flushing the hole with water through a rotating drill bit.

Needle sampling. In 2006, drilling was briefly interrupted at seven sites to increase the vertical resolution of both sediment and groundwater data using the needle sampler³¹. Groundwater was pressure-filtered under nitrogen directly from the sample tubes. As a measure of the pool of mobilizable As, sediment collected with the needle sampler was subjected to a single 24-hour extraction in a 1 M PO₄ solution at pH 5 (ref. 32).

Water level measurements. A theodolite elevation survey of the well and river measurement points were carried out in June 2010 by a surveying team from Hanoi University of Science. Water level data in both the wells and river were recorded using Solinst Levellogger pressure transducers. A barometric pressure logger was also deployed at the field site. Water level and barometric data were recorded at 5-min intervals and all water level data was barometrically corrected. The barometrically corrected water level data from each logger was then adjusted to the surveyed elevation of their respective measurement point so that all of the data was referenced to the same elevation datum.

Groundwater flow. The magnitude and direction of the head gradient within the 25–30-m depth of the aquifer at Van Phuc was calculated using the barometrically adjusted and survey-referenced water level data collected at 5-min intervals from September 2010 to June 2011 in three wells located near the centre of the transect (Fig. 1b). A least-squares fit of a plane was calculated for each set of simultaneous water levels at these three wells, and from this set of planes the magnitude and direction of the head gradient at 5-min intervals was directly computed.

Groundwater analysis. In 2006, a subset of the monitoring wells was sampled along a vertical transect for noble gas and tritium (³H) analysis. After purging the wells, the samples were taken using a submersible pump. To avoid degassing of the groundwater owing to bubble formation during sampling the water was pumped at high rates to maintain high pressure. The samples for noble gas and ³H analysis were put into copper tubes and sealed gastight using pinch-off clamps. All samples were analysed for noble gas concentrations and the isotope ratios ³He/⁴He, ²⁰Ne/²²Ne and ³⁶Ar/⁴⁰Ar using noble gas mass spectrometry in the Noble Gas Laboratory at ETH Zurich^{30,33}. ³H concentrations were determined by the ³He ingrowth method using a high-sensitivity compressor-source noble gas mass spectrometer. ³H–³He ages were calculated according to the equations listed in ref. 34, taking into account an excess air correction. When comparing the reconstructed original ³H content of each sample as a function of ³H–³He age with the ³H input function for south and southeast Asia (Supplementary Fig. 5), most samples follow the trend expected from simple plug flow^{34,35}.

Several days before analysis by high-resolution inductively coupled plasma mass spectrometry at LDEO, groundwater was acidified to 1% Optima HCl in the laboratory³⁶. This has been shown to re-dissolve entirely any precipitates that could have formed³⁷. In most cases, the difference between duplicates was within the analytical uncertainty of ~5%. With the exception of needle-sample data and the nest of ten wells in the Holocene portion of the aquifer, which had to yield to

construction, groundwater As, Fe and Mn concentrations reported here represent the average for samples collected without filtration in April and May 2012. Groundwater data from 2006 were previously reported in refs 6 and 31.

Dissolved organic carbon samples were collected in 25-ml glass vials combusted overnight at 450 °C and acidified to 1% HCl at the time of collection. Dissolved inorganic carbon samples were also collected in 25-ml glass vials with a Teflon septum but were not acidified. Both dissolved organic carbon (“NPOC”) and dissolved inorganic carbon (by difference of “TC-NPOC”) were analysed on a Shimadzu TOC-V carbon analyser calibrated with K phthalate standards.

Ammonium samples were collected in polypropylene bottles after passing through 0.45 µm cellulose acetate membrane filters and preserved by acidifying to pH < 2 with HNO₃. NH₄⁺ concentrations were analysed on a spectrophotometer (UV-3101, Shimadzu) at a wavelength of 690 nm after forming a complex with nitroferriicyanide³⁸.

Methane (CH₄) samples were filled up to about half of the pre-vacuumed glass vials and immediately frozen in dry ice. The analyses were performed no longer than ten days after sampling. Headspace CH₄ in the vials was measured on a Shimadzu 2014 gas chromatograph with a Porapak T packed column¹⁴.

Sediment analysis. As a measure of the redox state of Fe in acid-leachable oxyhydroxides, the diffuse spectral reflectance spectrum of cuttings from all sites was measured on samples wrapped in Saran wrap and kept out of the sun within 12 hours of collection using a Minolta 1600D instrument¹³. Starting in 2009, the coarse fractions of the drill cuttings were analysed by X-ray fluorescence for a suite of elements including Ca using an InnovX Delta instrument. The drill cuttings were resuspended in water several times to eliminate the overprint of Ca-enriched clays contained in the recycled water used for drilling. The washed samples were run as is, without drying or grinding to powder. Analyses of NIST reference material SRM2711 (28,800 ± 800 mg Ca per kg) analysed by X-ray fluorescence at the beginning and end of each run averaged 30,200 ± 400 mg Ca per kg (*n* = 16).

31. van Geen, A. *et al.* Comparison of arsenic concentrations in simultaneously-collected groundwater and aquifer particles from Bangladesh, India, Vietnam, and Nepal. *Appl. Geochem.* **23**, 3244–3251 (2008).
32. Zheng, Y. *et al.* Geochemical and hydrogeological contrasts between shallow and deeper aquifers in two villages of Araihaazar, Bangladesh: implications for deeper aquifers as drinking water sources. *Geochim. Cosmochim. Acta* **69**, 5203–5218 (2005).
33. Frei, F. Groundwater dynamics and arsenic mobilization near Hanoi (Vietnam) assessed using noble gases and tritium. Diploma thesis, ETH Zurich (2007).
34. Klump, S. *et al.* Groundwater dynamics and arsenic mobilization in Bangladesh assessed using noble gases and tritium. *Environ. Sci. Technol.* **40**, 243–250 (2006).
35. Stute, M. *et al.* Hydrological control of As concentrations in Bangladesh groundwater. *Wat. Resour. Res.* **43**, W09417 (2007).
36. Cheng, Z., Zheng, Y., Mortlock, R. & van Geen, A. Rapid multi-element analysis of groundwater by high-resolution inductively coupled plasma mass spectrometry. *Anal. Bioanal. Chem.* **379**, 512–518 (2004).
37. van Geen, A. *et al.* Monitoring 51 deep community wells in Araihaazar, Bangladesh, for up to 5 years: implications for arsenic mitigation. *J. Environ. Sci. Health A* **42**, 1729–1740 (2007).
38. Koroleff, F. In *Methods of Seawater Analysis* (ed. Grasshoff, K.) 126–133 (Chemie, 1974).

Non-chondritic sulphur isotope composition of the terrestrial mantle

J. Labidi¹, P. Cartigny¹ & M. Moreira²

Core-mantle differentiation is the largest event experienced by a growing planet during its early history. Terrestrial core segregation imprinted the residual mantle composition by scavenging siderophile (iron-loving) elements such as tungsten, cobalt and sulphur. Cosmochemical constraints suggest that about 97% of Earth's sulphur should at present reside in the core¹, which implies that the residual silicate mantle should exhibit fractionated $^{34}\text{S}/^{32}\text{S}$ ratios according to the relevant metal-silicate partition coefficients², together with fractionated siderophile element abundances. However, Earth's mantle has long been thought to be both homogeneous and chondritic for $^{34}\text{S}/^{32}\text{S}$, similar to Canyon Diablo troilite^{3–6}, as it is for most siderophile elements. This belief was consistent with a mantle sulphur budget dominated by late-accreted chondritic components. Here we show that the mantle, as sampled by mid-ocean ridge basalts from the south Atlantic ridge, displays heterogeneous $^{34}\text{S}/^{32}\text{S}$ ratios, directly correlated to the strontium and neodymium isotope ratios $^{87}\text{Sr}/^{86}\text{Sr}$ and $^{143}\text{Nd}/^{144}\text{Nd}$. These isotope trends are compatible with binary mixing between a low- $^{34}\text{S}/^{32}\text{S}$ ambient mantle and a high- $^{34}\text{S}/^{32}\text{S}$ recycled component that we infer to be subducted sediments. The depleted end-member is characterized by a significantly negative $\delta^{34}\text{S}$ of $-1.28 \pm 0.33\text{‰}$ that cannot reach a chondritic value even when surface sulphur (from continents, altered oceanic crust, sediments and oceans) is added. Such a non-chondritic $^{34}\text{S}/^{32}\text{S}$ ratio for the silicate Earth could be accounted for by a core-mantle differentiation record in which the core has a $^{34}\text{S}/^{32}\text{S}$ ratio slightly higher than that of chondrites ($\delta^{34}\text{S} = +0.07\text{‰}$). Despite evidence for late-veener addition of siderophile elements (and therefore sulphur) after core formation, our results imply that the mantle sulphur budget retains fingerprints of core-mantle differentiation.

Earlier reports of mid-ocean ridge basalts (MORBs) $\delta^{34}\text{S}$ (where $\delta^{34}\text{S} = [(^{34}\text{S}/^{32}\text{S})_{\text{sample}} / (^{34}\text{S}/^{32}\text{S})_{\text{CDT}} - 1] \times 1,000$ and CDT is Canyon Diablo troilite) yielded values statistically indistinguishable from the reported chondrite average of $0.04 \pm 0.31\text{‰}$ (refs 3–6), consistent with a late-veener origin for sulphur in the mantle. This view has been recently questioned in a study using improved sulphur-extraction techniques⁷. Worldwide MORBs exhibit exclusively negative $\delta^{34}\text{S}$ ranging down to -1.9‰ , with an approximately 2‰ variability⁷. These observations raise questions as to whether the terrestrial mantle is chondritic in sulphur isotopes, but the mechanisms controlling MORB $^{34}\text{S}/^{32}\text{S}$ variability remain unclear.

To address these issues, we investigated the sulphur isotope composition of 23 glasses dredged on the South Atlantic ridge between 40° and 55° S. Previous radiogenic isotopes^{8–10}, noble gases^{11,12}, volatiles¹³, major-element¹⁴ and trace-element¹⁵ measurements on these basalts illustrate interactions of the Shona–Discovery hotspots with the ridge. Several of the typical mantle end-members feed the mantle source of the two plumes, including HIMU ('high- μ ' where $\mu = ^{238}\text{U}/^{204}\text{Pb}$), LOMU ('low- μ '), and enriched-mantle components. The samples analysed were chosen to reflect this geochemical variability and thus offer an opportunity to address $^{34}\text{S}/^{32}\text{S}$ variations with respect to these mantle heterogeneities.

In our samples, sulphur occurs only in its reduced form, as commonly found in MORBs^{16–18}, and the sulphur content, from 642 to 1,388 parts per million (p.p.m.), correlates with the FeO content (Supplementary Fig. 3A), illustrating magmatic sulphide saturation¹⁶. The eruption depth of our samples precludes any significant sulphur degassing¹⁹, restricting the sulphur isotope discussion to primary magmatic considerations. $\delta^{34}\text{S}$ varies between -1.80‰ and $+1.05\text{‰}$, whereas both the quantifying mass-independent signatures $\Delta^{33}\text{S}$ and $\Delta^{36}\text{S}$ (where $\Delta^{33}\text{S} = \delta^{33}\text{S} - 1,000 \times [(\delta^{34}\text{S}/1,000 + 1)^{0.515} - 1]$ and $\Delta^{36}\text{S} = \delta^{36}\text{S} - 1,000 \times [(\delta^{34}\text{S}/1,000 + 1)^{1.889} - 1]$), are homogeneous and equal within uncertainty to those of Canyon Diablo troilite (Supplementary Table 1). Besides, $\delta^{34}\text{S}$ is remarkably correlated to source enrichment proxies such as $^{87}\text{Sr}/^{86}\text{Sr}$ or $^{143}\text{Nd}/^{144}\text{Nd}$ (Fig. 1). Seawater sulphate ($\delta^{34}\text{S} = +21\text{‰}$) assimilation by erupted basalts could result in an increase in $\delta^{34}\text{S}$; it would, however, scatter or erase any correlations between $\delta^{34}\text{S}$ and tracers that remain insensitive to seawater incorporation (such as $^{143}\text{Nd}/^{144}\text{Nd}$). It would also result in a relationship between $\delta^{34}\text{S}$ and proxies of seawater incorporation such as chlorine contents or Cl/K ratios, which is again not the case (Supplementary Fig. 4). Correlated $\delta^{34}\text{S}$ and radiogenic isotope enrichments thus reflect the variability of the MORB sources.

All the samples are saturated with immiscible sulphide¹⁶, and the extremely low osmium contents in the most primitive MORBs probably indicates that they were already sulphide-saturated during melting¹⁰. Such a saturation mechanism prevents us from constraining the sulphur contents of the mantle source, and because the fractionation factor between dissolved sulphur and magmatic sulphide might be significant, it raises the question of whether basalts can preserve the $^{34}\text{S}/^{32}\text{S}$ ratios of their mantle source. Those basalts investigated have such distinct differentiation and melting histories^{14,15} that the amount of sulphide left during both melting and differentiation is variable^{10,16}. If the high-temperature sulphur isotope fractionation during magmatic sulphide exsolution were significant, it would have erased the observed $\delta^{34}\text{S}$ – $^{87}\text{Sr}/^{86}\text{Sr}$ – $^{143}\text{Nd}/^{144}\text{Nd}$ trends (Fig. 1). The lack of correlation between $\delta^{34}\text{S}$ and sulphide segregation proxies indicates a fractionation factor, $\alpha_{\text{sulph-melt}}$, of between 1.0000 and 0.9995 ± 0.0005 , at most (Supplementary Information). The $\delta^{34}\text{S}$ of basalts hence provides direct information on mantle source composition, here displaying an average value of $-0.80 \pm 0.58\text{‰}$ (1σ).

The most ^{34}S -depleted samples correspond to depleted MORB and ^{34}S -enriched samples are related to the Discovery plume, whereas the Shona and LOMU basalts are of intermediate composition. Interestingly, samples from Shona and Discovery display similar $^3\text{He}/^4\text{He}$ and $^{21}\text{Ne}/^{22}\text{Ne}$ (refs 11 and 12) but have different ^{34}S enrichments, suggesting that these isotopic systems are decoupled. Such a lack of correlation between noble gases and S isotopes suggests that the primitive mantle is sulphur-poor compared to the recycled components. Hence, characterization of the primordial sulphur cannot be directly achieved from the present data set.

Our results can be explored in two ways. First, the south Atlantic depleted mantle has an average $\delta^{34}\text{S}$ of $-1.28 \pm 0.33\text{‰}$ (error is 1σ ,

¹Laboratoire de Géochimie des Isotopes Stables, Institut de Physique du Globe de Paris, Sorbonne Paris Cité, Université Paris Diderot, UMR 7154 CNRS, 1 rue Jussieu, 75005 Paris, France. ²Laboratoire de Géochimie et Cosmochimie, Institut de Physique du Globe de Paris, Sorbonne Paris Cité, Université Paris Diderot, UMR 7154 CNRS 1 rue Jussieu, 75005 Paris, France.

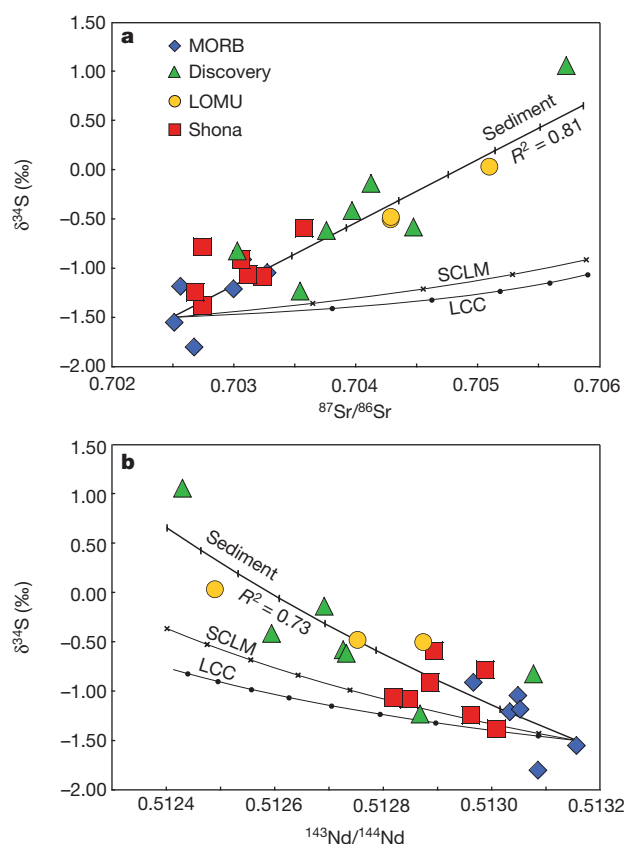


Figure 1 | $\delta^{34}\text{S}$ versus $^{87}\text{Sr}/^{86}\text{Sr}$ and $^{143}\text{Nd}/^{144}\text{Nd}$. Strontium and neodymium isotope data are from ref. 8. Sulphur-isotope uncertainties are estimated on the basis of replicate analysis for all samples, and are all within symbol sizes. The samples define a binary mixing relationship between a depleted-mantle and an enriched-mantle endmember. Mixing trends with sub-continental lithospheric mantle (SCLM) and lower continental crust (LCC) are also shown, illustrating that mixing with sediments account better for the geochemical composition of our samples. **a**, $\delta^{34}\text{S}$ versus $^{87}\text{Sr}/^{86}\text{Sr}$. **b**, $\delta^{34}\text{S}$ versus $^{143}\text{Nd}/^{144}\text{Nd}$. $\delta^{34}\text{S}$ is defined in the main text; the CDT standard is used. R , correlation coefficient. Data used for the mixing calculation is as follows, from refs 22–27 and Supplementary ref. 37. For depleted mantle, $\delta^{34}\text{S} = -1.5\text{‰}$, $^{87}\text{Sr}/^{86}\text{Sr} = 0.7025$, $^{143}\text{Nd}/^{144}\text{Nd} = 0.513156$, $\text{Sr} = 11.3$ p.p.m., $\text{Nd} = 1.12$ p.p.m. and $\text{S} = 200$ p.p.m. For LCC, $\delta^{34}\text{S} = +3\text{‰}$, $^{87}\text{Sr}/^{86}\text{Sr} = 0.7080$, $^{143}\text{Nd}/^{144}\text{Nd} = 0.511600$, $\text{Sr} = 348$ p.p.m., $\text{Nd} = 11$ p.p.m. and $\text{S} = 408$ p.p.m. For SCLM, $\delta^{34}\text{S} = +3\text{‰}$, $^{87}\text{Sr}/^{86}\text{Sr} = 0.7100$, $^{143}\text{Nd}/^{144}\text{Nd} = 0.511663$, $\text{Sr} = 49$ p.p.m., $\text{Nd} = 2.67$ p.p.m. and $\text{S} = 157$ p.p.m. For the sediment, $\delta^{34}\text{S} = +10\text{‰}$, $^{87}\text{Sr}/^{86}\text{Sr} = 0.7203$, $^{143}\text{Nd}/^{144}\text{Nd} = 0.511170$, $\text{Sr} = 327$ p.p.m., $\text{Nd} = 27$ p.p.m. and $\text{S} = 5,700$ p.p.m. Markers on the fits are separated by 0.1%, 1.0% and 4.0% for sediment, LCC and SCLM, respectively.

$n = 6$), defining a mean value consistently distinct from chondrites. We note that an extrapolation of Sr–Nd–S isotope trends to most depleted compositions would lead to a depleted-mantle endmember as low as -1.80‰ (Fig. 1). Second, the nature of classical mantle endmembers can be addressed. Whereas it is commonly accepted that HIMU features reflect the occurrence of subducted oceanic crust in plume sources²⁰, the enriched-mantle and LOMU cases remain much debated. In the south Atlantic mantle, a significant contribution of continental material has been invoked to account for the LOMU endmember, including either delaminated subcontinental lithospheric mantle^{8,9} or lower continental crust¹⁰. In S–Sr and S–Nd isotope spaces, however, the samples lie on a linear trend regardless of their locations or type of anomalies (Fig. 1), highlighting binary mixing between depleted mantle ($\delta^{34}\text{S} = -1.28\text{‰}$ or lower) and the enriched-mantle-type endmember ($\delta^{34}\text{S} = +1.05\text{‰}$ or higher).

Both LOMU basalts (having the lowest $^{206}\text{Pb}/^{204}\text{Pb}$) and Shona samples (HIMU-type⁸, having the highest $^{206}\text{Pb}/^{204}\text{Pb}$) cannot be distinguished from the other samples in the observed trends (Fig. 1). This

lack of correlation between $\delta^{34}\text{S}$ and $^{206}\text{Pb}/^{204}\text{Pb}$ (Supplementary Fig. 5), together with the preservation of the trends between $\delta^{34}\text{S}$ and Sr–Nd isotopes, argue in favour of relatively sulphur-poor HIMU and LOMU endmembers, overprinted by the contribution of a sulphur-rich enriched-mantle component. In this view, recycled oceanic crust carrying the radiogenic $^{206}\text{Pb}/^{204}\text{Pb}$ ratio is inferred to be relatively sulphur-depleted, consistent with its required high U/Pb. Sulphides are indeed the main Pb carrier in the oceanic crust²¹ and any Pb loss along subduction should occur through a concomitant sulphur loss.

The mixing trends being linear, the enriched-mantle component must be enriched in sulphur in the same way as it is enriched in strontium and neodymium. This allows a reliable estimate of its S/Sr and S/Nd, broadly equal to that of the depleted mantle. For simplicity, only the S/Sr ratio is used in the following. Taking 200 ± 40 p.p.m. (ref. 22) for sulphur and 11.3 p.p.m. (ref. 15) for strontium in depleted mantle, we obtain an S/Sr value for enriched mantle of 17 ± 4 . Both delaminated lithospheric mantle and lower continental crust have been suggested to account for enriched-mantle-type signals, especially in south Atlantic basalts^{8–10}. These reservoirs are, however, relatively sulphur-poor compared to incompatible trace elements, yielding S/Sr ratios of 3.2 ± 2.0 (ref. 23) and 0.8 ± 0.3 (ref. 24), respectively, that are low compared to the required value of 17 ± 4 (see above). Any occurrence of such a component in the south Atlantic mantle would have led to highly curved mixing relationships in S–Sr isotope space, especially given the range of $^{87}\text{Sr}/^{86}\text{Sr}$ displayed by the samples (Fig. 1a).

Alternatively, sediment may be a good candidate: sediments are enriched in trace elements²⁵ and can bear significant amounts of sulphur. In particular, many sediments deposited one to two billion years ago during the Proterozoic eon formed under reduced conditions and usually contain more than 1% of sulphur pyrite²⁶. A subducted sediment containing a realistic sulphur content of $5,700 \pm 1,000$ p.p.m. would satisfy the S/Sr of the enriched-mantle component. The fact that our estimate for recycled sediment falls within large uncertainties of non-subducted sediments suggests only moderate devolatilization, if any, during recycling (Supplementary Information). The best fits to our data are obtained for sediment having a $\delta^{34}\text{S}$ of $+10 \pm 3\text{‰}$, consistent with sediments one to two billion years old with an average $\delta^{34}\text{S}$ of $+5 \pm 10\text{‰}$ (ref. 27). This Proterozoic age for subducted sediments is also consistent with the observed lack of $\Delta^{33}\text{S}$ variability²⁸ best-fitted with a $\Delta^{33}\text{S}$ of $+0.06 \pm 0.03\text{‰}$ (Supplementary Fig. 6).

If subducted sediments are major ^{34}S carriers to the deep mantle, the depleted mantle is shown here to be significantly ^{34}S -depleted with respect to chondrites. This low $^{34}\text{S}/^{32}\text{S}$ ratio has fundamental implications for our understanding of the origin and processes affecting moderately volatile elements in the terrestrial mantle. In the following, we use the $-1.28 \pm 0.33\text{‰}$ depleted MORB average as the representative $\delta^{34}\text{S}$ of the depleted mantle, but further studies are needed to refine this value. Such a negative estimate allows us to discard a purely late-vener origin for sulphur in the mantle, because this scenario requires a strictly chondritic $^{34}\text{S}/^{32}\text{S}$ ratio for depleted mantle. According to the kinetic theory of gases, partial evaporation of sulphur during accretion could have modified the $^{34}\text{S}/^{32}\text{S}$ ratio of the accreted Earth, leaving the residual terrestrial mantle enriched in ^{34}S relative to chondrites. This would be at odds with the observed depletion in ^{34}S . Finally, assuming that the depleted mantle represents 25%–80% of the whole mantle²⁹, the complementary surface reservoirs (continents, oceans and altered oceanic crust) would need to have an average $\delta^{34}\text{S}$ of between $+8\text{‰}$ and $+25\text{‰}$ to balance the non-chondritic $\delta^{34}\text{S}$ of the depleted mantle. Current estimates, however, yield average $\delta^{34}\text{S}$ values of $-0.4 \pm 3.0\text{‰}$ (ref. 30) for the bulk surface reservoirs, a value that is far from being reconcilable with the above requirement, and emphasizing the non-chondritic character of the bulk silicate Earth.

In contrast to immiscible sulphide exsolution, sulphur dissolution into metal from silicate could fractionate the $^{34}\text{S}/^{32}\text{S}$ ratio owing to the distinct molecular environment of sulphur in a silicate versus a metallic liquid (and distinct vibrational partition functions). One likely possibility

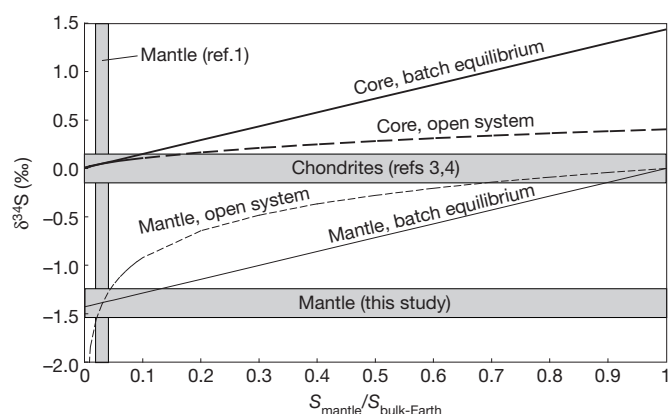


Figure 2 | Core-mantle sulphur partitioning model in batch equilibrium or open system. The $\delta^{34}\text{S}$ of the mantle is plotted against the sulphur content of the mantle S_{mantle} divided by the sulphur content of the bulk Earth $S_{\text{bulk-Earth}}$. According to ref. 1, S_{mantle} represents less than 3% of $S_{\text{bulk-Earth}}$. The sulphur isotope composition of chondrites (refs 3 and 4) and mantle (this study) values are both plotted, allowing a clear visualization of the sulphur isotope shift between these two reservoirs. Sulphur isotope and sulphur abundance observations coincide at an anchor point constraining the core-mantle fractionation. Under batch equilibrium, core $\delta^{34}\text{S}$ is +1.26‰ higher than the silicate value ($\alpha_{\text{core-mantle}} = 1.00130$). In an open system model, the core is treated as a cumulative product and $\alpha_{\text{core-mantle}}$ of 1.00035 is sufficient to explain the shift between mantle and chondrites.

involves the dissolution of sulphur in its metallic form (S^0) in the core, given that stable isotope fractionation theory predicts the more oxidized compound to be ^{34}S -enriched compared to sulphur dissolved as S^{2-} in the silicate mantle. The $\alpha_{\text{core-mantle}}$ can be inferred from a chondritic bulk Earth (that is, mantle and core) by combining the distribution of sulphur in the bulk Earth (ref. 1) and the re-evaluated $^{34}\text{S}/^{32}\text{S}$ of the mantle (this study), leading to a $\alpha_{\text{core-mantle}}$ of 1.00130 for a batch-equilibrium or 1.00035 for an open-system sulphur incorporation into the core (Fig. 2). In all cases, the core $\delta^{34}\text{S}$ is expected to be +0.07‰, almost indistinguishable from that of chondrites and iron meteorites, because this reservoir would contain most of the terrestrial sulphur¹.

Only Shahar *et al.*² experimentally addressed the $^{34}\text{S}/^{32}\text{S}$ fractionation between metal and silicate at high temperature, and estimated a $\alpha_{\text{core-mantle}}$ of 1.00220 ± 0.0014 at 1,850 °C (ref. 2). For 97% of the sulphur occurring in the core¹, such an estimate should lead to a mantle $\delta^{34}\text{S}$ of -2.10 ± 1.40 ‰, under batch-equilibrium fractionation. This value, despite a significant overlap, seems slightly lower than our observation. Because stable isotope fractionations scale with temperature T as $1/T^2$, such distinct estimates could reflect a core segregation occurring at a temperature higher than 1,850 °C: the average temperature for core-mantle segregation remains highly debated, with values up to 3,300 °C (ref. 31). Alternatively, such a distinction may require the involvement of 'hybrid models', as suggested for highly siderophile elements³¹, in which a fraction of the mantle sulphur is a fractionated leftover from core-mantle equilibrium, whereas the other fraction would have been delivered during the late-accretionary stage. For a $\alpha_{\text{core-mantle}}$ of 1.00220 (ref. 2), the proportion of late-accreted sulphur (that is, with chondritic $^{34}\text{S}/^{32}\text{S}$) in the mantle would reach approximately 40% of mantle sulphur, after batch-equilibrium core segregation.

At that stage, the most obvious implication of such a core-mantle differentiation record is that sulphur and elements of comparable volatilities (such as zinc, fluorine and lead) must have been present to some extent before the late-accretion event. This is a robust and independent constraint that will help to build more consistent models of timing for the origin of moderately volatile elements in Earth's mantle.

METHODS SUMMARY

Samples were analysed following the protocol described in ref. 7. Glassy rims of basalts were handpicked under a binocular microscope and if needed, cleaned

through a sonication in 99.9% ethanol. For each sample, about 300 mg was crushed to a fine powder (<100 µm) and dissolved in a 29 N HF + 2.1 M CrCl_3 solution. Under these conditions, sulphur is released as H_2S and subsequently trapped as precipitated Ag_2S . Sulphur extraction yields are $101 \pm 4\%$ for the 23 samples analysed in this study.

Weighed aliquots of silver sulphide were wrapped in aluminium foil and placed in Ni-reaction bombs for fluorination with purified F_2 at 250 °C overnight. The SF_6 produced was then purified using both cryogenic separation and gas chromatography. The purified SF_6 was then quantified and analysed using a dual-inlet ThermoFinnigan MAT 253 mass spectrometer where $m/z = 127^+$, 128^+ , 129^+ and 131^+ ion beams are monitored. All the samples were replicated, yielding a ± 0.1 , ± 0.005 and $\pm 0.1\%$ uncertainty for $\delta^{34}\text{S}$, $\Delta^{33}\text{S}$ and $\Delta^{36}\text{S}$, respectively, consistent with the basalt internal standards processed in ref. 7.

Online Content Any additional Methods, Extended Data display items and Source Data are available in the online version of the paper; references unique to these sections appear only in the online paper.

Received 25 April; accepted 18 July 2013.

Published online 4 September 2013.

- Dreibus, G. & Palme, H. Cosmochemical constraints on the sulfur content in the Earth's core. *Geochim. Cosmochim. Acta* **60**, 1125–1130 (1996).
- Shahar, A., Fei, Y., Liu, M. C. & Wang, J. Sulfur isotopic fractionation during the differentiation of Mars. *Geochim. Cosmochim. Acta* **73** (Suppl.), A1201 (2009).
- Gao, X. & Thiemens, M. Isotopic composition and concentration of sulfur in carbonaceous chondrites. *Geochim. Cosmochim. Acta* **57**, 3159–3169 (1993).
- Gao, X. & Thiemens, M. Variations of the isotopic composition of sulfur in enstatite and ordinary chondrites. *Geochim. Cosmochim. Acta* **57**, 3171–3176 (1993).
- Sakai, H., Marais, D. J., Ueda, A. & Moore, J. G. Concentrations and isotope ratios of carbon, nitrogen and sulfur in ocean-floor basalts. *Geochim. Cosmochim. Acta* **48**, 2433–2441 (1984).
- Chaussidon, M., Sheppard, S. M. F. & Michard, A. Hydrogen, sulphur and neodymium isotope variations in the mantle beneath the EPR at 12°50'N. *J. Geochem. Soc.* **3**, 325–337 (1991).
- Labidi, J., Cartigny, P., Birck, J. L., Assayag, N. & Bourrand, J. J. Determination of multiple sulfur isotopes in glasses: a reappraisal of the MORB $\delta^{34}\text{S}$. *Chem. Geol.* **334**, 189–198 (2012).
- Douglass, J., Schilling, J. G. & Fontignie, D. Plume-ridge interactions of the Discovery and Shona mantle plumes with the southern Mid-Atlantic Ridge (40°–55°S). *J. Geophys. Res.* **104**, 2941–2962 (1999).
- Andres, M., Blichert-Toft, J. & Schilling, J. G. Hafnium isotopes in basalts from the southern Mid-Atlantic Ridge from 40°S to 55°S: discovery and Shona plume-ridge interactions and the role of recycled sediments. *Geochem. Geophys. Geosyst.* **3**, 1–25 (2002).
- Escrig, S., Schiano, P., Schilling, J. G. & Allègre, C. Rhenium-osmium isotope systematics in MORB from the Southern Mid-Atlantic Ridge (40°–50°S). *Earth Planet. Sci. Lett.* **235**, 528–548 (2005).
- Moreira, M., Staudacher, T., Sarda, P., Schilling, J. G. & Allègre, C. J. A primitive plume neon component in MORB: the Shona ridge-anomaly, South Atlantic (51°–52°S). *Earth Planet. Sci. Lett.* **133**, 367–377 (1995).
- Sarda, P., Moreira, M., Staudacher, T., Schilling, J. G. & Allègre, C. J. Rare gas systematics on the southernmost Mid-Atlantic Ridge: constraints on the lower mantle and the Dupal source. *J. Geophys. Res.* **105**, 5973–5996 (2000).
- Dixon, J. E., Leist, L., Langmuir, C. & Schilling, J. G. Recycled dehydrated lithosphere observed in plume influenced mid-ocean-ridge basalt. *Nature* **420**, 385–389 (2002).
- le Roux, P. J., le Roex, A. P. & Schilling, J. G. MORB melting processes beneath the southern Mid-Atlantic Ridge (40°–55°S): a role for mantle plume-derived pyroxenite. *Contrib. Mineral. Petrol.* **144**, 206–229 (2002).
- le Roux, P. J. *et al.* Mantle heterogeneity beneath the southern Mid-Atlantic Ridge: trace element evidence for contamination of ambient asthenospheric mantle. *Earth Planet. Sci. Lett.* **203**, 479–498 (2002).
- Mathez, E. A. Sulfur solubility and magmatic sulfides in submarine basalt glass. *J. Geophys. Res.* **81**, 4269–4276 (1976).
- Wallace, P. & Carmichael, I. S. E. Sulfur in basaltic magmas. *Geochim. Cosmochim. Acta* **56**, 1863–1874 (1992).
- Métrich, N., Berry, A. J., O'Neill, H. S. C. & Susini, J. The oxidation state of sulfur in synthetic and natural glasses determined by X-ray absorption spectroscopy. *Geochim. Cosmochim. Acta* **73**, 2382–2399 (2009).
- Dixon, J. E., Clague, D. A. & Stolper, E. M. Degassing history of water, sulfur, and carbon in submarine lavas from Kilauea Volcano, Hawaii. *J. Geol.* **99**, 371–394 (1991).
- Cabral, R. A. *et al.* Anomalous sulphur isotopes in plume lavas reveal deep mantle storage of Archaean crust. *Nature* **496**, 490–493 (2013).
- Kelley, K., Plank, T., Ludden, J. & Staudigel, H. Composition of altered oceanic crust at ODP Sites 801 and 1149. *Geochem. Geophys. Geosyst.* **4**, 8910 (2003).
- O'Neill, H. S. C. The origin of the Moon and the early history of the Earth—a chemical model. Part 2: The Earth. *Geochim. Cosmochim. Acta* **55**, 1159–1172 (1991).
- McDonough, W. F. Constraints on the composition of the continental lithospheric mantle. *Earth Planet. Sci. Lett.* **101**, 1–18 (1990).
- Rudnick, R. L. & Gao, S. Composition of the continental crust. *Treat. Geochem.* **3**, 1–64 (2003).

25. Plank, T. & Langmuir, C. H. The chemical composition of subducting sediment and its consequences for the crust and mantle. *Chem. Geol.* **145**, 325–394 (1998).
26. Poulton, S. W., Fralick, P. W. & Canfield, D. E. The transition to a sulphidic ocean 1.84 billion years ago. *Nature* **431**, 173–177 (2004).
27. Canfield, D. E. & Farquhar, J. Animal evolution, bioturbation, and the sulfate concentration of the oceans. *Proc. Natl Acad. Sci. USA* **106**, 8123–8127 (2009).
28. Farquhar, J., Bao, H. & Thiemens, M. Atmospheric influence of Earth's earliest sulfur cycle. *Science* **289**, 756–758 (2000).
29. Caro, G. & Bourdon, B. Non-chondritic Sm/Nd ratio in the terrestrial planets: consequences for the geochemical evolution of the mantle–crust system. *Geochim. Cosmochim. Acta* **74**, 3333–3349 (2010).
30. Wedepohl, K. H. The composition of the continental crust. *Geochim. Cosmochim. Acta* **59**, 1217–1232 (1995).
31. Righter, K., Humayun, M. & Danielson, L. Partitioning of palladium at high pressures and temperatures during core formation. *Nature Geosci.* **1**, 321–323 (2008).

Supplementary Information is available in the online version of the paper.

Acknowledgements Support from the Region Ile de France (Sesame), CNRS (INSU-Mi-lourd and SEDIT-CNRS) and IPGP (BQR) is acknowledged. We thank M. G. Jackson for a review. We thank D. Calmels and M. Clog for discussion and comments. We also thank P. Richet, M. Chaussidon and P. Agrinier for comments on an early version of the manuscript. This is IPGP contribution number 3415.

Author Contributions J.L. performed sulphur isotope measurements. J.L. and M.M. performed sample preparation. P.C. conceived the project. J.L. took the lead in writing the paper, with substantial contributions from P.C. and M.M.

Author Information Reprints and permissions information is available at www.nature.com/reprints. The authors declare no competing financial interests. Readers are welcome to comment on the online version of the paper. Correspondence and requests for materials should be addressed to J.L. (labidi@ipgp.fr).

METHODS

Sample selection and preparation. Studied samples were chosen according to their degree of glassiness. They were cleaned in 99.9% ethanol to remove any room dust from the samples. Phenocrysts were removed under a binocular microscope or by magnetic separation, when needed. Samples were then crushed to a grain size smaller than 63 μm .

Electron microprobe measurement. Sulphur contents of MORB glasses were determined by electron micro-probe (EMP) analyses on polished sections with a Cameca SX100 at the CAMPARIS facility (Pierre et Marie Curie University). The analytical conditions used were 15 kV accelerating voltage, 100 nA sample current, 20 μm beam size, and 60 s counting time for each point. Ten spots were analysed on each polished section, the calculated mean value being taken as the sulphur content of the sample and the standard deviation of each series of measurements being taken as the 1σ uncertainty (around 25 p.p.m.).

A natural pyrite was used as a standard. Results were additionally calibrated using two reference samples: sample JDF D2 (high-sulphur-content standard, with 1,400 p.p.m. sulphur) and ED DR11 1–9 (low-sulphur-content standard, with 731 p.p.m. sulphur). These two standards were analysed alternately every 3 or 4 samples. For chlorine contents (see Supplementary Information), the analytical conditions used were 25 kV accelerating voltage, 500 nA sample current, 20 μm beam size, 100 s counting time for each point. A natural scapolite was used as a standard. In addition, results were systematically calibrated using one reference sample: the south Atlantic ridge sample EW9309 41D-1, for which the chlorine amount has been chemically determined at 55 ± 12 p.p.m. (ref. 32). Ten spots were analysed on each polished section. The calculated mean value was taken as the chlorine content of the sample and the standard deviation of each series of measurements is taken as the 1σ uncertainty (10 p.p.m.).

Sulphur extraction for isotope determination. Sulphur isotope measurement of sulphide inclusions in 300–400 mg of glass separates were performed after chemical extraction, by gas source isotope ratio mass spectrometry at the Stable Isotope

Laboratory at the Institut de Physique du Globe de Paris. Powdered samples were transferred to a Teflon apparatus like that in ref. 7, where they underwent sub-boiling HF–Cr(II) sulphur extraction. Sulphur released in this process as H_2S was trapped as silver sulphide, which was washed, dried and wrapped in clean Al foil. The sulphur-content measurement performed via the EMP value represents the bulk sulphur content of the sample, compared to our chemical extraction protocol, which is strictly specific to reduced sulphur (see details in ref. 7). Chemical extraction yields (that is, the ratio of chemically extracted reduced sulphur to sulphur determined by EMP) averaged $101 \pm 4\%$ (1σ , $n = 23$). Such a good match with EMP data supports the absence of significant amounts of oxidized sulphur in these basalts, in agreement with synchrotron spectroscopic results in worldwide samples¹⁸.

The sulphur isotope measurements were then performed using a dual-inlet MAT 253 gas-source mass spectrometer. Weighed silver sulphide wrapped in aluminium foil was placed into Ni-reaction bombs for fluorination with 250 torr of purified F_2 at 250 °C overnight. The produced SF_6 was then purified from impurities in a vacuum line using cryogenic methods and subsequently by gas chromatography separation). Purified SF_6 was then quantified and analysed in the mass spectrometer, where $m/z = 127+$, $128+$, $129+$ and $131+$ ion beams are monitored. The quality of the measurements was estimated on the basis of long-term reproducibility for IAEA reference materials. Repeated analyses gave $\delta^{34}\text{S} = -0.29 \pm 0.04\text{‰}$, $\Delta^{33}\text{S} = +0.082 \pm 0.004\text{‰}$, $\Delta^{36}\text{S} = -0.91 \pm 0.11\text{‰}$ for IAEA S1 (all errors are 1σ , $n = 43$) and $\delta^{34}\text{S} = +22.33 \pm 0.06\text{‰}$, $\Delta^{33}\text{S} = +0.030 \pm 0.006\text{‰}$, $\Delta^{36}\text{S} = -0.17 \pm 0.07\text{‰}$ for IAEA S2 (all errors are 1σ , $n = 20$). These values are in agreement with data reported by other laboratories worldwide.

For each MORB glass sample, the sulphur isotope measurement was duplicated and the standard deviation between the two duplicates was taken as the 1σ external uncertainty. The standard $\delta^{34}\text{S}$ uncertainty is 0.01‰–0.15‰, whereas it is approximately 0.010‰ and 0.100‰ for $\Delta^{33}\text{S}$ and $\Delta^{36}\text{S}$, respectively.

32. Bonifacie, M. *et al.* The chlorine isotope composition of Earth's mantle. *Science* **319**, 1518–1520 (2008).

Computational design of ligand-binding proteins with high affinity and selectivity

Christine E. Tinberg^{1*}, Sagar D. Khare^{1†*}, Jiayi Dou^{2,3}, Lindsey Doyle⁴, Jorgen W. Nelson⁵, Alberto Schena⁶, Wojciech Jankowski⁷, Charalampos G. Kalodimos⁷, Kai Johnsson⁶, Barry L. Stoddard⁴ & David Baker^{1,8}

The ability to design proteins with high affinity and selectivity for any given small molecule is a rigorous test of our understanding of the physicochemical principles that govern molecular recognition. Attempts to rationally design ligand-binding proteins have met with little success, however, and the computational design of protein–small-molecule interfaces remains an unsolved problem¹. Current approaches for designing ligand-binding proteins for medical² and biotechnological uses rely on raising antibodies against a target antigen in immunized animals^{3,4} and/or performing laboratory-directed evolution of proteins with an existing low affinity for the desired ligand^{5–7}, neither of which allows complete control over the interactions involved in binding. Here we describe a general computational method for designing pre-organized and shape complementary small-molecule-binding sites, and use it to generate protein binders to the steroid digoxigenin (DIG). Of seventeen experimentally characterized designs, two bind DIG; the model of the higher affinity binder has the most energetically favourable and pre-organized interface in the design set. A comprehensive binding-fitness landscape of this design, generated by library selections and deep sequencing, was used to optimize its binding affinity to a picomolar level, and X-ray co-crystal structures of two variants show atomic-level agreement with the corresponding computational models. The optimized binder is selective for DIG over the related steroids digitoxigenin, progesterone and β -oestradiol, and this steroid binding preference can be reprogrammed by manipulation of explicitly designed hydrogen-bonding interactions. The computational design method presented here should enable the development of a new generation of biosensors, therapeutics and diagnostics.

Computational design could provide a general approach for creating new small molecule binding proteins with rationally programmed specificities. Structural and biophysical characterization of previous computationally designed ligand-binding proteins revealed numerous discrepancies with the design models, however, and it was concluded that protein–ligand interaction design is an unsolved problem^{1,8}. The lack of accuracy in programming protein–small-molecule interactions also contributes to low catalytic efficiencies of computationally designed enzymes^{9–14}. The development of robust computational methods for the design of small-molecule-binding proteins with high affinity and selectivity would have wide-ranging applications.

We developed a computational method for designing ligand-binding proteins with three properties characteristic of naturally occurring binding sites: (1) specific energetically favourable hydrogen-bonding and van der Waals interactions with the ligand; (2) high overall shape complementarity to the ligand; and (3) structural pre-organization in the unbound protein state, which minimizes entropy loss upon ligand binding^{15,16}. To program in defined interactions with the small molecule,

disembodied binding sites are created by positioning amino acid side chains around the ligand in optimal orientations and then placed at geometrically compatible sites in a set of scaffold protein structures¹⁷. The surrounding side chain identities and conformations are then optimized to generate additional protein–ligand and buttressing protein–protein interactions (Fig. 1a). Designs with protein–small-molecule shape complementarity below those typical of native complexes¹⁸ or having interface side chain conformations with low Boltzmann-weighted probabilities in the unbound state¹⁶ are then discarded.

We used the method to design proteins that bind the steroid DIG (Supplementary Fig. 1), the aglycone of digoxin, a cardiac glycoside used to treat heart disease¹⁹ and a non-radioactive biomolecular labelling reagent²⁰. Anti-digoxigenin antibodies are administered to treat overdoses of digoxin, which has a narrow therapeutic window²¹, and are used to detect biomolecules in applications such as fluorescence *in situ* hybridization²⁰. We created idealized DIG-binding sites featuring hydrogen bonds from Tyr or His to the polar groups of DIG and hydrophobic packing interactions between Tyr, Phe or Trp and the steroid ring system (Fig. 1a). These interactions were embedded in designed binding sites with high shape complementarity to DIG, and 17 designs were selected for experimental characterization based on computed binding affinity, shape complementarity, and the extent of binding site pre-organization in the unbound state (Fig. 1b and Supplementary Tables 1 and 2).

Binding of the designed proteins to DIG was probed by yeast surface display²² and flow cytometry using DIG-functionalized bovine serum albumin (DIG-BSA) or RNase (DIG-RNase). Designed proteins DIG5 and DIG10 bound to both labels (Fig. 1c and Supplementary Fig. 2), and binding was reduced to background levels when unlabelled DIG was added as a competitor (Fig. 1c and Supplementary Fig. 3). Fluorescence polarization measurements with purified proteins and Alexa488-fluorophore-conjugated DIG (DIG-PEG₃-Alexa488) indicated affinities in the low-to-mid micromolar range, with DIG10 binding more tightly (Fig. 2a, b). Isothermal titration calorimetry (ITC) measurements confirmed that the affinity of DIG10 for DIG is identical to that for DIG-PEG₃-Alexa488 (Fig. 2b, Supplementary Fig. 4 and Supplementary Table 3). The scaffold from which both DIG5 and DIG10 derive, a protein of unknown function from *Pseudomonas aeruginosa* (Protein Data Bank (PDB) accession code 1Z1S), does not bind to either label (Fig. 1c and Supplementary Fig. 3a) when expressed on the yeast surface or to DIG-PEG₃-Alexa488 in solution (Fig. 2a), suggesting that the binding activities of both proteins are mediated by the computationally designed interfaces. Indeed, substitution of small nonpolar residues in the binding pockets of DIG5 and DIG10 with arginines resulted in complete loss of binding, and mutation of the designed hydrogen-bonding tyrosine and histidine residues to

¹Department of Biochemistry, University of Washington, Seattle, Washington 98195, USA. ²Department of Bioengineering, University of Washington, Seattle, Washington 98195, USA. ³Graduate Program in Biological Physics, Structure, and Design, University of Washington, Seattle, Washington 98195, USA. ⁴Division of Basic Sciences, Fred Hutchinson Cancer Research Center, Seattle, Washington 98109, USA. ⁵Department of Genome Sciences, University of Washington, Seattle, Washington 98195, USA. ⁶Ecole Polytechnique Fédérale de Lausanne, Institute of Chemical Sciences and Engineering, Institute of Bioengineering, National Centre of Competence in Research (NCCR) in Chemical Biology, 1015 Lausanne, Switzerland. ⁷Department of Chemistry and Chemical Biology, Center for Integrative Proteomics Research, Rutgers University, Piscataway, New Jersey 08854, USA. ⁸Howard Hughes Medical Institute, University of Washington, Seattle, Washington 98195, USA. [†]Present address: Department of Chemistry and Chemical Biology, Center for Integrative Proteomics Research, Rutgers University, Piscataway, New Jersey 08854, USA.

*These authors contributed equally to this work.

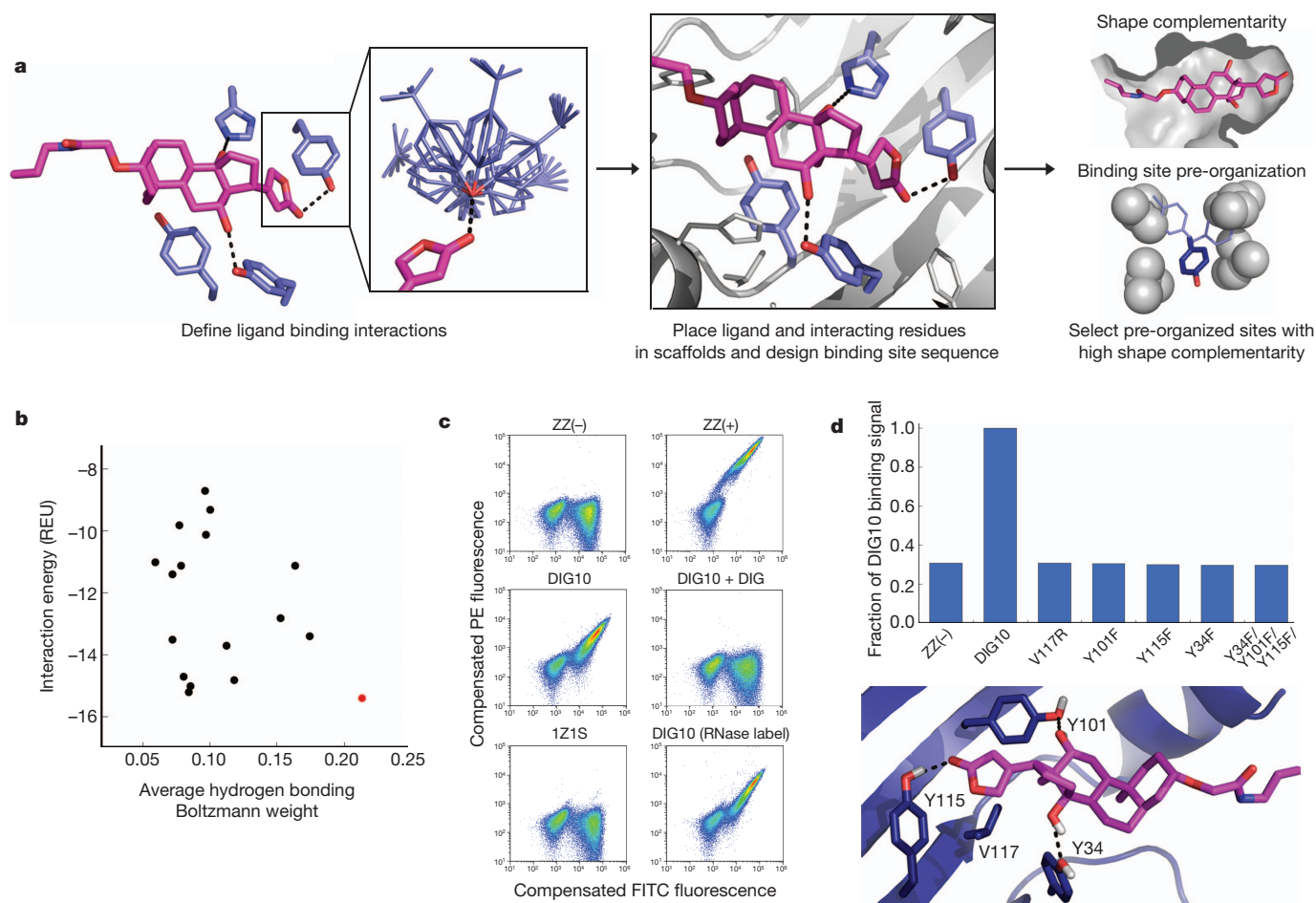


Figure 1 | Computational design methodology and experimental binding validation. **a**, Overview of the design procedure. **b**, Ranking of experimentally characterized DIG designs by computed ligand interaction energy (Rosetta energy units, REU) and average (geometric mean) side-chain Boltzmann weight of residues designed to hydrogen bond to DIG. DIG10 (red) scores the best by both metrics. **c**, Flow cytometric analysis of yeast cells expressing designed proteins. Yeast surface expression and DIG binding were probed by

labelling with anti-c-Myc-fluorescein (FITC) and a mixture of biotinylated DIG-functionalized BSA and phycoerythrin (PE)-streptavidin, respectively. ZZ(–), negative control; ZZ(+), positive control; 1Z1S, original scaffold. **d**, On-yeast substitutions of DIG10-designed interface residues reduce binding (phycoerythrin) signals to background negative control levels. See figure legends in Supplementary Information for details.

phenylalanine reduced (DIG5) or abolished (DIG10) binding (Fig. 1d and Supplementary Fig. 5). Optimization of DIG10 by site-saturation mutagenesis and selections using yeast surface display and fluorescence-activated cell sorting (FACS) identified several small-to-large hydrophobic amino acid changes that increase binding affinity 75-fold through enhanced binding enthalpy, yielding DIG10.1 (Fig. 2b, c, f, Supplementary Figs 4, 6–8 and Supplementary Table 3).

To provide feedback for improving the overall design methodology and to evaluate the contribution of each residue in the DIG10.1-binding site, we used next-generation sequencing to generate a comprehensive binding fitness map^{23–25}. A library of variants with approximately 1–3 substitutions at 39 designed interface positions in DIG10.1 was generated using doped oligonucleotide mutagenesis, displayed on yeast, and subjected to selections using a monovalent DIG-PEG₃-biotin conjugate (Supplementary Fig. 9). Variants with increased affinity for DIG were selected by FACS, and next-generation sequencing was used to quantify the frequency of every single point mutation in the unselected and selected populations. A large majority of the interrogated variants were depleted in the selected population relative to the unselected input library, suggesting that most of the DIG10.1-binding site residues are optimal for binding (Fig. 2d, e and Supplementary Fig. 10). In particular, mutation of the three designed hydrogen-bonding residues, Tyr 34, Tyr 101 and Tyr 115, to any other amino acid was disfavoured. Several large hydrophobic residues that pack against the ligand in the computational model

are also functionally optimal (for example, Phe66 and Phe119). Besides Ala 99, which contacts DIG directly, most of the observed mutations that improve binding are located in the second coordination shell of the ligand and fall into two categories: (1) protein core substitutions tolerating mutation to chemically similar amino acids (for example, Leu 105 and Cys 23), and (2) solvent-exposed loop residues having high sequence entropy (for example, His 90 and Val 92). The best clone obtained from sorting the library to homogeneity, DIG10.2, contains two of the most highly enriched mutations, Ala37Pro and His41Tyr (Fig. 2b, c and Supplementary Figs 4, 6, 8 and 11).

To increase binding affinity further, we constructed a library in which the residues at 11 positions that acquired beneficial substitutions in the deep sequencing experiment were varied in combination to allow for non-additive effects. Selections led to DIG10.3 (Supplementary Figs 4, 6, 8 and 12), which binds DIG and its cardiac glycoside derivative digoxin with picomolar affinity (Fig. 2b, Supplementary Fig. 13 and Supplementary Table 4), rivalling the affinities of anti-digoxin antibody therapeutics²¹ and an evolved single-chain variable anti-digoxin antibody fragment⁷. Fluorescence-polarization-based affinity measurements of DIG10.3 and Tyr knockouts suggest that the designed hydrogen bonds each contribute ~ 2 kcal mol^{–1} to binding energy (Supplementary Table 5 and Supplementary Fig. 8).

The crystal structures of DIG10.2 and DIG10.3 in complex with DIG were solved to 2.05 Å and 3.2 Å resolution, respectively (Fig. 3a, b and

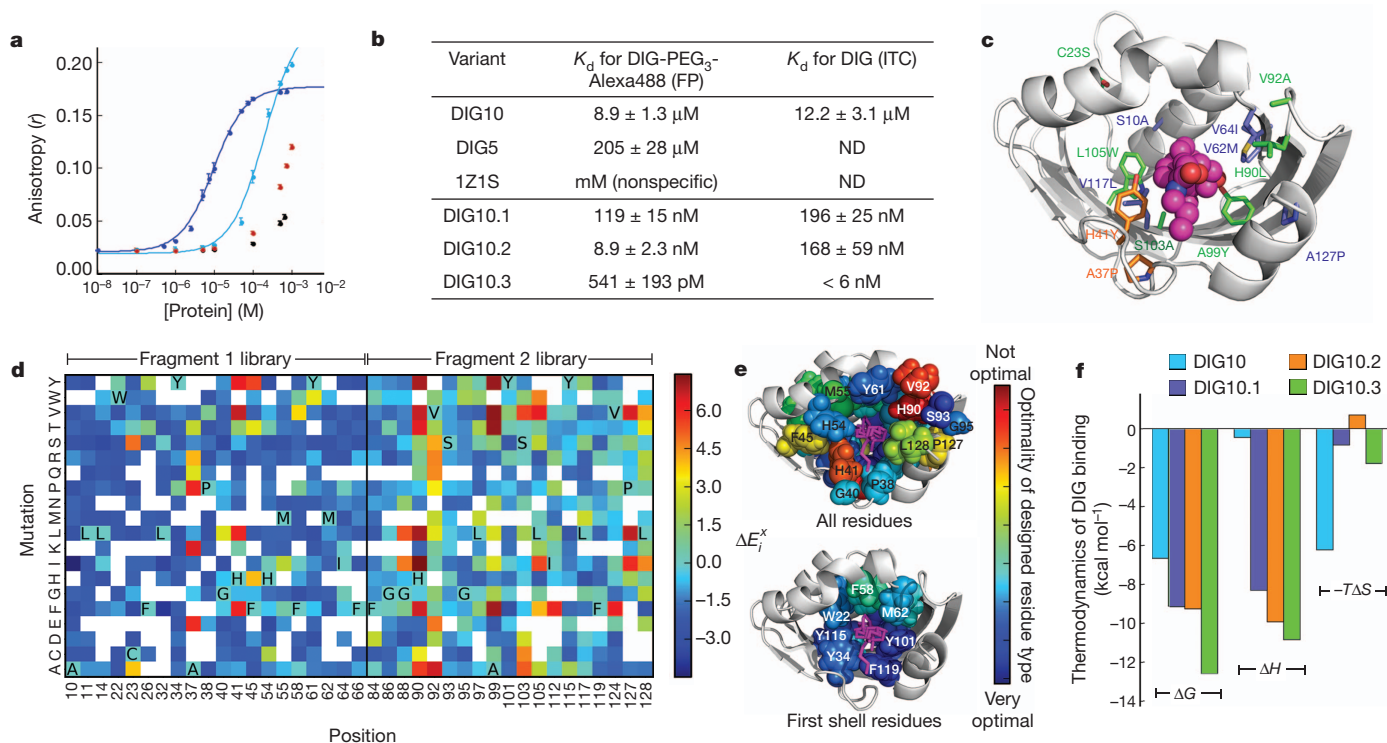


Figure 2 | Binding characterization and affinity maturation. **a**, Equilibrium fluorescence anisotropy of DIG-PEG₃-Alexa488 mixed with purified DIG10 (blue), DIG5 (cyan), 1Z1S scaffold (black) and BSA (red). Error bars represent s.d. for at least three independent measurements. **b**, Dissociation constants (K_d values) of designs. Differences in fluorescence polarization (FP)- and isothermal titration calorimetry (ITC)-derived K_d values probably result from enhanced interactions with the linker of DIG-PEG₃-Alexa488 used in the fluorescence polarization experiments. ND, not determined. **c**, Mutations identified during affinity maturation to generate DIG10.1 (blue), DIG10.2 (orange) and DIG10.3 (green) mapped onto the computational model of

DIG10.3. **d**, Fitness landscape of DIG10.1 showing the effects of single amino acid substitutions on binding (ΔE_i^x ; see equation (1) in Methods). Red and blue indicate enrichment and depletion, respectively. The original DIG10.1 amino acid at each position is indicated in bold. White indicates mutations for which there were not enough sequences in the unselected library to make a statistically significant conclusion about function. **e**, The optimality of each initial DIG10.1 residue type mapped onto the computational model of DIG10.1. **f**, DIG binding thermodynamic parameters determined by ITC. ΔG , free binding energy; ΔH , binding enthalpy; $-T\Delta S$, binding entropy. See figure legends in Supplementary Information for details.

Supplementary Figs 14–19). The structure of DIG10.2 bound to DIG shows atomic-level agreement with the design model (all-atom root mean squared deviation (r.m.s.d.) = 0.54 \AA ; Fig. 3c). The ligand–protein interface has high shape complementarity ($S_c = 0.66$) and no water molecules are observed in the binding pocket. The DIG binding mode is nearly identical in the X-ray structure and the computational model, with an average r.m.s.d. of 0.99 \AA for all ligand heavy atoms (Fig. 3d). As designed, Tyr 34, Tyr 101 and Tyr 115 hydrogen bond with O3, O2 and O1 of DIG, respectively. Tyr 41, a residue identified during affinity maturation, forms a weak hydrogen bond with the terminal hydroxyl group of DIG (O5) (Supplementary Fig. 16). Of 27 non-glycine/alanine residues within $\sim 10 \text{ \AA}$ of the ligand, 21 adopt the computationally designed conformations (Supplementary Fig. 17), including Tyr 101 and Tyr 115 (in chain B) as well as the first-shell packing residues Trp 22, Phe 58 and Phe 119. The structure of DIG10.3 bound to DIG (Supplementary Fig. 18) also agrees closely with the design model (r.m.s.d. = 0.68 \AA).

We assessed the binding specificity of DIG10.3 by determining affinities for a series of related steroids by equilibrium competition fluorescence polarization. Digitoxigenin, progesterone and β -oestradiol bind less tightly to DIG10.3 than DIG (Fig. 4a, b and Supplementary Table 4). The magnitudes of the affinity decreases are consistent with the loss of one, two and three hydrogen bonds, respectively (assuming $\sim 1.8 \text{ kcal mol}^{-1}$ per hydrogen bond²⁶), suggesting that these compounds bind in the same orientation as DIG. We next investigated whether the observed steroid selectivity could be reprogrammed by mutagenesis of the key hydrogen-bonding tyrosines. The variants Tyr101Phe, Tyr34Phe and Tyr34Phe/Tyr99Phe/Tyr101Phe show clear preferences for more hydrophobic

steroids in a predictable manner that depends on the hydrogen-bonding capabilities of both the protein and the steroid. Tyr101Phe eliminates the DIG-specific hydrogen bond with DIG O2 and provides a more hydrophobic environment that favours the other three steroids (Fig. 4c). Tyr34Phe removes a hydrogen bond common to DIG and digitoxigenin, thus enhancing the preference for progesterone (Fig. 4d). Tyr34Phe/Tyr99Phe/Tyr101Phe has decreased affinity for DIG and increased affinity for the more hydrophobic steroids (Fig. 4e). These results confirm that the selectivity of DIG10.3 for DIG is conferred through the designed hydrogen-bonding interactions and demonstrate how this feature can be programmed using positive design alone through the explicit placement of designed polar and hydrophobic interactions.

Comparison of the properties of successful and unsuccessful designs provides a test of the hypotheses underlying the design methodology. Although all 17 designed proteins had high computed shape complementarity to DIG by construction, the DIG10 design, which had the highest affinity for DIG, had the most favourable computed protein–ligand interaction energy and was predicted to have the most pre-organized binding site (Fig. 1b and Supplementary Table 6), suggesting that these attributes should continue to be the focus of future design methodology development. One potential avenue for obtaining more favourable interaction energies would be incorporating backbone flexibility during design to achieve more tightly packed binding sites: the fact that substitution of small hydrophobic interface residues to larger ones increased binding affinity indicates that the original DIG10 design was under-packed.

The binding fitness landscape in combination with the X-ray co-crystal structures highlight the importance of second shell interactions

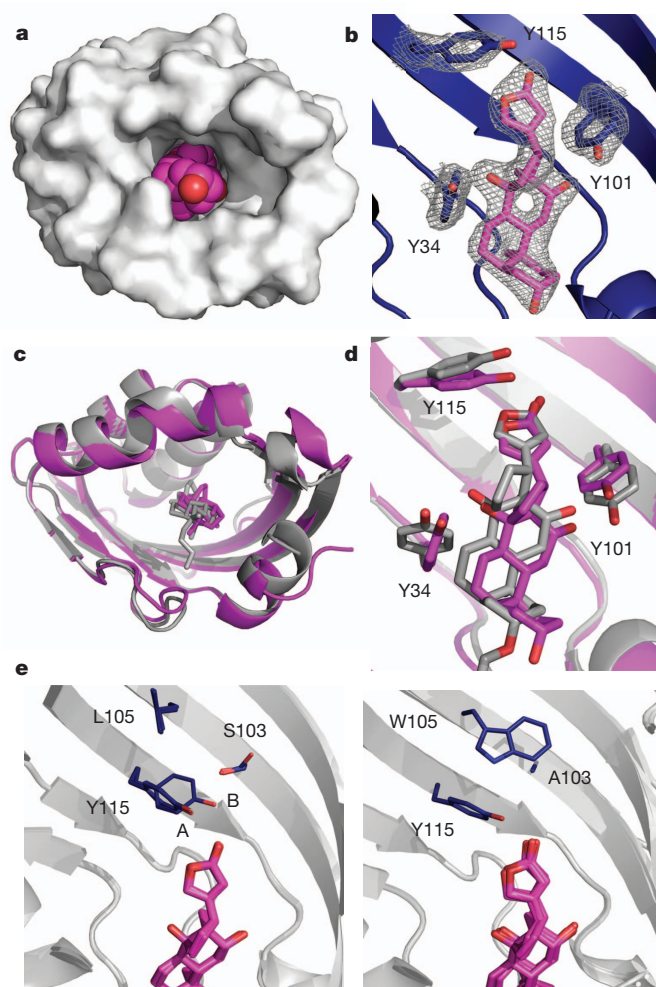


Figure 3 | Crystal structures of DIG10.2-DIG and DIG10.3-DIG. **a**, Surface representation of the DIG10.2-DIG complex. DIG is shown in magenta. DIG10.2 is a dimer and crystallized with four copies in the asymmetric unit. **b**, DIG10.2-DIG $2F_o - F_c$ omit map electron density showing DIG and interacting tyrosines contoured at 1.0σ . **c**, Backbone superposition of the crystal structure of DIG10.2-DIG (magenta) with the computational model (grey). **d**, DIG10.2-DIG-binding site backbone superposition. **e**, Comparison of an overlay of the four DIG10.2-DIG crystallographic copies (left) with that of DIG10.3-DIG chains A, B, C, H and I (right; the density was poorly resolved for the other four chains). DIG10.2 Tyr 115 conformation A has a more canonical hydrogen-bonding geometry than conformation B, and in DIG10.3 Tyr 115 is locked into conformation A by Trp 105.

in stabilizing binding competent conformations. For example, the enriched substitution Leu105Trp (Fig. 2d) causes the adjacent Tyr 115 side chain, which shows conformational variability in DIG10.2, to adopt a single conformation in DIG10.3 that makes a more canonical hydrogen bond to DIG than that of the DIG10.2 alternative state (Fig. 3e and Supplementary Fig. 19). The calculated side chain pre-organization of all three hydrogen-bonding tyrosine residues increases from DIG10.2 to DIG10.3 (Supplementary Table 7), suggesting that the increased affinity may arise in part from a higher proportion of the binding competent conformation of apo-DIG10.3 (refs 15, 27). Indeed, ITC studies confirm that entropic as well as enthalpic factors contribute to the enhanced binding affinity of DIG10.3 (Fig. 2f and Supplementary Table 3). Similarly, reduced backbone conformational entropy is probably responsible for the increased fitness of substitutions increasing β -sheet propensity at inter-strand loop positions 90 and 92 (Fig. 2d). That flexibility is selected against during affinity maturation suggests that maximizing the free-energy gap between binding-competent and alternative states of the binding site²⁸ by explicitly designing second shell interactions to buttress side

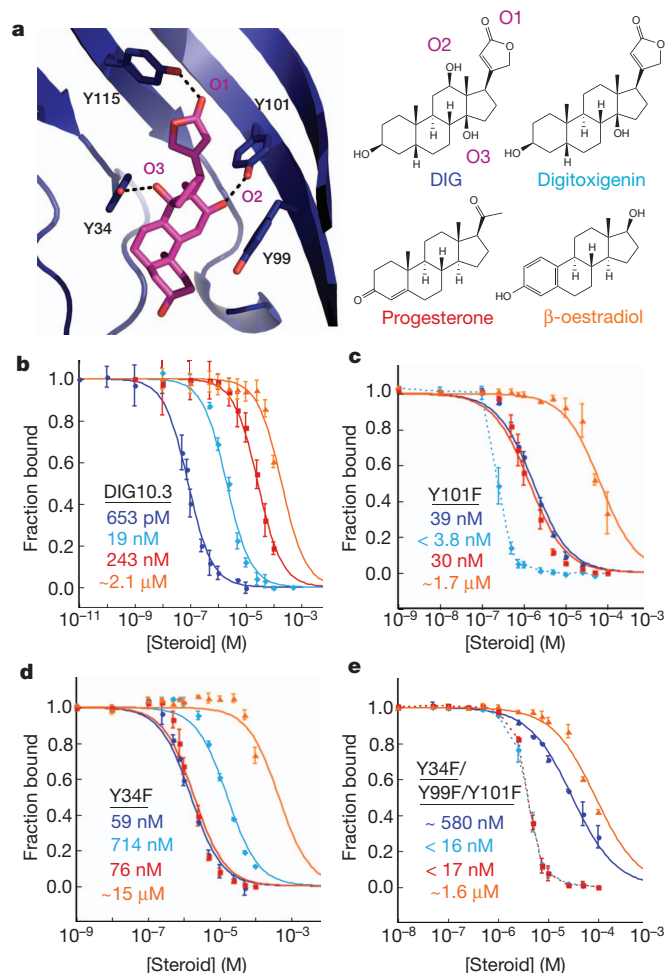


Figure 4 | Steroid binding selectivity. **a**, X-ray crystal structure of the DIG10.3-DIG complex (left) and chemical structures of related steroids (right). **b**, Steroid selectivity profile of DIG10.3 determined by measuring the equilibrium effects of unlabelled steroids on the anisotropy of the DIG-PEG₃-Alexa488-DIG10.3 complex. Solid lines represent fits of the data to a competitive binding model and error bars indicate s.d. for at least three independent measurements. Inhibition constants (K_i values, coloured numbers) were estimated from inhibitory half-maximal concentrations (IC_{50} values) obtained from the fits. **c**, Steroid selectivity profile of DIG10.3(Tyr101Phe). Dashed lines show qualitative assessments of the inhibitory effects for cases in which the data could not be fit due to overly strong inhibition (see Supplementary Methods). **d**, Steroid selectivity profile of DIG10.3(Tyr34Phe). **e**, Steroid selectivity profile of DIG10.3(Tyr34Phe/Tyr99Phe/Tyr101Phe).

chains making key ligand contacts should help to achieve high affinity in the next generation of computationally designed ligand-binding proteins.

The binding affinity of DIG10.3 is similar to those of anti-digoxin antibodies²¹, and because it is stable for extended periods (>3 months) at ambient temperatures (Supplementary Fig. 20) and can be expressed at high levels in bacteria, it could provide a more cost-effective alternative for biotechnological and for therapeutic purposes if it can be made compatible with the human immune response. With continued improvement in the methodology and feedback from experimental results, computational protein design should provide an increasingly powerful approach to creating small molecule receptors for synthetic biology, therapeutic scavengers for toxic compounds, and robust binding domains for diagnostic devices.

METHODS SUMMARY

Design calculations were performed using RosettaMatch¹⁷ to incorporate five pre-defined interactions to DIG into a set of 401 scaffolds. RosettaDesign²⁹ was then

used to optimize each binding site sequence for maximal ligand-binding affinity. Designs having low interface energy, high shape complementarity, and high binding site pre-organization were selected for experimental characterization. Example command lines and full design protocols are given in the Supplementary Data.

Designs were displayed on the surface of yeast strain EBY100 and examined for binding to a mixture of 2.7 μ M biotinylated DIG-conjugated BSA or DIG-conjugated RNase and streptavidin-phycoerythrin on an Accuri C6 flow cytometer. Binding clones from yeast-surface displayed libraries based on DIG10 were selected using highly avid DIG-BSA or DIG-RNase or monovalent DIG-conjugated biotin on a Cytopeia inFlux cell sorter. DIG10.1-derived library DNA was sequenced in paired-end mode on an Illumina MiSeq. For single mutations having ≥ 7 counts in the original input library, a relative enrichment ratio between the input library and each selected library was calculated^{23–25}. The effect of each amino acid substitution on binding, ΔE_i^x , was computed with equation (1),

$$\Delta E_i^x = \log_2 \left(\frac{f_i^{x,\text{sel}}}{f_i^{x,\text{unsel}}} \right) - \log_2 \left(\frac{f_i^{\text{orig},\text{sel}}}{f_i^{\text{orig},\text{unsel}}} \right) \quad (1)$$

in which $f_i^{x,\text{sel}}$ is the frequency of mutation x at position i in the selected population, $f_i^{x,\text{unsel}}$ is the frequency in the unselected population, $f_i^{\text{orig},\text{sel}}$ is the frequency of the original amino acid at position i in the selected population, and $f_i^{\text{orig},\text{unsel}}$ is the frequency of the original amino acid in the unselected population.

For biochemical assays, proteins were expressed in *E. coli* Rosetta 2 (DE3) cells with a carboxy-terminal tobacco etch virus (TEV) protease-cleavable His₆ tag. For crystallographic analysis of DIG10 variants, a 12-amino-acid structurally disordered C terminus deriving from the scaffold protein 1Z1S was replaced directly with a His₆ tag. Binding affinities were determined by equilibrium fluorescence polarization³⁰ on a SpectraMax M5e microplate reader by monitoring the anisotropy of DIG-conjugated Alexa488 as a function of protein concentration. Equilibrium fluorescence polarization competition assays were performed by examining the effect of increasing concentrations of unlabelled DIG, digitoxigenin, progesterone and β -oestradiol on the anisotropy of designed protein–DIG-conjugated Alexa488 complex. ITC studies were performed on an iTC200 microcalorimeter.

Full Methods and any associated references are available in the online version of the paper.

Received 27 February; accepted 11 July 2013.

Published online 4 September 2013.

- Schreier, B., Stumpp, C., Wiesner, S. & Höcker, B. Computational design of ligand binding is not a solved problem. *Proc. Natl Acad. Sci. USA* **106**, 18491–18496 (2009).
- de Wolf, F. A. & Brett, G. M. Ligand-binding proteins: their potential for application in systems for controlled delivery and uptake of ligands. *Pharmacol. Rev.* **52**, 207–236 (2000).
- Hunter, M. M., Margolies, M. N., Ju, A. & Haber, E. High-affinity monoclonal antibodies to the cardiac glycoside, digoxin. *J. Immunol.* **129**, 1165–1172 (1982).
- Shen, X. Y., Orson, F. M. & Kosten, T. R. Vaccines against drug abuse. *Clin. Pharmacol. Ther.* **91**, 60–70 (2012).
- Bradbury, A. R. M., Sidhu, S., Dübel, S. & McCafferty, J. Beyond natural antibodies: the power of *in vitro* display technologies. *Nature Biotechnol.* **29**, 245–254 (2011).
- Brustad, E. M. & Arnold, F. H. Optimizing non-natural protein function with directed evolution. *Curr. Opin. Chem. Biol.* **15**, 201–210 (2011).
- Chen, G. *et al.* Isolation of high-affinity ligand-binding proteins by periplasmic expression with cytometric screening (PECS). *Nature Biotechnol.* **19**, 537–542 (2001).
- Telmer, P. G. & Shilton, B. H. Structural studies of an engineered zinc biosensor reveal an unanticipated mode of zinc binding. *J. Mol. Biol.* **354**, 829–840 (2005).
- Baker, D. An exciting but challenging road ahead for computational enzyme design. *Protein Sci.* **19**, 1817–1819 (2010).
- Jiang, L. *et al.* De novo computational design of retro-Aldol enzymes. *Science* **319**, 1387–1391 (2008).
- Khare, S. D. & Fleishman, S. J. Emerging themes in the computational design of novel enzymes and protein–protein interfaces. *FEBS Lett.* **587**, 1147–1154 (2013).
- Khersonsky, O. *et al.* Bridging the gaps in design methodologies by evolutionary optimization of the stability and proficiency of designed Kemp eliminase KE59. *Proc. Natl Acad. Sci. USA* **109**, 10358–10363 (2012).

- Röthlisberger, D. *et al.* Kemp elimination catalysts by computational enzyme design. *Nature* **453**, 190–195 (2008).
- Wang, L. *et al.* Structural analyses of covalent enzyme–substrate analog complexes reveal strengths and limitations of *de novo* enzyme design. *J. Mol. Biol.* **415**, 615–625 (2012).
- Boehr, D. D., Nussinov, R. & Wright, P. E. The role of dynamic conformational ensembles in biomolecular recognition. *Nature Chem. Biol.* **5**, 789–796 (2009).
- Fleishman, S. J., Khare, S. D., Koga, N. & Baker, D. Restricted sidechain plasticity in the structures of native proteins and complexes. *Protein Sci.* **20**, 753–757 (2011).
- Zanghellini, A. *et al.* New algorithms and an *in silico* benchmark for computational enzyme design. *Protein Sci.* **15**, 2785–2794 (2006).
- Lawrence, M. C. & Colman, P. M. Shape complementarity at protein/protein interfaces. *J. Mol. Biol.* **234**, 946–950 (1993).
- The Digitalis Investigation Group. The effect of digoxin on mortality and morbidity in patients with heart failure. *N. Engl. J. Med.* **336**, 525–533 (1997).
- Eisel, D., Seth, O., Grünwald-Janho, S. & Kruchen, B. *DIG Application Manual for Nonradioactive in situ Hybridization* 4th edn (Roche Diagnostics, 2008).
- Flanagan, R. J. & Jones, A. L. Fab antibody fragments: some applications in clinical toxicology. *Drug Saf.* **27**, 1115–1133 (2004).
- Chao, G. *et al.* Isolating and engineering human antibodies using yeast surface display. *Nature Protocols* **1**, 755–768 (2006).
- Fowler, D. M. *et al.* High-resolution mapping of protein sequence-function relationships. *Nature Methods* **7**, 741–746 (2010).
- McLaughlin, R. N. Jr, Poelwijk, F. J., Raman, A., Gosal, W. S. & Ranganathan, R. The spatial architecture of protein function and adaptation. *Nature* **491**, 138–142 (2012).
- Whitehead, T. A. *et al.* Optimization of affinity, specificity and function of designed influenza inhibitors using deep sequencing. *Nature Biotechnol.* **30**, 543–548 (2012).
- Fersht, A. R. *et al.* Hydrogen bonding and biological specificity analysed by protein engineering. *Nature* **314**, 235–238 (1985).
- Frederick, K. K., Marlow, M. S., Valentine, K. G. & Wand, A. J. Conformational entropy in molecular recognition by proteins. *Nature* **448**, 325–329 (2007).
- Fleishman, S. J. & Baker, D. Role of the biomolecular energy gap in protein design, structure, and evolution. *Cell* **149**, 262–273 (2012).
- Kuhlman, B. & Baker, D. Native protein sequences are close to optimal for their structures. *Proc. Natl Acad. Sci. USA* **97**, 10383–10388 (2000).
- Rossi, A. M. & Taylor, C. W. Analysis of protein–ligand interactions by fluorescence polarization. *Nature Protocols* **6**, 365–387 (2011).

Supplementary Information is available in the online version of the paper.

Acknowledgements We thank E.-M. Strauch and P.-S. Huang for providing the ZZ/pETCON and S2/pETCON plasmids, respectively, and B. Shen for assistance with data processing, modelling and refinement of the X-ray crystal structures. We thank J. P. Sumida for assistance with analytical ultracentrifugation data collection, processing, and analysis. Analytical ultracentrifugation experiments were performed at the University of Washington Analytical Biopharmacy Core, which is supported by the Washington State Life Sciences Discovery Fund and the Center for the Intracellular Delivery of Biologics. We thank S. Fleishman, O. Khersonsky and P.-S. Huang for comments on the manuscript. J.W.N. acknowledges a pre-doctoral fellowship from the National Human Genome Research Institute under the Interdisciplinary Training in Genome Sciences program (T32 HG00035). This work was supported by grants from DTRA and DARPA to D.B., a grant from the Swiss National Science Foundation to K.J., and National Science Foundation grant MCB1121896 to C.G.K.

Author Contributions C.E.T., S.D.K. and D.B. designed the research. S.D.K., C.E.T. and J.D. performed computations. S.D.K. wrote program code. C.E.T. experimentally characterized the designs, constructed libraries, performed affinity maturation and deep sequencing selections, and conducted binding and biochemical studies of DIG10. J.D. characterized DIG5. J.W.N. analysed deep sequencing data. C.E.T. and J.D. prepared protein samples for crystallographic analysis. L.D. and B.S. crystallized the protein samples and analysed crystallographic data. A.S. and K.J. synthesized DIG-PEG₃-biotin and DIG-PEG₃-Alexa488. C.E.T. prepared protein samples for ITC studies, and W.J. and C.G.K. performed ITC experiments and analysed ITC data. C.E.T., S.D.K. and D.B. analysed data and wrote the manuscript. All authors discussed the results and commented on the manuscript.

Author Information The crystal structures of DIG10.2 and DIG10.3 bound to DIG have been deposited in the RCSB Protein Data Bank under the accession codes 4J8T (DIG10.2) and 4J9A (DIG10.3). Reprints and permissions information is available at www.nature.com/reprints. The authors declare no competing financial interests. Readers are welcome to comment on the online version of the paper. Correspondence and requests for materials should be addressed to D.B. (dabaker@u.washington.edu).

METHODS

General methods. Full details for all computational and experimental methods are given in Supplementary Methods. Design calculations were performed using RosettaDesign²⁹. Dissociation constants (K_d values) of designs were determined by equilibrium fluorescence polarization³⁰ and by ITC. Example command lines and RosettaScripts³¹ design protocols are provided in Supplementary Data. Source code is freely available to academic users through the Rosetta Commons agreement (<http://www.rosettacommons.org/>). Design models, the scaffold library, and scripts for running design calculations are provided on the Baker laboratory website.

Matching. RosettaMatch¹⁷ was used to identify backbone constellations in 401 protein scaffold structures where a DIG molecule and side chain conformations interacting with DIG in a pre-defined geometry could be accommodated. This set contained scaffolds previously used for design projects within our laboratory^{10,13,32}, as well as structural homologues of a subset of these scaffolds that are known to tolerate mutations. Full details are given in Supplementary Methods.

Rosetta sequence design. Two successive rounds of sequence design were used. The purpose of the first was to maximize binding affinity for the ligand³³. The goal of the second was to minimize protein destabilization due to aggressive scaffold mutagenesis while maintaining the binding interface designed during the first round. During the latter round, ligand–protein interactions were up-weighted by a factor of 1.5 relative to intra-protein interactions to ensure that binding energy was preserved. Two different criteria were used to minimize protein destabilization: (1) native scaffold residues identities were favoured by 1.5 REU, and (2) no more than five residues were allowed to change from residue types observed in a multiple sequence alignment (MSA) of the scaffold if (a) these residues were present in the MSA with a frequency greater than 0.6, or (b) if the calculated $\Delta\Delta G$ for mutation of the scaffold residue to alanine³⁴ was greater than 1.5 REU in the context of the scaffold sequence. In some design calculations, identities of the matched hydrogen-bonding residues were allowed to vary according to the MSA and $\Delta\Delta G$ criteria described above. In these cases, designs having fewer than three hydrogen bonds between the protein and the ligand were discarded.

Design evaluation. Designs were evaluated on interface energy, ligand solvent exposed surface area, ligand orientation, shape complementarity, and apo-protein binding site pre-organization. The latter was enforced by explicitly introducing second-shell amino acids that bolster the programmed interacting residues using Foldit³⁵ and by selecting designs having rotamer Boltzmann probabilities¹⁶ > 0.1 for at least one hydrogen-bonding residue (Supplementary Table 6). High shape complementarity was enforced by rejecting designs having $S_c < 0.5$. Shape complementarity was computed using the CCP4 package v.6.0.2 (ref. 36) using the S_c program¹⁸ and the Rosetta radii library. All designs were evaluated for local sequence secondary structure compatibility, and those predicted to have backbone conformations that varied by > 0.8 Å from their native scaffold were rejected (see Supplementary Methods).

General experimental methods. Detailed procedures for the syntheses of DIG-BSA-biotin, DIG-RNase-biotin, DIG-PEG₃-biotin, and DIG-PEG₃-Alexa488, as well as protein expression, purification, crystallization, cloning and mutagenesis methods are given in Supplementary Methods. Details about fluorescence polarization binding assays, ITC, gel filtration analysis, analytical ultracentrifugation experiments, and circular dichroism protein stability measurements are also provided in Supplementary Methods.

Yeast surface display. Designed proteins were tested for binding using yeast-surface display²². Yeast surface protein expression was monitored by binding of anti-c-Myc-FITC to the C-terminal Myc epitope tag of the displayed protein. DIG binding was assessed by quantifying the phycoerythrin (PE) fluorescence of the displaying yeast population following incubation with DIG-BSA-biotin, DIG-RNase-biotin, or DIG-PEG₃-biotin, and streptavidin-phycoerythrin (SAPE). In a typical experiment using DIG-BSA-biotin or DIG-RNase-biotin, cells were resuspended in a premixed solution of PBSF (PBS plus 1 g L⁻¹ of BSA) containing a 1:100 dilution of anti-c-Myc-FITC, 2.66 μM DIG-BSA-biotin or DIG-RNase-biotin, and 664 nM SAPE for 2–4 h at 4 °C. Cellular fluorescence was monitored on an Accuri C6 flow cytometer using a 488-nm laser for excitation and a 575-nm bandpass filter for emission. Phycoerythrin fluorescence was compensated to minimize bleed-over contributions from the FITC channel. Competition assays with free DIG were performed as above except that between 750 μM and 1.5 mM DIG was added to each labelling reaction mixture. Full details are given in Supplementary Methods.

Affinity maturation. Detailed procedures for constructing and selecting all libraries, including those for deep sequencing, are provided in Supplementary Methods. Yeast surface display library selections were conducted on a Cytopeia inFlux cell sorter using increasingly stringent conditions. In all labelling reactions for selections, care was taken to maintain at least a tenfold molar excess of label to cell surface protein. Cell surface protein molarity was estimated by assuming that

an attenuation at 600 nm ($D_{600\text{nm}}$) of $1.0 = 1 \times 10^7$ cells ml⁻¹, and that each cell displays 50,000 copies of protein²². For each round of sorting, we sorted at least 10 times the theoretical library size. FlowJo software v. 7.6 was used to analyse all data. Cell sorting parameters and statistics for all selections are given in Supplementary Table 9.

Next-generation sequencing. Two sequencing libraries based on DIG10.1 were assembled by recursive PCR: an amino-terminal library (fragment 1 library) and a carboxy-terminal library (fragment 2 library). To introduce mutations, we used degenerate PAGE-purified oligonucleotides in which the bases coding for 39 selected binding site amino acid residues were doped with a small amount of each non-native base at a level expected to yield 1–2 mutations per gene (TriLink BioTechnologies) (Supplementary Table 10). Yeast cells were transformed with DNA insert and restriction-digested pETCON³⁷. Surface protein expression was induced²² and cells were labelled with anti-c-Myc-FITC and sorted for protein expression. Expressing cells were recovered, induced, labelled with 100 nM of DIG-PEG₃-biotin for > 3 h at 4 °C and then SAPE and anti-c-Myc-FITC for 8 min at 4 °C, and then sorted. For each library, clones having binding signals higher than that of DIG10.1 were collected (Supplementary Fig. 9). To reduce noise from the first round of cell sorting, the sorted libraries were recovered, induced, and subjected to a second round of sorting using the same conditions (see Supplementary Methods).

Library DNA was prepared as described²⁵. Illumina adaptor sequences and unique library barcodes were appended to each library pool by PCR amplification using population-specific primers (Supplementary Table 11). DNA was sequenced in paired-end mode on an Illumina MiSeq using a 300-cycle reagent kit and custom primers (see Supplementary Methods). Of a total of 5,630,105 paired-end reads, 2,531,653 reads were mapped to library barcodes (Supplementary Table 12). For each library, paired-end reads were fused and filtered for quality (Phred ≥ 30). The resulting full-length reads were aligned against DIG10.1 using Enrich³⁸. For single mutations having ≥ 7 counts in the original input library, a relative enrichment ratio between the input library and each selected library was calculated^{23–25}. The effect of each amino acid substitution on binding, ΔE_i^x , was computed with equation (1),

$$\Delta E_i^x = \log_2 \left(\frac{f_i^{x,\text{sel}}}{f_i^{x,\text{unsel}}} \right) - \log_2 \left(\frac{f_i^{\text{orig},\text{sel}}}{f_i^{\text{orig},\text{unsel}}} \right) \quad (1)$$

in which $f_i^{x,\text{sel}}$ is the frequency of mutation x at position i in the selected population, $f_i^{x,\text{unsel}}$ is the frequency in the unselected population, $f_i^{\text{orig},\text{sel}}$ is the frequency of the original amino acid at position i in the selected population, and $f_i^{\text{orig},\text{unsel}}$ is the frequency of the original amino acid in the unselected population.

Fluorescence polarization binding assays. Fluorescence-polarization-based affinity measurements of designs and their evolved variants were performed as described³⁰ using Alexa488-conjugated DIG (DIG-PEG₃-Alexa488). Fluorescence anisotropy (r) was measured in 96-well plate format on a SpectraMax M5e microplate reader (Molecular Devices) with $\lambda_{\text{ex}} = 485$ nm and $\lambda_{\text{em}} = 538$ nm using a 515-nm emission cut-off filter. Fluorescence polarization equilibrium competition binding assays were used to determine the binding affinities of DIG10.3 and its variants for unlabelled DIG, digitoxigenin, progesterone, β -oestradiol and digoxin. The inhibition constant (K_i) for each protein–ligand interaction was calculated from the measured total unlabelled ligand producing 50% binding signal inhibition (I_{50} ; see Supplementary Methods) and the K_d of the protein–label interaction according to a model accounting for receptor-depletion conditions³⁰. Full details are provided in Supplementary Methods.

ITC. ITC studies were performed on an iTC200 microcalorimeter (MicroCal) at 25 °C in PBS, pH 7.4. Ligand solutions were prepared by diluting a stock solution of DIG (100 mM in 100% dimethylsulphoxide (DMSO)) into the flow-through of the last buffer aliquot used to exchange the protein (final DMSO concentrations were 1–3%). ITC titration data were integrated and analysed with Origin 7.0 (MicroCal). Full details are provided in Supplementary Methods.

1. Fleishman, S. J. *et al.* RosettaScripts: A scripting language interface to the Rosetta macromolecular modeling suite. *PLoS ONE* **6**, e20161 (2011).
2. Siegel, J. B. *et al.* Computational design of an enzyme catalyst for a stereoselective bimolecular Diels–Alder reaction. *Science* **329**, 309–313 (2010).
3. Richter, F., Leaver-Fay, A., Khare, S. D., Bjelic, S. & Baker, D. *De novo* enzyme design using Rosetta3. *PLoS ONE* **6**, e19230 (2011).
4. Kellogg, E. H., Leaver-Fay, A. & Baker, D. Role of conformational sampling in computing mutation-induced changes in protein structure and stability. *Proteins* **79**, 830–838 (2011).
5. Cooper, S. *et al.* Predicting protein structures with a multiplayer online game. *Nature* **466**, 756–760 (2010).
6. Collaborative Computational Project, Number 4. The CCP4 suite: programs for protein crystallography. *Acta Crystallogr. D* **50**, 760–763 (1994).

37. Benatuil, L., Perez, J. M., Belk, J. & Hsieh, C.-M. An improved yeast transformation method for the generation of very large human antibody libraries. *Protein Eng. Des. Sel.* **23**, 155–159 (2010).
38. Fowler, D. M., Araya, C. L., Gerard, W. & Fields, S. Enrich: software for analysis of protein function by enrichment and depletion of variants. *Bioinformatics* **27**, 3430–3431 (2011).

De novo mutations in epileptic encephalopathies

Epi4K Consortium* & Epilepsy Phenome/Genome Project*

Epileptic encephalopathies are a devastating group of severe childhood epilepsy disorders for which the cause is often unknown¹. Here we report a screen for *de novo* mutations in patients with two classical epileptic encephalopathies: infantile spasms ($n = 149$) and Lennox–Gastaut syndrome ($n = 115$). We sequenced the exomes of 264 probands, and their parents, and confirmed 329 *de novo* mutations. A likelihood analysis showed a significant excess of *de novo* mutations in the ~4,000 genes that are the most intolerant to functional genetic variation in the human population ($P = 2.9 \times 10^{-3}$). Among these are *GABRB3*, with *de novo* mutations in four patients, and *ALG13*, with the same *de novo* mutation in two patients; both genes show clear statistical evidence of association with epileptic encephalopathy. Given the relevant site-specific mutation rates, the probabilities of these outcomes occurring by chance are $P = 4.1 \times 10^{-10}$ and $P = 7.8 \times 10^{-12}$, respectively. Other genes with *de novo* mutations in this cohort include *CACNA1A*, *CHD2*, *FLNA*, *GABRA1*, *GRIN1*, *GRIN2B*, *HNRNPU*, *IQSEC2*, *MTOR* and *NEDD4L*. Finally, we show that the *de novo* mutations observed are enriched in specific gene sets including genes regulated by the fragile X protein ($P < 10^{-8}$), as has been reported previously for autism spectrum disorders².

Genetics is believed to have an important role in many epilepsy syndromes; however, specific genes have been discovered in only a small proportion of cases. Genome-wide association studies for both focal and generalized epilepsies have revealed few significant associations, and rare copy number variants explain only a few per cent of cases^{3–6}. An emerging paradigm in neuropsychiatric disorders is the major impact that *de novo* mutations have on disease risk^{7,8}. We searched for *de novo* mutations associated with epileptic encephalopathies, a heterogeneous group of severe epilepsy disorders characterized by early onset of seizures with cognitive and behavioural features associated with ongoing epileptic activity. We focused on two ‘classical’ forms of epileptic encephalopathies: infantile spasms and Lennox–Gastaut syndrome, recognizing that some patients with infantile spasms progress to Lennox–Gastaut syndrome.

Exome sequencing of 264 trios (Methods) identified 439 putative *de novo* mutations. Sanger sequencing confirmed 329 *de novo* mutations (Supplementary Table 2), and the remainder were either false positives, a result of B-cell immortalization, or in regions where the Sanger assays did not work (Supplementary Table 3).

Across our 264 trios, we found nine genes with *de novo* single nucleotide variant (SNV) mutations in two or more probands (*SCN1A*, $n = 7$; *STXBP1*, $n = 5$; *GABRB3*, $n = 4$; *CDKL5*, $n = 3$; *SCN8A*, $n = 2$; *SCN2A*, $n = 2$; *ALG13*, $n = 2$; *DNM1*, $n = 2$; and *HDAC4*, $n = 2$). Of these, *SCN1A*, *STXBP1*, *SCN8A*, *SCN2A* and *CDKL5* are genes that have a previously established association with epileptic encephalopathy^{9–14}. To assess whether the observations in the other genes implicate them as risk factors for epileptic encephalopathies, we determined the probability of seeing multiple mutations in the same gene given the sequence-specific mutation rate, size of the gene, and the number and gender of patients evaluated in this study (Methods). The number of observed *de novo* mutations in *HDAC4* and *DNM1* are not yet significantly greater than the null expectation. However, observing four unique *de novo* mutations in *GABRB3* and two identical *de novo* mutations in *ALG13*

were found to be highly improbable (Table 1 and Fig. 1). We performed the same calculations on all of the genes with multiple *de novo* mutations observed in 610 control trios and found no genes with a significant excess of *de novo* mutations (Supplementary Table 4). Although mutations in *GABRB3* have previously been reported in association with another type of epilepsy¹⁵, and *in vivo* mouse studies suggest that *GABRB3* haploinsufficiency is one of the causes of epilepsy in Angelman’s syndrome¹⁶, our observations implicate it, for the first time, as a single-gene cause of epileptic encephalopathies and provide the strongest evidence to date for its association with any epilepsy. Likewise, *ALG13*, an X-linked gene encoding a subunit of the uridine diphosphate-*N*-acetylglucosamine transferase, was previously shown to carry a novel *de novo* mutation in a male patient with a severe congenital glycosylation disorder with microcephaly, seizures and early lethality¹⁷. Furthermore, the same *ALG13 de novo* mutation identified in this study was observed as a *de novo* mutation in an additional female patient with severe intellectual disability and seizures¹⁸.

Each trio harboured on average 1.25 confirmed *de novo* mutations, with 181 probands harbouring at least one. Considering only *de novo* SNVs, each trio harboured on average 1.17 *de novo* mutations (Supplementary Fig. 1). Seventy-two per cent of the confirmed *de novo* SNV mutations were missense and 7.5% were putative loss-of-function (splice donor, splice acceptor, or stop-gain mutations). Compared to rates of these classes of mutations previously reported in controls (69.4% missense and 4.2% putative loss-of-function mutations)^{2,19,20}, we observed a significant excess of loss-of-function mutations in patients with infantile spasms and Lennox–Gastaut syndrome (exact binomial $P = 0.01$), consistent with data previously reported in autism spectrum disorder^{2,8,19,20}.

A framework was recently established for testing whether the distribution of *de novo* mutations in affected individuals differs from the general population⁸. Here, we extend the simulation-based approach of ref. 8 by developing a likelihood model that characterizes this effect and describes the distribution of *de novo* mutations among affected individuals in terms of the distribution in the general population, and a set of parameters describing the genetic architecture of the disease. These parameters include the proportion of the exome sequence that can carry disease-influencing mutations (η) and the relative risk (γ) of the mutations (Supplementary Methods). Consistent with what was reported in autism spectrum disorder⁸, we found no significant deviation in the overall distribution of mutations from expected ($\gamma = 1$ and/or $\eta = 0$). It is, however, now well established that some genes tolerate protein-disrupting mutations without apparent adverse phenotypic consequences, whereas others do not²¹. To take this into account, we used a simple scoring system that uses polymorphism data in the human population to assign a tolerance score to every considered gene (Methods). We then found that genes with a known association with epileptic encephalopathy rank among the most intolerant genes using this scheme (Supplementary Table 8). We therefore evaluated the distribution of *de novo* mutations within these 4,264 genes that are within the 25th percentile for intolerance and found a significant shift from the null distribution ($P = 2.9 \times 10^{-3}$). The maximum likelihood estimates of η (percentage of intolerant genes involved in epileptic encephalopathies) was 0.021 and γ (relative risk) was 81, indicating that there are 90 genes among the intolerant genes

*A list of authors and affiliations appears at the end of the paper.

Table 1 | Probability of observing the reported number of *de novo* mutations by chance in genes recurrently mutated in this cohort

Gene	Chromosome	Average effectively captured length (bp)	Weighted mutation rate	<i>De novo</i> mutation number	<i>P</i> value†	
<i>SCN1A</i>	2	6,063.70	1.61×10^{-4}	5‡	1.12×10^{-9}	***
<i>STXBP1</i>	9	1,917.51	6.44×10^{-5}	5	1.16×10^{-11}	***
<i>GABRB3</i>	15	1,206.86	3.78×10^{-5}	4	4.11×10^{-10}	***
<i>CDKL5</i>	X	2,798.38	5.44×10^{-5}	3	4.90×10^{-7}	**
<i>ALG13§</i>	X	475.05	1.03×10^{-5}	2	7.77×10^{-12}	***
<i>DNM1</i>	9	2,323.37	9.10×10^{-5}	2	2.84×10^{-4}	
<i>HDAC4</i>	2	2,649.82	1.16×10^{-4}	2	4.57×10^{-4}	
<i>SCN2A§</i>	2	5,831.21	1.52×10^{-4}	2	1.14×10^{-9}	***
<i>SCN8A</i>	12	5,814.48	1.64×10^{-4}	2	9.14×10^{-4}	

† Adjusted α is equivalent to $0.05/18,091 = 2.76 \times 10^{-6}$ (*), $0.01/18,091 = 5.53 \times 10^{-7}$ (**) and $0.001/18,091 = 5.53 \times 10^{-8}$ (***).

‡ Counts exclude three additional patients with an indel or splice site mutation as these are not accounted for in the mutability calculation.

§ Two *de novo* mutations occur at the same position. The probability of these special cases obtain $P = 7.77 \times 10^{-12}$ and $P = 1.14 \times 10^{-9}$ for *ALG13* and *SCN2A*, respectively (Methods).

that can confer risk of epileptic encephalopathies and that each mutation carries substantial risk. We also found that putatively damaging *de novo* variants in our cohort are significantly enriched in intolerant genes compared with control cohorts (Supplementary Methods).

We next evaluated whether the *de novo* mutations were drawn preferentially from six gene sets (Methods and Supplementary Table 10), including ion channels²², genes known to cause monogenic disorders with seizures as a phenotypic feature²³, genes carrying confirmed *de novo* mutations in patients with autism spectrum disorder^{2,8,19,20} and in patients with intellectual disability^{18,24}, and FMRP-regulated genes. Taking into account the size of regions with adequate sequencing coverage to detect a *de novo* mutation (Methods), we found significant over-representation for all gene lists in our data (Supplementary Table 10), and no over-representation in controls^{2,19,20,24}.

To determine possible interconnectivity among the genes carrying a *de novo* mutation, we performed a protein–protein interaction analysis and identified a single network of 71 connected proteins (Fig. 2 and Supplementary Fig. 7). These 71 proteins include six encoded by OMIM reported epileptic encephalopathy genes (<http://www.omim.org/>) where we identified one or more *de novo* mutations among the epileptic encephalopathy patients in this study. Genes in this protein–protein network were also found to have a much greater probability of overlap with the autism spectrum disorder^{2,8,19,20} and severe intellectual disability disorder^{18,24} exome sequencing study genes, and with FMRP-associated genes, than genes not in this network (Supplementary Table 11).

In support of a hypothesis that individual rare mutations in different genes may converge on biological pathways, we draw attention to six mutations that all affect subunits of the GABA (γ -aminobutyric acid) ionotropic receptor (four in *GABRB3*, and one each in *GABRA1* and

GABRB1), and highlight two interactions: *HNRNPU* interacting with *HNRNPH1*, and *NEDD4L* (identified here) binding to *TNK2*, a gene previously implicated in epileptic encephalopathies²⁵ (Fig. 2). Although the *HNRNPU* mutation observed here is a small insertion/deletion variant (indel) in a splice acceptor site, and therefore probably results in a modified protein, the *HNRNPH1 de novo* mutation is synonymous and thus of unknown functional significance (Supplementary Table 2). Notably, a minigene experiment indicates that this synonymous mutation induces skipping of exon 12 (Supplementary Methods).

Evaluation of the clinical phenotypes among patients revealed significant genetic heterogeneity underlying infantile spasms and Lennox–Gastaut syndrome, and begins to provide information about the range of phenotypes associated with mutations in specific genes (Supplementary Table 13). We identified four genes—*SCN8A*, *STXBP1*, *DNM1* and *GABRB3*—with *de novo* mutations in both patients with infantile spasms and patients with Lennox–Gastaut syndrome. Although infantile spasms may progress to Lennox–Gastaut syndrome, in three of these cases the patients with Lennox–Gastaut syndrome did not initially present with infantile spasms, indicating phenotypic heterogeneity associated with mutations in these genes yet supporting the notion of shared genetic susceptibility. Notably, in multiple patients we identified *de novo* mutations in genes previously implicated in other neurodevelopmental conditions, and in some cases with very distinctive clinical presentations (Supplementary Table 12). Most notably, we found a *de novo* mutation in *MTOR*, a gene recently found to harbour a causal variant in mosaic form in a case with hemimegalencephaly²⁶. Our patient however showed no detectable structural brain malformation. Similarly, we found one patient with a *de novo* mutation in *DCX* and another with a *de novo* mutation in *FLNA*, previously associated with lissencephaly and periventricular nodular heterotopia, respectively^{27,28}; neither patient had cortical malformations detected on magnetic resonance imaging.

In addition to *de novo* variants, we also screened for highly penetrant genotypes by identifying variants that create newly homozygous, compound heterozygous, or hemizygous genotypes in the probands that are not seen in parents or controls (Supplementary Methods). No inherited variants showed significant evidence of association. Additional studies evaluating a larger number of epileptic encephalopathy patients will be required to establish the role of inherited variants in the disease risk associated with infantile spasms and Lennox–Gastaut syndrome.

We have identified novel *de novo* mutations implicating at least two genes for epileptic encephalopathies, and also describe a genetic architecture that strongly suggests that we have identified additional causal mutations in genes intolerant to functional variation. Given that our sample size already shows many genes with recurrent mutations, it is clear that even modest increases in sample sizes will confirm many new genes now seen in only one of our trios. Our results also emphasize that it may be difficult to predict with confidence the responsible gene, even among known genes, based upon clinical presentation. This makes it clear that the future of genetic diagnostics in epileptic encephalopathies will need to focus on the genome as a whole as opposed to single genes or even gene panels. In particular, several of the genes with *de novo* mutations in our cohort have also been identified in patients with

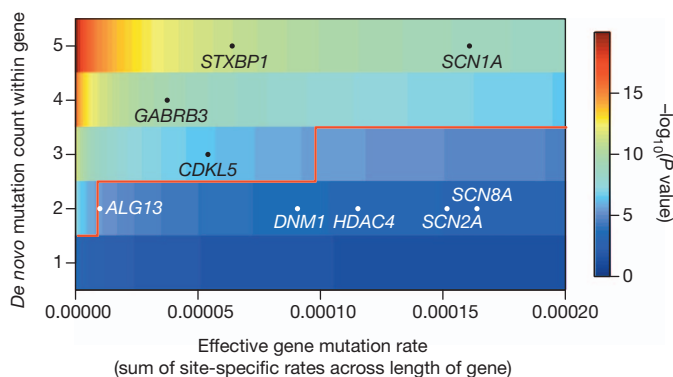


Figure 1 | Heat map illustrating the probability of observing the specified number of *de novo* mutations in genes with the specified estimated mutation rate. The number of *de novo* mutations required to achieve significance is indicated by the solid red line. The superimposed dots reflect positions of all genes found to harbour multiple *de novo* mutations in our study. *GABRB3*, *SCN1A*, *CDKL5* and *STXBP1* have significantly more *de novo* mutations than expected. The positions indicated for *ALG13* and *SCN2A* reflect only the fact that there are two mutations observed, not that there are two mutations affecting the same site (Methods).

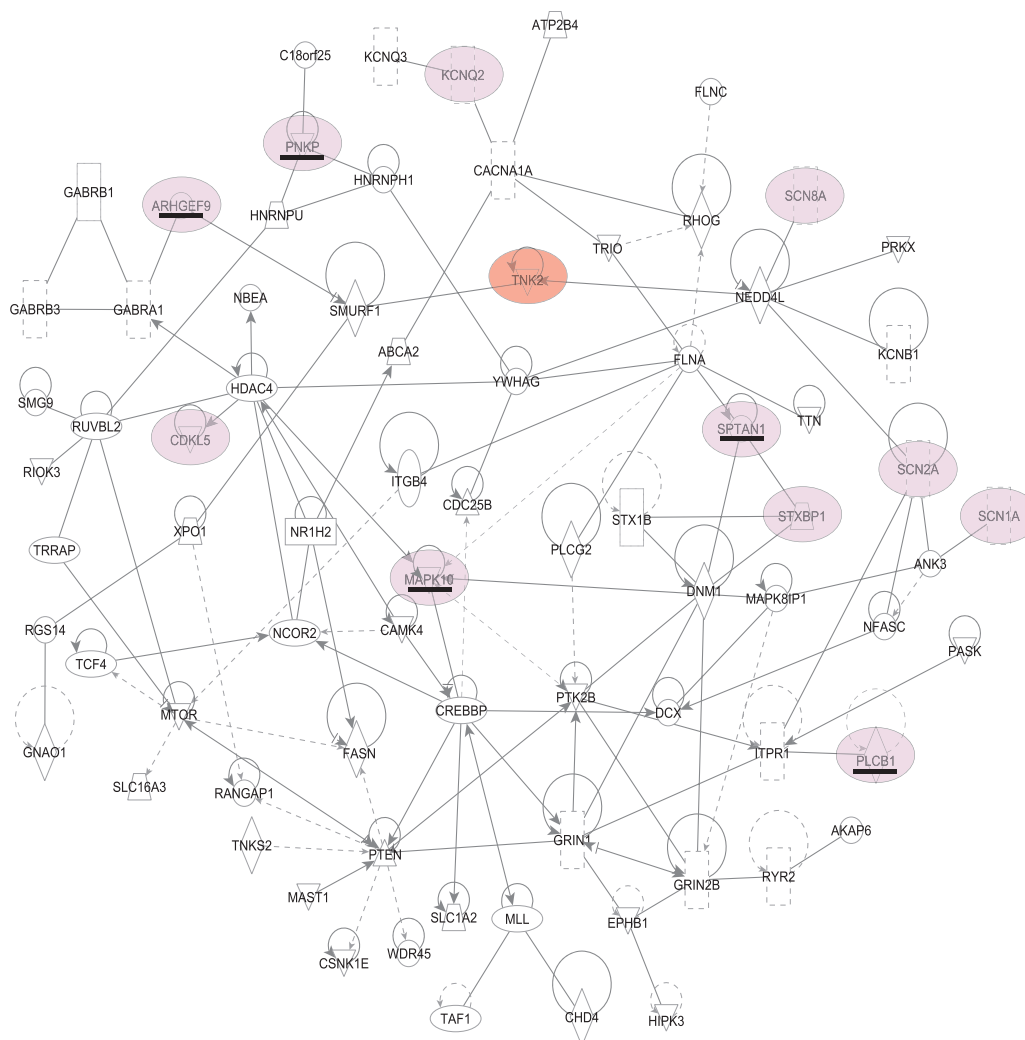


Figure 2 | A protein-protein interaction network of genes with *de novo* mutations found in infantile spasms and Lennox-Gastaut syndrome patients studied. The geometric shapes reflect differing protein roles, as defined by ingenuity pathway analysis (Ingenuity Systems): enzyme, rhombus; ion channel, vertical rectangle; kinase, inverted triangle; ligand-dependent nuclear receptor, horizontal rectangle; phosphatase, triangle; transcription regulator, horizontal oval; transmembrane receptor, vertical oval; transporter, trapezoid; and unknown, circle. Six of the genes found to harbour

de novo mutations in an infantile spasms or Lennox–Gastaut syndrome patient are known OMIM genes associated with epileptic encephalopathy (shaded circles). Five additional known OMIM genes associated with epileptic encephalopathy that were not found to be mutated in the 264 epileptic encephalopathy patients, but are involved in this network, are also shown (shaded circles with the gene underlined). The previously identified severe infantile epilepsy gene *TNK2* is superimposed into this network (red circle).

intellectual disability or autism spectrum disorder. Finally, and perhaps most importantly, this work suggests a clear direction for both drug development and treatment personalization in the epileptic encephalopathies, as many of these mutations seem to converge on specific biological pathways.

METHODS SUMMARY

All probands and family members were collected as part of the Epilepsy Phenome/Genome Project (EPGP) cohort²⁹ (Supplementary Table 1). Detailed inclusion and exclusion criteria are provided in Methods. Patient collection and sharing of specimens for research were approved by site-specific Institutional Review Boards.

We sequenced the exome of each trio, from DNA derived from primary cells ($n = 224$ trios) or from lymphoblastoid cell lines (LCLs) in one or more family members ($n = 40$ trios), using the TruSeq Exome Enrichment kit (Illumina). We aligned samples and called variants using established algorithms (Methods) and identified candidate *de novo* variants at sites included in the exons or splice sites of the consensus coding sequence (CCDS) as those called in the affected child and absent in both parents, despite each parent having at least tenfold coverage at the site. Variants created by the *de novo* mutation also had to be absent in our internal controls ($n = 436$), as well as the approximately 6,500 samples represented in the Exome Variant Server (<http://evs.gs.washington.edu/EVS>), and had to pass visual

inspection of alignment quality. Candidate *de novo* mutations were confirmed to be *de novo* mutations using Sanger sequencing. In all cases, primary DNA from the proband was used for the Sanger confirmation so that mutations appearing in the transformation process for the 40 trios sequenced from LCLs would be eliminated.

To determine whether our list of *de novo* mutations was preferentially located in genes contained in the six gene lists we calculated the proportion of CCDS *de novo* mutation opportunity space for each list (Additional Methods). A binomial probability calculation was used to determine whether the *de novo* mutations in CCDS transcripts identified in this cohort of epileptic encephalopathy patients were selectively enriched within the coding sequence of genes within a particular gene list (Supplementary Table 10).

Ingenuity Pathway Analysis (Ingenuity Systems) was used to assess the connectivity of proteins harbouring a *de novo* mutation.

Full Methods and any associated references are available in the online version of the paper.

Received 3 March; accepted 9 July 2013.

Published online 11 August 2013.

1. Berg, A.T. et al. Revised terminology and concepts for organization of seizures and epilepsies: report of the ILAE Commission on Classification and Terminology, 2005–2009. *Epilepsia* **51**, 676–685 (2010).

2. lossifov, I. *et al.* *De novo* gene disruptions in children on the autistic spectrum. *Neuron* **74**, 285–299 (2012).
3. EPICURE Consortium *et al.* Genome-wide association analysis of genetic generalized epilepsies implicates susceptibility loci at 1q43, 2p16.1, 2q22.3 and 17q21.32. *Hum. Mol. Genet.* **21**, 5359–5372 (2012).
4. Heinzen, E. L. *et al.* Exome sequencing followed by large-scale genotyping fails to identify single rare variants of large effect in idiopathic generalized epilepsy. *Am. J. Hum. Genet.* **91**, 293–302 (2012).
5. Mulley, J. C. & Mefford, H. C. Epilepsy and the new cytogenetics. *Epilepsia* **52**, 423–432 (2011).
6. Kasperaviciute, D. *et al.* Common genetic variation and susceptibility to partial epilepsies: a genome-wide association study. *Brain* **133**, 2136–2147 (2010).
7. Vissers, L. E. *et al.* A *de novo* paradigm for mental retardation. *Nature Genet.* **42**, 1109–1112 (2010).
8. Neale, B. M. *et al.* Patterns and rates of exonic *de novo* mutations in autism spectrum disorders. *Nature* **485**, 242–245 (2012).
9. Kalscheuer, V. M. *et al.* Disruption of the serine/threonine kinase 9 gene causes severe X-linked infantile spasms and mental retardation. *Am. J. Hum. Genet.* **72**, 1401–1411 (2003).
10. Claes, L. *et al.* *De novo* mutations in the sodium-channel gene *SCN1A* cause severe myoclonic epilepsy of infancy. *Am. J. Hum. Genet.* **68**, 1327–1332 (2001).
11. Saitsu, H. *et al.* *De novo* mutations in the gene encoding STXBP1 (*MUNC18-1*) cause early infantile epileptic encephalopathy. *Nature Genet.* **40**, 782–788 (2008).
12. Otsuka, M. *et al.* STXBP1 mutations cause not only Ohtahara syndrome but also West syndrome—result of Japanese cohort study. *Epilepsia* **51**, 2449–2452 (2010).
13. Veeramah, K. R. *et al.* *De novo* pathogenic *SCN8A* mutation identified by whole-genome sequencing of a family quartet affected by infantile epileptic encephalopathy and SUDEP. *Am. J. Hum. Genet.* **90**, 502–510 (2012).
14. Kamiya, K. *et al.* A nonsense mutation of the sodium channel gene *SCN2A* in a patient with intractable epilepsy and mental decline. *J. Neurosci.* **24**, 2690–2698 (2004).
15. Tanaka, M., DeLorey, T. M., Delgado-Escueta, A. & Olsen, R. W. In *Jasper's Basic Mechanisms of the Epilepsies* (eds Noebels, J. L. *et al.*) (2012).
16. DeLorey, T. M. *et al.* Mice lacking the β_3 subunit of the GABA_A receptor have the epilepsy phenotype and many of the behavioral characteristics of Angelman syndrome. *J. Neurosci.* **18**, 8505–8514 (1998).
17. Timal, S. *et al.* Gene identification in the congenital disorders of glycosylation type I by whole-exome sequencing. *Hum. Mol. Genet.* **21**, 4151–4161 (2012).
18. de Ligt, J. *et al.* Diagnostic exome sequencing in persons with severe intellectual disability. *N. Engl. J. Med.* **367**, 1921–1929 (2012).
19. O'Roak, B. J. *et al.* Sporadic autism exomes reveal a highly interconnected protein network of *de novo* mutations. *Nature* **485**, 246–250 (2012).
20. Sanders, S. J. *et al.* *De novo* mutations revealed by whole-exome sequencing are strongly associated with autism. *Nature* **485**, 237–241 (2012).
21. Petrovski, S. *et al.* Genic intolerance to functional variation and the interpretation of personal genomes. *PLoS Gen.* (in the press) (2013).
22. Klassen, T. *et al.* Exome sequencing of ion channel genes reveals complex profiles confounding personal risk assessment in epilepsy. *Cell* **145**, 1036–1048 (2011).
23. Lemke, J. R. *et al.* Targeted next generation sequencing as a diagnostic tool in epileptic disorders. *Epilepsia* **53**, 1387–1398 (2012).
24. Rauch, A. *et al.* Range of genetic mutations associated with severe non-syndromic sporadic intellectual disability: an exome sequencing study. *Lancet* **380**, 1674–1682 (2012).
25. Hitomi, Y. *et al.* Mutations in *TNKS2* in severe autosomal recessive infantile-onset epilepsy. *Ann. Neurol.* <http://dx.doi.org/doi:10.1002/ana.23934> (2013).
26. Lee, J. H. *et al.* *De novo* somatic mutations in components of the PI3K-AKT3-mTOR pathway cause hemimegalencephaly. *Nature Genet.* **44**, 941–945 (2012).
27. Gleeson, J. G. *et al.* Doublecortin, a brain-specific gene mutated in human X-linked lissencephaly and double cortex syndrome, encodes a putative signaling protein. *Cell* **92**, 63–72 (1998).
28. Fox, J. W. *et al.* Mutations in filamin 1 prevent migration of cerebral cortical neurons in human periventricular heterotopia. *Neuron* **21**, 1315–1325 (1998).
29. The EPGP Collaborative. The Epilepsy Phenome/Genome Project. *Clin. Trials* **10**, 568–586 (2013).

Supplementary Information is available in the online version of the paper.

Acknowledgements We are grateful to the patients, their families, clinical research coordinators and referring physicians for participating in the Epilepsy Phenome/Genome Project (EPGP) and providing the phenotype data and DNA samples used in this study. We thank the following professional and lay organizations for substantial assistance in publicizing EPGP and therefore enabling us to recruit participants effectively: AED Pregnancy Registry, American Epilepsy Society, Association of Child Neurology Nurses, California School Nurses Organization, Child Neurology Society, Citizens United for Research in Epilepsy, Dravet Syndrome Foundation, Epilepsy Alliance of Orange County, Epilepsy Foundation, Epilepsy Therapy Project, Finding a Cure for Epilepsy and Seizures, IDEA League, InfantileSpasms.com, Lennox-Gastaut Syndrome Foundation, PatientsLikeMe, People Against Childhood Epilepsy, PVNH Support & Awareness, and Seizures & Epilepsy Education. We thank the EPGP Administrative Core (C. Freyer, K. Schardein, R.N., M.S., R. Fahlstrom, M.P.H., S. Cristofaro, R.N., B.S.N. and K. McGovern), EPGP Bioinformatics Core (G. Nesbitt, K. McKenna, V. Mays), staff at the Coriell Institute – NINDS Genetics Repository (C. Tarn, A. Scutti), and members of the Duke Center for Human Genome Variation (B. Krueger, J. Bridgers, J. Keebler, H. Shin Kim, E. Campbell, K. Cronin, L. Hong and M. McCall) for their dedication and commitment to this work. We also thank S. Shinnar (Albert Einstein College of Medicine) and N. Risch (University of California, San Francisco) for valuable

input into the creation of EPGP and Epi4K, and R. Stewart, K. Gwinn and R. Corriveau from the National Institute of Neurological Disorders and Stroke for their careful oversight and guidance of both EPGP and Epi4K. This work was supported by grants from the National Institute of Neurological Disorders and Stroke (The Epilepsy Phenome/Genome Project NS053998; Epi4K Project 1—Epileptic Encephalopathies NS077364; Epi4K—Administrative Core NS077274; Epi4K—Sequencing, Biostatistics and Bioinformatics Core NS077303 and Epi4K—Phenotyping and Clinical Informatics Core NS077276); Finding a Cure for Epilepsy and Seizures; and the Richard Thalheimer Philanthropic Fund. We would like to acknowledge the following individuals and groups for their contribution of control samples: J. Hoover-Fong, N. Sobreira and D. Valle; The MURDOCK Study Community Registry and Biorepository (D. Murdock); S. Sisodiya; D. Attix; O. Chiba-Falek; V. Shashi; P. Lugal; W. Lowe; S. Palmer; D. Marchuk; Z. Farfel; D. Lancet; E. Pras; Q. Zhao; D. Daskalakis; R. Brown; E. Holtzman; R. Gbadegesin; M. Winn; S. Kerns; and H. Oster. The collection of control samples was funded in part by ARRA 1RC2NS070342, NIAID R56AI098588, the Ellison Medical Foundation New Scholar award AG-NS-0441-08, an award from SAID-Frederick, Inc. (M11-074), and with federal funds by the Center for HIV/AIDS Vaccine Immunology ("CHAVI") under a grant from the National Institute of Allergy and Infectious Diseases, National Institutes of Health (U01AI067854).

Author contributions Initial design of EPGP: B.K.A., O.D., D.D., M.P.E., R.Kuz., D.H.L., R.O., E.H.S. and M.R.W. EPGP patient recruitment and phenotyping: B.A.-K., J.F.B., S.F.B., G.C., D.C., P.Cr., O.D., D.D., M.F., N.B.F., D.F., E.B.G., T.G., S.G., S.R.H., J.H., S.L.H., H.E.K., R.C.K., E.H.K., R.Kup., R.Kuz., D.H.L., S.M.M., P.V.M., E.J.N., J.M.Pao., J.M.Par., K.P., A.P., I.E.S., J.J.S., R.S., J.Si., M.C.S., L.L.T., A.V., E.P.G.V., G.K.V.A., J.L.W. and P.W.-W. Phenotype data analysis: B.A.-K., B.K.A., A.B., G.C., O.D., D.D., J.F., T.G., S.J., A.K., R.C.K., R.Kuz., D.H.L., R.O., J.M.Pao., A.P., I.E.S., R.A.S., E.H.S., J.J.S., J.Su., P.W.-W. and M.R.W. Initial design of Epi4K: S.F.B., P.Co., N.D., D.D., E.E.E., M.P.E., T.G., D.B.G., E.L.H., M.R.J., R.Kuz., D.H.L., A.G.M., H.C.M., T.J.O., R.O., A.P., I.E.S. and E.H.S. Epileptic encephalopathy phenotyping strategy: S.F.B., P.Co., D.D., R.Kuz., D.H.L., R.O., I.E.S. and E.H.S. Encephalopathy phenotyping: D.D., K.B.H., M.R.Z.M., H.C.M., A.P., I.E.S., E.H.S. and C.J.Y. Sequence data analysis and statistical interpretation: A.S.A., D.B.G., Y.Ha., E.L.H., S.E.N., S.P., E.K.R. and E.H.S. Functional evaluation of identified mutations: D.B.G., E.L.H., Y.Hi. and Y.-F.L. Writing of manuscript: A.S.A., S.F.B., D.D., D.B.G., Y.Ha., E.L.H., M.R.J., D.H.L., H.C.M., R.O., A.P., S.P., E.K.R., I.E.S. and E.H.S.

Author Information Exome sequence data will be available in dbGAP (Epi4K: Gene Discovery in 4,000 Epilepsy Genomes). Reprints and permissions information is available at www.nature.com/reprints. The authors declare no competing financial interests. Readers are welcome to comment on the online version of the paper. Correspondence and requests for materials should be addressed to Epi4K (epi4k@duke.edu).

Epi4K Consortium

Andrew S. Allen¹, Samuel F. Berkovic², Patrick Cossette³, Norman Delanty⁴, Dennis Dlugos⁵, Evan E. Eichler⁶, Michael P. Epstein⁷, Tracy Glauser⁸, David B. Goldstein⁹, Yujun Han⁹, Erin L. Heinzen⁹, Yuki Hitomi⁹, Katherine B. Howell¹⁰, Michael R. Johnson¹¹, Ruben Kuzniecky¹², Daniel H. Lowenstein¹³, Yi-Fan Lu⁹, Maura R. Z. Madou¹³, Anthony G. Marson¹⁴, Heather C. Mefford¹⁵, Sahar Esmaeili Nieh¹⁶, Terence J. O'Brien¹⁷, Ruth Ottman¹⁸, Slavé Petrovski^{29,17}, Annapurna Poduri¹⁹, Elizabeth K. Ruzzo⁹, Ingrid E. Scheffer^{20,21}, Elliott H. Sherr²² & Christopher J. Yuskaitis²³

Epilepsy Phenome/Genome Project

Bassel Abou-Khalil²⁴, Brian K. Alldredge²⁵, Jocelyn F. Bautista²⁶, Samuel F. Berkovic², Alex Borot²⁷, Gregory D. Cascino²⁸, Damian Consalvo²⁹, Patricia Crumrine³⁰, Orrin Devinsky³¹, Dennis Dlugos⁵, Michael P. Epstein⁷, Miguel Fiol³², Nathan B. Fountain³³, Jacqueline French¹², Daniel Friedman¹², Eric B. Geller³⁴, Tracy Glauser⁸, Simon Glynn³⁵, Sheryl R. Haut³⁶, Jean Hayward³⁷, Sandra L. Helmers³⁸, Sucheta Joshi³⁹, Andres Kanner⁴⁰, Heidi E. Kirsch^{13,41}, Robert C. Knowlton⁴², Eric H. Kossoff⁴³, Rachel Kuperman⁴⁴, Ruben Kuzniecky¹², Daniel H. Lowenstein¹³, Shannon M. McGuire⁴⁵, Paul V. Motika⁴⁶, Edward J. Novotny⁴⁷, Ruth Ottman¹⁸, Juliann M. Paolicchi^{24,48}, Jack M. Parent^{49,50}, Kristen Park⁵¹, Annapurna Poduri¹⁹, Ingrid E. Scheffer^{20,21}, Renée A. Shellhaas⁵², Elliott H. Sherr²², Jerry J. Shih⁵³, Rani Singh⁵⁴, Joseph Sirven⁵⁵, Michael C. Smith⁴⁰, Joseph Sullivan¹³, Liu Lin Thio⁵⁶, Anu Venkat⁵, Eileen P. G. Vining³⁷, Gretchen K. Von Allmen⁵⁸, Judith L. Weisenberg⁵⁹, Peter Widdess-Walsh³⁴ & Melodie R. Winawer⁶⁰

¹Department of Biostatistics and Bioinformatics, Duke Clinical Research Institute, and Center for Human Genome Variation, Duke University Medical Center, Durham, North Carolina 27710, USA. ²Epilepsy Research Centre, Department of Medicine, University of Melbourne (Austin Health), Heidelberg, Victoria 3084, Australia. ³Centre of Excellence in Neuroimaging and CHUM Research Center, Université de Montréal, CHUM-Hôpital Notre-Dame Montréal, Québec H2L 4M1, Canada. ⁴Department of Neurology, Beaumont Hospital and Royal College of Surgeons, Dublin 9, Ireland. ⁵Department of Neurology and Pediatrics, The Children's Hospital of Philadelphia, Perelman School of Medicine at the University of Pennsylvania, Philadelphia, Pennsylvania 19104, USA. ⁶Department of Genome Sciences, University of Washington School of Medicine, Seattle, and Howard Hughes Medical Institute, University of Washington, Seattle, Washington 98195, USA. ⁷Department of Human Genetics, Emory University School of Medicine, Atlanta, Georgia 30322, USA. ⁸Division of Neurology, Cincinnati Children's Hospital Medical Center, Cincinnati, Ohio 45229, USA. ⁹Center for Human Genome Variation, Duke University School of Medicine, Durham, North Carolina 27708, USA. ¹⁰Department of Neurology,

The Royal Children's Hospital Melbourne, Parkville, 3052 Victoria, Australia. ¹¹Centre for Clinical Translation Division of Brain Sciences, Imperial College London, London SW7 2AZ, UK. ¹²Comprehensive Epilepsy Center, Department of Neurology, NYU School of Medicine, New York, New York 10016, USA. ¹³Department of Neurology, University of California, San Francisco, San Francisco, California 94143, USA. ¹⁴Department of Molecular and Clinical Pharmacology, University of Liverpool, Clinical Sciences Centre, Lower Lane, Liverpool L9 7LJ, UK. ¹⁵Department of Pediatrics, Division of Genetic Medicine, University of Washington, Seattle, Washington 98115, USA. ¹⁶University of California, San Francisco, California 94143, USA. ¹⁷Departments of Medicine and Neurology, The Royal Melbourne Hospital, Parkville, Victoria 3146, Australia. ¹⁸Departments of Epidemiology and Neurology, and the G. H. Sergievsky Center, Columbia University; and Division of Epidemiology, New York State Psychiatric Institute, New York, New York 10032, USA. ¹⁹Division of Epilepsy and Clinical Neurophysiology, Department of Neurology Boston Children's Hospital, Boston, Massachusetts 02115, USA. ²⁰Epilepsy Research Centre, Department of Medicine, University of Melbourne (Austin Health), Heidelberg, Victoria 3084, Australia. ²¹Florey Institute and Department of Pediatrics, Royal Children's Hospital, University of Melbourne, Victoria 3052, Australia. ²²Departments of Neurology, Pediatrics and Institute of Human Genetics, University of California, San Francisco, San Francisco, California 94158, USA. ²³Department of Neurology, Boston Children's Hospital Harvard Medical School, Boston, Massachusetts 02115, USA. ²⁴Department of Neurology, Vanderbilt University Medical Center, Nashville, Tennessee 37232, USA. ²⁵Department of Clinical Pharmacy, UCSF School of Pharmacy, Department of Neurology, UCSF School of Medicine, San Francisco, California 94143, USA. ²⁶Department of Neurology, Cleveland Clinic Lerner College of Medicine & Epilepsy Center of the Cleveland Clinic Neurological Institute, Cleveland, Ohio 44195, USA. ²⁷Department of Neurology, Montefiore Medical Center, Albert Einstein College of Medicine, Bronx, New York 10467, USA. ²⁸Division of Epilepsy, Mayo Clinic, Rochester, Minnesota 55905, USA. ²⁹Epilepsy Center, Neurology Division, Ramos Mejia Hospital, Buenos Aires 1221, Argentina. ³⁰Medical Epilepsy Program & EEG & Child Neurology, Children's Hospital of Pittsburgh of UPMC, Pediatrics, University of Pittsburgh School of Medicine, Pittsburgh, Pennsylvania 15224, USA. ³¹NYU and Saint Barnabas Epilepsy Centers, NYU School of Medicine, New York, New York 10016, USA. ³²Department of Neurology, Epilepsy Care Center, University of Minnesota Medical School, Minneapolis 55414, USA. ³³FE Dreifuss Comprehensive Epilepsy Program, University of Virginia, Charlottesville, Virginia 22908, USA. ³⁴Division of Neurology, Saint Barnabas Medical Center, Livingston, New Jersey 07039, USA. ³⁵Department of Neurology, Comprehensive Epilepsy Program, University of Michigan Health System, Ann Arbor, Michigan 48109, USA. ³⁶Comprehensive Epilepsy Center, Montefiore Medical Center, Bronx, New York 10467, USA. ³⁷The Kaiser Permanente Group, Oakland, California 94618, USA. ³⁸Neurology and Pediatrics, Emory University School of Medicine, Atlanta, Georgia 30322, USA. ³⁹Pediatrics & Communicable Diseases, University of Michigan, Ann Arbor, Michigan 48109, USA. ⁴⁰Department of Neurological Sciences, Rush Epilepsy Center, Rush University Medical Center, Chicago, Illinois 60612, USA. ⁴¹Department of Radiology, University of California, San Francisco, California 94143, USA. ⁴²Neurology, University of Texas Medical School, Houston, Texas 77030, USA. ⁴³Neurology and Pediatrics, Child Neurology, Pediatric Neurology Residency Program, Johns Hopkins Hospital, Baltimore, Maryland 21287, USA. ⁴⁴Epilepsy Program, Children's Hospital & Research Center Oakland, Oakland, California 94609, USA. ⁴⁵Clinical Neurology, Children's Hospital Epilepsy Center of New Orleans, New Orleans, Louisiana 70118, USA. ⁴⁶Comprehensive Epilepsy Center, Oregon Health and Science University, Portland, Oregon 97239, USA. ⁴⁷Departments of Neurology and Pediatrics, University of Washington School of Medicine, Seattle Children's Hospital, Seattle, Washington 98105, USA. ⁴⁸Weill Cornell Medical Center, New York, New York 10065, USA. ⁴⁹Department of Neurology and Neuroscience Graduate Program, University of Michigan Medical Center, Ann Arbor, Michigan 49108, USA. ⁵⁰Ann Arbor Veterans Administration Healthcare System, Ann Arbor, Michigan 48105, USA. ⁵¹Departments of Neurology and Pediatrics, University of Colorado School of Medicine, Children's Hospital Colorado, Denver, Colorado 80045, USA. ⁵²University of Michigan, Pediatric Neurology, Ann Arbor, Michigan 48109, USA. ⁵³Department of Neurology, Mayo Clinic, Jacksonville, Florida 32224, USA. ⁵⁴Division of Pediatric Neurology, University of Michigan Health System, Ann Arbor, Michigan 48109, USA. ⁵⁵Department of Neurology, Mayo Clinic, Scottsdale, Arizona 85259, USA. ⁵⁶Department of Neurology, Washington University School of Medicine, St Louis, Missouri 63110, USA. ⁵⁷Department of Neurology, Johns Hopkins Hospital, Baltimore, Maryland 21287, USA. ⁵⁸Division of Child & Adolescent Neurology, Departments of Pediatrics, University of Texas Medical School, Houston, Texas 77030, USA. ⁵⁹Department of Neurology, Division of Pediatric Neurology, Washington University School of Medicine, St Louis, Missouri 63110, USA. ⁶⁰Department of Neurology and the G.H. Sergievsky Center, Columbia University, New York, New York 10032, USA.

METHODS

Study subjects. Infantile spasms and Lennox–Gastaut syndrome patients evaluated in this study were collected through the Epilepsy Phenome/Genome Project (EPGP, <http://www.epgp.org>)²⁹. Patients were enrolled across 23 clinical sites. Informed consent was obtained for all patients in accordance with the site-specific Institutional Review Boards. Phenotypic information has been centrally databased and DNA specimens stored at the Coriell Institute–NINDS Genetics Repository (Supplementary Table 1). Infantile spasms patients were required to have hypsarrhythmia or a hypsarrhythmia variant on EEG. Lennox–Gastaut syndrome patients were required to have EEG background slowing or disorganization for age and generalized spike and wave activity of any frequency or generalized paroxysmal fast activity (GPFA). Background slowing was defined as <8 Hz posterior dominant rhythm in patients over 3 years of age, and <5 Hz in patients over 2 years of age. EEGs with normal backgrounds were accepted if the generalized spike and wave activity was 2.5 Hz or less and/or if GPFA was present.

All patients were required to have no evidence of moderate-to-severe developmental impairment or diagnosis of autistic disorder or pervasive developmental disorder before the onset of seizures. Severe developmental delay was defined by 50% or more delay in any area: motor, social, language, cognition, or activities of living; or global delay. Mild delay was defined as delay of less than 50% of expected milestones in one area, or less than 30% of milestones across more than one area. All patients had no confirmed genetic or metabolic diagnosis, and no history of congenital TORCH infection, premature birth (before 32 weeks gestation), neonatal hypoxic-ischaemic encephalopathy or neonatal seizures, meningitis/encephalitis, stroke, intracranial haemorrhage, significant head trauma, or evidence of acquired epilepsy. All infantile spasms and Lennox–Gastaut syndrome patients had an MRI or CT scan interpreted as normal, mild diffuse atrophy or focal cortical dysplasia. (Our case with the mutation in *HNRNPU* had had a reportedly normal MRI but on review of past records, a second more detailed MRI was found showing small regions of periventricular nodular heterotopia.) To participate, both biological parents had to have no past medical history of seizures (except febrile or metabolic/toxic seizures).

A final diagnosis form was completed by the local site EPGP principal investigator based on all collected information. A subset of cases was reviewed independently by two members of the EPGP Data Review Core to ensure data quality and consistency. All EEGs were reviewed by a site investigator and an EEG core member to assess data quality and EEG inclusion criteria. EEGs accepted for inclusion were then reviewed and scored by two EEG core members for specific EEG phenotypic features. Disagreements were resolved by consensus conference among two or more EEG core members before the EEG data set was finalized. MRI scans were reviewed by local investigators and an MRI core member to exclude an acquired symptomatic lesion.

Exome-sequenced unrelated controls ($n = 436$) used to ascertain mutation frequencies were sequenced in the Center for Human Genome Variation as part of other genetic studies.

Exome sequencing, alignment and variant calling. Exome sequencing was carried out within the Genomic Analysis Facility in the Center for Human Genome Variation (Duke University). Sequencing libraries were prepared from primary DNA extracted from leukocytes of parents and probands using the Illumina TruSeq library preparation kit following the manufacturer's protocol. Illumina TruSeq Exome Enrichment kit was used to selectively amplify the coding regions of the genome according to the manufacturer's protocol. Six individual barcoded samples (two complete trios) were sequenced in parallel across two lanes of an Illumina HiSeq 2000 sequencer.

Alignment of the sequenced DNA fragments to Human Reference Genome (NCBI Build 37) was performed using the Burrows–Wheeler Alignment Tool (BWA) (version 0.5.10). The reference sequence we use is identical to the 1000 Genomes Phase II reference and it consists of chromosomes 1–22, X, Y, MT, unplaced and unlocalized contigs, the human herpesvirus 4 type 1 (NC_007605), and decoy sequences (hs37d5) derived from HuRef, Human Bac and Fosmid clones and NA12878.

After alignments were produced for each individual separately using BWA, candidate *de novo* variants were jointly called with the GATK Unified Genotyper for all family members in a trio. Loci bearing putative *de novo* mutations were extracted from the variant call format files (VCFs) that met the following criteria: (1) the read depth in both parents should be greater than or equal to 10; (2) the depth of coverage in the child should be at least one-tenth of the sum of the coverage in both parents; (3) for *de novo* variants, less than 5% of the reads in either parent should carry the alternate allele; (4) at least 25% of the reads in the child should carry the alternate allele; (5) the normalized, phred-scaled likelihood (PL) scores for the offspring genotypes AA, AB and BB, where A is the reference allele and B is the alternate allele, should be >20, 0 and >0, respectively; (6) the PL scores for both parents should be 0, >20 and >20; (7) at least three variant alleles must be observed in the proband; and (8) the *de novo* variant had to be located in a CCDS exon targeted by the exome enrichment kit. PL scores are assigned such that the most likely genotype is given a score of 0, and the score for the other two genotypes

represent the likelihood that they are not the true genotypes. SnpEff (version 3.0a) was used to annotate the variants according to Ensembl (version 69) and consensus coding sequencing (CCDS release 9, GRCh37.p5) and limited analyses to exonic or splice site (2 bp flanking an exon) mutations. All candidate *de novo* mutations that were absent from population controls, including a set of 436 internally sequenced controls and the ~6,500 individuals whose single nucleotide variant data are reported in the Exome Variant Server, NHLBI Exome Sequencing Project (<http://evs.gs.washington.edu/EVS/>; August 2012) were also visually inspected using Integrative Genomics Viewer (IGV). All candidate *de novo* mutations were confirmed with Sanger sequencing of the relevant proband and parents. For comparison, we also called *de novo* variants from probands and parents individually for a subset of trios. Using this individual calling approach we identified and confirmed an additional 46 *de novo* mutations. These were included in all the downstream *de novo* mutation analyses.

Calculation of gene-specific mutation rate. Point mutation rates were scaled to per base pair, per generation, based on the human genome sequences matrix³⁰ (provided by S. Sunyaev and P. Polak), and the known human average genome *de novo* mutation rate (1.2×10^{-8})³¹. The mutation rate (M) of each gene was calculated by adding up point mutation rates in effectively captured CCDS regions in the offspring of trios, and then dividing by the total trio number ($S = 264$). The P value was calculated as $[1 - \text{Poisson cumulative distribution function}(x - 1, \lambda)]$, where x is the observed *de novo* mutation number for the gene, and λ is calculated as $2SM$ for genes on autosome or $(2f + m)M$ for genes on chromosome X (f and m are the number of sequenced female and male probands, respectively). Genes on Y chromosome were not part of these analyses. Two *de novo* mutations in gene *ALG13* are at the same position, likewise in gene *SCN2A*. We calculated the probability of this special case as $[1 - \text{Poisson cumulative distribution function}(1, (2f + m)r)]$, where r reflects the point mutation rate on that specific *de novo* mutation position. Further investigations indicated that it is unlikely for these *de novo* mutations, which occur at the same site across distinct probands, to have been caused by sequencing or mapping errors (Supplementary Methods).

Calculation of mutation tolerance for HGNC genes. To assign quantitatively a mutation tolerance score to genes in the human genome (HGNC genes), we calculated an empirical penalty based on the presence of common functional variation using the aggregate sequence data available from the 6,503 samples reported in the Exome Variant Server, NHLBI Exome Sequencing Project (<http://evs.gs.washington.edu/EVS/>; accessed August 2012). We first filtered within the EVS database and eliminated from further consideration genes where the number of tenfold average covered bases was less than 70% of its total extent. In calculating a score, we focused on departures from the average common functional variant frequency spectrum, corrected for the total mutation burden in a gene. We construct this score as follows. Let Y be the total number of common, minor allele frequency >0.1%, missense and nonsense (including splice) variants and let X be total number of variants (including synonymous) observed within a gene. We regress Y on X and take the studentized residual as the score (S). Thus, the raw residual is divided by an estimate of its standard deviation and thus account for differences in variability that comes with differing mutational burdens. S measures the departure from the average number of common functional mutations found in genes with a similar amount of mutational burden. Thus, when $S = 0$ the gene has the average number of common functional variants given its total mutational burden. Genes where $S < 0$ have less common functionals than average for their mutational burden and thus, would seem to be less tolerant of functional mutation, indicating the presence of weak purifying selection. We further investigated how different 'intolerance' thresholds of S captured known epileptic encephalopathy genes (Supplementary Table 8). Supplementary Fig. 6 illustrates how different percentiles of S lead to the classification of different proportions of the known epileptic encephalopathy genes as 'intolerant'. Note that *ARX* is not in these analyses as this gene did not meet a 70% of gene coverage threshold. The dashed vertical line in Supplementary Fig. 6 illustrates the 25th percentile of S and shows that using this threshold results in 12 out of the 14 assessed known genes being considered 'intolerant'. On the basis of this analysis, we used this 25th percentile threshold in classifying genes as intolerant in all subsequent analyses. Supplementary Table 9 lists the 25th percentile of most intolerant genes that had Sanger confirmed *de novo* mutations among the infantile spasms/Lennox–Gastaut syndrome probands.

Defining the CCDS opportunity space for detecting *de novo* mutations. For each trio, we defined callable exonic bases that had the opportunity for identification of a coding *de novo* mutation, by restricting to bases where each of the three family members had at least tenfold coverage, obtained a multi-sampling (GATK) raw phred-scaled confidence score of ≥ 20 in the presence or absence of a variant, and were within the consensus coding sequence (CCDS release 9, GRCh37.p5) or within the two base pairs at each end of exons to allow for splice acceptor and donor variants. Using these three criteria, the average CCDS-defined *de novo* mutation opportunity space across 264 trios was found to be 28.84 ± 0.92 Mb (range of 25.46–30.25 Mb).

To explore at the gene level, we similarly assessed the *de novo* calling opportunity within any given trio for every gene with a CCDS transcript. For genes with instances of non-overlapping CCDS transcripts, we merged the corresponding regions into a consensus summary of all CCDS-defined bases for that gene. Using these criteria, over 85% of the CCDS-defined exonic regions were sequenced to at least tenfold coverage across the three family members in over 90% of trios. All 264 trios covered at least 79% of the CCDS-defined regions under the CCDS opportunity space criteria.

Calculations of CCDS opportunity space for calling a *de novo* mutation, aside from the Y chromosome, were used in both the gene-list enrichment and architecture calculations.

30. Kryukov, G. V., Pennacchio, L. A. & Sunyaev, S. R. Most rare missense alleles are deleterious in humans: implications for complex disease and association studies. *Am. J. Hum. Genet.* **80**, 727–739 (2007).
31. Kong, A. *et al.* Rate of *de novo* mutations and the importance of father's age to disease risk. *Nature* **488**, 471–475 (2012).

Induction of mouse germ-cell fate by transcription factors *in vitro*

Fumio Nakaki¹, Katsuhiko Hayashi^{1,2,3}, Hiroshi Ohta^{1,4}, Kazuki Kurimoto^{1,4}, Yukihiro Yabuta^{1,4} & Mitinori Saitou^{1,2,4,5}

The germ-cell lineage ensures the continuity of life through the generation of male and female gametes, which unite to form a totipotent zygote. We have previously demonstrated that, by using cytokines, embryonic stem cells and induced pluripotent stem cells can be induced into epiblast-like cells (EpiLCs) and then into primordial germ cell (PGC)-like cells with the capacity for both spermatogenesis and oogenesis^{1,2}, creating an opportunity for understanding and regulating mammalian germ-cell development in both sexes *in vitro*. Here we show that, without cytokines, simultaneous overexpression of three transcription factors, *Blimp1* (also known as *Prdm1*), *Prdm14* and *Tfap2c* (also known as *AP2γ*), directs EpiLCs, but not embryonic stem cells, swiftly and efficiently into a PGC state. Notably, *Prdm14* alone, but not *Blimp1* or *Tfap2c*, suffices for the induction of the PGC state in EpiLCs. The transcription-factor-induced PGC state, irrespective of the transcription factors used, reconstitutes key transcriptome and epigenetic reprogramming in PGCs, but bypasses a mesodermal program that accompanies PGC or PGC-like-cell specification by cytokines including bone morphogenetic protein 4. Notably, the transcription-factor-induced PGC-like cells contribute to spermatogenesis and fertile offspring. Our findings provide a new insight into the transcriptional logic for PGC specification, and create a foundation for the transcription-factor-based reconstitution and regulation of mammalian gametogenesis.

In mice, PGCs, the precursors for spermatozoa and oocytes, arise in the epiblasts in response to cytokines, including bone morphogenetic protein 4 (BMP4), from extraembryonic tissues³. Gene-knockout studies have identified transcription factors (TFs) essential for PGC specification³. However, the TFs sufficient for PGC induction and the precise mechanism of action of key TFs remain unknown. Using the *in vitro* PGC specification system^{1,2}, we set out to identify TFs whose forced expression may be sufficient to confer the PGC fate onto EpiLCs. We focused on the three TFs BLIMP1 (hereafter referred to as B), PRDM14 (P14) and TFAP2C (A) because they show specific expression in PGCs and are necessary for PGC specification^{4–7}. We derived embryonic stem (ES) cells expressing mVenus and enhanced cyan fluorescent protein (eCFP) under the control of *Blimp1* and *stella* (also known as *Dppa3* and *PGC7*) regulatory elements, respectively (*Blimp1*-mVenus (BV) and *stella*-eCFP (SC), or BVSC)^{1,2,8–10}, and reverse tetracycline transactivator (rtTA) under the control of the constitutively active *Rosa26* locus¹¹ (BVSCR26rtTA ES cells) (Fig. 1a). During mouse development, *Blimp1* expression signifies the onset of PGC specification, whereas *stella* begins expression in the established PGCs^{5,8,9}. We transfected the BVSCR26rtTA ES cells (XY karyotype) (Supplementary Fig. 1a–c) with *piggyBac* transposon-based vectors expressing *Blimp1*, *Prdm14* or *Tfap2c* under the control of tetracycline regulatory elements to isolate BVSCR26rtTA ES cells bearing transgenes for all three TFs (BP14A), or two (BP14, BA and P14A) or one (B, P14 and A) of the three TFs (Fig. 1a and Supplementary Fig. 1d, e).

We first examined the effect of simultaneous forced expression of the three TFs. We induced BP14A cells (line 3-3) into EpiLCs, and

generated floating aggregates of ~2,000 EpiLCs in the absence of relevant cytokines with or without doxycycline (Dox; 1.5 $\mu\text{g ml}^{-1}$), a tetracycline analogue (Supplementary Fig. 2a). The aggregates without Dox did not show BVSC expression over the six-day period (Fig. 1b). By contrast, remarkably, those with Dox exhibited robust BVSC expression as early as day 2 of the Dox treatment (Fig. 1b). We confirmed that Dox induces exogenous TFs rapidly and at high levels in nearly all EpiLCs (Supplementary Fig. 2b, c). Fluorescence activated cell sorting (FACS) revealed that at day 2, more than ~80% and ~30% of the cells expressed BV and SC, respectively (Fig. 1c), and the efficiency of BVSC induction was dependent on the Dox dosage (Supplementary Fig. 2d, e). The BVSC induction by Dox was much more efficient/faster than that by the cytokines^{1,2} (Supplementary Fig. 2f). The Dox-induced BVSC-positive cells showed proliferation and persisted until day 4, but decreased thereafter (Fig. 1b and Supplementary Fig. 2g). The other BP14A lines showed similar BVSC induction by Dox (Supplementary Fig. 3a, b). As in the case of the induction by cytokines¹, the Dox-induced EpiLCs adhering to the culture dish tended to detach, and the remaining cells did not activate BVSC as efficiently (data not shown). Thus, under the floating aggregate condition, the three TFs are sufficient for robust activation of the BVSC transgenes in EpiLCs.

We analysed the expression of genes relevant for PGC specification in TF (BP14A)-induced BV-positive cells (including SC-positive cells; Fig. 1c) by quantitative PCR (qPCR). Like cytokine-induced BV-positive cells, TF-induced BV-positive cells upregulated key genes for PGC specification/development (*Blimp1*, *Prdm14*, *Tfap2c*, *Nanos3*, *stella*, *Pou5f1*, *Sox2* and *Nanog*) and downregulated epigenetic modifiers (*Dnmt3a* and *Dnmt3b*)¹ (Fig. 1d). Interestingly, unlike cytokine-induced cells and PGCs *in vivo*^{1,8,12,13}, TF-induced cells did not show transient upregulation of mesodermal genes such as *Hoxa1*, *Hoxb1* and *T* (also known as *brachyury*), but continued to express them at low/undetectable levels (Fig. 1d and Supplementary Fig. 3d), indicating that the TF (BP14A)-induced BV-positive cells acquire a transcriptional program similar to PGCs, but lack a mesodermal program.

We next examined whether the forced expression of two or one of the three TFs would induce BVSC (three lines for each). We found that P14A, and to a lesser extent, BP14 and BA, and, notably, P14 alone, activated BVSC, although all at lower efficiencies than all three TFs combined (BP14A) (Supplementary Fig. 3a–c). The BA-induced aggregates (two out of three lines) looked fragile and remained small (Supplementary Fig. 3a), and B or A alone did not activate BVSC (Supplementary Fig. 3a–c). We confirmed that all the lines showed uniform induction of exogenous TF(s) after Dox treatment (Supplementary Fig. 4a–f). It should be noted that we could not isolate B cells that express exogenous *Blimp1* after Dox treatment at levels as high as those of exogenous *Prdm14* in P14 cells (Supplementary Fig. 4c–e). The two TFs (P14A, BP14, BA)- and single TF (P14)-induced BV-positive cells (including SC-positive cells (Supplementary Fig. 3c)) exhibited gene expression dynamics similar to those of BP14A-induced BV-positive cells (Fig. 1d and Supplementary Fig. 4g), suggesting that once the key regulators for

¹Department of Anatomy and Cell Biology, Graduate School of Medicine, Kyoto University, Yoshida-Konoe-cho, Sakyo-ku, Kyoto 606-8501, Japan. ²Center for iPS Cell Research and Application, Kyoto University, 53 Kawahara-cho, Shogoin Yoshida, Sakyo-ku, Kyoto 606-8507, Japan. ³JST, PRESTO, Yoshida-Konoe-cho, Sakyo-ku, Kyoto 606-8501, Japan. ⁴JST, ERATO, Yoshida-Konoe-cho, Sakyo-ku, Kyoto 606-8501, Japan. ⁵Institute for Integrated Cell-Material Sciences, Kyoto University, Yoshida-Ushinomiya-cho, Sakyo-ku, Kyoto 606-8501, Japan.

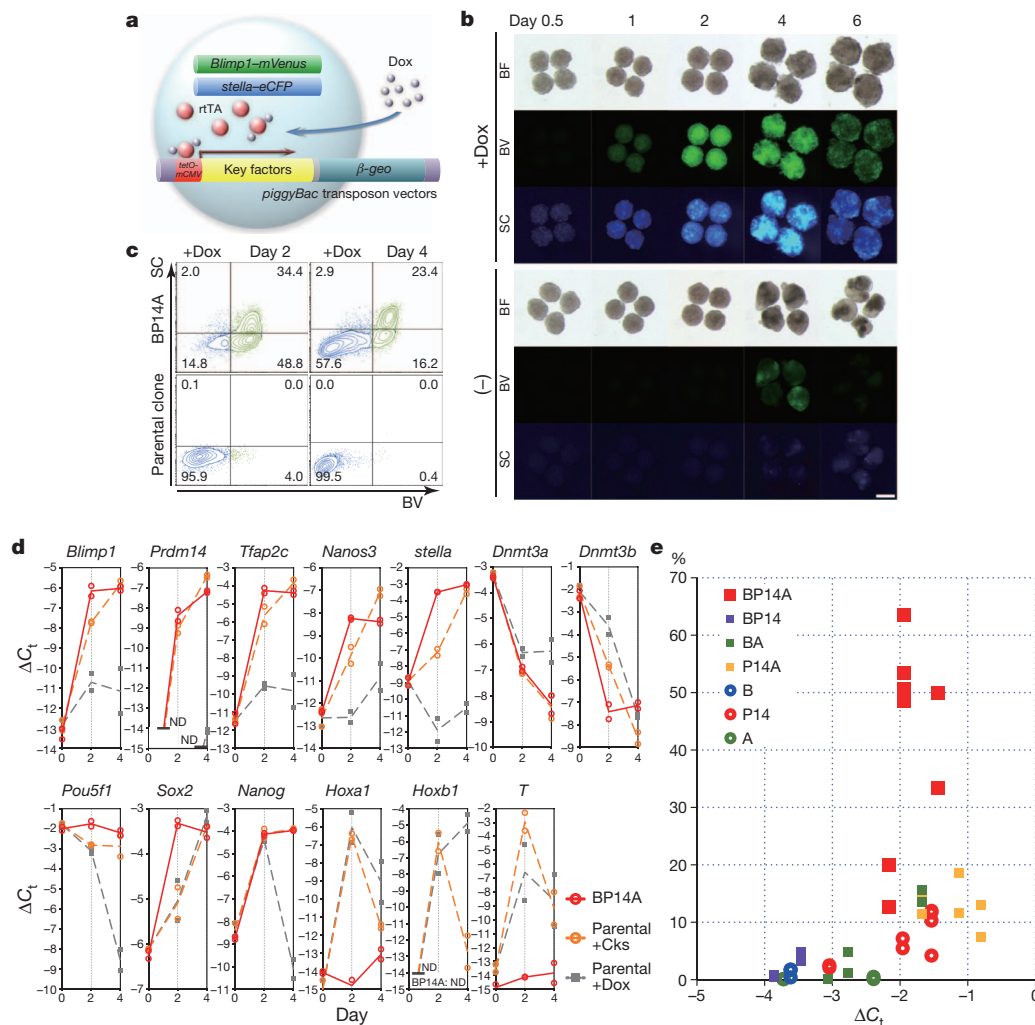


Figure 1 | Induction of a PGC-like state by TFs. **a**, Scheme for the BVSCR26rtTA cells and the *piggyBac* transposon-based vectors with tetracycline-responsive promoters driving TF and β -geo expression. **b**, Induction of BVSC with (top) or without (bottom) Dox ($1.5 \mu\text{g ml}^{-1}$) in floating aggregates of EpiLCs induced from BP14A cells during the 6-day period. BF, bright field. Scale bar, $200 \mu\text{m}$. **c**, FACS analysis of BVSC induction by Dox ($1.5 \mu\text{g ml}^{-1}$) in floating aggregates of EpiLCs from BP14A cells (line 3-3) (top) or parental BVSCR26rtTA cells (bottom). **d**, Expression of the indicated genes measured by qPCR in TF (BP14A)- and cytokine-induced BV-positive cells (red and orange, respectively) or in the whole aggregates of parental BVSCR26rtTA EpiLCs with Dox (grey) during the 4-day period. For each gene, the ΔC_t from the average C_t values of *Arbp* and *Ppia* is shown (\log_2 scale, the mean value of two independent experiments with two technical replicates). Cks, cytokines; ND, not detectable. **e**, BVSC induction rates (%) at day 2 plotted against whole exogenous TF transcript levels (ΔC_t) 12 h after induction in several independent clones of the indicated cells.

PGC specification is activated, the induced cells acquire similar transcriptional profiles. We determined the relationship between the BVSC induction rate and the exogenous TF expression level. As shown in Fig. 1e (data based on Supplementary Figs 3b and 4c), BP14A induced BVSC much more efficiently than P14A or BA or P14 at similar whole exogenous TF levels, indicating that BP14A shows a synergistic effect on the activation of PGC-like transcriptional profiles in EpiLCs.

To exclude the possibility that the TFs activate BMP4 signalling, which in turn induces EpiLCs into a PGC-like state, we induced BP14A in EpiLCs with an inhibitor for BMP4 signalling—LDN193189, which inhibits activin receptor-like kinase 2/3. LDN193189 blocked BV, *Blimp1* and *Prdm14* induction by BMP4, but not by BP14A (Supplementary Fig. 5a, b). These findings, together with the much faster kinetics of BVSC induction by the TFs than by the cytokines (Fig. 1b and Supplementary Fig. 2f), indicate that the TFs directly activate a PGC program. We then examined whether induction of a PGC-like state by TFs requires an EpiLC state. Although BP14A induced EpiLCs robustly into a PGC-like state, BP14A induction in ES cells resulted in a peculiar phenotype: intense SC activation with no BV (Supplementary Fig. 5c, d), demonstrating that a proper cellular context (for example, a proper epigenetic background, presence/absence of *trans*-acting factors) is essential for the robust induction of a PGC-like state by TFs.

To characterize further the TF-induced PGC-like cells (hereafter referred to as TF-PGCLCs), we determined their transcriptomes (BV-positive cells (including SC-positive cells) induced by BP14A (days 2 and 4), BP14 (day 2), P14A (day 2) and P14 (day 2) (Supplementary Fig. 6a)) and compared them with those of PGCs at embryonic day (E) 9.5 (ref. 1) and cytokine-induced day 2, 4 and 6 PGCLCs (hereafter

referred to as Ck-PGCLCs)¹. Principal component analysis (PCA) revealed that all the TF-PGCLCs, irrespective of the TF combinations or of the induction period, bear similar transcriptomes, which are also similar to the transcriptomes of day 4 and 6 Ck-PGCLCs and, to a lesser extent, of E9.5 PGCs (Fig. 2a and Supplementary Table 1), indicating that the exogenous TFs, at varying efficiencies depending on their combinations, creates a similar PGC-like transcriptome. Notably, day 2 Ck-PGCLCs showed a more similar transcriptome to E5.75 epiblasts than to TF-PGCLCs, day 4 and 6 Ck-PGCLCs, and E9.5 PGCs, indicating that day 2 Ck-PGCLCs represent a transient state towards the acquisition of a PGC-like state from the EpiLC/epiblast states (Fig. 2a). The transcriptomes of the SC-positive cells induced by BP14A in ES cells (SC ES cells by BP14A) (Supplementary Fig. 5c, d) were different from those of PGCLCs/PGCs, and closer to those of ES cells (Fig. 2a).

We looked at individual genes upregulated in day 2 TF (BP14A)-PGCLCs in comparison to those in EpiLCs/control EpiLCs without exogenous TFs but treated with Dox, and found that genes such as *Blimp1*, *Prdm14*, *Tfap2c*, *stella*, *Sox2*, *Klf2*, *Tcl1*, *Esrrb*, *Elf3*, *Kit*, *Lifr*, *Nr5a2*, *Gjb3*, *Tdh*, *Spnb3*, *Pygl*, *Mbp*, *Npnt* and *AU015386* showed robust upregulation. All of these genes ('core PGC genes') were upregulated in day 4 and 6 Ck-PGCLCs and in E9.5 PGCs (Supplementary Fig. 6b, Supplementary Table 2). We examined the genes upregulated in day 2 Ck-PGCLCs but not in day 2 TF-PGCLCs in comparison to those in EpiLCs, which revealed that the genes *Hoxa1*, *Hoxb1*, *Hoxb2*, *Evx1*, *T*, *Cdx1*, *Cdx2*, *Hand1*, *Snai1*, *Mesp1*, *Id1*, *Mx1*, *Mx2*, *Nkx1-2*, *Isl1*, *Mixl1*, *Rspo3*, *Wnt5a*, *Fgf8* and *Bmp4*—all of which show transient upregulation in PGC precursors at around E7.0 and represent a somatic

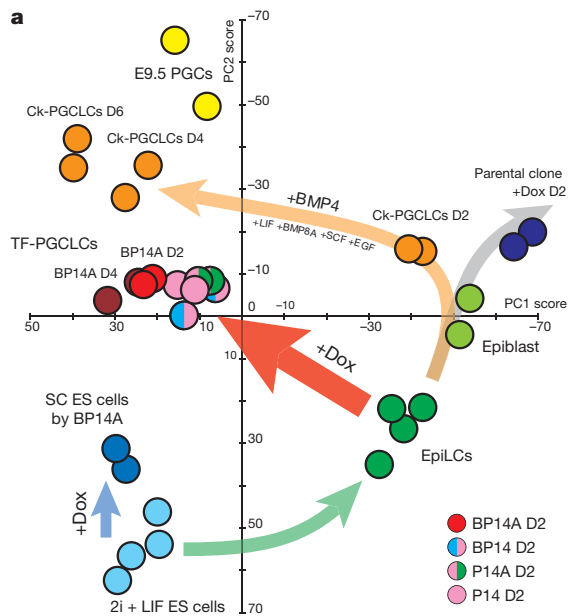
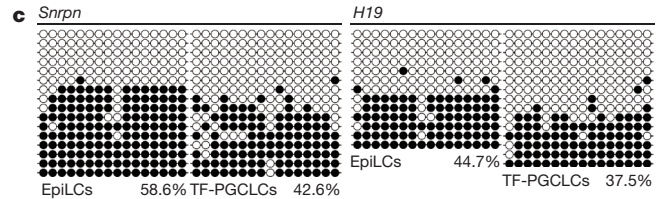
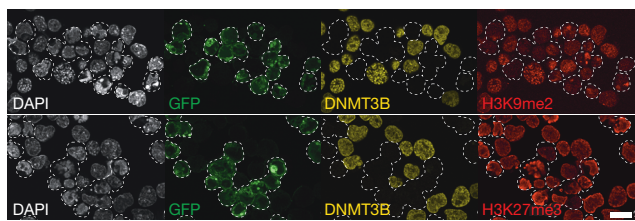


Figure 2 | Global transcription profiles for TF- and Ck-PGCLCs and epigenetic properties of TF-PGCLCs. **a**, PCA of the transcriptomes of the indicated cells. PGCLCs were sorted by BV. D, day. **b**, Immunofluorescence analysis for H3K9me2 (top) or H3K27me3 (bottom) in day 4 TF (BP14A)-PGCLCs (green fluorescent protein (GFP)-positive, dotted lines, line 3-3) compared to those in EpiLCs (DNMT3B-positive, line 3-3). Left,



mesodermal program¹³—were transiently upregulated in day 2 Ck-PGCLCs but not in day 2 TF-PGCLCs, and most of these genes were downregulated in day 4 and 6 Ck-PGCLCs and in E9.5 PGCs (Supplementary Fig. 6b and Supplementary Table 2). Genes up-/downregulated in SC ES cells by BP14A showed no correlation to those in TF-PGCLCs (Supplementary Fig. 6c and Supplementary Table 3). These findings demonstrate on a genome-wide scale that PGC/PGCLC specification by BMP4 activates both a key PGC program and a somatic mesodermal program,

the latter of which is eventually repressed by the former, and that the direct activation of key TFs confers EpiLCs with the key PGC program but not the somatic mesodermal program.

We evaluated the epigenetic profiles of TF-PGCLCs. Compared to EpiLCs showing high DNMT3B, BV-positive day 4 TF-PGCLCs were extremely weak for DNMT3B and showed reduced histone H3 lysine 9 di-methylation (H3K9me2) and increased H3K27 tri-methylation (H3K27me3) (Fig. 2b and Supplementary Fig. 7). BV-positive day 4

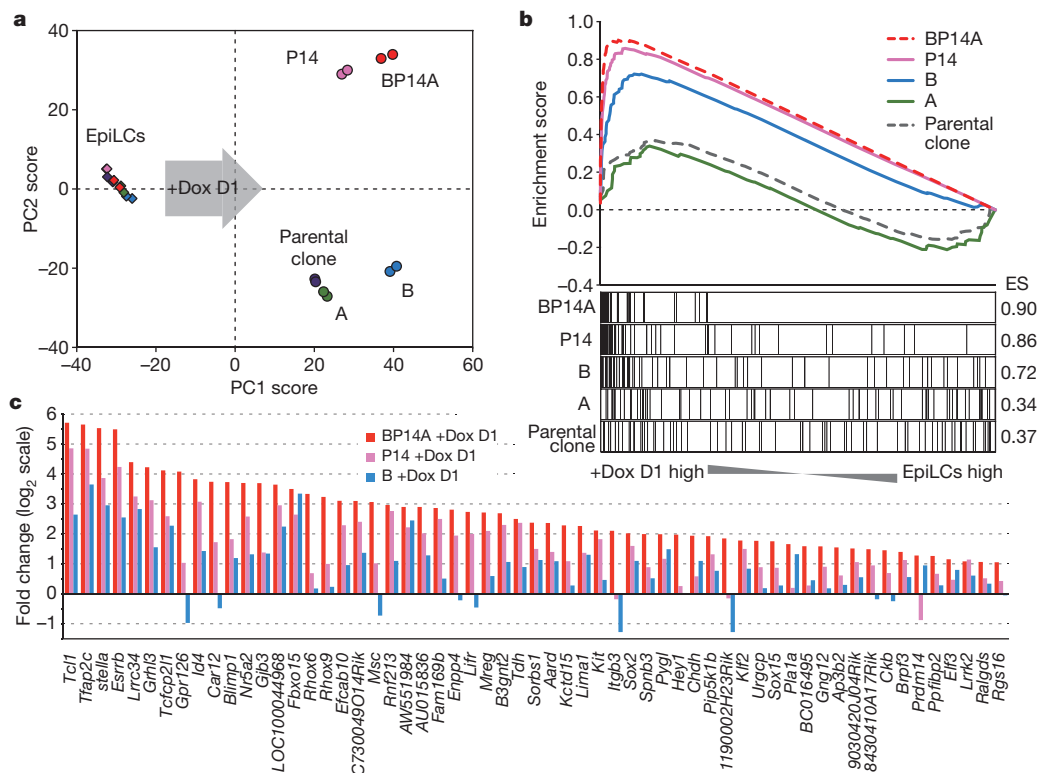


Figure 3 | Global transcriptional target analyses of the three TFs. **a**, PCA of the transcriptomes of whole EpiLC aggregates induced by the indicated factors and of corresponding parental EpiLCs. **b**, GSEA on core PGC genes of the transcriptomes of whole EpiLC aggregates induced by the indicated factors at 24 h. Genes were ranked by the difference of the expression level (\log_2) between day 1 aggregates and EpiLCs for each line. ES, enrichment score. **c**, Induction levels of core PGC genes in whole EpiLC aggregates by the indicated factors at 24 h. The mean values of two biological replicates for core PGC genes upregulated more than twofold in induced aggregates compared to uninduced aggregates are shown.

TF-PGCLCs retained the imprints on paternally imprinted *H19* and maternally imprinted *Snrpn* (Fig. 3c). These findings suggest that the BV-positive day 4 TF-PGCLCs acquire an epigenome similar to day 6 Ck-PGCLCs and to migrating PGCs at E8.5–E9.5 (refs 1, 14).

We went on to gain insights into the targets of the three TFs. The induction kinetics by the TFs of endogenous *Blimp1*, *Prdm14* and *Tfap2c* in whole EpiLC aggregates showed that (1) BLIMP1 and PRDM14 activate *Blimp1* gradually and *Tfap2c* rapidly, whereas TFAP2C does not activate *Blimp1* nor *Tfap2c*, but enhances the activity of BLIMP1 to induce *Tfap2c* and *Blimp1*; (2) activation of *Prdm14* by the TFs occurs relatively late (after 24 h); and (3) BP14A has the strongest effect on the activation of *Blimp1*, *Tfap2c* and subsequently *Prdm14* (Supplementary Fig. 8). We determined the transcriptomes induced by the TFs at 24 h in whole EpiLC aggregates. Unsupervised hierarchical clustering and PCA showed that PRDM14 alone induces a transcriptome similar to that induced by BP14A (Fig. 3a, Supplementary Fig. 9a and Supplementary Table 4). Accordingly, Gene Set Enrichment Analysis (GSEA)¹⁵ showed that core PGC genes are enriched in genes induced by PRDM14 and, to a lesser extent, in genes induced by BLIMP1, but show no significant enrichment in genes induced by TFAP2C (Fig. 3b). Thus, PRDM14 has a central role in the BP14A-induced PGCLC formation.

We analysed individual genes regulated by PRDM14 and BLIMP1 with regard to the regulation of corresponding genes by BP14A. We classified the genes regulated by PRDM14 and BLIMP1 into those regulated in the same (a) (up or down by both P14 and B) and opposite (b) (up by P14 and down by B, or vice versa) direction. This revealed a trend in which the expression-level changes of the type (a) genes were enhanced (Fig. 3c and Supplementary Fig. 9b–d), whereas the type (b) genes were ‘balanced’ (Supplementary Fig. 9e, f) by BP14A. Importantly, the core PGC genes were overrepresented by genes upregulated by both PRDM14 and BLIMP1 (Fig. 3c). We scrutinized individual genes up/downregulated by PRDM14 and BLIMP1. We found that PRDM14 upregulates genes associated with pluripotency (such as *Epas1*, *Tcl1*, *Esrrb*, *Klf5*, *Nr5a2*, *Zfp42*, *Klf4*, *Lifr*, *Dppa2*, *Dppa5a* and *Nanog*), and downregulates genes associated with neural differentiation (*Zfp521*, *Sox3*, *Nrcam* and *Hs6st2*). Although we did not find a clear functional category of genes upregulated by BLIMP1, we noted that BLIMP1 represses targets of OCT4 and SOX2 (*Fgf4*, *Lefty1* and *Lefty2*), among others (Supplementary Fig. 9c–f and Supplementary Table 5). Some of the targets of PRDM14 were in common between ES cells and EpiLCs (upregulated: *Tcl1*, *Esrrb* and *Klf5*; downregulated: *Hs6st2* and *Dnmt3b*)¹⁶ (Supplementary Fig. 9c–f). These findings reveal that PRDM14 and BLIMP1 function primarily and co-operatively, whereas TFAP2C has an auxiliary role, at least for BLIMP1, for the acquisition of the TF-PGCLC transcriptome. The finding that BLIMP1 makes a relatively small contribution to the TF-PGCLC transcriptome would be attributable to TF-PGCLCs lacking the cytokine-induced somatic mesodermal program, which BLIMP1 has an essential role in repressing¹³.

After Dox withdrawal, the TF-PGCLCs shut off exogenous TFs, but continue their endogenous transcription program, and may therefore serve as precursors for proper spermatogenesis. To explore this possibility, we induced TF-PGCLCs (BP14A, BP14, P14A, P14), purified the BV-positive cells (including SC-positive cells, at days 3, 4 and 6) (Fig. 4a and Supplementary Table 6), and transplanted them into seminiferous tubules of neonatal W/W^u mice lacking endogenous germ cells^{1,17}. Notably, ten weeks after transplantation, the testes transplanted with the TF-PGCLCs, particularly those sorted at days 3 and 4, irrespective of the TFs used, contained numerous tubules with signs of spermatogenesis (Fig. 4b, Supplementary Fig. 10a and Supplementary Table 6). These tubules showed normal spermatogenesis and contained spermatozoa with proper morphology (Fig. 4c, d and Supplementary Fig. 10b). The control day 6 Ck-PGCLCs also contributed to spermatogenesis (Supplementary Table 6). By contrast, SC ES cells induced by BP14A did not contribute to spermatogenesis, but formed foci of teratomas in six out of eight transplanted testes (Supplementary Fig. 10d, e and Supplementary Table 6). The inability of day 6 TF-PGCLCs to contribute

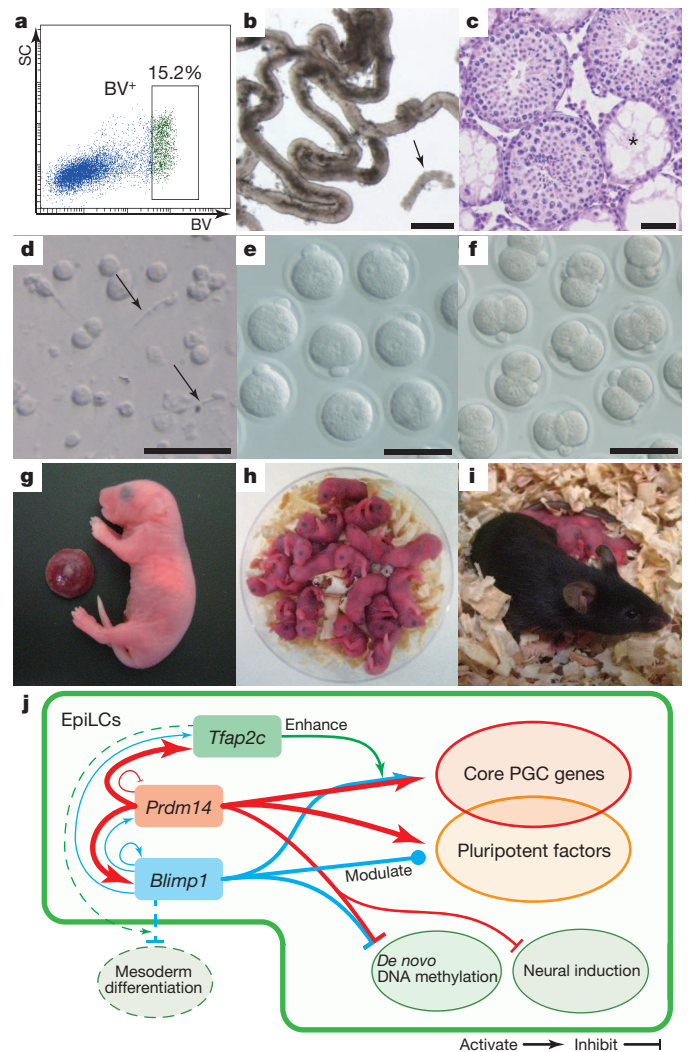


Figure 4 | Spermatogenesis and fertile offspring from TF (BP14A)-PGCLCs. **a**, FACS of BV-positive TF (BP14A, line 3–10)-PGCLCs for injection. **b**, Seminiferous tubules of a W/W^u mouse injected with TF-PGCLCs showing spermatogenesis. An arrow indicates an empty tubule. Scale bar, 500 μ m. **c**, Haematoxylin and eosin staining of a section of a W/W^u mouse testis injected with TF-PGCLCs showing spermatogenesis. The asterisk indicates an empty tubule. **c–e**, Scale bar, 50 μ m. **d**, Spermatozoa (arrows) from TF-PGCLCs. **e**, Zygotes at pronuclear stages generated by injection of TF-PGCLC-derived spermatozoa into wild-type oocytes by intracytoplasmic sperm injection. **f**, Two-cell embryos from zygotes in **e**. **g, h**, Apparently normal offspring (**g, h**) and placenta (**g**) derived from TF-PGCLC-derived spermatozoa. **i**, A fertile female derived from a TF-PGCLC-derived spermatozoan. **j**, A proposed model for TF-PGCLC induction.

to spermatogenesis may result from a prolonged non-optimal culture of TF-PGCLCs (Supplementary Table 6). We fertilized wild-type oocytes with TF-PGCLC-derived spermatozoa by intracytoplasmic sperm injection¹⁸. The resultant zygotes developed into two-cell embryos, and we transferred these embryos into pseudopregnant female mice, and 18 days later, obtained healthy offspring with grossly normal placenta and imprinting states (Fig. 4e–h, Supplementary Fig. 10c, f and Supplementary Table 7). These offspring bore transgenes for the exogenous TFs and the BVSCR26rtTA (Supplementary Fig. 10g), and grew up normally into fertile adults (Fig. 4i, Supplementary Fig. 10h, i and Supplementary Table 7). We conclude that the TF-PGCLCs function as bona fide precursors for the spermatogenesis and healthy offspring.

We have demonstrated the transcriptional logic by which BLIMP1, PRDM14 and TFAP2C activate a key PGC program and create the TF-PGCLCs (Fig. 4j). On the basis of our findings, it should be feasible to

explore TF-based regulation of further crucial processes of germ-cell development. The TF-based control of germ-cell development may be applicable to mammals other than mice, including humans.

METHODS SUMMARY

BVSCR26rtTA ES cells were established and maintained under the N2B27 '2i + LIF' condition¹⁹. PB-TET vectors²⁰ with *Avi-Blimp1*, 3×*FLAG-Prdm14* and *V5-Tfap2c* (Supplementary Table 8) were transfected into the BVSCR26rtTA ES cells (XY karyotype) on feeders with Lipofectamine2000 (Invitrogen) together with pPBCAG-hph and pCAGGS-mPB plasmids. Transgene integration was determined by PCR and Southern blotting. Transfected ES cells were adapted to a feeder-free condition and differentiated into EpiLCs as reported¹. After 36 h of differentiation, cells were aggregated (2,000 cells per aggregate) in GK15 medium¹ with Dox (1.5 µg ml⁻¹) (Clonotect). Ck-PGCLCs were induced by BMP4, BMP8A, SCF, LIF and EGF as described¹. Transcriptomes were analysed by GeneChip Mouse Genome 430 2.0 Array (Affymetrix)^{1,21}. Published data (Gene Expression Omnibus (GEO) accessions GSM744093–GSM744096 and GSM744099–GSM744104)¹ were included in the analysis. Seminiferous tubule injection and intracytoplasmic sperm injection were performed as described^{1,17,18}. All primer sequences for PCR are listed in Supplementary Table 9.

Full Methods and any associated references are available in the online version of the paper.

Received 19 January; accepted 26 June 2013.

Published online 4 August 2013.

- Hayashi, K., Ohta, H., Kurimoto, K., Aramaki, S. & Saitou, M. Reconstitution of the mouse germ cell specification pathway in culture by pluripotent stem cells. *Cell* **146**, 519–532 (2011).
- Hayashi, K. *et al.* Offspring from oocytes derived from *in vitro* primordial germ cell-like cells in mice. *Science* **338**, 971–975 (2012).
- Saitou, M. & Yamaji, M. Primordial germ cells in mice. *Cold Spring Harb. Perspect. Biol.* **4**, 223–241 (2012).
- Vincent, S. D. *et al.* The zinc finger transcriptional repressor Blimp1/Prdm1 is dispensable for early axis formation but is required for specification of primordial germ cells in the mouse. *Development* **132**, 1315–1325 (2005).
- Ohinata, Y. *et al.* Blimp1 is a critical determinant of the germ cell lineage in mice. *Nature* **436**, 207–213 (2005).
- Yamaji, M. *et al.* Critical function of Prdm14 for the establishment of the germ cell lineage in mice. *Nature Genet.* **40**, 1016–1022 (2008).
- Weber, S. *et al.* Critical function of AP-2γ/TCFAP2C in mouse embryonic germ cell maintenance. *Biol. Reprod.* **82**, 214–223 (2010).
- Saitou, M., Barton, S. C. & Surani, M. A. A molecular programme for the specification of germ cell fate in mice. *Nature* **418**, 293–300 (2002).
- Sato, M. *et al.* Identification of PGC7, a new gene expressed specifically in preimplantation embryos and germ cells. *Mech. Dev.* **113**, 91–94 (2002).
- Ohinata, Y., Sano, M., Shigeta, M., Yamanaka, K. & Saitou, M. A comprehensive, non-invasive visualization of primordial germ cell development in mice by the *Prdm1*-mVenus and *Dppa3*-ECFP double transgenic reporter. *Reproduction* **136**, 503–514 (2008).
- Hochedlinger, K., Yamada, Y., Beard, C. & Jaenisch, R. Ectopic expression of Oct-4 blocks progenitor-cell differentiation and causes dysplasia in epithelial tissues. *Cell* **121**, 465–477 (2005).
- Yabuta, Y., Kurimoto, K., Ohinata, Y., Seki, Y. & Saitou, M. Gene expression dynamics during germline specification in mice identified by quantitative single-cell gene expression profiling. *Biol. Reprod.* **75**, 705–716 (2006).
- Kurimoto, K. *et al.* Complex genome-wide transcription dynamics orchestrated by Blimp1 for the specification of the germ cell lineage in mice. *Genes Dev.* **22**, 1617–1635 (2008).
- Seki, Y. *et al.* Cellular dynamics associated with the genome-wide epigenetic reprogramming in migrating primordial germ cells in mice. *Development* **134**, 2627–2638 (2007).
- Subramanian, A. *et al.* Gene set enrichment analysis: a knowledge-based approach for interpreting genome-wide expression profiles. *Proc. Natl Acad. Sci. USA* **102**, 15545–15550 (2005).
- Yamaji, M. *et al.* PRDM14 ensures naive pluripotency through dual regulation of signaling and epigenetic pathways in mouse embryonic stem cells. *Cell Stem Cell* **12**, 368–382 (2013).
- Chuma, S. *et al.* Spermatogenesis from epiblast and primordial germ cells following transplantation into postnatal mouse testis. *Development* **132**, 117–122 (2005).
- Kimura, Y. & Yanagimachi, R. Intracytoplasmic sperm injection in the mouse. *Biol. Reprod.* **52**, 709–720 (1995).
- Ying, Q. L. *et al.* The ground state of embryonic stem cell self-renewal. *Nature* **453**, 519–523 (2008).
- Woltjen, K. *et al.* piggyBac transposition reprograms fibroblasts to induced pluripotent stem cells. *Nature* **458**, 766–770 (2009).
- Kurimoto, K. *et al.* An improved single-cell cDNA amplification method for efficient high-density oligonucleotide microarray analysis. *Nucleic Acids Res.* **34**, e42 (2006).

Supplementary Information is available in the online version of the paper.

Acknowledgements We thank A. Bradley, A. Smith, G. Guo, H. Niwa and G. Nagamatsu for providing plasmids. We are grateful to the Center for Anatomical Studies (Graduate School of Medicine, Kyoto University) for performing the histological analyses. We thank M. Yamaji for advice and T. Mori for encouragement. F.N. is a Japan Society for the Promotion of Science (JSPS) Research Fellow. This study was supported in part by a Grant-in-Aid from the Ministry of Education, Culture, Sports, Science, and Technology of Japan; by JST-CREST/ERATO; by the Takeda Science Foundation; and by the Academia for Repro-regenerative Medicine.

Author Contributions F.N. designed and conducted the experiments, analysed the data, and wrote the manuscript. K.H. designed the experiments and analysed the data. K.K. conducted the microarray experiments. H.O. performed the transplantation of cells into seminiferous tubules. Y.Y. analysed the data. M.S. conceived the project, designed the experiments and wrote the manuscript.

Author Information The accession number for the microarray data presented in this study is available from the Gene Expression Omnibus (GEO) database under accession GSE46855. Reprints and permissions information is available at www.nature.com/reprints. The authors declare no competing financial interests. Readers are welcome to comment on the online version of the paper. Correspondence and requests for materials should be addressed to M.S. (saitou@anat2.med.kyoto-u.ac.jp).

METHODS

Animals. All animal experiments were conducted according to the Guidelines for Animal Experiments of Kyoto University. The BVSC transgenic mice (C57BL/6 background, acc. no. BV, CDB0460T; SC CDB0465T: <http://www.cdb.riken.jp/arg/TG%20mutant%20mice%20list.html>) were established as reported previously¹⁰. B6;129-Gt(Rosa)26Sor^{tm1(rtTA_gM2)}lac⁺Col1a1^{tm2(tetO-Pou5f1)}lac⁺/J mice¹¹ (stock number: 006911) were purchased from the Jackson Laboratory. WBB6F1-W/W^v mice were purchased from SLC.

Establishment of ES cells. Mice homozygous for the *Rosa26-rtTA* knock-in allele were obtained by crossing of B6;129-Gt(Rosa)26Sor^{tm1(rtTA_gM2)}lac⁺Col1a1^{tm2(tetO-Pou5f1)}lac⁺/J mice heterozygous for both loci. They were mated with BVSC transgenic mice and blastocysts were recovered at E2.5. BVSC-R26rtTA ES cells were selected by PCR genotyping, and established and maintained under the N2B27'2i + LIF' condition¹⁹. A male cell line was used in this study.

Chimaera formation assay. BVSC-R26rtTA ES cells were trypsinized and a single-cell suspension was prepared. Approximately 15 ES cells per embryo were injected into blastocysts of E3.5 blastocysts obtained from ICR (albino) female mice with a piezo-actuating micromanipulator. Injected embryos were transferred into the uteri of E2.5 pseudopregnant ICR female mice. Chimaeric mice were delivered by caesarean section at E18.5. Chimaerism was determined by coat-colour. The chimaeric mice were subjected to test breeding with ICR female mice to confirm the germ-line contribution.

Vector construction. The mouse *Blimp1* (from ATG in exon 3) and *Tfap2c* variant 1 (accession number: NM_009335.2) coding sequences were cloned by PCR flanked with SalI-AviTag-XhoI and NotI sites and EcoRI sites, respectively. The *Prdm14* coding sequence was obtained from AG-P14 (ref. 16).

The SalI-Avi-*Blimp1*-NotI cassette was subcloned into XhoI/NotI sites of the pPyCAG-CHA-IP plasmid²², and this cassette was subcloned again into the EcoRI/NotI sites of the pENTR1A dual selection vector (Invitrogen). For *Prdm14* and *Tfap2c*, KpnI-3×FLAG-XhoI-S(G4S)₃-Linker-SpeI and BamHI-V5-S(G4S)₃-Linker-NotI fragments, respectively, were attached to the amino termini by PCR or synthesized oligonucleotide linker ligation. 3×FLAG-*Prdm14* and V5-*Tfap2c* cassettes were subcloned into the KpnI/NotI and BamHI/EcoRI sites of pENTR1A, respectively. Lastly, they were shuttled into the PB-TET destination vector (Addgene)²⁰ with LR clonase II enzyme mix (Invitrogen). To construct pPBCAG-hph, a CAG promoter fragment from the pCAGGS plasmid obtained by digestion of SpeI and EcoRI (filled) was inserted into the GG131 vector^{23,24} digested with SpeI/MscI. All sequences engineered by PCR or oligonucleotide synthesis were confirmed. All attached sequences are shown in Supplementary Table 8 and primer sequences for cloning are listed in Supplementary Table 9.

Transfection and selection of subclones. BVSC-R26rtTA ES cells were transfected with PB-TET vectors containing key factors, pPBCAG-hph and pCAGGS-mPB using Lipofectamine2000 (Invitrogen) on feeder cells (mouse embryonic fibroblasts) in a 60-mm dish under a 2i + LIF condition. The total amount of vector DNA was below 8 µg. Transfectants were selected with hygromycin B (150 µg ml⁻¹) (Sigma) and genotyped with PCR for transgenes. The primer sequences for the genotype are shown in Supplementary Table 9.

Southern blotting. Eight micrograms of genomic DNA was isolated and digested with BamHI. DNA fragments were electrophoresed in 0.7% agarose gel, transferred to Hybond N⁺ (GE Healthcare) and ultraviolet-crosslinked. The β-geo probe was obtained by digestion of PB-TET with RsrII/SmaI, labelled with ³²P (PerkinElmer) by a random primer DNA labelling kit ver. 2.0 (TaKaRa) and purified with an Illustra ProbeQuant spin column (GE Healthcare). Radioisotope images were captured with a BAS system (Fujifilm).

Karyotyping. Metaphase chromosome spreads of ES cells were prepared by treating them with demecolcin solution (0.03 µg ml⁻¹) for 2 h at 37 °C, followed by hypotonic treatment with 75 mM potassium chloride for 15 min at room temperature. Cells were fixed in Carnoy's solution (3:1 mixture of methanol and acetic acid) and dropped onto glass slides soaked in 50% ethanol before the analysis. The presence of the Y chromosome was determined by PCR with *Ubel* primers. Cell lines including 2-4, 7-1, 7-5 and 7-8 were found to have the XO karyotype. The primer sequences are described in Supplementary Table 9.

TF- and Ck-PGCLCs. Transfected ES cells were adapted to a feeder-free condition before induction. EpiLC differentiation was performed as reported previously¹. After 36 h of differentiation, cells were collected and cultured in a Lipidure-Coat 96-well plate (NOF) to be aggregated (started with 2,000 cells per well) in GK15 (ref. 1) with 1.5 µg ml⁻¹ of Dox (Clonetechn). The TF-PGCLCs can be induced as 1,000–5,000 (possibly more) cells per well. We used 2,000 cells per well in this study, as this condition was most efficient for obtaining BVSC-positive TF-PGCLCs. PGCLCs were induced by BMP4 (500 ng ml⁻¹), BMP8A (500 ng ml⁻¹), SCF (100 ng ml⁻¹), LIF (1,000 U ml⁻¹) and EGF (50 ng ml⁻¹) as previously described¹. LDN193189 (120 pM; Stemgent) was added concurrently with Dox or cytokines. Aggregates

from ground-state ES cells were also cultured in GK15 with Dox as described above.

Reverse transcription and qPCR. For evaluating endogenous transcripts, TF-induced BV-positive cells were FACS-sorted on days 2 and 4 with the gates shown in Fig. 1c and Supplementary Fig. 3c. The sorting gates used for day 2 and 4 Ck-PGCLCs are shown in Supplementary Fig. 6a. Aggregates were trypsinized and lysated as a whole unless otherwise specified. Total RNA was purified with an RNeasy Micro kit (QIAGEN) and reverse transcription was performed with SuperScript III (Invitrogen) primed with oligo-dT primer according to the manufacturer's protocol. Real-time PCR was performed with Power SYBR (Applied Biosystems) and CFX384 (BioRad). The gene expression levels are presented as ΔC_t (in log₂ scale) normalized with the average C_t values of *Arbp* and *Ppia*¹².

To discriminate endogenous transcripts from exogenous ones, both the oligo-dT primer (Invitrogen) and gene-specific primers of interest were used for reverse transcription to reduce the reverse transcription bias due to differences in the distance between reverse transcription priming sites and amplified regions. The amplification efficiency of the newly designed primer sets was determined with pGEM-T-Easy plasmids containing the corresponding amplicons as templates. To verify both the endogenous and exogenous expression levels, samples were tested with CDS primers concurrently (data not shown). We found that the amplification efficiency of the 3×FLAG-*Prdm14* primer set was slightly lower than that of the other primer sets. Therefore, we adjusted the C_t value of 3×FLAG-*Prdm14* using the equation:

$$cC_{(3 \times \text{FLAG-Prdm14})} = 1.017 \times C_{(3 \times \text{FLAG-Prdm14})} - 1.039$$

in which $cC_{(3 \times \text{FLAG-Prdm14})}$ and $C_{(3 \times \text{FLAG-Prdm14})}$ are the adjusted C_t values and original C_t values obtained by the experiment using the 3×FLAG-*Prdm14* primer set, respectively. This equation was determined by linear regression between the $C_{(3 \times \text{FLAG-Prdm14})}$ and C_t values of the β-geo primer set in cell lines containing 3×FLAG-*Prdm14* but not the other two TFs (data not shown). In this paper, $cC_{(3 \times \text{FLAG-Prdm14})}$ was used for calculation of the ΔC_t values for the 3×FLAG-*Prdm14* primer set.

The primer sequences are listed in Supplementary Table 9 (refs 12, 21).

LacZ staining. Cell aggregates at 12 h were trypsinized and fixed with 2% paraformaldehyde and 0.2% glutaraldehyde. Fixed cells were spread with cytospin4 (Thermo Scientific) and stained with LacZ staining solution overnight²⁰.

Flowcytometric analysis and cell sorting. The sample preparations from cell aggregates were performed essentially as described previously¹. FACS was performed with a FACSARIA or FACSARIAIII (BD) cell sorter. BV and SC fluorescence were detected with the FITC and AmCyan Horizon V500 channel, respectively. Data were analysed with FACSDiva (BD) or Flowjo (Tree Star) software.

Immunofluorescent staining. BV-positive cells from BP14A-induced day 4 aggregates were sorted with the gate shown in Supplementary Fig. 7, mixed with EpiLCs at a ratio of 1:1 and spread onto MAS-coated glass slides (Matsunami). Immunofluorescent staining was performed as reported previously¹. The primary antibodies used in this study were as follows: anti-GFP (rat monoclonal antibody; Nacalai Tesque GF_090R), anti-DNMT3B (mouse monoclonal antibody; Imgenex IMG-184A), anti-H3K27me3 (rabbit, polyclonal antibody; Millipore 07-449), and anti-H3K9me2 (rabbit, polyclonal antibody; Millipore 07-441). Secondary antibodies were as follows: Alexa Fluor 568 anti-rabbit IgG, Alexa Fluor 488 anti-rat IgG and Alexa Fluor 647 anti-mouse IgG (all three from Invitrogen, A11011, A11006 and A21235, respectively). Images were captured with a confocal laser scanning microscope (Olympus FV1000).

Bisulphite sequencing. Genomic DNA was isolated and bisulphite treatment was conducted with an EpiTect bisulphite kit (QIAGEN) according to the manufacturer's protocol. The differentially methylated regions of *Snrpn*, *H19*, *Igf2r*, *Peg1* and *Peg3* were amplified by PCR as previously reported²⁵. Sequences were determined and analysed with QUMA (<http://quma.cdb.riken.jp/top/index.html>)²⁶.

cDNA amplification and microarray analysis. For characterization of TF-PGCLCs, the cell populations surrounded with red rectangles in Supplementary Fig. 6a were sorted by FACS. Note that the background level was different in sorting of Ck-PGCLCs and TF-PGCLCs on day 2. Total RNA was isolated with an RNeasy micro kit (QIAGEN) and reverse transcription and cDNA amplification were conducted as previously described^{1,21}. Samples were analysed with a GeneChip Mouse Genome 430 2.0 Array (Affymetrix). Data were normalized with dChip software and are shown in log₂ scale²⁷. Probes that exhibited a 'present' call in at least one sample were included in the analysis. Probe selection criteria for further analysis were as follows: (1) maximum expression score ≥ 8; (2) maximum differential expression level ≥ 2; and (3) exhibiting the highest expression level among multiple probes for a gene, if any. Published data (GEO accession GSE30056 (two replicates of ES cells (GSM744093 and GSM744094), EpiLCs (GSM744095 and GSM744096), epiblast (GSM744099 and GSM744100), Ck-PGCLCs d6 (GSM744101 and GSM744102), and E9.5 PGCs (GSM744103 and GSM744104)))

were also included¹. We selected 4,464 probes and performed PCA with R (version 2.15.1)²⁸. For the differential gene expression analysis, we averaged biological duplicates or quadruplicates and selected core PGC genes (Supplementary Fig. 6b, top) and 'somatic mesodermal genes' (Supplementary Fig. 6b, bottom) according to the following criteria. Core PGC genes were (1) upregulated in BP14A-induced day 2 more than fourfold compared with both EpiLCs and the parental clone with Dox day 2; and (2) not downregulated in E9.5 PGCs (the expression level was not less than a half of BP14A-induced day 2). Somatic mesodermal genes exhibited at least fourfold upregulation in day 2 PGCLCs as compared with both EpiLCs and BP14A-induced day 2. Representative genes are specified. The complete list is shown in Supplementary Table 2. To compare the genes whose expression was altered by BP14A between EpiLCs and ES cells, differences in log₂ scale between the averaged expression value of day 2 TF-PGCLCs and EpiLCs, between that of SC-positive cells induced by BP14A in ES cells and ES cells, and between that of Ck-PGCLCs day 4 and EpiLCs were calculated. The 100 genes exhibiting the most altered expression in EpiLCs and ES cells are listed in Supplementary Table 3.

To identify the target genes of each transcription factor, total RNA was isolated with an RNeasy Micro kit (QIAGEN) from both EpiLCs and whole cells from day 1 aggregates on each of the BP14A (line 3-3), B (line 2-4), P14 (line 7-109), and A (line 8-2) cell lines and the parental clone cultured with Dox. Data acquisition with microarray and data normalization was performed as described above. We first selected 38,769 probes that exhibited a present call in at least one sample and performed GSEA¹⁵ with core PGC genes defined above as a gene set. Genes were ranked by the difference of the expression levels (in log₂ scale) between day 1 aggregates and EpiLCs for each cell line. For further analysis, 4,211 probes were selected according to the following criteria: (1) maximum expression score ≥ 6 ; (2) maximum differential expression level ≥ 1 ; (3) *P* value of one-way analysis of variance for 10 groups (each group containing two biological replicates) ≤ 0.10 (false discovery rate ≤ 0.10 , calculated by the 'qvalue' software package²⁹ in the program R); and (4) exhibiting the highest expression level among multiple probes for a gene, if any. Unsupervised hierarchical clustering and PCA were performed with R (version 2.15.1)²⁸. To identify a gene whose expression was altered by each of the transcription factors, we averaged biological replicates and calculated the differential expression level between day 1 aggregates and EpiLCs in each cell line. The differential expression level of the parental clone was further subtracted (in log₂ scale) from that of the transfected lines to exclude the effects of aggregation formation. We defined a gene exhibiting this value (fold change from the parental clone) ≥ 1 or ≤ 1 as up- or downregulated by each factor, respectively. The accession number for the microarray data presented in this study is GSE46855 (GEO database).

Seminiferous tubule injection. After the designated cell populations were sorted by FACS, 1×10^4 cells per testis were injected into the neonatal testes of W/W^v mice (7 days post partum) basically as previously described¹⁷. Anti-mouse CD4 antibody (50 mg per dose, clone GK1.5; eBioscience or Biolegend) was injected intraperitoneally at day 0, 2 or 4 for immunosuppression as necessary³⁰. The transplanted testes were analysed 10 weeks after injection. For haematoxylin and eosin staining, testis samples were fixed with Bouin's solution, embedded in paraffin, and sectioned.

Intracytoplasmic sperm injection. Intracytoplasmic sperm injection was performed basically as reported previously¹⁸. In brief, seminiferous tubules with spermatogenesis colonies were gently minced and a spermatogenic cell suspension was prepared. Spermatozoa were injected into oocytes recovered from BDF1 mice. After *in vitro* embryo culture, two-cell-stage embryos were transferred into the oviducts of pseudopregnant mice at 0.5 days post coitum (d.p.c.) (ICR). Pups were delivered by caesarean section at 18.5 d.p.c. The primer sequences used for genotyping PCR are described in Supplementary Table 9.

22. Niwa, H., Masui, S., Chambers, I., Smith, A. G. & Miyazaki, J. Phenotypic complementation establishes requirements for specific POU domain and generic transactivation function of Oct-3/4 in embryonic stem cells. *Mol. Cell Biol.* **22**, 1526–1536 (2002).
23. Guo, G. & Smith, A. A genome-wide screen in EpiSCs identifies Nr5a nuclear receptors as potent inducers of ground state pluripotency. *Development* **137**, 3185–3192 (2010).
24. Niwa, H., Yamamura, K. & Miyazaki, J. Efficient selection for high-expression transfectants with a novel eukaryotic vector. *Gene* **108**, 193–199 (1991).
25. Lucifero, D., Mertineit, C., Clarke, H. J., Bestor, T. H. & Trasler, J. M. Methylation dynamics of imprinted genes in mouse germ cells. *Genomics* **79**, 530–538 (2002).
26. Kumaki, Y., Oda, M. & Okano, M. QUMA: quantification tool for methylation analysis. *Nucleic Acids Res.* **36**, W170–W175 (2008).
27. Li, C. & Wong, W. H. Model-based analysis of oligonucleotide arrays: expression index computation and outlier detection. *Proc. Natl Acad. Sci. USA* **98**, 31–36 (2001).
28. R. Development Core Team. *R: A Language and Environment for Statistical Computing* <http://www.R-project.org> (R Foundation for Statistical Computing, 2012).
29. Storey, J. D. & Tibshirani, R. Statistical significance for genomewide studies. *Proc. Natl Acad. Sci. USA* **100**, 9440–9445 (2003).
30. Kanatsu-Shinohara, M. *et al.* Allogeneic offspring produced by male germ line stem cell transplantation into infertile mouse testis. *Biol. Reprod.* **68**, 167–173 (2003).

The pluripotent genome in three dimensions is shaped around pluripotency factors

Elzo de Wit^{1*}, Britta A. M. Bouwman^{1*}, Yun Zhu¹, Petra Klous¹, Erik Splinter¹, Marjon J. A. M. Verstegen¹, Peter H. L. Krijger¹, Nicola Festuccia², Elphège P. Nora³, Maaïke Welling¹, Edith Heard³, Niels Geijsen^{1,4}, Raymond A. Poot⁵, Ian Chambers² & Wouter de Laat¹

It is becoming increasingly clear that the shape of the genome importantly influences transcription regulation. Pluripotent stem cells such as embryonic stem cells were recently shown to organize their chromosomes into topological domains that are largely invariant between cell types^{1,2}. Here we combine chromatin conformation capture technologies with chromatin factor binding data to demonstrate that inactive chromatin is unusually disorganized in pluripotent stem-cell nuclei. We show that gene promoters engage in contacts between topological domains in a largely tissue-independent manner, whereas enhancers have a more tissue-restricted interaction profile. Notably, genomic clusters of pluripotency factor binding sites find each other very efficiently, in a manner that is strictly pluripotent-stem-cell-specific, dependent on the presence of Oct4 and Nanog protein and inducible after artificial recruitment of Nanog to a selected chromosomal site. We conclude that pluripotent stem cells have a unique higher-order genome structure shaped by pluripotency factors. We speculate that this interactome enhances the robustness of the pluripotent state.

In recent years, several technological advances have made it possible to delineate the three-dimensional shape of the genome³. Spatial organization of DNA has been recognized as an additional regulatory layer of chromatin, important for gene regulation and transcriptional competence^{4,5}. In somatic cells active and inactive chromosomal regions are spatially segregated^{6,7}. Recently, the genome was further shown to be subdivided into evolutionarily conserved topological domains^{1,2}.

4C (chromosome conformation capture combined with sequencing) is a genome-scale variant of the 3C technology⁸, which examines the spatial organization of DNA and measures the contact frequencies of a chosen genomic site, or 'viewpoint', with the rest of the genome. To assess chromosome topology in mouse E14 embryonic stem cells (IB10), we generated high-resolution contact maps using 4C sequencing⁹ for a series of individual sites representative of different chromosomal regions on various chromosomes (Supplementary Fig. 1 and Methods). All 4C experiments show the typical result of a chromosome conformation capture experiment, with the bulk of the signal close to the viewpoint, intrachromosomal captures outnumbering interchromosomal captures, and clustering of captures at distal sites^{6,7} (Supplementary Fig. 2 and Supplementary Table 1). To identify significant intra- and interchromosomal contacts, we used a windowing approach in combination with a false discovery rate (FDR) analysis that determines significant clustering of independently captured sequences (FDR, $\alpha = 0.01$; ref. 10). Contacts in this case can mean either direct interactions between the chromatin of chromosomal regions or indirect contacts via intermediate protein complexes. 3D-DNA fluorescence *in situ* hybridization (FISH) experiments validated the 4C results (Supplementary Fig. 3).

Different from what is observed in somatic cells, in embryonic stem cells we find that transcriptionally inactive regions form low numbers of specific long-range contacts (Fig. 1a, b). This is not due to their inability to reach over large distances, but instead to a more random organization of their long-range captures (Supplementary Fig. 4), suggesting that inactive chromatin is spatially less organized in pluripotent nuclei. We confirmed these results in an independent, 129/Cast, embryonic stem (ES) cell line¹¹ (Supplementary Fig. 5a). We furthermore show that this is not an intrinsic feature of the selected regions as they do engage in many long-range contacts in astrocytes (Fig. 1c and Supplementary Fig. 6). For example, the chemoreceptor *Tas2r110* gene, part of a cluster of taste receptors that is specifically expressed in taste buds, engages in only three contacts in ES cells but shows 34 specific contacts in astrocytes (Fig. 1d).

We assessed whether the lack of long-range contacts is a global feature of ES cells, by analysing a recently published mouse ES cell Hi-C data set¹. 'Virtual 4C' contact profiles extracted from the Hi-C data set (see Methods for details) correlate strongly to our 'true 4C' profiles (Supplementary Fig. 7), emphasizing the high level of agreement between the data sets. The Hi-C data confirm on a global scale that inactive and active chromatin differ in their propensity to form specific long-range contacts in ES cells. Similar to our 4C data, this difference is abolished in differentiated cells (cortex), where both active and inactive chromatin engage equally well in specific long-range contacts (Fig. 1e, f and Supplementary Fig. 8).

We next asked whether chromosomal organization is reversed during cellular reprogramming. 129/Cast neural precursor cells (NPCs)⁹ were transduced with a lentivirus containing a multicistronic transcript encoding *Oct4* (also known as *Pou5f1*), *Klf4*, *Sox2* and *c-Myc*, to generate induced pluripotent stem (iPS) cells. Quantitative PCR (qPCR) expression analysis of several marker genes confirmed reprogramming (Supplementary Fig. 9). A reactivated gene (*Nanog*) gains contacts during iPS cell reprogramming, whereas a resiled gene (*Ptprz1*) loses all but two contacts (Supplementary Fig. 10), demonstrating that cellular reprogramming is accompanied by the reemergence of a pluripotency-specific spatial organization of the genome.

A closer inspection of the intrachromosomal contacts made by the *Nanog* gene revealed another aspect of the 3D pluripotent genome; *Nanog* was found to interact with many genes that are known to have an important role in maintenance of ES cell pluripotency, including *Rybp*, *Ezh2*, *Tcf3* and *Smadcad1*. The ES-cell-specific nature of these contacts becomes obvious from a comparison between the ES cell and NPC contact profiles of the *Nanog* gene. Most of the ES-cell-specific interacting regions have a high density of binding sites for the pluripotency factors Oct4, Sox2 and Nanog (Fig. 2a, b). Importantly, we also find such preferential associations when we apply 4C to the *Sox2* enhancer (Supplementary Fig. 11). The ES cell Hi-C data¹ show that

¹Hubrecht Institute-KNAW & University Medical Center Utrecht, Uppsalalaan 8, 3584 CT Utrecht, The Netherlands. ²MRC Centre for Regenerative Medicine, Institute for Stem Cell Research, School of Biological Sciences, University of Edinburgh, 5 Little France Drive, Edinburgh EH16 4UU, UK. ³Mammalian Developmental Epigenetics Group, Institut Curie CNRS UMR3215 INSERM U934, Paris, France.

⁴Utrecht University, School of Veterinary Medicine, 3584 CL Utrecht, The Netherlands. ⁵Department of Cell Biology, Erasmus Medical Center, Rotterdam 3015 GE, The Netherlands.

*These authors contributed equally to this work.

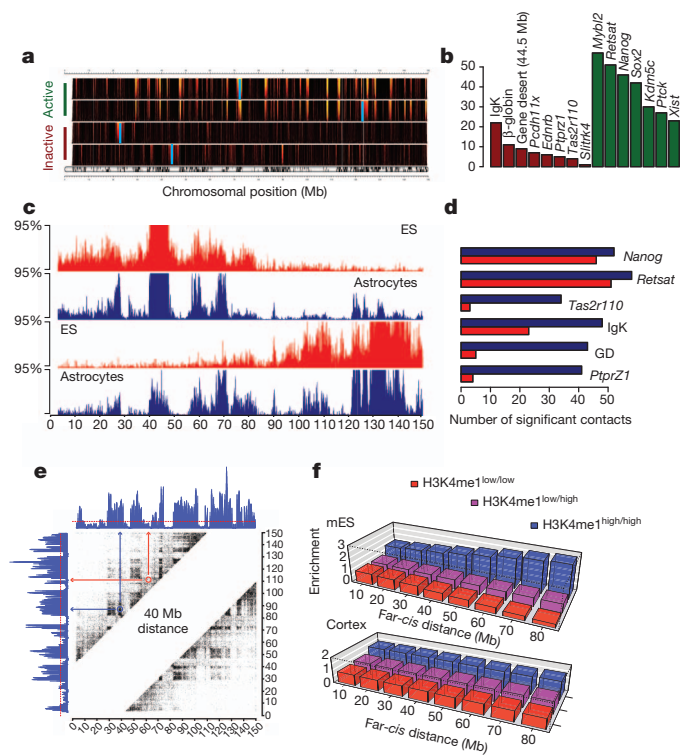


Figure 1 | Inactive regions lack specific long-range interactions in embryonic stem cells. **a**, Domainogram analysis (see Methods) shows 4C profiles of *Retsat*, *Nanog*, *Ptpz1* and gene desert (top to bottom) in ES cells. Plots represent contact profiles of active (dark green; $n = 7$) and inactive (dark red; $n = 8$) viewpoints. Below the domainograms, a map of the chromosomal position of the genes is plotted. **b**, Quantification of the number of significantly contacted regions for different viewpoints in ES cells. Green bars denote viewpoints in active regions, red bars denote viewpoints in inactive regions. **c**, Chromosomal maps show read count distribution for a gene desert (at 44.5 Mb) and for *Tas2r110*, for ES cells (red) and astrocytes (blue). The 4C signal is calculated using a sliding window average (running mean) of the read counts (window size is 51). The vertical axis is maximized at the ninety-fifth percentile. **d**, Quantification of the number of far-cis regions that are significantly contacted by a given viewpoint in ES cells (red) or astrocytes (blue). GD, gene desert. **e**, A pairwise contact matrix was generated to calculate disorganization scores from the Hi-C data (see Methods). Chromosome 6 was segmented into regions with high density of H3K4me1 and low density of H3K4me1, as a proxy for active and inactive chromatin. The pairwise contact matrix was subdivided into contacts between two regions of high H3K4me1 density ($\text{H3K4me1}^{\text{high/high}}$) or low H3K4me1 density ($\text{H3K4me1}^{\text{low/low}}$) or between a region with low H3K4me1 density and a region with high H3K4me1 density ($\text{H3K4me1}^{\text{low/high}}$). **f**, From the distribution of H3K4me1 high and low regions, we calculated an expected distribution of long-range contacts, under the null hypothesis that there is no difference between active and inactive regions with respect to their long-range contacts. An enrichment score is calculated by dividing the observed scores by these expected values.

Nanog-contacting regions also form preferential contacts among each other (Fig. 2c). Among the interchromosomal contacts made by the *Nanog* gene are again a large number of pluripotency related genes: *Mybl2*, *Dppa5*, *Rex1* (also known as *Zfp42*), *Zfp281*, *Lefty1*, *Lin28a*, *Esrrb*, *Klf5*, *Sall1*, *Cbx5* and *Cbx7* (Fig. 2d and Supplementary Fig. 12; see Supplementary Table 2 for a full list of contacted regions). The contacts of *Nanog* with *Esrrb* and *Zfp281* were verified by 3D-DNA FISH (Supplementary Fig. 12). GREAT analysis¹² of these interchromosomal contacts reveals strong enrichment for genes involved in pluripotency and early embryogenesis, which is not observed for unrelated viewpoints or in other tissues (Supplementary Table 3). This suggests that pluripotency genes prefer to cluster with other pluripotency-specific genes.

We designed a computational strategy, paired-end spatial chromatin analysis (PE-SCAN) (Fig. 2e), which combines chromatin factor

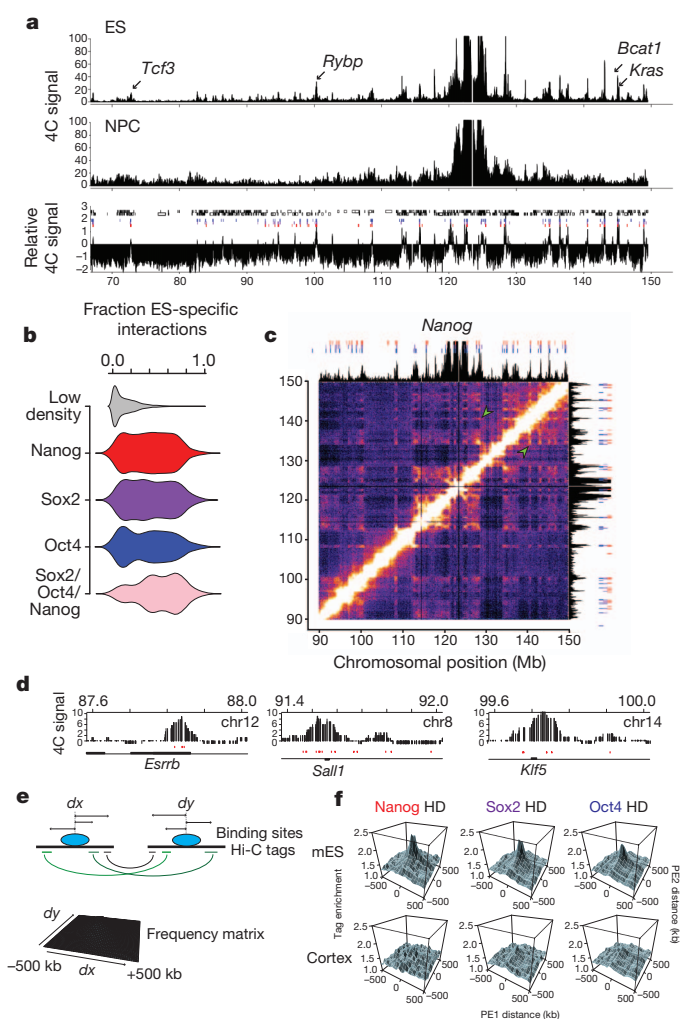


Figure 2 | Expressed *Nanog* gene shows preferential interaction with other pluripotency genes. **a**, Chromosomal map of 4C signal for the *Nanog* gene in ES cells and NPCs. Representative 4C data ($n = 6$ (ES cell) and $n = 2$ (NPC) biological replicates) is normalized to reads per million and plotted as a running mean with a window of 31. Bottom panel shows the ES cell to NPC ratio. Red, purple and blue rectangles denote the windows with a high density of *Nanog*-, *Sox2*- and *Oct4*-binding sites, respectively. High-density is defined as >5 sites per 100 kb. **b**, Violin plots show quantification of ES cell/NPC ratios for regions with a high density of binding sites for *Nanog*, *Sox2*, *Oct4* and all three combined. **c**, Combined Hi-C-4C plot for the telomeric region of chromosome 6, shows a normalized Hi-C contact matrix (see Methods) with the 4C data for *Nanog* superimposed. Red, purple and blue rectangles show the high-density regions, as in **a**. Green arrowheads point to *Nanog* high-density (HD) Hi-C interactions other than with the *Nanog* enhancer. **d**, Examples of interchromosomal contacts made by *Nanog* with pluripotency genes *Esrrb*²⁷, *Sall1* (ref. 28) and *Klf5* (ref. 29). See methods for the definition of the 4C enrichment score. *Nanog*-, *Sox2*- and *Oct4*-binding sites are again highlighted with red, purple and blue rectangles. **e**, Schematic depiction of paired-end spatial chromatin analysis (PE-SCAN). Hi-C di-tags are sequentially aligned to ChIP-seq binding sites. From the total set of distances dx and dy , a normalized two-dimensional frequency matrix is calculated (see Methods). Hi-C pairs within 5 Mb were excluded to focus the analysis on contacts between, rather than within topological domains. **f**, PE-SCAN plots show the alignment of intrachromosomal Hi-C data to high-density clusters of pluripotency factors (≥ 5 sites in 50 kb, *Nanog*: $n = 423$, *Sox2*: $n = 607$, *Oct4*: $n = 1025$). Top row shows alignment of ES cell Hi-C data, bottom row shows alignment of cortex Hi-C data.

binding data and Hi-C data to analyse, on a global scale, whether given genomic sites (bound by a protein of interest) in different topological domains have a preference to interact among each other. PE-SCAN shows that individual *Nanog*-, *Sox2*- or *Oct4*-binding sites have little

preference to contact each other over such large chromosomal distances (Supplementary Fig. 13a). However, clusters of *Nanog*-, *Oct4*- or *Sox2*- binding sites (5 or more per 50 kilobases (kb)) do show a strong preference to interact with each other in ES cells (Fig. 2f). When we circularly permute the positions of the *Nanog*, *Sox2* or *Oct4* clusters, this preference is not observed, confirming that these interactions are specific (data not shown). Moreover, these contacts are tissue-specific as they are absent in the cortex (Fig. 2f).

We also used PE-SCAN to investigate the contribution of other factors to the shape of the pluripotent genome. Although CTCF and cohesin have both been implicated in higher-order chromatin folding¹³, CTCF has been suggested to predominantly form chromatin loops over shorter distances^{14,15}. Indeed, we find that CTCF, but also cohesin-binding sites, contribute little to chromosome folding over larger distances (Fig. 3a and Supplementary Fig. 13b). Recent chromosome architecture experiments have revealed a central role for promoters in chromosome topology¹⁶. PE-SCAN for histone H3 trimethyl Lys 4 (H3K4me3) confirmed that active transcriptional start sites are engaged in specific long-range contacts (Fig. 3b). However, their contribution is largely tissue-invariant, because promoters marked by H3K4me3 in either ES cells or cortex also find each other equally well in the corresponding tissue (Fig. 3b). This is different for active enhancer sites (H3K27ac¹⁷), which contribute to genome topology in a more tissue-restricted manner (Fig. 3b). Pluripotency factors, but also cohesin, often bind to enhancer sequences. For *Oct4*, *Sox2*, *Nanog* and cohesin we find that 41%, 38%, 35% and 27%, respectively, of binding sites overlap with active enhancer sites. All intersected enhancer sites show an equal preference for homotypic contacts as the unselected enhancers (Fig. 3c). Importantly, the preferred contacts among *Nanog* enhancers were not dependent on cohesin (Fig. 3d). Finally, we assessed chromosomal contacts among, respectively, enhancer and cohesin clusters (5 or more per 50 kb). We found that they have no advantage over isolated sites to interact with each other, and that their contact preference is not as pronounced as seen for clusters of pluripotency-factor-binding sites (Supplementary Fig. 13b).

To investigate whether this pluripotency-specific genome configuration is dependent on pluripotency factors, we used ZHBTc4 (ref. 18) and RCNβH (ref. 19) ES cell lines, which allow the acute depletion of *Oct4* and *Nanog* protein, respectively (Fig. 4a, b and Supplementary Fig. 14a, b). After *Oct4* or *Nanog* protein removal, the overall chromosome topology is largely unaffected (Fig. 4c and Supplementary Fig. 14c). However, a close comparison between factor-depleted and wild-type contact profiles reveals a decrease in contact frequencies specifically at clusters where pluripotency factors normally bind (Fig. 4d, e). Quantification confirms that the regions with reduced contact frequency after removal of *Oct4* or *Nanog* protein are those with a high density of cognate binding sites and not, for example, regions with a high density of CTCF-binding sites (Fig. 4f, see Methods for details). Of note, partial loss of *Nanog* by short interfering RNA (siRNA)-mediated knockdown (78%) has no effect (Supplementary Fig. 15), indicating that full knockout of *Nanog* protein is required to affect chromosome topology in ES cells.

To test further whether pluripotency factor binding has a direct role in this pluripotent-stem-cell-specific genome configuration, we made use of a C56Bl/6–129S1/SvImJ ES cell line with a 256× lacO repeat cassette integrated into the C56Bl/6 *Nfix* allele on chromosome 8 (Fig. 4g and Supplementary Fig. 16). We targeted green fluorescent protein (GFP)–LacR–*Nanog* fusion proteins to these lacO repeats and performed allele-specific 4C (ref. 20) to simultaneously analyse the contact spectra of the targeted C56Bl/6 and the non-targeted 129S1/SvImJ allele. Again, the overall chromosome topology for both alleles was highly similar, but several new specific contacts were found for the C56Bl/6 allele. Notably, these contacts coincide with high-density *Nanog*-binding sites around the pluripotency genes *Sall1* and *Klf2* and the *Irfx* cluster of developmental regulators. Circular permutation

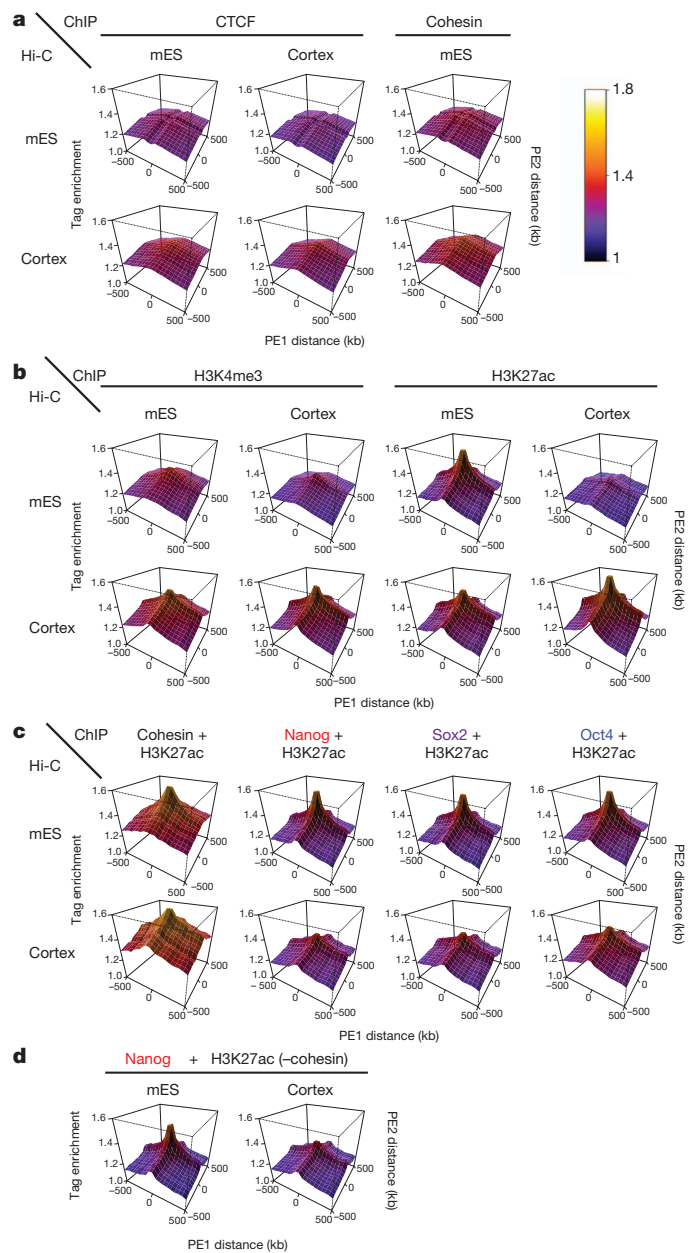


Figure 3 | Spatial interactome of chromatin factors is revealed by PE-SCAN. **a–d**, PE-SCAN plots for various chromatin factors. Plots are the same as in Fig. 2e, but with a different scale on the vertical axis. Note that the height of the data is colour-coded according to the colour bar shown in **a**. Top row represents mouse ES cell Hi-C data, bottom row represents cortex Hi-C data. **a**, PE-SCAN plots for known looping factors CTCF and cohesin (Smc1). **b**, PE-SCAN plots for promoter (H3K4me3) and active enhancer (H3K27ac) marks in mouse ES cells and cortex. **c**, PE-SCAN plots for active enhancer sites co-bound by cohesin (Smc1), *Nanog*, *Sox2* or *Oct4*. **d**, PE-SCAN plots for genomic sites with active enhancer marks and *Nanog* binding, but which are devoid of cohesin. Left, mouse ES cell Hi-C data; right, cortex Hi-C data.

of the positions of the high-density *Nanog* clusters showed that increased contact frequency was significantly enriched at these sites ($P < 0.001$), demonstrating that *Nanog* has a direct role in bringing together distantly located clusters of *Nanog*-binding sites.

Our data show that pluripotency transcription factors shape the pluripotent genome via spatial intra- and interchromosomal gathering of high-density binding sites. It has been suggested previously that transcription factors position tissue-specific and co-regulated genes in somatic cells^{21–23}. However, in contrast to previous studies, we validated this concept by comparing genome-wide contact maps

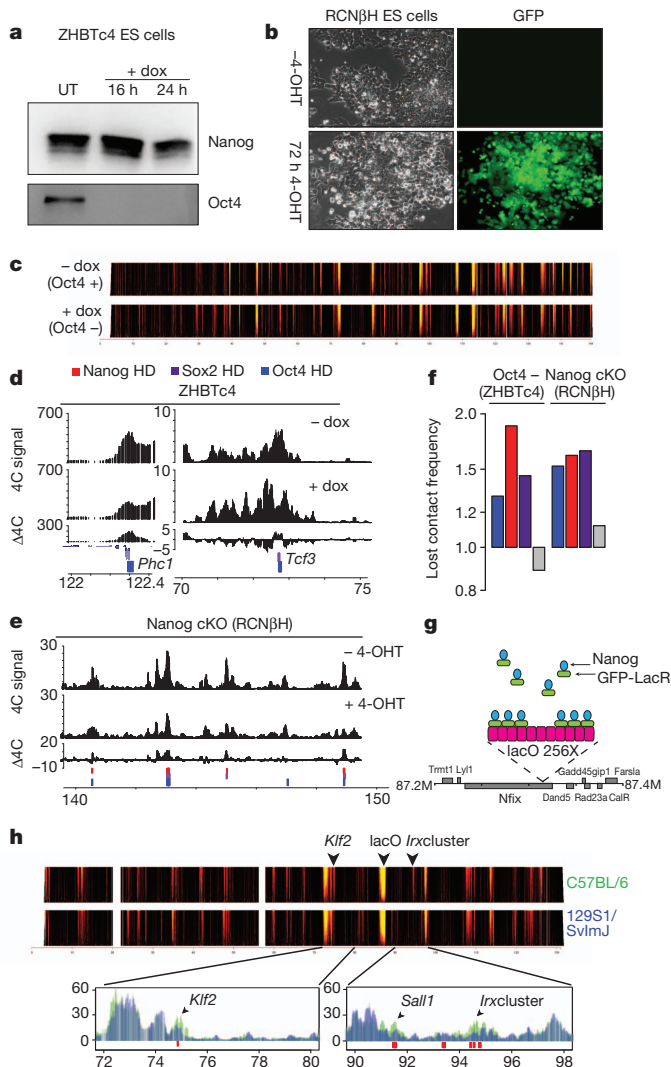


Figure 4 | Pluripotency factors influence the 3D organization of the genome. **a**, Immunoblot analysis before and after treatment of ZHBTc4 cells with $1 \mu\text{g ml}^{-1}$ doxycycline for the indicated times. Oct4 and Nanog proteins were detected using anti-Oct4 and anti-Nanog antibodies. UT, untreated. **b**, Morphology and GFP expression of RCNβH cells before and 72 h after treatment with $1 \mu\text{M}$ tamoxifen (4-OHT, 4-hydroxytamoxifen). **c**, 4C domainograms for Oct4-positive (–dox) and Oct4-negative (+dox) ZHBTc4 cells ($n = 2$ biological replicates) show that overall chromosome topology is maintained in Oct4-depleted cells. **d**, Zoomed-in regions show 4C signal (reads per million) for Oct4-positive (top) and Oct4-negative (middle) cells. Bottom, the difference (Δ) between the 4C signal of the Oct4-positive and -negative cells. Red, purple and blue rectangles show high-density Nanog, Sox2 and Oct4 regions, respectively. **e**, Same as **d** but for Nanog conditional knockout (cKO) ($n = 1$). Note that gene information is left out at this scale. **f**, Chromosome-wide analysis of differential 4C interactions for the Nanog enhancer viewpoint. Loss of 4C contact frequency is defined as a lower 4C signal in the knockout compared to the non-depleted reference cell line. Loss of contact frequency is determined for high-density Oct4, Nanog, Sox2 and CTCF (control) clusters for the Oct4-ablated and Nanog-conditional knockout cell lines and the enrichment over the background is calculated (see Methods for details). **g**, Schematic drawing depicting the integration site of the lacO repeat cassette in the C57Bl/6 allele of the *Nfix* locus and the targeting of GFP–LacR–Nanog fusion proteins. **h**, Domainograms showing allele-specific 4C (ref. 20) for the C57Bl/6 (containing the lacO cassette) and the 129 allele present in the hybrid ES cells ($n = 1$). Bottom panels show zoomed-in 4C profiles (C57Bl/6 green, 129 blue) for example differential regions. Red rectangles indicate high-density Nanog clusters (6 sites per 100 kb).

generated in wild-type and transcription factor knockout cells and by studying an artificially induced cluster of binding sites. Our observation that targeting or removing a given factor to or from the genome

only changes specific contacts while the overall folding of chromosomes remains intact is in accordance with a recently proposed model for chromosome topology. This ‘dog-on-a-lead’ model predicts that chromosomes are dominant over their individual segments (genes, domains, enhancers) in dictating the overall shape of the genome, but that segments can search the nuclear subvolumes they occupy for preferred contact partners²⁴. There is accumulating evidence that stochastically determined nuclear environments can influence the transcriptional output of resident genes, leading to cell-to-cell variability^{25,26}. We propose that the observed spatial clustering of pluripotency factor binding sites in pluripotent stem cells enhances the transcription efficiency of nearby genes and thereby contributes to the robustness of the pluripotent state.

METHODS SUMMARY

4C sequencing and mapping. 4C sequencing was performed as previously described⁹. We used HindIII as the first restriction enzyme to generate the 3C template, which was further trimmed with DpnII. Sequencing was performed on Illumina GAI and HiSeq 2000 over multiple runs. Raw sequencing data and mapped wig files can be found under Gene Expression Omnibus (GEO) accession GSE37275. **PE-SCAn.** To assess which factors are associated with genome organization, we aligned ChIP data to the Hi-C data. For this, intrachromosomal captures that are >5 Mb from each other are aligned to transcription-factor-binding sites. Only captures where both di-tags mapped within 500 kb of a ChIP peak were considered in the analysis. As a result we get for every pair of ChIP peaks on the same chromosome a set of two distances (dx , dy), to all the Hi-C di-tags that are found within 500 kb of these peaks. From the distribution of dx and dy a frequency matrix is calculated with a bin size of 50 kb, which is normalized by dividing by a randomized data set that is calculated by aligning the Hi-C data to a circularly permuted ChIP-seq data set, that is, the ChIP peaks are linearly shifted 10 Mb along the chromosome. In this manner the structure of the Hi-C data is preserved; the structure of the ChIP data is also preserved, only shifted.

Depletion of pluripotency factors. RCNβH cells were treated with tamoxifen and replated the next day. Seventy-two hours after initial tamoxifen treatment, cells were collected for 4C template preparation and analyses. ZHBTc4 cells were collected after 48 h of treatment with $1 \mu\text{g ml}^{-1}$ doxycycline.

Full Methods and any associated references are available in the online version of the paper.

Received 4 April 2012; accepted 26 June 2013.

Published online 24 July 2013.

- Dixon, J. R. *et al.* Topological domains in mammalian genomes identified by analysis of chromatin interactions. *Nature* **485**, 376–380 (2012).
- Nora, E. P. *et al.* Spatial partitioning of the regulatory landscape of the X-inactivation centre. *Nature* **485**, 381–385 (2012).
- de Wit, E. & de Laat, W. A decade of 3C technologies: insights into nuclear organization. *Genes Dev.* **26**, 11–24 (2012).
- van Steensel, B. & Dekker, J. Genomics tools for unraveling chromosome architecture. *Nature Biotechnol.* **28**, 1089–1095 (2010).
- Splinter, E. & de Laat, W. The complex transcription regulatory landscape of our genome: control in three dimensions. *EMBO J.* **30**, 4345–4355 (2011).
- Simonis, M. *et al.* Nuclear organization of active and inactive chromatin domains uncovered by chromosome conformation capture-on-chip (4C). *Nature Genet.* **38**, 1348–1354 (2006).
- Lieberman-Aiden, E. *et al.* Comprehensive mapping of long-range interactions reveals folding principles of the human genome. *Science* **326**, 289–293 (2009).
- Dekker, J., Rippe, K., Dekker, M. & Kleckner, N. Capturing chromosome conformation. *Science* **295**, 1306–1311 (2002).
- Splinter, E. *et al.* The inactive X chromosome adopts a unique three-dimensional conformation that is dependent on Xist RNA. *Genes Dev.* **25**, 1371–1383 (2011).
- Splinter, E., de Wit, E., van de Werken, H. J., Klous, P. & de Laat, W. Determining long-range chromatin interactions for selected genomic sites using 4C-seq technology: from fixation to computation. *Methods* **58**, 221–230 (2012).
- Wutz, A., Rasmussen, T. P. & Jaenisch, R. Chromosomal silencing and localization are mediated by different domains of Xist RNA. *Nature Genet.* **30**, 167–174 (2002).
- McLean, C. Y. *et al.* GREAT improves functional interpretation of cis-regulatory regions. *Nature Biotechnol.* **28**, 495–501 (2010).
- Apostolou, E. *et al.* Genome-wide chromatin interactions of the Nanog locus in pluripotency, differentiation, and reprogramming. *Cell Stem Cell* **12**, 699–712 (2013).
- Handoko, L. *et al.* CTCF-mediated functional chromatin interactome in pluripotent cells. *Nature Genet.* **43**, 630–638 (2011).
- Lin, Y. C. *et al.* Global changes in the nuclear positioning of genes and intra- and interdomain genomic interactions that orchestrate B cell fate. *Nature Immunol.* **13**, 1196–1204 (2012).

16. Li, G. *et al.* Extensive promoter-centered chromatin interactions provide a topological basis for transcription regulation. *Cell* **148**, 84–98 (2012).
17. Shen, Y. *et al.* A map of the *cis*-regulatory sequences in the mouse genome. *Nature* **488**, 116–120 (2012).
18. Niwa, H., Miyazaki, J. & Smith, A. G. Quantitative expression of Oct-3/4 defines differentiation, dedifferentiation or self-renewal of ES cells. *Nature Genet.* **24**, 372–376 (2000).
19. Chambers, I. *et al.* Nanog safeguards pluripotency and mediates germline development. *Nature* **450**, 1230–1234 (2007).
20. Holwerda, S. J. *et al.* Allelic exclusion of the immunoglobulin heavy chain locus is independent of its nuclear localization in mature B cells. *Nucleic Acids Res.* <http://dx.doi.org/10.1093/nar/gkt491> (7 June 2013).
21. Schoenfelder, S. *et al.* Preferential associations between co-regulated genes reveal a transcriptional interactome in erythroid cells. *Nature Genet.* **42**, 53–61 (2010).
22. Xu, M. & Cook, P. R. Similar active genes cluster in specialized transcription factories. *J. Cell Biol.* **181**, 615–623 (2008).
23. Dhar, S. S. & Wong-Riley, M. T. Chromosome conformation capture of transcriptional interactions between cytochrome c oxidase genes and genes of glutamatergic synaptic transmission in neurons. *J. Neurochem.* **115**, 676–683 (2010).
24. Krijger, P. H. & de Laat, W. Identical cells with different 3D genomes; cause and consequences? *Curr. Opin. Genet. Dev.* **23**, 191–196 (2013).
25. Noordermeer, D. *et al.* Variegated gene expression caused by cell-specific long-range DNA interactions. *Nature Cell Biol.* **13**, 944–951 (2011).
26. Kind, J. *et al.* Single-cell dynamics of genome-nuclear lamina interactions. *Cell* **153**, 178–192 (2013).
27. Feng, B. *et al.* Reprogramming of fibroblasts into induced pluripotent stem cells with orphan nuclear receptor Esrrb. *Nature Cell Biol.* **11**, 197–203 (2009).
28. Karantzali, E. *et al.* Sall1 regulates embryonic stem cell differentiation in association with nanog. *J. Biol. Chem.* **286**, 1037–1045 (2011).
29. Parisi, S. *et al.* Klf5 is involved in self-renewal of mouse embryonic stem cells. *J. Cell Sci.* **121**, 2629–2634 (2008).

Supplementary Information is available in the online version of the paper.

Acknowledgements We would like to thank C. Vermeulen and S. Holwerda for counting FISH slides; G. Geeven for the analysis of sequencing data; J. Brandsma for technical assistance; P. Verschure for the LacR–GFP backbone construct; and H. Niwa for providing ZHBTc4 ES cells. We also thank the Netherlands Institute for Regenerative Medicine (NIRM) network for supporting the R.A.P. laboratory and the Medical Research Council UK for supporting the I.C. laboratory. This work was financially supported by grants from the Dutch Scientific Organization (NWO) to E.d.W. (700.10.402, 'Veni') and W.d.L. (91204082 and 935170621), InteGer FP7 Marie Curie ITN (PITN-GA-2007-214902) and a European Research Council Starting Grant (209700, '4C') to W.d.L.

Author Contributions E.d.W. conceived the study, analysed the data and wrote the manuscript. B.A.M.B. designed and performed reprogramming and knockout experiments, and helped to write the manuscript. Y.Z. and P.H.L.K. designed and performed LacR–Nanog experiments. E.S. and P.H.L.K. performed cell culture and 4C experiments. M.J.A.M.V., E.P.N. and E.H. designed, performed and analysed FISH experiments. M.W. and N.G. assisted with reprogramming experiments. R.A.P. shared Oct4 conditional knockout cells and assisted with depletion experiments. N.F. and I.C. shared conditional knockout cells and assisted with Nanog depletion experiments. W.d.L. conceived the study and wrote the manuscript.

Author Information 4C sequencing data and mapped wig files have been submitted to the Gene Expression Omnibus (GEO) under accession number GSE37275. Reprints and permissions information is available at www.nature.com/reprints. The authors declare no competing financial interests. Readers are welcome to comment on the online version of the paper. Correspondence and requests for materials should be addressed to W.d.L. (w.delaat@hubrecht.eu).

METHODS

Cell culture. E14 ES cells (129/Ola background) and C56Bl/6-129 ES cells were grown in BRL-conditioned DMEM (high glucose, Gibco) supplemented with 15% FBS, 1× non-essential amino acids (NEAA; Gibco), 1× penicillin–streptomycin (Gibco), 1:1,000 β-mercaptoethanol (Invitrogen), 1× L-glutamine (Gibco) and 1,000 U ml⁻¹ leukaemia inhibitory factor (LIF; Gibco). Independently derived 129/Cast ES cells (129SVJ/Castaneus background) were grown on irradiated mouse embryonic fibroblasts in DMEM supplemented with 15% FBS, 1× NEAA, 1× penicillin–streptomycin, 1:1,000 β-mercaptoethanol and 1,000 U ml⁻¹ LIF. RCNβH cells were cultured in GMEM, β-mercaptoethanol, 10% FCS and LIF as described previously^{19,30}. ZHBTc4 (ref. 18) cells were cultured in GMEM, β-mercaptoethanol, 15% FCS, sodium bicarbonate and LIF. Culture medium was supplemented with 1 μg ml⁻¹ doxycycline or 1 μM tetracycline when applicable. NPCs (E14 and 129/Cast) were grown in DMEM/F12 supplemented with 1:100 N2 (Gibco), 20 ng ml⁻¹ bFGF (Peprotech), 20 ng ml⁻¹ murine EGF (Peprotech). For the 129/Cast NP cells 1× B-27 (Gibco) was added⁹. We generated astrocytes by growing E14NP cells to confluency and washing twice with DMEM before adding astrocyte medium (DMEM/F12 supplemented with 1:100 N2 and 2% FBS)³¹. The culture medium was changed twice and cells were grown for 5 days to make sure differentiation was complete, which was confirmed by immunofluorescence.

Generation of iPS cells. For generation of iPS cells, 10,000 129/Cast NPCs were seeded on gelatin-coated dishes in N2B27 medium (StemCell Resources). Cells were infected overnight with lentivirus expressing a multicistronic reprogramming cassette, encoding the iPS factors Oct4, Klf4, Sox2 and c-Myc³². After 5 days, cells were collected and plated on irradiated mouse embryonic fibroblasts. On day 6, N2B27 medium was replaced with mouse ES cell medium (DMEM with 15% FBS, 1× NEAA, 1× penicillin–streptomycin, 1:1,000 β-mercaptoethanol and 1,000 U ml⁻¹ LIF). iPS cell colonies were picked for clonal expansion on days 20–22 after infection. At passage 11 after colony picking, proper iPS cell reprogramming was examined by qPCR analysis on a panel of marker genes on total RNA (pluripotency markers: *Nanog*, *Zic3*, *Dppa4*, *Sall4*, *Cer1*, *Sox17* and *Fgf5*, neuronal lineage markers: *Olig2*, *Nestin*, *Blbp* and *Glast*). Cells were collected for 4C at passage 11.

siRNA knockdown of *Nanog*. For our knockdown experiments we used a pool of siRNA oligonucleotides targeting *Nanog* (M-057004-01) and a control pool containing non-targeting siRNAs (D-001206-13, siGENOME SMARTpool, Dharmacon). 129/Cast ES cells were seeded without feeders in 100-mm culture dishes at ~20% confluency on the day before transfection. Cells were transfected according to the manufacturer's protocol using 25 nM final siRNA concentration combined with 50 μl DharmaFECT 1. Transfection mixtures were added directly into the culture medium and plates were incubated at 37 °C with 5% CO₂. Forty-eight hours after transfection, cells were collected for protein level analysis and 4C template preparation.

Conditional ablation of *Nanog* and *Oct4*. RCNβH cells were treated with tamoxifen and replated the next day. Seventy-two hours after initial tamoxifen treatment, cells were collected for 4C template preparation and analyses. ZHBTc4 cells were collected after 48 h of treatment with 1 μg ml⁻¹ doxycycline.

Protein analysis. Protein levels before and after conditional deletion were analysed in cells collected at the time points as described above. Immunoblot analysis was carried out on nuclear extracts that were made as described in³³. Extracts were subjected to SDS–PAGE³⁴, and proteins were transferred to a methanol-activated PVDF membrane. Blots were blocked in blocking buffer (5% non-fat dry milk in TBST (50 mM Tris, pH 7.4, 150 mM NaCl, 0.1% Tween)) for 1 h at room temperature or overnight at 4 °C, while tumbling. Primary antibody was diluted in blocking buffer and incubated for 1–3 h at room temperature or overnight at 4 °C, while tumbling. Blots were washed four times with TBST and incubated with secondary antibody for 1 h in blocking buffer. Membranes were then incubated with SuperSignal West Pro (Thermo Scientific) and digitally analysed using an LAS 4000 ECL ImageQuant imager and ImageJ software. Used antibodies: anti-*Nanog* (A300-397A, Bethyl Laboratories) at 1:5,000, anti-*Oct4* (C30A3, Cell Signaling Technology) at 1:1,000, anti-histone H3 (Abcam 1791) at 1:2,000.

Flow cytometry. Tamoxifen-treated and -untreated RCNβH cells were trypsinized and pellets were resuspended as single cells in regular ES cell medium at about 10⁶ per ml. For each condition, 50,000 live cells were analysed for GFP fluorescence, using a Becton Dickinson FACSCalibur flow cytometer and FloJo software.

Generation of lacO targeted cell line. Homology arms were excised (KpnI digest) from bacterial artificial chromosome (BAC) RP24-136A15, and ligated into a low-copy bluescript plasmid. A total of 256 copies of a lacO array were inserted into a unique AatII site of the homology arms. F₁ ES cells derived from C56Bl/6 and 129 mouse strains were transfected with the linearized targeting construct by electroporation. After 14 days of selection with neomycin, positive colonies were picked and screened by Southern blotting. The GFP–LacR–*Nanog* construct was generated in the backbone of pHAGE2-IRES-puro with an EF1α promoter³⁵. LacO cells were

stably transduced with the GFP–LacR–*Nanog* construct, and positive cells were selected with puromycin for 10 days after which cells were collected and tested for purity of by flow cytometry (90% GFP-positive). Allelic paired-end 4C technology was performed as described²⁰, using HindIII–DpnII digestion and the following 4C primers: 5'-AATGATACGGCGACCACCGAGATCTACACTCTTTCCCTACA CGACGCTCTTCGATCGGAACCTAAATGGAGGATC-3' and 5'-CAAGCAG AAGACGGCATAACGAGATCGGTCTCGGCATTCTCTGTAACCGCTCTTC CGATCTTACCAGGACCCCTGGGACCC-3'.

3D-DNA FISH. 3D-DNA FISH for interchromosomal interaction was performed essentially as described in ref. 2. For slide preparation, ES cells were spotted on polylysine microscopy slides after which slides were washed in PBS. Cells were fixed in 3% paraformaldehyde/PBS and washed twice with PBS, after which cells were permeabilized on ice using ice-cold 0.5% Triton X-100 for 6 min. Slides were then washed for 3 min with 70% ethanol and stored in 70% ethanol at –20 °C. For preparation of probes, 10 μl of both labelled BACs was combined with 5 μl mouse Cot1 DNA and mixtures were speedvaccinated until pellets were dry. Pellets were resuspended in 12.5 μl 50+ hybmix, incubated for 5 min at 95 °C, cooled on ice, and incubated for 30 min at 37 °C.

For FISH hybridization, slides were dehydrated for 3 min in 70% ethanol, 3 min in 90% ethanol, 3 min in 100% ethanol, after which slides were air-dried. One-hundred microliters of 70+ hybmix was then added to the dried slides, and slides were covered with a coverslip and incubated for 3 min at 85 °C. Slides were washed on ice, using ice-cold 2× saline-sodium citrate buffer (SSC) for 5 min, then using ice cold 70% ethanol for 5 min, after which slides were dehydrated again as described above. After air drying, 10 μl probe was added and covered with a coverslip and hybridizing slides were incubated overnight at 37 °C in a humid box containing 50% formamide/2× SSC. After hybridization, slides were washed in 2× SSC for 5 min, which also removes the coverslip. Subsequently, slides were washed three times for 10 min in 50% formamide/2× SSC at 37 °C. Slides were then dehydrated as described above, and air-dried slides were mounted using 40 μl DAPI/Vectashield. Slides were covered with new coverslips and sealed with transparent nail polish. We performed manual distance measurements in ImageJ using the Image5D plugin.

General 4C template information. For high-quality 4C experiments library complexity is crucial; by applying 4C to 1 million genome equivalents (3 μg DNA), we analyse a large number of ligation products per viewpoint. The generated DNA contact profiles are therefore a true population average³. The observed ligation products are the result of spatial proximity. Note that these ligation products can be a reflection of direct DNA contacts (such as promoter–enhancer interactions) or indirect contacts mediated by large macromolecular complexes or nuclear particles.

Experimental and primer design is done as previously described¹⁰. For the allele-specific 4C we have used a paired-end 4C strategy²⁰. To this end, we designed forward and reverse primers compatible with the Illumina flow cell. The forward primer analyses the ligation product and the reverse primer is selected such that it sequences an SNP that distinguishes the C57Bl/6 allele from the 129S1/SvImJ allele. After sequencing, this SNP is used to demultiplex the two alleles, to create two separate 4C profiles.

Definitions. To make this methods section clearer to non-experts we present the following definitions. Fragment: a genomic region (or sequence) that is generated after the first restriction. In this case, the first restriction enzyme, that generates the 3C template, is always HindIII. Fragment end: to generate the 4C template, the 3C template is further digested with a frequent cutter, in our case DpnII. The resulting HindIII–DpnII restriction fragment is referred to as the fragment end, because this restriction fragment represents the end of the 3C fragment. Capture frequency: captures are defined as the ligations in the 3C protocol resulting from 3D genome conformation. The 4C primers directly interrogate the ligation junction. Therefore the resulting capture frequency can be estimated from counting the number of reads coming from a given fragment end.

4C sequencing and mapping. 4C sequencing was performed as previously described⁹. We used HindIII as the first restriction enzyme to generate the 3C template, which was further trimmed with DpnII. Sequencing was performed on Illumina GAI and HiSeq 2000 over multiple runs. Primer sequence (internal barcode) is removed from the sequence and the trimmed reads were aligned to a reduced genome consisting of sequences that flank HindIII restriction sites. The mouse mm9 genome was used as the reference genome for mapping 4C sequence captures. Non-unique sequences (repeats) that flank a restriction site were removed from the analysis. From the mapping a frequency distribution along the genome is calculated, which is the input for all downstream analyses. Raw sequencing data and mapped wig files can be found under GEO accession GSE37275.

Statistical analysis of 4C data. Statistical analyses of 4C data (that is, domainograms and target identification) was performed as described previously^{9,10}. For formal definitions we refer the reader to these articles. Here we will briefly describe underlying principles of the data analysis. An inherent challenge of 4C data (and

genome-wide chromosome capture data in general) is the highly non-uniform data distribution. Close to the viewpoint the signal is very high, whereas the signal rapidly decreases as a function of the distance from the viewpoint. Therefore, we statistically define significant interactions as regions that have an increased number of captures compared to the local background. To this end we must estimate the local background capture frequency. To minimize potential PCR artefacts we transform the 4C-seq read count at HindIII-DpnII fragment ends to binary data (that is, captured or not captured). From this it is clear that 0s play an essential role in determining significant interactions. Local background is then determined as the frequency of captured fragment ends (1s) in a large window, typically 3,000 fragment ends. Following the binomial distribution, we can estimate μ and σ (for details see ref. 10, which is used to determine a z-score for a window of fragment ends of fixed size).

To visualize the 4C data using domainograms, z-scores are calculated using windows with a range of size (from 3 to 200). The z-scores are subsequently transformed to P-values with a one-tailed normal test. The $-\log_{10}$ -transformed P-values are colour-coded and visualized along the linear chromosome. As such regions can be visualized with a high likelihood of interaction with the viewpoint.

To distill discrete regions of significant interaction we choose a fixed window size of 100 fragment ends and calculate the z-scores for this window size across the chromosome. To select significant regions we determine the z-score threshold based on a FDR level of 0.01. The FDR is determined based on the z-score distribution in 100 randomly permuted chromosomes. The windows exceeding the z-score threshold are selected as significantly contacted regions.

Analysis of 4C trans-interactions. In our data set we find highly specific inter-chromosomal interactions. Like the intrachromosomal profiles we calculate an enrichment score over the background capture frequency. However, because the background capture frequency is distributed more or less uniformly across the chromosome, we can use a single background frequency per chromosome. The 4C enrichment score is calculated in the following way:

$$E_{\text{trans},i} = \frac{w p_{w,i} - (p_{\text{chrom}} \cdot w)}{\sqrt{w p_{\text{chrom}} (1 - p_{\text{chrom}})}} \quad (1)$$

in which w is the window size, and i is window index along the chromosome. p_{chrom} is defined as follows:

$$p_{\text{chrom}} = \frac{N_{\text{captured}}}{N_{\text{chrom}}} \quad (2)$$

in which N_{captured} is the number of fragment ends captured on the chromosome and N_{chrom} is the total number fragment ends on the chromosome. $p_{w,i}$ is defined as follows:

$$p_{w,i} = \frac{n_{w,i,\text{captured}}}{w} \quad (3)$$

in which $n_{w,i,\text{captured}}$ is the number of fragments captured in genomic window i of size w .

Windows with an $E_{\text{trans},i}$ larger than 6 were chosen for subsequent analysis in GREAT.

4C/Hi-C alignment to ChIP profiles. To test enrichment of 4C signal along ChIP peaks we aligned the *trans* fragments to nearest ChIP peak. We used several ES cell ChIP-seq profiles from various sources. For Oct4, Sox2 and Nanog we used the data described in ref. 36 (GSE11724). H3K27ac was taken from ref. 37 (GSE24165). Smc1 data³⁸ (GSE22557), H3K4me3 (ref. 39) (GSE12241), RNA PolII and CTCF (mES cell and cortex), H3K27ac and H3K4me3 (cortex)¹⁷ (GSE29218).

4C data was binarized because *in trans* the capture frequency is so low that read count more likely represent differences in PCR efficiency rather than genuine unique captures. For the binarized data the distance to the nearest ChIP peak was calculated. To calculate enrichment scores, the distances to the nearest ChIP peak were sorted (that is, aligned) and a sliding average was calculated. The window size of the sliding average was set to 1% of the total data set.

Hi-C normalization and analysis. Hi-C data¹ was downloaded from GEO (accession GSE35156). We removed all read pairs that are mapped within 500 bp of each other on the chromosome, because these read pairs are probably genomic background sequence, rather than bona fide Hi-C captures. For the virtual 4C and disorganization analysis we average the data to bins of 100 kb, which results in a matrix of pairwise capture frequencies between all the genomic bins. A proper analysis of the Hi-C data requires that we correct the Hi-C matrix for genomic biases. For this normalization we assume that the capture probability in a given genomic bin is dependent on the number of restriction sites in this bin. The strong positive correlation between the restriction site density and the number of captures for that given bin is evidence that this assumption is correct (data not shown). We therefore normalize the bins by dividing by the capture probability. First we

calculate the restriction density in 100-kb bins along the chromosome, which gives us a capture probability for in a given bin ($p_{\text{capture},i}$). The capture probability between two bins on the chromosome ($P_{\text{capture},i,j}$) can now be calculated by taken the product of the capture probabilities of the two single bins ($p_{\text{capture},i} p_{\text{capture},j}$). Before normalization the correlation between the diagonals of the the Hi-C matrices for the NcoI and HindIII experiments from mouse ES cells is 0.32. However, after normalization this correlation has jumped to 0.86.

For the virtual 4C based on the Hi-C data, we combine the three normalized matrices ($2 \times$ HindIII, $1 \times$ NcoI). Because the data are too sparse to perform a virtual 4C analysis for a single fragment, we analyse a single row from the Hi-C interaction matrix. For comparison, we also calculate the average 4C signal in 100-kb genomic bins.

For the analysis of genomic disorganization we use the two HindIII experiments for mouse ES cell and cortex (GSE35156). In this analysis we want to compare the propensity of active and inactive regions to contact regions over large genomic distances. To this end we segment the chromosomes in active and inactive bins of 100 kb, based on the density of H3K4me1 sites⁴⁰. On the basis of this segmentation we can create a matrix with similar in size to the Hi-C matrix. In this matrix three classes of interaction bins can be created: (1) H3K4me1 high in both: interaction bin between two active genomic regions; (2) H3K4me1 low in both: interaction bin between two inactive genomic regions; and (3) H3K4me1 low/H3K4me1 high: interaction bin between active and inactive.

Because we perform a 50/50 segmentation, the classes H3K4me1^{high/high} and H3K4me1^{low/low} will both be 25% of the interaction bins, H3K4me1^{high/low} class will be 50% of the interaction bins. In addition, the Hi-C matrix is segmented into high-contact and low-contact bins by setting an arbitrary threshold (75% quantile value of the entire matrix). Next, we overlay the segmented Hi-C matrix and the contact bins to determine the number of long-range contacts made for each of the classes. We use various minimal distance cut-offs running from 10–70 Mb with step sizes of 10 Mb. This process is schematically explained in Fig. 1e.

Alignment of Hi-C data to ChIP peaks (PE-SCAN). To assess which factors are associated with genome organization, we aligned ChIP data to the Hi-C data. To this end we selected the intrachromosomal captures, however, because of the strongly non-uniform distribution we removed the captures that lie within 5 Mb of each other. This has the effect that we only analyse interactions between, rather than within, topological domains. The Hi-C pairs were aligned to the ChIP data in two iterations. First, one end of the paired reads was aligned to the ChIP data. Only reads that mapped within 500 kb up- or downstream of the ChIP peaks were selected for further analysis. Of this reduced set the corresponding read was also aligned to the ChIP peaks within 500 kb. As a result we get for every intrachromosomal pair of ChIP peak a set of two distances (dx , dy), to all the Hi-C ditags that are found within 500 kb of these peaks. From the distribution of dx and dy a frequency matrix is calculated, which is the result of our two-dimensional alignment, with a bin size of 50 kb. To calculate whether the binding sites of a given factor show preferential spatial contacts, we calculate an enrichment score over a randomized data set. The randomized data set is calculated by aligning the Hi-C data to a circularly permuted ChIPseq data set, that is, the ChIP peaks are linearly shifted 10 Mb along the chromosome. It is important to note that in this manner the structure of the Hi-C data are preserved; the structure of the ChIP data are also preserved, only shifted. The resulting frequency matrix serves as an internal normalization for the observed Hi-C data alignment scores.

30. Smith, A. G. Culture and differentiation of embryonic stem cells. *J. Tissue Cult. Methods* **13**, 89–94 (1991).
31. Peric-Hupkes, D. *et al.* Molecular maps of the reorganization of genome-nuclear lamina interactions during differentiation. *Mol. Cell* **38**, 603–613 (2010).
32. Warlich, E. *et al.* Lentiviral vector design and imaging approaches to visualize the early stages of cellular reprogramming. *Mol. Ther.* **19**, 782–789 (2011).
33. Andrews, N. C. & Faller, D. V. A rapid micropreparation technique for extraction of DNA-binding proteins from limiting numbers of mammalian cells. *Nucleic Acids Res.* **19**, 2499 (1991).
34. Laemmli, U. K. Cleavage of structural proteins during the assembly of the head of bacteriophage T4. *Nature* **227**, 680–685 (1970).
35. Wilson, A. A. *et al.* Sustained expression of α_1 -antitrypsin after transplantation of manipulated hematopoietic stem cells. *Am. J. Respir. Cell Mol. Biol.* **39**, 133–141 (2008).
36. Marson, A. *et al.* Connecting microRNA genes to the core transcriptional regulatory circuitry of embryonic stem cells. *Cell* **134**, 521–533 (2008).
37. Creighton, M. P. *et al.* Histone H3K27ac separates active from poised enhancers and predicts developmental state. *Proc. Natl Acad. Sci. USA* **107**, 21931–21936 (2010).
38. Kagey, M. H. *et al.* Mediator and cohesin connect gene expression and chromatin architecture. *Nature* **467**, 430–435 (2010).
39. Mikkelsen, T. S. *et al.* Genome-wide maps of chromatin state in pluripotent and lineage-committed cells. *Nature* **448**, 553–560 (2007).
40. Meissner, A. *et al.* Genome-scale DNA methylation maps of pluripotent and differentiated cells. *Nature* **454**, 766–770 (2008).

Mechanism of MEK inhibition determines efficacy in mutant KRAS- versus BRAF-driven cancers

Georgia Hatzivassiliou¹, Jacob R. Haling², Huifen Chen³, Kyung Song¹, Steve Price⁴, Robert Heald⁴, Joanne F. M. Hewitt^{4†}, Mark Zak³, Ariana Peck^{2†}, Christine Orr¹, Mark Merchant¹, Klaus P. Hoeflich¹, Jocelyn Chan¹, Shih-Ming Luoh¹, Daniel J. Anderson^{5†}, Mary J. C. Ludlam^{5†}, Christian Wiesmann^{6†}, Mark Ultsch⁶, Lori S. Friedman¹, Shiva Malek² & Marcia Belvin¹

KRAS and BRAF activating mutations drive tumorigenesis through constitutive activation of the MAPK pathway. As these tumours represent an area of high unmet medical need, multiple allosteric MEK inhibitors, which inhibit MAPK signalling in both genotypes, are being tested in clinical trials. Impressive single-agent activity in BRAF-mutant melanoma has been observed; however, efficacy has been far less robust in KRAS-mutant disease¹. Here we show that, owing to distinct mechanisms regulating MEK activation in KRAS- versus BRAF-driven tumours^{2,3}, different mechanisms of inhibition are required for optimal antitumour activity in each genotype. Structural and functional analysis illustrates that MEK inhibitors with superior efficacy in KRAS-driven tumours (GDC-0623 and G-573, the former currently in phase I clinical trials) form a strong hydrogen-bond interaction with S212 in MEK that is critical for blocking MEK feedback phosphorylation by wild-type RAF. Conversely, potent inhibition of active, phosphorylated MEK is required for strong inhibition of the MAPK pathway in BRAF-mutant tumours, resulting in superior efficacy in this genotype with GDC-0973 (also known as cobimetinib), a MEK inhibitor currently in phase III clinical trials. Our study highlights that differences in the activation state of MEK in KRAS-mutant tumours versus BRAF-mutant tumours can be exploited through the design of inhibitors that uniquely target these distinct activation states of MEK. These inhibitors are currently being evaluated in clinical trials to determine whether improvements in therapeutic index within KRAS versus BRAF preclinical models translate to improved clinical responses in patients.

The MAPK/ERK kinase (MEK) signalling cascade is a key regulator of cellular proliferation, differentiation and survival downstream of RAS activation⁴. Upregulation of this pathway occurs in a large fraction of tumours, frequently owing to oncogenic activating mutations in KRAS, NRAS, HRAS and BRAF⁵. Whereas BRAF inhibitors have shown remarkable efficacy against melanomas with BRAF(V600E) mutations, these compounds are not effective against KRAS-mutant tumours owing to inhibitor-mediated priming of wild-type RAF signalling^{6–8}. As MEK is a common effector downstream of wild-type and mutant RAF^{9,10}, MEK inhibitors have the potential to target all tumours dependent on MAPK pathway signalling. Hence, MEK inhibitors show efficacy against both BRAF- and KRAS-mutant cancer cell lines and xenograft models¹¹. Although the sensitivity of BRAF-mutant models is typically greater than that of KRAS-mutant models^{9,12}, the relative potency between the two genotypes varies for different inhibitors^{13–15}. This difference is evident when comparing three allosteric MEK inhibitors in tumour models that have mutations in either BRAF or KRAS (Table 1 and Fig. 1). All three inhibitors are potent, ATP-uncompetitive inhibitors of MEK1 but show distinct shifts in cellular activity, with GDC-0973

having 100-fold weaker potency against a KRAS-mutant versus BRAF-mutant cell line, whereas GDC-0623 and G-573 show only 6- and 15-fold half-maximum effective concentration (EC₅₀) decreases, respectively (Table 1 and Supplementary Fig. 1). We profiled the MEK inhibitors across a panel of BRAF and KRAS-mutant cancer cell lines (Fig. 1a and Supplementary Table 1) and consistently found that GDC-0973 was less potent in KRAS versus BRAF-mutant cell lines, whereas GDC-0623 and G-573 had similar efficacy in the two genotypes. We tested clinically relevant doses of GDC-0973 and GDC-0623: the average plasma concentration of GDC-0973 over 24 h at its maximum tolerated dose (MTD) is 0.37 μ M and for GDC-0623 is 0.63 μ M (Musib *et al.*, manuscripts in preparation).

To test whether these differences translate to *in vivo* tumour models, we compared GDC-0973, GDC-0623 and G-573 in three KRAS-mutant xenograft models (Fig. 1b and Supplementary Fig. 2). Compounds were evaluated at their MTDs, and superior antitumour activity was observed with GDC-0623 and G-573 compared to GDC-0973 in all three KRAS models.

Treatment of KRAS-mutant cells with MEK inhibitors is expected to lead to an increase in phosphorylated MEK (pMEK) through feedback-mediated RAF activation^{15,16}. We observed the expected increase in pMEK in response to GDC-0973 (Fig. 2a, top panel), but not GDC-0623 or G-573. This block of pMEK accumulation resulted in more effective inhibition of pERK by GDC-0623 and G-573. Release of negative feedback mediators occurred normally in response to all inhibitors (Supplementary Fig. 3). In a BRAF(V600E) cell line, where wild-type RAF activity is low¹⁶, all inhibitors reduced pMEK levels (Fig. 2a lower panel)¹³. Knockdown experiments revealed that BRAF and CRAF, but not ARAF, were responsible for pMEK induction (Supplementary Fig. 4), in agreement with BRAF–CRAF heterodimers being the major mediators of signalling through activated KRAS⁴.

Given that GDC-0623 and G-573 prevent MEK phosphorylation in cells, we tested whether these compounds directly inhibit RAF activity *in vitro*. Only GDC-0623 and G-573 were able to prevent MEK phosphorylation by CRAF *in vitro* (Fig. 2b, upper panel), whereas all three inhibitors were able to block MEK phosphorylation by BRAF(V600E) (Fig. 2b, lower panel). The inhibitors did not block phosphorylation of MEK(K97R) (Supplementary Fig. 5a), which is kinase dead and does not effectively bind the inhibitors (Supplementary Figs 5b and 10). These studies confirm that the MEK inhibitors do not block RAF activation directly, but rather through their effects on MEK. Furthermore, none of the inhibitors had off-target effects against other kinases (Supplementary Table 3).

Because the MEK inhibitors affect RAF activity, we proposed that they might affect RAF–MEK protein interactions. *In vitro* dimerization assays revealed that GDC-0623 and G-573 stabilize the RAF–MEK

¹Department of Translational Oncology, Genentech, Inc., 1 DNA Way, South San Francisco, California 94080, USA. ²Department of Biochemical and Cellular Pharmacology, Genentech, Inc., 1 DNA Way, South San Francisco, California 94080, USA. ³Department of Discovery Chemistry, Genentech, Inc., 1 DNA Way, South San Francisco, California 94080, USA. ⁴Argenta, 8/9 Spire Green Centre, Flex Meadow, Harlow, Essex CM19 5TR, UK. ⁵Department of Discovery Oncology, Genentech, Inc., 1 DNA Way, South San Francisco, California 94080, USA. ⁶Department of Structural Biology, Genentech, Inc., 1 DNA Way, South San Francisco, California 94080, USA. [†]Present addresses: WestCHEM, School of Chemistry, University of Glasgow, Joseph Black Building, University Avenue, Glasgow G12 8QQ, UK (J.F.M.H.); MRC Mitochondrial Biology Unit, Wellcome Trust/MRC Building, Hills Road, Cambridge CB2 0XY, UK (A.P.); Novartis Institutes for Biomedical Research, Fabrikstrasse 16, CH-4002 Basel, Switzerland (C.W.); Cairn Biosciences Inc., 3534 24th Street, San Francisco, California 94110, USA (M.J.C.L.); Cleve Biosciences, 866 Malcolm Road suite 100, Burlingame, California 94010, USA (D.J.A.).

Table 1 | Biochemical and Cellular Potency of GDC-0973, GDC-0623, and G-573.

Compound	MEK1 (-ATP) K_i (nM)	MEK1 (+ATP) K_i (nM)	Proliferation EC ₅₀ (μM)		KRAS(G13D)/ BRAF(V600E) EC ₅₀
			A375 (BRAF(V600E))	HCT116 (KRAS(G13D))	
GDC-0973	262.5	0.05	0.005	0.520	104
GDC-0623	217.5	0.13	0.007	0.042	6
G-573	196.3	0.30	0.011	0.167	15

complex whereas GDC-0973 does not (Fig. 2c and Supplementary Fig. 6a, b). RAF–MEK complex formation was specific to wild-type RAF and not BRAF(V600E), which does not form stable complexes in the presence of inhibitors (Fig. 2d and Supplementary Fig. 6a, b). These *in vitro* findings were confirmed in cells. In KRAS-mutant cells GDC-0623, and more markedly, G-573, induced dimerization of MEK with both BRAF and CRAF, whereas GDC-0973 reduced baseline heterodimer levels (Fig. 2e), coincident with elevated pMEK levels (Fig. 2f, top panel, and Supplementary Fig. 7a, b). Consistent with the biochemical data, G-573 did not affect the basal BRAF(V600E)–MEK complex in BRAF(V600E) homozygous cells, whereas it was able to effectively stabilize the CRAF–MEK complex (Supplementary Fig. 6c, d).

We theorized that RAF–MEK complex stabilization by GDC-0623 and G-573 may disfavour BRAF–CRAF complex formation in response to MEK inhibitors, and thus dampen feedback-induced signalling. Indeed, only GDC-0973 promoted BRAF–CRAF heterodimer formation (Fig. 2f, lower panel, and Supplementary Fig. 7b). Furthermore, whereas GDC-0973 induced CRAF translocation to the plasma membrane as previously described¹⁵, G-573 treatment blocked it (Supplementary Fig. 7c). Thus, a subset of MEK inhibitors, in addition to blocking MEK activation by RAF, also block RAF activation through inhibition of BRAF–CRAF heterodimer formation and RAF plasma membrane translocation.

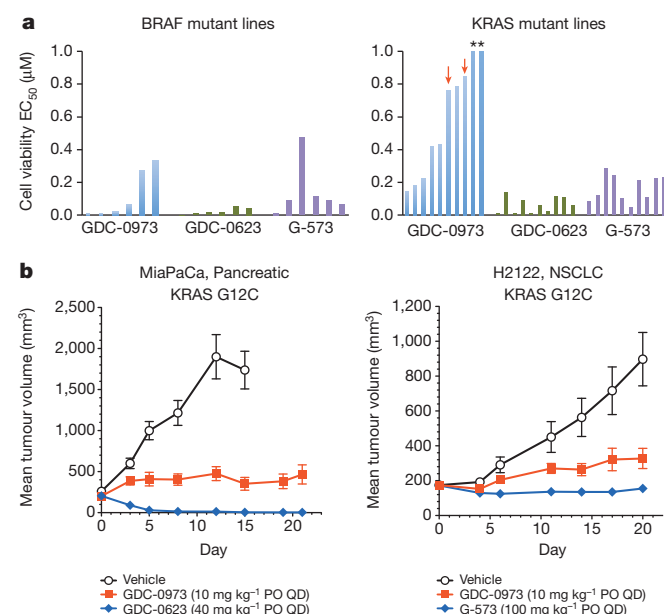


Figure 1 | Allosteric MEK inhibitors show distinct relative potencies in KRAS-mutant and BRAF-mutant cancer models. **a**, EC₅₀ values (μM) in a cell viability assay of indicated MEK inhibitors against a panel of BRAF(V600E) and KRAS-mutant cancer cell lines. *EC₅₀ values >1 μM. Red arrows: MiaPaCa-2 (left), H2122 (right). **b**, Antitumour efficacy of GDC-0973 in the MiaPaCa-2 and H2122 xenograft models, GDC-0623 in MiaPaCa-2 ($n = 5$ per group) or G-573 in H2122 ($n = 10$ per group). Percent tumour growth inhibition (%TGI) was 78% for GDC-0973 and 120% for GDC-0623 in MiaPaCa-2. GDC-0973 had no partial or complete regressions (PR/CR), whereas GDC-0623 had 3 PR, 2 CR. In H2122 xenografts, GDC-0973 treatment led to 80% TGI, 1 PR, 0 CR; G-573 treatment led to 118% TGI, 3 PR, 0 CR. Group mean is plotted with error bars representing the standard error of mean (s.e.m.). PO QD, by mouth once a day.

We obtained a crystal structure of GDC-0973 with the MEK1 kinase domain and compared its binding mode to that of GDC-0623 and G-573 based on molecular modelling (Fig. 3a and Supplementary Fig. 10). The three inhibitors bind in a similar orientation with respect to the nucleotide and the activation loop (A-loop) helix that contains S218, one of the two MEK sites phosphorylated by RAF. S222, the second phosphorylation site, lies in a part of the activation loop that is not well defined in the

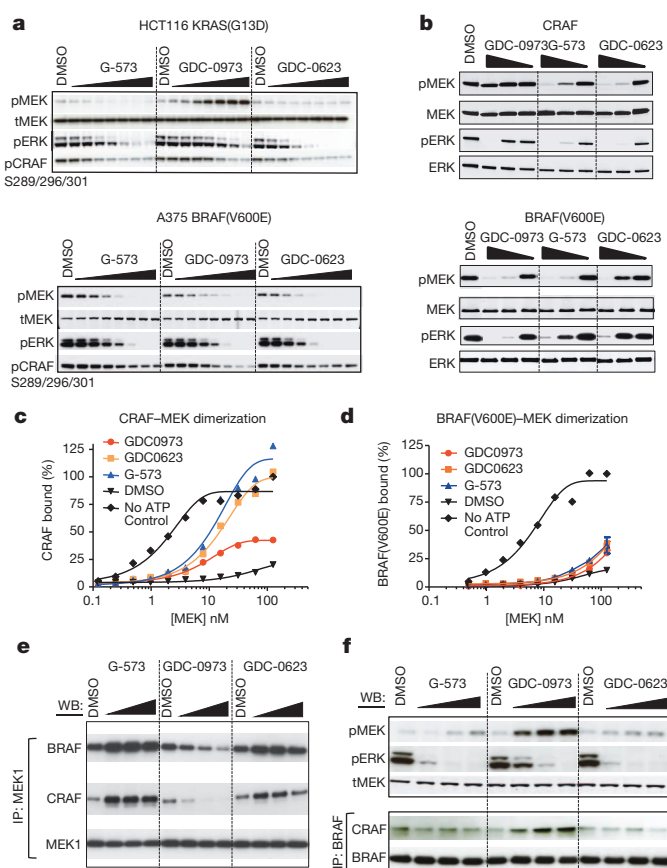


Figure 2 | MEK inhibitor efficacy in KRAS-mutant models correlates with the ability to block feedback-induced phosphorylation of MEK by RAF.

a, Western blot (WB) of phosphorylated MEK (pMEK) and total MEK (tMEK) in HCT116 KRAS(G13D) cells (top) and A375 BRAF(V600E) cells (bottom) after overnight treatment with inhibitors (range: 0.00045–0.33 μM in threefold increments) shows pMEK induction selectively by GDC-0973 in HCT116 cells. **b**, *In vitro* cascade kinase assays using recombinant inactive MEK and ERK and recombinant kinase domains of either CRAF (top) or BRAF(V600E) (bottom) in the presence of 0.01, 0.1 and 1 μM of the indicated MEK inhibitors. **c**, **d**, Recombinant kinase domain (KD) CRAF^{KD}–MEK dimer formation (**c**) or BRAF(V600E)^{KD}–MEK dimer formation (**d**) are detected by homogenous time-resolved fluorescence *in vitro*, either in the absence (No ATP control) or presence of 100 μM ATP with and without MEK inhibitors (GDC-0973, GDC-0623, G-573, DMSO). **e**, Immunoprecipitation (IP)/WB of endogenous MEK1 from lysates of HCT116 (KRAS(G13D)) cells treated overnight with DMSO or indicated MEK inhibitors at 0.1, 1, 10 μM. **f**, IP/WB of endogenous BRAF from lysates of HCT116 (KRAS(G13D)) cells treated overnight with DMSO or indicated MEK inhibitors at 0.1, 1, 10 μM (lower panel). Immunoprecipitates were immunoblotted for BRAF and CRAF, showing that GDC-0973 promotes BRAF–CRAF complex formation. Total lysates were immunoblotted for pMEK, pERK and tMEK (upper panel).

crystal structure. In our structure/models, the inhibitors form an interaction with the backbone amide of S212, at the beginning of the A-loop helix^{17,18}. Whereas GDC-0623 and G-573 are predicted to engage S212 with an aromatic nitrogen (N) to form a hydrogen bond, GDC-0973 engages S212 with an aromatic fluorine (F) forming a much weaker interaction, given the high electronegativity and low polarizability of F¹⁹. The importance of this interaction for inhibitor activity was highlighted by disrupting it through substitution of a carbon at this site, which abolished activity (Supplementary Fig. 8).

We proposed that the interaction with the S212 backbone might constrain the movement of the A-loop helix and prevent MEK phosphorylation by RAF. To test this, we mutated S212 to proline to disrupt the hydrogen bond with the inhibitors (Supplementary Fig. 9). Based on modelling, S212P also disrupts the hydrogen-bond network between the S212 side chain, the A-loop helix, and E114 in the α -C helix, and is predicted to allow greater accessibility of the A-loop to RAF (Supplementary Fig. 9). In contrast, a S212A mutation should not affect the inhibitor hydrogen-bond interaction, but would affect the hydrogen-bond network between S212, the A-loop helix and E114 and lead to increased

A-loop helix dynamics and higher basal MEK activity, as previously reported²⁰. In cellular studies, transfected wild-type MEK1 became highly phosphorylated in the presence of GDC-0973 (Fig. 3b). The S212P and S212A mutants showed higher basal pMEK levels, consistent with the disruption of the S212/A-loop/C-helix interactions. As predicted, GDC-0623 and G-573 were unable to inhibit the phosphorylation of MEK1(S212P) but were able to block the phosphorylation of MEK1(S212A). Our model suggests this is because of the hydrogen bonds to the alanine backbone that are lost with the proline backbone (Fig. 3b and Supplementary Fig. 9c). We propose that the stronger interaction of GDC-0623 and G-573 with S212 reduces the flexibility of the MEK A-loop helix, thus preventing RAF from accessing S218/S222.

We evaluated additional compounds with an N (G-530) or F (PD-901) at this position (Supplementary Fig. 10). As predicted by our model, G-530 prevented pMEK accumulation and stabilized a RAF–MEK complex, whereas PD-901 led to increased pMEK and lower levels of RAF–MEK dimers (Fig. 3c). In biochemical studies, RAF–MEK complexes stabilized by G-573 and G-530 were lost upon introduction of a S212P mutation in MEK (Fig. 3d). Additionally, the relative potencies of PD-901 and G-530 in KRAS versus BRAF-mutant cells track with those of GDC-0973 and GDC-0623/G-573, respectively (Supplementary Fig. 11). These data support the conclusion that a strong hydrogen bond between MEK inhibitors and S212 is important for stabilizing a RAF–MEK complex and blocking RAF-mediated MEK phosphorylation in KRAS-mutant cells.

Interestingly, the clinical MEK inhibitor AZD6244, which has an N rather than a F at the S212-interacting site, was previously reported to have lower potency in a panel of oncogenic KRAS mutant cell lines (KRAS^{MT}) versus BRAF(V600E) cells and to allow the induction of pMEK in KRAS^{MT} cells^{9,15}. Despite the presence of an N at this position, AZD6244 is predicted to form a weaker hydrogen bond with S212 compared to GDC-0623 due to a longer hydrogen-bond distance from the S212 backbone NH (Supplementary Fig. 12). This leads us to refine our model by concluding that it is the strength of the inhibitor–MEK S212 interaction, rather than the exact identity of the atom interacting with MEK that is critical for the ability of MEK inhibitors to block pMEK induction and show strong potency in KRAS-mutant cells.

Importantly, whereas GDC-0973 showed reduced efficacy in KRAS-mutant *in vivo* models compared to GDC-0623 and G-573, the reverse was found in BRAF(V600E) mutant models (Fig. 4a). In BRAF(V600E) xenografts, GDC-0973 showed the greatest efficacy at its MTD, with an increased rate of regressions. Because the rank order of compounds in efficacy studies was reversed in KRAS versus BRAF-mutant models, pharmacokinetic differences between the molecules do not account for these differences.

Given that BRAF(V600E) tumour models have high basal levels of pMEK¹⁶ (Supplementary Fig. 13a), we proposed that GDC-0973 may have a higher binding affinity for activated pMEK, and thus greater efficacy in BRAF(V600E) cells compared to MEK inhibitors that preferentially bind to the inactive form of MEK^{13,21}. To test this directly, we generated a phosphomimetic construct encoding constitutively active MEK(S218D S222D) (thereafter MEK-DD). In fluorescence polarization assays GDC-0623 and G-573 bound tenfold less strongly to MEK-DD than wild-type MEK, whereas GDC-0973 bound equivalently to both forms (Fig. 4b). We proposed that the reduction in binding affinity for GDC-0623 and G-573 against MEK-DD might be due to the weakening of their hydrogen-bond interaction with S212 as a result of increased dynamics of the A-loop and α -C helix in the MEK-DD conformation²². To test this, we introduced an additional mutation, E114D, to the MEK-DD protein, predicted to further increase A-loop/ α -C helix dynamics and further weaken the S212 interaction with inhibitors. As predicted, GDC-0623 and G-573 lost substantial binding affinity against MEK-DD(E114D), whereas GDC-0973 was minimally affected. We attribute the strong binding of GDC-0973 to the additional interactions it makes with the nucleotide and with residues within the MEK HRD motif of the catalytic loop (Fig. 4c;

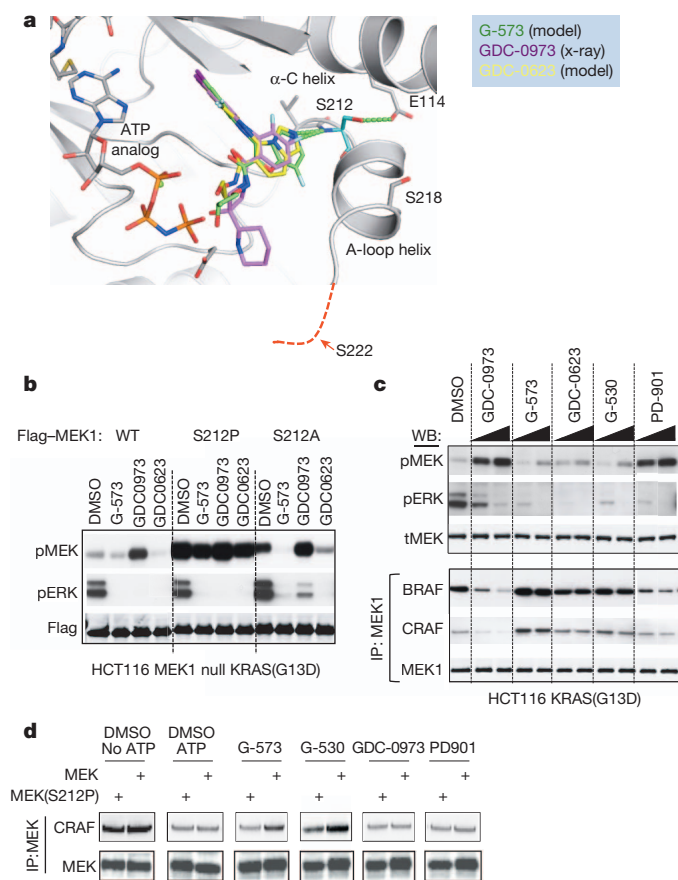
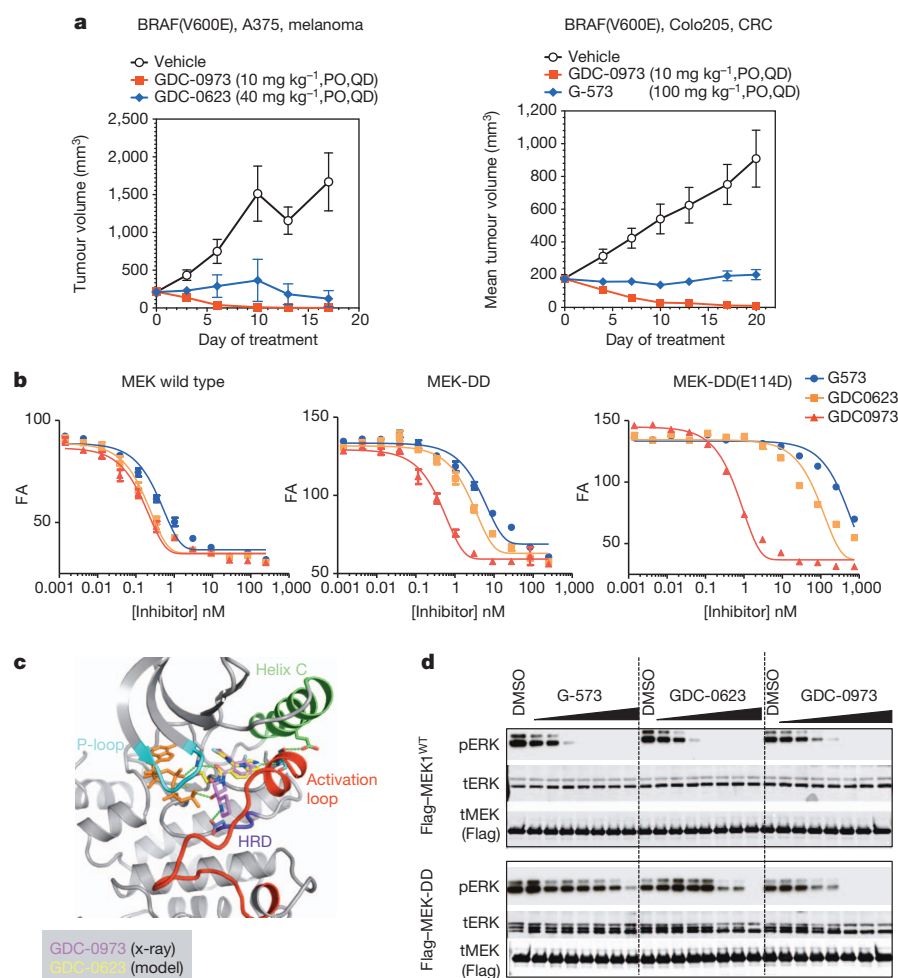


Figure 3 | Distinct inhibitor interactions with MEK determine their individual effects on RAF–MEK complex formation, MEK activation and inhibition of ERK phosphorylation. **a**, MEK1 crystal structure of GDC-0973 (magenta) with models of GDC-0623 (yellow) and G-573 (green) show key hydrogen-bond interactions of inhibitors with S212 on the MEK activation segment. S222 is shown in its approximate location based on modelled conformations. **b**, WB of lysates from HCT116 MEK1 null cells transiently transfected with wild-type MEK1 (WT), S212P or S212A mutant MEK1 and treated with 1 μ M of the indicated MEK inhibitors for 24 h. **c**, Upper panel, WB of HCT116 (KRAS(G13D)) cells treated for 24 h with the indicated MEK inhibitors (0.1, 1 μ M); lower panel, IP/WB of endogenous MEK1 from lysates of HCT116 (KRAS(G13D)) cells treated overnight with DMSO or indicated inhibitors. **d**, Recombinant protein pull-down assays using wild-type or S212P MEK after incubation with recombinant CRAF in the presence or absence of ATP (100 μ M) and the indicated inhibitors.

Figure 4 | Potency of MEK inhibitors in BRAF-mutant versus KRAS-mutant tumours correlates with high inhibitor binding affinity against dually phosphorylated MEK (S218/S222) compared to un-phosphorylated MEK.

a, Antitumour efficacy of GDC-0973 in A375 and Colo205 xenograft models, GDC-0623 in A375 ($n = 5$ per group) or G-573 in Colo205 ($n = 10$ per group). In A375, GDC-0973 treatment led to 127% TGI, with 3 PR, 2 CR; GDC-0623 treatment led to 102% TGI with 3 PR, 0 CR. In Colo-205, GDC-0973 treatment led to 141% TGI with 4 PR, 6 CR; G-573 treatment led to 109% TGI with 3 PR, 0 CR. Group mean is plotted with error bars representing standard error of mean (SEM). CRC, colorectal cancer. **b**, Binding curves of GDC-0973, GDC-0623 and G-573 against MEK1^{WT}, MEK-DD and MEK-DD(E114D) using fluorescence anisotropy (FA). K_i (nM) for inhibitor are GDC-0973: 0.05, 0.18, 0.48; GDC-0623: 0.13, 1.33, ~62.0; G-573: 0.30, 3.53, ~284.0 for the MEK WT, MEKDD and MEK-DD(E114D) constructs, respectively. **c**, MEK1 crystal structure of GDC-0973 (magenta) with a model of GDC-0623 (yellow) showing GDC-0973 reaching towards the HRD motif in the catalytic loop of MEK1. **d**, WB of 293-T cells transfected with either vector, Flag-MEK1^{WT} or Flag-MEK-DD and treated for 24 h with the indicated inhibitors (range: 0.01–10 μ M in threefold increments).



Supplementary Fig. 10)²³, and suggest that GDC-0973 is less affected by A-loop/ α -C helix dynamics such as occurs during MEK activation.

To confirm these findings in cells, we transfected wild-type MEK or MEK-DD into cells (note: MEK-DD(E114D) is catalytically dead and thus not used) and assessed the ability of the inhibitors to prevent phosphorylation of ERK (Fig. 4d). Consistent with the binding studies, we found that GDC-0623 and G-573, but not GDC-0973, lost potency against MEK-DD.

We proposed that the strong binding of GDC-0973 to activated MEK might also explain its variable potency in KRAS-mutant cell lines. Comparison of pMEK levels in KRAS^{MT} lines that were sensitive versus resistant to GDC-0973 (Fig. 1a) demonstrated that the most sensitive lines had high basal pMEK and pERK levels comparable to those in the A375 BRAF(V600E) line (Supplementary Fig. 13). Therefore, cells with high levels of activated MEK are sensitive to GDC-0973 even in the KRAS genotype.

In conclusion, our study elucidates the mechanisms of distinct classes of allosteric MEK inhibitors that control their efficacy in KRAS versus BRAF-mutant tumours. We demonstrate that MEK inhibitors that form a strong hydrogen bond to S212 prevent phosphorylation of MEK by RAF and stabilize a RAF–MEK complex, leading to greater efficacy in KRAS-mutant tumours. Why this interaction is needed for strong inhibition of MEK activity downstream of WT RAF is not entirely understood. Other MEK inhibitors have been shown to inhibit RAF phosphorylation of MEK^{13,24}, although the mechanism had not previously been elucidated. Furthermore, whereas the interaction of MEK inhibitors with S212 has been previously observed^{18,25}, our study is the first to link directly the strength of this interaction to the prevention of RAF-mediated MEK activation and increased potency in KRAS-mutant cells.

In the context of BRAF(V600E) mutant tumours, we discovered that the superior efficacy of GDC-0973 against BRAF-mutant tumour models correlates with its potent binding and inhibition of activated MEK. Because of the high basal activity of MEK in BRAF(V600E) mutant tumours, this results in increased efficacy in this genetic background. Our data are consistent with previous studies demonstrating that MEK is activated differently by oncogenic BRAF(V600E) compared to wild-type BRAF and CRAF in tumours with oncogenic KRAS^{26,27}. We demonstrate that these differences can be exploited by targeting MEK inhibitors against distinct activated states of MEK, leading to increased efficacy in BRAF or KRAS-mutant preclinical models.

With respect to the implications of these findings for the clinic, our studies were carried out with clinically relevant doses. Importantly, GDC-0973 has already shown strong clinical efficacy in BRAF(V600E) melanoma patients, with partial responses observed in 7/12 melanoma patients treated at MTD where 6 of the 7 responders had BRAF(V600E) mutations (Rosen, L. *et al.*, unpublished data)²⁸. Clinical trials with GDC-0973 and GDC-0623 will assess whether the observed differences in mechanism of action translate to differential therapeutic benefit for cancer patients.

METHODS SUMMARY

GDC-0973 and G-573 were synthesized at Genentech and have been described previously^{23,29}. GDC-0623 and G-530 were synthesized according to the procedure in patent number US7803839 (2010). PD0325901 (PD901) was purchased from Active Biochem. Cells were obtained from the Genentech cell line repository and were cultured according to ATCC specifications. The establishment of MiaPaCa, H2122, A375 and Colo 205 xenografts is described in detail in Methods in the Supplementary Information. Kinase reactions, immunoprecipitations and western

blots were conducted as described previously¹⁹. The binding studies of MEK1 to small-molecule inhibitors were performed by competitive fluorescence polarization and described in Methods in the Supplementary Information. MEK1 purification and crystallization conditions are described in Methods in the Supplementary Information. Structure determination, refinement and modelling are described in Methods in the Supplementary Information and Supplementary Table 2.

Received 28 December 2012; accepted 10 July 2013.

Published online 11 August 2013.

- Akinleye, A., Furqan, M., Mukhi, N., Ravella, P. & Liu, D. MEK and the inhibitors: from bench to bedside. *J. Hematol. Oncol.* **6**, 27 (2013).
- Blasco, R. B. *et al.* c-Raf, but not B-Raf, is essential for development of *K-Ras* oncogene-driven non-small cell lung carcinoma. *Cancer Cell* **19**, 652–663 (2011).
- Davies, H. *et al.* Mutations of the *BRAF* gene in human cancer. *Nature* **417**, 949–954 (2002).
- Downward, J. Targeting RAS signalling pathways in cancer therapy. *Nature Rev. Cancer* **3**, 11–22 (2003).
- Bamford, S. *et al.* The COSMIC (Catalogue of Somatic Mutations in Cancer) database and website. *Br. J. Cancer* **91**, 355–358 (2004).
- Hatzivassiliou, G. *et al.* RAF inhibitors prime wild-type RAF to activate the MAPK pathway and enhance growth. *Nature* **464**, 431–435 (2010).
- Heidorn, S. J. *et al.* Kinase-dead BRAF and oncogenic RAS cooperate to drive tumor progression through CRAF. *Cell* **140**, 209–221 (2010).
- Poulikakos, P. I., Zhang, C., Bollag, G., Shokat, K. M. & Rosen, N. RAF inhibitors transactivate RAF dimers and ERK signalling in cells with wild-type BRAF. *Nature* **464**, 427–430 (2010).
- Solit, D. B. *et al.* BRAF mutation predicts sensitivity to MEK inhibition. *Nature* **439**, 358–362 (2006).
- Wellbrock, C., Karasarides, M. & Marais, R. The RAF proteins take centre stage. *Nature Rev. Mol. Cell Biol.* **5**, 875–885 (2004).
- Chapman, M. S. & Miner, J. N. Novel mitogen-activated protein kinase kinase inhibitors. *Expert Opin. Investig. Drugs* **20**, 209–220 (2011).
- Engelman, J. A. *et al.* Effective use of PI3K and MEK inhibitors to treat mutant *Kras* G12D and *PIK3CA* H1047R murine lung cancers. *Nature Med.* **14**, 1351–1356 (2008).
- Gilmartin, A. G. *et al.* GSK1120212 (JTP-74057) is an inhibitor of MEK activity and activation with favorable pharmacokinetic properties for sustained *in vivo* pathway inhibition. *Clin. Cancer Res.* **17**, 989–1000 (2011).
- Hoeflich, K. P. *et al.* Intermittent administration of MEK inhibitor GDC-0973 plus PI3K inhibitor GDC-0941 triggers robust apoptosis and tumor growth inhibition. *Cancer Res.* **72**, 210–219 (2012).
- Friday, B. B. *et al.* BRAF V600E disrupts AZD6244-induced abrogation of negative feedback pathways between extracellular signal-regulated kinase and Raf proteins. *Cancer Res.* **68**, 6145–6153 (2008).
- Pratils, C. A. *et al.* V600E BRAF is associated with disabled feedback inhibition of RAF–MEK signaling and elevated transcriptional output of the pathway. *Proc. Natl Acad. Sci. USA* **106**, 4519–4524 (2009).
- Delaney, A. M., Printen, J. A., Chen, H., Fauman, E. B. & Dudley, D. T. Identification of a novel mitogen-activated protein kinase kinase activation domain recognized by the inhibitor PD 184352. *Mol. Cell. Biol.* **22**, 7593–7602 (2002).
- Heald, R. A. *et al.* Discovery of novel allosteric mitogen-activated protein kinase kinase (MEK) 1,2 inhibitors possessing bidentate Ser212 interactions. *J. Med. Chem.* **55**, 4594–4604 (2012).
- O'Hagan, D. Understanding organofluorine chemistry. An introduction to the C–F bond. *Chem. Soc. Rev.* **37**, 308–319 (2008).
- Gopalbhai, K. *et al.* Negative regulation of MAPKK by phosphorylation of a conserved serine residue equivalent to Ser212 of MEK1. *J. Biol. Chem.* **278**, 8118–8125 (2003).
- Sheth, P. R. *et al.* Fully activated MEK1 exhibits compromised affinity for binding of allosteric inhibitors U0126 and PD0325901. *Biochemistry* **50**, 7964–7976 (2011).
- Resing, K. A. & Ahn, N. G. Deuterium exchange mass spectrometry as a probe of protein kinase activation. Analysis of wild-type and constitutively active mutants of MAP kinase kinase-1. *Biochemistry* **37**, 463–475 (1998).
- Rice, K. D. *et al.* Novel carboxamide-based allosteric MEK inhibitors: discovery and optimization efforts toward XL518 (GDC-0973). *ACS Med. Chem. Lett.* **3**, 416–421 (2012).
- Alessi, D. R., Cuenda, A., Cohen, P., Dudley, D. T. & Saltiel, A. R. PD 098059 is a specific inhibitor of the activation of mitogen-activated protein kinase kinase *in vitro* and *in vivo*. *J. Biol. Chem.* **270**, 27489–27494 (1995).
- Ohren, J. F. *et al.* Structures of human MAP kinase kinase 1 (MEK1) and MEK2 describe novel noncompetitive kinase inhibition. *Nature Struct. Mol. Biol.* **11**, 1192–1197 (2004).
- Garnett, M. J., Rana, S., Paterson, H., Barford, D. & Marais, R. Wild-type and mutant B-RAF activate C-RAF through distinct mechanisms involving heterodimerization. *Mol. Cell* **20**, 963–969 (2005).
- Röring, M. *et al.* Distinct requirement for an intact dimer interface in wild-type, V600E and kinase-dead B-Raf signalling. *EMBO J.* **31**, 2629–2647 (2012).
- Rosen, L. *et al.* A first-in-human phase 1 study to evaluate the MEK1/2 inhibitor GDC-0973 administered daily in patients with advanced solid tumors. *Cancer Res.* **71**, 4716 (2011).
- Choo, E. F. *et al.* Preclinical disposition and pharmacokinetics-pharmacodynamic modeling of biomarker response and tumour growth inhibition in xenograft mouse models of G-573, a MEK inhibitor. *Xenobiotica* **40**, 751–762 (2010).

Supplementary Information is available in the online version of the paper.

Acknowledgements The authors would like to acknowledge the Genentech IVCC group, IVP dosing group, as well as B. Liu and I. Yen and for technical support. SSRL is supported by the Department of Energy, the National Institutes of Health, the National Institute of General Medical Sciences and the National Center for Research Resources.

Author Contributions J.R.H., K.S., S.-M.L., J.C., A.P., C.O. J.F.M.H., D.J.A., M.J.C.L., M.Z. and M.U. performed the experiments; M.M., S.P., R.H., C.W., M.Z. and K.P.H. analysed data; L.S.F. provided comments; G.H., J.R.H., H.C., S.M. and M.B. directed the studies, analysed data, and wrote the manuscript.

Author Information The structure of the MEK1:GDC-0973 complex has been deposited with the PDB and assigned accession code 4LMN. Reprints and permissions information is available at www.nature.com/reprints. Readers are welcome to comment on the online version of the paper. Correspondence and requests for materials should be addressed to M.B. (belvin.marcia@gene.com) or G.H. (hatzivassiliou.georgia@gene.com).

Completion of the entire hepatitis C virus life cycle in genetically humanized mice

Marcus Dorner^{1†}, Joshua A. Horwitz^{1*}, Bridget M. Donovan^{1*}, Rachael N. Labitt¹, William C. Budell¹, Tamar Friling¹, Alexander Vogt¹, Maria Teresa Catanese¹, Takashi Satoh², Taro Kawai², Shizuo Akira², Mansun Law³, Charles M. Rice¹ & Alexander Ploss^{1†}

More than 130 million people worldwide chronically infected with hepatitis C virus (HCV) are at risk of developing severe liver disease. Antiviral treatments are only partially effective against HCV infection, and a vaccine is not available. Development of more efficient therapies has been hampered by the lack of a small animal model. Building on the observation that CD81 and occludin (OCLN) comprise the minimal set of human factors required to render mouse cells permissive to HCV entry¹, we previously showed that transient expression of these two human genes is sufficient to allow viral uptake into fully immunocompetent inbred mice². Here we demonstrate that transgenic mice stably expressing human CD81 and OCLN also support HCV entry, but innate and adaptive immune responses restrict HCV infection *in vivo*. Blunting antiviral immunity in genetically humanized mice infected with HCV results in measurable viraemia over several weeks. In mice lacking the essential cellular co-factor cyclophilin A (CypA), HCV RNA replication is markedly diminished, providing genetic evidence that this process is faithfully recapitulated. Using a cell-based fluorescent reporter activated by the NS3-4A protease we visualize HCV infection in single hepatocytes *in vivo*. Persistently infected mice produce *de novo* infectious particles, which can be inhibited with directly acting antiviral drug treatment, thereby providing evidence for the completion of the entire HCV life cycle in inbred mice. This genetically humanized mouse model opens new opportunities to dissect genetically HCV infection *in vivo* and provides an important preclinical platform for testing and prioritizing drug candidates and may also have utility for evaluating vaccine efficacy.

The narrow species tropism of HCV is incompletely understood. Mouse cells do not support viral entry and inefficiently replicate HCV RNA, but do support virion assembly and release. HCV uses numerous cellular factors to enter hepatocytes in a coordinated multistep process, including glycosaminoglycans³, low-density lipoprotein receptor⁴, scavenger receptor class B type I (SCARB1)⁵, the tetraspanin CD81 (ref. 6), the tight junction proteins claudin 1 (CLDN1)⁷ and occludin (OCLN)^{1,8}, the receptor tyrosine kinases epidermal growth factor receptor⁹ and ephrin receptor A2 (ref. 9), and the cholesterol uptake receptor Niemann–Pick C1 like 1 (ref. 10). Of these, CD81 and OCLN comprise the minimal human factors needed for HCV uptake into rodent cells¹.

We recently demonstrated that adenoviral delivery of HCV entry factors renders mice susceptible to HCV infection². This transient approach is high-throughput and allows the possibility of rapidly evaluating mutant versions of HCV entry factors. However, adenoviral gene delivery strongly induces interferon-stimulated genes, creating an environment that may antagonize HCV replication. To limit variability and to prevent vector-mediated immune activation, we generated transgenic mice stably expressing human CD81, SCARB1, CLDN1 and/or OCLN under the control of a liver-specific albumin promoter.

Transgenic expression of the human orthologues of the HCV entry factors resulted in similar mRNA levels of the human and endogenous mouse genes in the murine liver (Supplementary Fig. 1) and expression of all four proteins (Supplementary Fig. 2) with the expected subcellular distribution in the liver (Supplementary Fig. 3). Next, we aimed to test the susceptibility of entry factor transgenic (EFT) mice to HCV infection. To identify founder lines supporting viral entry we took advantage of a previously generated, highly sensitive detection system which is based on the activation of a *loxP*-flanked STOP-luciferase reporter in the genome of ROSA26-Fluc mice by Cre recombinase encoded in recombinant HCV genomes². We crossed EFT mice to a ROSA26-Fluc background and challenged these animals with a bicistronic HCV genome expressing Cre (HCV-Cre). Consistent with previous data², the bioluminescent reporter was activated in mice expressing human CD81 and OCLN (Fig. 1a and Supplementary Fig. 4a). The addition of human SCARB1 and CLDN1 (Supplementary Fig. 4b) did not increase the entry signal, demonstrating that their murine orthologues are functional for HCV entry *in vivo*. For subsequent experiments, founder lines Alb-hCD81/hOCLN#941 (2hEF) and Alb-hCD81/hSCARB1/hCLDN1/hOCLN#100 (4hEF), which supported the most efficient viral uptake (Supplementary Fig. 4a), were used. To estimate the number of HCV-infected liver cells, we used an indicator mouse strain in which Cre leads to activation of a nuclear-localized green fluorescent protein/ β -galactosidase (GNZ) reporter (ROSA26-GNZ)¹¹. Similar to our previous observations², HCV-Cre infection resulted in reporter activation in approximately 1–1.5% of murine hepatocytes in 2hEF or 4hEF mice (Fig. 1b and Supplementary Fig. 5). To provide additional evidence that viral uptake into EFT mice is mediated by the specific interaction of HCV glycoproteins with host entry factors, we administered antibodies directed against the HCV envelope glycoprotein complex E1E2 or the host entry factor CD81. Delivery of anti-human CD81 or anti-E1E2 (AR4A; ref. 12) antibodies resulted in a dose-dependent inhibition of HCV-Cre infection (Fig. 1c), whereas isotype control immunoglobulins had no effect. These data further affirm that HCV is taken up in a viral glycoprotein-specific fashion *in vivo* and underscore the utility of this model for evaluation of passive immunization strategies.

Direct measurement of HCV genome levels by quantitative reverse transcription (qRT)–PCR demonstrated a slight increase in HCV RNA in the serum (at 4 h) and liver (at 3 h and 24 h) of inoculated mice expressing the human entry factors; at 72 h, however, the signal was reduced to background levels (Fig. 1d, e). HCV infection resulted in the upregulation of several interferon-stimulated genes (Fig. 1f, g and Supplementary Fig. 6), infiltration of immune cells, especially natural killer (NK) cells, into the liver (Fig. 1i), and elevated proinflammatory cytokine levels in the serum (Fig. 1h and Supplementary Fig. 7), which could antagonize HCV replication. This hypothesis is further supported by the previous observation that HCV replicons,

¹Center for the Study of Hepatitis C, The Rockefeller University, New York, New York 10065, USA. ²Laboratory of Host Defense, WPI Immunology Frontier Research Center, Osaka University, 3-1 Yamada-oka, Suita, Osaka 565-0871, Japan. ³Department of Immunology and Microbial Science, The Scripps Research Institute, La Jolla, California 92037, USA. [†]Present addresses: Imperial College London, Department of Medicine, London W2 1NY, UK (M.D.); Department of Molecular Biology, Princeton University, Princeton, New Jersey 08544, USA (A.P.).

*These authors contributed equally to this work.

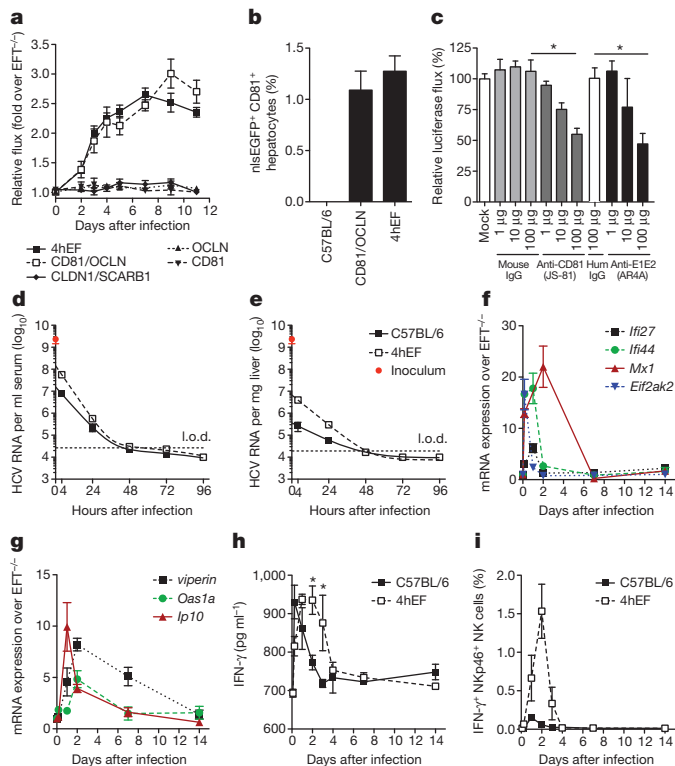
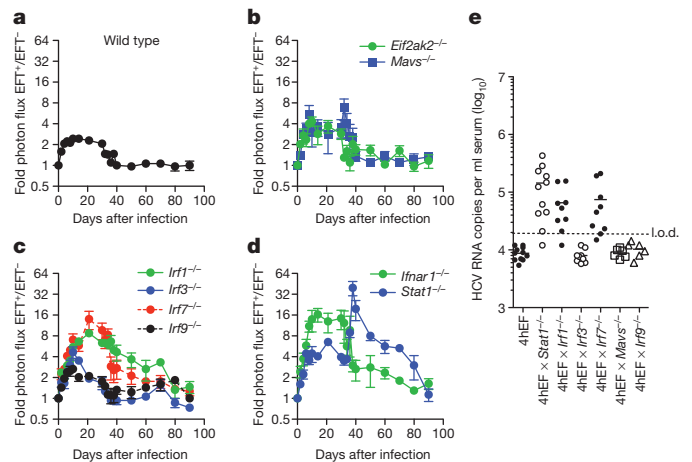


Figure 1 | Transgenic expression of human CD81 and OCLN renders mice permissive to HCV entry. **a**, Longitudinal bioluminescence imaging of ROSA26-Fluc mice expressing either human CD81 plus OCLN, SCARB1 plus CLDN1, CD81 alone, OCLN alone, or all four HCV entry factors (4hEF). **b**, Quantification of viral uptake into murine hepatocytes expressing human CD81 and OCLN or all four human entry factors determined by flow cytometry 72 h after infection with BiCre-Jc1. **c**, Blocking of HCV infection *in vivo* by either blocking antibodies against CD81 (JS-81) or neutralizing antibodies against HCV E1E2 (AR4A). ROSA26-Fluc 4hEF mice were injected with the indicated amounts of antibodies 24 h and 4 h before infection with BiCre-Jc1. **d, e**, Longitudinal quantification of HCV RNA by RT-qPCR in (d) serum and (e) liver of either wild-type or mice expressing all four HCV entry factors; dotted lines indicate the limit of detection (l.o.d.). **f, g**, Expression of the interferon-stimulated genes *Irf1*, *Irf3*, *Irf7*, *Irf9*, *Stat1* (f) and *viperin* (also known as *Rsd2*), *Oas1a* and *Ip10* (g) in the liver after infection with BiCre-Jc1 in wild-type or 4hEF mice. **h**, Serum levels of IFN- γ in wild-type or 4hEF mice infected with BiCre-Jc1. **i**, Analysis of liver-infiltrating IFN- γ -secreting NKp46-positive NK cells in BiCre-Jc1-infected wild-type or 4hEF mice. All data shown are mean \pm s.d. of four independent experiments. For panels e–g, four mice were used per time point. * $P < 0.05$.

selectable HCV RNA genomes, replicate more efficiently in murine cells with impaired antiviral signalling^{13,14}.

To identify a murine environment more conducive to HCV replication we crossed 4hEF ROSA26-Fluc mice to strains carrying targeted disruptions in *Eif2ak2*, *Mavs*, *Irf1*, *Irf3*, *Irf7*, *Irf9*, *Stat1* or the *Ifn- α* receptor (Fig. 2). These strains are viable and known to be hypersusceptible to RNA viruses, due to impaired innate immune responses. The luminescent reporter signal was slightly elevated during the early phase after infection with HCV-Cre in most EFT strains impaired in antiviral signalling as compared to EFT mice on a wild-type background (Fig. 2a–d). Between 20 and 40 days after infection there was a marked increase in the luciferase signal, particularly in IRF1 (eightfold), IRF7 (16-fold) (Fig. 2c), IFN- α receptor (20-fold) and STAT1 (40-fold) deficient mice (Fig. 2d) compared to non-transgenic littermate controls. The increased reporter signal, which presumably reflects a transient burst in viral replication and spread, eventually returned to background levels, possibly marking clearance of HCV-infected cells by the murine immune system. The elevated luminescent signal correlated with increases in serum HCV RNA levels at peak time points (Fig. 2e).



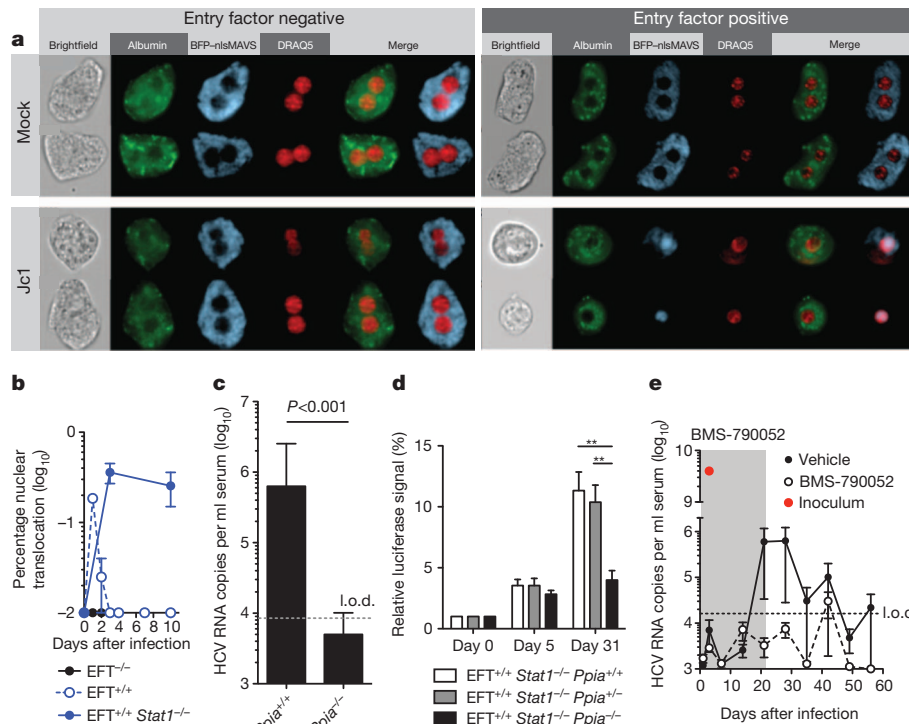


Figure 3 | Visualization and genetic and pharmacological interference with HCV infection. **a, b**, Quantification of murine hepatocytes actively replicating HCV in wild-type, 4hEF and 4hEF Stat1^{-/-} mice as measured by the HCV NS3-4a-dependent cleavage of the TagBFP-nlsMAVS transgenic reporter construct by ImageStream X analysis. **c–e**, Longitudinal HCV RNA levels and

luciferase signal in 4hEF Stat1^{-/-} mice lacking PPIA (**c, d**), and longitudinal HCV RNA levels in 4hEF Stat1^{-/-} mice treated with an HCV NS5A inhibitor (BMS-790052) for 20 days (**e**). Data shown are mean \pm s.d. of $n = 10$ –18 mice from two independent experiments. $**P < 0.01$.

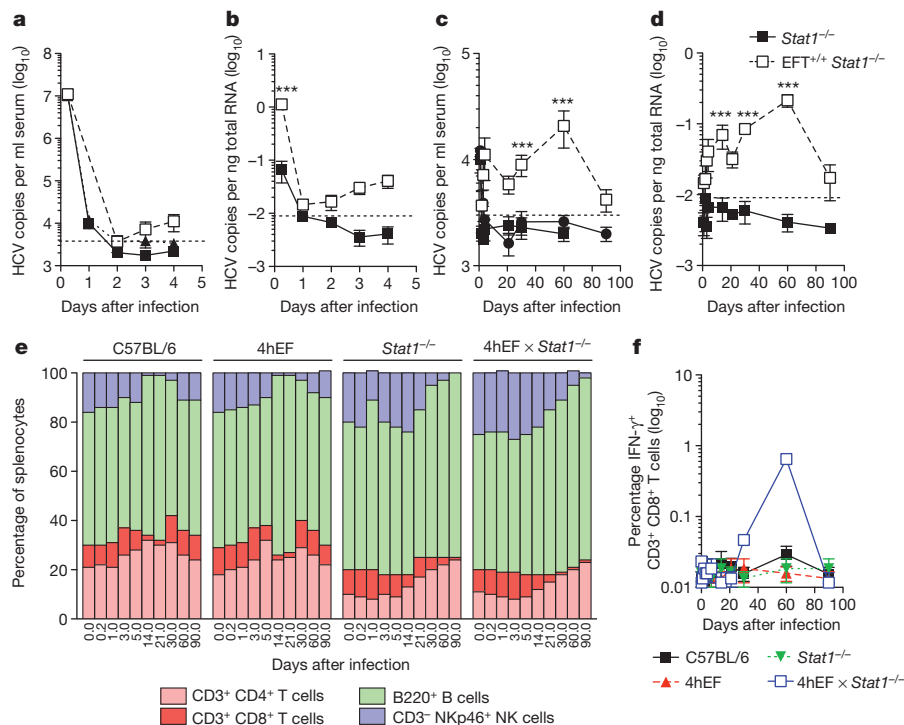


Figure 4 | HCV infection in 4hEF Stat1^{-/-} mice leads to immune activation. **a–d**, HCV RNA copies in serum (**a, c**) and liver (**b, d**) of 4hEF Stat1^{-/-} mice during early (**a, b**) or late (**c, d**) infection with Con1/Jc1. **e**, Relative frequencies of the indicated lymphocyte subsets in spleens of wild-type, 4hEF, Stat1^{-/-} or Stat1^{-/-} 4hEF mice isolated at the indicated time

points after infection with Con1/Jc1. **f**, Analysis of liver-infiltrating IFN- γ -producing CD3⁺CD8⁺ T cells of wild-type, 4hEF, Stat1^{-/-} and 4hEF Stat1^{-/-} mice after infection with Con1/Jc1. Data shown are mean \pm s.d. of three independent experiments. $***P < 0.001$.

in STAT1 sufficient mice, the signal persisted at least until day 10 in mice on a *Stat1*^{-/-} background (Fig. 3b). Taken together, these results indicate that HCV can replicate in immunocompromised mice expressing human CD81 and OCLN and highlight the value of the model for studying HCV replication *in vivo*.

We further characterized viral kinetics in mice infected with a monoclonal cell-culture-derived HCV (HCVcc). HCV RNA rose approximately tenfold over the limit of quantification in serum (Fig. 4a, c) and liver (Fig. 4b, d) of EFT *Stat1*^{-/-} mice as compared to non-transgenic *Stat1*^{-/-} controls. Mice remained persistently infected for most of the observation period, with HCV RNA becoming nearly undetectable after 90 days (Fig. 4c, d). Sequence analysis of HCV RNA detected at late time points in mice infected with HCV-Cre revealed mutations in some viral genomes, but none was shared among the five mice that were analysed (Supplementary Fig. 12). Whether any of these are adaptive mutations that increase viral fitness *in vivo* will be the subject of future studies. HCV infection caused splenomegaly in some innate immune-deficient mice expressing HCV entry factors, but not in non-EFT mice (Supplementary Fig. 10a), indicative of HCV-specific immune activation. Indeed we observed increased frequencies of NK cells and subsequently B cells in the spleens of 4hEF *Stat1*^{-/-} mice in the early and late phases of infection, respectively (Fig. 4e and Supplementary Fig. 10b). Consistent with results in humans and chimpanzees, primarily NK and IFN- γ -producing CD8⁺ T cells (Fig. 4f) infiltrated the livers of 4hEF *Stat1*^{-/-} mice with a skewing towards an effector memory phenotype near the end of the time course (Supplementary Fig. 10c). These data indicate that HCV infection elicits cellular immune responses, albeit potentially confounded by the STAT1 deficiency, which may contribute to eventual viral clearance.

To determine whether primary hepatocytes in EFT mice on immunodeficient backgrounds were capable of producing infectious virions, sera collected at day 40 after infection were used to inoculate naive Huh-7.5 cells. Infectious virus was detected in sera of 4hEF mice deficient for STAT1, IRF1 and IRF7 (Fig. 5a), consistent with the increased levels of luminescent reporter activity (Fig. 2c, d) and HCV RNA load (Fig. 2e) in these strains. In HCV-infected 4hEF *Stat1*^{-/-} mice titres reached approximately 100 tissue culture infectious dose 50 (TCID₅₀) per ml (Fig. 5b). Sera from HCV-infected non-EFT littermates, or directly acting antiviral (DAA)-treated 4hEF *Stat1*^{-/-} or 4hEF *Stat1*^{-/-} *Ppia*^{-/-} mice collected at the same time points, did not yield NS5A-positive cells (data not shown), indicating *de novo* virus production rather than

carry-over of the inoculum. To demonstrate that the lack of HCV NS5A-positive cells in the infectivity assay cannot simply be attributed to residual quantities of the DAA in circulation, we spiked the sera from the BMS-790052-treated animals with tissue-culture-produced BiCre-Jc1 virus (Fig. 5b) and found no inhibitory effect. Furthermore, in Huh-7.5 cells expressing an TagRFP-nlsMAVS reporter¹⁶, infection with sera from infected mice resulted in re-localization of the reporter signal whereas inoculation with sera from non-infected, DAA-treated or *Ppia*^{-/-} mice did not (Supplementary Fig. 11). These data are in accordance with previous *in vitro* observations demonstrating that mouse hepatoma cells support late stages of the HCV life cycle¹⁷.

This study represents an important step forward in developing an animal model for HCV infection and immunity. To our knowledge this is the first time that the entire HCV life cycle has been recapitulated in inbred mice with inheritable susceptibility to HCV. Previously developed xenotransplant mouse models can also be infected with HCV. However, these models are hampered by intra- and inter-experimental variability, donor-to-donor variability, low throughput, and high costs. The inbred mouse model presented here can overcome many of these challenges, is amenable to genetic manipulations and can be used for preclinical assessment of the efficacy of antiviral drug candidates and entry inhibitors. To study unperturbed HCV-specific immune responses and HCV-associated pathogenesis it will be necessary to establish persistent HCV infection in fully immunocompetent mice. By harnessing the remarkable genetic plasticity of HCV it may be possible to select for viral variants that replicate more robustly in sufficiently immunocompromised rodent strains. High titre sera could subsequently be passaged through progressively more immunocompetent hosts to produce this outcome. Future studies will address the capacity of different, genetically diverse HCV genotypes to establish chronicity in genetically humanized mice.

METHODS SUMMARY

Mice. Construction of all mice expressing HCV entry factors under the control of a liver-specific albumin promoter or CAGGS-TagBFP-nlsMAVS and the source of all other mouse mutant strains is described in the Methods. Mice were bred and maintained at the Comparative Bioscience Center of The Rockefeller University according to guidelines established by the Institutional Animal Committee.

Hepatitis C virus. Plasmids encoding chimaeric HCV genomes, including Jc1, Con1-Jc1 and bicistronic HCV genomes expressing Cre, were linearized with XbaI and *in vitro* transcribed. RNA was electroporated into Huh-7.5 cells and infectious virus was collected from supernatants 48–72 h after transfection¹⁸.

RT-PCR quantification of HCV RNA. Total RNA was isolated from mouse brain, liver and sera using the RNeasy kit (Qiagen). HCV genome copy number was quantified by one-step RT-PCR.

Full Methods and any associated references are available in the online version of the paper.

Received 2 November 2012; accepted 2 July 2013.

Published online 31 July 2013.

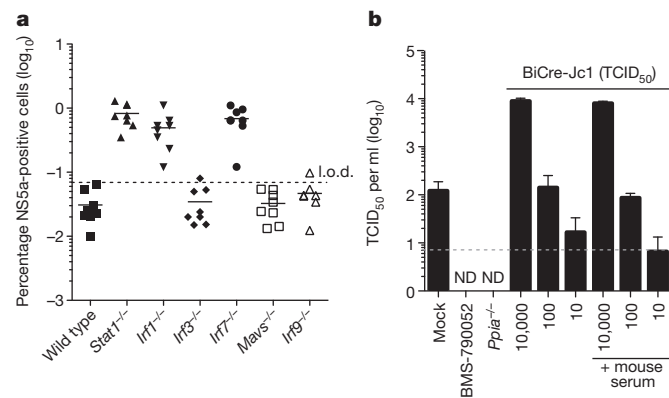


Figure 5 | Evidence for production of infectious particles. **a**, *Stat1*^{-/-}, *Irf1*^{-/-}, *Irf3*^{-/-}, *Irf7*^{-/-}, *Irf9*^{-/-} and *Mavs*^{-/-} mice expressing all four human HCV entry factors were infected with BiCre-Jc1. Sera were collected 6 weeks after infection and were used to infect naive Huh-7.5 cells. NS5A staining was performed 72 h after infection and the frequency of HCV antigen-bearing cells quantified by flow cytometry. **b**, HCV infectious particles released into the serum of 4hEF *Stat1*^{-/-} mice, 4hEF *Stat1*^{-/-} mice lacking PPIA or 4hEF *Stat1*^{-/-} mice treated with BMS-790052 for 20 days as determined by limiting dilution assay. Data shown are mean \pm s.d. of four independent experiments. ND, not detectable.

- Ploss, A. *et al.* Human occludin is a hepatitis C virus entry factor required for infection of mouse cells. *Nature* **457**, 882–886 (2009).
- Dörner, M. *et al.* A genetically humanized mouse model for hepatitis C virus infection. *Nature* **474**, 208–211 (2011).
- Barth, H. *et al.* Cellular binding of hepatitis C virus envelope glycoprotein E2 requires cell surface heparan sulfate. *J. Biol. Chem.* **278**, 41003–41012 (2003).
- Agnello, V., Abel, G., Elfahal, M., Knight, G. B. & Zhang, Q.-X. Hepatitis C virus and other Flaviviridae viruses enter cells via low density lipoprotein receptor. *Proc. Natl Acad. Sci. USA* **96**, 12766–12771 (1999).
- Scarselli, E. *et al.* The human scavenger receptor class B type I is a novel candidate receptor for the hepatitis C virus. *EMBO J.* **21**, 5017–5025 (2002).
- Pileri, P. *et al.* Binding of hepatitis C virus to CD81. *Science* **282**, 938–941 (1998).
- Evans, M. J. *et al.* Claudin-1 is a hepatitis C virus co-receptor required for a late step in entry. *Nature* **446**, 801–805 (2007).
- Liu, S. *et al.* Tight junction proteins claudin-1 and occludin control hepatitis C virus entry and are downregulated during infection to prevent superinfection. *J. Virol.* **83**, 2011–2014 (2009).
- Lupberger, J. *et al.* EGFR and EphA2 are host factors for hepatitis C virus entry and possible targets for antiviral therapy. *Nature Med.* **17**, 589–595 (2011).
- Sainz, B. Jr *et al.* Identification of the Niemann-Pick C1-like 1 cholesterol absorption receptor as a new hepatitis C virus entry factor. *Nature Med.* **18**, 281–285 (2012).

11. Awatramani, R., Soriano, P., Mai, J. J. & Dymecki, S. An FLP indicator mouse expressing alkaline phosphatase from the *ROSA26* locus. *Nature Genet.* **29**, 257–259 (2001).
12. Giang, E. *et al.* Human broadly neutralizing antibodies to the envelope glycoprotein complex of hepatitis C virus. *Proc. Natl Acad. Sci. USA* **109**, 6205–6210 (2012).
13. Lin, L. T. *et al.* Replication of subgenomic hepatitis C virus replicons in mouse fibroblasts is facilitated by deletion of interferon regulatory factor 3 and expression of liver-specific microRNA 122. *J. Virol.* **84**, 9170–9180 (2010).
14. Chang, K. S. *et al.* Replication of hepatitis C virus (HCV) RNA in mouse embryonic fibroblasts: protein kinase R (PKR)-dependent and PKR-independent mechanisms for controlling HCV RNA replication and mediating interferon activities. *J. Virol.* **80**, 7364–7374 (2006).
15. Yang, F. *et al.* Cyclophilin A is an essential cofactor for hepatitis C virus infection and the principal mediator of cyclosporine resistance *in vitro*. *J. Virol.* **82**, 5269–5278 (2008).
16. Jones, C. T. *et al.* Real-time imaging of hepatitis C virus infection using a fluorescent cell-based reporter system. *Nature Biotechnol.* **28**, 167–171 (2010).
17. Long, G. *et al.* Mouse hepatic cells support assembly of infectious hepatitis C virus particles. *Gastroenterology* **141**, 1057–1066 (2011).
18. Lindenbach, B. D. *et al.* Complete replication of hepatitis C virus in cell culture. *Science* **309**, 623–626 (2005).

Supplementary Information is available in the online version of the paper.

Acknowledgements We thank J. Sable, E. Castillo, B. Flatley, S. Shirley, A. Webson and E. Giang for laboratory support. A. North and the Rockefeller University Bioimaging Core Facility, S. Mazel and the Rockefeller University Flowcytometry Core Facility,

C. Yang and the Gene Targeting Center and R. Tolwani and the staff of the Comparative Bioscience Center provided technical support. This study was supported in part by award number RC1DK087193 (to C.M.R. and A.P.) from the National Institute of Diabetes and Digestive and Kidney Diseases, R01AI072613, R01AI099284 (to C.M.R.), R01AI079031 (to M.L.) from the National Institute for Allergy and Infectious Disease, R01CA057973 (to C.M.R.) from the National Cancer Institute, The Starr Foundation, the Greenberg Medical Research Institute, the Richard Salomon Family Foundation, the Ronald A. Shellow, M.D. Memorial Fund, the MGM Mirage Voice Foundation, Gregory F. Lloyd Memorial contributions, and anonymous donors. M.D. was supported by a postdoctoral fellowship from the German Research Foundation (Deutsche Forschungsgesellschaft). M.T.C. is a recipient of The Rockefeller University Women & Science Fellowship. A.P. is a recipient of the Astella Young Investigator Award from the Infectious Disease Society of America and a Liver Scholar Award from the American Liver Foundation. The funding sources were not involved in the study design, collection, analysis and interpretation of data or in the writing of the report.

Author Contributions M.D. and J.A.H. planned and performed experiments and contributed to writing the manuscript. B.M.D., R.N.L., W.C.B., T.F., A.V. and M.T.C. performed the experimental work; T.K., T.S., S.A. and M.L. provided reagents. C.M.R. provided laboratory infrastructure, space, reagents, advice and edited the manuscript. A.P. planned and performed experiments and wrote the manuscript.

Author Information Reprints and permissions information is available at www.nature.com/reprints. The authors declare competing financial interests: details are available in the online version of the paper. Readers are welcome to comment on the online version of the paper. Correspondence and requests for materials should be addressed to A.P. (aploss@princeton.edu) or C.M.R. (ricec@rockefeller.edu).

METHODS

Animals and cell lines. Gt(ROSA)26Sor^{tm1(Luc)Kaelin} (ref. 19) (ROSA26-Fluc), B6;129-Gt(ROSA)26Sor^{tm1Joc}/J (ref. 20) (Rosa26-GNZ) and C57BL/6 (wild type) mice were obtained from The Jackson Laboratory. J. Colgan (University of Iowa) made the Ppia^{tm1Lubn} (Ppia^{-/-})²¹ mice available. ROSA26-Fluc mice contain the firefly luciferase (*luc*) gene inserted into the Gt(ROSA)26Sor locus. Expression of the luciferase gene is blocked by a *loxP*-flanked STOP fragment placed between the *luc* sequence and the Gt(ROSA)26Sor promoter. Cre-recombinase-mediated excision of the transcriptional stop cassette results in luciferase expression in Cre-expressing tissues. ROSA26-GNZ knock-in mice have widespread expression of a nuclear-localized green fluorescent protein- β -galactosidase fusion protein (nlsGFP-GNZ) once an upstream *loxP*-flanked STOP sequence is removed. When Cre recombinase is introduced into cells the resulting GNZ fusion protein expression allows for enhanced (single cell level) visualization. Mice were bred and maintained at the Comparative Bioscience Center of the Rockefeller University according to guidelines established by the Institutional Animal Committee. Huh-7.5 (ref. 22), Huh-7.5.1 (ref. 23) and Huh-7.5 stably expressing the TagRFP-nlsMAVS reporter¹⁶ were maintained in DMEM with 10% fetal bovine serum (FBS) and 1% nonessential amino acids (NEAA).

Mutant mice with targeted disruptions in genes involved in antiviral defences. Irf1^{tm1Mak} (Irf1^{-/-})²⁴ mice were obtained from the Jackson Laboratory. Ifnar1^{tm1Agt} (Ifnar1^{-/-})²⁵ from B&K Universal Ltd, and Stat1^{tm1Dlv} (Stat1^{-/-})²⁶ from Taconic. Bcl2l12/Irf3^{tm1Tg} (Irf3^{-/-})²⁷, Irf7^{tm1Tg} (Irf7^{-/-})²⁸ and Irf9^{tm1Tg} (Irf9^{-/-})²⁹ mice were provided by T. Taniguchi. T. Satoh and S. Akira provided Dlx58^{tm1(A30K)Aki} (LGP2A30K/A30K)³⁰ and T. Kawai and S. Akira provided Mavs^{tm1Aki} (Mavs^{-/-})³¹ mice. A. Garcia-Sastre (Mount Sinai School of Medicine) made the Eif2ak2^{tm1Cwe} (Eif2ak2^{-/-})³² and A. Berns (Netherlands Cancer Institute) the Rag2^{-/-} IL2R^{Null} (ref. 33) mice available.

Generation of HCV entry factor transgenic mice. cDNAs encoding human CD81, SCARB1, CLDN1 or OCLN were cloned into a vector between a chimaeric intron and the 3' flanking regions of human growth hormone (GH1), in which the mouse albumin enhancer/promoter drives gene expression³⁴. Vector-free human CD81, SCARB1, CLDN1 and/or OCLN expression fragments were prepared by NotI and KpnI digestion and microinjected alone or in combination into fertilized C57BL/6 mouse eggs. Transgenic offspring were mated with C57BL/6 wild-type animals to select for founder lines stably inheriting the transgene(s). In some mice that were co-injected with multiple expression constructs, transgenes did not segregate in the F₁ generation, indicating separate insertions in close proximity or insertion as concatemers. The founder lines were designated as follows: C57BL/6-Tg(Alb-hCD81)976^{Plo/RO} (Alb-hCD81), C57BL/6-Tg(Alb-hSCARB1)^{Plo/RO} (Alb-hSCARB1), C57BL/6-Tg(Alb-hOCLN)70^{Plo/RO} (Alb-hOCLN), C57BL/6-Tg(Alb-hCD81/hOCLN)941^{Plo/RO} (Alb-hCD81/hOCLN), C57BL/6-Tg(Alb-hSCARB1/hCDN1)935^{Plo/RO} (Alb-hSCARB1/hCDN1), C57BL/6-Tg(Alb-hCD81/hSCARB1/hCDN1/hOCLN)100^{Plo/RO} (Alb-EFT4x).

Generation of TagBFP-nlsMAVS reporter mice (C57BL/6-Tg(TagBFP-nlsMAVS)4065). The TagRFP-NLS-MAVS(WT) cassette¹⁶ was inserted into pCR2.1-TOPO (Invitrogen) and modified to contain TagBFP in place of TagRFP. The resulting TagBFP-NLS-MAVS cassettes was inserted into the pCAGGS vector (Addgene) to yield pCAGGS-TagBFP-NLS-MAVS(WT). The pCAGGS backbone drives transgene expression from a ubiquitously active chimaeric CMV/ β actin promoter³⁵ and has been used to create transgenic mice successfully (for example, ref. 36). The pCAGGS-TagBFP-NLS-MAVS(WT) internal transgenesis cassette was isolated by linearization with SalI/PstI enzymes and injected into C57BL/6 pronuclei. Founder animals were identified by PCR and bred with congenic C57BL/6J animals.

HCV generation and infections. Construction of BiCre-Jc1 (ref. 2), Jc1 (ref. 37), Con1-Jc1 (ref. 38) and Jc1 5AB Ypet³⁹ was described elsewhere. Huh-7.5.1 (ref. 23) or Huh-7.5 (ref. 22) cells were electroporated with *in vitro* transcribed full-length HCV RNA. Seventy-two hours after electroporation, the medium was replaced with DMEM containing 1.5% FBS and supernatants were collected every 6 h starting from 72 h. Pooled supernatants were clarified by centrifugation at 1,500g, filtered through a 0.45 μ m bottle top filter (Millipore) and concentrated using a stirred cell (Millipore). Viral titres (TCID₅₀) were determined using Huh-7.5 cells as previously described¹⁸. All infections of mice with the indicated genotypes were performed intravenously.

Antibodies and inhibitors. Blocking antibodies against CD81 (JS81) and IgG1 control antibodies were obtained from BD Biosciences. Antibodies against NS5A (ref. 18) and E2 (clone AR4A)¹² and the human IgG1 isotype control (b12 (ref. 40), provided by D. Burton, The Scripps Research Institute) have been described previously. Antibodies for the detection of human CD81 were purchased from BD Biosciences, OCLN from BD Biosciences (for histology) and from Invitrogen (for western blotting), CLDN1 from Invitrogen (for western blotting) and Abcam (for histology), and SCARB1 from Genetex (for histology) and from BD

Biosciences (for western blotting). The HCV NS5A inhibitor BMS-790052 (ref. 41) was obtained from Selleck Chemicals.

Adenovirus constructs. Adenoviral constructs encoding HCV JFH1 NS3-4A were created using the AdEasy Adenoviral Vector System (Agilent Technologies) according to the manufacturer's instructions. Briefly, JFH1 NS3-4A cDNA was PCR-amplified from pCR3.1-NS3/4A and inserted into the pShuttle-CMV using KpnI/NotI sites. Recombinant pShuttle-CMV plasmids were linearized with PmeI and ligated to pAdEasy by homologous recombination followed by electroporation into BJ5183 cells (Agilent). Recombinant pShuttle-pAdEasy constructs were identified by PacI restriction analysis. All plasmid constructs were verified by DNA sequencing.

Histological detection of HCV entry factors. Liver and spleen of mice injected with adenoviruses encoding human entry factors were collected 24 h after injection and fixed using 4% paraformaldehyde. Tissue sections (8 μ m) were deparaffinized and subjected to antigen retrieval by boiling for 30 min in citrate buffer (10 mM sodium citrate, 0.05% Tween 20, pH 6.0). Entry factors were stained with human-specific primary antibodies for 16 h at 4 °C followed by secondary antibody staining using Alexa 488 or Alexa 633-conjugated antibodies for 2 h at room temperature. For *in situ* detection of eGFP fluorescence, mouse tissue was immediately frozen in OCT (Optimal Cutting Temperature) compound at -80 °C. Tissue sections (~5–6 μ m) were cut on poly-L-lysine-coated slides. Secondary antibodies goat-anti-mouse or goat-anti-rabbit Alexa 488- or rhodamine conjugates (Invitrogen; 1:1,000) were used for immunofluorescence. Nuclei were detected using DAPI in VectaShield Mounting medium (Vector Laboratories). Images were captured on an Axioplan 2 imaging fluorescence microscope (Zeiss) using Metavue Software (Molecular Devices). Images were processed using ImageJ software (NIH).

Isolation of murine hepatocytes. Mice were anaesthetized by intraperitoneal injection of a mixture of 100 mg kg⁻¹ ketamine and 10 mg kg⁻¹ xylazine. Livers were perfused through the inferior vena cava for 5 min each with chelating buffer (0.5 mM EGTA, 0.05 M HEPES pH 7.3 in Ca/Mg-free HBSS) at a flow rate of 2 ml min⁻¹ followed by collagenase solution (4.8 mM CaCl₂, 100 U ml⁻¹ collagenase type IV, 0.05 M HEPES pH 7.3 in Ca/Mg-free HBSS). The resulting cell suspension was passed through a 100 μ m cell strainer, washed twice in HBSS and was fixed in 4% paraformaldehyde. Purity of isolated hepatocytes was over 90% in all preparations as confirmed by intracellular staining for murine albumin.

Immune activation. Lymphocytes were isolated from liver and spleen by digestion with 0.1% collagenase (Sigma) for 30 min at 37 °C. Lymphocytes were then isolated from the cell suspensions as well as from peripheral blood by density gradient centrifugation. Cells were stained with directly fluorochrome-conjugated antibodies against CD3, CD4, CD8, B220 (eBioscience) and NKp46 (BD Biosciences). After cell surface staining, cells were fixed and permeabilized using BD Cytofix/Cytoperm (BD Biosciences) and stained with antibodies against IFN- γ and TNF- α . Samples were measured using a BD LSR2 flow cytometer (BD Biosciences) and data were analysed using Flowjo (Treestar Software).

Western blotting. Perfused murine liver tissue was homogenized in lysis buffer containing 1% Triton X-100, 50 mM Tris-HCl pH 8, 150 mM NaCl and Mini EDTA-free Protease Inhibitor Cocktail (Roche) for 30 min on ice. Thirty micrograms of protein lysate was separated on 4–12% Bis/Tris NuPage polyacrylamide gels (Invitrogen). Proteins were transferred to nitrocellulose membranes and entry factors were detected using antibodies against human SCARB1 (1:500) and CLDN1 (1:200). β -actin (1:10,000) was probed as a loading control. After secondary antibody staining with HRP-conjugated anti-mouse IgG Fc (JIR, 1:10,000), western blots were visualized using SuperSignal West Pico (Thermo Scientific).

RT-PCR quantification of HCV entry factors and interferon-stimulated genes. To quantify expression of human and murine genes (entry factors and interferon-stimulated genes), the livers of FVB/NJ mice were collected at the indicated time points. Total liver RNA was isolated using RNeasy isolation kit (Qiagen) and cDNA was synthesized from 0.5 μ g RNA using a SuperScript VILO cDNA Synthesis kit (Invitrogen) according to manufacturer's instructions. Quantitative PCR was performed with a light cycler LC480 (Roche Applied Science) using an Applied Biosystems SYBR Green PCR Master Mix and the following primer pairs: human *CD81* forward 5'-TGTTCTTGAGCACTGAGGTGGTC-3', reverse 5'-TGGTGGATGATGACGCCAAC-3'; human *SCARB1* forward 5'-CGGATTTGGCAGATGACAGG-3', reverse 5'-GGGGAGAGACTCTTCACACATTCTAC-3'; human *CLDN1* forward 5'-CACCTCATCGTCTTCCAAGCAC-3', reverse 5'-CCTGGGAGTGATAGCAATCTTTG-3'; human *OCLN* forward 5'-CGGCAATGAAACAAAAGGCAG-3', reverse 5'-GGCTATGGTTATGGCTATGGCTAC-3'; mouse *Cd81* forward 5'-GGCTGTTCTCAGTATGGTGGTAG-3', reverse 5'-CCAAGGCTGTGGTGAAGACTTTC-3'; mouse *Scarb1* forward 5'-CAAAAAGCATTTCTCTGGCTG-3', reverse 5'-AATCTGTCAAGGCATCGGG-3'; mouse *Cldn1* forward 5'-TTATGCCCAATGACAGCC-3', reverse 5'-ATGAGGTGCCTGGAAGATGATG-3'; mouse *Ocln* forward 5'-ACTAAGGAAGCGATGAAGCAGAAG-3', reverse 5'-GCTCTTTGGAGGAAGCCTAACTAC-3'; mouse

Gapdh forward 5'-ACGGCCGCATCTTCTTGTGCA-3', reverse 5'-ACGGCCA AATCCGTTACACACC-3'; mouse *viperin* forward 5'-TGCTGGCTGAGAATAG CATTAGG-3', reverse 5'-GCTGAGTGTCTCCCATCT-3'; mouse *Irf1* forward 5'-GCTTGTGGGAACCTGTTTG-3', reverse 5'-GGATGGCATTTGTTGAT GTGGAG-3'; mouse *Irf4* forward 5'-AACTGACTGCTCGCAATAATGT-3', reverse 5'-GTAACACAGCAATGCCTCTTGT-3'; mouse *Mx1* forward 5'-GAC CATAGGGGTCTTGACCA-3', reverse 5'-AGACTTGCTCTTTCTGAAAAG CC-3'; mouse *Eif2ak2* forward 5'-ATGCACGGAGTAGCCATTACG-3', reverse 5'-TGACAATCCACCTTGTTCGT-3'; mouse *Oas1a* forward 5'-ATGGAGC ACGGACTCAGGA-3', reverse 5'-TCACACACGACATTGACGGC-3'; mouse *Irfn1* forward 5'-CAGCTCCAAGAAAGGACGAAC-3', reverse 5'-GGCAGTG TAACCTTCTGCAT-3'; mouse *Irf1* forward 5'-CCAAGTGTGCGCTCATT TTC-3', reverse 5'-GGCTCGCAGGGATGATTCAA-3'.

RT-PCR quantification of HCV RNA. Total RNA was isolated from the indicated mouse tissues using the RNeasy kit (Qiagen). HCV genome copy number was quantified by one step RT-PCR using Multicode-RTx HCV RNA kit (Eragen) and a light cycler LC480 (Roche Applied Science), according to the manufacturers' instructions.

ImageStream. Hepatocytes were isolated as described above. Hepatocytes were fixed in 4% paraformaldehyde, permeabilized using 0.1% Triton X-100 and stained with antibodies against mouse albumin (Cedarlane) and DRAQ5 (eBioscience) before ImageStream acquisition using an ImageStream X with Multimag (Amnis).

Bioluminescence imaging. Unless otherwise specified, mice were injected with 10^{11} adenoviral particles 24 h before intravenous injection with 2×10^7 TCID₅₀ HCV-Cre. At 72 h after infection, mice were anaesthetized using ketamin/xylazine and injected intraperitoneally with 1.5 mg luciferin (Caliper Lifesciences). Bioluminescence was measured using an IVIS Lumina II platform (Caliper Lifesciences).

HCV genome sequencing. Total RNA isolated from mouse sera was used to synthesize cDNA covering the HCV genome using the SuperScript III First-Strand Synthesis System for RT-PCR (Invitrogen Life Technologies). Briefly, cDNA fragments were synthesized covering the BiCre HCV genome, using the following primer sets: 10526/17376, 16768/12470, 5928/17377 and 6993/15692, or 10526/17375, 15356/17376, 15695/6986, 3949/5996, 17119/12470, 5928/6815, 6993/16864, 16863/17388, depending on the mouse (see below).

The following primers were used for cDNA synthesis: RU-O-10526, 5'-ACCTG CCCCTAATAGGGGCGAC-3' (sense, 5' UTR); RU-O-17376, 5'-TGCTGGCGT TGAAGTCAGCTC-3' (antisense, E2); RU-O-16768, 5'-CGCACCATCATGT TGGGGG-3' (sense, E2); RU-O-12470, 5'-AAGCCTCATACAGGACCTCC-3' (antisense, NS4A); RU-O-5928, 5'-GATGCTACCTCCATTCTCG-3' (sense, NS5B); RU-O-17377, 5'-GCAATGTGGGCGCAACTATCC-3' (antisense, NS5B); RU-O-6993, 5'-CCGCCCTCACCAGTCCGTTGT-3' (sense, NS4B); RU-O-15692, 5'-TATT CACGCCCTTTAGTGAGTGA-3' (antisense, 3' UTR); RU-O-17375, 5'-CCG AACACGGGGACGTGGTT-3' (antisense, EMCV); RU-O-15356, 5'-GCAAG GTCTGTGAATGTCG-3' (sense, EMCV); RU-O-15695, 5'-CGAATGTGGCC GTGCAGCGGC-3' (sense, E1); RU-O-6986, 5'-AGTCTTTGAGCCGTCGAA GT-3' (antisense, NS3); RU-O-3949, 5'-GCATCCTGATACCACTTACCTC-3' (sense, E2); RU-O-5996, 5'-CAGGTAGAGGAAGACAGGGCA-3' (antisense, NS3); RU-O-17119, 5'-GCTCCCATCACTGCTTATGCC-3' (sense, NS3); RU-O-6815, 5'-CAACACCTATGACGTGGACATG-3' (antisense, NS5A); RU-O-16864, 5'-GT AACTGCTGTTGCGATACC-3' (antisense, NS5B); RU-O-16863, 5'-CAGGT AGAGCTTCAACCTCCC-3' (sense, NS5A); RU-O-17388, 5'-ATTGCCGGAGG CGCGCTACT-3' (antisense, 3' UTR).

Resulting cDNA fragments were then amplified by PCR using Taq polymerase and a combination of the PCR primers listed below. m44 and m55 primer pairs: 3949/5996, 14317/17435, 7086/17376, 15355/16490, 16253/17377, 6993/6815, 3949/6986, 17119/5996. m46 and m64 primer pairs: 3949/5996, 16768/6986, 15354/16490, 6993/16864, 10526/17374, 15356/17376, 17119/12470, 14317/17435, 5928/6815, 7086/17376. m54 primer pairs: 15355/17375, 7086/17376, 3949/6986, 3949/10215, 17119/5996, 5928/12470, 6993/6815, 17391/16864, 14317/17388.

Primers used for sub-fragment PCR amplification: RU-O-3949, 5'-GCATCC TGATACCACTTACCTC-3' (sense, E2); RU-O-5996, 5'-CAGGTAGAGGAAG ACAGGCA-3' (antisense, NS3); RU-O-14317, 5'-CGGGTGGAGTATCTCTTGA A-3' (sense, NS5B); RU-O-17435, 5'-CTGTGTGAAATTGTTATCCGC-3' (antisense, 3' UTR); RU-O-7086, 5'-TGGGCAGGATGGCTCCTGTC-3' (sense, core); RU-O-17376, 5'-TGCTGGCGTTGAAGTCAGCTC-3' (antisense, E2); RU-O-15355, 5'-TGGCAGAACGAAAACGCTG-3' (sense, nlsCre); RU-O-16490, 5'-CGCTG CCGAAGTGAAGAACA-3' (antisense, E1); RU-O-17377, 5'-GCATTGTGGGC GCAACTATCC-3' (antisense, NS5B); RU-O-6993, 5'-CCGCCCTCACCAGTC CGTTGT-3' (sense, NS4B); RU-O-6815, 5'-CAACACCTATGACGTGGACATG-3'

(antisense, NS5A); RU-O-16253, 5'-CATAGGTTTGCACCCACA-3' (sense, NS5A); RU-O-6986, 5'-AGTCTTTGGAGCCGTGCAAGT-3' (antisense, NS3); RU-O-17119, 5'-GCTCCCATCACTGCTTATGCC-3' (sense, NS3); RU-O-16768, 5'-CGCAC CCATCACTGTTGGGGG-3' (sense, E2); RU-O-15354, 5'-CAAGAAGAAGAGG AAGGTGTC-3' (sense, nlsCre); RU-O-10526, 5'-ACCTGCCCCCTAATAGGGG CGAC-3' (sense, 5' UTR); RU-O-16864, 5'-GTAACCTCGCTGTTGCGATACC-3' (antisense, NS5B); RU-O-17374, 5'-CGGTCCAGCCACGTGGAAGGC-3' (antisense, core); RU-O-15356, 5'-GCAAGGTCTGTTGAATGTCG-3' (sense, EMCV); RU-O-12470, 5'-AAGCCTCATACAGGACCTCC-3' (antisense, NS4A); RU-O-5928, 5'-GATGCTACCTCCATTCTCG-3' (sense, NS5B); RU-O-17375, 5'-CCGAAC CACGGGGACGTGGTT-3' (antisense, EMCV); RU-O-10215, 5'-CATCTATGA CCACCTACACC-3' (antisense, NS2); RU-O-17391, 5'-CATAGGTTTGCAACC CACACCA-3' (sense, NS5A); RU-O-17388, 5'-ATTGCCGGAGGCGCGCTTA CT-3' (antisense, 3' UTR).

The resulting PCR amplicons were cloned into the pCR2.1 vector using the TOPO TA Cloning kit (Invitrogen Life Technologies). Resulting clones were screened for proper amplicon insertion size by EcoRI digestion, and sequenced using M13F/R primers, as well as additional internal primers for full genomic coverage (MacrogenUSA).

Statistical analysis. Statistical analyses were performed using Graphpad Prism Software. Statistics were calculated using Kruskal-Wallis one-way analysis of variance. *P* values below 0.05 were considered statistically significant.

- Safran, M. *et al.* Mouse reporter strain for noninvasive bioluminescent imaging of cells that have undergone Cre-mediated recombination. *Mol. Imaging* **2**, 297–302 (2003).
- Stoller, J. Z. *et al.* Cre reporter mouse expressing a nuclear localized fusion of GFP and beta-galactosidase reveals new derivatives of Pax3-expressing precursors. *Genesis* **46**, 200–204 (2008).
- Colgan, J. *et al.* Cyclophilin A regulates TCR signal strength in CD4⁺ T cells via a proline-directed conformational switch in Itk. *Immunity* **21**, 189–201 (2004).
- Blight, K. J., McKeating, J. A. & Rice, C. M. Highly permissive cell lines for subgenomic and genomic hepatitis C virus RNA replication. *J. Virol.* **76**, 13001–13014 (2002).
- Zhong, J. *et al.* Robust hepatitis C virus infection *in vitro*. *Proc. Natl Acad. Sci. USA* **102**, 9294–9299 (2005).
- Matsuyama, T. *et al.* Targeted disruption of IRF-1 or IRF-2 results in abnormal type I IFN gene induction and aberrant lymphocyte development. *Cell* **75**, 83–97 (1993).
- Muller, U. *et al.* Functional role of type I and type II interferons in antiviral defense. *Science* **264**, 1918–1921 (1994).
- Durbin, J., Hadden, R., Simon, M. C. & Levy, D. E. Targeted disruption of the mouse Stat1 gene results in compromised innate immunity to viral disease. *Cell* **84**, 443–450 (1996).
- Sato, M. *et al.* Distinct and essential roles of transcription factors IRF-3 and IRF-7 in response to viruses for *IFN- α/β* gene induction. *Immunity* **13**, 539–548 (2000).
- Honda, K. *et al.* IRF-7 is the master regulator of type-I interferon-dependent immune responses. *Nature* **434**, 772–777 (2005).
- Kimura, T. *et al.* Essential and non-redundant roles of p48 (ISGF3 gamma) and IRF-1 in both type I and type II interferon responses, as revealed by gene targeting studies. *Genes Cells* **1**, 115–124 (1996).
- Satoh, T. *et al.* LPS2 is a positive regulator of RIG-I and MDA5-mediated antiviral responses. *Proc. Natl Acad. Sci. USA* **107**, 1512–1517 (2010).
- Kumar, H. *et al.* Essential role of IPS-1 in innate immune responses against RNA viruses. *J. Exp. Med.* **203**, 1795–1803 (2006).
- Yang, Y. L. *et al.* Deficient signaling in mice devoid of double-stranded RNA-dependent protein kinase. *EMBO J.* **14**, 6095–6106 (1995).
- Gimeno, R. *et al.* Monitoring the effect of gene silencing by RNA interference in human CD34⁺ cells injected into newborn RAG2^{-/-} γ c^{-/-} mice: functional inactivation of p53 in developing T cells. *Blood* **104**, 3886–3893 (2004).
- Suemizu, H. *et al.* Establishment of a humanized model of liver using NOD/Shi-scid IL2R^{gull} mice. *Biochem. Biophys. Res. Commun.* **377**, 248–252 (2008).
- Niwa, H., Yamamura, K. & Miyazaki, J. Efficient selection for high-expression transfectants with a novel eukaryotic vector. *Gene* **108**, 193–199 (1991).
- Okabe, M., Ikawa, M., Kominami, K., Nakanishi, T. & Nishimune, Y. 'Green mice' as a source of ubiquitous green cells. *FEBS Lett.* **407**, 313–319 (1997).
- Pietschmann, T. *et al.* Construction and characterization of infectious intragenotypic and intergenotypic hepatitis C virus chimeras. *Proc. Natl Acad. Sci. USA* **103**, 7408–7413 (2006).
- Gottwein, J. M. *et al.* Development and characterization of hepatitis C virus genotype 1-7 cell culture systems: role of CD81 and scavenger receptor class B type I and effect of antiviral drugs. *Hepatology* **49**, 364–377 (2009).
- Horwitz, J. A. *et al.* Expression of heterologous proteins flanked by NS3-4A cleavage sites within the hepatitis C virus polyprotein. *Virology* **439**, 23–33 (2013).
- Burton, D. R. *et al.* Efficient neutralization of primary isolates of HIV-1 by a recombinant human monoclonal antibody. *Science* **266**, 1024–1027 (1994).
- Gao, M. *et al.* Chemical genetics strategy identifies an HCV NS5A inhibitor with a potent clinical effect. *Nature* **465**, 96–100 (2010).

Pathogen blocks host death receptor signalling by arginine GlcNAcylation of death domains

Shan Li^{1,2*}, Li Zhang^{2,3*}, Qing Yao^{1,2}, Lin Li², Na Dong², Jie Rong⁴, Wenqing Gao², Xiaojun Ding², Liming Sun², Xing Chen⁴, She Chen² & Feng Shao²

The tumour necrosis factor (TNF) family is crucial for immune homeostasis, cell death and inflammation. These cytokines are recognized by members of the TNF receptor (TNFR) family of death receptors, including TNFR1 and TNFR2, and FAS and TNF-related apoptosis-inducing ligand (TRAIL) receptors¹. Death receptor signalling requires death-domain-mediated homotypic/heterotypic interactions between the receptor and its downstream adaptors, including TNFR1-associated death domain protein (TRADD) and FAS-associated death domain protein (FADD)². Here we discover that death domains in several proteins, including TRADD, FADD, RIPK1 and TNFR1, were directly inactivated by NleB, an enteropathogenic *Escherichia coli* (EPEC) type III secretion system effector known to inhibit host nuclear factor- κ B (NF- κ B) signalling^{3,4}. NleB contained an unprecedented *N*-acetylglucosamine (GlcNAc) transferase activity that specifically modified a conserved arginine in these death domains (Arg 235 in the TRADD death domain). NleB GlcNAcylation (the addition of GlcNAc onto a protein side chain) of death domains blocked homotypic/heterotypic death domain interactions and assembly of the oligomeric TNFR1 complex, thereby disrupting TNF signalling in EPEC-infected cells, including NF- κ B signalling, apoptosis and necroptosis. Type-III-delivered NleB also blocked FAS ligand and TRAIL-induced cell death by preventing formation of a FADD-mediated death-inducing signalling complex (DISC). The arginine GlcNAc transferase activity of NleB was required for bacterial colonization in the mouse model of EPEC infection. The mechanism of action of NleB represents a new model by which bacteria counteract host defences, and also a previously unappreciated post-translational modification.

EPEC contains several type-III-secreted effectors, including NleC/D^{5–8}, Tir^{9,10}, NleE and NleB^{3,4,11,12}, all of which can inhibit host NF- κ B signalling and pro-inflammatory cytokine production. Among these effectors, NleB is required for virulence *in vivo*^{13–15}. NleB homologues are present in *Salmonella* and pathogenic *E. coli* strains¹⁶. Consistent with previous studies^{4,9}, the expression of NleB (E2348C_3231) in HeLa cells selectively blocked TNF- α but not interleukin (IL)-1 β activation of NF- κ B signalling (Supplementary Fig. 1a, b). TNF- α -induced I κ B- α phosphorylation and degradation were both severely inhibited (Supplementary Fig. 1c). NleB blocked TRAF2- but not TRAF6-induced NF- κ B activation (Supplementary Fig. 2a). TNF- α - but not IL-1 β -stimulated TAK1 phosphorylation, downstream of the receptor and TRAF complex, was diminished by NleB (Supplementary Fig. 2b). TNFR can also induce apoptosis or necroptosis (in cells deficient in caspase activity), playing an important role in microbial infection and inflammation¹⁷. NleB efficiently blocked TNF- α plus cycloheximide-induced 293T cell apoptosis (Fig. 1a), and also blocked necroptosis of HeLa cells stably expressing the RIP3 protein kinase (HeLa-RIP3 cells) (Fig. 1b). This agrees with NleB targeting upstream of TAK1, as TAK1 is not required for TNF- α -induced cell death¹⁸. Thus, NleB differs from

other NF- κ B-targeting effectors and can block both NF- κ B signalling and TNF- α -induced cell death.

A yeast two-hybrid screen of a HeLa complementary DNA library identified a cDNA clone encoding the death domain of TRADD, a universal component of the TNFR1 but not IL-1R complex^{19–21}. NleB also interacted with full-length TRADD, but not with components of the TAK1 and I κ B kinase (IKK) complexes; no interaction occurred between NleE and TRADD (Fig. 1c). Endogenous TRADD was readily precipitated by NleB (Supplementary Fig. 3a). The TRADD death domain (residues 195–312) was required and sufficient for precipitation by enhanced green fluorescent protein (eGFP)-NleB (Fig. 1d and Supplementary Fig. 3b). Similar to that observed with TNF- α stimulation, NleB completely abolished TRADD overexpression-induced NF- κ B activation (Fig. 1e) and apoptosis in 293T cells (Fig. 1f and Supplementary Fig. 4a). Thus, NleB can target TRADD and disrupt multiple signalling pathways downstream of TNFR1.

NleB did not affect TRADD stability or turnover (Supplementary Fig. 5a). TRADD contains an amino-terminal TRAF2-binding domain and a carboxy-terminal death domain. The TRADD death domain oligomerizes with itself and also with death domains of TNFR1 and FADD²². Death-domain-mediated TRADD recruitment to TNFR1 initiates TNF- α signalling, and TRADD-FADD complex formation triggers apoptosis²³. TRADD readily precipitated TNFR1c (the intracellular death-domain-containing region) from 293T cells, and this was abolished by NleB (Supplementary Fig. 5b). A similar blocking effect was observed in TRADD-FADD but not in TRADD-TRAF2 co-immunoprecipitation (Supplementary Fig. 5c, 6). TRADD oligomerization is crucial for TNFR1 complex assembly²². TRADD or TRADD death domain expressed in 293T cells appeared as a large oligomer on a blue native polyacrylamide gel electrophoresis (PAGE) gel, and NleB co-expression shifted TRADD and also the TRADD death domain to a lower molecular mass position that roughly corresponded to the monomer form (Fig. 2a). Consistently, NleB inhibited the recruitment of TRADD, TRAF2, HOIP, SHAPPIN, HOIL-1L and ubiquitinated RIPK1 to TNFR1 (Fig. 2b). Thus, NleB inactivates the TRADD death domain and disrupts homotypic/heterotypic death domain interactions and the TNFR1 complex assembly.

In these TRADD oligomerization and binding assays, the amount of NleB was considerably lower than those of TRADD, indicating that NleB may act in a catalytic manner on the TRADD death domain. Mass spectrometry analysis identified a 203-dalton (Da) mass increase on TRADD death domain co-expressed with NleB in either *E. coli* (Supplementary Fig. 7) or 293T cells (Fig. 2c), whereas control TRADD death domain showed the theoretic molecular mass. The 203-Da mass increase indicated a GlcNAc modification. Consistently, recombinant NleB efficiently transferred ³H-GlcNAc, but not ³H-glucose, from radiolabelled sugar donors onto purified TRADD (Fig. 2d). Cold UDP-GlcNAc, but not UDP-GalNAc, UDP-glucose, UDP-galactose and UDP-GlcA,

¹College of Biological Sciences, China Agricultural University, Beijing 100094, China. ²National Institute of Biological Sciences, Beijing 102206, China. ³Graduate School of Chinese Academy of Medical Sciences and Beijing Union Medical College, Beijing 100730, China. ⁴Beijing National Laboratory for Molecular Sciences, Department of Chemical Biology, College of Chemistry and Molecular Engineering, Peking University, Beijing 100871, China.

*These authors contributed equally to this work.

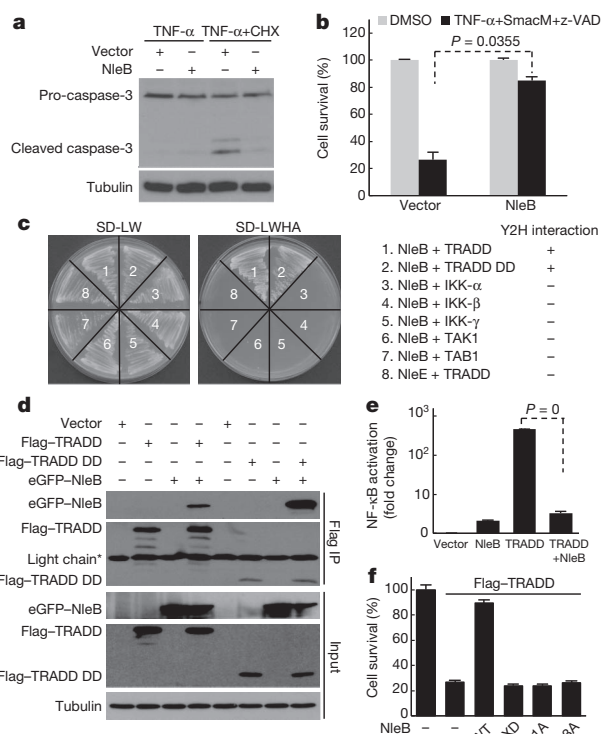


Figure 1 | NleB blocks TNF- α signalling by directly targeting the TRADD death domain. **a**, Effects of NleB transfection on TNF- α -induced caspase-3 activation in 293T cells. CHX, cycloheximide. **b**, Vector- or NleB-transfected HeLa-RIP3 cells were stimulated with TNF- α plus Smac mimetic (SmacM) and z-VAD, dimethylsulphoxide. **c**, Yeast strain was transformed with indicated plasmid combinations (bait plus prey) to assay the interaction of NleB with TRADD or other components downstream of TNFR. Yeast strains were grown on SD-LW (non-selective) and SD-LWHA (selective) media. DD, death domain; Y2H, yeast two-hybrid. **d**, Co-immunoprecipitation of NleB with TRADD and TRADD death domain in 293T cells. **e**, NF- κ B luciferase activity of NleB- and/or TRADD-transfected 293T cells is shown as fold change normalized to that in vector-transfected cells. **f**, Viability of NleB- and/or TRADD-transfected 293T cells was determined by measuring ATP levels. $P < 0.0001$ for all (TRADD plus NleB versus TRADD plus DXD, versus TRADD plus Asp221Ala, and versus TRADD plus Asp223Ala). For **b**, **e** and **f**, $n = 3$; data are mean \pm s.d.; P value determined by Student's t -test. Data in **a**, **c** and **d** are representative from at least three repetitions.

abolished ^3H -GlcNAc labelling of TRADD by NleB (Fig. 2d and Supplementary Fig. 8). TRADD purified from NleB-expressing cells was resistant to further *in vitro* ^3H -GlcNAc labelling by recombinant NleB in the 'back glycosylation' assay²⁴ (Fig. 2e), confirming the complete modification of TRADD in NleB-expressing 293T cells. Thus, NleB is a glycosyltransferase that GlcNAcylates the TRADD death domain.

Extensive mutagenesis of potentially catalytic residues identified NleB Asp221Ala and Asp223Ala mutants that lost the activity of inhibiting TNF- α -NF- κ B signalling (Supplementary Fig. 9). Interestingly, the GT-A family of glycosyltransferases²⁵, including the large clostridial toxins that modify Rho/Ras small GTPases²⁶, feature a catalytic Asp-X-Asp (DXD) motif that coordinates manganese (Mn^{2+}) and/or the sugar donor. The NleB(Asp221Ala/Asp223Ala) (DXD) mutant could not block the death-domain-mediated TRADD interaction with TNFR1c and FADD (Supplementary Fig. 5b, c) or TRADD self-oligomerization (Fig. 2a). Recombinant NleB DXD mutant exhibited no catalytic activity of GlcNAcylating TRADD (Fig. 2d); these two aspartate residues were required for NleB interaction (Supplementary Fig. 3a) and modification of TRADD in transfected 293T cells (Fig. 2e), as well as for inhibiting TRADD-induced apoptosis (Fig. 1f and Supplementary Fig. 4a). Concurrent to our analysis, another study²⁷ also

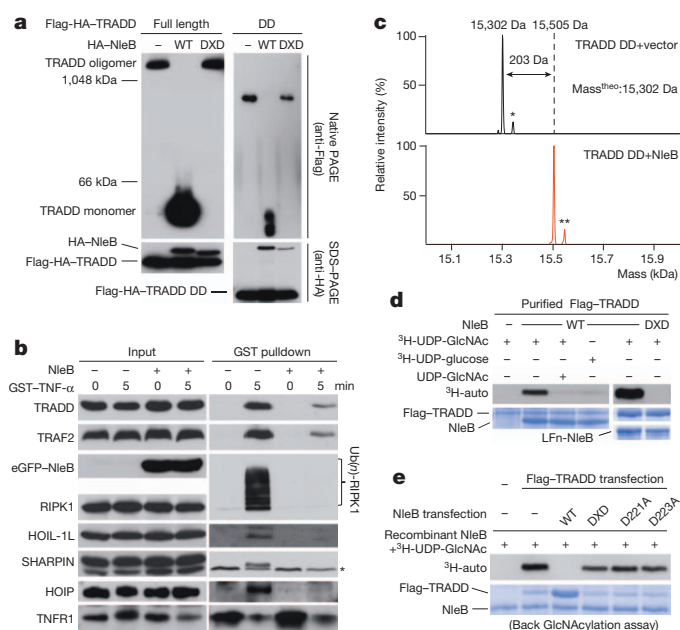
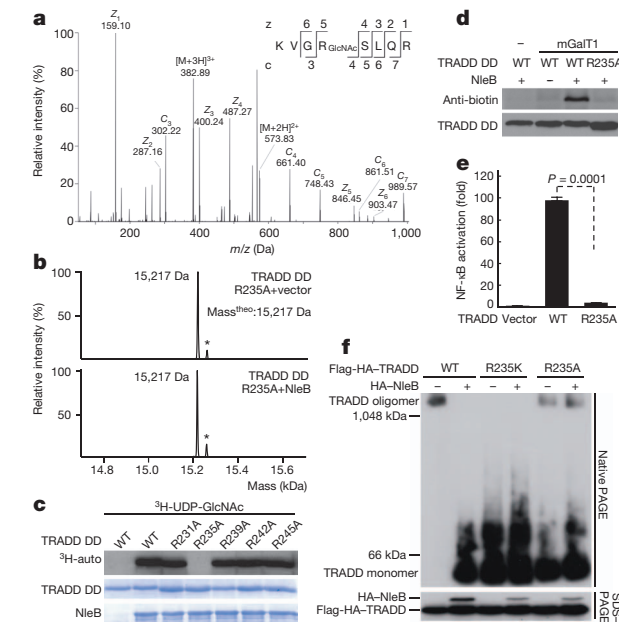


Figure 2 | NleB GlcNAcylates the TRADD death domain and disrupts its oligomerization. **a**, Effects of NleB transfection on TRADD oligomerization in 293T cells. Shown are immunoblots of cell lysates loaded onto native (top) and SDS-PAGE (bottom) gels. HA, haemagglutinin; WT, wild type. **b**, Effects of NleB transfection on TNFR1 complex formation in HeLa cells. Ub(n)-RIPK1 denotes polyubiquitinated RIPK1; asterisk marks a nonspecific band. GST, glutathione S-transferase. **c**, Electrospray ionization (ESI)-mass spectrometry determination of the total mass of TRADD death domain immunopurified from NleB- or vector-transfected 293T cells. Single and double asterisks denote the acetylated TRADD death domain. **d**, *In vitro* ^3H -UDP-GlcNAc labelling of TRADD by recombinant NleB. LFn-NleB refers to NleB protein fused C-terminally to the N-terminal domain of anthrax lethal factor. **e**, TRADD immunopurified from NleB-transfected 293T cells was subjected to further *in vitro* ^3H -UDP-GlcNAc labelling by recombinant NleB. Data in **a**, **b**, **d** and **e** are representative from at least three repetitions.

proposes that NleB is a GT-A-type glycosyltransferase according to fold recognition prediction. This study identifies glyceraldehyde-3-phosphate dehydrogenase (GAPDH) as a host binding partner of NleB. In *O*-GlcNAc antibody blotting, ^3H -GlcNAc labelling and mass spectrometric assays, GAPDH was not glycosylated by NleB *in vitro* and *in vivo* (Supplementary Fig. 10). GAPDH binding may represent a regulatory mechanism of NleB function, or be a target of NleB homologue. EPEC contains an NleB paralogue known as NleB2 (E2348C_1041) and an NleB homologue, SseK1, is present in *Salmonella enterica* serovar Typhimurium. Although SseK1 functioned comparably to NleB in inhibiting TNF- α -NF- κ B signalling and GlcNAcylating the TRADD death domain, NleB2 showed a lower enzymatic activity and only a fraction of TRADD was modified by NleB2 in 293T cells (Supplementary Fig. 11).

Protein *O*-GlcNAcylation is an *O*-linked GlcNAc modification generally occurring on serine/threonine residues of intracellular proteins. *O*-GlcNAcylation is abundant from bacteria to mammals, and has been proposed to be a phosphorylation-like modification in regulating transcription or signalling in response to nutrients and cellular stresses^{28,29}. The 203-Da mass increase indicates a single GlcNAc modification to the TRADD death domain by NleB (Fig. 2c and Supplementary Fig. 7a). To pinpoint the exact modification site, mutagenesis analyses were first used given that mapping the *O*-GlcNAcylation site by the conventional collision-assisted dissociation (CAD) mass spectrometry is technically difficult owing to the labile nature of GlcNAc modification²⁹. Surprisingly, no single mutation in all the ten serine/threonine residues in the TRADD death domain disrupted its modification by NleB (Supplementary Fig. 12). The ST10A mutant (all ten serine/threonine residues



were mutated simultaneously) was still GlcNAcylated to a considerable extent (Supplementary Fig. 12). Thus, NleB-induced modification may not be a canonical O-GlcNAcylation. The NleB-modified TRADD death domain (Supplementary Fig. 13) was then subjected to in-depth mass spectrometry analyses. Among the 13 tryptic peptides that cover the large majority of the TRADD death domain sequence, two overlapping ones (232-KVGRSLQR-239 and 233-VGRSLQR-239) showed a 203-Da mass increase (Supplementary Fig. 14). Electron-transfer dissociation (ETD) tandem mass spectrometry, which works better in preventing loss of the labile GlcNAc during peptide fragmentation²⁹, revealed that the 203-Da mass increase occurred on Arg 235 (Fig. 3a).

Figure 3 | NleB GlcNAcylation of Arg235 that is required for TRADD function. **a**, ETD tandem mass spectrum of a triply charged Arg-235-containing tryptic peptide from NleB-modified TRADD death domain in bacteria. The fragmentation patterns that generate the observed *c* and *z* ions are illustrated along the peptide sequence shown on top of the spectrum. **b**, ESI-mass spectrometry determination of the total mass of TRADD arginine mutants immunopurified from NleB- or vector-transfected 293T cells. All arginine residues in the TRADD death domain were individually mutated into alanine (also see Supplementary Fig. 17). Asterisk denotes the acetylated TRADD death domain Arg235Ala mutant. **c**, *In vitro* ³H-UDP-GlcNAc labelling of TRADD death domain arginine mutants by recombinant NleB. **d**, TRADD death domain or its Arg235Ala mutant immunopurified from NleB-transfected 293T cells was subjected to chemoenzymatic UDP-GalNAz labelling followed by reaction with an alkyne-biotin derivative. **e**, **f**, TRADD or its Arg 235 mutants were expressed in TRADD-knockdown 293T cells. **e**, NF-κB luciferase activity (fold change) is normalized to that in vector-transfected cells (*n* = 3; mean ± s.d.; Student's *t*-test). Data in **c**, **d** and **f** are representative from at least three repetitions.

When the Arg-235-containing tryptic peptide was purified and sequentially digested by proteinase K and carboxypeptidase, the GlcNAc-modified dipeptide (234-Gly-Arg-235) and even Arg 235 alone were identified by higher-energy collision dissociation tandem mass spectrometry (Supplementary Fig. 15). When the modification was performed in cells metabolically labelled with 2-(acetyl-*d*₃-amino)-2-deoxy-1,3,4,6-tetra-*O*-acetyl-D-glucopyranose (Ac₄GlcNAc-*d*₃), a mass increase of 206 Da, corresponding to modification by the deuterium-labelled GlcNAc, occurred on Arg235 in the TRADD death domain (Supplementary Fig. 16).

NleB GlcNAcylation of TRADD Arg235 was supported by four additional evidences. Arg235Ala and Arg235Lys mutations in the TRADD death domain abolished the GlcNAc modification by NleB in 293T cells, whereas mutation in any of the other ten arginine residues had no such effect (Fig. 3b and Supplementary Fig. 17). The purified TRADD(Arg235Ala) mutant resisted NleB-catalysed *in vitro* GlcNAcylation (Fig. 3c). When chemoenzymatic labelling of the terminal GlcNAc was used to detect GlcNAcylation, the wild-type TRADD

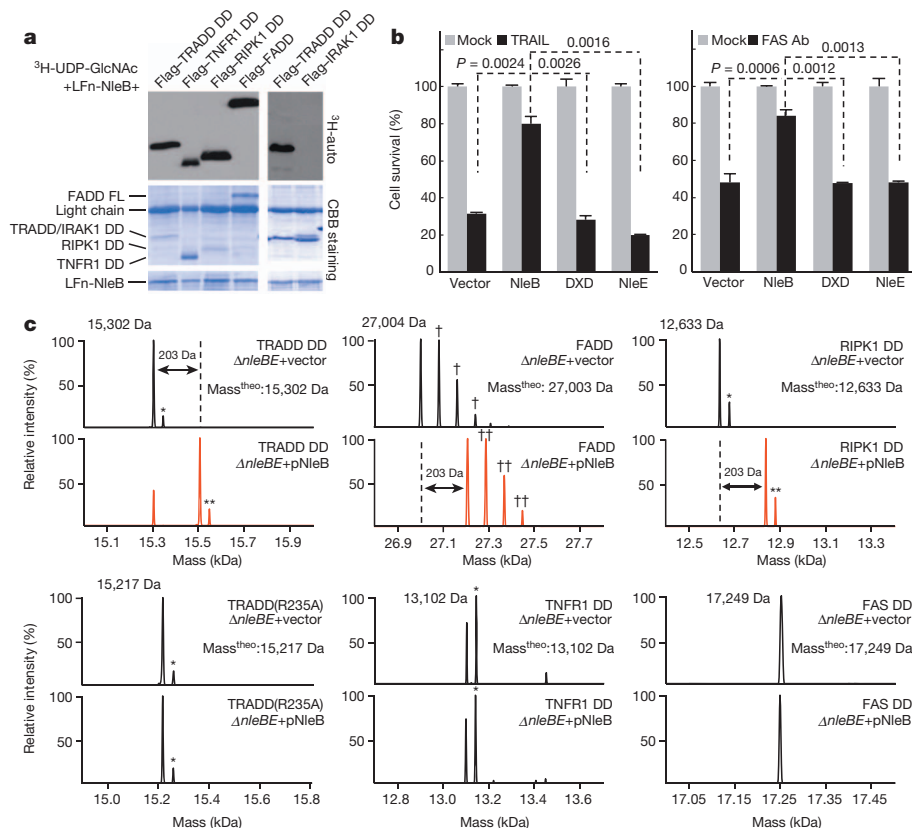


Figure 4 | NleB GlcNAcylation of FADD and other death domain proteins, and blocks FAS- and TRAIL-induced apoptosis. **a**, *In vitro* ³H-UDP-GlcNAc labelling of indicated death domains or death-domain-containing proteins by recombinant NleB. Data represent at least three repetitions. **b**, NleB-, NleE- or vector-transfected HeLa cells were stimulated with FAS antibody (Ab) or TRAIL, and cell viability was determined by measuring ATP levels (*n* = 3; mean ± s.d.; Student's *t*-test). **c**, ESI-mass spectrometry determination of the total mass of indicated death domain proteins purified from EPEC-infected 293T cells. Δ nleBE, NleB and NleE double-deletion EPEC E2348/69 strain; pNleB, NleB rescue plasmid. Dagger symbols denote the phosphorylated FADD; asterisks mark the corresponding acetylated proteins.

death domain from NleB-expressing 293T cells was readily labelled with *N*-azidoacetylgalactosamine (GalNAz) by an engineered galactosyl-transferase (Tyr289Leu mutant of GalT1), whereas no evident GalNAz labelling occurred on TRADD(Arg235Ala) (Fig. 3d). Lastly, NleB-catalysed GlcNAc modification was not reversed by *O*-GlcNAcase, β -*N*-acetylglucosaminidase and β -*N*-acetylhexosaminidase_f (a recombinant protein fusion of β -*N*-acetylhexosaminidase and maltose binding protein) (Supplementary Fig. 18), enzymes that are capable of removing *O*-linked or terminal GlcNAc.

TRADD-knockdown 293T cells were generated (Supplementary Fig. 19a). Knockdown of endogenous TRADD minimized its hetero-oligomerization and interference with transfected TRADD mutants. In contrast to wild-type TRADD, expression of TRADD(Arg235Ala) in TRADD-knockdown cells was largely deficient in activating the NF- κ B signalling (Fig. 3e and Supplementary Fig. 19b). Consistently, lysine or alanine substitution of Arg 235 in TRADD completely or nearly completely disrupted TRADD self-oligomerization, and the residual Arg235Ala oligomer was insensitive to further NleB expression (Fig. 3f). Thus, Arg 235 is important for TRADD function and activity.

Arg 235 is conserved in one-third of the total of more than 30 death-domain-containing proteins in humans²² (Supplementary Fig. 20), including FADD, TNFR1, RIPK1, FAS and death receptor-3/4/5 (DR3/4/5) that function in death receptor signalling. NleB completely modified the death domains of TNFR1 and RIPK1 as well as full-length FADD in bacteria (Supplementary Fig. 21) or 293T cells (Supplementary Fig. 22); a considerable portion of FAS death domain was also GlcNAc-modified. Death domains of MYD88 and IRAK1 devoid of the conserved arginine were not modified by NleB (Supplementary Fig. 22). In the ³H-GlcNAc labelling assay, FADD and death domains of TNFR1 and RIPK1 were GlcNAcylated by recombinant NleB, with efficiency comparable to that of the TRADD death domain (Fig. 4a). Induction of apoptosis by FAS ligand (FasL) and TRAIL require death-domain-mediated FADD interaction with the receptors and formation

of a caspase-8-containing death-inducing signalling complex (DISC). Consistently, anti-FAS antibody and TRAIL-stimulated HeLa cell apoptosis was inhibited by NleB, but not by the GlcNAc-transferase-deficient DXD mutant or the NleE effector (Fig. 4b).

293T cells expressing various death domains or death domain proteins were infected with an NleB-proficient or -deficient EPEC strain. FADD, RIPK1 death domain and a portion of TRADD death domain from NleB-positive infection showed a 203-Da mass increase (Fig. 4c). Modification of these proteins was not observed with the NleB-deficient strain. Importantly, no GlcNAc modification occurred on TRADD(Arg235Ala) (Fig. 4c). Consistent with these observations, expression of NleB, but not the DXD mutant, in a NleB/E double-deletion EPEC strain blocked p65 nuclear translocation in infected mouse embryonic fibroblast (MEF) cells (Fig. 5a and Supplementary Fig. 23a). GlcNAc-transferase-active NleB inhibited apoptosis in EPEC-infected HeLa cells after stimulation by TNF- α , FasL or TRAIL (Fig. 5b and Supplementary Fig. 4b). Type-III-delivered NleB, but not the DXD mutant, also effectively blocked TNF- α -induced necroptosis in HeLa-RIP3 or HT-29 cells (Supplementary Fig. 24). Furthermore, TNF- α -induced recruitment of TRADD, TRAF2, SHARPIN and ubiquitinated RIPK1 to TNFR1 as well as TRAIL-induced DISC formation were both disrupted by EPEC expressing the catalytically active NleB, and disruption of DISC formation was more severe (Fig. 5c and Supplementary Fig. 23b). When expressed in the type III secretion-deficient Δ escN strain, NleB did not affect cell death and death receptor complex assembly (Fig. 5a–c and Supplementary Figs 23b and 24).

Deletion of *nleB* from *Citrobacter rodentium* results in severely reduced bacterial colonization in infected mice¹³. *C. rodentium* NleB (NleBc) inhibited TNF- α signalling to an extent comparable to that of EPEC NleB (Supplementary Fig. 25a); NleBc also GlcNAcylated several death domain proteins, including FADD, TNFR1 and RIPK1, despite a slightly different substrate preference (Supplementary Fig. 25b). In *C. rodentium*-inoculated C57BL/6 mice, the Δ nleB mutant showed a significantly reduced colonization compared to the wild-type strain,

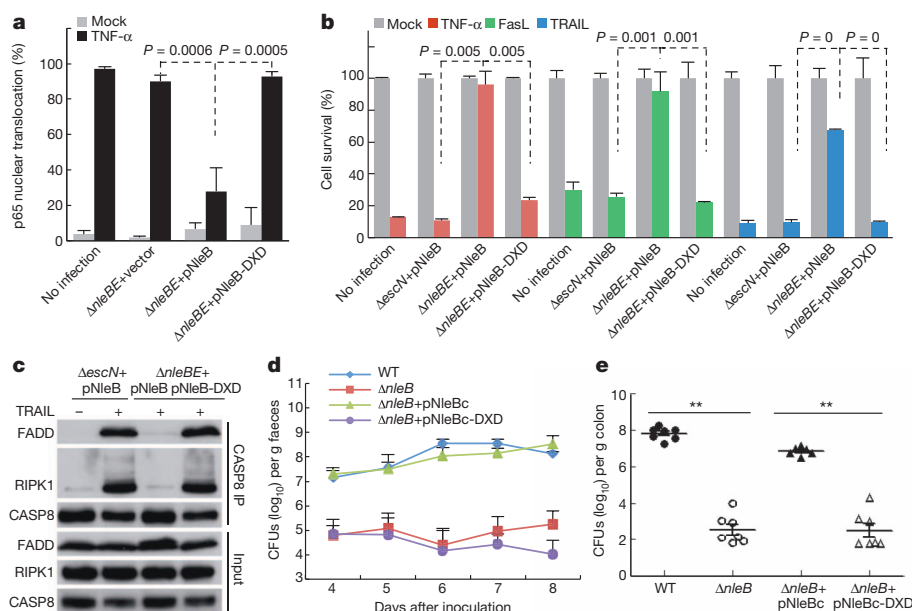


Figure 5 | Disrupting several death receptor pathways by NleB GlcNAc transferase activity that is required for bacterial colonization *in vivo*. **a**, MEF cells infected with indicated EPEC strains were stimulated with TNF- α , and statistics of cells with nuclear-localized p65 are shown. Representative fluorescence images are in Supplementary Fig. 23a. **b**, HeLa cells infected with indicated EPEC strains were stimulated with TNF- α , FasL or TRAIL, and cell viability was determined by measuring ATP levels. For **a** and **b**, $n = 3$; mean \pm s.d. **c**, Lysates of EPEC-infected HeLa cells stimulated with TRAIL were subjected to anti-caspase-8 (CASP8) immunoprecipitation. Data

represent at least three repetitions. **d**, **e**, Five–six-week-old C57BL/6 mice were oral gavaged with indicated *C. rodentium* DBS100 strains. Viable stool bacterial counts (**d**), measured at indicated points after inoculation, are shown as mean \pm s.e.m. of log₁₀ colony-forming units (CFU) per gram faeces, and bacterial colonization of the intestine 8 days after infection (**e**) is shown as the mean \pm s.e.m. of log₁₀ CFU per gram colon ($n > 6$). ** $P < 0.01$ (Student's *t*-test). pNleB(c) and pNleB(c)-DXD are rescue plasmids expressing wild-type and the DXD mutant of NleB(c), respectively.

demonstrated by colony-forming units of bacteria recovered from stool samples and colons from infected mice (Fig. 5d, e). Complementation of $\Delta nleB$ with NleBc or EPEC NleB, but not the DXD mutant, recovered stool counts to the level of the wild-type strain and restored bacterial colonization in the intestinal tract of mice (Fig. 5d, e and Supplementary Fig. 26). Thus, the arginine GlcNAc transferase activity of NleB is crucial for bacterial colonization and virulence in mice.

We discover that the EPEC type III effector NleB targets several death-domain-containing proteins in TNFR, FAS and TRAIL death receptor complexes to block host cell death. NleB probably functions as part of a network of effectors during EPEC interaction with the host. NleB is the first bacterial virulence factor hijacking the death receptor complex. Such distinguished feature may account for the unique virulence activity of NleB^{13–15}. TRADD and FADD are central adaptors in death receptor signalling. TRADD also mediates Toll-like receptor signalling in macrophages^{19–21}, suggesting an even broader function of NleB in EPEC modulation of host defences. NleB modifies its death domain targets by GlcNAcylation on a conserved arginine. Discovering arginine GlcNAcylation is conceptually unexpected despite one early preliminary study proposing such modification on a corn protein³⁰. The labile GlcNAc modification is refractory to conventional mass-spectrometry-based proteomic identifications that are performed in the absence of an arginine GlcNAcylation hypothesis. Thus, arginine GlcNAcylation might be widely used and represent a previously unappreciated mechanism in signalling.

METHODS SUMMARY

The EPEC E2348/69 $\Delta nleB/E$ SC3909 strain ($\Delta IE2::kan$ and $nleBE IE6::tet$)³ was used for cell culture infection. A single bacterial colony was inoculated into 0.5 ml of LB medium and statically cultured overnight at 37 °C. Bacterial cultures were then diluted by 1:40 in DMEM supplemented with 1 mM isopropyl- β -D-thiogalactoside (IPTG) and cultured for an additional 4 h at 37 °C in the presence of 5% CO₂. Infection was performed at a multiplicity of infection of 200:1 in the presence of 1 mM IPTG for 2 h. Cells were washed four times with PBS and bacteria were killed by 200 μ g ml⁻¹ gentamicin. To assay NleB-induced modification, 293T cells were transfected with pCS2-Flag-TRADD death domain plasmids 24 h before infection. z-VAD (Sigma) (20 μ M) was added to inhibit apoptosis. Lysates of infected cells were subjected to anti-Flag immunoprecipitation to purify the TRADD death domain for mass spectrometry analysis. All independent experiments carried out in this study and indicated in the figure legends were biological replicates.

Full Methods and any associated references are available in the online version of the paper.

Received 25 March; accepted 8 July 2013.

Published online 18 August 2013.

- Wilson, N. S., Dixit, V. & Ashkenazi, A. Death receptor signal transducers: nodes of coordination in immune signaling networks. *Nature Immunol.* **10**, 348–355 (2009).
- Kersse, K., Verspurten, J., Vanden Bergh, T. & Vandenabeele, P. The death-fold superfamily of homotypic interaction motifs. *Trends Biochem. Sci.* **36**, 541–552 (2011).
- Nadler, C. *et al.* The type III secretion effector NleE inhibits NF- κ B activation. *PLoS Pathog.* **6**, e1000743 (2010).
- Newton, H. J. *et al.* The type III effectors NleE and NleB from enteropathogenic *E. coli* and *OspZ* from *Shigella* block nuclear translocation of NF- κ B p65. *PLoS Pathog.* **6**, e1000898 (2010).
- Yen, H. *et al.* NleC, a type III secretion protease, compromises NF- κ B activation by targeting p65/RelA. *PLoS Pathog.* **6**, e1001231 (2010).
- Baruch, K. *et al.* Metalloprotease type III effectors that specifically cleave JNK and NF- κ B. *EMBO J.* **30**, 221–231 (2011).
- Mühlen, S., Ruchaud-Sparagano, M. H. & Kenny, B. Proteasome-independent degradation of canonical NF- κ B complex components by the NleC protein of pathogenic *Escherichia coli*. *J. Biol. Chem.* **286**, 5100–5107 (2011).
- Pearson, J. S., Riedmaier, P., Marches, O., Frankel, G. & Hartland, E. L. A type III effector protease NleC from enteropathogenic *Escherichia coli* targets NF- κ B for degradation. *Mol. Microbiol.* **80**, 219–230 (2011).

- Ruchaud-Sparagano, M. H., Mühlen, S., Dean, P. & Kenny, B. The enteropathogenic *E. coli* (EPEC) Tir effector inhibits NF- κ B activity by targeting TNF α receptor-associated factors. *PLoS Pathog.* **7**, e1002414 (2011).
- Yan, D., Wang, X., Luo, L., Cao, X. & Ge, B. Inhibition of TLR signaling by a bacterial protein containing immunoreceptor tyrosine-based inhibitory motifs. *Nature Immunol.* **13**, 1063–1071 (2012).
- Vossenköpfer, A. *et al.* Inhibition of NF- κ B signaling in human dendritic cells by the enteropathogenic *Escherichia coli* effector protein NleE. *J. Immunol.* **185**, 4118–4127 (2010).
- Zhang, L. *et al.* Cysteine methylation disrupts ubiquitin-chain sensing in NF- κ B activation. *Nature* **481**, 204–208 (2012).
- Kelly, M. *et al.* Essential role of the type III secretion system effector NleB in colonization of mice by *Citrobacter rodentium*. *Infect. Immun.* **74**, 2328–2337 (2006).
- Misyurina, O. *et al.* The role of Tir, EspA, and NleB in the colonization of cattle by Shiga toxin producing *Escherichia coli* O26:H11. *Can. J. Microbiol.* **56**, 739–747 (2010).
- Wickham, M. E. *et al.* Bacterial genetic determinants of non-O157 STEC outbreaks and hemolytic-uremic syndrome after infection. *J. Infect. Dis.* **194**, 819–827 (2006).
- Kujat Choy, S. L. *et al.* SseK1 and SseK2 are novel translocated proteins of *Salmonella enterica* serovar Typhimurium. *Infect. Immun.* **72**, 5115–5125 (2004).
- Lamkanfi, M. & Dixit, V. M. Manipulation of host cell death pathways during microbial infections. *Cell Host Microbe* **8**, 44–54 (2010).
- Aggarwal, B. B. Signalling pathways of the TNF superfamily: a double-edged sword. *Nature Rev. Immunol.* **3**, 745–756 (2003).
- Chen, N. J. *et al.* Beyond tumor necrosis factor receptor: TRADD signaling in toll-like receptors. *Proc. Natl Acad. Sci. USA* **105**, 12429–12434 (2008).
- Ermolaeva, M. A. *et al.* Function of TRADD in tumor necrosis factor receptor 1 signaling and in TRIF-dependent inflammatory responses. *Nature Immunol.* **9**, 1037–1046 (2008).
- Pobezinskaya, Y. L. *et al.* The function of TRADD in signaling through tumor necrosis factor receptor 1 and TRIF-dependent Toll-like receptors. *Nature Immunol.* **9**, 1047–1054 (2008).
- Park, H. H. *et al.* The death domain superfamily in intracellular signaling of apoptosis and inflammation. *Annu. Rev. Immunol.* **25**, 561–586 (2007).
- Hsu, H., Shu, H. B., Pan, M. G. & Goeddel, D. V. TRADD domain-TRAF2 and TRADD domain-FADD interactions define two distinct TNF receptor 1 signal transduction pathways. *Cell* **84**, 299–308 (1996).
- Belyi, Y. *et al.* *Legionella pneumophila* glucosyltransferase inhibits host elongation factor 1A. *Proc. Natl Acad. Sci. USA* **103**, 16953–16958 (2006).
- Lairson, L. L., Henrissat, B., Davies, G. J. & Withers, S. G. Glycosyltransferases: structures, functions, and mechanisms. *Annu. Rev. Biochem.* **77**, 521–555 (2008).
- Belyi, Y. & Aktories, K. Bacterial toxin and effector glycosyltransferases. *Biochim. Biophys. Acta* **1800**, 134–143 (2010).
- Gao, X. *et al.* NleB, a bacterial effector with glycosyltransferase activity, targets GAPDH function to inhibit NF- κ B activation. *Cell Host Microbe* **13**, 87–99 (2013).
- Love, D. C. & Hanover, J. A. The hexosamine signaling pathway: deciphering the “O-GlcNAc code”. *Sci. STKE* **2005**, re13 (2005).
- Hart, G. W., Slawson, C., Ramirez-Correa, G. & Lagerlof, O. Cross talk between O-GlcNAcylation and phosphorylation: roles in signaling, transcription, and chronic disease. *Annu. Rev. Biochem.* **80**, 825–858 (2011).
- Singh, D. G. *et al.* β -Glucosylarginine: a new glucose-protein bond in a self-glucosylating protein from sweet corn. *FEBS Lett.* **376**, 61–64 (1995).

Supplementary Information is available in the online version of the paper.

Acknowledgements We thank I. Rosenshine for providing *nleBE* deletion EPEC strains, H. Wu for the TNFR1/2 plasmid, K. Iwai for LUBAC antibodies, H. Sakurai for the p-TAK1 antibody, Z. Yang for yeast two-hybrid screen, L. Feng for synthesizing Ac₄GlcNAc-d₃, M. Dong for accessing the ETD instrument and X. Liu for assistance with mass spectrometry data analyses. We also thank members of the Shao laboratory for discussions and technical assistance. The research was supported in part by an International Early Career Scientist grant from the Howard Hughes Medical Institute to F.S. This work was also supported by the National Basic Research Program of China 973 Programs 2010CB835400 and 2012CB518700 to F.S. and 2010CB835204 to S.C.

Author Contributions S.L. and L.Z. performed most experiments, assisted by Q.Y., N.D. and W.G. L.L., X.D. and S.C. performed mass spectrometry analyses and S.C. analysed the data. L.S., J.R. and X.C. contributed reagents and analytic tools. S.L., L.Z. and F.S. analysed the data and wrote the manuscript. All authors discussed the results and commented on the manuscript.

Author Information Reprints and permissions information is available at www.nature.com/reprints. The authors declare no competing financial interests. Readers are welcome to comment on the online version of the paper. Correspondence and requests for materials should be addressed to S.C. (chenshe@nibs.ac.cn) or F.S. (shaofeng@nibs.ac.cn).

METHODS

Plasmid, antibodies and reagents. DNA for NleB and NleB homologue genes was amplified from genomic DNA of EPEC E2348/69, *C. rodentium* DBS100 and *S. enterica* Typhimurium LT2 strains, and inserted into pCS2-EGFP, pCS2-HA and pCDNA4-Flag-HA vectors for mammalian expression, and pGEX-6P-2, pET28a-LFn and pSUMO for expression in *E. coli*. NleB DNA was also ligated into the pTRC99A vector for complementation in EPEC (under the *trc* promoter) and pET28a for complementation in *C. rodentium* (under the *C. rodentium* NleB promoter). cDNAs for TRADD, RIPK1, TRAF2/5/6, IKK- $\alpha/\beta/\gamma$, TAK1, TAB2/3 and I κ B- α were amplified from a HeLa cDNA library as previously described^{12,31}. TRADD death domain refers to residue 195–312 of human TRADD. cDNAs for cIAP1/2 and TNFRI were gifts from X. Wang and H. Wu, respectively. cDNAs for FAS, FADD, IRAK1, GAPDH, MYD88 and OGT were amplified from human ultimate ORF clones (Invitrogen). For mammalian expression, cDNAs were cloned into pCS2-EGFP and pCS2-3Flag vectors. DNA encoding residues 31–624 of *O*-GlcNAcase was amplified from the *Clostridium perfringens* genome, and cloned into the pGEX6p-2 vector for recombinant expression. For yeast two-hybrid analysis, DNAs encoding NleB, TAK1 and NleE were cloned into the bait vector pGBKT7; cDNAs for TRADD, RIPK1, TRAF2/5, IKK- $\alpha/\beta/\gamma$, TAK1, TAB1, cIAP1/2 and FADD were cloned into the prey vector pGAD-GH. The yeast two-hybrid interaction assay was performed using the Matchmaker 2-hybrid system (Clontech) following the manufacturer's instruction. All single point mutations were generated by QuickChange site-directed mutagenesis kit (Stratagene), and multiple point mutations and truncation mutants were generated by standard molecular biology procedures. NF- κ B reporter plasmids were previously described³². Plasmids were prepared by GoldHi endofree plasmid maxi kit (CW2104, Beijing CoWin Bioscience) for transfection. All plasmids were verified by DNA sequencing.

Antibodies for I κ B- α (44D4, catalogue number 4812), p-I κ B- α (S32) (14D4, 2589), PARP (9542), caspase-8 (1C12, 9746, for immunoblotting) and caspase-3 (9662) were purchased from Cell Signaling Technology. Antibodies for GFP (sc-8334), p65 (sc-372), TNFRI (H271, sc-7895), TRAF2 (C-20, sc-876), TRAF6 (H274, sc-7221), haemagglutinin probe (Y-11, sc-805), caspase-8 (C-20, sc-6136, for immunoprecipitation), FADD (H-181, sc-5559) and TAK1 (sc-7162) were all from Santa Cruz Biotechnology. Antibodies for TRADD (610573) and RIPK1 (610459) were from BD Transduction Laboratories. Flag (M2), tubulin and actin antibodies were from Sigma. Horseradish peroxidase (HRP)-conjugated anti-biotin antibody was from Abcam (ab19221); p-TAK1 (Thr187) antibody was a gift from H. Sakurai; antibodies for HOIL-1L (2E2), HOIP (N1) and SHARPIN were provided by K. Iwai. Homemade SmacM compound was described previously³³. Caspase-8 peptide (FFIQACQGDNYQKGPVETD) was commercially synthesized (SciLight-Peptide). Cell culture products were from Invitrogen, all other reagents were Sigma unless noted.

Cell culture and luciferase reporter assay. 293T and HeLa cells obtained from the American Type Culture Collection (ATCC) and MEF cells from S. Ghosh were grown in DMEM (HyClone) supplemented with 10% FBS, 2 mM L-glutamine, 100 U ml⁻¹ penicillin and 100 mg ml⁻¹ streptomycin. HT-29 cells (ATCC) were maintained in McCoy's 5A media supplemented with 10% FBS and 2 mM L-glutamine. Cells were cultivated in a humidified atmosphere containing 5% CO₂ at 37 °C. Vigofect (Vigorus) was used for transfection following the manufacturer's instructions. Luciferase activity was determined 24 h after transfection by using the dual luciferase assay kit (Promega) according to the manufacturer's instructions. Detailed procedures were previously described^{31,32}. One-hour CHX pretreatment (1 μ g ml⁻¹) was used to sensitize TRAIL (200 ng ml⁻¹) and FAS antibody (1 μ g ml⁻¹) stimulation of apoptosis, and the concentration of CHX used for TNF- α (10 ng ml⁻¹) was 4 μ g ml⁻¹. SmacM (100 μ M) and z-VAD (20 μ M; Sigma) were used to induce necroptosis.

Stable cell-line construction. To generate NleB stable expression cells, empty pCDNA4 vector or pCDNA4-NleB plasmid was transfected into 293T cells. Forty-eight hours after transfection, cells were subcultured in the complete DMEM medium supplemented with 100 μ g ml⁻¹ zeocin (Invitrogen). Two-to-three weeks later, clones were lifted and tested for expression of the transgene. To generate TRADD stable knockdown cells, pLKO.1 or pLKO.1-shTRADD (TRC number TRCN0000008020, Sigma) was transfected into 293T cells. Forty-eight hours after transfection, cells were subcultured in the complete DMEM medium containing 1 μ g ml⁻¹ puromycin. Two-to-three weeks later, clones were lifted, the culture was expanded, and expression of endogenous TRADD was tested by immunoblotting analysis. The HeLa-RIP3 stable cell line used for TNF- α induction of necroptosis was generated as previously described^{33,34} and maintained in DMEM medium supplemented with 10% tetracycline-free FBS, 2 mM L-glutamine, 100 U ml⁻¹ penicillin, 100 mg ml⁻¹ streptomycin, 10 μ g ml⁻¹ blasticidin and 1 mg ml⁻¹ G418.

Immunoprecipitation and receptor complex pulldown. For co-immunoprecipitation, 293T cells at a confluency of 60–70% in 6-well plates were transfected

with a total of 5 μ g plasmids. Twenty-four hours after transfection, cells were washed once in PBS and lysed in buffer A containing 25 mM Tris-HCl, pH 7.6, 150 mM NaCl, 10% glycerol and 1% Triton X-100, supplemented with a protease inhibitor mixture (Roche Molecular Biochemicals). Pre-cleared lysates were subjected to anti-Flag M2 immunoprecipitation following the manufacturer's instructions. The beads were washed four times with lysis buffer and the immunoprecipitates were eluted by 2 \times SDS sample buffer followed by standard immunoblotting analysis. All the immunoprecipitation assays were performed more than three times and representative results are shown.

To purify death domains or death-domain-containing proteins for mass spectrometry, 293T cells overexpressing death domain or death-domain-containing proteins were collected in buffer B containing 50 mM Tris-HCl, pH 7.5, 150 mM NaCl, 20 mM *n*-octyl- β -D-glucopyranoside (INALCO) and 5% glycerol, supplemented with an EDTA-free protease inhibitor mixture (Roche Molecular Biochemicals). Cells were lysed by ultrasonication. The supernatant was pre-cleared by protein G-sepharose at 4 °C for 1 h and subjected to anti-Flag (M2) immunoprecipitation. After 4 h incubation, the beads were washed once with buffer B and then four times with TBS buffer (50 mM Tris-HCl, pH 7.5, and 150 mM NaCl). Bound proteins were eluted with 600 μ g ml⁻¹ Flag peptide (Sigma) in TBS buffer. The eluted protein was verified by Coomassie brilliant blue staining on an SDS-PAGE gel before mass spectrometry analysis.

For TNFR complex pulldown, HeLa cells were treated with 1 μ g ml⁻¹ recombinant GST-TNF- α for indicated lengths of time (for $t = 0$, GST-TNF- α was added after the cells were lysed). Cells were lysed in the GST pulldown buffer containing 25 mM Tris-HCl, pH 7.6, 150 mM NaCl, 25 mM β -glycerophosphate, 1 mM sodium orthovanadate, 10% glycerol, 0.5 mM dithiothreitol (DTT), 1 mM phenylmethylsulphonyl fluoride (PMSF) and 1% Triton X-100, supplemented with the protease inhibitor mixture. Total cell lysates were incubated with glutathione sepharose 4B beads and mixed at 4 °C for 4 h. The beads were washed once with PBS plus 1% Triton X-100, and twice with PBS plus 0.5% Triton X-100. Bead-bound proteins were analysed by immunoblotting using indicated antibodies. For DISC complex pulldown, HeLa cells infected with indicated EPEC strains were stimulated with 200 ng ml⁻¹ TRAIL for 2 h. Anti-caspase-8 immunoprecipitation was then performed according to published literatures with minor modifications^{35,36}. Cells were lysed in DISC immunoprecipitation buffer (50 mM Tris-HCl, pH 7.5, 150 mM NaCl, 10% glycerol and 1% Triton X-100) supplemented with 1% protease inhibitor, 10 mM NaF, 2 mM Na₃VO₄, 0.1 mM PMSF and 1 mM EDTA. Caspase-8 antibody (1.5 μ g) was coupled to 20 μ l protein G-sepharose in TBS (supplemented with 7 mg ml⁻¹ BSA). The pre-coupled sepharose was then washed and incubated with 2 mg of cell lysates overnight at 4 °C. Following extensive washes with DISC immunoprecipitation buffer (four times) and TBS (once), the immunocomplex were eluted using 40 μ l of TBS containing 1 mg ml⁻¹ caspase-8 peptide and 1% protease inhibitor at room temperature for 1 h. The eluted proteins were analysed by SDS-PAGE and immunoblotting.

Immunofluorescence. For immunofluorescence, rhodamine-phalloidin (Invitrogen) staining of actin in transfected HeLa cells or pedestal in EPEC-infected HeLa cells and p65 staining of NF- κ B activation in TNF- α -treated HeLa cells were performed as previously described^{31,37}.

Expression and purification of recombinant proteins. Protein expression was induced in *E. coli* BL21 (DE3) strain (Novagen) at 23 °C for 15 h with 0.4 mM isopropyl- β -D-thiogalactopyranoside (IPTG) after absorbance at 600 nm ($A_{600\text{nm}}$) reached 0.8–1.0. Affinity purification of GST-TRADD death domain or 6 \times His-SUMO-NleB and LFn-NleB proteins was performed using glutathione sepharose (GE Healthcare) and Ni-NTA agarose (Qiagen), respectively, following the manufacturer's instructions. GST-TRADD death domain was further purified by ion exchange chromatography and concentrated in a buffer containing 20 mM HEPES, pH 7.5, 150 mM NaCl and 5% glycerol.

Native PAGE. Blue native gel electrophoresis was performed to examine TRADD oligomerization using the NativePAGE Bis-Tris gel system from Invitrogen. In brief, Flag-TRADD was transfected into intact 293T or TRADD knockdown 293T cells for 24 h. Transfected cells were washed twice with cold PBS and lysed in 1% digitonin-containing native lysis buffer (50 mM Bis-Tris, pH 7.2, 50 mM NaCl, 10% (w/v) glycerol, 0.001% Ponceau S, 1% digitonin, 2 mM Na₃VO₄ and 25 mM NaF) supplemented with the EDTA-free protease inhibitor cocktail. Cell lysis was performed on ice for 30 min, and cell debris was removed by centrifugation (16,000g, 20 min) at 4 °C. Lysates were separated by NativePAGE using the Novex Bis-Tris gel system (Invitrogen). Native gels were soaked in 10% SDS for 5 min before transfer to PVDF membrane (Millipore) for immunoblotting analysis.

Chemoenzymatic labelling-based GlcNAcylation detection. To detect NleB GlcNAcylation of TRADD death domain in 293T cells, immunopurified TRADD death domain was chemoenzymatically labelled using the Click-iT O-GlcNAc enzymatic labelling system (Invitrogen) and GlcNAc modification was detected by Click-iT protein analysis detection kits (Invitrogen) following the manufacturer's

protocol. In brief, 1×10^8 293T cells were transfected with indicated plasmids and anti-Flag immunoprecipitation was carried out as described earlier. The immunoprecipitates (~200 µg) were eluted with 1% SDS in 20 mM HEPES, pH 7.9, at 95 °C for 5 min, and then subjected to UDP-GalNAz labelling using the mGalT1 enzyme (Tyr289Leu mutant of galactosyltransferase GalT1) and a biotinylated-alkyne/azide click chemistry conjugation. The GlcNAc modification was detected by immunoblotting analysis using an anti-biotin antibody.

In vitro ^3H -UDP-GlcNAc labelling. Flag-TRADD or other death domain proteins expressed in 293T cells were immunopurified and immobilized on the Flag M2 beads. The beads were incubated with 5 µg NleB for 2 h at 37 °C in 40 µl buffer containing 20 mM HEPES, pH 7.5, 100 mM KCl, 2 mM MgCl_2 , 1 mM MnCl_2 and 0.4 µCi (0.2 µM) of ^3H -UDP-GlcNAc (Perkin Elmer). The reaction mixtures were separated on a 12% SDS-PAGE gel followed by Coomassie blue staining. Incorporation of ^3H -UDP-GlcNAc was visualized by ^3H autoradiography. For the ligand competition, 10 µM cold UDP-activated sugars were included in the GlcNAcylation reaction.

Liquid chromatography-mass spectrometry analysis. *E. coli* or 293T-cell purified death domain proteins were loaded onto a homemade capillary column (150 µm ID, 3-cm long) packed with Poros R2 media (AB-Sciex), and eluted by an Agilent 1100 binary pump system with the following solvent gradient: 0–100% B in 60 min (A = 0.1 M acetic acid in water; B = 0.1 M acetic acid, 40% acetonitrile and 40% isopropanol). The eluted proteins were sprayed into a QSTAR XL mass spectrometer (AB-Sciex) equipped with a Turbo Electrospray ion source. The instrument was acquired in mass spectrometry mode under 5 K volts spray voltage. The protein charge envelop was averaged across the corresponding protein elution peaks, and de-convoluted into non-charged forms by the BioAnalyst software provided by the manufacturer.

MALDI-TOF mass spectrometry analysis of tryptic peptides. Purified GST-TRADD death domain proteins were in-solution cleaved by PreScission, and GST was depleted by glutathione sepharose 4B. TRADD death domain co-expressed with SUMO-NleB was completely soluble, whereas TRADD death domain expressed alone aggregated to some extent after PreScission cleavage. After centrifugation at 3,200g for 1 min to remove the beads, the supernatant containing TRADD death domain was digested with sequencing-grade modified trypsin (Promega) at 37 °C for at least 3 h in 50 mM ammonium bicarbonate. The digested peptide samples were analysed on an Autoflex II MALDI-TOF/TOF (matrix-assisted laser desorption/ionization-time of flight) mass spectrometer (Bruker) equipped with a nitrogen pulsed laser. In brief, equal volumes of the peptide samples and 2,5-dihydroxybenzoic acid solution (Agilent) were mixed together and spotted on a Bruker MTP 384 massive stainless steel MALDI target. The matrix spots were allowed to dry at room temperature and then washed on-target with 0.1% trifluoroacetic acid to remove salts and other water soluble contaminations. Peptide mass fingerprinting spectra were acquired in the positive reflector mode with pulsed ion extraction.

To identify GlcNAcylated arginine and arginine-containing peptides, the trypsin-digested TRADD death domain (modified by NleB in bacteria) was separated on an Agilent Ellipse C18 reversed phase column (4.6 × 150 mm) using the Agilent 1260 Infinity HPLC system. The HPLC gradient was as follows: 0–20% B in 10 min, 20–100% B in 20 min (solvent A = 10 mM ammonium acetate, solvent B = 10 mM ammonium acetate in 80% acetonitrile). The ultraviolet detector wavelength was 215 nm and the fractionation size was 300 µl. Peptides from each fraction were detected by MALDI-TOF on Autoflex II mass spectrometer. The HPLC fraction containing peptide with *m/z* matching 233-VGR-GlcNAc.SLQR-239 with GlcNAc modification was concentrated to ~50 µl and then digested with proteinase K (New England Biolabs) overnight at 37 °C. To obtain the single arginine with GlcNAc modification, the proteinase-K-treated peptides were digested further with carboxypeptidase A (Sigma) overnight at 37 °C. The digests were loaded into a nanoES emitter and sprayed directly into LTQ Orbitrap Velos mass spectrometer equipped with a nanoESI ion source. The dipeptide $\text{GR}_{\text{GlcNAc}}$ and the single arginine with a GlcNAc modification were manually selected for high-energy collision dissociation tandem mass analysis.

ETD-MS analysis of GlcNAc-modified peptides. To determine the exact GlcNAcylation site on TRADD proteins after NleB modification, purified TRADD death domain protein co-expressed with SUMO-NleB in *E. coli* was

trypsin digested and the resulting tryptic peptides were analysed on a LTQ Orbitrap XL mass spectrometer (Thermo Fisher) equipped with an ETD ion source and a nanoESI ion source. The peptide solution was loaded into a nanoES emitter and sprayed directly into the instrument. The peptides with *m/z* matched to calculated GlcNAc-modified TRADD peptides were manually selected for ETD fragmentation with a 2-Da mass selection window.

Stable isotope labelling. Isotope-labelled Ac_4GlcNAc (2-(acetyl- d_3 -amino)-2-deoxy-1,3,4,6-tetra-*O*-acetyl-D-glucopyranose) ($\text{Ac}_4\text{GlcNAc-}d_3$) was synthesized as previously described³⁸ and the spectroscopic data were consistent with that in the literature³⁸. 293T cells (5×10^8) were pretreated with 100 µM isotope-labelled $\text{Ac}_4\text{GlcNAc-}d_3$ for 12 h and transfected with Flag-TRADD death domain and NleB for another 12 h. Flag-TRADD death domain was immunopurified as that for mass spectrometry measurement of the total mass and prepared into the 50 mM NH_4HCO_3 , pH 8.0, buffer. Flag peptide was depleted with Flag M2 beads and the supernatant was subjected to trypsin digestion at 37 °C for 1 h. The resulting tryptic peptides were analysed by ETD as described earlier.

Mice infection and *C. rodentium* colonization assays. All animal experiments were conducted following the Ministry of Health national guidelines for housing and care of laboratory animals and performed in accordance with institutional regulations after review and approval by the Institutional Animal Care and Use Committee at National Institute of Biological Sciences. Male C57BL/6 mice, 5–6 weeks old, maintained in the specific pathogen-free environment were used. All animals were housed in individually high efficiency particulate air (HEPA)-filtered cages with sterile bedding. Mice were randomized into each experimental group with no blinding. Independent experiments were performed using 7–8 mice per group.

Deletion of the gene encoding NleBc in *C. rodentium* strain DBS100 (ATCC51459; ATCC) was generated by standard homologous recombination using the suicide vector pCVD442, as described previously³². The DNA of pNleBc was amplified by PCR from genomic DNA of DBS100 strain to include a putative upstream promoter sequence (~300 bp), using the forward primer 5'-TCAGGGCCGGCCGACTGG AACATATGCGGG-3' and reverse primer 5'-TGACGGCGCGCCTTACCATGA ACTGTTGGTATACATACTG-3'. For oral inoculation and harvesting, *C. rodentium* wild-type strain and represented derivatives were prepared by overnight shaking of bacterial culture at 37 °C in LB broth. Mice were orally inoculated using a gavage needle with 200 µl suspension of bacteria in PBS (~ 2×10^9 CFU). The number of viable bacteria used as the inoculum was determined by retrospective plating onto LB agar containing the appropriate antibiotics. Stool samples were recovered aseptically at various time points after inoculation, and the number of viable bacteria per gram of stool was determined after homogenization in PBS and plating onto LB agar containing the appropriate antibiotics. Eight days after inoculation, colons were removed aseptically, weighed and homogenized in PBS. Homogenates were serially diluted and plated to determine CFU counts. Colonization data were analysed using a Student's *t*-test in the commercial software GraphPad Prism. *P* < 0.05 was considered significant.

- Ge, J. *et al.* A *Legionella* type IV effector activates the NF-κB pathway by phosphorylating the IκB family of inhibitors. *Proc. Natl Acad. Sci. USA* **106**, 13725–13730 (2009).
- Li, H. *et al.* The phosphothreonine lyase activity of a bacterial type III effector family. *Science* **315**, 1000–1003 (2007).
- Sun, L. *et al.* Mixed lineage kinase domain-like protein mediates necrosis signaling downstream of RIP3 kinase. *Cell* **148**, 213–227 (2012).
- Wang, Z., Jiang, H., Chen, S., Du, F. & Wang, X. The mitochondrial phosphatase PGAM5 functions at the convergence point of multiple necrotic death pathways. *Cell* **148**, 228–243 (2012).
- Wang, G. *et al.* Small-molecule activation of the TRAIL receptor DR5 in human cancer cells. *Nature Chem. Biol.* **9**, 84–89 (2013).
- Wang, L., Du, F. & Wang, X. TNF-α induces two distinct caspase-8 activation pathways. *Cell* **133**, 693–703 (2008).
- Cui, J. *et al.* Glutamine deamidation and dysfunction of ubiquitin/NEDD8 induced by a bacterial effector family. *Science* **329**, 1215–1218 (2010).
- Horton, D., Hughes, J. B., Jewell, J. S., Phillips, K. D. & Turner, W. N. Anomeric equilibria in derivatives of amino sugars. Nuclear magnetic resonance studies on acetylated amino sugars and specifically deuterated analogs. *J. Org. Chem.* **32**, 1073–1080 (1967).

A type III effector antagonizes death receptor signalling during bacterial gut infection

Jaclyn S. Pearson¹, Cristina Giogha¹, Sze Ying Ong¹, Catherine L. Kennedy¹, Michelle Kelly¹, Keith S. Robinson², Tania Wong Fok Lung¹, Ashley Mansell³, Patrice Riedmaier¹, Clare V. L. Oates¹, Ali Zaid¹, Sabrina Mühlen¹, Valerie F. Crepin², Olivier Marches⁴, Ching-Seng Ang⁵, Nicholas A. Williamson⁵, Lorraine A. O'Reilly^{6,7}, Aleksandra Bankovacki⁶, Ueli Nachbur⁶, Giuseppe Infusini⁶, Andrew I. Webb^{6,7}, John Silke^{6,7}, Andreas Strasser^{6,7}, Gad Frankel² & Elizabeth L. Hartland^{1,8}

Successful infection by enteric bacterial pathogens depends on the ability of the bacteria to colonize the gut, replicate in host tissues and disseminate to other hosts. Pathogens such as *Salmonella*, *Shigella* and enteropathogenic and enterohaemorrhagic (EPEC and EHEC, respectively) *Escherichia coli* use a type III secretion system (T3SS) to deliver virulence effector proteins into host cells during infection that promote colonization and interfere with antimicrobial host responses^{1–3}. Here we report that the T3SS effector NleB1 from EPEC binds to host cell death-domain-containing proteins and thereby inhibits death receptor signalling. Protein interaction studies identified FADD, TRADD and RIPK1 as binding partners of NleB1. NleB1 expressed ectopically or injected by the bacterial T3SS prevented Fas ligand or TNF-induced formation of the canonical death-inducing signalling complex (DISC) and proteolytic activation of caspase-8, an essential step in death-receptor-induced apoptosis. This inhibition depended on the *N*-acetylglucosamine transferase activity of NleB1, which specifically modified Arg 117 in the death domain of FADD. The importance of the death receptor apoptotic pathway to host defence was demonstrated using mice deficient in the FAS signalling pathway, which showed delayed clearance of the EPEC-like mouse pathogen *Citrobacter rodentium* and reversion to virulence of an *nleB* mutant. The activity of NleB suggests that EPEC and other attaching and effacing pathogens antagonize death-receptor-induced apoptosis of infected cells, thereby blocking a major antimicrobial host response.

Members of the death receptor family such as FAS and TNFR1 contain an intracellular death domain and require caspase-8 for the activation of effector caspases and consequent cell death by the extrinsic apoptotic pathway^{4,5}. Within seconds of engagement by Fas ligand (FasL), pre-associated FAS trimers undergo multimerization and recruit the death-domain-containing adaptor protein FADD through heterotypic death domain interactions⁶. FADD then recruits pro-caspase-8 forming the death-inducing signalling complex (DISC), whereupon caspase-8 undergoes conformational change, auto-proteolytic processing and release from the DISC to allow cleavage of cytosolic substrates, including pro-caspase-3 and Bid⁷. Similarly, upon stimulation by TNF, TNFR1 recruits the adaptor protein TRADD and the receptor kinase, RIPK1, leading to NF- κ B activation. Alternatively, cell death may be induced through TNFR1 internalisation and formation of a secondary complex that contains TRADD/RIPK1/FADD and caspase-8 (refs 6, 7).

Previously, we reported that the EPEC T3SS effector NleB1 inhibited I κ B degradation in cells upon stimulation with TNF but not IL-1 β , suggesting that NleB1 interfered with death receptor signalling⁸. To identify host cell binding partners of NleB1, we screened a yeast two-hybrid complementary DNA (cDNA) library derived from HeLa cells using NleB1 as bait. FADD and RIPK1, were recovered several times.

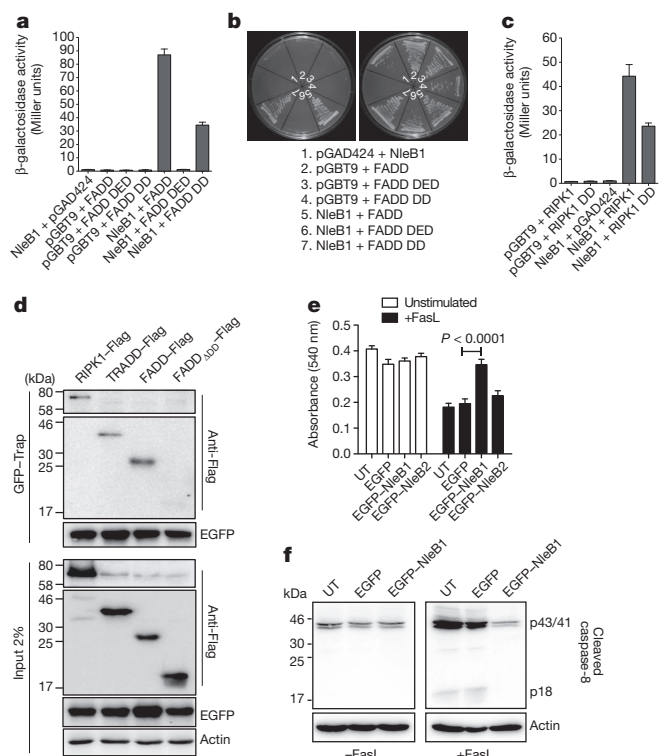


Figure 1 | NleB1 binds death domain proteins and inhibits caspase-8 activation. **a**, Yeast two-hybrid analysis of protein–protein interactions in *S. cerevisiae* PJ69-4A. Results are mean \pm s.e.m. β -galactosidase activity from at least three independent experiments performed in triplicate. DD, death domain; DED, death effector domain. **b**, Growth of *S. cerevisiae* PJ69-4A on medium to select for protein–protein interactions (left panel) or plasmid maintenance (right panel). Representative images from at least three independent experiments. **c**, Yeast two-hybrid analysis of protein interactions in *S. cerevisiae* PJ69-4A. Results are mean \pm s.e.m. β -galactosidase activity from at least three independent experiments performed in triplicate. **d**, GFP-Trap of EGFP–NleB1 and detection of FADD–Flag, TRADD–Flag and RIPK1–Flag in HEK293T cells. Actin, loading control. Representative immunoblot from at least three independent experiments. **e**, MTT reduction in HeLa cells expressing EGFP, EGFP–NleB1 or EGFP–NleB2. UT, untransfected. Results are the mean \pm s.e.m. of absorbance at 540 nm from three independent experiments performed in triplicate. * $P < 0.0001$, unpaired, two-tailed *t*-test. **f**, Cleaved caspase-8 in HeLa cells expressing EGFP or EGFP–NleB1. p43/41 and p18 are products of processed caspase-8. UT, untransfected. Representative immunoblot from at least three independent experiments.

¹Department of Microbiology and Immunology, University of Melbourne, Victoria 3010, Australia. ²MRC Centre for Molecular Bacteriology and Infection, Department of Life Sciences, Imperial College, London SW7 2AZ, UK. ³Centre for Innate Immunity and Infectious Diseases, Monash Institute of Medical Research, Victoria 3010, Australia. ⁴Centre for Immunology and Infectious Disease, Blizard Institute, Barts and The London School of Medicine and Dentistry, Queen Mary University of London, London E1 2AT, UK. ⁵Bio21 Molecular Science and Biotechnology Institute, University of Melbourne, Victoria 3010, Australia. ⁶The Walter and Eliza Hall Institute of Medical Research, Parkville, Victoria 3052, Australia. ⁷Department of Medical Biology, University of Melbourne, Victoria 3010, Australia. ⁸Murdoch Children's Research Institute, Royal Children's Hospital, Parkville, Victoria 3052, Australia.

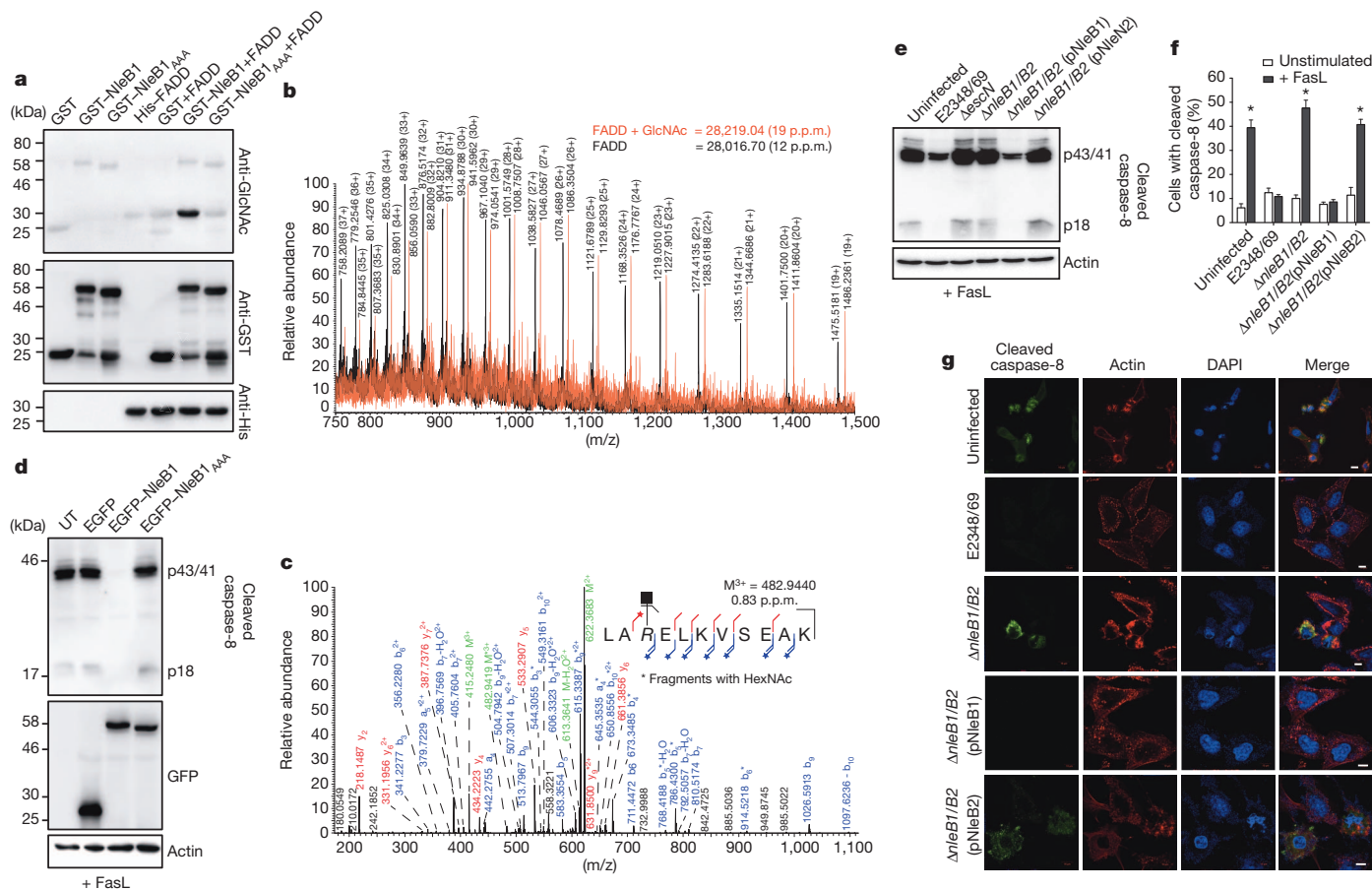


Figure 2 | Enzymatic activity of NleB1. **a**, *In vitro* assay for NleB1 N-acetylglucosamine (GlcNAc) modification of FADD using recombinant proteins and 1 mM UDP-GlcNAc. Representative immunoblot from at least three independent experiments. **b**, Intact protein mass spectrometry of FADD incubated with GST-NleB1 and UDP-GlcNAc. **c**, High resolution collision-induced dissociation (CID) spectrum of the peptide corresponding to FADD¹¹⁵⁻¹²⁵. The * denotes diagnostic fragment ions that carry the GlcNAc modification. **d**, Cleaved caspase-8 in FasL-treated HeLa cells expressing EGFP, EGFP-NleB1 or EGFP-NleB1^{AAA}. UT, untransfected. Actin; loading control. Representative immunoblot from at least three independent experiments. **e**, Cleaved caspase-8 in HeLa cells infected with derivatives of EPEC and treated

Transformation into a different yeast strain demonstrated that the interaction of NleB1 with FADD and RIPK1 occurred through their respective death domains (Fig. 1a–c). Studies in transfected HEK293T cells showed that FADD-Flag, TRADD-Flag and RIPK1-Flag co-purified with an EGFP-NleB1 (EGFP, enhanced green fluorescent protein) fusion protein as well as a 2HA-tagged NleB1 translocated during EPEC E2348/69 infection (Fig. 1d and Extended Data Fig. 1a, b). The death domain of FADD was required for binding to NleB1 from different attaching and effacing pathogens (Fig. 1d and Extended Data Fig. 1b). As TRADD and RIPK1 are critical components of the TNFR1 signalling complex, we investigated the influence of NleB1 on inhibition of the NF- κ B dependent cytokine, IL-8, during EPEC infection. Unlike NleE, a known inhibitor of NF- κ B activation^{8,9}, neither NleB1 nor its close homologue NleB2 appeared to inhibit IL-8 production during EPEC infection (Extended Data Fig. 1c). Therefore we focused our attention on FADD-dependent apoptosis signalling. After treatment with FasL, HeLa cells transfected with pEGFP-NleB1 showed significantly higher levels of MTT (3-(4,5-dimethylthiazol-2-yl)-2,5-diphenyltetrazolium bromide) reduction (mitochondrial activity assay) compared to pEGFP transfected cells (Fig. 1e), suggesting that NleB1 blocked cell death. Immunoblot analysis with an antibody that recognizes only cleaved caspase-8, revealed that FasL-induced

with FasL. Representative immunoblot from at least three independent experiments. pNleB1, pTrc99A carrying *nleB1*. pNleB2, pTrc99A carrying *nleB2*. **f**, Quantification of cleaved caspase-8 by immunofluorescence microscopy of HeLa cells infected with derivatives of EPEC and treated with FasL. Results are mean \pm s.e.m. of the percentage of cells with cleaved caspase-8 from two independent experiments counting \sim 200 cells in triplicate. * $P < 0.0001$ compared to uninfected, unstimulated control, one-way ANOVA. **g**, Immunofluorescence staining for detection of cleaved caspase-8 induced by FasL in HeLa cells infected with derivatives of EPEC. Scale bar, 10 μ m. Representative images are shown from at least three independent experiments.

caspase-8 cleavage was substantially reduced in HeLa cells transfected with pEGFP-NleB1 (Fig. 1f). By immunofluorescence microscopy, fewer cells expressing EGFP-NleB1 contained cleaved caspase-8 after treatment with FasL (Extended Data Fig. 1d, e). In contrast, a comparable number of cells contained cleaved caspase-3 in untransfected, EGFP and EGFP-NleB1 expressing cells treated with tunicamycin (Extended Data Fig. 1e). This indicated that NleB1 had no effect on activation of the intrinsic apoptotic pathway.

NleB from the murine attaching and effacing pathogen *C. rodentium* was recently described as an N-acetylglucosamine (GlcNAc) transferase and a member of the glycogenin family of enzymes¹⁰. Given the ability of NleB1 to bind FADD and inhibit proteolytic activation of caspase-8, we examined whether FADD was post-translationally modified by NleB1. Following incubation with GST-NleB1 and UDP-GlcNAc, we observed GlcNAc modification of His-FADD (Fig. 2a). This modification was not present upon incubation with an NleB1 catalytic site mutant (NleB1^{AAA})¹⁰. Similar modification of FADD-Flag occurred upon ectopic expression of EGFP-NleB1 in HeLa cells (Extended Data Fig. 1f). Intact protein liquid chromatography-mass spectrometry (LC-MS) of His-FADD incubated with GST-NleB1 and UDP-GlcNAc revealed a mass shift matching a single GlcNAc modification on FADD (Fig. 2b). Peptide sequencing of multiple spectra

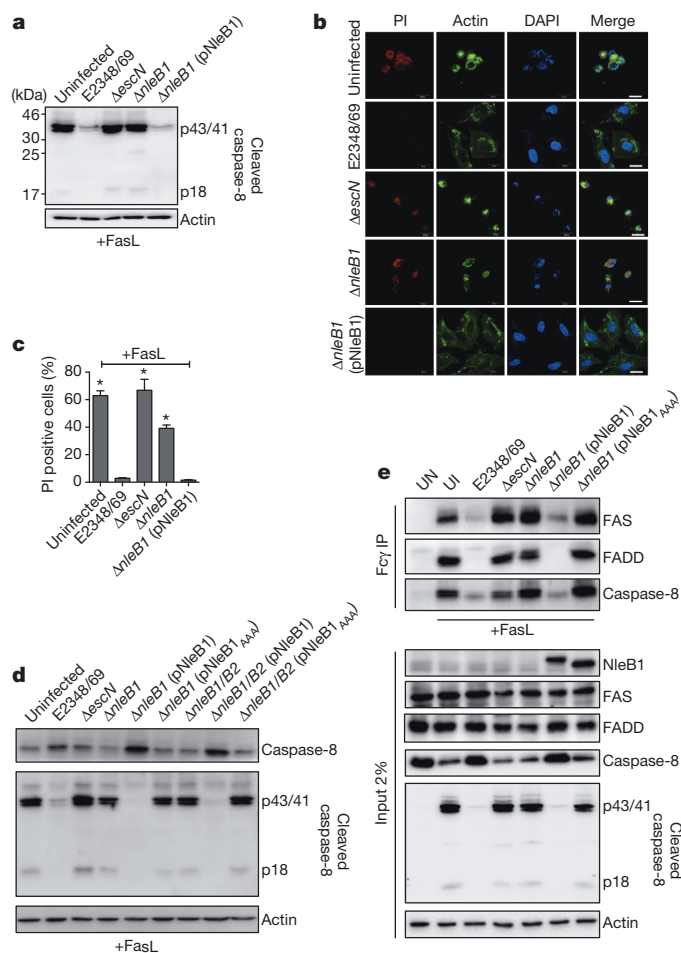


Figure 3 | Inhibition of FasL-induced DISC formation and cell death by EPEC. **a**, Cleaved caspase-8 in HeLa cells infected with derivatives of EPEC. Actin; loading control. Representative immunoblot from at least three independent experiments. **b**, Cell death visualized by propidium iodide (PI) staining in HeLa cells infected with derivatives of EPEC and treated with FasL. Scale bar, 20 μ m. Representative images shown from at least three independent experiments. **c**, Quantification of PI staining and microscopic analysis in HeLa cells infected with derivatives of EPEC and treated with FasL. Results are mean \pm s.e.m. of percentage cells with PI staining from two independent experiments counting ~ 200 cells in triplicate. * $P < 0.0001$ compared to E2348/69 infected cells, one-way ANOVA. **d**, Cleaved and full-length caspase-8 in HeLa cells infected with derivatives of EPEC and treated with FasL. Representative immunoblot from at least three independent experiments. **e**, DISC components induced by FasL coupled to Fc γ and precipitated with protein G beads. UN, untreated and uninfected; UI, uninfected. Representative immunoblot from at least three independent experiments.

from in-gel digests unambiguously identified Arg 117 as the site of *N*-acetylglucosylation (Fig. 2c, Extended Data Figs 2–3, Supplementary Table 1). This was confirmed by substitution of Arg 117 in FADD with alanine, whereas alanine substitution at Ser 122 had no effect on NleB-mediated *N*-acetylglucosylation (Extended Data Fig. 4). Arg 117 is located at the interface of the FAS–FADD death domain interaction and is critical for assembly of the FAS–FADD oligomeric complex and formation of the DISC^{11,12}. Accordingly, EGFP–NleB1 but not catalytically inactive EGFP–NleB1_{AAA} inhibited caspase-8 activation (Fig. 2d).

During infection, NleB1 delivered by the EPEC T3SS inhibited FasL-induced caspase-8 activation in HeLa cells. This inhibition was lost in cells infected with an Δ escN mutant that has a non-functional T3SS, or an Δ nleB1/B2 double mutant (Fig. 2e–g). Complementation of the Δ nleB1/B2 mutant with *nleB1* but not *nleB2* restored the ability of EPEC to inhibit caspase-8 activation (Fig. 2e–g), demonstrating that the two NleB proteins have distinct functions. This mirrored our protein

interaction studies, which showed that NleB2 did not interact with FADD or TRADD and bound only weakly to RIPK1 (Extended Data Fig. 5a–d).

Arg 117 in FADD is essential for FAS–FADD and TRADD–FADD death domain interactions^{11,12}. Consistent with the role of NleB1 in inhibition of FADD-dependent caspase-8 activation, an *nleB1* mutant was unable to inhibit FasL- or TNF-induced activation of caspase-8 whereas the complemented strain was as effective as wild-type EPEC (Fig. 3a and Extended Data Fig. 5e, f). EPEC expressing NleB1 also inhibited FasL-induced apoptosis as measured by propidium iodide (PI) staining (Fig. 3b, c). These phenotypes were not due to differences in adherence (Extended Data Fig. 5g).

NleB1 *N*-acetylglucosamine transferase activity was required for inhibition of FasL-induced caspase-8 processing during infection (Fig. 3d). To examine the influence of NleB1 on FAS DISC assembly, which precedes caspase-8 activation, we immunoprecipitated the FAS receptor complex from infected HeLa cells treated with FasL (Fig. 3e). Prior infection of cells with EPEC substantially inhibited FasL-induced DISC formation and this required NleB1 *N*-acetylglucosamine transferase activity (Fig. 3e).

We next examined the effect of NleB on inhibition of caspase-8 processing *in vivo* by infecting wild-type C57BL/6 mice with *C. rodentium* or a Δ nleB mutant of *C. rodentium* and staining tissue sections for cleaved caspase-8. Although few cells were positive for cleaved caspase-8 during *C. rodentium* infection, significant numbers of cells were positive for cleaved caspase-8 during infection with the Δ nleB mutant (Fig. 4a). Many of these caspase-8 positive cells were present as sloughed cells in the gut lumen (Extended Data Fig. 6a).

The observation that NleB1 inhibited FasL-induced caspase-8 cleavage suggested that FAS-mediated apoptosis contributes to host defence against attaching and effacing pathogens. We tested this by infecting FAS-deficient *Fas*^{lpr/lpr} mutant mice with *C. rodentium*¹³. As shown previously, *nleB* was essential for efficient colonization of wild-type C57BL/6 mice¹⁴ (Fig. 4b). Although there was no difference in faecal shedding of *C. rodentium* between C57BL/6 and *Fas*^{lpr/lpr} mice during the acute phase of infection (first 12 days) (Fig. 4b), *Fas*^{lpr/lpr} mice developed severe, watery diarrhoea (Fig. 4c). In addition, *C. rodentium* penetrated the crypts in *Fas*^{lpr/lpr} mice, unlike in C57BL/6 mice in which the bacteria were predominantly located at the tips of the villi (Fig. 4d). To study the resolving phase of infection (post day 12), C57BL/6 and *Fas*^{lpr/lpr} mice were infected with a lower dose of *C. rodentium* to avoid the rapid onset of severe diarrhoea and monitored for up to 33 days. *Fas*^{lpr/lpr} mice were impaired in their ability to clear *C. rodentium* compared to C57BL/6 mice (Fig. 4e and Extended Data Fig. 6b).

The development of severe diarrhoea in *C. rodentium*-infected *Fas*^{lpr/lpr} mice was unexpected and sections of colon from mice infected with *C. rodentium* for 10 days were examined to identify differences in pathology between *Fas*^{lpr/lpr} mice and C57BL/6 mice. Histological analysis of colons from *Fas*^{lpr/lpr} mice revealed greater erosion of the epithelium (tissue damage) as well as increased colon weight and crypt height compared to C57BL/6 mice (measures of *C. rodentium* induced intestinal hyperplasia¹⁴) (Extended Data Fig. 7a–d). In addition, *Fas*^{lpr/lpr} mice showed more pronounced neutrophil infiltration, which penetrated across the muscularis mucosa (Extended Data Fig. 7e). Similar phenotypes were observed in FasL-deficient *Fas*^{gld/gld} mice and Bid-deficient mice (Fig. 4d, e and Extended Data Fig. 8). Bid is not required for FasL-induced apoptosis in lymphoid cells, but is required for FasL-induced apoptosis in several other cell types^{15,16}. This suggests that FAS signalling in epithelial cells rather than lymphoid cells limits *C. rodentium*-induced colitis.

We reasoned that if NleB interfered with FAS-mediated apoptosis signalling during infection, then *C. rodentium* Δ nleB mutant bacteria would no longer be attenuated in mice that carry defects in this apoptosis pathway. Indeed, *Fas*^{lpr/lpr} mice infected with the Δ nleB mutant showed comparable levels of bacterial colonization and severity of diarrhoea compared to their littermates infected with *C. rodentium* (Extended

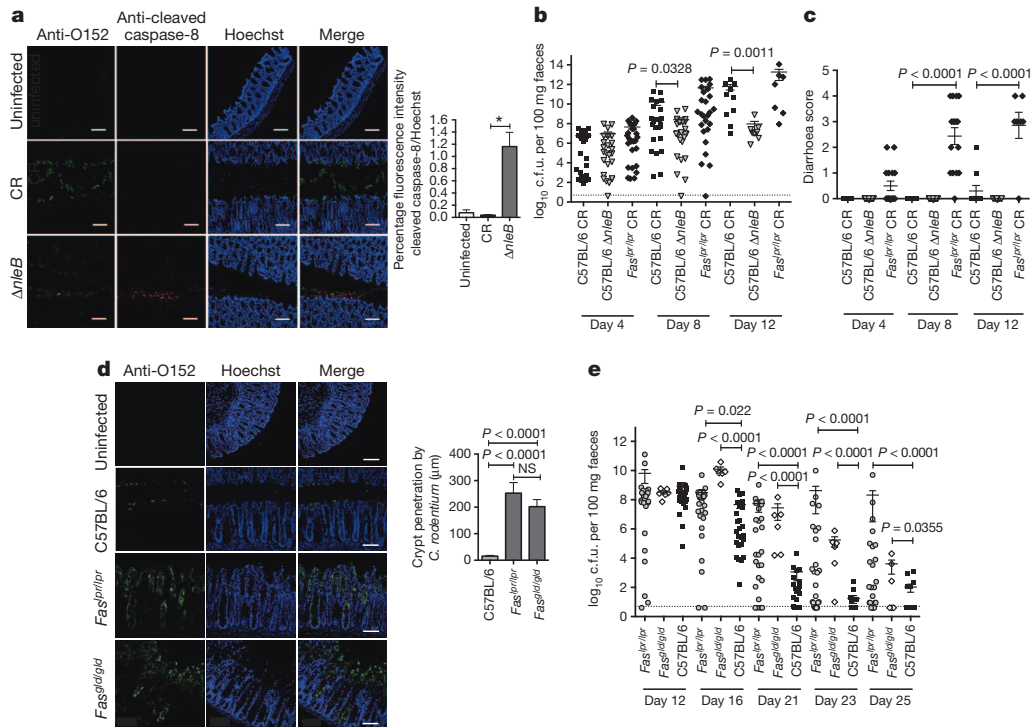


Figure 4 | Infection of mice deficient for FAS signalling with *C. rodentium*.

a, Immunofluorescence staining and quantification of cleaved caspase-8 in colonic sections from C57BL/6 mice infected with *C. rodentium* (CR) or a *C. rodentium nleB* mutant. Representative images from at least three separate sections of colon at least 100 μm apart (transverse or longitudinal), per animal from five individual mice per group. Results are mean \pm s.e.m. of percentage fluorescence intensity of cleaved caspase-8 staining relative to Hoechst staining of five fields with *C. rodentium* infection from three mice per group.

* $P = 0.0001$, unpaired two-tailed *t*-test. **b**, Bacterial load in the faeces during acute infection with *C. rodentium*. Each data point represents \log_{10} c.f.u. per 100 mg faeces per individual animal on days 4, 8 and 12 after infection (c.f.u., colony forming units). Mean \pm s.e.m. are indicated, dotted line represents the detection limit. *P* values from Mann–Whitney *U*-test. **c**, Diarrhoea score at day 4, 8 and 12 post-infection. The scoring system is described in the Methods.

Data Figs 6b and 9a, b). The same was not true for $\Delta espI$ or $\Delta espF$ mutants of *C. rodentium*, which retained their known colonization defects in $Fas^{lpr/lpr}$ mice (Extended Data Fig. 9c, d)^{17,18}. EspI and EspF are T3SS effector proteins with functions unrelated to NleB1 and the inhibition of FAS signalling.

During infection with attaching and effacing pathogens, the predominant site of NleB activity is in enterocytes where the translocation of bacterial effector proteins occurs¹. NleB-mediated inhibition of FasL/FAS-induced apoptosis may prolong bacterial attachment to host cells and thereby promote bacterial shedding in the faeces. Indeed NleB is associated with the transmission of *C. rodentium* amongst littermates¹⁹ and is epidemiologically associated with outbreaks of haemolytic uraemic syndrome caused by EHEC^{20,21}. Conversely, the reduced colonization of C57BL/6 mice by *C. rodentium* $\Delta nleB$ mutants and increased numbers of activated caspase-8 positive cells may reflect partial protection by the FAS apoptotic pathway through the elimination of infected cells¹⁴. This is consistent with the prolonged shedding of *C. rodentium* in FAS-deficient animals compared to C57BL/6 mice. The increased intestinal pathology observed in *C. rodentium*-infected FAS-, FasL- and Bid-deficient mice has also revealed a function for the FAS apoptotic pathway in limiting the extent of colitis during gastrointestinal infection. This aggravation of disease may be mirrored in humans, as nucleotide polymorphisms in the *FASLG* gene, encoding FasL, have been associated with the development of inflammatory bowel disease²². In summary, the discovery of a bacterial T3SS effector that specifically modifies death domain containing proteins through a

Mean \pm s.e.m. are indicated. *P* values from one-way ANOVA.

d, Immunofluorescence staining and quantification of *C. rodentium* penetration into intestinal crypts in colonic sections from C57BL/6, $Fas^{lpr/lpr}$ and $Fas^{gld/gld}$ mice. Representative images from at least two separate sections of colon at least 100 μm apart (transverse or longitudinal), per animal from five individual mice per group. Results are the mean \pm s.e.m. maximum distance of *C. rodentium* staining from the epithelial surface (in μm) of five independent sections with at least three measurements per section. $P = 0.0001$, unpaired two-tailed *t*-test. **e**, Bacterial load in the faeces during the resolving phase of *C. rodentium* infection. Each data point represents \log_{10} c.f.u. per 100 mg faeces per individual animal on days 12, 16, 21, 23 and 25 post-infection. Mean \pm s.e.m. are indicated, dotted line represents detection limit. *P* values from Mann–Whitney *U*-test. Scale bars, 100 μm .

newly identified post-translational modification and thereby inhibits death receptor mediated apoptosis has revealed a new virulence mechanism in bacterial infection.

METHODS SUMMARY

Detailed information including bacterial mutant construction, immunofluorescence, immunoblot details, mouse infections, histology and pathology scoring, imaging and image analysis, and associated references are included in the Methods. Protein interaction assays were investigated using the yeast two-hybrid system and co-immunoprecipitation. Activation of caspase-8 was assessed by immunoblot and immunofluorescence microscopy using antibodies specific for cleaved caspase-8. Cell death was examined by MTT reduction and propidium iodide staining. Post-translational modifications of FADD were identified by intact protein mass spectrometry and collision-induced dissociation (CID) and electron transfer dissociation (ETD) peptide fragmentation. All genetically modified and spontaneous mutant mice are on a C57BL/6 background and all animals were inoculated by oral gavage with 200 μl containing approximately 1×10^9 or 1×10^8 c.f.u. of *C. rodentium*. All animal experimentation was approved by the University of Melbourne Animal Ethics Committee, applications 0808209 and 1112062.

Online Content Any additional Methods, Extended Data display items and Source Data are available in the online version of the paper; references unique to these sections appear only in the online paper.

Received 8 April; accepted 2 August 2013.

- Wong, A. R. *et al.* Enteropathogenic and enterohaemorrhagic *Escherichia coli*: even more subversive elements. *Mol. Microbiol.* **80**, 1420–1438 (2011).

2. Srikanth, C. V., Mercado-Lubo, R., Hallstrom, K. & McCormick, B. A. *Salmonella* effector proteins and host-cell responses. *Cell. Mol. Life Sci.* **68**, 3687–3697 (2011).
3. Ashida, H. *et al.* *Shigella* deploy multiple countermeasures against host innate immune responses. *Curr. Opin. Microbiol.* **14**, 16–23 (2011).
4. Park, H. H. *et al.* The death domain superfamily in intracellular signaling of apoptosis and inflammation. *Annu. Rev. Immunol.* **25**, 561–586 (2007).
5. Strasser, A., Jost, P. J. & Nagata, S. The many roles of FAS receptor signaling in the immune system. *Immunity* **30**, 180–192 (2009).
6. Schneider-Brachert, W. *et al.* Compartmentalization of TNF receptor 1 signaling: internalized TNF receptosomes as death signaling vesicles. *Immunity* **21**, 415–428 (2004).
7. Micheau, O. & Tschopp, J. Induction of TNF receptor I-mediated apoptosis via two sequential signaling complexes. *Cell* **114**, 181–190 (2003).
8. Newton, H. J. *et al.* The type III effectors NleE and NleB from enteropathogenic *E. coli* and OspZ from *Shigella* block nuclear translocation of NF- κ B p65. *PLoS Pathog.* **6**, e1000898 (2010).
9. Zhang, L. *et al.* Cysteine methylation disrupts ubiquitin-chain sensing in NF- κ B activation. *Nature* **481**, 204–208 (2012).
10. Gao, X. *et al.* NleB, a bacterial effector with glycosyltransferase activity, targets GAPDH function to inhibit NF- κ B activation. *Cell Host Microbe* **13**, 87–99 (2013).
11. Imtiyaz, H. Z., Zhang, Y. & Zhang, J. Structural requirements for signal-induced target binding of FADD determined by functional reconstitution of FADD deficiency. *J. Biol. Chem.* **280**, 31360–31367 (2005).
12. Wang, L. *et al.* The Fas–FADD death domain complex structure reveals the basis of DISC assembly and disease mutations. *Nature Struct. Mol. Biol.* **17**, 1324–1329 (2010).
13. Strasser, A., Harris, A. W., Huang, D. C., Krammer, P. H. & Cory, S. Bcl-2 and Fas/APO-1 regulate distinct pathways to lymphocyte apoptosis. *EMBO J.* **14**, 6136–6147 (1995).
14. Kelly, M. *et al.* Essential role of the type III secretion system effector NleB in colonization of mice by *Citrobacter rodentium*. *Infect. Immun.* **74**, 2328–2337 (2006).
15. Jost, P. J. *et al.* XIAP discriminates between type I and type II FAS-induced apoptosis. *Nature* **460**, 1035–1039 (2009).
16. Kaufmann, T. *et al.* The BH3-only protein bid is dispensable for DNA damage- and replicative stress-induced apoptosis or cell-cycle arrest. *Cell* **129**, 423–433 (2007).
17. Mundy, R. *et al.* Identification of a novel *Citrobacter rodentium* type III secreted protein, EspI, and roles of this and other secreted proteins in infection. *Infect. Immun.* **72**, 2288–2302 (2004).
18. Deng, W. *et al.* Dissecting virulence: systematic and functional analyses of a pathogenicity island. *Proc. Natl Acad. Sci. USA* **101**, 3597–3602 (2004).
19. Wickham, M. E., Brown, N. F., Boyle, E. C., Coombes, B. K. & Finlay, B. B. Virulence is positively selected by transmission success between mammalian hosts. *Curr. Biol.* **17**, 783–788 (2007).
20. Wickham, M. E. *et al.* Bacterial genetic determinants of non-O157 STEC outbreaks and hemolytic-uremic syndrome after infection. *J. Infect. Dis.* **194**, 819–827 (2006).
21. Karmali, M. A. *et al.* Association of genomic O island 122 of *Escherichia coli* EDL 933 with verocytotoxin-producing *Escherichia coli* seropathotypes that are linked to epidemic and/or serious disease. *J. Clin. Microbiol.* **41**, 4930–4940 (2003).
22. Jostins, L. *et al.* Host–microbe interactions have shaped the genetic architecture of inflammatory bowel disease. *Nature* **491**, 119–124 (2012).

Supplementary Information is available in the online version of the paper.

Acknowledgements We gratefully acknowledge P. Bouillet for the gift of *Bid*^{−/−} mice and T. Cumming for assistance with animal work. This work was supported by the Australian National Health and Medical Research Council (Program Grant no.606788 to E.L.H., Project Grants no.637332, no.1009145 to A.S., no.1009145 to L.O.R., Australia Fellowship to A.S.), the Wellcome Trust to G.F., the Juvenile Diabetes Foundation; the Leukaemia and the Lymphoma Society (New York; SCOR grant no.7413) to A.S. E.L.H. was supported by an Australian Research Council Future Fellowship. J.S.P., M.K., T.W., C.G. and P.R. were supported by Australian Postgraduate Awards. This work was made possible through Victorian State Government Operational Infrastructure Support and Australian Government NHMRC IRISS.

Author Contributions J.S.P., C.G., S.Y.O., C.L.K., M.K., K.S.R., T.W.F.L., P.R., C.V.O. and A.B. designed and performed the experiments. V.F.C. and O.M. generated reagents. C.S.A., N.A.W., G.I. and A.I.W. performed mass spectrometry analyses. L.A.O., A.Z., S.M., U.N., A.M., A.S., J.S., G.F., J.S.P. and E.L.H. contributed to experimental design. J.S.P., A.S., J.S., G.F. and E.L.H. wrote the manuscript.

Author Information Reprints and permissions information is available at www.nature.com/reprints. The authors declare no competing financial interests. Readers are welcome to comment on the online version of the paper. Correspondence and requests for materials should be addressed to E.L.H. (hartland@unimelb.edu.au).

METHODS

Bacterial strains, plasmids, yeast strains and growth conditions. The bacterial strains, yeast strains and plasmids used in this study are listed in Supplementary Table 2. All PCR primers are listed in Supplementary Table 3. Bacteria were grown at 37 °C in Luria–Bertani (LB) medium or Dulbecco's modified Eagle's medium (DMEM) (Gibco) where indicated and supplemented with ampicillin (100 µg ml⁻¹), kanamycin (100 µg ml⁻¹), nalidixic acid (50 µg ml⁻¹) or chloramphenicol (25 µg ml⁻¹) when necessary. Yeast strains were grown at 30 °C in YPD (yeast extract/peptone/dextrose) medium or yeast nitrogen minimal medium supplemented with 2% glucose and amino acids including histidine (20 µg ml⁻¹), methionine (20 µg ml⁻¹), tryptophan (20 µg ml⁻¹), adenine (20 µg ml⁻¹), uracil (20 µg ml⁻¹) and leucine (30 µg ml⁻¹) when necessary. For infection of HeLa cells, overnight cultures of EPEC grown in LB medium were subcultured 1:50 into DMEM and grown statically for 3–4 h at 37 °C with 5% CO₂. The optical density ($D_{600\text{ nm}}$) of the bacterial cultures was measured to standardize the inoculum before infection. Cultures were induced with 1 mM isopropyl-β-D-thiogalactopyranoside (IPTG) for 30 min before infection.

Construction of NleB, TRADD, RIPK1 and FADD expression vectors. The plasmids and primers used in this study are listed in Supplementary Tables 2 and 3, respectively. The *nleB1* gene from EPEC E2348/69 (GenBank accession CAS10779), *nleB1* from EHEC O157:H7 EDL933 (GenBank accession NP_289553.1) and *nleB* from *C. rodentium* (GenBank accession NC_013716.1) were amplified from genomic DNA by PCR using the primer pairs NleB1_F/NleB1_R, NleB1_{EHF}/NleB1_{EHR} or NleB_{CRF}/NleB_{CCR}, respectively and ligated into EcoRI/BamHI digested pEGFP-C2 to generate N-terminal EGFP fusions to NleB (EGFP–NleB1, EGFP–NleB1_{EHEC}, EGFP–NleB_{CR}). The *nleB2* gene was amplified from EPEC E2348/69 genomic DNA (GenBank accession CAS08589) using primer pairs NleB2_F/NleB2_R and ligated into EcoRI/BamHI digested pEGFP-C2. To generate the complementing vectors, pNleB1 and pNleB2, *nleB1* and *nleB2* were amplified from EPEC E2348/69 genomic DNA by PCR using the primer pairs NleB1_F/NleB1_R and NleB2_F/NleB2_R and ligated into EcoRI/BamHI digested pTrc99A. To create pNleB1–2HA and pNleB2–2HA, *nleB1* or *nleB2* was amplified from EPEC E2348/69 genomic DNA by PCR using the primer pairs NleB1_F/NleB1_{R-2HA} and NleB2_F/NleB2_{R-2HA}, respectively, and ligated into EcoRI/BamHI digested pTrc99A. To generate GST tagged NleB, *nleB1* was amplified from EPEC E2348/69 genomic DNA by PCR using the primer pairs NleB1_F/NleB1_{PGEXR} and ligated into EcoRI/SalI digested pGEX-4T-1.

TRADD–Flag was kindly provided by J. Tschopp. FADD–Flag and RIPK1–Flag were provided by A. Mansell. To generate FADD_{ADD}–Flag, the coding region for amino acids 1–96 of FADD was amplified by PCR from FADD–Flag using the primer pairs FADD_F/FADD_{DDR} and ligated into EcoRI/BamHI digested p3×Flag–Myc–CMV to generate an N-terminal 3×Flag fusion to FADD_{1–96} (FADD_{ADD}–Flag). To generate His–FADD, FADD was amplified from FADD–Flag using the primer pairs FADD_{HISF}/FADD_{HISR} and ligated into BamHI/SalI digested pET28a.

To generate pGBT–NleB1, *nleB1* was amplified from EPEC E2348/69 or EHEC O157:H7 EDL933 genomic DNA by PCR using primer pairs NleB1_{EPGBT}/NleB1_R or NleB1_{EHGBT}/NleB1_{EHR} (pGBT–NleB1 and pGBT–NleB1_{EH}). The PCR products were digested with SmaI/EcoRI and EcoRI/BamHI, respectively and ligated into pGBT9. The plasmids pGAD–FADD_{DED} and pGAD–FADD_{DD} were generated from the template pGAD–FADD recovered from the cDNA library screen using primer pairs FADD_{GADF}/FADD_{DEDR} and FADD_{DDF}/FADD_{GADR}, respectively. The FADD_{DED} and FADD_{DD} PCR products were digested with EcoRI/HindIII and EcoRI/SalI, respectively, and ligated into pGAD424. The pGAD–RIPK1_{DD} plasmid was generated using primers RIPK1_{DDF}/RIPK1_{GADR} using pGAD–RIPK1 recovered from the cDNA library screen as template DNA, and cloned using the EcoRI and BamHI restriction sites.

Construction of non-polar deletion mutants. *C. rodentium* strain ICC169 Δ*nleB* (ICC911) was constructed using the lambda Red-based mutagenesis system²³. The *nleB* gene was replaced by a kanamycin resistance cassette following integration of a linear PCR product generated using the primers pair crNleB–pKD4–Fw/crNleB–pKD4–Rv, which contain 50 nucleotide homology extensions corresponding to regions in 5' and 3' of the *nleB* open reading frame and priming sequences for the kanamycin cassette of plasmid pKD4 (Supplementary Table 3)²³. The PCR product was DpnI-digested to remove residual template, gel purified and electroporated into ICC169 carrying the temperature-sensitive lambda Red helper plasmid pKD46 following induction of lambda Red recombinase with 10 mM L-arabinose at 30 °C. The deletion mutant of *C. rodentium nleB* was confirmed by PCR and DNA sequencing and the growth rates of the mutant and parental strains were assessed in rich and minimal media. The *C. rodentium* strains ICC169 Δ*espI* (ICC179) and ICC169 Δ*espF* (ICC177) have been described previously¹⁷. EspI binds to Sec24 and inhibits COPII-dependent vesicle trafficking while EspF is a multifunctional effector that has been associated with destabilization of mitochondria, induction of apoptosis, activation of sorting nexin 9 and disruption of tight

junctions¹. These mutants were chosen as controls because they exhibit varying degrees of attenuation in the mouse model of *C. rodentium* infection and have functions unrelated to NleB.

The EPEC E2348/69 *nleB1* mutant was created with the one step PCR lambda Red method using primers NleB1 E69FRT_{F155} and NleB1 E69FRT_{R156}. pKD3 was used as template DNA to amplify the chloramphenicol cassette. The cassette was electroporated into wild-type EPEC E2348/69 and positive clones were selected on LB agar with 5 µg ml⁻¹ chloramphenicol. The mutations were checked by PCR using primer pairs from outside and inside the mutation. The EPEC E2348/69 *nleB2* mutant was created using primers NleB2 E69FRT_{F115} and NleB2 E69FRT_{R116}. pKD4 was used as template DNA to amplify the kanamycin cassette. The cassette was electroporated into wild-type EPEC E2348/69 and positive clones selected for on LB agar with 50 µg ml⁻¹ kanamycin. The mutations were checked by PCR with a combination of primers from outside and inside the mutation. The EPEC E2348/69 *nleB1/nleB2* double mutant was generated using the one step PCR method by amplifying the *nleB2* mutation from the *nleB2* mutant with primers NleB2₂₁₂ and NleB2₂₁₃. The PCR product was transferred into the *nleB1* mutant strain by electroporation. Mutants were first selected on LB agar plates with 20 µg ml⁻¹ of kanamycin and then grown with chloramphenicol (25 µg ml⁻¹) and kanamycin (50 µg ml⁻¹) to select for *nleB1* and *nleB2* allelic replacement.

Site-directed mutagenesis. The His–FADD_{R117A} and His–FADD_{S122A} mutants, and the NleB1 mutants, pNleB1_{AAA}, EGFP–NleB1_{AAA} and pGEX–NleB1_{AAA} were generated using the Stratagene QuikChange II Site-Directed Mutagenesis Kit. FADD_{R117A} and FADD_{S122A} were generated by PCR using the primer pairs FADD_{(R117A)F}/FADD_{(R117A)R} and FADD_{(S122A)F}/FADD_{(S122A)R}, respectively with His–FADD as template DNA. For the NleB mutants, pNleB1, EGFP–NleB1 or pGEX–NleB1 were used as template DNA and amplified by PCR using the primer pair pNleB1_{(AAA)F}/pNleB1_{(AAA)R}. Plasmids were digested with DpnI at 37 °C overnight before subsequent transformation into the appropriate *E. coli* strain.

Yeast two-hybrid screening and β-galactosidase assay. NleB1 from EPEC strain E2348/69 (GenBank accession CAS10779) and NleB1 from EHEC O157:H7 strain EDL933 (GenBank accession NP_289553.1) were used as bait. The BD Matchmaker pre-transformed HeLa cDNA library (Clontech) was screened according to the manufacturer's protocols (Clontech PT3183–1 manual) to identify HeLa proteins interacting with NleB. The yeast strain AH109 (MATα) was transformed with pGBT–NleB using the lithium acetate method and mated with Y187 (MATα) carrying the cDNA library in pGADT7 Rec plasmid. The mating mixtures were plated onto quadruple drop-out plates (Trp⁻, Leu⁻, Ade⁻, His⁻) to select for diploids expressing reporter genes. The pGADT7–Rec cDNA plasmids were selectively rescued from those diploids with positive protein interactions into *E. coli* KC8. The pGADT7–Rec cDNA plasmids were then sequenced using primer Rec744 to identify the cDNA inserts.

β-galactosidase assays were performed according to the manufacturer's protocols (Clontech PT3024–1 manual). Briefly, pGADT7–Rec plasmid alone or with pGBT–NleB (or pGBT9, pGAD–FADD, pGAD–FADD_{DED}, pGAD–FADD_{DD} when necessary) were transformed into *Saccharomyces cerevisiae* strain PJ69–4A using the lithium acetate method. Transformants were selected on Trp⁻ Leu⁻ plates and grown to an optical density ($D_{600\text{ nm}}$) of 0.6 before lysis and assay for the level of β-galactosidase activity using ONPG as a substrate. Data are from at least three biological replicates performed in triplicate.

Bacterial adherence assay. Standard lines of HeLa and HEK293T cells are maintained in our laboratory and regularly tested for mycoplasma contamination. To assess the level of bacterial replication during infection and treatment with FasL, bacterial cultures grown in DMEM for were standardised by measurement of $D_{600\text{ nm}}$ and plated on selective media for assessment by viable count. HeLa cell monolayers were infected in duplicate with the same cultures for 3 h before being incubated for 1.5 h in media supplemented with or without 20 ng ml⁻¹ Fcγ–FasL. Following treatment, cells were washed three times and attached bacteria were resuspended in DMEM by pipetting and subsequently spread on selective media for assessment of bacterial viable count. Data are from at least three biological replicates performed in triplicate.

Immunoprecipitation and detection of HA-, EGFP-, Flag-tagged proteins. All immunoprecipitation experiments were performed as at least three biological replicates. For immunoprecipitation by GFP–Trap–M (Chromotek), HEK293T cells were grown in 10-cm tissue culture dishes (Greiner Bio One) and co-transfected with pEGFP–NleB1 or pEGFP–NleB2 in combination with pRIPK1–Flag, pTRADD–Flag, pFADD–Flag or pFADD_{ADD}–Flag. Following transfection (after 18–24 h), lysis and immunoprecipitation were carried out according to instructions for immunoprecipitation of GFP-fusion proteins provided by the GFP–Trap–M supplier.

For immunoprecipitation of 2× haemagglutinin (HA) tagged proteins, HeLa cells cultured in T-75 cm² tissue culture flasks (Corning) were first transfected with FADD–Flag, RIPK1–Flag or TRADD–Flag expression constructs for 18 h followed

by infection with various EPEC derivatives for 90–120 min. Cells were then washed three times with cold PBS and lysed in 1 ml cold lysis buffer (1% Triton X-100, 50 mM Tris-HCl, pH 7.4, 1 mM EDTA, 150 mM NaCl and Complete Protease Inhibitor (Roche)) and incubated on ice for 10 min before collection. Cell debris was pelleted and equal volumes of supernatant collected. 100 μ l of the supernatant was kept as input and 60 μ l of monoclonal anti-HA-agarose (Clone HA-7, Sigma-Aldrich) was added to the remainder of the supernatant which was incubated on a rotating wheel at 4 °C overnight. The agarose was washed three times with lysis buffer and resuspended in 50 μ l of 2 \times SDS sample buffer.

For immunoprecipitation of Fas receptor complexes (DISC) by protein G, HeLa cells were grown in 10-cm tissue culture dishes and infected with various EPEC derivatives for 2 h. Cells were then treated with 50 μ g ml⁻¹ gentamycin and 1 μ g of Fc γ -FasL for 1 h. An uninfected control was left untreated. Cells were lysed in 400 μ l of 2 \times DISC lysis buffer (20 mM Tris-HCl, pH 7.4, 150 mM NaCl, 2 mM EDTA, 1% TritonX-100, 10% glycerol and Complete Protease Inhibitor (Roche)) and incubated on ice for 10 min before centrifugation to remove cell debris. An aliquot (80 μ l) of the supernatant was kept as input and 40 μ l of Protein G Dynabeads (Invitrogen) was added to the remainder of the sample which was placed on a rotating wheel at 4 °C overnight. Beads were washed three times with lysis buffer and finally resuspended in 75 μ l of DISC lysis buffer with 25 μ l of 5 \times SDS sample buffer.

All samples were boiled for 5 min, subjected to SDS-PAGE and transferred to nitrocellulose membranes. Membranes were probed with the following primary antibodies as necessary: mouse monoclonal anti-HA.11 (16B12) (Covance), mouse monoclonal anti-Flag M2-HRP (Sigma-Aldrich), mouse monoclonal anti-FADD (BD Transduction Laboratories), rabbit monoclonal anti-Fas (C18C12) (Cell Signaling), rabbit polyclonal anti-caspase-8 (D35G2) (Cell Signaling), mouse monoclonal anti-GFP (7.1 and 13.1) (Roche) or mouse monoclonal anti- β -actin (AC-15) diluted 1:1,000 in TBS with 5% BSA and 0.1% Tween. Images were visualized using an MFChemibis imaging station (DNR).

Preparation of GST and His tagged proteins, demonstration of N-acetylglucosylation of recombinant FADD by NleB1 and detection by immunoblotting. Overnight cultures of BL21 (pGEX-4T-1), BL21 (pGEX-NleB1), BL21 (pGEX-NleB1_{AAA}) and BL21 (pET-FADD), BL21 (pET-FADD_{R117A}), BL21 (pET-FADD_{S122A}) grown in LB were diluted 1:100 in 200 ml of LB supplemented with either kanamycin (pET) or ampicillin (pGEX) (100 mg ml⁻¹) with shaking to an optical density of ($D_{600\text{nm}}$) 0.6 at 37 °C. Cells were incubated with 1 mM IPTG and grown for a further 2 h then pelleted by centrifugation. Proteins were purified by either nickel or glutathione affinity chromatography in accordance with the manufacturer's instructions (Novagen). Protein concentrations were determined using a bicinchoninic acid (BCA) kit (Thermo Scientific).

For detection of N-acetylglucosylation of FADD by NleB1, 2 μ g of purified recombinant proteins were incubated either alone or in combination at 37 °C for 4 h in the presence of 1 mM UDP-GlcNAc. 5 \times SDS sample buffer was added to the samples before boiling for 5 min. Samples were subjected to SDS-PAGE and transferred to nitrocellulose membranes which were subsequently probed with the following primary antibodies: mouse monoclonal anti-GlcNAc (CTD110.6) (Cell Signaling), which recognizes O-linked and N-linked GlcNAc²⁴, rabbit polyclonal anti-GST (Cell Signaling), or mouse monoclonal anti-His (AD1.1.10) (AbD Serotech) diluted 1:1,000 in TBS with 5% BSA and 0.1% Tween. Detection and visualization were performed as previously mentioned. Detection of N-acetylglucosylated recombinant FADD was performed as three technical replicates.

For detection of N-acetylglucosylation during transient transfection with NleB1 and FADD, HEK293T cells were grown in 10-cm tissue culture dishes (Greiner Bio One) and co-transfected with pEGFP-NleB1 or pEGFP-NleB1_{AAA} in combination with pFADD-Flag. Cells were washed three times with cold PBS and lysed in 600 μ l of cold lysis buffer (1% Triton X-100, 50 mM Tris-HCl, pH 7.4, 1 mM EDTA, 150 mM NaCl and Complete Protease Inhibitor (Roche)) and incubated on ice for 10 min before collection. Cell debris was pelleted and equal volumes of supernatant collected. Then 80 μ l of the supernatant was kept as input and 40 μ l of monoclonal anti-Flag M2 magnetic beads (Sigma-Aldrich) was added to the remainder of the supernatant which was incubated on a rotating wheel at 4 °C overnight. The beads were washed three times with cold lysis buffer followed by elution of bound proteins with 80 μ g of Flag peptide (Sigma-Aldrich) to which 16 μ l of 5 \times SDS sample buffer was added. Samples were boiled for 5 min, subjected to SDS-PAGE and transferred to nitrocellulose membranes. Membranes were probed with the following primary antibodies as necessary: mouse monoclonal anti-O/N-GlcNAc (CTD110.6) (Cell Signaling), mouse monoclonal anti-Flag M2-HRP (Sigma-Aldrich), mouse monoclonal anti-GFP (7.1 and 13.1) (Roche) or mouse monoclonal anti- β -actin (AC-15) diluted 1:1,000 in TBS with 5% BSA and 0.1% Tween. Images were visualized using an MFChemibis imaging station (DNR).

Glyco-site specific analysis of FADD. Intact protein analysis was performed by the Proteomics Laboratory at the Walter and Eliza Hall Institute (Fig. 2b and

Extended Data Fig. 4). 10 μ g of intact recombinant His-FADD, His-FADD_{R117A} or His-FADD_{S122A} incubated with GST-NleB1 and UDP-GlcNAc, was injected and separated by nano-flow reversed-phase liquid chromatography on a nano LC system (1200 series, Agilent) using a custom packed C4 capillary column (15 cm \times 0.15 mm inner diameter (I.D.), packed with Resprosil 300 Å C4 5- μ m resin, Dr Maisch GmbH) using a linear 45 min gradient from 5 to 100% buffer B at a flow rate of 1.2 μ l min⁻¹ (A: 0.1% Formic acid in Milli-Q water B: 0.1% Formic acid, 80% acetonitrile, (Mallinckrodt Baker) 20% Milli-Q water). The nano HPLC was coupled online to a Q-Exactive mass spectrometer equipped with a nano-electrospray ion source (Thermo Fisher Scientific) set to acquire full scan and all-ion-fragmentation (AIF) sequentially. Mass accuracy of the intact protein was achieved by summing multiple lower resolution (35,000) full scan MS events. The intact mass and error calculation was facilitated by the open source program mMass.

Tryptic peptide analysis was performed by the Proteomics Laboratory at the Walter and Eliza Hall Institute (Fig. 2c and Extended Data Fig. 2). Reacted and unreacted mixtures of recombinant FADD and NleB1 were purified by SDS-PAGE and bands corresponding to FADD were excised and manual in-gel reduction, alkylation and tryptic digestion was performed. Extracted peptides were injected and separated by nano flow reversed-phase liquid chromatography on a nano LC system (1200 series, Agilent) using a nanoAcquity C18 150 mm \times 0.15 mm I.D. column (Waters) with a linear 45-min gradient from 5 to 100% buffer B set at a flow rate of 1.2 μ l min⁻¹ (A: 0.1% Formic acid in Milli-Q water, B: 0.1% Formic acid, 80% acetonitrile, (Mallinckrodt Baker, New Jersey, USA) 20% Milli-Q water). The nano HPLC was coupled online to an LTQ-Orbitrap XL mass spectrometer equipped with a nano-electrospray ion source (Thermo Fisher Scientific) for automated MS/MS using multi-stage activation (MSA) setting. The Orbitrap was run in a data-dependent acquisition mode with the Orbitrap resolution set at 30,000 and the top-three multiply charged species selected for fragmentation in the linear ion trap by collision-induced dissociation (CID) (single charged species were ignored). Fragment ions were analysed on the Orbitrap with the resolution set at 7,500 with the ion threshold set to 15,000 counts. The activation time was set to 30 ms, normalized collision energy set to 35. Raw files consisting of full-scan MS and high resolution MS/MS spectra were converted to the MGF data format with Proteome Discoverer 1.4 and searched against UniProt database (2013/02) limiting the search to mouse taxonomy and custom FASTA database containing the protein constructs of FADD and NleB1 using Mascot v2.4. Mascot parameters for each search included Trypsin/no P enzyme with six missed cleavages, a fixed modification in the form of carbamidomethyl at cysteine residues and variable modification of HexNAc at Ser/Thr/Asn/Arg residues, acetyl at protein N-terminal, oxidation at methionine residues. Spectra were searched with a mass tolerance of 20 p.p.m. in MS mode and 40 m.m.u. in MS/MS mode. The MS/MS fragmentation of modified peptides obtained from the Mascot search was manually sequenced using mMass to assign ion peaks and confirm the site of modification. Detection of N-acetylglucosylated recombinant FADD by mass spectrometry was performed as two technical replicates.

The site of modification was verified independently using electron transfer dissociation (ETD) fragmentation on an Orbitrap Elite mass spectrometer by the Bio21 Mass Spectrometry and Proteomics Facility at the University of Melbourne (Extended Data Fig. 3). The protein complex was digested with Endoproteinase AspN (Roche) at an enzyme to protein ratio of 1:5 at 37 °C overnight. The reaction contained FADD, NleB1 and UDP-GlcNAc and the incubation was performed as described earlier for anti-GlcNAc immunoblot analysis. LC-MS/MS was carried out on a LTQ Orbitrap Elite (Thermo Scientific) with an EASY nano electrospray interface coupled to an Ultimate 3000 RSLC nanosystem (Dionex). The nanoLC system was equipped with a Acclaim Pepmap nano-trap column (Dionex – C18, 100 Å, 75 μ m \times 2 cm) and a Thermo EASY-Spray column (Pepmap RSLC C18, 2 μ m, 100 Å, 75 μ m \times 25 cm). 4 μ l of the peptide mix was loaded onto the enrichment (trap) column at an isocratic flow of 4 μ l min⁻¹ of 3% CH₃CN containing 0.1% formic acid for 5 min before the enrichment column was switched in-line with the analytical column. The eluents used for the liquid chromatography were 0.1% (v/v) formic acid (solvent A) and 100% CH₃CN/0.1% formic acid (v/v). 0.1% formic acid (v/v). The flow following gradient was used: 3% B to 12% B for 1 min, 12% B to 35% B in 20 min, 35% B to 80% B in 2 min and maintained at 80% B for 2 min and equilibration at 3% B for 7 min before the next sample injection. The LTQ Orbitrap Elite mass spectrometer was operated in the data dependent mode with nano ESI spray voltage of +2.0 kV, capillary temperature of 250 °C and S-lens RF value of 60%. A sequential mode whereby spectra were acquired first in positive mode with full scan scanning from m/z 300–1650 in the FT mode at 120,000 resolution followed by CID, ETD and high energy collision dissociation (HCD). CID in the linear ion trap was carried out in parallel with three most intense peptide ions with charge states ≥ 2 isolated and fragmented using normalized collision energy of 35 and activation Q of 0.25. The decision tree procedure for ETD activation was also applied whereby peptides with charge state

3 of <650 m/z, charge state 4 of <900 m/z and charge state 5 of <1,000 m/z were subjected to 100 ms of ETD activation. HCD at 15,000 resolution using normalized collision energy of 35 and 0.1 ms activation time was carried out on every precursor selected. The mass spectra were searched against the Uniprot database using the Sequest HT (V1.3) search algorithm as part of the Proteome Discoverer 1.4 Workflow (Thermo Scientific). Searching parameters used were: variable modifications (HexNAc of N, S, T and R; 203.079), 2 missed tryptic cleavages, 10 p.p.m. peptide mass tolerance and 0.6 Da fragment ion mass tolerance. The false-discovery rate (derived from corresponding decoy database search) was less than 1%. Peptides of interest were manually inspected and validated.

IL-8 secretion assay. For analysis of IL-8 secretion, HeLa cell monolayers were infected for 3 h before being incubated for 8–12 h in media supplemented with 50 $\mu\text{g ml}^{-1}$ gentamycin with or without 20 ng ml^{-1} TNF (Calbiochem, EMD4Biosciences). Following this, the HeLa cell supernatant was collected and either used immediately or stored at -20°C for subsequent analysis of IL-8 secretion. IL-8 secretion was measured using the Quantikine Human IL-8 Immunoassay (R&D Systems) according to the manufacturer's instructions. Samples were measured on a FLUOstar Omega microplate reader (BMG Labtech). Differences in IL-8 secretion were assessed for significance by one-way analysis of variance (ANOVA) with Dunnett's multiple comparison post-test. Data are from at least three biological replicates performed in triplicate.

Detection of cleaved caspase-8 by immunoblotting. For detection of cleaved caspase-8 during EPEC infection, HeLa cells were grown in 24-well tissue culture plates (Greiner Bio One) and infected for 3 h with various EPEC derivatives. Cells were then treated with 50 $\mu\text{g ml}^{-1}$ gentamicin, and either 20 ng ml^{-1} of Fc γ -FasL, 20 ng ml^{-1} TNF or a combination of 20 ng ml^{-1} TNF and 10 $\mu\text{g ml}^{-1}$ cycloheximide for a further 60 min and lysed in 60 μl of 2 \times SDS sample buffer. For detection of cleaved caspase-8 by transfection, HeLa cells were grown in 24-well tissue culture plates and either left untransfected or transfected with pEGFP-C2, pEGFP-NleB1 or pEGFP-NleB1_{AAA} for 18–24 h using FuGENE 6 (Roche). Cells were then treated with 20 ng ml^{-1} of Fc γ -FasL for a further 60 min and collected by lysis in 60 μl of 2 \times SDS sample buffer. All samples were boiled for 5 min and subjected to SDS-PAGE followed by transfer to nitrocellulose membranes (PALL). Membranes were incubated at least overnight at 4°C with rabbit polyclonal anti-cleaved caspase-8 (Asp391) (18C8) (Cell Signaling) diluted 1:1,000 in TBS with 5% skimmed milk and 0.1% Tween (Sigma-Aldrich), rabbit polyclonal anti-caspase-8 (D35G2) (Cell Signaling) diluted 1:1,000 or mouse monoclonal anti- β -actin (AC-15) (Sigma-Aldrich) diluted 1:5,000 in TBS with 5% BSA (Sigma-Aldrich) and 0.1% Tween. Proteins were detected using anti-rabbit or anti-mouse IgG secondary antibodies conjugated to horseradish peroxidase (PerkinElmer) and developed with either enhanced chemiluminescence (ECL) western blotting reagent (Amersham) or Western Lightning Ultra reagent (PerkinElmer). All secondary antibodies were diluted 1:3,000 in TBS with 5% BSA and 0.1% Tween. Images were visualized using an MFCHEMIBis imaging station (DNR). At least three biological replicates were performed for all experiments.

Detection of cleaved caspase-8 and caspase-3 in vitro by immunofluorescence microscopy. For visualization of caspase-8 cleavage by immunofluorescence microscopy, HeLa cells were either infected with EPEC E2348/69 derivatives for 3 h or transfected for 16 h followed by an additional 1 h of treatment with 20 ng ml^{-1} Fc γ -FasL. One experiment used recombinant rhFasL to treat transfected HeLa cells for comparison with tunicamycin treatment (Extended Data Fig. 1d, e). For this, HeLa cells were transfected for 16 h and treated with 200 ng ml^{-1} of rhFasL (R&D Systems). For visualization of caspase-3 cleavage induced by tunicamycin, HeLa cells were transfected for 16 h, followed by 18 h treatment with 5 $\mu\text{g ml}^{-1}$ tunicamycin (Sigma-Aldrich). Cells were then fixed in 3.7% (w/v) formaldehyde (Sigma-Aldrich) in PBS for 10 min and permeabilized with 0.2% Triton (Sigma-Aldrich) for 4 min. Following 30 min blocking in PBS with 3% (w/v) BSA, samples were exposed to primary antibodies (specific to cleaved caspase-8 or cleaved caspase-3; Cell Signaling Technology) diluted in blocking solution for 1 h at 20°C , except for cleaved caspase-3, which was incubated overnight at 4°C . For fluorescent actin staining in EPEC infected cells, 0.5 $\mu\text{g ml}^{-1}$ of phalloidin conjugated to rhodamine (Sigma-Aldrich) was added during primary antibody incubation. 4',6-diamidino-2-phenylindole (DAPI, Invitrogen) was applied at 0.5 $\mu\text{g ml}^{-1}$ in blocking solution for 5 min at 20°C post-secondary antibody treatment. Secondary antibodies were all coupled to Alexa Fluor dyes (Invitrogen) applied to cells at 1:2,000 in blocking solution for 1 h at 20°C . Coverslips were mounted onto microscope slides with Prolong Gold anti-fade reagent (Invitrogen). Images were acquired using a Zeiss confocal laser scanning microscope with a 100 \times /EC Epiplan-Apochromat oil immersion objective. Cleavage of caspase-8 or caspase-3 was quantified from at least three biological replicates performed in duplicate for both transfection and infection studies counting at least 100 cells per field.

Cell viability assays (MTT and propidium iodide staining). HeLa cells were transfected in 24-well tissue culture plates for 18–24 h before being left untreated or treated with 20 ng ml^{-1} of Fc γ -FasL for a further 60 min. The cells were washed once with PBS and replaced with DMEM containing 0.1 $\mu\text{g ml}^{-1}$ 3-(4,5-dimethylthiazol-2-yl)-2,5-diphenyltetrazolium bromide (MTT) (Sigma) for 1 h, after which the medium was removed and 100 μl of dimethylsulphoxide (DMSO, Sigma) was added to each well. After thorough mixing on an orbital shaker for 1 min, the absorbance at 540 nm for each well was obtained using a FLUOstar Omega microplate reader (BMG Labtech). Results were obtained from at least three biological replicates performed in triplicate.

For analysis of cell viability by PI staining, HeLa cell monolayers were infected for 3 h before being incubated for 1 h in media supplemented with 50 $\mu\text{g ml}^{-1}$ gentamycin with 20 ng ml^{-1} Fc γ -FasL. Propidium iodide (50 $\mu\text{g ml}^{-1}$) was added for the final 15 min of treatment. Cells were fixed and stained for confocal microscopy as previously mentioned. Phalloidin conjugated to FITC (Sigma-Aldrich) was used at 0.5 $\mu\text{g ml}^{-1}$ to stain for actin. Duplicate coverslips were counted for PI positive cells, and results were obtained from at least three biological replicates counting at least 100 cells per field.

Animal experiments. All animal experimentation was approved by the University of Melbourne Animal Ethics Committee, applications 0808209 and 1112062. All genetically modified and spontaneous mutant mice are on a C57BL/6 background. Overnight cultures of bacterial strains were pelleted by centrifugation and resuspended in PBS. C57BL/6 (wild-type), Fas^{lpr/pr}, Fas^{gld/gld} and Bid^{-/-} mutant mice (6 to 8 weeks old, male and female mice) were inoculated by oral gavage with 200 μl containing approximately 1×10^9 c.f.u. of *C. rodentium*, or a lower dose of 1×10^8 c.f.u. when testing for prolonged infection (up to 33 days). The viable count of the inoculum was determined retrospectively by plating dilutions of the inoculum on plates with appropriate antibiotics. Animals were allocated to experimental groups to ensure even distribution of age, sex and weight. Investigators were not blinded to group allocation. Sample size was at least five animals per group for statistical power per biological replicate. Larger sample sizes (up to 12 mice per group) were used if mice were available. Infection experiments were repeated at least twice regardless of sample size to ensure reproducibility and results represent all experimental data combined from repeated infections. Mice were weighed every 2 days and faeces collected every 2 or 4 days for enumeration of c.f.u. The viable bacterial count per 100 mg of faeces was determined by plating serial dilutions in duplicate of faeces onto medium containing selective antibiotics.

Histological analysis and scoring of tissue pathology and diarrhoea. The increased intestinal pathology observed in *C. rodentium*-infected Fas-, FasL- and Bid-deficient mice revealed a function for the Fas apoptotic pathway in limiting the extent of colitis during gastrointestinal infection. This exacerbated disease compared to *C. rodentium* infection of wild-type mice likely arose from the difference between a complete block of Fas signalling in the gut epithelium of Fas-deficient mice as opposed to less complete inhibition of Fas signalling in the gut epithelium by NleB in wild-type mice, which depends on the timing and efficiency of *C. rodentium* attachment and NleB translocation. A grading system for diarrhoea was developed in which a score of diarrhoea severity from 0–4 was recorded every 4 days. The scoring system can be interpreted as follows, (0) (no diarrhoea): solid stool with no sign of soiling around the anus. The stool is very firm when subjected to pressure with tweezers; (1) (very mild diarrhoea): formed stools that appear moist on the outside, and no sign of soiling around the anus. Stool is less firm when considerable pressure applied with tweezers; (2) (mild diarrhoea): formed stools that appear moist on the outside, and some signs of soiling around anus. Stools will easily submit to pressure applied with tweezers; (3) (diarrhoea): no formed stools with a mucous-like appearance. Considerable soiling around the anus and the fur around tail. Mouse takes a long time to pass stool; (4) (severe, watery diarrhoea): mostly clear or mucous-like liquid stool with very minimal solid present and considerable soiling around anus. Mouse may not be able to pass stool at all and may have a hunched appearance. Occasionally, blood may be observed in the stool.

For histological analysis, mice inoculated with the higher dose of *C. rodentium* (1×10^9 c.f.u.) were culled at day 10 or 12 post-infection and the distal portion of colon from the caecum to the rectum removed aseptically and weighed after removal of faecal pellets. Colons and spleens were homogenized mechanically in PBS using a Seward 80 stomacher, and the bacterial c.f.u. per 100 mg of organ homogenate was enumerated by plating onto LB containing the appropriate antibiotics. Colons from a representative group of these mice were collected and fixed in 4% (w/v) paraformaldehyde (Sigma-Aldrich) and sectioned for haematoxylin and eosin staining and assessment of gut pathology. A scoring system (0–3) was used by a veterinary pathologist to assess the extent of tissue damage: (0) no damage; (1) discrete lesion; (2) mucosal erosion; and (3) extensive mucosal damage/ulceration (extending into muscularis and deeper).

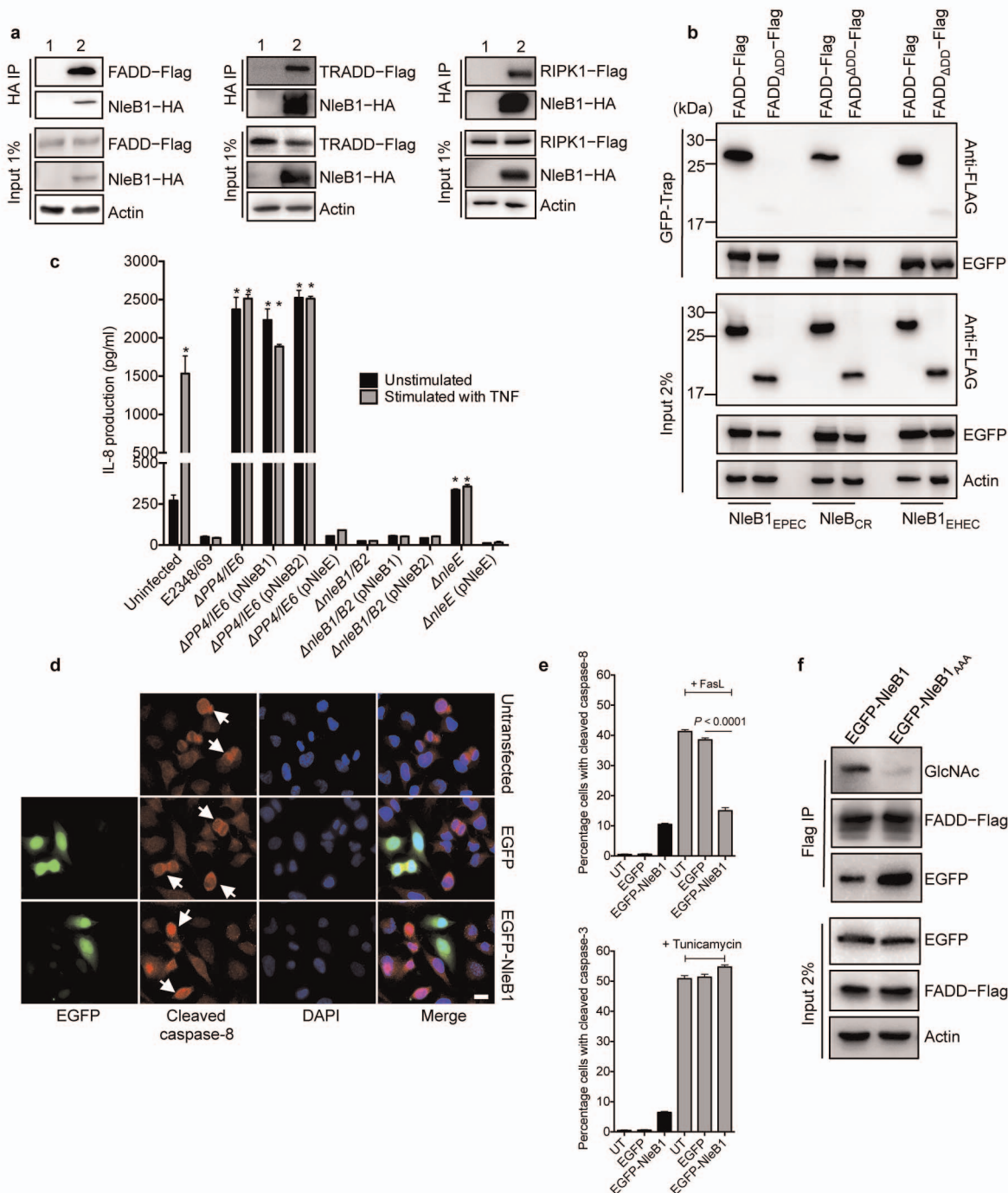
Detection of *C. rodentium* and cleaved caspase-8 in mouse colon tissue by immunofluorescence microscopy. For immunofluorescence staining of mouse colons, the distal portion of colon from the caecum to the rectum was removed from representative groups of infected and uninfected C57BL/6 (wild-type) and *Fas*^{lpr/lpr} mice, gently flushed with a 1:1 mix of OCT compound (Tissue-Tek) and PBS and frozen at -80°C in full strength OCT compound. 10- μm sections were cut on a Leica CM3050S cryostat and mounted onto Menzel-Gläser Superfrost Plus slides (Thermo Fisher Scientific). Slide sections were dried for at least 2 h before fixing in absolute acetone at -20°C , followed by a 30 min block with Dako Protein-Free Block Serum (Dako). Sections were incubated with primary antibody; polyclonal rabbit anti-*C. rodentium* O152 (Statens Serum Institute) diluted 1:100 or mouse specific monoclonal rabbit anti-cleaved caspase-8 (Asp387) (D5B2) XP diluted 1:500 in 2.5% normal donkey serum (NDS) (Jackson ImmunoResearch Laboratories) in PBS. Secondary antibody coupled to Alexa Fluor-488 was applied at 1:1,000 in 2.5% NDS followed by 2 min of exposure to Hoechst 33258 (Invitrogen) diluted at 1:2,000 in 2.5% NDS. Slides were mounted with glass coverslips using Prolong Gold anti-fade reagent (Invitrogen) and images were acquired using a Zeiss LSM700 inverted Axio Observer with LED laser lines at 405 nm and 488 nm, and a Plan-Apochromat 20 \times /0.8 objective. To determine the average depth of penetration by *C. rodentium* in mouse intestinal crypts, ImageJ was used to measure the distance of bacterial staining from the epithelial surface on immunofluorescent images. Results are from five independent sections with at least three

measurements taken from each section. To quantify the amount of cleaved caspase-8 in infected mouse colons, the relative fluorescence intensity of cleaved caspase-8 staining was expressed as a percentage of the relative fluorescence intensity of Hoechst staining from 5 independent infected fields of 3 mice for each bacterial strain.

Hyperplasia of colonic crypts (crypt height) was measured using MIRAX software on haematoxylin and eosin stained sections at day 10 and 12 post-infection. Data are from 4 sections of distal colon measured at least 50 μm apart per animal from at least three individual mice per group.

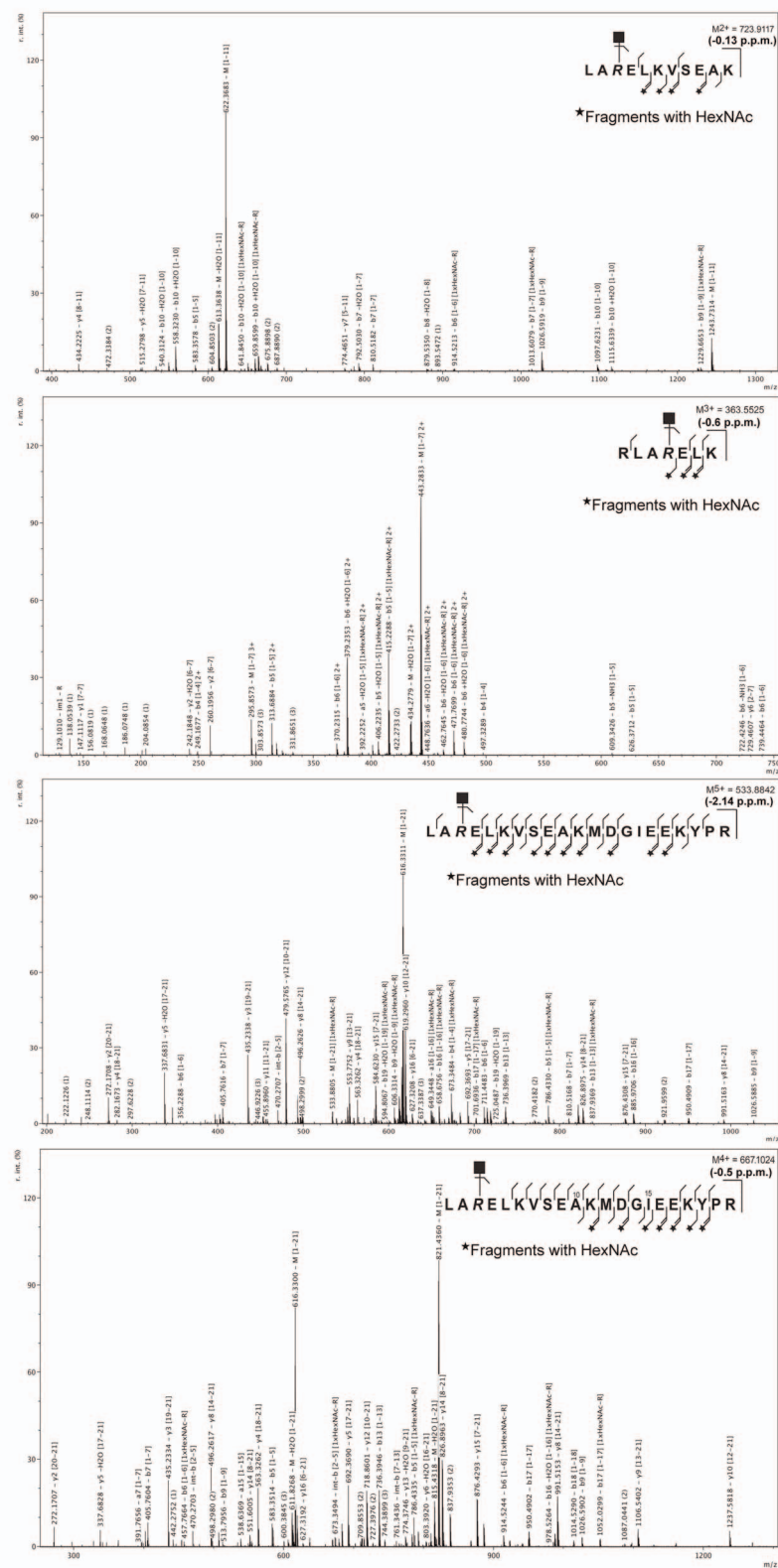
Statistical analysis. All statistical analyses were performed using GraphPad Prism version 6.0. Statistical tests used were unpaired two-tailed Student's *t*-test for pairwise comparisons between groups or one-way ANOVA with Dunnett's multiple comparison test for multiple comparisons as indicated. Variance was similar in all comparisons. Differences in faecal counts of *C. rodentium* from mice and diarrhoea scores were assessed using a Mann-Whitney *U*-test, in which normal distribution was not assumed. $P < 0.05$ was considered to be significant.

23. Datsenko, K. A. & Wanner, B. L. One-step inactivation of chromosomal genes in *Escherichia coli* K-12 using PCR products. *Proc. Natl Acad. Sci. USA* **97**, 6640–6645 (2000).
24. Isono, T. O-GlcNAc-specific antibody CTD110.6 cross-reacts with N-GlcNAc₂-modified proteins induced under glucose deprivation. *PLoS ONE* **6**, e18959 (2011).

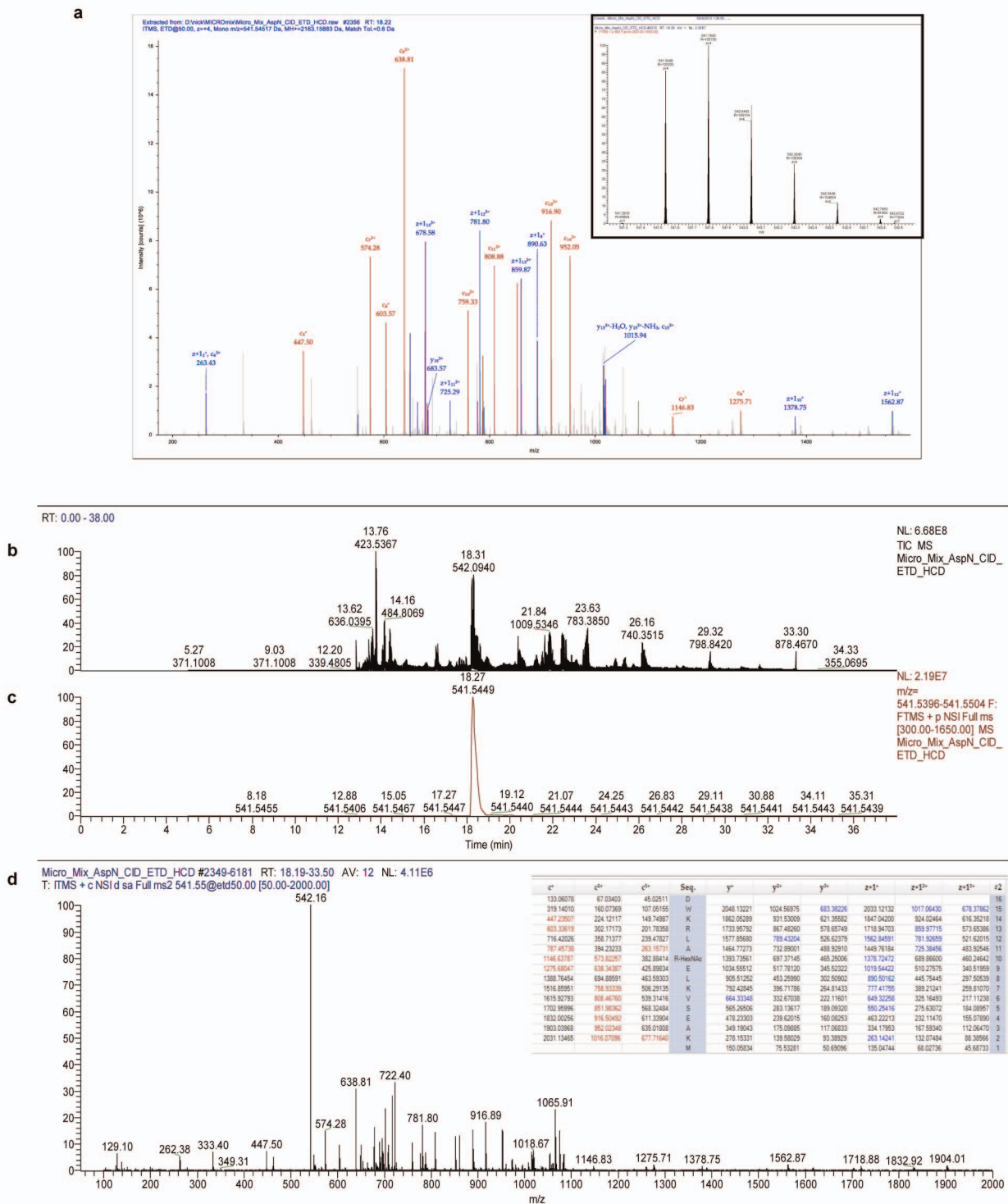


Extended Data Figure 1 | NleB1 binds FADD, TRADD and RIPK1 and blocks extrinsic apoptosis. **a**, Co-immunoprecipitation of bacterially delivered NleB1-2HA with FADD-Flag, TRADD-Flag and RIPK1-Flag in HeLa cells. Lane 1, HeLa cells infected with EPEC Δ nleB1 (pNleB1) (negative control). Lane 2, HeLa cells infected with EPEC Δ nleB1 (pNleB1-2HA). Actin, loading control. Representative immunoblot from at least three independent experiments. **b**, GFP-Trap pull-down of FADD-Flag or FADD Δ DD-Flag. NleB1 from EPEC E2348/69, EHEC O157:H7 EDL933 and *C. rodentium* ICC169 fused with EGFP were used as indicated. Actin, loading control. Representative immunoblot from at least three independent experiments. **c**, HeLa cells were infected with derivatives of EPEC as indicated for 4 h and left unstimulated (dark grey bars) or stimulated with TNF for 8 h (light grey bars). Results are the mean \pm s.e.m. of at least three independent experiments carried out in duplicate. The * indicates significantly greater than uninfected,

unstimulated cells, $P < 0.0001$, one-way ANOVA with Dunnett's multiple comparison test. **d**, Apoptosis was induced by FasL and HeLa cells were stained with antibodies to cleaved caspase-8. Arrows indicate cells with cleaved caspase-8. Scale bar, 5 μ m. Representative images from at least three independent experiments. **e**, Quantification of cleaved caspase-8 or cleaved caspase-3 by immunofluorescence microscopy in HeLa cells expressing EGFP or EGFP-NleB1. UT, untransfected; Results are the mean \pm s.e.m. of percentage of cells with cleaved caspase-8 or cleaved caspase-3 from at least three independent experiments counting ~ 200 cells in triplicate. * $P < 0.0001$, unpaired, two-tailed *t*-test. **f**, N-acetylglucosylation of FADD-Flag detected using a monoclonal antibody to GlcNAc of immunoprecipitated lysate from HEK293T cells. Actin, loading control. Representative immunoblot from at least three independent experiments.

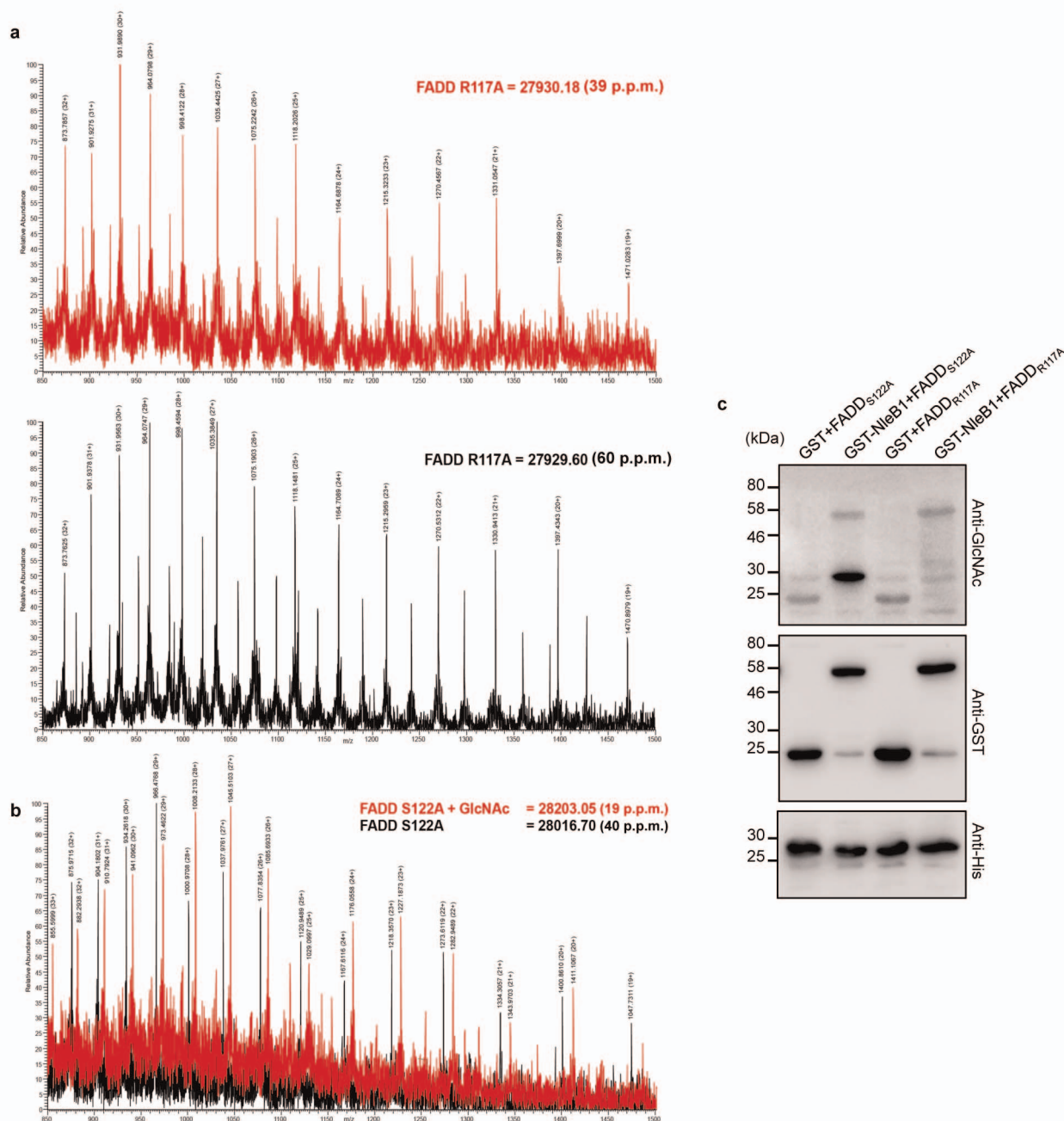


Extended Data Figure 2 | Mass spectra of peptides identifying FADD Arg 117 GlcNAc modification. Fragment ions of overlapping tryptic missed cleaved peptides confirm Arg 117 of FADD as the modification site.



Extended Data Figure 3 | Mass spectra obtained using electron transfer dissociation fragmentation on the Orbitrap Elite mass spectrometer. a, Red and blue spectra represent the c and z series ions that matches the peptide sequence DWKRLAR-HexNAc-ELKVSEAKM (addition of 203.0793 Da) produced from an AspN endoproteinase digest of FADD incubated with NleB1. Insert box shows the precursor ion present as a 4+ charge isotope series with a delta mass of 0.15 p.p.m. between the measured and theoretical mass of

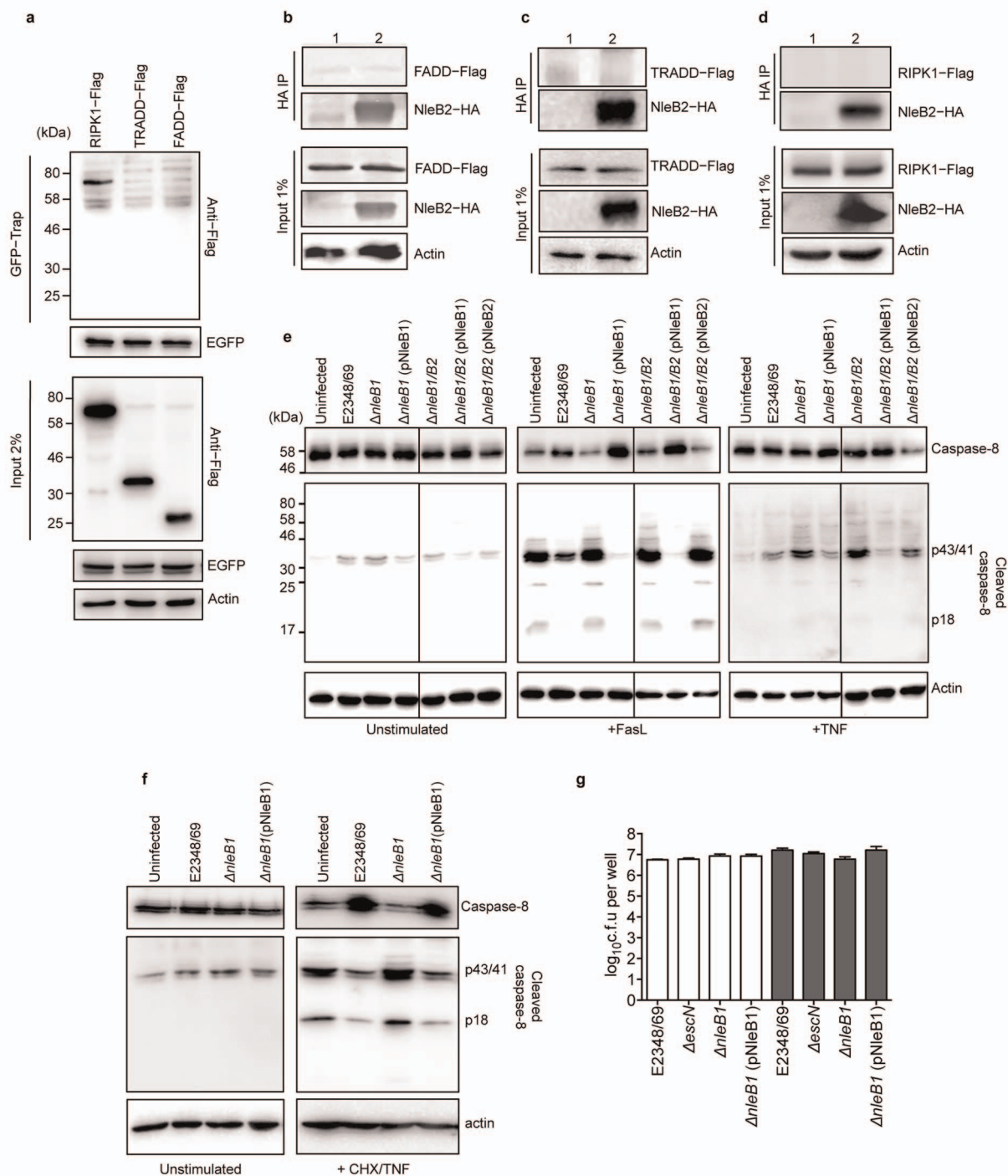
the modified peptide. Xcorr score of 6.26 was obtained using the Sequest HT (V1.3) search engine. **b**, Total ion current of the AspN digest. **c**, Extracted ion chromatogram of mass 541.5449 belonging to the HexNAc modified peptide DWKRLARELVSEAKM using isolation mass tolerance of 10 p.p.m. **d**, ETD fragmentation spectra of the 541.55 precursor ion. Insert table shows the theoretical masses associated with the respective fragmentation ions.



Extended Data Figure 4 | GlcNAc modification of FADD by GST-NleB1.

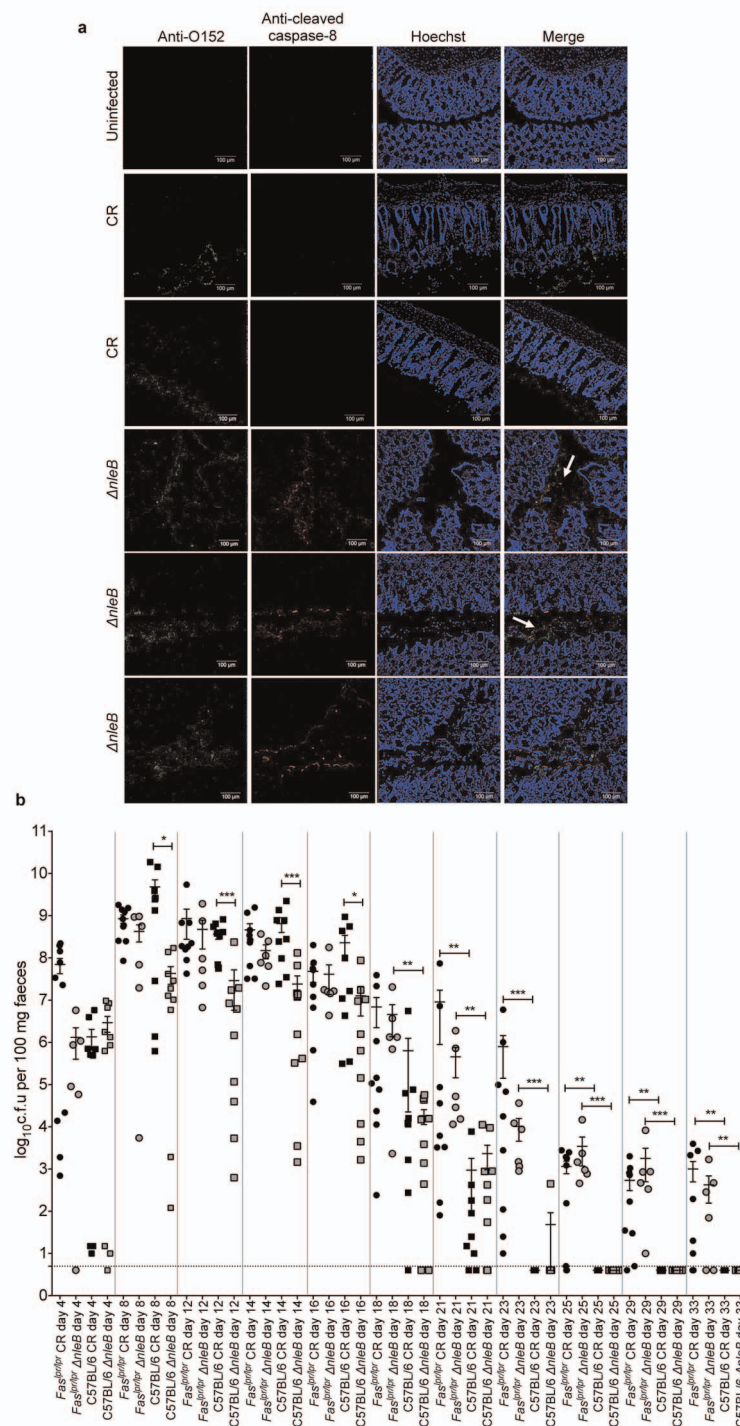
a, Intact protein mass spectrometry of FADD with an R117A substitution incubated with GST-NleB1 and UDP-GlcNAc reveals no GlcNAc modification. **b**, Intact protein mass spectrometry of FADD with S122A

substitution incubated with GST-NleB1 and UDP-GlcNAc reveals a single GlcNAc modification. **c**, *In vitro* assay for NleB1 GlcNAc modification of mutated forms of FADD as indicated. Representative immunoblot from at least three independent experiments.



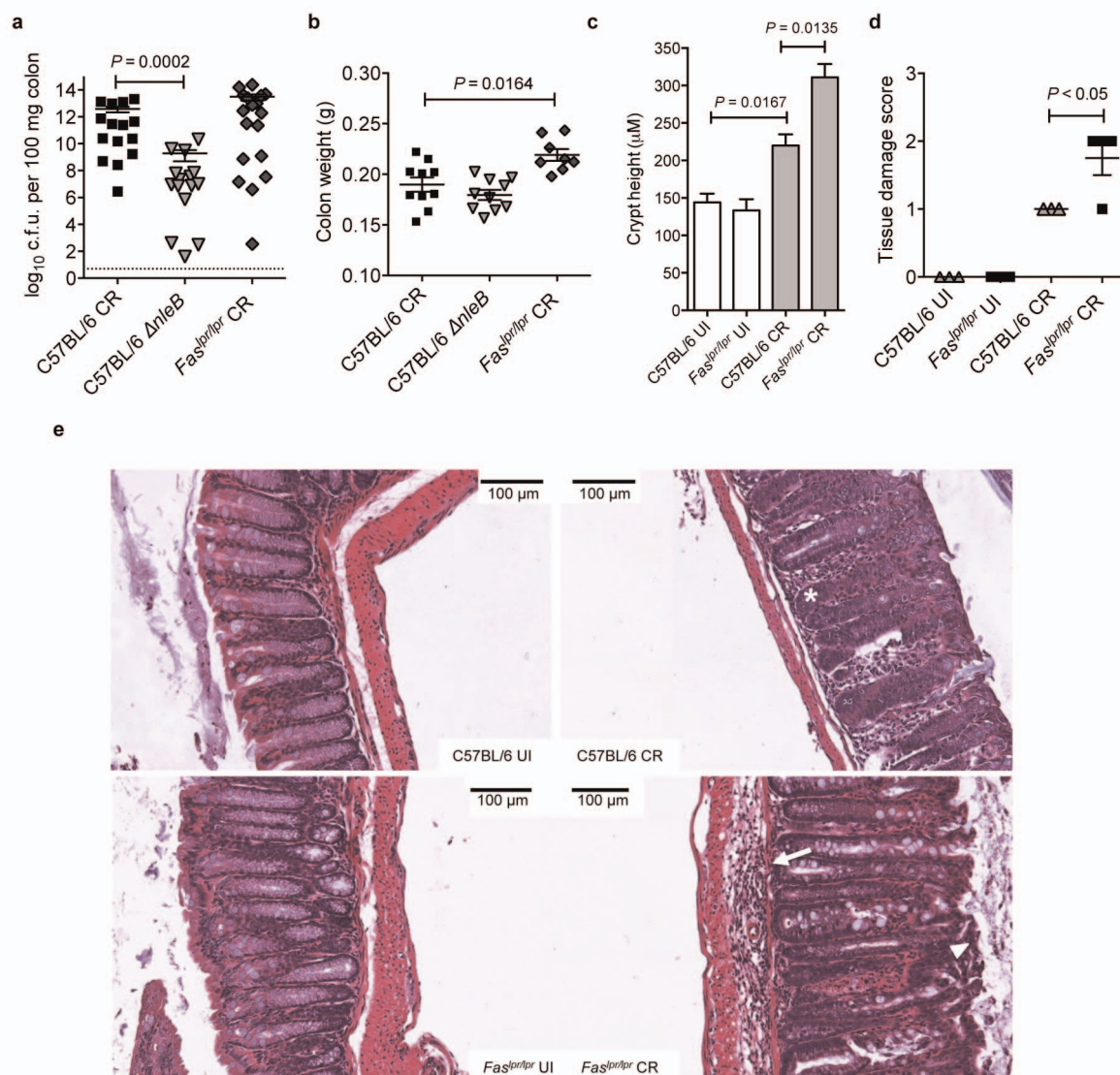
Extended Data Figure 5 | Comparison of FasL and TNF-mediated caspase-8 processing and analysis of NleB2. **a**, GFP-Trap pull-down of FADD-Flag, TRADD-Flag or RIPK1-Flag with EGFP-NleB2 in HEK293T cells. Actin, loading control. Representative immunoblot from at least three independent experiments. **b-d**, Co-immunoprecipitation of bacterially delivered NleB2-2HA with FADD-Flag, TRADD-Flag and RIPK1-Flag in HeLa cells using HA antibodies. Lane 1, HeLa cells infected with EPEC *ΔnleB2* (pNleB2) (negative control). Lane 2, HeLa cells infected with EPEC *ΔnleB2* (pNleB2-2HA). Actin, loading control. Representative immunoblots from at least three independent experiments. **e**, Unprocessed and cleaved caspase-8 in HeLa cells infected for 3 h with derivatives of EPEC and left untreated or treated with Fcγ-FasL or

TNF for 1 h, as indicated. Representative immunoblot from at least three independent experiments. **f**, Unprocessed and cleaved caspase-8 in HeLa cells infected for 45 min with derivatives of EPEC and left untreated or treated with TNF and cyclohexamide (CHX) for 1 h as indicated. Actin, loading control. Representative immunoblot from at least three independent experiments. **g**, Adherence of EPEC to HeLa cells. HeLa cells were infected with derivatives of EPEC for 3 h followed by treatment with FasL for 1 h. Number of recovered bacteria and the inoculum are shown for comparison. Mean \pm s.e.m. are indicated. Data are from three independent experiments performed in triplicate.



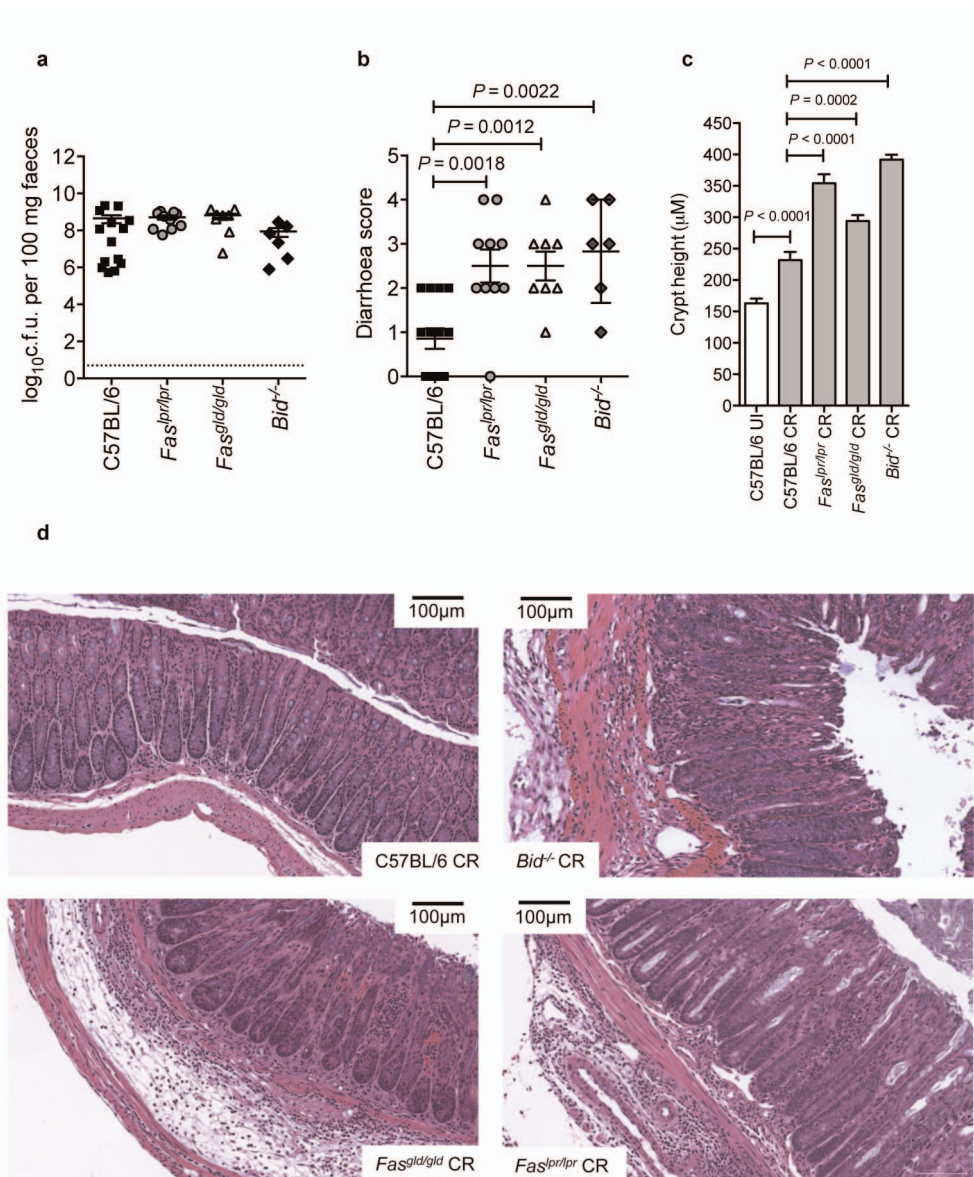
Extended Data Figure 6 | Infection of C57BL/6 and *Fas^{lpr/lpr}* mice with *C. rodentium*. **a**, Immunofluorescence staining of cleaved caspase-8 in different colonic sections from C57BL/6 mice infected with wild type *C. rodentium* and an *nleB* mutant as indicated, using antibodies to *C. rodentium* O-antigen (anti-O152, green) and cleaved caspase-8 (red). Intestinal tissue was visualized with Hoechst staining for DNA (blue). Arrows indicate cleaved caspase-8 positive cells sloughed into the gut lumen. Scale bar, 100 μ m. Representative images from at least three separate sections of colon at least

100 μ m apart (transverse or longitudinal), per animal from five individual mice per group. **b**, Time course of infection of C57BL/6 and *Fas^{lpr/lpr}* mutant mice with *C. rodentium*. Each data point represents log₁₀ c.f.u. per 100 mg faeces per individual animal on the indicated days. Mean \pm s.e.m. are indicated, dotted line represents detection limit. *C. rodentium*, mice infected with wild type *C. rodentium*; $\Delta nleB$ mice infected with *C. rodentium nleB* mutant. * $P < 0.05$, ** $P < 0.01$, *** $P < 0.001$. P values from Mann-Whitney U -test. Dotted line represents the detection limit.



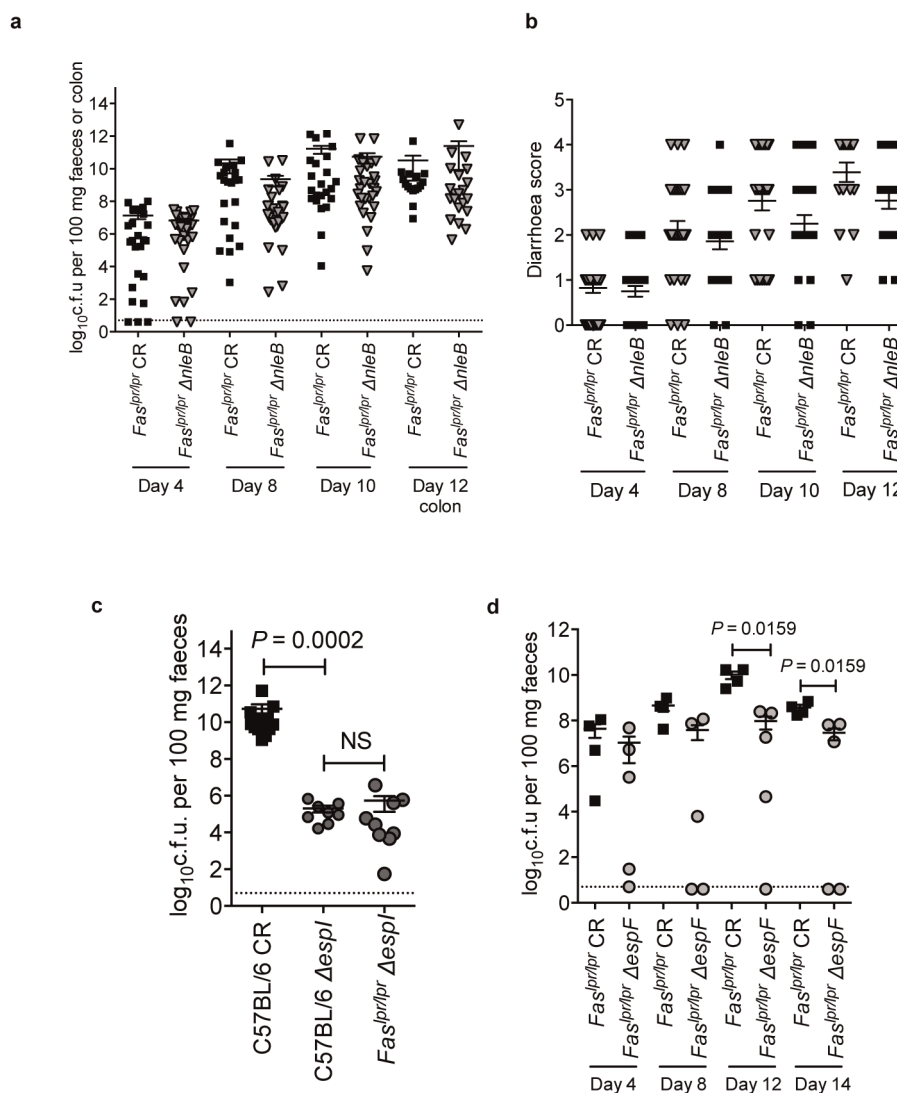
Extended Data Figure 7 | Histological analysis of intestinal sections at day 10 from FAS-deficient mice infected with *C. rodentium*. **a**, Bacterial load in the colon of mice infected with *C. rodentium* (CR). Each data point represents \log_{10} c.f.u. per 100 mg colon per individual animal on day 10 post-infection. C57BL/6 CR, wild-type mice infected with wild-type *C. rodentium*; C57BL/6 $\Delta nleB$, wild-type mice infected with *C. rodentium nleB* mutant; $Fas^{lpr/lpr}$ CR, $Fas^{lpr/lpr}$ mice infected with wild-type *C. rodentium*, dotted line is the detection limit. $P = 0.0002$, Mann–Whitney *U*-test. Mean \pm s.e.m. are indicated. **b**, Resected colon weights (between rectum and caecum) of individual animals on day 10 post-infection. C57BL/6 CR, wild-type mice infected with wild-type *C. rodentium*; C57BL/6 $\Delta nleB$, wild-type mice infected with *C. rodentium nleB* mutant; $Fas^{lpr/lpr}$ CR, $Fas^{lpr/lpr}$ mice infected with wild type *C. rodentium*. $P = 0.0164$, Mann–Whitney *U*-test. Mean \pm s.e.m. are indicated.

c, Mean \pm s.e.m. crypt height in μm in haematoxylin and eosin stained sections from C57BL/6 and $Fas^{lpr/lpr}$ mice infected with wild type *C. rodentium*. UI, uninfected. Data are from 4 sections of colon measured at least 50 μm apart per animal from at least 3 individual mice per group. **d**, Mean \pm s.e.m. tissue damage score in colon sections for individual mice infected with wild type *C. rodentium*. Scoring system is described in the Methods. UI, uninfected. $P < 0.05$, Mann–Whitney *U*-test. **e**, Haematoxylin and eosin stained sections of colon from C57BL/6 (wild-type) or $Fas^{lpr/lpr}$ mice uninfected or infected with wild type *C. rodentium* (day 10 post-infection). UI, uninfected. Scale bar, 100 μm . Mucosal inflammation (asterisk), neutrophil invasion of the muscularis mucosa (arrow), erosion of the epithelium (arrowhead). Representative images from two sections of colon at least 100 μm apart (transverse or longitudinal) from at least three individual mice per group.



Extended Data Figure 8 | Diarrhoea score and histological analysis of intestinal sections at day 12 from C57BL/6 (wild-type), *Fas^{lpr/lpr}*, *Fas^{gld/gld}* and *Bid^{-/-}* mice infected with *C. rodentium*. **a**, Bacterial load in the faeces of different mouse strains infected with wild-type *C. rodentium* as indicated. Each data point represents log₁₀ c.f.u. per 100 mg colon per individual animal. Dotted line is detection limit. Mean \pm s.e.m. are indicated. **b**, Diarrhoea score at day 12 post-infection of different strains of mice infected with *C. rodentium*. Scoring system is described in the Methods. Mean \pm s.e.m. are indicated.

P values from one-way ANOVA. **c**, Mean \pm s.e.m. crypt height in μ m in haematoxylin and eosin stained sections from different mouse strains infected with wild-type *C. rodentium*. UI, uninfected. Data are from 4 sections of colon measured at least 50 μ m apart per animal from at least three individual mice per group. **d**, Haematoxylin and eosin stained sections of colon from different mouse strains infected with wild type *C. rodentium*. Scale bar, 100 μ m. Representative images from two sections of colon at least 100 μ m apart (transverse or longitudinal) from at least three individual mice per group.



Extended Data Figure 9 | Bacterial load in the faeces of *Fas^{Δpr/Δpr}* mice infected with wild-type *C. rodentium*, an *espI* mutant and an *espF* mutant.

a, Bacterial load in the faeces of mice during infection with derivatives of *C. rodentium*. Each data point represents \log_{10} c.f.u. per 100 mg faeces or colon as indicated per individual animal on days 4, 8, 10 and 12 post-infection. Mean \pm s.e.m. are indicated, dotted line represents detection limit.

b, Diarrhoea score at day 4, 8, 10 and 12 post-infection. Scoring system is described in the Methods. Mean \pm s.e.m. are indicated. P values from one-way ANOVA. **c**, **d**, Bacterial load in the faeces of mice infected with derivatives of *C. rodentium*. Each data point represents \log_{10} c.f.u. per 100 mg faeces per individual animal on day 8 post-infection. Mean \pm s.e.m. are indicated, dotted line represents detection limit. P values from Mann-Whitney U -test.

Stability and function of regulatory T cells is maintained by a neuropilin-1–semaphorin-4a axis

Greg M. Delgoffe¹*, Seng-Ryong Woo¹*, Meghan E. Turnis¹, David M. Gravano¹, Cliff Guy¹, Abigail E. Overacre^{1,2}, Matthew L. Bettini¹, Peter Vogel³, David Finkelstein⁴, Jody Bonnevier⁵, Creg J. Workman¹ & Dario A. A. Vignali¹

Regulatory T cells (T_{reg} cells) have a crucial role in the immune system by preventing autoimmunity, limiting immunopathology, and maintaining immune homeostasis¹. However, they also represent a major barrier to effective anti-tumour immunity and sterilizing immunity to chronic viral infections¹. The transcription factor Foxp3 has a major role in the development and programming of T_{reg} cells^{2,3}. The relative stability of T_{reg} cells at inflammatory disease sites has been a highly contentious subject^{4–6}. There is considerable interest in identifying pathways that control the stability of T_{reg} cells as many immune-mediated diseases are characterized by either exacerbated or limited T_{reg} -cell function. Here we show that the immune-cell-expressed ligand semaphorin-4a (Sema4a) and the T_{reg} -cell-expressed receptor neuropilin-1 (Nrp1) interact both *in vitro*, to potentiate T_{reg} -cell function and survival, and *in vivo*, at inflammatory sites. Using mice with a T_{reg} -cell-restricted deletion of Nrp1, we show that Nrp1 is dispensable for suppression of autoimmunity and maintenance of immune homeostasis, but is required by T_{reg} cells to limit anti-tumour immune responses and to cure established inflammatory colitis. Sema4a ligation of Nrp1 restrained Akt phosphorylation cellularly and at the immunologic synapse by phosphatase and tensin homologue (PTEN), which increased nuclear localization of the transcription factor Foxo3a. The Nrp1-induced transcriptome promoted T_{reg} -cell stability by enhancing quiescence and survival factors while inhibiting programs that promote differentiation. Importantly, this Nrp1-dependent molecular program is evident in intra-tumoral T_{reg} cells. Our data support a model in which T_{reg} -cell stability can be subverted in certain inflammatory sites, but is maintained by a Sema4a–Nrp1 axis, highlighting this pathway as a potential therapeutic target that could limit T_{reg} -cell-mediated tumour-induced tolerance without inducing autoimmunity.

It was suggested initially that T_{reg} -cell-mediated suppression was contact-dependent, and soluble factors were insufficient, as purified T_{reg} cells failed to suppress across a permeable transwell membrane^{3,7}. However, we have shown previously that additional signals, derived from co-cultured T cells, are required to potentiate maximal T_{reg} -cell suppression by soluble factors across a transwell membrane⁸. Indeed, T_{reg} cells stimulated in the presence of fixed or live $CD4^+$ conventional T cells (T_{conv} cells) in the top chamber of a transwell plate can suppress T_{conv} cells in the bottom chamber (Supplementary Fig. 1a). To determine the T_{conv} -cell-derived signals responsible for potentiating or boosting T_{reg} -cell-mediated suppression, we compared the T_{conv} - and T_{reg} -cell transcriptomes and identified Sema4a as a potential ligand that could boost T_{reg} -cell function (Supplementary Fig. 1b–d). Sema4a is involved in neural patterning and has been implicated in modulating immune function, with haematopoietic cell expression restricted to $CD4^+$ and $CD8^+$ T cells, natural killer cells and dendritic cells⁹. Using RNA interference, loss-variant selection and overexpression in hybridomas, and

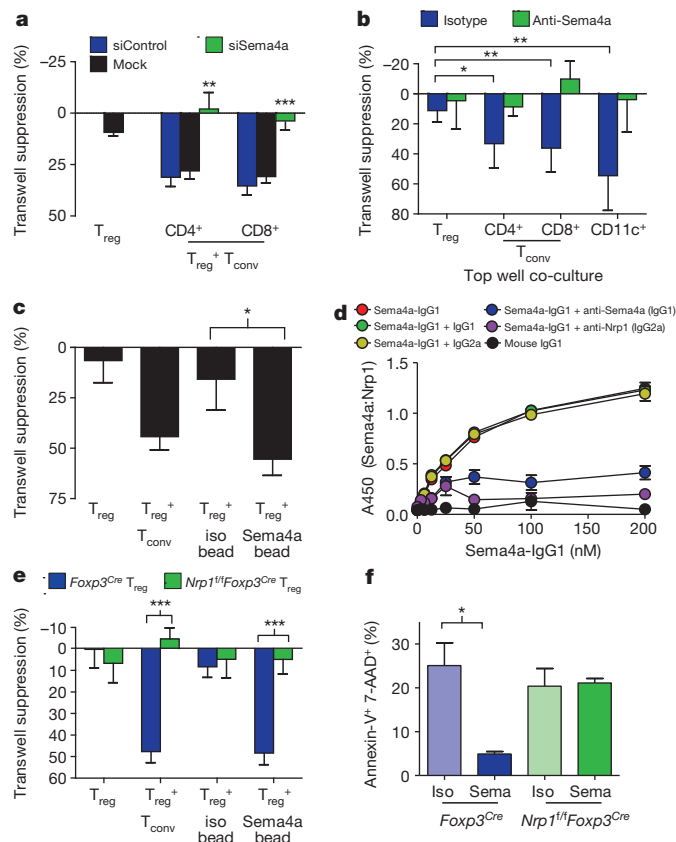


Figure 1 | Sema4a binds Nrp1 to potentiate T_{reg} -cell function and survival *in vitro*. **a**, Transwell suppression assay in which T_{reg} cells were co-cultured in the top chamber of a transwell plate with anti-CD3- and anti-CD28-coated beads in the presence or absence of $CD4^+$ or $CD8^+$ T_{conv} cells that had been transfected previously with scrambled or siRNA to Sema4a. Proliferation of T_{conv} cells stimulated with anti-CD3- and anti-CD28-coated beads in the bottom chambers was measured by [³H]-thymidine uptake. **b**, Transwell suppression assay with T_{reg} cells co-cultured in top chamber with $CD4^+$, $CD8^+$ or $CD11c^+$ cells including anti-Sema4a or its isotype control. **c**, Transwell suppression assay in which T_{reg} cells were co-cultured in the absence of T_{conv} cells but in the presence of beads coated with Sema4a-IgG1 or its isotype control. **d**, ELISA-based binding assay in which plates coated with Nrp1 were incubated with Sema4a-IgG1 or its isotype control in the presence of various blocking antibodies. Sema4a-IgG1 was detected using an isotype specific antibody. **e**, Transwell suppression assay in which T_{reg} cells were purified by flow cytometry from Foxp3^{Cre} or Nrp1^{fl/fl}Foxp3^{Cre} mice. **f**, Annexin V-7-AAD staining of T_{reg} cells stimulated for 48 h *in vitro* in the presence of Sema4a-IgG1 or its isotype control. Results represent the mean of five independent experiments. **P* < 0.05, ***P* < 0.01, ****P* < 0.001 by unpaired *t*-test. Error bars indicate s.e.m.

¹Department of Immunology, St Jude Children's Research Hospital, Memphis, Tennessee 38105, USA. ²Integrated Biomedical Sciences Program, University of Tennessee Health Science Center, Memphis, Tennessee 38163, USA. ³Department of Pathology, St Jude Children's Research Hospital, Memphis, Tennessee 38105, USA. ⁴Computational Biology, St Jude Children's Research Hospital, Memphis, Tennessee 38105, USA. ⁵R&D Systems Inc., Minneapolis, Minnesota 55413, USA.

*These authors contributed equally to this work.

antibody blockade, we confirmed that Sema4a was necessary for T_{reg} -cell-mediated transwell suppression (Fig. 1a, b and Supplementary Fig. 2a–e). Sema4a is also sufficient to potentiate suppression, as T_{reg} cells cultured in the presence of beads coated with a Sema4a-immunoglobulin-G1 (IgG1) fusion protein, instead of fixed T_{conv} cells, potentiated transwell suppression (Fig. 1c). In contrast, soluble Sema4a-IgG1 inhibited T_{conv} -cell-potentiated, T_{reg} -cell-mediated transwell suppression (Supplementary Fig. 2f). These data demonstrate that Sema4a is required and sufficient to potentiate T_{reg} -cell function by soluble factors *in vitro*.

Nrp1 is a homogeneously expressed marker of thymically derived T_{reg} cells, and has also been shown to bind Sema3a, which shares homology with Sema4a, and vascular endothelial growth factor (VEGF) in mediating neural axon growth and angiogenesis (Supplementary Fig. 3a)^{10–13}. We therefore proposed that Nrp1 functions as a receptor for Sema4a on T_{reg} cells. Sema4a could directly and specifically bind to Nrp1, albeit with slightly lower avidity to Sema3a, as demonstrated in an enzyme-linked immunosorbent assay (ELISA)-based binding assay with recombinant Nrp1 and Sema family proteins and blocking antibodies to Nrp1 or Sema4a (Fig. 1d and Supplementary Fig. 3b–d). We bred mice harbouring a loxP-flanked ('floxed') *Nrp1* gene (*Nrp1*^{fl/f}) to mice expressing a yellow fluorescent protein (YFP)-codon-improved Cre (iCre) fusion protein driven by an IRES following *Foxp3* (*Foxp3*^{YFP-iCre}), which we refer to as *Foxp3*^{Cre} to obtain a T_{reg} -cell-restricted deletion of Nrp1 (*Foxp3*^{YFP-iCre} × *Nrp1*^{fl/f}, which we refer to as *Nrp1*^{fl/f}*Foxp3*^{Cre}). Sema4a-IgG1 also bound to control but not Nrp1-deficient T_{reg} cells in a flow cytometric assay (Supplementary Fig. 3e). These data support a direct interaction between Nrp1 and Sema4a.

Although Nrp1-deficient T_{reg} cells develop normally and can suppress in a 'classical' contact-dependent suppression assay (Supplementary

Fig. 4a), they were unable to suppress across a transwell membrane in the presence of either T_{conv} cells or Sema4a-IgG1-coated beads (Fig. 1e). Transwell suppression can be blocked by anti-Nrp1 and, as reported previously, is dependent on interleukin-10 (IL-10) and IL-35 (Supplementary Fig. 4b–d)⁸. Sema4a–Nrp1 ligation substantially reduced cell death and modestly increased proliferation, and, although single-cell levels of IL-10 and IL-35 did not change, increased survival resulted in greater amounts of IL-10 and IL-35 in Sema4a-treated T_{reg} -cell cultures (Fig. 1f and Supplementary Fig. 4e–i). Expression of NRP1 on human T_{reg} cells has been a contentious subject^{14,15}. We observed sustained NRP1 expression, albeit modest, on optimally suppressive T_{reg} cells that could mediate transwell suppression in response to human Sema4a in a NRP1-dependent manner (Supplementary Fig. 5). Taken together, these data suggest Sema4a–Nrp1 interaction promotes T_{reg} -cell survival and function.

Nrp1^{fl/f}*Foxp3*^{Cre} mice did not show any autoimmune phenotype for at least 16 months after birth (data not shown). In addition, the capacity of *Foxp3*^{Cre} and *Nrp1*^{fl/f}*Foxp3*^{Cre} T_{reg} cells to limit the development of the autoimmune sequelae caused by *Foxp3* deletion was comparable (Supplementary Fig. 6), suggesting that maintenance of immune homeostasis and prevention of autoimmunity may not require Nrp1 signalling.

We reasoned that Nrp1 signalling may regulate T_{reg} -cell function under inflammatory conditions. T_{reg} cells are recruited to and are induced by tumour cells, which consequently hamper protective anti-tumour immunity¹⁶. *Foxp3*^{DTR-GFP} mice, which allow for conditional T_{reg} -cell deletion following diphtheria toxin treatment¹⁷, can clear MC38 adenocarcinoma, EL4 thymoma, and B16 melanoma tumours when treated with diphtheria toxin at the time of inoculation, although they invariably succumb to autoimmune disease (Fig. 2a–c). Notably, *Nrp1*^{fl/f}*Foxp3*^{Cre} mice showed reduced, delayed tumour growth and increased survival,

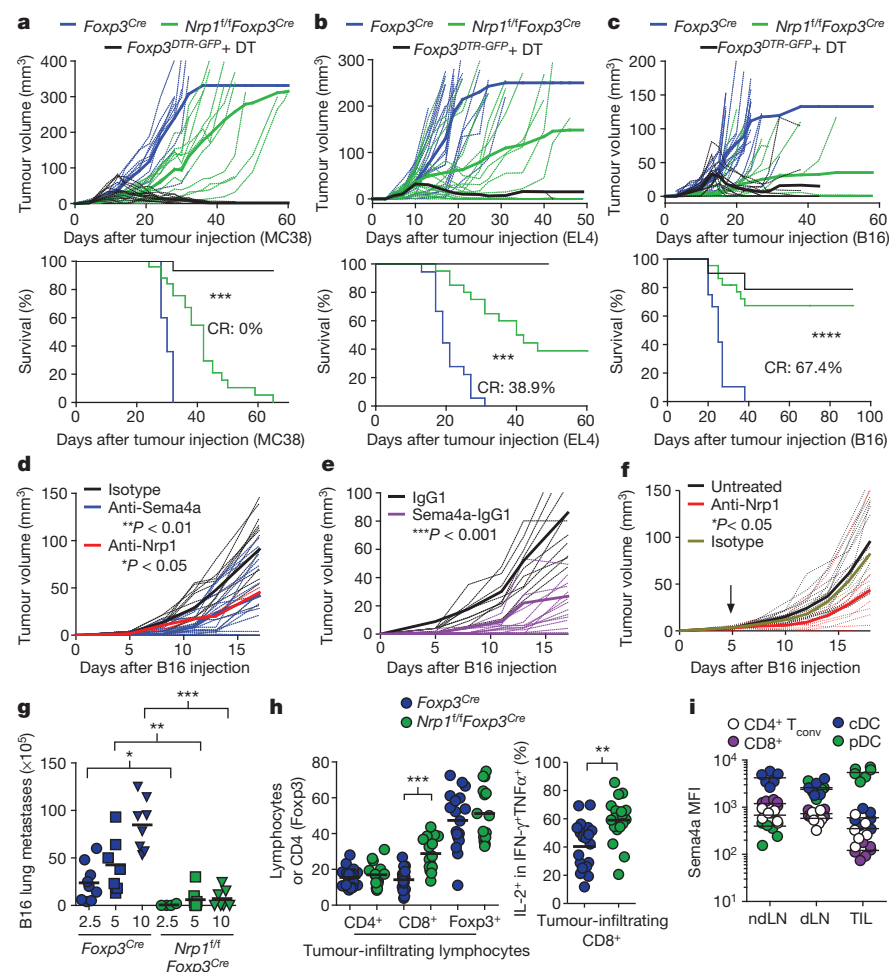


Figure 2 | Nrp1-deficient T_{reg} cells fail to suppress anti-tumour immune responses.

a, Tumour growth curve (top) and survival plot (bottom) of *Foxp3*^{Cre}, *Nrp1*^{fl/f}*Foxp3*^{Cre}, or *Foxp3*^{DTR-GFP} mice receiving 1.25 × 10⁵ MC38 melanoma cells subcutaneously and (for *Foxp3*^{DTR-GFP}) 100 μg diphtheria toxin (DT) intraperitoneally, twice weekly. **b**, As in **a**, but mice received 1.25 × 10⁵ EL4 thymoma intradermally. **c**, As in **a**, but mice received 1.25 × 10⁵ B16 melanoma intradermally. **d**, Tumour growth curve of C57/BL6 mice receiving 1.25 × 10⁵ B16 melanoma intradermally concomitant with injections of isotype control, anti-Sema4a, or anti-Nrp1 (100 μg) twice weekly. **e**, Tumour growth curve as in **d** except mice received Sema4a-IgG1 twice weekly. **f**, Tumour growth curve of C57/BL6 mice receiving 1.25 × 10⁵ B16 melanoma intradermally. When tumours were palpable (day 5, indicated by arrow), mice began receiving injections of anti-Nrp1 or its isotype control (400 μg initially, 200 μg every 3 days). **g**, Lung metastasis counts from *Foxp3*^{Cre} or *Nrp1*^{fl/f}*Foxp3*^{Cre} mice injected with 2.5–10 × 10⁵ B16 cells intravenously, 17–20 days earlier. **h**, Tabulation of flow cytometric analysis of tumour-infiltrating lymphocytes from *Foxp3*^{Cre} or *Nrp1*^{fl/f}*Foxp3*^{Cre} mice injected intradermally with B16 18 days earlier. **i**, Sema4a expression of various immune cells in non-draining lymph node (ndLN), draining lymph node (dLN) or tumour-infiltrating lymphocytes (TIL). Results represent the mean of five (a–c, n = 10–25 mice), three (d–h, n = 8–20 mice), or three (i) experiments. *P < 0.05, **P < 0.01, ***P < 0.001, by (a–f) one-way analysis of variance (ANOVA) or (g–i) unpaired t-test. CR, complete response. Error bars indicate s.e.m.

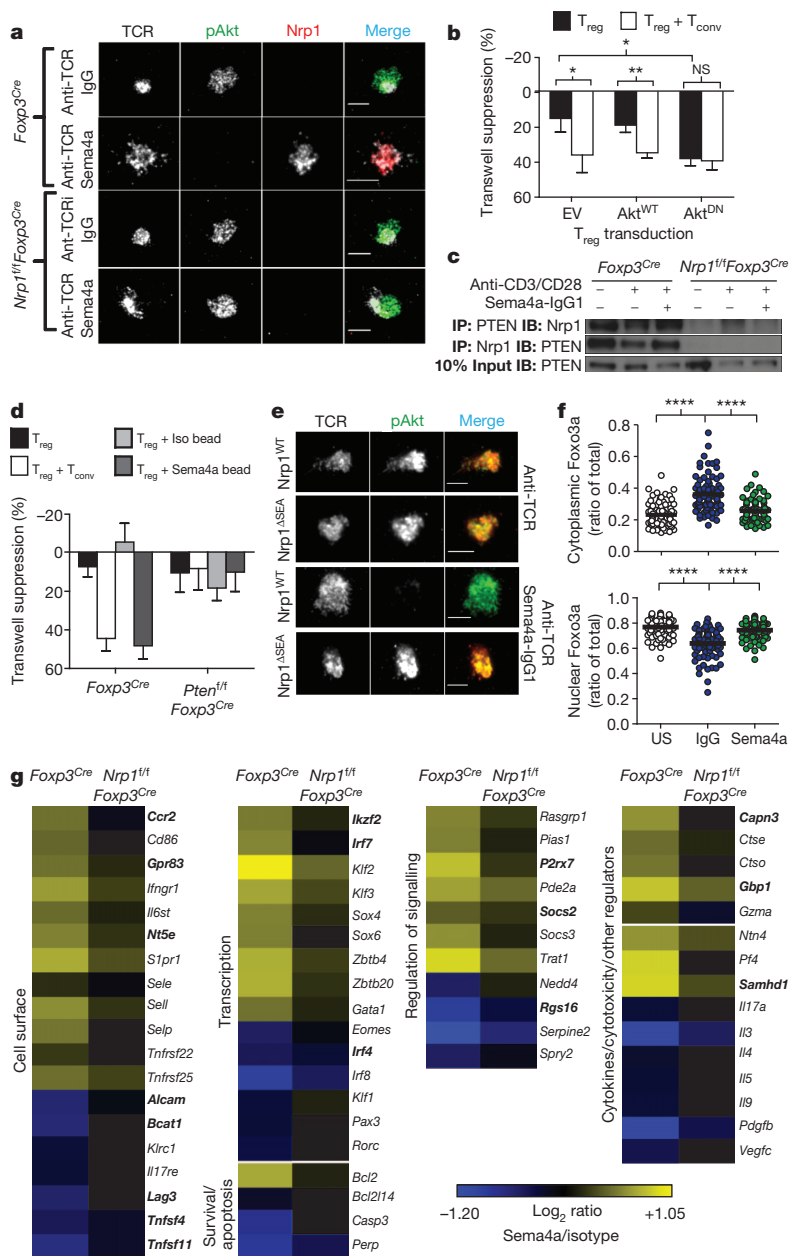


Figure 3 | Ligand of Nrp1 by Sema4a promotes T_{reg} -cell stability through modulation of Akt-mTOR signalling. **a**, Total internal reflection fluorescence (TIRF) microscopic analysis of immunologic synapse Akt phosphorylation in T_{reg} cells stimulated 20 min on a lipid bilayer coated with anti-TCR antibodies in the presence or absence of Sema4a-IgG1. **b**, Transwell suppression assay using T_{reg} cells retrovirally expressing wild-type (WT) or dominant-negative (DN)-Akt. Transductants were selected and expanded using puromycin and IL-2. NS, not significant. **c**, Immunoprecipitation (IP) analysis of Nrp1 using *in vitro* expanded T_{reg} cells that were serum starved for 3 h, then stimulated as indicated for 6 h before IP. **d**, Transwell suppression assay using $Foxp3^{Cre}$ or $Pten^{fl/fl}Foxp3^{Cre}$ T_{reg} cells. **e**, TIRF microscopic analysis of immunologic synapse Akt phosphorylation as in **a**, of $Nrp1^{fl/fl}Foxp3^{Cre}$ T_{reg} cells retrovirally reconstituted with wild-type (WT) or SEA-deficient (ASEA) Nrp1. **f**, Foxo3a cytoplasmic (top) and nuclear (bottom) localization signals, as defined by masking using actin and DNA staining. Arbitrary Units represent fluorescence intensity calculated volumetrically through 20 to 30 slices of T_{reg} cells. $n = 70-93$. US, unstimulated (control). IgG, unstimulated (control). Sema4a, stimulated for 48 h with anti-CD3, anti-CD28, 100 units per ml rhIL-2, and immobilized IgG1 or Sema4a-IgG1. RNA was subjected to Affymetrix gene profiling. T_{reg} -cell signature genes are in bold. All genes shown met false discovery rate (FDR) < 0.10 and compared using two-way ANOVA. Results represent at least three independent experiments (**a**, **c**, **e**, **f**) or represent means of three (**b**, **d**) or seven (**g**) experiments. * $P < 0.05$, ** $P < 0.01$ by unpaired *t*-test. Error bars indicate s.e.m.

particularly with B16 melanoma, without any detectable autoimmune consequences (Fig. 2a–c and data not shown). In wild-type C57BL/6 mice, blockade of this pathway using Sema4a monoclonal antibody, Nrp1 monoclonal antibody (which does not block Nrp1–VEGF interaction), and Sema4a-IgG1 (which acts as a soluble antagonist), significantly decreased tumour growth (Fig. 2d–f and Supplementary Fig. 2f, 3b, c). Nrp1-deficient T_{reg} cells also failed to suppress clearance of B16 lung metastases, even with very high tumour cell inoculates (Fig. 2g and Supplementary Fig. 7a). $Nrp1^{fl/fl}Foxp3^{Cre}$ mice displayed increased intratumoral CD8⁺ T cells, particularly in the IFN- γ -IL-2⁺ TNF- α ⁺ tumoricidal subset (Fig. 2h)¹⁸. Although we originally presumed the source of Sema4a would be tumour-infiltrating T cells and conventional dendritic cells, the majority of Sema4a⁺ cells infiltrating tumours were plasmacytoid dendritic cells (57.4% of intratumoral Sema4a⁺ cells), consistent with previous suggestions highlighting mechanistic links between T_{reg} cells and plasmacytoid dendritic cells in mediating tumour-induced tolerance (Fig. 2i and Supplementary Fig. 7b, c)¹⁹. Indeed, plasmacytoid dendritic cells can potentiate T_{reg} -cell function *in vitro* in a Sema4a–Nrp1-dependent manner (Supplementary Fig. 7d). Treatment with Sema4a-IgG1 also resulted in an increased number of intratumoral

CD8⁺ T cells, consistent with observations with $Nrp1^{fl/fl}Foxp3^{Cre}$ mice (Supplementary Fig. 7e). Nrp1-deficient T_{reg} cells also fail to cure established inflammatory colitis, suggesting that the utilization of this pathway is not restricted to the tumour microenvironment (Supplementary Fig. 8). Thus, although Nrp1 seems to be dispensable for regulating immune homeostasis, it is required for maximal T_{reg} -cell-mediated control of inflammatory environments.

We next sought to determine the signalling pathway downstream of Nrp1. Given the importance of limiting Akt–serine/threonine-protein kinase mTOR signalling in T_{reg} -cell function, and previous suggestions that Nrp1 modulates Akt signalling, we proposed that Nrp1 inhibits Akt function in T_{reg} cells^{20–22}. Indeed, T-cell receptor (TCR)- and CD28-activation-induced whole-cell Akt–mTOR signalling (as determined by phosphorylation of Akt and S6K1) was reduced to baseline levels in freshly isolated T_{reg} cells (as well as 47–54% in IL-2-expanded T_{reg} cells) by Sema4a-mediated Nrp1 ligation (Supplementary Fig. 9a, b). Furthermore, T_{reg} -cell activation on stimulatory lipid bilayers containing Sema4a-IgG1, but not an isotype control, recruited Nrp1 to the immunologic synapse and inhibited immunologic synapse Akt phosphorylation, while sparing global immunologic synapse tyrosine

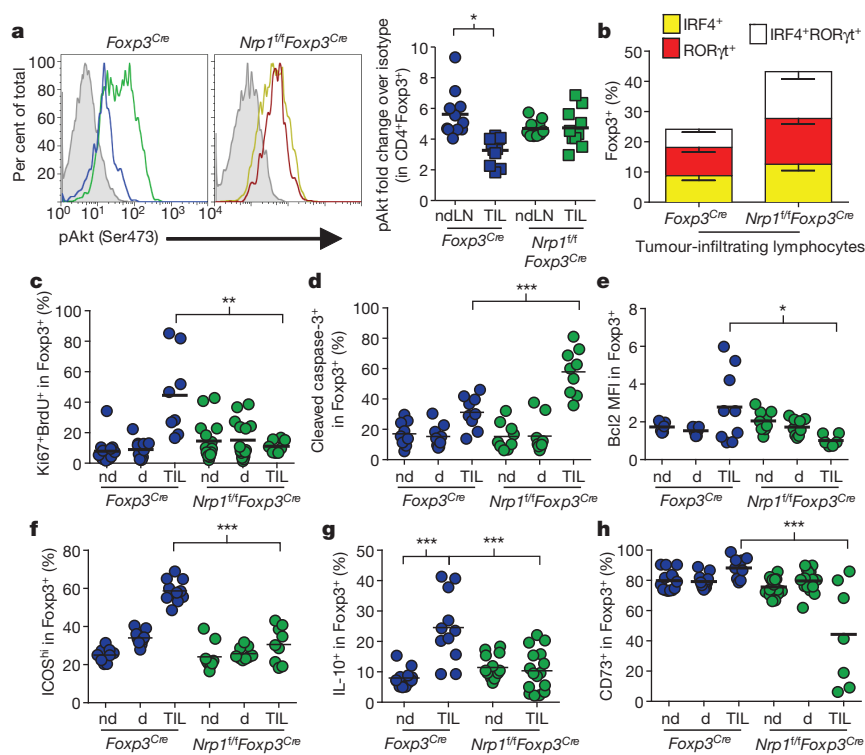


Figure 4 | Tumour-infiltrating T_{reg} cells bear a signature similar to Sema4a–Nr1p1 ligation.
a, Akt phosphorylation in T_{reg} cells. TIL (blue and maroon) and ndLN (green and gold) were collected from tumour-bearing $Foxp3^{Cre}$ or $Nrp1^{fl}/Foxp3^{Cre}$ mice. Cells were immediately fixed and stained for phosphorylated Akt (pAkt). **b–h**, Shaded histogram indicates isotype control. Results are tabulated normalized to isotype control staining. IRF4 and ROR γ T (**b**), Ki67 and BrdU (**c**), cleaved caspase-3 (**d**), Bcl2 (**e**), ICOS (**f**), IL-10 (**g**) and CD73 (**h**) staining from ndLN, dLN, or TIL from tumour-bearing $Foxp3^{Cre}$ or $Nrp1^{fl}/Foxp3^{Cre}$ mice. Ki67 and BrdU analysis included injection with BrdU 14 h before harvest. IL-10 staining included restimulation with phorbol myristate acetate (PMA) and ionomycin for 16 h in the presence of brefeldin A. Results represent the mean of 3–5 independent experiments. * $P < 0.05$, ** $P < 0.01$, *** $P < 0.001$ by paired t -test (**a**, $n = 10–11$) or unpaired t -test (**b–h** $n = 7–17$). MFI, mean fluorescence intensity. Error bars indicate s.e.m.

phosphorylation (Fig. 3a and Supplementary Fig. 9c, d). Retroviral overexpression of a dominant-negative Akt mutant²³ in T_{reg} cells expanded with IL-2 limited the requirement for Nr1p1 ligation, at least in transwell suppression assays, suggesting that Akt may be a dominant pathway that limits T_{reg} -cell transwell suppression (Fig. 3b and Supplementary Fig. 9e). As immunologic synapse phosphorylated-Akt diminution in response to Sema4a was rapid, we reasoned that Nr1p1 recruits the phosphatase PTEN to the immunologic synapse, restraining Akt–mTOR signalling²⁴. Nr1p1 constitutively bound PTEN in resting T_{reg} cells, which was reduced upon activation but maintained in the presence of Sema4a–Nr1p1 interaction (Fig. 3c). PTEN-deficient T_{reg} cells failed to inhibit Akt phosphorylation at the immunologic synapse in the presence of Sema4a, and failed to suppress across a transwell membrane in response to Sema4a- or T_{conv} -cell-mediated potentiation (Fig. 3d and Supplementary Fig. 10a, b). Nr1p1 has a small cytoplasmic domain consisting of an evolutionarily conserved PDZ domain-binding motif (carboxy-terminal amino acid sequence: Ser–Glu–Ala)²⁵. Nr1p1 mutants lacking this motif could not inhibit Akt phosphorylation at the immunologic synapse or recruit PTEN (Fig. 3e and Supplementary Fig. 10c, d). Activated Akt can phosphorylate Foxo transcription factors, promoting their exclusion from the nucleus²⁶. Foxo transcription factors are critical for T_{reg} -cell development, through interaction with Foxp3 as well as inducing several T_{reg} -cell signature genes^{26–28}. Indeed, Sema4a–IgG1 limited the activation-induced nuclear export of Foxo3a (Fig. 3f). We propose that, during activation, Nr1p1 ligation restrains Akt phosphorylation through PTEN, facilitates Foxo nuclear localization, and thereby potentiates T_{reg} -cell function.

Gene-expression analysis revealed an Nr1p1-induced transcriptional profile that was consistent with promoting T_{reg} -cell survival, stability and quiescence, and that was similar to a Foxo-dependent transcriptional signature (Fig. 3g)^{26–28}. Gene Ontology and Gene Set Enrichment Analysis revealed that Nr1p1 ligation modulated multiple pathways and programs, including the IL-2- and IL-7-related transcriptional programs, repression of cytokine transcripts and modulated Foxp3 targets (Fig. 3g, Supplementary Fig. 11–13, and Supplementary Tables 1 and 2). Of particular interest was the stabilization of the transcription factor Kruppel-like Factor 2 (KLF2) (and its targets *Sell*, *Ccr7*, *Il7r*), the T_{reg} -cell regulator Helios (*Irf2*; also known as IKAROS family zinc

finger 2), and the anti-apoptotic protein Bcl2, accompanied by a concomitant repression of the lineage defining transcription factors Eomes, IRF4 and ROR γ T (nuclear receptor ROR γ T, encoded by *Rorc*), suggesting a role for Nr1p1 in stabilizing the T_{reg} -cell program and repressing terminal differentiation (Fig. 3g and Supplementary Fig. 13b–d).

Finally, we sought to determine whether the molecular fingerprints of Nr1p1 signalling could be observed *in vivo*. Tumour-infiltrating T_{reg} -cells restrained Akt phosphorylation in an Nr1p1-dependent manner (Fig. 4a). Likewise, tumour-infiltrating T_{reg} cells showed Nr1p1-dependent upregulation of Helios and downregulation of IRF4 and ROR γ T (Fig. 4b and Supplementary Fig. 14a, b). This was associated with an increase in intratumoural T_{reg} -cell proliferation, as revealed by Ki67–BrdU (5-bromodeoxyuridine) staining, reduced caspase-3-dependent programmed cell death, and increased expression of the anti-apoptotic protein Bcl2 (Fig. 4c–e and Supplementary Fig. 14c–e). We also observed an Nr1p1-dependent increase in the percentage of ICOS⁺, IL-10⁺ and CD73⁺ intratumoural T_{reg} cells (Fig. 4f–h and Supplementary Fig. 14f–h). Taken together, our data support a role for Nr1p1 in modulating T_{reg} -cell stability, survival and function in certain tumour microenvironments.

Our data demonstrate that cell contact-dependent potentiation of T_{reg} -cell stability and function is mediated by Sema4a–Nr1p1 ligation through a PTEN–Akt–Foxo axis (Supplementary Fig. 15). This pathway enhances T_{reg} -cell function indirectly by enforcing stability and promoting survival, and this is most evident in inflammatory sites such as certain tumours and colitic intestinal mucosa. However, Nr1p1 signalling may also boost T_{reg} -cell function directly by enhancing some suppressive mechanisms (for example, CD73). Apart from haematopoietic lineages, Sema4a seems to have a pattern of expression consistent with sites in which T_{reg} -cell tolerogenic activity would be desired, such as the nervous system, eye and intestine²⁹. The issue of T_{reg} -cell stability has been highly contentious, and the mechanisms that maintain T_{reg} -cell stability remain elusive^{4–6}. As Foxo family members enhance Foxp3 function and promote T_{reg} -cell homeostasis and function^{26–28}, it is intriguing that Nr1p1 signalling may counteract the negative impact of Akt on Foxo nuclear localization, resulting in substantial overlap between the transcriptional profiles induced by Foxo and Nr1p1 signalling²⁸. It is possible that the Nr1p1–Sema4a pathway may be perturbed genetically or under certain pathologic circumstances; this could also provide a

basis for the seemingly contradictory perceptions of T_{reg}-cell stability in a variety of normal and diseased states.

Previous studies have shown that plasmacytoid dendritic cells promote tolerance, T_{reg}-cell differentiation and function, and their ablation has been shown to correlate with enhanced antitumour immunity^{19,30}. Given that the dominant intratumoral source of Sema4a was plasmacytoid dendritic cells, this raises the possibility that Nrp1-induced T_{reg}-cell stability and survival provides a mechanistic explanation for these observations. As T_{reg} cells represent a major barrier to anti-tumour immunity in many cancers, a clinically relevant and critical question is whether it is possible to limit T_{reg}-cell function in tumours while preventing inflammatory or autoimmune adverse events. Recently, a role for Nrp1 in T_{reg} cells was proposed to limit tumour growth in the MT/ret murine melanoma model²⁹, although contrary to the findings in that study we did not observe any differences in T_{reg}-cell prevalence in B16 melanoma tumours (Fig. 2h). However, further studies will be required to delineate in which tumours and under what conditions these two disparate functions of Nrp1 in T_{reg} cells—regulation of T_{reg}-cell migration and the maintenance of T_{reg}-cell survival and stability—are used. Our identification of Nrp1–Sema4a as a pivotal pathway required for intratumoral T_{reg}-cell stability, but dispensable for the maintenance of immune homeostasis, suggests that Sema4a–Nrp1 blockade via antibodies or soluble antagonists may be a viable therapeutic strategy to limit tumour-induced tolerance without evoking autoimmunity.

METHODS SUMMARY

Mice. C57/BL6 and dnTGFβRII mice were purchased from the Jackson Laboratories. *Foxp3*^{YFP-iCre}, *Foxp3*^{−/−} and *Foxp3*^{DTR-GFP} mice were obtained from A.Y. Rudensky. *Il10*^{−/−} mice were obtained from T. Geiger. *Nrp1*^{fl/fl} mice were obtained from D. Cheresch. *Pten*^{fl/fl} × *Foxp3*^{YFP-iCre} mice were obtained from H. Chi. Animal experiments were performed in American Association for the Accreditation of Laboratory Animal Care-accredited, specific-pathogen-free facilities in the St Jude Animal Resource Center. Animal protocols were approved by the St Jude Animal Care and Use Committee.

Full Methods and any associated references are available in the online version of the paper.

Received 20 September 2012; accepted 2 July 2013.

Published online 4 August 2013.

- Vignali, D. A., Collison, L. W. & Workman, C. J. How regulatory T cells work. *Nature Rev. Immunol.* **8**, 523–532 (2008).
- Fontenot, J. D., Gavin, M. A. & Rudensky, A. Y. Foxp3 programs the development and function of CD4⁺CD25⁺ regulatory T cells. *Nature Immunol.* **4**, 330–336 (2003).
- Hori, S., Nomura, T. & Sakaguchi, S. Control of regulatory T cell development by the transcription factor Foxp3. *Science* **299**, 1057–1061 (2003).
- Miyao, T. *et al.* Plasticity of Foxp3⁺ T cells reflects promiscuous Foxp3 expression in conventional T cells but not reprogramming of regulatory T cells. *Immunity* **36**, 262–275 (2012).
- Rubtsov, Y. P. *et al.* Stability of the regulatory T cell lineage *in vivo*. *Science* **329**, 1667–1671 (2010).
- Zhou, X. *et al.* Instability of the transcription factor Foxp3 leads to the generation of pathogenic memory T cells *in vivo*. *Nature Immunol.* **10**, 1000–1007 (2009).
- Qiao, M., Thornton, A. M. & Shevach, E. M. CD4⁺CD25⁺ regulatory T cells render naive CD4⁺CD25[−] T cells anergic and suppressive. *Immunology* **120**, 447–455 (2007); corrigendum **121**, 146 (2007).
- Collison, L. W., Pillai, M. R., Chaturvedi, V. & Vignali, D. A. Regulatory T cell suppression is potentiated by target T cells in a cell contact, IL-35- and IL-10-dependent manner. *J. Immunol.* **182**, 6121–6128 (2009).
- Kumanogoh, A. *et al.* Class IV semaphorin Sema4A enhances T-cell activation and interacts with Tim-2. *Nature* **419**, 629–633 (2002).
- Bruder, D. *et al.* Neuropilin-1: a surface marker of regulatory T cells. *Eur. J. Immunol.* **34**, 623–630 (2004).
- Kolodkin, A. L. *et al.* Neuropilin is a semaphorin III receptor. *Cell* **90**, 753–762 (1997).
- Weiss, J. M. *et al.* Neuropilin 1 is expressed on thymus-derived natural regulatory T cells, but not mucosa-generated induced Foxp3⁺ T reg cells. *J. Exp. Med.* **209**, 1723–1742 (2012).
- Yadav, M. *et al.* Neuropilin-1 distinguishes natural and inducible regulatory T cells among regulatory T cell subsets *in vivo*. *J. Exp. Med.* **209**, 1713–1722 (2012).

- Milpied, P. *et al.* Neuropilin-1 is not a marker of human Foxp3⁺ Treg. *Eur. J. Immunol.* **39**, 1466–1471 (2009).
- Piechnik, A. *et al.* The VEGF receptor neuropilin-1 (NRP1) represents a promising novel target for chronic lymphocytic leukemia patients. *Int. J. Cancer* <http://dx.doi.org/10.1002/ijc.28135> (28 February 2013).
- Nishikawa, H. & Sakaguchi, S. Regulatory T cells in tumor immunity. *Int. J. Cancer* **127**, 759–767 (2010).
- Kim, J. M., Rasmussen, J. P. & Rudensky, A. Y. Regulatory T cells prevent catastrophic autoimmunity throughout the lifespan of mice. *Nature Immunol.* **8**, 191–197 (2007).
- Wilde, S. *et al.* Human antitumor CD8⁺ T cells producing Th1 polycytokines show superior antigen sensitivity and tumor recognition. *J. Immunol.* **189**, 598–605 (2012).
- Demoulin, S., Herfs, M., Delvenne, P. & Hubert, P. Tumor microenvironment converts plasmacytoid dendritic cells into immunosuppressive/tolerogenic cells: insight into the molecular mechanisms. *J. Leukoc. Biol.* **93**, 343–352 (2013).
- Castro-Rivera, E., Ran, S., Brekken, R. A. & Minna, J. D. Semaphorin 3B inhibits the phosphatidylinositol 3-kinase/Akt pathway through neuropilin-1 in lung and breast cancer cells. *Cancer Res.* **68**, 8295–8303 (2008).
- Crellin, N. K., Garcia, R. V. & Levings, M. K. Altered activation of AKT is required for the suppressive function of human CD4⁺CD25⁺ T regulatory cells. *Blood* **109**, 2014–2022 (2007).
- Haxhinasto, S., Mathis, D. & Benoist, C. The AKT-mTOR axis regulates de novo differentiation of CD4⁺Foxp3⁺ cells. *J. Exp. Med.* **205**, 565–574 (2008).
- Franke, T. F. *et al.* The protein kinase encoded by the Akt proto-oncogene is a target of the PDGF-activated phosphatidylinositol 3-kinase. *Cell* **81**, 727–736 (1995).
- Stambolic, V. *et al.* Negative regulation of PKB/Akt-dependent cell survival by the tumor suppressor PTEN. *Cell* **95**, 29–39 (1998).
- Pellet-Many, C., Frankel, P., Jia, H. & Zachary, I. Neuropilins: structure, function and role in disease. *Biochem. J.* **411**, 211–226 (2008).
- Merkenschlager, M. & von Boehmer, H. PI3 kinase signalling blocks Foxp3 expression by sequestering Foxo factors. *J. Exp. Med.* **207**, 1347–1350 (2010).
- Kerdiles, Y. M. *et al.* Foxo transcription factors control regulatory T cell development and function. *Immunity* **33**, 890–904 (2010); erratum **34**, 135 (2011).
- Ouyang, W. *et al.* Foxo proteins cooperatively control the differentiation of Foxp3⁺ regulatory T cells. *Nature Immunol.* **11**, 618–627 (2010).
- Heng, T. S. & Painter, M. W. The Immunological Genome Project: networks of gene expression in immune cells. *Nature Immunol.* **9**, 1091–1094 (2008).
- Sawant, A. *et al.* Depletion of plasmacytoid dendritic cells inhibits tumor growth and prevents bone metastasis of breast cancer cells. *J. Immunol.* **189**, 4258–4265 (2012).

Supplementary Information is available in the online version of the paper.

Acknowledgements The authors would like to thank E. J. Wherry and H. Chi for advice; A. Rudensky, D. Cheresch, K. Yang, T. Geiger and H. Chi for mice; D. R. Green for plasmids; and B. Triplett, M. Howard and M. McKenna at St Louis Cord Blood Bank for cord blood samples. The authors also thank K. Forbes and A. McKenna for maintenance, breeding and genotyping of mouse colonies; A. Castellaw for preparation of human cord blood samples; K. M. Vignali for assistance with cloning; A. Herrada for generating Nrp1-IgG1; A. L. Szymczak-Workman for assistance with histological analysis; S. Morgan, G. Lennon and R. Cross of the St Jude Immunology Flow Lab for cell sorting; the staff of the Shared Animal Resource Center at St Jude Children's Research Hospital for the animal husbandry; the Hartwell Center for Biotechnology and Bioinformatics at St Jude Children's Research Hospital for Affymetrix microarray analysis; the Veterinary Pathology Core for histological preparation; and the Immunology Department at St Jude Children's Research Hospital for helpful discussions. This work was supported by the National Institutes of Health (R01 AI091977 and AI039480 to D.A.A.V.; F32 AI098383 to G.M.D.), NCI Comprehensive Cancer Center Support CORE grant (CA21765, to D.A.A.V.) and ALSAC (to D.A.A.V.).

Author Contributions G.M.D. designed and performed most of the experiments and wrote the manuscript. S.-R.W. performed critical initial experiments and identified Sema4a and Nrp1 as the ligand–receptor pair. M.E.T. conducted many of the tumour experiments. D.M.G. performed a substantial portion of the colitis experiments. C.G. performed TIRF microscopy. M.L.B. assisted with the *Foxp3*-deficiency rescue experiments. A.E.O. assisted with several experiments. P.V. performed histological analysis. D.F. performed computational analysis of the microarray data. J.B. provided the blocking monoclonal antibodies to Sema4a and Nrp1. C.J.W. conducted and curated the initial microarray analysis. D.A.A.V. conceived the project, directed the research and wrote the manuscript. All authors edited and approved the manuscript.

Author Information The data discussed in this publication have been deposited in the NCBI Gene Expression Omnibus and are accessible through GEO Series accession number GSE41185. Reprints and permissions information is available at www.nature.com/reprints. The authors declare competing financial interests: details are available in the online version of the paper. Readers are welcome to comment on the online version of the paper. Correspondence and requests for materials should be addressed to D.A.A.V. (vignali.lab@stjude.org).

METHODS

Mice. C57/BL6 and dnTGF β RII mice were purchased from the Jackson Laboratories. *Foxp3*^{YFP-iCre}, *Foxp3*^{-/-} and *Foxp3*^{DTR-GFP} mice were obtained from A.Y. Rudensky. *Il10*^{-/-} mice were obtained from T. Geiger. *Nrp1*^{fl/fl} mice were obtained from D. Cheresh. *Pten*^{fl/fl} \times *Foxp3*^{YFP-iCre} mice were obtained from H. Chi. Animal experiments were performed in American Association for the Accreditation of Laboratory Animal Care-accredited, specific-pathogen-free facilities in the St Jude Animal Resource Center. Animal protocols were approved by the St Jude Animal Care and Use Committee.

Antibodies. Sema4a staining antibody was purchased from MBL (clone 5E3), and conjugated to biotin or Alexa Fluor 647 in-house. Polyclonal anti-Nrp1 was purchased from R&D Systems (AF566). Monoclonal antibodies were obtained from R&D Systems (Sema4a, 757129; Nrp1, 761704, MAB59941). Most flow cytometric antibodies were purchased from BioLegend. Anti-Foxp3 and anti-Eomes were purchased from eBioscience. KLF2 antibody was purchased from Millipore. Phospho-Akt (Ser473), phospho-S6K1 (Thr421-Ser424), Foxo3a, and pan Akt antibodies were purchased from Cell Signaling Technologies. PTEN-HRP (horseradish peroxidase) antibody was purchased from Santa Cruz Biotechnology.

RNA interference. Control siRNA (catalogue no. 4390843) and pools of Sema4a (catalogue no. 4390771, siRNA no. s73547) siRNA were purchased from Life Technologies and resuspended per the manufacturer's instructions. CD4⁺ and CD8⁺ conventional T cells were sorted magnetically by negative selection and transfected by Amaxa (Lonza) with 300 pMol siRNA and 2 μ g of pMaxGFP control plasmid, rested overnight in Amaxa nucleofector media. Cells were then sorted based on GFP, CD25, and CD45RB expression and co-cultured with T_{reg} cells in the top well of a transwell suppression assay.

Plasmids. Nrp1-mCherry was obtained from Addgene and used as a template to generate retroviral overexpression constructs. Nrp1^{WT} was generated by adding the native signal sequence and cloned into pMCherry (MSCV-driven retroviral construct with an IRES-driven mCherry gene). Nrp1^{ΔSEA} was generated from the WT construct, deleting the terminal SEA motif by mutation of the serine codon to a stop codon. Akt^{WT}, Akt^{DN} (dominant-negative kinase dead K179M; described previously²³), and pBabe empty vector were obtained from D. R. Green.

Human T-cell populations. Human umbilical cord samples were provided by B. Triplett, M. Howard and M. McKenna at the St Louis Cord Blood Bank, and were obtained from the umbilical vein immediately after vaginal delivery with the informed consent of the mother and approved by St Louis Cord Blood Bank Institutional Review Board (IRB). Research use was approved by the St Jude Children's Research Hospital IRB.

Transwell suppression. 1.25×10^4 T_{reg} cells purified flow cytometrically (CD4⁺ CD45RB^{lo} *Foxp3*^{YFP-iCre+}) were stimulated in the top chamber of a Millipore Millicell 96 (0.4 μ m pore size) in the presence of flow cytometrically purified T_{conv} cells (CD45RB^{hi} CD25⁻ CD4⁺ or CD8⁺), B cells (B220⁺), or T_{reg} cells at a 1:4 ratio, Sema4a-IgG1- or IgG-conjugated latex beads (1:1 ratio), anti-CD3 ϵ (145.2C11) and anti-CD28 (37.51) conjugated latex beads (1:1 ratio), and/or neutralizing antibodies. In some experiments, the top well co-cultured cells were fixed with 2% paraformaldehyde for 15 min and washed extensively before co-culture with T_{reg} cells. Purified T_{conv} cells (5×10^4) were stimulated in the bottom well with anti-CD3- and anti-CD28-coated beads at a 1:1 ratio. Cells were cultured for 72 h and pulsed with [³H]-thymidine for the final 8 h. The bottom chambers were harvested and read with a beta counter.

For human studies, flow cytometrically purified umbilical cord blood T_{conv} cells (CD4⁺ CD25⁻) and T_{reg} cells (CD4⁺ CD25⁺) were activated with 3 μ g ml⁻¹ plate-bound anti-CD3 (clone OKT3), 2 μ g ml⁻¹ soluble anti-CD28 (clone CD28.1), and 100 units per ml rIL-2 for 7–9 days. After collection and washing, T_{reg} cells were stimulated at a 1:10 ratio with fixed autologous T_{conv}-cell- or IgG- or Sema4a-IgG1-coated latex beads in the top well of a transwell plate. 2.5×10^4 T_{conv} cells were stimulated in the bottom well at a 1:1 ratio with OKT3- and CD28.1-coated latex beads. Cells were cultured for 5 d and pulsed with [³H]-thymidine for the final 8 h. The cells from the bottom chambers were collected and read with a beta counter. 'Transwell suppression' is defined as $100 - 100 \times ((\text{counts per min of a particular well}) / (\text{Average counts per min of unsuppressed cells}))$ to normalize across experiments.

Fusion proteins. The sequence encoding the extracellular domains of Sema4a and Nrp1 were cloned in-frame to pX-Ig to create a Sema4a- or Nrp1-mouse IgG1 fusion protein construct (Sema4a-IgG1 and Nrp1-IgG1). J558L B cells were electroporated with this construct, and high-producing clones were selected by single-cell sorting. High-producing clones were seeded into Sartorius Bioreactors and collected for protein G purification and concentration. Sulphate latex 4- μ m beads (Life Technologies) were conjugated with isotype control (mouse IgG1, MOPC21, R&D Systems) or Sema4a-Ig overnight with 3 μ g protein per bead, blocked with 10% FBS, and stored in media. Mouse Sema-3a-Fc, Sema4a-Fc, mouse Nrp1, and human Sema4a-Fc was purchased from R&D Systems.

Binding assays. High protein binding ELISA plates were coated with 500 ng ml⁻¹ recombinant murine Nrp1 (R&D Systems) overnight in PBS. After a 1–2-h block in 1% BSA in PBS at 4 $^{\circ}$ in the dark, coated plates were incubated with various concentrations of Sema4a-IgG1 or mouse IgG1 for 2–4 h in the presence of anti-Sema4a, anti-Nrp1, or isotype control antibodies. Plates were then washed with PBS plus 0.05% Tween-20 10 times and incubated with 500 ng ml⁻¹ biotinylated anti-mouse IgG1 antibody (BD Biosciences) to bind the fusion protein (or mouse IgG1 control). After 7 washes, Streptavidin-HRP (GE Healthcare) was added at 500 ng ml⁻¹ to detect the biotinylated antibody. After another 7 washes, TMB substrate (Thermo Scientific) was added and stopped with 1 N H₂SO₄.

For VEGF binding, the same protocol was followed, except that rather than Sema4a-IgG1 being used, VEGF₁₆₅ (R&D Systems) was used at 50 ng ml⁻¹ in PBS and detected with 500 ng ml⁻¹ anti-VEGF-biotin (R&D Systems) followed by SA-HRP for detection.

For comparisons across Sema family members, plates were coated with varying concentrations of Sema3a-Fc, Sema4d-Fc, Sema4a-IgG1, or isotype control overnight. Biotinylated Nrp1-IgG1 was added and incubated for 3 h, and SA-HRP was used for detection.

mRNA analysis. RNA was extracted from cells lysed in TRIzol reagent (Life Technologies) and reverse transcribed with the High Capacity Reverse Transcription kit (Applied Biosystems). Real-time polymerase chain reaction (PCR) was carried out using primers and probes and TaqMan master mix or SYBR green chemistry (Applied Biosystems).

Rescue of Foxp3-deficient autoimmunity. CD45.1 \times *Foxp3*^{+/-} female mice were bred with CD45.1 male mice in timed breedings. Male progeny were genotyped at birth for *Foxp3*^{-/-} status. Purified *Foxp3*^{Cre} (1×10^6) or *Nrp1*^{fl/fl}/*Foxp3*^{Cre} CD45.2⁺ T_{reg} cells, purified by flow cytometry, were injected intraperitoneally into *Foxp3*^{-/-} male pups within 3 days of birth. Mice were monitored for the scurfy phenotype (scaly skin, eye inflammation, runted phenotype, and lack of mobility). For some experiments, all mice were killed at 5 weeks for histological analysis of the ear pinna, liver and lung.

Tumour models. *Foxp3*^{Cre}, *Nrp1*^{fl/fl}/*Foxp3*^{Cre}, or *Foxp3*^{DTR-GFP} mice were injected with B16.F10 melanoma (1.25×10^5 cells intradermally), EL4 thymoma (1.25×10^5 cells intradermally), or MC38 colon carcinoma (2.5×10^5 cells subcutaneously). Tumours were measured regularly with digital calipers and tumour volumes were calculated; this was done blind but not randomized. Tumours and lymph nodes were collected for analysis. TILs were prepared using a Percoll gradient from tumour samples after mechanical disruption. For metastasis studies, B16.F10 was injected intravenously at various doses. After 17–20 days, lungs were harvested, inflated with H₂O₂, and metastases were counted. Therapeutic B16 experiments were conducted by injecting 1.25×10^5 B16 melanoma cells intradermally and waiting until tumours were palpable (5 days). On day 5, mice began to receive intraperitoneal injections of either rat IgG2a, or anti-Nrp1 (R&D Systems clone 761704, MAB59941) (400 μ g initial dose and 200 μ g every 3 days). Prophylactic experiments included anti-Sema4a (R&D Systems clone 757129) and Sema4a-IgG1 consisting of twice weekly injections of 100 μ g of protein starting on the day of tumour inoculation. To achieve reasonable power, at least 15 mice were used in each group, at least 5 mice per experiment. Additional mice were added to experiments as appropriate.

Experimental colitis. Six- to eight-week-old RAG2^{-/-} mice were injected intraperitoneally with 4×10^5 congenically marked CD45RB^{hi} CD25⁻ T_{conv} cells. When the majority of the mice had lost 10% body weight and had colitis symptoms (21 to 28 days later), 1×10^6 *Foxp3*^{Cre} or *Nrp1*^{fl/fl}/*Foxp3*^{Cre} T_{reg} cells were injected intraperitoneally. Mice that did not lose 10% body weight at this time received no injection and were excluded from analysis, and mice received randomized injections (different genotypes of transferred cells per cage). Body weight was measured daily in a blinded fashion, and 28 days after T_{reg}-cell rescue, sections were stained for histology. To achieve reasonable power, at least 15 mice were used in each group, and at least 5 mice per experiment. Additional mice were added to experiments as appropriate.

Signalling analysis. For flow cytometry, T_{reg} cells were stimulated with anti-CD3- and anti-CD28-coated beads and IgG1-coated or Sema4a-IgG1-coated beads overnight, then fixed with 1% PFA for 15 min at 37 $^{\circ}$ C. Cells were then permeabilized in ice-cold 90% MeOH for 20 min at -20 $^{\circ}$ C. After extensive washing in PBS, cells were blocked with 10% normal mouse serum in PBS for 10 min at room temperature. Cells were then stained with antibodies in 1% BSA in PBS (phosphorylated S6K1 (pS6K1) (Thr421-Ser424), pAkt (Ser473), or pAkt (Thr308)) for 1 h at room temperature, in the dark. Finally, cells were stained with appropriate secondary antibodies for 30 min at room temperature, in the dark, then washed and analysed. For immunoblot analysis, T_{reg} cells were expanded with 1 ng ml⁻¹ phorbol-13-myristol acetate and 10 ng ml⁻¹ ionomycin with 500 units recombinant human interleukin-2 (IL-2) for 3 days, then washed extensively with media, and expanded to 10 \times volume in 500 units recombinant human IL-2. After an overnight rest with no IL-2, T_{reg} cells were stimulated with plate-bound anti-CD3, soluble anti-CD28,

and bead-bound Sema4a-IgG1 for 6 h, and lysed in whole-cell lysis buffer (1% NP40, 5 mM EDTA, 5 mM EGTA, Tween-20) for 15 min on ice, then subjected to immunoblot analysis. In some experiments, $1-3 \times 10^6$ T_{reg} cells were lysed in a larger volume, and cleared. Nrp1 was immunoprecipitated using a polyclonal anti-Nrp1 antibody (R&D Systems, AF566) 6–16 h followed by a 3 h incubation with Protein G beads. Beads were washed with lysis buffer before elution. In brief, precipitates or input lysates were incubated at 96 °C with 0.1 M dithiothreitol (DTT) and 4× LDS sample buffer (Life Technologies), then loaded into 4–12% Bis-Tris NuPAGE gels (Life Technologies), and run for 1 h at 200 V. Separated gels were electrotransferred to polyvinylidene difluoride (PVDF) membranes using the Criterion Gel Blotting System (Biorad), and blocked for 1 h at room temperature with 3% BSA in Tris-buffered saline (TBS) supplemented with 0.1% Tween-20. Blocked membranes were incubated overnight with anti-PTEN conjugated directly to HRP (Santa Cruz Biotechnologies), washed three times with TBS-Tween, and imaged using Western Lightning ECL (enhanced chemiluminescence). For other immunoblot analysis, blocked membranes were incubated with varying primary antibodies (anti-Nrp1, anti-phosphorylated or total Akt, anti-phosphorylated S6K1) overnight, washed three times with TBS-Tween, and incubated with appropriate HRP-conjugated secondary antibody controls. After three additional washes membranes were imaged using Western Lightning ECL.

Retroviral transduction. 293T cells were transfected with pPAM-EQ and pVSV-G packaging plasmids with various retroviral constructs to transduce GPE86 retroviral producer cells. T_{reg} cells were purified flow cytometrically. T_{reg} cells were activated and cycled with PMA and ionomycin in the presence of 500 units per ml recombinant human IL-2 for 24 h in 96-well flat-bottom plates at 5×10^4 per well in 100 µl. Viral supernatants were concentrated 10-fold using 100-kilodalton (kDa) MWCO concentrators (Millipore) and added in equal volume to cycling T_{reg} cells in the presence of 500 units per ml recombinant human IL-2 and $6 \mu\text{g ml}^{-1}$ polybrene and centrifuged at 1,000g for 60 min at 37 °C, then incubated for 24 h. The transduction process was repeated twice every 24 h, removing 100 µl of supernatant from the cultured T_{reg} cells each day to keep the culture volume at 200 µl per well. T_{reg} cells were then washed in media and sorted based on fluorescent protein expression or selected with $1 \mu\text{g ml}^{-1}$ puromycin and expanded further in IL-2. Fluorescent protein or intracellular epitope staining (anti-HA, Sigma) was confirmed before use. Functional assays were performed after a 24 h rest without IL-2.

Microscopy. TIRF illumination of immunologic synapse activation was performed as described previously³¹. In brief, lipid bilayers containing anti-TCR and an anti-mouse IgG1 capture antibody loaded with Sema4a-IgG1 or isotype control were prepared. T_{reg} cells were stimulated on the bilayer for 20 min, then fixed, permeabilized, and stained for phosphorylated Akt (Ser473), global phosphotyrosine (4G10), or Nrp1. The 'percentage of pAkt⁺ TCR clusters' represents the ratio of synapses positive for phosphorylated Akt (Ser473) to the total number of synapses formed, as read-out by TCR clustering.

Foxo3a was carried out on freshly isolated T_{reg} cells that were left unstimulated in media overnight or stimulated with immobilized anti-CD3 and anti-CD28 in the presence or absence of immobilized Sema4a-IgG1 or its isotype control. Cells were collected, fixed in 1% PFA, and permeabilized with 0.1% Triton X-100 in TBS.

After blocking with normal mouse serum, cells were stained with anti-Foxo3a (Cell Signaling Technologies) overnight in Tris-buffered 1% BSA. After several washes, cells were stained with Alexa Fluor 647 conjugated anti-rabbit IgG (Life Technologies), and then washed several times. Cells were then loaded with 4',6-diamidino-2-phenylindole (DAPI) and phalloidin-Alexa Fluor 546 or 488 before microscopy. Random fields of 10 to 30 cells were visualized using spinning-disc laser-scanning confocal microscopy. Blinded masks were generated using phalloidin and DAPI staining to determine cytoplasmic and nuclear volume, respectively, and only then was the Foxo3a staining visualized. The nuclear and cytoplasmic volumes of Foxo3a fluorescence of 20 to 30 stacks were calculated using Slidebook (3i) software in arbitrary fluorescence units and analysed in Graphpad Prism.

Affymetrix array and analysis. *Foxp3^{Cre}* or *Nrp1^{fl/fl}Foxp3^{Cre}* T_{reg} cells were flow cytometrically sorted to 99.0% purity from 6- to 8-week-old mice, and stimulated for 48 h with plate-bound anti-CD3, anti-CD28, 100 units per ml recombinant human IL-2, and either isotype or Sema4a-IgG1-coated latex beads. Cells were collected, washed three times with PBS, and lysed in TRIzol reagent (Life Technologies). Quality was confirmed by ultraviolet spectrophotometry and by analysis on an Agilent 2100 Bioanalyzer (Agilent Technologies). Total RNA (100 ng) was processed and labelled in the Hartwell Center for Biotechnology & Bioinformatics according to the Affymetrix 3' IVT Express protocol and arrayed on a mouse high-throughput 430 PM GeneChip array. Signal data were RMA summarized, visualized, quality checked by principal components analysis (PCA) (Partek Genomics Suite 6.6). Batch correction was applied as needed to correct differences in completely replicated experiments scanned on distinct dates. To compare T_{conv} cells to resting T_{reg} cells and unequal variance, a *t*-test was applied to each probe set and the log₂ ratio calculated. This same analysis was used to compare T_{conv} cells to activated T_{reg} cells. To compare the effect of Sema4a treatment in wild-type T_{reg} cells to the effect of Sema treatment in Nrp1-deficient cells, a two-factor analysis of variance (ANOVA) interaction of treatment and genotype was applied to each probeset and the Storey *q* value was found to be correct for multiple comparisons. The categorical mean of each probe set was found, transformed to a Z-score, hierarchically clustered and visualized by heat-map in Spotfire DecisionSite 9.1 (Tibco). The heat map in Fig. 5f was composed of the top named genes that had the passed *P*-value interaction FDR at 10%, had a minimum mean expression of 6 in one class and a minimum absolute value logratio difference of at least 0.5. The volcano plots were generated using STATA/s.e. 11.1. For all volcano plots, genes without official symbols or names were removed. In these plots, score refers to the $-\log_{10}$ -transformed *P* value. For the interaction volcano plot genes a metric for distance from the origin was applied to colour code the graph $|(\text{score}/10 + |\log \text{ratio difference}|)/2| > 0.5$. Statistical tests and multiple comparison corrections were performed using Partek Genomics Suite 6.6. Sequences were retrieved for probe sets that showed at least a threefold difference between T_{conv} and activated T_{reg} cells. and a *P* value of 0.01 and these sequences were then tested with SignalP 3.0 software to identify transmembrane domains.

- Guy, C. S. *et al.* Distinct TCR signaling pathways drive proliferation and cytokine production in T cells. *Nature Immunol.* **14**, 262–270 (2013).

Interactome map uncovers phosphatidylserine transport by oxysterol-binding proteins

Kenji Maeda¹, Kanchan Anand^{1†}, Antonella Chiapparino¹, Arun Kumar¹, Mattia Poletto¹, Marko Kaksonen¹ & Anne-Claude Gavin¹

The internal organization of eukaryotic cells into functionally specialized, membrane-delimited organelles of unique composition implies a need for active, regulated lipid transport. Phosphatidylserine (PS), for example, is synthesized in the endoplasmic reticulum and then preferentially associates—through mechanisms not fully elucidated—with the inner leaflet of the plasma membrane^{1–3}. Lipids can travel via transport vesicles. Alternatively, several protein families known as lipid-transfer proteins (LTPs) can extract a variety of specific lipids from biological membranes and transport them, within a hydrophobic pocket, through aqueous phases^{4–7}. Here we report the development of an integrated approach that combines protein fractionation and lipidomics to characterize the LTP–lipid complexes formed *in vivo*. We applied the procedure to 13 LTPs in the yeast *Saccharomyces cerevisiae*: the six Sec14 homology (Sfh) proteins and the seven oxysterol-binding homology (Osh) proteins. We found that Osh6 and Osh7 have an unexpected specificity for PS. *In vivo*, they participate in PS homeostasis and the transport of this lipid to the plasma membrane. The structure of Osh6 bound to PS reveals unique features that are conserved among other metazoan oxysterol-binding proteins (OSBPs) and are required for PS recognition. Our findings represent the first direct evidence, to our knowledge, for the non-vesicular transfer of PS from its site of biosynthesis (the endoplasmic reticulum) to its site of biological activity (the plasma membrane). We describe a new subfamily of OSBPs, including human ORP5 and ORP10, that transfer PS and propose new mechanisms of action for a protein family that is involved in several human pathologies such as cancer, dyslipidaemia and metabolic syndrome.

To determine LTP specificity, we purified LTP–lipid complexes from extracts of yeast strains expressing physiological amounts of LTPs fused to the tandem-affinity purification (TAP) tag (Supplementary Fig. 1a)^{8,9}. This approach combines high-affinity purification using an immunoglobulin G (IgG) resin, elution with a site-specific protease, and separation by size-exclusion chromatography (SEC). Proteins and lipids in the SEC fractions were then analysed by denaturing gel electrophoresis (SDS–PAGE) and high performance thin layer chromatography (HPTLC) or mass spectrometry, respectively (Supplementary Figs 2–4). The SEC elution profiles discriminate any background binding to IgG and only lipids co-eluting with LTPs were considered to represent specific ligands. Importantly, the procedure allows LTPs to be maintained in conditions that closely approximate normal physiology and preserves their ability to form multiprotein complexes. For example, Sec14 was found to co-elute with a known interaction partner Ptc7 (systematic name Yhr076w), a 38-kDa type 2C protein phosphatase (Supplementary Fig. 3). The analysis confirmed many other known or predicted interactions, such as the ones between Kes1 (also known as Osh4, systematic name Ypl145c) and sterol¹⁰ and between Sec14 (systematic name Ymr079w) or Sfh1 (systematic name Ykl091c; 64% primary sequence identity with Sec14) and phosphatidylinositol (PI)/phosphatidylcholine (PC)¹¹ (Supplementary Figs 1b, 2 and 3).

Among proteins with an OSBP domain, Osh6 (systematic name Ykr003w) and Osh7 (systematic name Yhr001w)—two paralogues that have poor sterol-transfer activity *in vitro*¹²—formed stoichiometric and specific complexes with PS but not with sterols (Supplementary Figs 1c, 2 and 4). For Osh6, the amount of PS in the pull-downs was ~100-fold higher than in the controls Kes1 and Sec14, no other lipids co-eluted at significant levels and the protein only associated with PS species with long aliphatic chains (C34) (Supplementary Figs 1d and 4). Osh6 and Osh7 seem to participate in lipid metabolic pathways *in vivo* that are distinct from those of other OSBPs. Kes1 fused to green fluorescent protein (GFP) localizes to the cytosol¹³, whereas Osh6–GFP resides in structures at the cell periphery that overlap with cortical endoplasmic reticulum (ER) and represent ER–plasma membrane (PM) contact sites¹² (Supplementary Fig. 5a). Upon perturbations of either ergosterol or PI phosphate metabolism, Kes1–GFP translocated to juxtanuclear patches¹³, whereas only mutations targeting PS metabolism specifically affected Osh6–GFP localization at the cell periphery (Supplementary Fig. 5b). These data indicate a new role for the OSBP family in the transport of PS, an important signalling lipid. This forms the basis for the more detailed mechanistic and structural studies discussed below.

To confirm the interaction between Osh6 and PS, we produced Osh6 in *Escherichia coli*. The recombinant Osh6 co-purified with phosphatidylglycerol (PG) and phosphatidylethanolamine (PE), two abundant lipids in bacteria, and with PS (Supplementary Fig. 6a). These complexes were resistant to exposure to a non-ionic detergent, indicating that the ligands are poorly accessible. We measured Osh6 lipid-binding specificity *in vitro* using liposomes containing PS, PG, PE, PI, cardiolipin (CA), ergosterol or mixtures of lipids originating from yeast membranes (in which PG exists in trace amounts¹⁴). We found that only PS bound efficiently to recombinant Osh6 and that PS could replace bacterially produced and co-purifying PG and PE (Fig. 1a, b). As a control in the same assay, recombinant Kes1 bound ergosterol, but not PS. This shows that *in vitro*, Osh6 specifically binds PS and exchanges lipids with membrane bilayers.

We then determined whether Osh6/Osh7 can transfer PS between membranes *in vitro*. For this purpose, we used either recombinant Osh6 (Fig. 1c and Supplementary Fig. 6b) or native Osh6–TAP and Osh7–TAP (Fig. 1d) purified from yeast. We designed two different lipid-transfer assays. First, we monitored the transfer of lipids from ‘heavy’ donor liposomes (that contained different putative lipid cargoes) to ‘light’ acceptor liposomes (Fig. 1c, d). The donor liposomes were filled with sucrose so that they could readily be separated by centrifugation¹². In the second assay, we measured the amount of PS transferred from donor to immobilized and fluorescently labelled (green) acceptor liposomes. We visualized the presence of PS in the acceptor liposome with a specific probe, the fluorescently labelled annexin V (red, Cy3) (Supplementary Fig. 6b). Overall, the data demonstrate that *in vitro* both Osh6 and Osh7, but neither Kes1 nor Sec14, specifically transfer PS between donor and acceptor membranes.

Osh6 and Osh7 localize at membrane contact sites that bridge PS synthesis (the ER) with areas of PS accumulation and biological

¹European Molecular Biology Laboratory, EMBL, Meyerhofstrasse 1, D-69117 Heidelberg, Germany. †Present address: Center of Advanced European Studies and Research (Caesar), Ludwig-Erhard-Allee 2, 53175 Bonn, Germany.

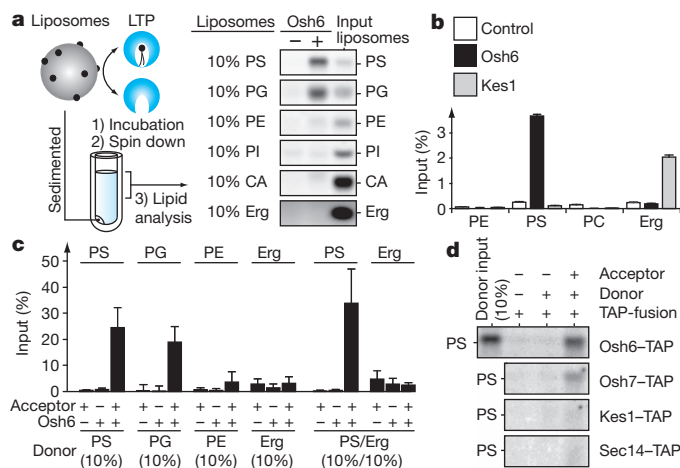


Figure 1 | Recombinant Osh6/Osh7 bind and specifically transfer PS *in vitro*. **a**, Osh6 specifically associates with phosphatidylserine (PS) and phosphatidylglycerol (PG). Osh6-associated lipids were determined by HPTLC. Liposomes (2% of the input) were loaded as references. **b**, Osh6 extracts PS from liposomes containing yeast total lipid extract. Kes1 associates with ergosterol (Erg). Control: without lipid-transfer proteins (LTPs). **c**, Recombinant Osh6 specifically transfers PS from heavy donor liposomes to light acceptor liposomes. **d**, Transfer of PS from the donor to acceptor liposomes by Osh6-TAP and Osh7-TAP purified from yeast. CA, cardiolipin; PE, phosphatidylethanolamine; PI, phosphatidylinositol. Error bars represent standard deviation, $n \geq 3$.

activity (the PM)¹² (Supplementary Figs 5a and 7a). We first examined whether Osh6 and Osh7 contribute *in vivo* to the subcellular compartmentalization of PS by measuring the content of the lipid in different subcellular membranes (Fig. 2a and Supplementary Fig. 7a). In wild-type cells, PS is more concentrated in the PM- than in the ER-enriched fractions. By contrast, in the absence of Osh6/Osh7, PS accumulation at the PM was reduced ($\sim 30\%$), whereas the distribution of other glycerophospholipids was largely unaffected. We also performed additional tests using an *in vivo* probe for cellular PS: the lactadherin C2 domain fused to GFP (Lact C2-GFP)¹. Consistent with the biochemical data, PS predominantly localized at the PM in the unperturbed, *osh6Δ*, *osh7Δ* and *kes1Δ* (control) strains², where it laterally partitioned into domains (Fig. 2b and Supplementary Fig. 7a). Deletion of both Osh6 and Osh7 induced PS delocalization from the PM and the Lact C2-GFP probe adhered to intracellular membrane structures representing the ER and vacuoles (Fig. 2b and Supplementary Fig. 7a, b). PS mislocalization was rescued by the reintroduction of wild-type Osh6, but not the mutants Osh6 Lys126Ala or Leu69Asp that are deficient in PS binding (see below; Supplementary Fig. 7c) or of an engineered Osh6 that localizes at vacuolar membranes (see below; Supplementary Fig. 7d). Collectively, these results indicate that *in vivo*, active Osh6/Osh7 at the ER-PM contact sites contribute to the delivery and accumulation of PS at the PM.

PS is also transported from the ER to sites of PS decarboxylation, where PS serves as a precursor for the biosynthesis of PE and PC (Fig. 2c). If Osh6 and Osh7 contribute to PS decarboxylation, then their deletions should lead to a drop in the cellular levels of PE/PC. However, in *osh6Δosh7Δ* cells, the total amounts of PE/PC were largely unaffected (Fig. 2a). We observed instead a significant decrease in PS levels that could be reversed by the deletion of the main decarboxylase in yeast, the mitochondrial Psd1 or the addition of choline (a precursor for the Kennedy pathway, that is, an alternative, PS-independent route of PC synthesis). These results disprove a major role for Osh6/Osh7 in the delivery of PS to the main sites of decarboxylation in yeast¹⁰. This is also consistent with the notion that Osh6/Osh7 contribute to the accumulation of PS at the PM so that it avoids decarboxylation in the mitochondria. Our data support the view that

there are distinct routes for regulated PS delivery to its different sites of biological activity (Fig. 2c). Cellular processes implying intracellular PS transport, that is, PS decarboxylation into PE (mitochondria) or the vesicular trafficking-, cell cycle-dependent polarization of PS at the buds^{3,15}, were largely unaffected in *osh6Δosh7Δ* strains (data not shown).

We then investigated whether Osh6/Osh7 directly transport newly synthesized PS between cellular membranes *in vivo*. We first depleted endogenous PS by deleting the PS synthase (Cho1, systematic name Yer026c). Lyso-PS (derivatives of phosphatidylserine in which one acyl chain have been removed by hydrolysis) subsequently added to the media was incorporated into the cells and was rapidly converted to PS in the ER (wild-type cellular levels of PS were restored within 10 min; Supplementary Fig. 8a)^{16,17}. We were then able to measure the kinetics of Osh6/Osh7-mediated transfer of newly synthesized PS using the Lact C2-GFP probe¹. In the absence of Osh6/Osh7, or in the presence of a mutated Osh6 deficient in PS binding (Leu69Asp; see below), newly formed PS remained trapped in the ER (Fig. 2d and Supplementary Fig. 8b, c). By contrast, functional Osh6/Osh7 triggered a rapid (within 2 min) translocation of PS from the ER to the PM. The rate at which newly synthesized PS equilibrates in the PM was slower in the Osh6/Osh7 double mutant than in wild-type cells (Supplementary Fig. 8b). Osh6/Osh7-mediated PS transfer took place at 4 °C, further indicating that PS transport is largely independent of vesicular trafficking. In *osh6Δosh7Δ* strains at 4 °C, a small fraction of the Lact C2-GFP probe remained bound to the PM, indicating that additional, Osh6/Osh7-independent, non-vesicular mechanisms of PS transport may exist. Finally, we also examined whether the translocation of Osh6 to other cellular membranes is sufficient to redirect PS to this new location (Fig. 2e, f). In an Osh7-knockout strain, we co-expressed Osh6 fused to human FKBP (FK506-binding protein) and Vph1 (a trans-membrane, vacuolar protein) fused to human FRB (FKBP-rapamycin-binding domain). Rapamycin induced the relocalization of Osh6-FKBP to vacuoles, particularly to regions adjacent to the ER (Fig. 2e). Upon Osh6 translocation, newly synthesized PS also became quickly (within 5 min) redirected to this organelle (Fig. 2f), indicating that Osh6/Osh7 can directly transport PS between cellular membranes *in vivo*. Together, these results provide the first direct evidence for non-vesicular transfer of PS from its site of biosynthesis (the ER) to its site of biological activity (the PM). We propose that members of the Osh protein family are integral parts of the cellular machinery regulating PS homeostasis and signalling and are responsible for its accumulation at the PM.

To gain insights into the mechanisms for specific PS recognition, we determined the structure of the Osh6-PS complex by X-ray crystallography at 1.95 Å resolution (Supplementary Fig. 9a and Supplementary Table 1). Similar to Kes1^{18,19} (20% sequence identity to Osh6), the Osh6 structure consists of an incomplete β -barrel that forms the ligand-binding tunnel (residues 74–327), an amino-terminal 'lid' (residues 35–73) covering the tunnel entrance and a carboxy-terminal mainly α -helical region that does not contact the ligand (residue 328–434) (Supplementary Fig. 9a). The structure also revealed a clear electron density map in the ligand-binding pocket of Osh6 in which we could model PS with a 17 carbon-long saturated acyl chain (*sn*-1 position) and an 18 carbon-long unsaturated acyl chain (oleic acid; *sn*-2 position). The Osh6 tunnel, which can accommodate the long aliphatic chain of PS, is predominantly hydrophobic and is about 8–10 Å deeper than the one reported for Kes1 (Supplementary Fig. 9b)^{18,19}. The head group and the *sn*-2 acyl group of PS are oriented towards the tunnel entrance and the *sn*-1 acyl group towards the bottom of the tunnel (Supplementary Fig. 9a). The entire PS molecule is involved in extensive interactions with 36 residues from Osh6 (Fig. 3a). In particular, the α 1- β 1 loop in the lid and the region near the tunnel entrance are crucial for PS recognition (see below). This implies a series of hydrophobic residues in the α 1- β 1 loop (Leu 64, Ile 67, Leu 69 and Ile 73) and at the tunnel entrance (Val 124) that form

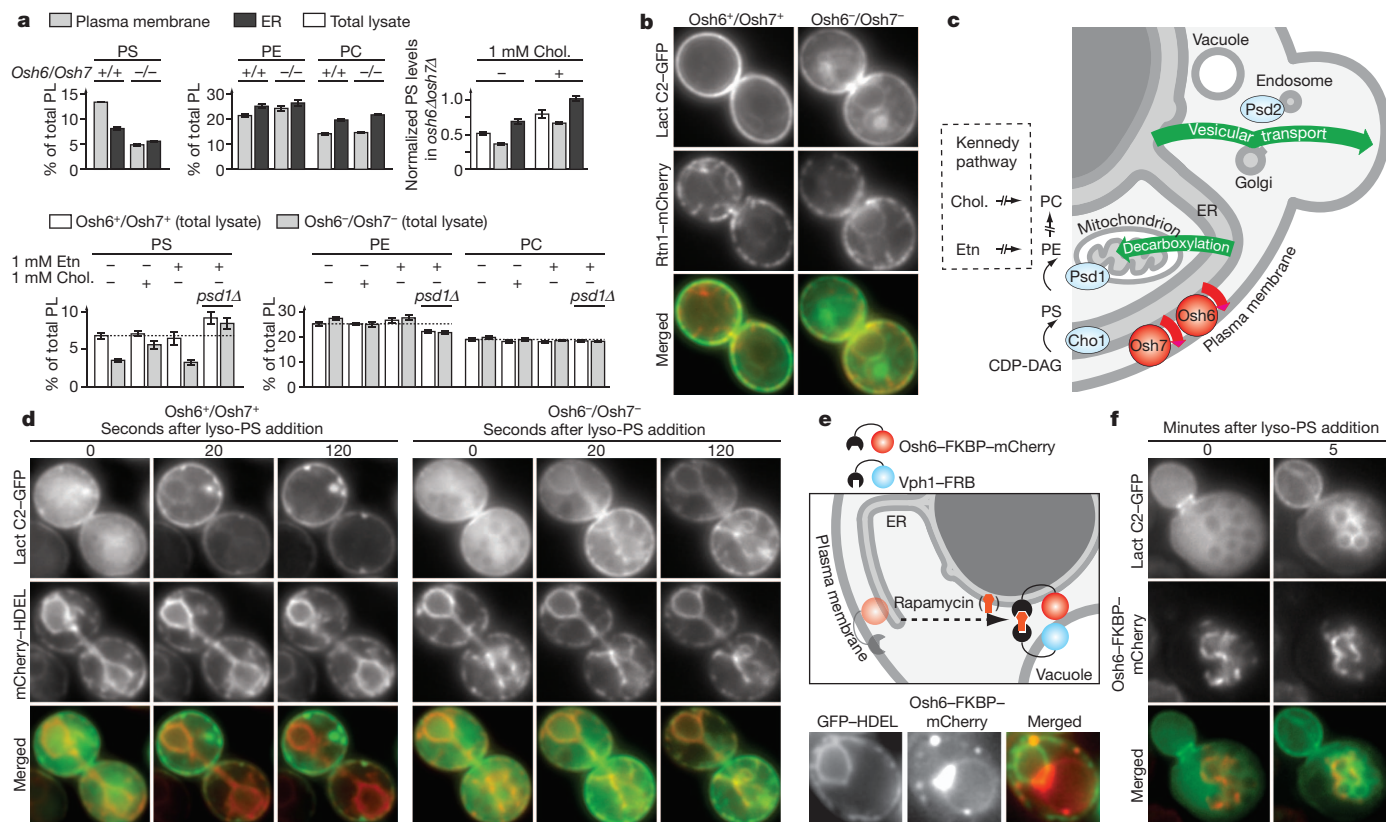


Figure 2 | *In vivo*, Osh6/Osh7 transport PS from the ER to the PM.

a, Lipidomics analyses (glycerophospholipid, PL) of PM or ER fractions (top), and of total cell extracts (bottom). **b**, Osh6/Osh7 are required for the accumulation of PS to the PM. Rtn1-mCherry marks the ER. **c**, Schematic view of the role of Osh6/Osh7 in PS trafficking. CDP-DAG, cytidine diphosphate-diacylglycerol. **d**, Kinetics of Osh6-mediated PS transfer *in vivo*. Lact C2-GFP re-localization after the addition of 18:1 lyso-phosphatidylserine (Lyso-PS) in

PS-depleted cells (*cho1Δ*). mCherry-HDEL marks the ER. **e**, Rapamycin induces Osh6-FKBP-mCherry to dimerize with Vph1-FRB and to translocate to vacuolar membranes adjacent to the ER. GFP-HDEL marks the ER. **f**, The vacuolar translocation of Osh6 is followed by an accumulation of newly synthesized PS (from lyso-PS) in vacuoles. Error bars represent standard deviation, $n \geq 3$. Chol., choline; Etn, ethanolamine.

extensive non-polar contacts with the *sn*-2 acyl group of PS (Fig. 3b). Several residues in the α 1- β 1 loop (Leu 64, Ile 67 and Leu 69) and at the tunnel entrance (Lys 126, Asn 129 and Ser 183) are also engaged in polar interactions with the PS head group, especially with the carboxylate anion. This could explain the specificity of Osh6 for PS versus the related PE and PC, which are products of PS decarboxylation (Supplementary Fig. 10).

Only nine of the PS-interacting residues in Osh6 are conserved in Kes1. Not surprisingly, Osh6 in which these conserved interacting residues are mutated—including Lys126Ala, Asn129Ala (polar contacts with the PS carboxylate anion) or Ile73Asp (hydrophobic contact with PS)—binds very poorly to PS *in vitro* (Fig. 3c), indicating that they have conserved roles in ligand binding. By contrast, mutations of conserved, polar amino acids located near the PS head group, but not interacting with it (His 157, His 158, Lys 351 and Lys 182), had no effect. Importantly, most Osh6 residues that bind to PS are not conserved in Kes1 and probably give rise to Osh6 specificity. In particular, the α 1- β 1 loop in the lid region, which is poorly conserved in Kes1 (where it partially folds as a short 3/10 helix^{18,19}), makes extensive polar and non-polar contacts to PS (Fig. 3b). Osh6 in which Leu 69 is substituted for a charged residue (Asp) or for the corresponding Kes1 residue (Ala) interacted poorly with PS, whereas substitution for another hydrophobic residue (Phe) had no effect (Fig. 3c). Further supporting the notion that the α 1- β 1 loop has a key role in specific PS binding, additional mutations of Thr 71 (to Pro) or the substitution of the entire α 1- β 1 loop with the corresponding loop of Kes1 completely abrogated the association with PS. In total, we replaced six Osh6-specific, PS-contacting residues (Leu 69, Arg 82, Gln 86, Val 124, Ser 183 and Met 194) with the corresponding ones in Kes1

and for five of these, this led to significant decreases in PS binding (Fig. 3c). The crystal structure of Osh6 demonstrates that binding to PS involves a series of amino acids that are not conserved in Kes1

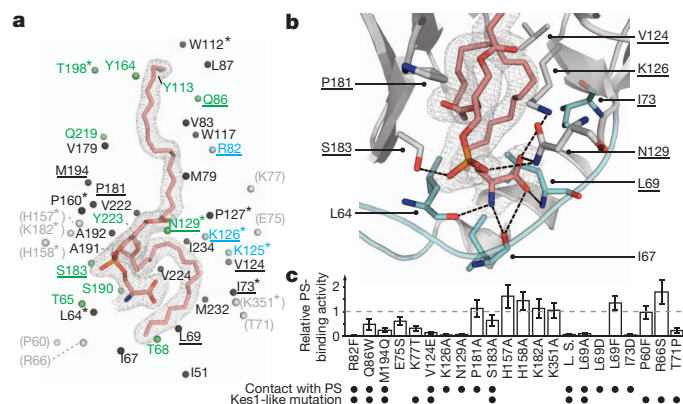


Figure 3 | Structure of the Osh6-PS complex. **a**, An overview of Osh6-PS interactions. α atoms (spheres) of polar (green), positively charged (blue) and hydrophobic (black) residues that form contacts to PS (sticks). Underlined, mutated residues. Grey, mutated residues not forming contact. Light grey isomesh map: PS 2F_o - F_c electron density map at the 1.0 σ level. Stars, residues conserved in Kes1. **b**, Close-up of region forming key contacts with PS (sticks). Blue, α 1- β 1 loop. Dashed lines, hydrogen bonds <3.5 Å. **c**, *In vitro* PS-binding activities of Osh6 mutants. Kes1-like mutants introduce corresponding Kes1 amino acids. The 'loop-swap' (L.S.) mutant: Osh6 α 1- β 1 loop was swapped for the corresponding segment in Kes1. Error bars represent standard deviation, $n \geq 3$.

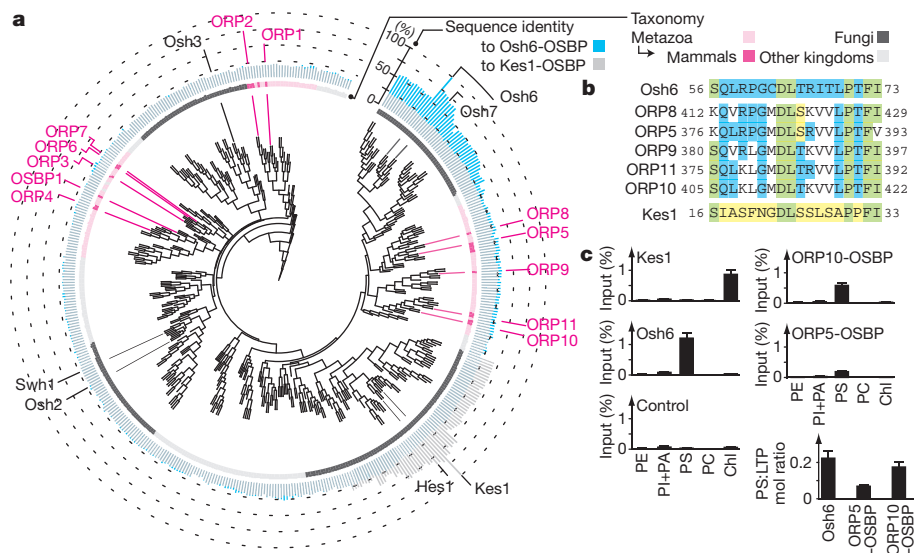


Figure 4 | Osh6/Osh7 are the first representatives of a PS-binding OSBP subfamily conserved in humans. **a**, A phylogenetic analysis of all OSBP domains. Black, *S. cerevisiae* OSBPs; magenta, human OSBPs. Bar graphs, sequence identities derived from pair-wise alignment with Osh6-OSBP (blue) and Kes1-OSBP (grey). **b**, Sequence features of the Osh6 $\alpha 1$ - $\beta 1$ loop are conserved in the five clustered human OSBP domains. Blue and yellow:

and may represent the signature of a new subfamily of OSBPs with specificity for PS.

Our results show that in yeast, Osh6 and Osh7 define a unique OSBP subfamily with structural features adapted for PS recognition. To determine whether this subfamily is conserved in other kingdoms, we performed a phylogenetic analysis with all OSBP domains entered in the Pfam database²⁰ (see Methods). The seven OSBP domains of Osh proteins in *S. cerevisiae* distribute broadly across the entire tree (Fig. 4a). Those of Osh6/Osh7 and Kes1 belong to two clades, consistent with the view that they define distinct subfamilies. Importantly, the Osh6/Osh7 clade also contains OSBP domains in metazoans, including five human proteins, ORP5, ORP8, ORP9, ORP10 and ORP11, suggesting a broad conservation across eukaryotes. In particular, we observed a high degree of conservation of the sequence signature that is required for Osh6 to bind specifically to PS (see above) (Fig. 4b). Within the $\alpha 1$ - $\beta 1$ loop, we could define sequence motifs characteristic of the Osh6/Osh7 and Kes1 subfamilies (Supplementary Fig. 11). We selected two human OSBP domains that clustered within the Osh6/Osh7 subfamily, one from ORP5 and one from ORP10, and measured their binding specificity *in vitro*, using liposomes derived from brain total lipid extract. We observed that the recombinant OSBP domains from ORP5 and ORP10 efficiently and specifically extracted PS (Fig. 4c). This supports the notion that Osh6 and Osh7 are the first representatives of a broader subfamily of OSBPs that transport PS and which are also conserved in humans.

Other members of the OSBP family are known to bind sterols and PI lipids¹⁹. In humans, many are involved in diseases^{21,22} and in yeast they share a common, essential function, as only one of the seven proteins is required for yeast survival²³. We demonstrate that PS transport represents a new function for some members of this protein family, but clearly, binding to a specific lipid is not a common and essential task. *De facto*, the name 'oxysterol-binding protein' is a misnomer that should be revised and we propose that 'lipid sensing and sorting' (Lss) protein could be more appropriate. Several models could account for the Osh6/Osh7-mediated PS transport against an apparent concentration gradient. A likely scenario relies on the fact that PS associates with specific PM microdomains^{17,24}. This may contribute to its sequestration from the pool of 'free' PS. Consistent with this hypothesis, we observed that Osh6 and PS (Lact C2-GFP) partition in

Osh6- and Kes1-specific residues, respectively. Green, residues common to both. **c**, The OSBP domains of ORP5 and ORP10 bind PS *in vitro*. OSBP-bound fractions of individual lipids are quantified. Bottom: the PS:OSBP molar ratios for recombinant Osh6, ORP5-OSBP and ORP10-OSBP. Chl, cholesterol. Error bars represent standard deviation, $n \geq 3$.

spatially discrete domains with distinct dynamic properties (Supplementary Fig. 7a). In addition, in the ER, the spatial confinement of PS-synthesizing enzymes, for example, Cho1, at PM contact sites²⁵ may produce high, local PS concentrations that also contribute to the transfer of PS from ER to the PM. An important outcome of our study is the ease by which *in vivo*-assembled LTP-lipid complexes can be retrieved from cells. This work clearly demonstrates the feasibility of broader efforts that would include all LTPs in higher eukaryotes^{26–30}.

METHODS SUMMARY

Purification of LTP-TAP fusions and lipid analysis by HPTLC. The TAP fusions were affinity purified on IgG agarose resins and eluted with 20 μ g tobacco etch virus protease (TEV) at 4 °C. The eluates (100 μ l) were loaded on a gel filtration column and 150 μ l fractions were collected. Lipids were extracted from samples by sequential addition of solvents. The lipid fraction was sprayed on HPTLC silica gel 60 plates that were developed with solvent systems for neutral lipids and phospholipids. The plates were dripped in 10% (w/v) CuSO₄ in 8% (v/v) aqueous phosphoric acid, charred at 145 °C for 4.5 min, and scanned for fluorescence detection at 488 nm extinction and 530 nm emission wavelengths.

Crystallization of Osh6-PS complex. The purified Osh6 was treated with tenfold molar excess of PS. The Osh6-PS complexes were purified with Ni-NTA resins followed by gel filtration, and crystallized using vapour diffusion techniques. Diffraction data were collected at beamline ID23-1 of the European Synchrotron Radiation Facility (ESRF, Grenoble, France). The structure was solved by molecular replacement.

The protocols for the production of recombinant proteins, the *in vitro* binding and transfer assays, the cell fractionation, lipidomics, the visualization of intracellular PS and the phylogenetic analysis of OSBP domains are described in the Methods section.

Full Methods and any associated references are available in the online version of the paper.

Received 23 July 2012; accepted 4 July 2013.

Published online 11 August 2013.

1. Yeung, T. *et al.* Membrane phosphatidylserine regulates surface charge and protein localization. *Science* **319**, 210–213 (2008).
2. Leventis, P. A. & Grinstein, S. The distribution and function of phosphatidylserine in cellular membranes. *Annu Rev Biophys* **39**, 407–427 (2010).
3. Fairn, G. D., Hermansson, M., Somerharju, P. & Grinstein, S. Phosphatidylserine is polarized and required for proper Cdc42 localization and for development of cell polarity. *Nature Cell Biol.* **13**, 1424–1430 (2011).

4. D'Angelo, G., Vicinanza, M. & De Matteis, M. A. Lipid-transfer proteins in biosynthetic pathways. *Curr. Opin. Cell Biol.* **20**, 360–370 (2008).
5. Lev, S. Non-vesicular lipid transport by lipid-transfer proteins and beyond. *Nature Rev. Mol. Cell Biol.* **11**, 739–750 (2010).
6. Holthuis, J. C. & Levine, T. P. Lipid traffic: floppy drives and a superhighway. *Nature Rev. Mol. Cell Biol.* **6**, 209–220 (2005).
7. Stefan, C. J. *et al.* Osh proteins regulate phosphoinositide metabolism at ER-plasma membrane contact sites. *Cell* **144**, 389–401 (2011).
8. Gavin, A. C. *et al.* Proteome survey reveals modularity of the yeast cell machinery. *Nature* **440**, 631–636 (2006).
9. Gavin, A. C. *et al.* Functional organization of the yeast proteome by systematic analysis of protein complexes. *Nature* **415**, 141–147 (2002).
10. Raychaudhuri, S., Im, Y. J., Hurley, J. H. & Prinz, W. A. Nonvesicular sterol movement from plasma membrane to ER requires oxysterol-binding protein-related proteins and phosphoinositides. *J. Cell Biol.* **173**, 107–119 (2006).
11. Li, X. *et al.* Identification of a novel family of nonclassic yeast phosphatidylinositol transfer proteins whose function modulates phospholipase D activity and Sec14p-independent cell growth. *Mol. Biol. Cell* **11**, 1989–2005 (2000).
12. Schulz, T. A. *et al.* Lipid-regulated sterol transfer between closely apposed membranes by oxysterol-binding protein homologues. *J. Cell Biol.* **187**, 889–903 (2009).
13. Li, X. *et al.* Analysis of oxysterol binding protein homologue Kes1p function in regulation of Sec14p-dependent protein transport from the yeast Golgi complex. *J. Cell Biol.* **157**, 63–78 (2002).
14. Ejlsing, C. S. *et al.* Global analysis of the yeast lipidome by quantitative shotgun mass spectrometry. *Proc. Natl Acad. Sci. USA* **106**, 2136–2141 (2009).
15. Slaughter, B. D. *et al.* Non-uniform membrane diffusion enables steady-state cell polarization via vesicular trafficking. *Nature Commun.* **4**, 1380 (2013).
16. Riekhof, W. R. *et al.* Lysophosphatidylcholine metabolism in *Saccharomyces cerevisiae*: the role of P-type ATPases in transport and a broad specificity acyltransferase in acylation. *J. Biol. Chem.* **282**, 36853–36861 (2007).
17. Spira, F. *et al.* Patchwork organization of the yeast plasma membrane into numerous coexisting domains. *Nature Cell Biol.* **14**, 640–648 (2012).
18. Im, Y. J., Raychaudhuri, S., Prinz, W. A. & Hurley, J. H. Structural mechanism for sterol sensing and transport by OSBP-related proteins. *Nature* **437**, 154–158 (2005).
19. de Saint-Jean, M. *et al.* Osh4p exchanges sterols for phosphatidylinositol 4-phosphate between lipid bilayers. *J. Cell Biol.* **195**, 965–978 (2011).
20. Punta, M. *et al.* The Pfam protein families database. *Nucleic Acids Res.* **40**, D290–D301 (2012).
21. Ngo, M. H., Colbourne, T. R. & Ridgway, N. D. Functional implications of sterol transport by the oxysterol-binding protein gene family. *Biochem. J.* **429**, 13–24 (2010).
22. Burgett, A. W. *et al.* Natural products reveal cancer cell dependence on oxysterol-binding proteins. *Nature Chem. Biol.* **7**, 639–647 (2011).
23. Beh, C. T., Cool, L., Phillips, J. & Rine, J. Overlapping functions of the yeast oxysterol-binding protein homologues. *Genetics* **157**, 1117–1140 (2001).
24. Fairn, G. D. *et al.* High-resolution mapping reveals topologically distinct cellular pools of phosphatidylserine. *J. Cell Biol.* **194**, 257–275 (2011).
25. Pichler, H. *et al.* A subfraction of the yeast endoplasmic reticulum associates with the plasma membrane and has a high capacity to synthesize lipids. *Eur. J. Biochem.* **268**, 2351–2361 (2001).
26. Yu, J. W. & Lemmon, M. A. All phox homology (PX) domains from *Saccharomyces cerevisiae* specifically recognize phosphatidylinositol 3-phosphate. *J. Biol. Chem.* **276**, 44179–44184 (2001).
27. Yu, J. W. *et al.* Genome-wide analysis of membrane targeting by *S. cerevisiae* pleckstrin homology domains. *Mol. Cell* **13**, 677–688 (2004).
28. Park, W. S. *et al.* Comprehensive identification of PIP3-regulated PH domains from *C. elegans* to *H. sapiens* by model prediction and live imaging. *Mol. Cell* **30**, 381–392 (2008).
29. Gallego, O. *et al.* A systematic screen for protein–lipid interactions in *Saccharomyces cerevisiae*. *Mol. Syst. Biol.* **6**, 430 (2010).
30. Li, X., Gianoulis, T. A., Yip, K. Y., Gerstein, M. & Snyder, M. Extensive *in vivo* metabolite–protein interactions revealed by large-scale systematic analyses. *Cell* **143**, 639–650 (2010).

Supplementary Information is available in the online version of the paper.

Acknowledgements We are grateful to C. Schultz and C. Müller for inspiring comments on the manuscript, and to the EMBL Proteomics and the Protein Expression and Purification Core Facilities, E. M. Vilalta, V. Rybin, O. Gallego, M. Skruzny, A. Picco, S. Glatt, F. Voigt and A. Scholz for expert help and the sharing of reagents. The authors thank the beam line staff at the European Synchrotron Radiation Facility (ESRF), beam line ID23–1, Grenoble, France where crystallographic data collection was performed. We also thank C. Müller's group and other members of M.K.'s and A.-C.G.'s groups for continuous discussions and support. We are grateful to C. Boone, S. Emr and E. Hurt for sharing reagents. This work was partially funded by the Federal Ministry of Education and Research (BMBF; 01GS0865) in the framework of the IG-Cellular System genomics to A.-C.G.; A.K. is supported by the European Molecular Biology Laboratory and the EU Marie Curie Actions Interdisciplinary Postdoctoral Cofunded Programme. K.A. acknowledges support from Marie Curie reintegration grant (ERG). K.M. is supported by the Danish Natural Science Research Council (09-064986/FNU).

Author Contributions K.M. and A.-C.G. designed the research; K.M., A.C. and A.K. conducted the experiments and performed the analysis; K.A. and K.M. performed X-ray crystallography; M.P. supported the development of the biochemical protocols; M.K. provided technical expertise with instrumentation; and K.M. and A.-C.G. discussed results and wrote the manuscript with support from all the authors.

Author Information The atomic coordinates and structure factors have been deposited in the Protein Data Bank at entry 4B2Z. Reprints and permissions information is available at www.nature.com/reprints. The authors declare no competing financial interests. Readers are welcome to comment on the online version of the paper. Correspondence and requests for materials should be addressed to A.-C.G. (e-mail: gavin@embl.de).

METHODS

Purification of LTP-TAP fusions. Yeast TAP strains⁸ were grown in 181 YPAD medium to $D_{600} = 3.5$ ($OD_{600} = 3.5$). Yeast pellets were resuspended in one volume of yeast lysis buffer (50 mM Tris.HCl pH 7.5, 500 mM NaCl, 1.5 mM $MgCl_2$, protease inhibitor cocktail (Complete, EDTA-free; Roche), 1.0 mM AEBSE, and 0.5 mM dithiothreitol (DTT)) and lysed using a planet mill and 0.5-mm zirconia/silica beads (BioSpec Products). The lysates were centrifuged at 27,000g for 20 min and at 200,000g for 1 h. The supernatants were clarified using 0.22- μ m Express PLUS filters (Millipore), and loaded (at ~ 1 ml min⁻¹) on 100 μ l IgG agarose resins (GE Healthcare) packed in Mobicols columns (MoBiTec). The resins were washed with 10 ml yeast lysis buffer without protease inhibitors, and incubated with 20 μ g tobacco etch virus protease (TEV) for 1 h at 4 °C for elution. The eluates (100 μ l) were loaded on an analytical Superdex 200 SEC column (3.9 ml column volume) equilibrated with 50 mM Tris.HCl pH 7.5, 500 mM NaCl, and 150 μ l fractions were collected.

Lipid analysis by HPTLC. All solvents for HPTLC were from Merck Chemicals (HPLC grade). All lipids were purchased from Avanti Polar Lipids unless otherwise stated. Lipids were extracted from samples by sequential addition of 3.75 volume chloroform:methanol (1:2 v/v), 1.25 volume chloroform, and 1.25 volume 0.5% acetic acid in 500 mM NaCl followed by 30 s vortexing after each step. After centrifugation at 1,200 r.p.m. for 10 min, the bottom layer was sprayed on HPTLC silica gel 60 plates (10 cm \times 10 cm) (Merck) in 3-mm bands using the TLC sampler 4 (Camag). The plates were developed with a solvent system of hexanes:diethyl-ether:acetic acid 80:20:2 for the analysis of neutral lipids. For phospholipids, the plates were sequentially developed with (1) dichloromethane:ethyl acetate:acetone 80:16:4 and (2) chloroform:acetone:isopropanol:ethyl acetate:ethanol: methanol: H_2O :acetic acid 30:6:6:16:28:6:2³¹. The plates were dried in vacuum and dripped in 10% (w/v) $CuSO_4$ in 8% (v/v) aqueous phosphoric acid, charred at 145 °C for 4.5 min, and scanned for fluorescence detection³² using Pharos FX Plus molecular imager (Bio-Rad) (488 nm extinction and 530 nm emission wave lengths). Lipids applied as standards were detected with a sensitivity of <10 picomole. HPTLC images were analysed and processed using ImageJ.

Assessment of protein-lipid interactions from SEC elution profiles. Only lipids co-eluting with LTPs were considered to represent specific ligands. Abundant yeast lipids (PC, PI, PE and ergosterol) that eluted near the void volume peak were filtered out as background. All interactions were detected in at least two independent experiments, except the binding of Sfh5 (systematic name Yjl145w) to PI which was only detected in one of the duplicates.

Phospholipid analysis by LC/MS/MS. Phospholipids in the SEC peak fractions of Osh6-TAP (fractions 9–10), Kes1-TAP (fractions 9–10) and Sec14-TAP (fractions 11–12) were analysed using LC/MS/MS by Avanti Polar Lipids. The two peak fractions for each TAP-fusion were pooled, and 200 μ l were subjected to lipid extraction. The samples were mixed with one volume each of methanol and chloroform (HPLC grade) and vortexed for 30 s. The mixture was centrifuged at 1,000 r.p.m. for 5 min, and the bottom layer was transferred to a new test tube. The upper layer was subjected to re-extraction using 200 μ l chloroform. The two bottom layers were combined and washed twice with 500 μ l water (HPLC grade). Appropriate and known quantities of phospholipids were added to the washed bottom layer as internal standards. The samples were dried to a residue under nitrogen at room temperature. Lipids were dissolved in 200 μ l methanol. The samples were analysed for PC, PE, PI, PA, PS and PG on a Waters Acquity UPLC/AB Sciex 5500 LC/MS system. Each phospholipid group was assayed by individual reverse phase chromatography/multiple reaction monitoring methods (MRM) and quantified against the respective internal standard compounds. Identified compounds exhibiting >3:1 signal to noise response were quantified.

Production of recombinant proteins in *E. coli*. Codon-optimized synthetic genes for Osh6, Kes1, ORP5-OSBP (Uniprot entry code Q9H0X9, residues 357–788), and ORP10-OSBP (Uniprot entry code Q9XB5, residues 340–764) (GenScript, Entelechon) were inserted into the pETM11-SUMO3GFP vector using BamHI and NotI sites. Expression vectors for Osh6 mutants were constructed on the pETM11-SUMO3GFP vector with Osh6 insertion using QuikChange Lightning Site-Directed Mutagenesis Kit (Agilent Technologies). The N-terminal hexahistidine-SUMO3 tagged proteins were expressed in BL21 Star cells (Invitrogen) grown in LB medium by induction (at $D_{600} = 0.6$) with 0.4 mM isopropyl-1-thio- β -D-galactopyranoside at 22 °C for 5 h (Osh6 and Osh6 mutants), at 18 °C overnight or at 28 °C for 3 h (ORP5-OSBP and ORP10-OSBP). Collected cells were suspended in the lysis buffer (50 mM Tris pH 7.5, 500 mM NaCl, 20 mM imidazole, 0.5 mM DTT, protease inhibitor cocktail (Complete, EDTA-free; Roche)) and lysed by sonication. The expressed proteins in the soluble fractions were captured on Ni-NTA agarose resins (Qiagen) and eluted in 50 mM Tris pH 7.5, 250 mM NaCl, 300 mM imidazole. After tag cleavage with 1:200 molar ratio of hexahistidine-tagged SenP2 protease (EMBL) and dialysis against 50 mM Tris pH 7.5, 250 mM NaCl, 20–80 mM imidazole, the proteins were loaded on the

Ni-NTA agarose resins. The flow-through was loaded on the Superdex 200 16/60 SEC column (GE Healthcare) equilibrated with 50 mM HEPES pH 7.5, 250 mM NaCl. For the preparation of crystallization sample, Osh6 was further purified on the Mono S 5/50 GL cation exchange chromatography column (GE Healthcare).

Liposome preparation. PC and indicated mol% of additional lipids were mixed and dried into thin films in glass-vials using argon-flow and then under vacuum for at least 30 min. Liposomes were formed by rehydrating the lipid films in the rehydration buffer (10 mM HEPES pH 7.4, 250 mM NaCl unless otherwise specified) to the total lipid concentration of 3.8 mM at 62 °C for 1 h. Liposomes were filtered 21 times through the Nuclepore Track-Etched Membranes (Waters) on Mini-extruder (Avanti Polar Lipids) to define the sizes (when specified). Liposomes of 50% (w/w) yeast total lipid extract (Avanti Polar Lipids) or 50% (w/w) porcine brain total lipid extract (Avanti Polar Lipids) were prepared to 3.0 mg ml⁻¹ total lipid concentration and filtered to 400 nm.

Lipid-profiling of recombinant Osh6. Recombinant Osh6 was incubated overnight at 25 °C with 0.2% (v/v) Nonidet P40 Substitute (Fluka) or liposomes solely consisting of PS at tenfold molar excess, and re-purified using the affinity of untaged Osh6 to Ni-NTA agarose resins. The treated and untreated recombinant Osh6 (250 μ g) was loaded on the analytical Superdex 200 SEC column, and the peak fractions were analysed for lipid contents using HPTLC.

In vitro lipid-binding assay. Recombinant Osh6 (20 μ M) were incubated with liposomes containing 10 mol% (0.20 mM) PS, PE, PG, PI, CA or Erg in 200 μ l assay buffer (10 mM HEPES pH 7.4, 250 mM NaCl) at 25 °C for 30 min. OSBP proteins were incubated with liposomes of 50% (w/w) yeast total lipid extract or 50% (w/w) porcine brain total lipid extract (total lipid concentration of 0.15 mg ml⁻¹). After centrifugation at 80,000 r.p.m. for 30 min (TLA 100 rotor) to pellet the liposomes, the supernatant (110 μ l) was analysed by HPTLC (lipids) and SDS-PAGE (proteins). Lipids were densitometrically quantified relatively to the individual lipids in the input liposomes (applied on the same HPTLC plates). Proteins were densitometrically quantified relatively to the protein standards (loaded on the same Coomassie stained gels). Standard deviations are derived from assays performed at least in triplicates.

Biochemical lipid-transfer assay. The 'heavy' donor liposomes (400 nm) were prepared with PC and 10 mol% of PS, PE, PG or Erg, in the rehydration buffer containing 0.75 M sucrose, and pelleted at 16,100g for 15 min and washed twice with the rehydration buffer. The 'light' acceptor liposomes (100 nm) were prepared with PC. Recombinant Osh6 (1.0 μ M) was incubated with the donor and acceptor liposomes (each corresponding to 2.0 mM total lipids) in 150 μ l assay buffer (10 mM HEPES pH 7.4, 250 mM NaCl) at 25 °C for 30 min. After pelleting the donor liposomes at 16,100g for 30 min, lipids in the supernatants (100 μ l) were analysed (HPTLC). Transferred lipids were densitometrically quantified relatively to the individual lipids in the input liposomes loaded on the same HPTLC plates. The lipid transfer activities of yeast TAP-fusions were determined using the same assay (the donor and acceptor liposomes each correspond to 1.3 mM total lipids). The TAP-strains were grown and lysed as described above. The TAP-fusions were captured on IgG agarose resins and washed with the lysis buffer (without protease inhibitors) with 0.15% (v/v) Nonidet P40 Substitute and eluted with 10 μ l TEV in \sim 200 μ l assay buffer. Fifty microlitre eluates were used for each assay.

PS-transfer assay using fluorescence microscopy. The 'heavy' acceptor liposomes were prepared of 0.1% BODIPY FL DHPE (Invitrogen), and 1.0% DSPE-PEG-Biotin (Avanti Polar Lipids) in the assay buffer (10 mM HEPES pH 7.4, 300 mM NaCl) with 0.75 M sucrose. After sonication for 30 s, the liposomes were pelleted at 16,100g and washed three times in the assay buffer. The 'light' donor liposomes (100 nm) with 30% PS were prepared in assay buffer. Recombinant Osh6 (1.0 μ M) was incubated with the donor and acceptor liposomes (corresponding to 2.0 mM and 1.0 mM total lipids, respectively) in 200 μ l assay buffer at 25 °C for 3 h. The acceptor liposomes were then pelleted at 16,100g for 15 min and washed three times in 10 mM HEPES pH 7.4, 150 mM NaCl, and immobilized on glass slides coated with biotin-labelled bovine albumin (Sigma) and streptavidin (Sigma). The immobilized acceptor liposomes were incubated in 0.5 μ g ml⁻¹ solution of annexin V-Cy3.18 (Sigma) in 10 mM HEPES pH 7.5, 140 mM NaCl, 2.5 mM $CaCl_2$ for at least 10 min and imaged on the Olympus IX81 microscope equipped with a \times 100/NA 1.45 objective lens and Hamamatsu Orca-ER camera.

Creation of yeast strains. Yeast strains with deleted or depleted lipid metabolizing, *OSH6*, *OSH7* and *KES1* genes, or C-terminally mCherry-tagged *RTN1* and *VPH1* were created in the SGA Y7039 strain (a gift from C. Boone) derived from the BY4741 background³³ (*MAT α can1 Δ :: STE2pr-LEU2 lyp1 Δ ura3 Δ 0 leu2 Δ 0 his3 Δ 1 met15 Δ 0*) using standard yeast molecular biology procedures³⁴. Strains used for rapamycin-inducible heterodimerization³⁵ carried *Fpr1 Δ* and Ser1972Arg mutation on the *TOR1* gene (*MAT α his3200 leu2-3 112 ura3-52 lys2-801 tor1-1 fpr1::*). For the overexpression of Osh6 and Osh6 mutants, the cloned Osh6 gene was inserted into the plasmid pRS315. The QuikChange Lightning Site-Directed Mutagenesis Kit (Agilent Technologies) was used to introduce mutations. Osh6

and its mutants were expressed with C-terminal mCherry-tag from the *ADHI* promoter. The ER-markers GFP- and mCherry-HDEL were constructed as previously described³⁶ into the plasmid pRS315 and expressed from the *ADHI* promoter. Lact C2-GFP and PLC δ -PH-GFP were expressed from plasmids p416-GFP-Lact-C2¹ (Haematologic technologies) and pRS426-PLC δ -PH³⁷ (a gift from S. Emr), respectively.

Phospholipid analysis and subcellular fractionations. All experiments were performed in triplicates. To ensure reproducible determination of phospholipids, yeast strains were grown in litter scales and lysed mechanically with a planet mill and 0.5-mm zirconia/silica beads (BioSpec Products) (>90% lysis efficiency). Strains were grown in 1.0 l synthetic defined (SD) medium to D_{600} of ~ 1.5 . The pellets were suspended in 10 ml 25 mM imidazole pH 7.0, 0.4 M sucrose (supplemented with protease inhibitor cocktail (Complete, EDTA-free; Roche), 1.0 mM AEBSF). After lysis, the extracts (100 μ l) were subjected for phospholipid extraction and profiling on HPTLC as described above. Ethanolamine or choline was added to the growth medium to 1.0 mM as indicated.

For fractionation of PM and microsomes, strains were grown and lysed as described above. The lysates were subjected to differential centrifugation and sucrose step gradient centrifugation as described previously^{38,39}. The mouse anti-DMP1 yeast monoclonal antibody (Invitrogen, catalogue no. A-6429) and goat anti-Pma1 polyclonal antibody (Santa Cruz Biotechnology; catalogue no. sc-19389) were used to assess the enrichment of membrane fractions with western blot.

For determination of PS produced in *cho1 Δ* strains from exogenously added lyso-PS, strains were grown to D_{600} of ~ 1 in 1.0 ml SD medium supplemented with 1.0 mM ethanolamine. Lyso-PS was dried under vacuum to remove the solvent and suspended in the SD medium to 54 μ M. 1.0 ml of the yeast culture was mixed with same volume of lyso-PS solution and incubated for 10 min at room temperature. The cells were then cooled on ice, pelleted and washed twice in ice-cold water, resuspended in 200 μ l water, and lysed mechanically (vortexing) using 0.5-mm zirconia/silica beads. PS levels were determined (in 100 μ l lysate) as described above.

Visualization of intracellular PS. Yeast strains were grown overnight at 30 °C in relevant SD medium (plasmid selection) and diluted to $D_{600} < 0.05$ for further growth for ~ 5 h. The cells were adhered on glass slides coated with Concavalin A (Sigma) and imaged with an Olympus IX81 microscope equipped with a $\times 100$ /NA 1.45 objective lens and Hamamatsu Orca-ER camera. Total internal reflection fluorescence microscopy was performed on 488 nm and 561 nm solid-state lasers (Coherent). For Osh6-translocation (rapamycin-inducible heterodimerization), the adhered cells were incubated for 30 min at 30 °C in the SD medium containing 1.4 μ M rapamycin. To monitor cellular localizations of PS produced from exogenously added lyso-PS in the *cho1 Δ* strains, lyso-PS was dissolved in SD medium as described above, and the resultant solutions were centrifuged for 2 min to remove insoluble materials. Equal volumes of Lyso-PS solution were added to cultures of the adhered cells (performed at the room temperature or on ice). Images were processed with ImageJ.

Visualization of Osh localizations upon perturbed lipid metabolism. Yeast strains harbouring both GFP-fused *OSH* genes and deletions/depletions of genes of lipid metabolic enzymes were generated using robot facilitated mating, sporulation and strain selection of the standard SGA protocols^{33,40}. The genotypes of the final strains were confirmed by PCR. For live-cell imaging, cells were inoculated in SD medium without tryptophan and histidine and grown overnight at 30 °C. Cells were diluted to $D_{600} = 0.1$, adhered on Concavalin A (Sigma)-coated 96 well glass bottom plates, and imaged on fully motorized Olympus fluorescence microscope system (Olympus IX81) at 30 °C (temperature controlled incubator, EMBL manufacture). Images with 16-bit readout were acquired using a $\times 100$ oil objective with an NA of 1.45, low noise highly sensitive ORCA-R camera (Hamamatsu), MT20 illumination system, and Uniblitz Electro-Programmable Shutter system. Acquired images were processed with ImageJ.

Phylogenetic analysis of OSBP domains. A sequence alignment file containing all OSBP domain entries were obtained from the Pfam database (<http://pfam.sanger.ac.uk/>), and processed in Jalview⁴¹ to reduce redundancy, eliminate entries shorter than 320 amino acids or containing unassigned amino acids. A phylogenetic analysis was performed on the processed sequence alignment at the PHYLIP 3.67: protdist server⁴² (<http://mobyle.pasteur.fr/cgi-bin/portal.py#forms::protdist>). The generated tree was visualized in iTOL⁴³ (<http://itol.embl.de/upload.cgi>). Sequence logos were created in WebLogo⁴⁴ (<http://weblogo.berkeley.edu/>) after the realignment of protein groups using T-coffee⁴⁵ (<http://www.ebi.ac.uk/Tools/msa/tcoffee/>).

Crystallization of Osh6-PS complex. The purified Osh6 (12 mg ml⁻¹) was treated with tenfold molar excess of PS in liposomes at 25 °C overnight in 20 mM HEPES pH 7.4, 500 mM NaCl, and 0.5 mM DTT. Osh6 was purified using Ni-NTA resins, and Superdex 200 SEC column equilibrated with 10 mM HEPES pH 7.4, 250 mM NaCl.

Screening (mosquito crystallization robot, TTP Labtech) using the sitting drop vapour diffusion technique in 96 well plate format gave initial microcrystals of Osh6-PS with drop and reservoir volumes of 0.2 μ l and 100 μ l, respectively. Later crystals were optimized to larger size in 24 well plates (Hampton Research) at 15 °C by the hanging drop vapour diffusion technique. Equal volumes (0.75 μ l/0.75 μ l) of protein (13 mg ml⁻¹) and crystallization buffer (0.1 M MES, 13% (w/v) PEG6000, 5% (w/v) MPD, pH 6.5) were mixed on a coverslip, which was subsequently equilibrated against a reservoir containing 500 μ l of crystallization buffer. Few microcrystals appeared in ~ 3 days. At this stage 1 μ l of reservoir was added into the drop. This delayed the crystal growth and gave optimal monoclinic crystals grew in about eight days to a size of about 80 μ m \times 70 μ m \times 50 μ m. They were harvested by transfer to a cryoprotectant solution (15% ethylene glycol in the mother-liquor), rapidly recovered in a nylon loop (Hampton Research) and flash-frozen in liquid nitrogen.

Data collection, crystal characterization and refinement. Data were collected at beamline ID23-1 of the European Synchrotron Radiation Facility (ESRF, Grenoble, France) using ADSC Quantum Q105 CCD detector, at a wavelength of 0.93340 Å (Supplementary Table 1). Crystals were kept at a temperature of 100 K in a stream of nitrogen gas for data collection. The diffraction data clearly suggested for space group 5. A Matthews coefficient of 2.42 Å³ Da⁻¹ and a solvent content of 49% were obtained, assuming two molecules were present in the asymmetric unit. The data were processed and scaled using the XDS program package⁴⁶. The phase problem was solved by molecular replacement⁴⁷ using PHASER⁴⁸ with the individual structure of Kes1 (PDB code 1ZHT) as search model (20% sequence identity to Osh6). Flexible loops (60–76, 124–133, 292–311, 367–381 and 390–416) of the search model were truncated for the phase solution. The cycles of adjustments to the electron density were done using graphical program COOT⁴⁹.

The alternate rounds of computational-refinement were performed using PHENIX⁵⁰. The first electron density map already showed interpretable density for the major fold of the Osh6 molecule. Most of the amino acid residues were clearly visible in the electron density map, except side chains of few residues at the N-terminal region and β 11- β 12 which were disordered. Therefore, side-chain occupancies of these atoms were kept at zero. Water molecules were modelled using COOT⁴⁹ and included in the refinement cycles at the later stage. Manual fitting of the model, following the refinement cycles eventually lead to final R_{work} of 19.7% and R_{free} of 23.5% with a good stereochemistry (Supplementary Table 1). In the final model (residues 36–434 (molecule A) and 35–434 (molecule B)), no residue fall in disallowed regions of Ramachandran space (95.2% preferred, 100% allowed) (using PROCHECK⁵¹). Molecular diagrams were drawn using PyMOL (<http://pymol.sourceforge.net>). Structure-based sequence alignment was produced using PROMALS3D⁵² and corrected manually on the basis of the three-dimensional structures.

- Weerheim, A. M., Kolb, A. M., Sturk, A. & Nieuwland, R. Phospholipid composition of cell-derived microparticles determined by one-dimensional high-performance thin-layer chromatography. *Anal. Biochem.* **302**, 191–198 (2002).
- Churchward, M. A., Brandman, D. M., Rogasevskaja, T. & Coorsen, J. R. Copper (II) sulfate charring for high sensitivity on-plate fluorescent detection of lipids and sterols: quantitative analyses of the composition of functional secretory vesicles. *J. Chem. Biol.* **1**, 79–87 (2008).
- Tong, A. H. & Boone, C. in *Yeast Gene Analysis, Methods in Microbiology* 2nd edn, Vol. 36 (eds Stansfield, I. and Stark, M.) 369–386; 706–707 (Elsevier, 2007).
- Janke, C. et al. A versatile toolbox for PCR-based tagging of yeast genes: new fluorescent proteins, more markers and promoter substitution cassettes. *Yeast* **21**, 947–962 (2004).
- Chen, J., Zheng, X. F., Brown, E. J. & Schreiber, S. L. Identification of an 11-kDa FKBP12-rapamycin-binding domain within the 289-kDa FKBP12-rapamycin-associated protein and characterization of a critical serine residue. *Proc. Natl Acad. Sci. USA* **92**, 4947–4951 (1995).
- Rossanese, O. W. et al. A role for actin, Cdc1p, and Myo2p in the inheritance of late Golgi elements in *Saccharomyces cerevisiae*. *J. Cell Biol.* **153**, 47–62 (2001).
- Stefan, C. J., Audhya, A. & Emr, S. D. The yeast synaptotagmin-like proteins control the cellular distribution of phosphatidylinositol (4,5)-bisphosphate. *Mol. Biol. Cell* **13**, 542–557 (2002).
- Fischl, A. S. & Carman, G. M. Phosphatidylinositol biosynthesis in *Saccharomyces cerevisiae*: purification and properties of microsome-associated phosphatidylinositol synthase. *J. Bacteriol.* **154**, 304–311 (1983).
- Panaretou, B. & Piper, P. Isolation of yeast plasma membranes. *Methods Mol. Biol.* **313**, 27–32 (2006).
- Huh, W. K. et al. Global analysis of protein localization in budding yeast. *Nature* **425**, 686–691 (2003).
- Waterhouse, A. M., Procter, J. B., Martin, D. M., Clamp, M. & Barton, G. J. Jalview Version 2—a multiple sequence alignment editor and analysis workbench. *Bioinformatics* **25**, 1189–1191 (2009).
- Felsenstein, J. PHYLIP (Phylogeny Inference Package) version 3.5c. Distributed by the author. Department of Genetics, University of Washington, Seattle, Washington, USA (1993).

43. Letunic, I. & Bork, P. Interactive Tree Of Life (iTOL): an online tool for phylogenetic tree display and annotation. *Bioinformatics* **23**, 127–128 (2007).
44. Crooks, G. E., Hon, G., Chandonia, J. M. & Brenner, S. E. WebLogo: a sequence logo generator. *Genome Res.* **14**, 1188–1190 (2004).
45. Di Tommaso, P. *et al.* T-Coffee: a web server for the multiple sequence alignment of protein and RNA sequences using structural information and homology extension. *Nucleic Acids Res.* **39**, W13–W17 (2011).
46. Kabsch, W. Automatic processing of rotation diffraction data from crystals of initially unknown symmetry and cell constants. *J. Appl. Cryst.* **26**, 795–800 (1993).
47. Rossmann, M. G. The molecular replacement method. *Acta Crystallogr. A* **46**, 73–82 (1990).
48. Read, R. J. Pushing the boundaries of molecular replacement with maximum likelihood. *Acta Crystallogr. D* **57**, 1373–1382 (2001).
49. Emsley, P. & Cowtan, K. Coot: model-building tools for molecular graphics. *Acta Crystallogr. D* **60**, 2126–2132 (2004).
50. Adams, P. D. *et al.* PHENIX: building new software for automated crystallographic structure determination. *Acta Crystallogr. D* **58**, 1948–1954 (2002).
51. Laskowski, R. A., MacArthur, M. W., Moss, D. S. & Thornton, J. M. PROCHECK: a program to check the stereochemical quality of protein structures. *J. Appl. Cryst.* **26**, 283–291 (1993).
52. Pei, J., Kim, B. H. & Grishin, N. V. PROMALS3D: a tool for multiple protein sequence and structure alignments. *Nucleic Acids Res.* **36**, 2295–2300 (2008).

CORRIGENDUM

doi:10.1038/nature12498

Corrigendum: A CRISPR/Cas system mediates bacterial innate immune evasion and virulence

Timothy R. Sampson, Sunil D. Saroj, Anna C. Llewellyn, Yih-Ling Tzeng & David S. Weiss

Nature **497**, 254–257 (2013); doi:10.1038/nature12048

In this Letter, we described two small RNAs (scaRNA and tracrRNA) within the *Francisella novicida* CRISPR/Cas locus that are necessary for repression of an endogenous transcript. Concurrent to our studies, E. Charpentier's group performed RNA sequencing analyses of multiple type II CRISPR loci to identify tracrRNA in *F. novicida* and other species¹, based in part on the co-processing of tracrRNA:crRNA by RNase III (ref. 2). These observations indicate that the regulatory RNA we annotated as scaRNA is the tracrRNA, and that the RNA we annotated as tracrRNA is the scaRNA. Furthermore, RNAseq data show that the transcriptional direction of the crRNA array is the opposite of what was predicted. Finally, our predictions of tracrRNA and scaRNA within Supplementary Table 2 are incorrect based on this transcriptional analysis; the scaRNAs predicted in *Neisseria meningitidis* 92045, *Listeria monocytogenes* SLCC2482 and *Streptococcus pyogenes* M1 GAS are in fact within the crRNA array transcript, as is the predicted tracrRNA in *Campylobacter jejuni* NCTC11168, whereas the predicted *C. jejuni* scaRNA is actually the tracrRNA. We include a corrected annotated Fig. 1a below, and apologize for any confusion about our incorrect nomenclature. We are grateful to E. Charpentier and her group for alerting us to the errors.

1. Chylinski, K., Le Rhun, A. & Charpentier, E. The tracrRNA and Cas9 families of type II CRISPR-Cas immunity systems. *RNA Biol.* **10**, 726–737 (2013).
2. Deltcheva, E. *et al.* CRISPR RNA maturation by *trans*-encoded small RNA and host factor RNase III. *Nature* **471**, 602–607 (2011).

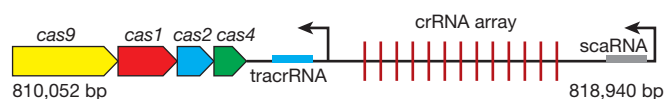


Figure 1 | This is the corrected Fig. 1a of the original Letter.

CORRIGENDUM

doi:10.1038/nature12527

Corrigendum: X-ray analysis on the nanogram to microgram scale using porous complexes

Yasuhide Inokuma, Shota Yoshioka, Junko Ariyoshi, Tatsuhiko Arai, Yuki Hitora, Kentaro Takada, Shigeki Matsunaga, Kari Rissanen & Makoto Fujita

Nature **495**, 461–466 (2013); doi:10.1038/nature11990

Previously unnoticed ambiguities in the crystallographic data in our Article (specifically, non-negligible disorder of the miyakosyne A molecule), along with further work by three of the authors (Y.H., K.T. and S.M.) have revealed that the stereochemistry we assigned at C14 of miyakosyne A is incorrect. Our new investigations confirm that we can indeed determine the molecular skeleton of miyakosyne A. However, we can only tentatively and not unambiguously identify all of the stereochemistry of miyakosyne A based on the data included in the original paper. A future publication will confirm the stereochemistry at the C14 moiety of miyakosyne A. The other conclusions of our paper are not affected by this correction.

RETRACTION

doi:10.1038/nature12497

Retraction: Bird-like fossil footprints from the Late Triassic

Ricardo N. Melchor, Silvina de Valais & Jorge F. Genise

Nature **417**, 936–938 (2002); doi:10.1038/nature00818

In this Letter, we considered the bird-like footprints from the former Santo Domingo Formation of northwest Argentina to be of Late Triassic age. Recent radiometric dating¹ of the sedimentary sequence containing these bird-like footprints (renamed as the Laguna Brava Formation) indicated a Late Eocene age. Further geological studies² suggest that the region suffered a complex deformation during the Andean orogeny, including block rotation. In consequence, our previous inferences about the possible implications of this finding for the fossil record of Aves are no longer supported. This Retraction has not been signed by J.F.G. Correspondence should be addressed to R.N.M. (rmelchor@exactas.unlpam.edu.ar).

1. Melchor, R. N., Buchwaldt, R. & Bowring, S. A. A Late Eocene date for Late Triassic bird tracks. *Nature* **495**, E1–E2 (2013).
2. Vizán, H. *et al.* Geological setting and paleomagnetism of the Eocene red beds of Laguna Brava Formation (Quebrada Santo Domingo, northwestern Argentina). *Tectonophysics* **583**, 105–123 (2013).

TECHNOLOGY FEATURE

THE GENOME JIGSAW

Advances in high-throughput sequencing are accelerating genomics research, but crucial gaps in data remain.

WATCHARA/SHUTTERSTOCK



BY VIVIEN MARX

To understand why high-throughput gene-sequencing technology often produces frustrating results, says Titus Brown, imagine that 1,000 copies of Charles Dickens' novel *A Tale of Two Cities* have been shredded in a woodchipper. "Your job is to put them back together into a single book," he says.

That task is relatively easy if the volumes are identical and the shreds are large, says Brown, a microbiologist and bioinformatician at Michigan State University in East Lansing. It is harder with smaller shreds, he says, "because if the sentence fragments are too small, then you can't uniquely place them in the book". There

are too many ways they might fit together. "And it's harder still if the original pile of books includes multiple editions," he says.

Researchers in genetic sequencing today face a similar task. An organism's DNA — made up of four basic building blocks, or bases, denoted by the letters A, T, C and G — is chopped into short snippets, sequenced to determine the order of its bases and reassembled into what researchers hope is a good approximation of the organism's actual genome.

Today's high-throughput sequencing technology is remarkably powerful and has led to an explosion of sequencing projects in laboratories around the world, says Jay Shendure, a molecular biologist who develops

sequencing methods at the University of Washington School of Medicine in Seattle. Thousands of patient tumours and more than 10,000 vertebrate species have been or are being sequenced. High-throughput sequencing is now an essential tool for basic and clinical research, with applications ranging from detection of microbial 'bio-threats' to finding better biofuels¹.

But some types of genomic DNA cannot be sequenced by high-throughput methods, leaving many frustrating gaps in data (see 'What makes a tough genome?'). For example, a genome might contain long stretches in which the sequence simply repeats — as if Dickens had filled whole pages with a word or sentence

written over and over — making that passage hard, if not impossible, to reconstruct by the usual technologies. And the widespread adoption of next-generation sequencing has meant that the quality of genome assemblies has declined significantly over the past six years, says Evan Eichler, a molecular biologist also at the University of Washington. Although “we can generate much, much more sequence, the short sequence-read data translate into more gaps, missing data and more incomplete references,” he says.

Incomplete genomes make it harder for researchers to identify and interpret sequence variations. “Instead,” Eichler says, “we focus only on the accessible portions, creating a biased view,” which in turn hinders efforts to study the genetic basis of disease or how species have evolved. For example, the human-genome sequence, used as a reference by scientists around the world, has more than 350 gaps, says Deanna Church, a genomicist at the US National Center for Biotechnology Information. An updated reference genome is filling in much of the missing data, but “even with the release of the new assembly, there will still be gaps and regions that aren’t well represented,” she says. “It is definitely a work in progress.”

More than 900 human genes are in regions where there is much repetition. About half of these genes are in areas so poorly understood that they are often excluded from biomedical study, says Eichler. Certain regions of chromosomes, notably those near centromeres (where the two halves of a chromosome connect) and telomeres (the ends of chromosomes) are especially incomplete in the reference genome.

This lack of information can have medical consequences. For example, researchers have known for more than a decade that medullary cystic kidney disease — a rare disorder that occurs in mid-life — can be caused by mutations in a gene hidden somewhere along a 2-million-base-pair stretch of chromosome 1. Early detection of the mutation is the first step towards preventative therapies, but would require a DNA test. The gene, however, lies within a region rich in sequence repeats as well as in the bases guanine (G) and cytosine (C). Such ‘GC-rich’ regions, like repetitions, are difficult to sequence.

Only by reverting to Sanger sequencing — a classic but more laborious approach — and combining it with special assembly methods were researchers able to decipher the DNA

region involved in the disease. The results, which were published in February², mean that a test to screen younger members of families affected by the disorder is now a possibility.

Sanger sequencing is a painstaking process in which each type of DNA base is labelled with a different compound. The labelled DNA is then separated and the sequence is read. For the Human Genome Project, researchers combined Sanger sequencing with techniques to establish markers that locate where the sequences fit. The approach, which has been in use for decades, delivers a read accuracy and contiguity of sequence that are unmatched by current technology, Shendure says. “I couldn’t do anything remotely approaching the quality of what resulted from the project.” But the art of Sanger sequencing and its associated methods cannot be scaled up for the high-throughput sequencing projects done today. “We need to think about how to ‘next-generation-ify’ all of this,” he says.

Research to do just that is well under way, with a variety of methodologies that address problems such as repetitive sequences and GC-rich regions, as well as the knotty task of assembling complete genomes for organisms that have four or even eight copies of each chromosome, for example, as opposed to humans’ two.

Some of the technologies on the horizon promise to deliver longer reads and, possibly, fewer headaches for researchers trying to assemble them. But until those instruments are on bench tops, scientists are combining new and old approaches to refine sequencing.

RICH IS POOR

Some of the newer approaches aim to tackle GC-rich regions. For high-throughput sequencing, DNA is often first chopped into short fragments, which are then amplified by polymerase chain reaction (PCR). But the enzyme used in PCR “has trouble getting through” GC-rich regions, says Shendure. As a result, GC-rich stretches can end up poorly represented in the DNA sample delivered to the sequencer, thus skewing the data. Some sequencing technologies, such as those made by Illumina, based in San Diego, California, use amplification before and during the sequencing process, causing further bias against GC regions.

A number of sample-preparation approaches reduce this GC bias. The amplification step is cut out completely in platforms made by Pacific Biosciences, based in Menlo Park, California, and in a method being developed at Oxford Nanopore Technologies in Oxford, UK. And although DNA read lengths differ among platforms, the most widely used bench top sequencers — which are made by Illumina — generate short reads, of around 150 base pairs.

“The killer with short reads is that they’re very sensitive to repeated content,” says Brown.

What makes a tough genome?

Certain features of DNA are challenging for high-throughput sequencing.

- Long sequences of repeated bases
- Missing bases in the original sequence
- Degraded or damaged DNA
- Regions rich in guanine and cytosine

If the read length is shorter than a repeat — or, to draw on the book analogy, if the shreds of the novel are only a fraction as long as a repeated paragraph — it is hard or even impossible to uniquely place. “That’s where things like long reads or other technologies can be helpful,” says Shendure. Long DNA fragments can bridge repetitive regions and thus help to map them. As another way to ease assembly, researchers in Shendure’s group and elsewhere are exploring different methods to tag and group DNA fragments before sequencing. “There are more on the horizon,” says Shendure, but he prefers to divulge the details in research publications.

The terms ‘short’ and ‘long’ are in a state of flux in this fast-moving industry. The first generation of Illumina machines generated reads of around 25 base pairs in length; the latest ones have upped that to around 150 base pairs (see ‘Extended sequence’). But it is still hard to assemble a complete genome from reads of this length.

Geoff Smith, who directs technology development at Illumina in Cambridge, UK, acknowledges the drawbacks of short-read technology for sequencing repetitive regions and various types of genomic rearrangements. He says that the company aims to address issues that crop up as researchers compare genomes they sequence to reference genomes, or sequence organisms from scratch without references.

Illumina has launched a service to allow longer reads with its current short-read technology. Last year the firm bought Moleculo, a company based in San Francisco, California, which has developed a process to create long reads by stitching together short ones through a proprietary sample-preparation and computational process. In July Illumina began offering Moleculo’s process as a service for customers.

The Moleculo process first creates DNA fragments about 10,000 bases (10 kilobases) in length. The fragments are sheared and amplified, then grouped and tagged with a unique barcode that helps to identify which larger fragment they originated from and aids in assembly.

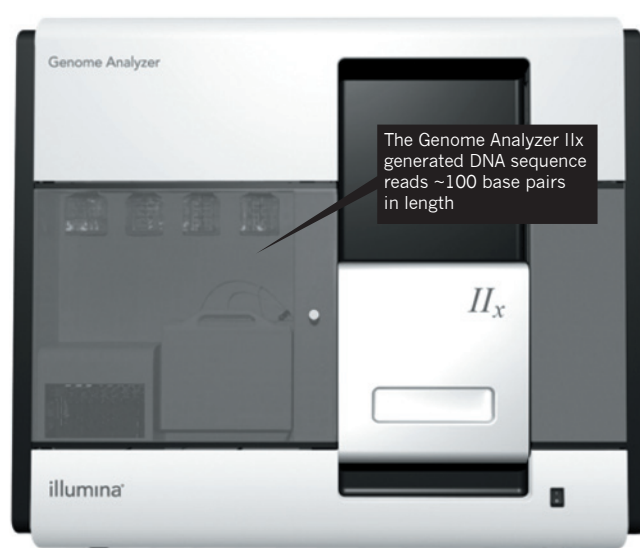


Jay Shendure is working to develop the next generation of sequencing methods.

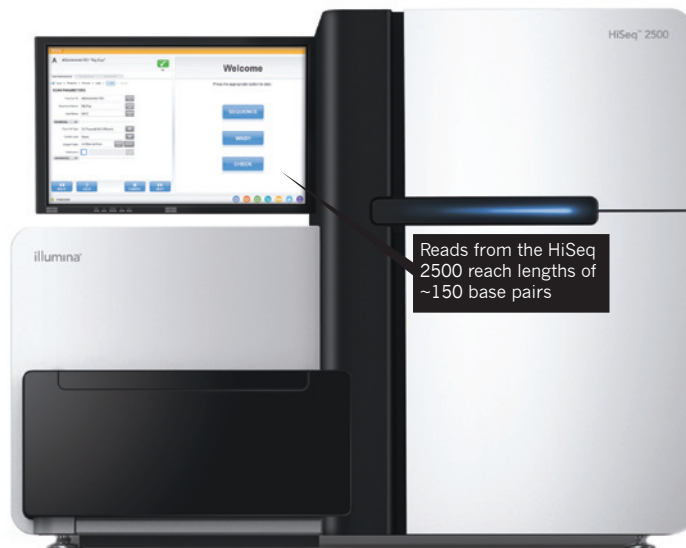
UNIV. WASHINGTON

EXTENDED SEQUENCE

Illumina's first high-throughput sequencers produced very short reads.



2009



2013

At present, sample preparation for the Molecule process takes around two days. Smith says that he and his team are refining the process and that by the end of the year Illumina will launch Molecule as a stand-alone sample-preparation kit. He says that company scientists are now evaluating the kit's performance by sequencing a well-known genome, but he prefers not to say which one.

"We suspect you will be able to uncover a lot more of the genome with 10-kilobase reads versus the [150-base-pair] read length that we currently have," says Smith. He adds that the company plans to increase the fragment length to 20 kilobases. He and his team hope to "develop better molecular-biology tools to allow us to reach into these difficult-to-sequence parts of the genome but also use those tools on well-characterized genomes," he says. The team is also tuning the Illumina software to better distinguish between false and correct reads.

The company's initiative comes at a time of intense commercial and academic activity around long-read sequencing technology and new assembly methods. Finished genomes have taken a back seat, leaving many highly fragmented assemblies that need completing, says Jonas Korfach, chief scientific officer of sequencing manufacturer Pacific Biosciences in Menlo Park, California, whose sequencer generates read lengths of around 5 kilobases.

Korfach agrees that long reads will help to sequence repetitive regions, such as those that characterize many plant genomes, for example. They will also help with the challenge of distinguishing between copies of chromosomes, important in identifying the tiny variants that can affect biological function. Humans are diploid, meaning they have

two copies of each chromosome, but "many organisms, especially plants, have even more copies, which makes resolving all the different chromosomes so much harder", Korfach says.

TOUGH NUTS

Plant sequencing, in particular, will benefit from improvements³. The spruce genome is a "real nightmare", says Stefan Jansson, a plant biologist at the Umeå Plant Science Centre in Sweden. Jansson led a study that generated a draft assembly of the Norway spruce genome (*Picea abies*)⁴. In addition to being the largest genome yet sequenced, it also contains many repeats, and the differences between its chromosomes are larger than in the human genome. "Sequencing diploid spruce is like mixing human and chimpanzee DNA and then trying to assemble them simultaneously," Jansson says.

Many plants have more than two copies of chromosomes. Bread wheat (*Triticum aestivum*), for example, is hexaploid, and sequencing and assembling the six sets of chromosomes to completion has proven extremely difficult. And although some strawberry species are diploid, the commercial strawberry (*Fragaria × ananassa*) is octoploid: it has eight sets of seven chromosomes, four sets from each parent, says Thomas Davis, a plant biologist at the University of New Hampshire in Durham. "Good thing Mendel didn't use octoploid strawberries to try to understand heredity," he says.

Davis and his colleagues have published a draft genome of the diploid woodland strawberry (*Fragaria vesca*), and now want to apply their experience to the octoploid strawberry⁵. Assembling this tough-nut genome will require high-quality reads longer than 500 base

pairs, Davis says. He believes he can succeed, although he does not want to share his methodology just yet. "If anyone cracks that nut, he'll do it," says Kevin Folta, a molecular biologist at the University of Florida in Gainesville, who led the woodland-strawberry project.

The plant world has many other challenging genomes to offer. The onion genome is massive, Folta says, and sugarcane has 12 copies of each chromosome. "Those will take special techniques," he says.

Every platform has benefits and drawbacks, and scientists must weigh the costs, sample-preparation time and sequencing-error rates for each. To sequence the woodland strawberry, for example, the scientists used a combination of three platforms.

But for polyploid genomes, short-read sequencing is almost a waste of time, says Clive Brown, chief technology officer at Oxford Nanopore. "You don't know where your short read comes from, which chromosome it is from," he says. "It's very hard to piece that together." He believes that the problem will be helped by instruments, including those in development in his company, that can generate long reads without the need for special sample preparation or complex assembly. The longer the reads, the easier the assembly, because the overlapping sequences will help researchers to determine which sequence belongs to which chromosome.

Fresh approaches were needed to crack the genome of the oil palm (*Elaeis guineensis*), reported last month in *Nature*⁶. The effort was more than a decade in the making. Oil palm is an important source of food, fuel and jobs in southeast Asia, and the industry is under pressure to produce it sustainably and avoid increased rainforest logging, says study

ILLUMINA

co-leader Ravigadevi Sambanthamurthi, director of the advanced biotechnology and breeding centre at the Malaysian Palm Oil Board in Kajang, which works with the country's oil-palm industry.

With millions of repeats distributed throughout the plant's genome, short reads could fit in many possible spots in the assembled DNA sequence. "It is as if you were assembling a jigsaw puzzle in which most of the pieces are identical," says Robert Martienssen, a geneticist at Cold Spring Harbor Laboratory in New York, who co-led the project with Sambanthamurthi.

Classic sequencing methods were too laborious and expensive for the oil-palm project. So Martienssen suggested applying a technique based on a finding he had made in 1998 — that repeats in plant genomes can be distinguished from genes because the cytosine bases in the repeats usually carry methyl groups. Before fragments are sent to the sequencer, they are treated with enzymes that digest methylated DNA and thereby remove the repeats from the samples.

To complete the oil-palm project, the scientists applied this methylation-filtration technique and then sequenced the DNA regions housing genes. The technique has now been commercialized through Orion Genomics, a company based in St Louis, Missouri, which Martienssen co-founded.

The researchers used a high-throughput sequencer made by 454 Life Sciences, a company owned by Roche and based in Branford, Connecticut, that generates short reads from longer, filtered fragments. In preparing the samples, the researchers used bacteria to amplify DNA in large chunks on bacterial artificial chromosomes — an approach also used in the Human Genome Project — to pin down hard-to-map regions by retaining them next to genes with known positions to act as signposts.

Assembly of the oil-palm genome called

for extensive computational resources, which crashed multiple times, the researchers say. But now, with the genome in hand, they have located a gene that encodes the shell of the palm fruit, knowledge they hope to harness to increase the plant's yield.

Sambanthamurthi says that when the researchers finally pinned down the shell gene, they popped a bottle of champagne, then celebrated with a traditional Malaysian meal served on a banana leaf.

THE LONG AND THE SHORT

Bacterial genomes are smaller and less complex than those of plants and other multicellular organisms, but they, too, have regions that are tough to sequence. For example, *Bordetella pertussis*, which causes whooping cough, has hundreds of insertion sequence elements — stretches of mobile DNA inserted into various locations in the genome — each more than 1 kilobase long. Proponents of long-read technology say that spanning these regions with long reads will deliver sequencing efficiency gains.

Korlach points out that it took a team of more than 50 scientists to solve the bacterium's complete genome⁷. But long-read technology can make assembly of highly repetitive genomes faster and easier, he says. He says that he and scientists in the Netherlands were able to assemble nine whooping-cough bacterial strains in one month.

Whether a read is classified as 'long' or 'short' is in great flux. Two years ago, scientists might have said that a long read was 1 kilobase, Korlach says. "Now [Pacific Biosciences] customers are generating an average of 5,000 bases, with some reads longer than 20,000 bases — and we are working to deliver even more than that." Ultimately, a 'long read' will be as long as is needed to sequence a given genome, he says.

Korlach knows that some scientists say his

company's sequencers are pricey, but he says that the newer versions have seen a significant drop in price and an increase in throughput. He says that the question of price is often raised "in the context of pure cost per sequenced base". And, he adds, if a certain sequencing technology is the only one that will work to solve a medically important question, "then

there is no price tag that can be put on this medically relevant information".

Last year, researchers collaborating with Pacific Biosciences used the company's sequencer to distinguish the repetitive genomic region involved in fragile X syndrome, a developmental disorder that is caused by repeats in a particular region on the X chromosome, and that worsens in severity with higher numbers of repeats⁸.

As technology developers get closer to instruments that produce longer reads, scientists will need longer DNA fragments at the beginning of their sequencing experiments. Several companies focus on helping researchers to prepare DNA fragments for sequencing. For example, Sage Science, based in Beverly, Massachusetts, has a platform that uses pulsed-field electrophoresis to select and sort DNA fragments of sizes ranging from 50 base pairs to 50,000 base pairs. In May, the company began marketing its instrument to accompany the Pacific Biosciences sequencing platform.

Steve Siembieda, who is responsible for business development at Advanced Analytical Technologies in Ames, Iowa, says that his company sees the trend towards longer reads as writing on the wall. The company has licensed patents from Iowa State University, also in Ames, to develop an instrument to assess the integrity, fragment length and concentration of DNA samples.

With this instrument, an electric field is applied to a tiny amount of DNA so that it is pulled into a long, hair-thin capillary tube containing a gel with a fluorescent dye that binds to DNA molecules. As the DNA fragments move through the gel, they separate according to size. "Small molecules move fast, big molecules move slowly," Siembieda says. As the molecules pass by a window in the capillary, a flash of light excites the dye and a camera records the DNA fragment length (see 'Bits and pieces').

The instrument's readout tells scientists whether the size distribution of the DNA fragments is in the range needed for a given sequencing platform and whether the DNA



Titus Brown likens high-throughput sequencing to piecing together 1,000 shredded copies of a novel.



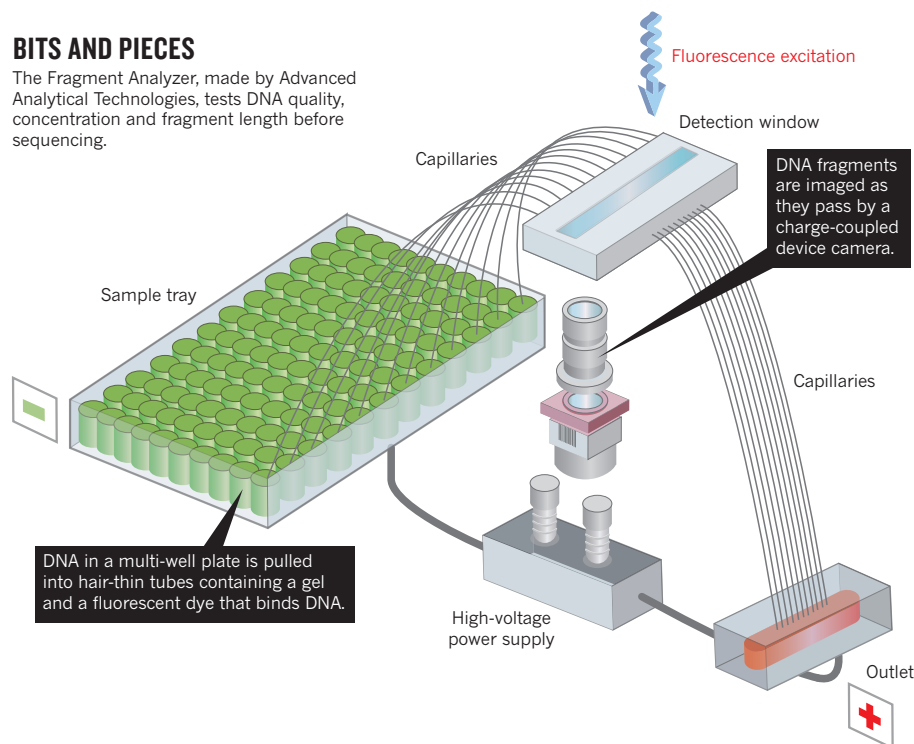
Oil palm has a complex and repeat-riddled genome that took more than ten years to sequence.

MICHIGAN STATE UNIV.

ROBERT MARTIENSSEN/CSHL

BITS AND PIECES

The Fragment Analyzer, made by Advanced Analytical Technologies, tests DNA quality, concentration and fragment length before sequencing.



has the right concentration. Siembieda says that skipping these measurements can be the wrong experimental shortcut — if the concentration or fragment size is off, “a sequencer may run for nine days, it will cost them thousands of dollars, plus all the time wasted to not make sure they have the appropriate material”. The instrument will possibly be used in developing the Molecule process, but negotiations between the two companies are still under way.

Technology development at Advanced Analytical is focusing increasingly on long DNA fragments, which are challenging to resolve, Siembieda says. One solution is to customize gels for different applications. At present, the company’s instrument can resolve lengths of up to 20 kilobases and the company is working on resolving longer fragments, he says.

ASSEMBLY REQUIRED

Scientists are applying many methods and tricks to create longer fragments. “Unfortunately, these technology tricks create erroneous data at points, so now you’re stuck with some data that may be wrong,” says Michigan State’s Titus Brown. He was part of an effort, published in April⁹, to sequence the lamprey (*Petromyzon marinus*) genome, one-third of which is covered by long repeats. Obtaining an assembly even with Sanger sequencing, which generates 1-kilobase reads, was difficult, he says. In addition, the lamprey genome has many GC-rich regions. The team used several types of software to assemble the complete DNA sequence.

In July, scientists published a comparison of software programs used to assemble sequence reads¹⁰. The researchers found that different assemblers give different results — even when fed the same sequence reads. Brown says that

biologists should never forget that assemblies are not certainties. Every new sequencing technology — from how the DNA sample is prepared to the sequencing chemistry — has the potential for error and bias. “If you have short reads, or bad biology, you’re going to have a very hard time getting a good assembly, even in theory,” he says.

Ideally, a genome assembly should deliver end-to-end chromosomal sequences, says Shendure. What worries him more than the discordance among assemblers in the comparison study is that all of the assemblies were very fragmented. “That’s not a fault of the assemblers, that’s a fault of the data that we’re putting into the assemblers and the fact that we’re not capturing contiguity at these longer scales,” he says. “The algorithms can only make do with the ingredients that they are provided by the technologies.”

Brown is hopeful about the potential impact of longer-read technology. If Pacific Biosciences or Oxford Nanopore “deliver on many inexpensive long reads — more than 10 kilobases, I’d say — regardless of accuracy, you would end up revolutionizing the genome-assembly field, because it would give you so much more information to work with,” he says. However, he adds, assembly software has to be compatible with each sequencing method. “So we’re continually playing catch up, where new sequencing technologies lead to new sequence-analysis approaches a year or three later.”

Eichler agrees that sequencing and assembly must continue to improve. Read lengths longer than 200 kilobases and with 99.9% accuracy rates will be needed to unpick repeats and other complications, he says. He says that the Pacific Biosciences instrument and what he

knows of Molecule “fall short of this, but are on the right track”. All read-length requirements depend on the genome and complexity, he adds. For many bacterial genomes, current read lengths and accuracy are already sufficient, he says.

THE NEXT TELESCOPE

Oxford Nanopore plans to launch its new sequencing technology in the near future, but no date has been given. The technology expands on findings by researchers at Harvard University in Cambridge, Massachusetts, the University of Oxford, UK, and the University of California in Santa Cruz to harness the abilities of pore-forming proteins for DNA-sequencing devices.

One of the weaknesses of current high-throughput sequencing technology is amplification chemistry, says Oxford Nanopore’s Clive Brown. Although DNA is made up of four bases, it is possible that more than those canonical four — such as bases that are methylated — should be detected, he says.

And in some sections of genomes, bases are naturally missing. But current sequencers do not capture such variations — instead, says Brown, they produce the equivalent of a four-colour photocopy of a picture with many more colours. “A lot of the detail is lost immediately, as soon as you make a four-colour copy,” he says. Ideally, “you take a chromosome and run it through the sequencer. You can’t quite do that yet.” He, too, says that the next crucial phase of sequencing technology will be about long reads.

Brown says that to his mind, sequencers are just opening the door to characterizing the genome. People can get “very cosy about what they can see”, with scientific instruments, he says. He likens today’s sequencers to the first telescopes, which offered a view of the Moon’s features and exploration of the visible spectrum. “It gets you a long way, you can count the stars, see the planets,” he says. But the telescope does not show other celestial phenomena — such as dark matter or galactic movement.

Like astronomers with their telescopes, genome researchers will get a clearer picture of the genome as the sequencing technologies improve, he says. And, inspired by that picture, they will strive to see even more. ■

Vivien Marx is technology editor for *Nature* and *Nature Methods*.

- Shendure, J. & Aiden, E. L. *Nature Biotechnol.* **30**, 1084–1094 (2012).
- Kirby, A. et al. *Nature Genet.* **45**, 299–303 (2013).
- Schatz, M. C., Witkowski, J. & McCombie, W. R. *Genome Biol.* **13**, 243 (2012).
- Nystedt, B. et al. *Nature* **497**, 579–584 (2013).
- Shulaev, V. et al. *Nature Genet.* **43**, 109–116 (2011).
- Singh, R. et al. *Nature* **500**, 335–339 (2013).
- Parkhill, J. et al. *Nature Genet.* **35**, 32–40 (2003).
- Loomis, E. W. et al. *Genome Res.* **23**, 121–128 (2013).
- Smith, J. J. et al. *Nature Genet.* **45**, 415–421 (2013).
- Bradnam, K. R. et al. *GigaScience* **2**, 10 (2013).

CAREERS

RESEARCH NASA launches programme to study effects of spaceflight **p.271**

FUNDING MacArthur 'genius grant' to rise to US\$625,000 this year **p.271**

NATUREJOBS For the latest career listings and advice www.naturejobs.com

MARK AIRS/GETTY



ADMINISTRATION

A watchful eye on grant funding

Researchers disillusioned with the lab and eager to engage their soft skills can find promise in scientific administration.

BY PAUL SMAGLIK

Most scientists worry about how to secure grants. But a select few make a career out of managing those grants to ensure that the money is well spent. This is the job of the scientific administrator.

Broadly speaking, scientific administration involves the awarding, spending and tracking of funding at the grant, programme or policy level. Grant-level administrators assign or manage funds given to individual investigators. Programme administrators look after the needs of multi-investigator or multi-institution projects. And policy administrators oversee funding for entire departments, institutions or even university systems.

Jobs at all levels exist at universities, federal agencies and foundations, and scientific administrators often flip between these worlds at different stages of their careers — perhaps awarding grants at institutions such as the US National Institutes of Health (NIH) or UK biomedical charity the Wellcome Trust at one time, and managing funds at universities at another.

Scientific administrators have a crucial role in the research process, says Ginny Cox Delaney, an organizational consultant in the Oakland Office of the President of the University of California system, which administers ten research universities and five medical centres. “For me, science administration means the value-added role of advancing an organization’s research goal, besides doing the actual science,” she says.

HUMBLE BEGINNINGS

Almost no one sets out to be a scientific administrator. Instead, they realize at some point that they would rather support the scientific process away from the bench than at it.

When Elizabeth Prescott started her PhD, she had trouble visualizing where she would be in five years. After graduating, she deliberately chose a postdoc in the lab of a young investigator, at Yale University in New Haven, Connecticut. “I got a first-hand view of what it looked like to be a junior faculty member,” says Prescott, noting the long hours the job entailed. “I don’t think I love this enough,” she thought.

She was considering leaving her fellowship and searching for a job in industry when the director of the postdoctoral-affairs office at Yale told her about an upcoming position. The university was establishing numerous core facilities in fields including DNA sequencing and high-performance computing, and the ►

► provost's office needed someone to act as a liaison. Apart from a requirement to monitor how effectively the facilities served the needs of the university's scientists, the position was not well defined. So when Prescott got the job, she had a bit of a baptism of fire. "I learned about non-profit accounting; I learned about grant compliance," she says. She also learned to evaluate investigators' needs, and then sort them into different priorities.

In doing so, she became a link between the investigator, the granting agency and other parts of the university. These days, Prescott works as a foundation relations adviser at the Fred Hutchinson Cancer Research Center in Seattle, Washington, where she also acts as a liaison — this time between the centre and the companies and foundations that want to donate to it. Having scientific knowledge gives her credentials with all sides, she says. "It helps to have an understanding, to know what it is like to work in the lab. You don't want to be perceived as a bean counter or a barrier."

'Liaison' is one of many roles of scientific administrators. 'Head of logistics' is another. As a scientific review officer for the NIH in Bethesda, Maryland, Shiv Prasad recruits qualified scientists three times a year to review grant applications. To say that organizational skills are essential in his work would be an understatement, he notes. "When you have 20 or more scientists coming to a study section from around the world, you want to make sure things run like clockwork. That means getting them their applications to review on time, giving them enough notice to make travel plans and making sure rooms are booked."

It takes a certain kind of person to excel in administration — someone who enjoys repeatedly arranging and following up on meetings, and who understands how something as mundane as the wording on a form can affect the application experience, says Jonathan Best, grant operations manager at the Wellcome Trust in London. "I enjoy taking a process and making it work as efficiently as it can," he says. "It takes me to a whole new level of geekdom and challenges me in a totally different way to my previous scientific positions." Best provides help at every step, from application, making sure that the applicant has filed the correct information, to evaluation — seeing that members of the review committee get the applications in time. Currently his office is updating forms and revising deadlines to make the process less onerous for the applicant.

Administering grants also involves monitoring their success and implementation — activities that require attention to detail and a willingness to police recipients. After a grant has been awarded, Best helps to monitor how effective it was in advancing the investigator's field. He examines metrics such as publications and citations, as well as less tangible outcomes, including whether recipients have led effectively in their fields rather than following trends.

An ability to deal with deadlines is essential, says Diane McFadden, associate director of the Northeast Biodefense Center at Columbia University in New York — an NIH centre of excellence that involves 28 investigators and 3 postdocs at 12 institutions. With so many different components to manage, deadlines "are constantly hitting you", she says. And attention to detail is paramount: if someone does not fill out a form correctly and McFadden misses the error, funds or equipment could be delayed, slowing down projects.

All these things can be learned on the job, as can an understanding of how the funding and follow-up processes work. What cannot be taught, says Prasad, is a passion for science. Keeping up with the latest advances, helping to shepherd promising ideas through funding and seeing the research turn into successful publications and applications are the most satisfying parts of the job, he says.

ADVANCED ADMINISTRATION

As administrators gain seniority, they tend to take on broader responsibilities. High-level scientific administrators need to be able to see the big picture, says Carl Rhodes, a senior scientific officer at the Howard Hughes Medical Institute (HHMI) in Chevy Chase, Maryland. He helps the institution to select and review new investigators, who are funded by the HHMI but based at universities. Until recently,



"Science administration means the value-added role of advancing an organization's research goal."

Ginny Cox Delaney

he also helped to plan and run seven scientific meetings a year. "You need to decide what the agenda is and if it makes sense," he says. "You need to decide how to advertise it, what is the most logical progression for the programme."

Administrators often learn to deal with increasing complexity as they move from monitoring and giving grants to single investigators, to focusing on whole programmes, departments or agencies.

Rhodes started his teaching and administration career at Stanford University in California, where he focused on "things other faculty didn't want to do", he says, such as coordinating teaching assistants, refining the curriculum and dealing with the occasional disciplinary problem. He viewed himself as a service provider. "I made myself useful," he says.

In that role, Rhodes developed key skills and insights that would serve him well in a later job as a grants officer at the NIH, where he managed a review panel that evaluated

ROBERT DURELL/COPE

joint PhD–medical doctorate programmes. It was also useful later on: sifting through 1,000 graduate-school applications at a time at Stanford was at least as difficult as triaging hundreds of new-investigator applications at the HHMI, he says. He now oversees scientific advisory panels that evaluate the strengths and weaknesses of each investigator's application and the contributions that they would make to their fields. The review officer combines the panel's comments into a single document — and all the documents go through Rhodes for final approval.

The ability to understand, create and evaluate budgets is essential to scientific administrators — especially as they move up the career ladder. McFadden has become adept at budgeting to make sure that her investigators' needs are met. "I've learned a tremendous amount about building a budget and how to do that with fairness," she says. Some projects deserve extra attention — and providing that, without belittling or alienating other projects in the consortium, can be a delicate process.

Having concrete goals — while keeping in mind a broader picture — is another hallmark of success in upper policy-level administration, says Sue Rosser, provost and vice-president for academic affairs at San Francisco State University in California. "The higher up you get in administration, the more emphasis there is on having a goal and getting things done and on time," she adds. Rosser works to make sure that the myriad meetings that populate her days are not empty exercises, but produce something tangible. "I like to have agendas, outcomes, follow-ups, results," she says. For example, last year her institution decided not to renew funding for a multi-year, multimillion-dollar project that did not fit the university's mission. More than a year before the programme was due to end, Rosser and her team began to have meetings about the closure, with detailed timelines to complete the programme's activities and ensure a smooth transition to an interim grantee. Rosser, like Rhodes, has a service mindset — but she is not so closely connected to the people she helps.

"I am trying to help the faculty under me succeed," she says. "And I am not even directly doing that, I am helping deans help chairs help faculty."

A WAY IN

Most people who move from a research career to scientific administration do so when they realize that lab work does not meet their life and career goals. There is no obvious, well-worn career path that reliably culminates in an administrative post, but there are ways to get a foothold — and to find out whether it is the right route. When Cox Delaney recognized that she did not have "the golden hands" needed to succeed in the lab, she got a public-policy fellowship from the American

Association for the Advancement of Science in Washington DC. That had her working on science-policy cooperation between the United States and western Europe, which helped her to develop her interpersonal communication skills. A subsequent job at the Alfred P. Sloan Foundation, a non-profit granting organization based in New York, taught her about scientific funding.

Cox Delaney says that graduate students and postdocs who think they might be interested in administration can gather experience by running symposia, planning



"You need to decide what is the most logical progression for the programme."

Carl Rhodes

talks, dealing with caterers or booking speakers and venues for conferences. "There are a lot of opportunities to step up into leadership roles," she says. "That will give you a sense of whether you like the organizing piece."

Even pulling authors together for a paper or coordinating a simple event such as a journal club can help, if the organizers can observe the people they are working with and find out what motivates them, or can build new skills, says Cox Delaney. She is currently working with all the University of California campuses to find ways to share and save on administrative costs, so that they can pass the savings on to research and education.

Advancing in administration often means nurturing a skill set that goes well beyond research. Cox Delaney puts people who go into scientific administration into two categories: people with a strong understanding of science and good interpersonal skills; and people adept at accounting and funding. Administrators who have both sets of traits are relatively rare — and they are the ones who tend to rise to the highest levels, she says.

Many universities — especially publicly funded, research-based ones — recruit their leading managers from a pool of scientists, who tend to be detail-oriented and adept at handling complexity, and researchers with a particular appetite and aptitude for managing budgets and people will have multiple career options in administration. The path to broader responsibilities, or even a university presidency, could begin with shepherding a single grant. ■

Paul Smaglik is a freelance writer based in Milwaukee, Wisconsin.

RESEARCH

Biology in space

NASA is launching an open-ended research programme to investigate how human and other tissue reacts to time spent in space. The geneLAB project will begin seeking grant applications by autumn 2014, says D. Marshall Porterfield, director of space life and physical sciences research at NASA in Washington DC. It will award 'innovation exploration' grants of US\$100,000 for one year; full grants will be for up to 5 years and worth a maximum of \$500,000. The agency wants to send organisms including fruitflies and roundworms to the International Space Station to learn how spaceflight affects living tissue at the biomolecular and genetic level. Future grant recipients would also study bone loss and examine tissue from crew members to look for changes to their DNA that occurred while in space and after returning to Earth.

GENDER

Mothers' careers stalled

Attitudes about motherhood can impede women's career aspirations, even at companies that purport to have family-friendly policies, a study suggests (C. Herman *et al. Gender Work Organ.* 20, 467–478; 2013). Women working in science, engineering and technology at multinational corporations in the Netherlands, France and Italy adopted potentially career-damaging tactics including, for example, avoiding big projects and disguising the need to leave early or come in late because of childcare obligations, the study found. Firms must take stock of how attitudes stymie women who are looking to advance, says study co-author Anne Laure Humbert, a gender researcher at the European Institute for Gender Equality in Vilnius.

FUNDING

Genius grant grows

Awards for the MacArthur Fellows Program, known as genius grants, will this year rise from US\$500,000 to \$625,000. The John D. and Catherine T. MacArthur Foundation in Chicago, Illinois, makes unrestricted 5-year grants to recipients chosen for their creativity, innovation and potential to shape the future. Spokesman Andrew Solomon says that the increase is partly a response to inflation and is the programme's fourth rise since it began in 1981. The 2013 fellows will be announced on 25 September.

LACUNAE

The rhythm of life.

BY WILLIAM MEIKLE

What Frank Green did wasn't difficult. All it took was a large amount of computing power and many weeks of meticulous research in musty book stacks. By mid-July he felt ready to test his findings.

He wasn't sure quite what he'd found, but the pattern was unmistakable. For most of recorded history, people have been disappearing without trace, often right in front of astonished friends and acquaintances.

The pair of professors tasked with reviewing Frank's work proved sceptical in the extreme, even after he showed them the simulation — the one that tracked the lacunae over time and space, the one that then predicted where and when these holes in space and time might occur. But two days later Frank was in Alberta, standing outside his tent where he'd bivouacked halfway up a deer trail at nearly 6,000 feet, still stunned that they had said yes.

"Trust us son," Professor Wagner had said. "We've had stranger requests. Just bring back good hard data. That's what the bean-counters like."

And there lay the problem in a nutshell.

How do I collect data on the absence of something?

It wouldn't be for want of trying. He was armed with cameras, EMF meters and as much computing power as he was able to carry around with him. Now all he had to do was wait, and trust in his theory.

As he lay in his tent that night he pondered the wisdom of even being here. Yes, it might prove his theory. But there was also a chance, a very real chance, that he too would become one of the *disappeared*, just another name on a list of unsolved vanishings. It was a chance he was willing to take, for if he was right, he was on the verge of solving some of the great mysteries, from the missing Roman legion all the way to the *Marie Celeste*. Fortune and glory might wait just around the corner.

As night fell he daydreamed; of book deals and chat shows, of front-page headlines and TV appearances. He found that he was too energized to sleep and eventually, after an hour of

tossing and turning in his sleeping bag, he got up and checked over some of the cases that had brought him to this place. He spent the next few hours studying the apocryphal tales surrounding the Flannan lighthouse in



Scotland, and the supposed disappearance of three of the keepers in 1900 — another dot on his map.

He'd worked for many long hours on the map, approaching it from many angles, looking for a pattern, a rhythm that might correlate the disappearances with some physical aspect that could be measured by his instruments. He'd cross-referenced his pattern with changes in the magnetic field, with sunspot activity, with lunar cycles, even with daily fluctuations in the stock market. He only hit the jackpot when he took into account the orbit around the Sun, and the long variations caused by the precession of the equinoxes. He found that there was a certain region of space that, whenever Earth passed through it, caused the now famous disappearances. The scale of the vanishing seemed to depend on how close the planet brushed against this spatial anomaly. And it was that anomaly that Frank hoped to measure over the coming day.

He finally fell asleep with dreams of

fortune and glory, and woke at dawn to a sparkling clear morning, and the sound of his meters clicking.

It was happening. It was really happening.

The air tingled, as if suddenly supercharged with static, and the hairs Frank's arms and neck all stood up at once. Reality seemed to slide and slip, as if the very fabric of nature was melting and becoming blurred. Frank struggled to focus on his equipment, but that too seemed to blur and fade, so much so that no meter readings were possible.

Just bring back good hard data. That's what the bean-counters like.

Frank wailed. His dream of glory was fading fast, and without data all would be for nothing. He scrambled among the equipment, desperate to reach his laptop. He was so preoccupied that he failed to notice that the world outside his tent had gone.

The laptop went away just as he put a hand on it. Blue static ran across his skin and crackled like damp sticks in a fire.

Frank blinked. In that time, he too went away.

He floated, in darkness filled with swirling fog containing occasional flashes of blue lightning. There was no sound, but there was a profound feeling of being at rest, of being *cod-*

dled by the thick fog.

There was no panic, and Frank's curiosity overcame any sense of fear. He examined the timing of the lightning, hoping once again to discern a pattern, a rhythm that he might identify and use to find a way out of his predicament.

The fog started to part and clear. A blue haze hung ahead of him, and Frank drifted towards it, carried by an unseen tide. He was eagerly awaiting what would come next.

Right up until the moment when the blue haze parted and a vast mouth filled with banks of razor teeth opened up.

He realized his main mistake even as the jaws clamped shut at his waist.

There was one rhythm common throughout nature that he'd failed to take into account.

Feeding time. ■

William Meikle is a Scottish writer resident in Canada with 10 novels published in the genre press and more than 200 short-story credits in 13 countries.

JACEY